The Low-Temperature Tectonic Evolution of the Western Tian Shan (Kazakhstan, Kyrgyzstan, Uzbekistan, Tajikistan)

Gilby Jepson

November 30, 2018

Thesis submitted for the degree of

Doctor of Philosophy

in

Earth Sciences

at The University of Adelaide

Faculty of Sciences, School of Physical Sciences

Department of Earth Sciences

THE UNIVERSITY
of ADELAIDE

Contents

List of Tables

List of Figures

Signed Statement

I certify that this work contains no material which has been accepted for the award of any other degree or diploma in my name in any university or other tertiary institution and, to the best of my knowledge and belief, contains no material previously published or written by another person, except where due reference has been made in the text. In addition, I certify that no part of this work will, in the future, be used in a submission in my name for any other degree or diploma in any university or other tertiary institution without the prior approval of the University of Adelaide and where applicable, any partner institution responsible for the joint award of this degree.

I give consent to this copy of my thesis, when deposited in the University Library, being made available for loan and photocopying, subject to the provisions of the Copyright Act 1968.

I also give permission for the digital version of my thesis to be made available on the web, via the University's digital research repository, the Library Search and also through web search engines, unless permission has been granted by the University to restrict access for a period of time.

Signed: ..... Date: .....

Acknowledgements

In late 2014, sitting in a cold, dimly lit office in the subterranean halls of the Mawson Building (the University of Adelaide), pouring over a map of Central Asia, the offer of a PhD was put forward to me. With little understanding of the regions that the project would focus, and even less on the techniques being employed, I dived in. Nestled around sweeping ranges and expansive deserts, Central Asia is a melting pot of cultures, religions, traditions, and geopolitics. Working in these remote regions has proved to be enlightening beyond measure, forever shaping my personal heuristics. Three and a half years later, after three field seasons covering Uzbekistan, Kazakhstan, Kyrgyzstan, and Xinjiang, and I am still as enamoured with Central Asia as when I started.

I must first of all thank Stijn Glorie for introducing me to the wonders of Central Asia. None of this would have been possible without Stijn taking a chance on a very naïve student. Stijn provided immense assistance in developing my understanding in both thermochronology and tectonics, as well as greatly improving my scientific writing and critical thinking. Supporting me as a supervisor and a mentor, Stijn pushed me and inspired me to make the most of my brief time in graduate research.

Numerous colleagues at the University of Adelaide provided valuable discussion, insights, and support throughout this project. My thanks go to Morgan Blades, Ben Wade, and Sarah Gilbert for their endless and gracious laboratory and analysis support, and to Derrick Hasterok for fielding any and all questions regarding geophysics and software. A special thank you goes to my long time primary supervisor and now secondary supervisor Alan Collins. Alan always pushed me to think about my project in a broader, more regional context, encouraging discussion and collaboration with researchers outside my sphere. Alan fostered a positive and enjoyable research environment, with regular TRaX meetings and

lunches that provided both a formal and informal space to practise talks and discuss ideas.

I would like to thank Jack Gillespie and Sheree Armistead, the value of our regular field excursions, numerous morning coffees, and cheeky evening drinks can not be understated. Such a reliable level of camaraderie became an integral part of this research project, and a part that I am forever grateful blossomed.

Thank you to the Australian thermochronology community for welcoming and supporting me throughout this project; my research benefited greatly from the both the technical AHe and ZHe assistance of Martin Danišík and Noreen Evans, while Andrew Gleadow and Barry Kohn always had time for thoughtful discussion. None of this would have been possible without the assistance of researchers and field contacts in Europe, Russia and Central Asia; Johan De Grave, Andrei Khudoley, Sergey Malychev, Fedor Zhimulev, Dmitry Gurevich, Yunus Mamadjanov, Farid Divaev, Vladimir Chirikin, and Dongfang Song provided logistics, feedback, assistance, and discussion in a truly beautiful part of the world. In particular I would like to thank Dmitry Konopelko, not only did Dmitry give insightful and valuable input into the papers that comprise this thesis, but he also became a major, positive personal influence.

This study was supported by an Australian Research Council Discovery grant (DP150101730). D. Konopelko was supported by the Ministry of Education and Science of the Russian Federation (project No 14.Y26.31.0018) and by travel grant (mer. 6-2018) from Saint Petersburg State University.

Undertaking this project was a labour of love. One that I have been truly privileged to delve into and freely explore. Ultimately, this thesis represents the small interactions and experiences that cumulate to drastically shape who we are today.

Abstract

The evolution of intracontinental mountain ranges represent a unique challenge in our understanding of the Earth's history. One of the largest of these intracontintal mountain ranges on Earth is the Tian Shan in Central Asia. The crustal architecture of the Tian Shan formed during the closure of the Palaeo-Asian Ocean in the Palaeozoic and underwent multiple reactivations in response to distant tectonic events at the Eurasian plate margin, to give rise to the modern expression of the Tian Shan we see today. Most of the previous thermochronological studies in the Tian Shan focused on the core of the mountain range, deciphering a punctuated tectonic history throughout the Mesozoic, with a dominant Cenozoic overprint as a result of the India-Eurasia collision. However, little work has been done on the eastern and western extents of the Tian Shan. These regions are characterised by low relief and record less Cenozoic overprint, providing opportunity to better constrain the Mesozoic thermo-tectonic history of the Tian Shan.

In this project, we used multiple thermochronometers (apatite uranium-lead, zircon (U-Th-Sm)/He), zircon fission track, apatite fission track, and apatite (U-Th-Sm)/He) on >100 basement samples taken along the western-most extent of the Tian Shan. More specifically, samples from the Karatau–Talas range in the north (Kazakhstan and Uzebkistan), the Chaktal–Kurama range (Uzbekistan and Tajikistan) and the Kyzylkum–Nurata Segment (Uzbekistan and Tajikistan) in the middle, and the Garm region in the south, were analysed to decipher key periods of deformation and mountain building in the Tian Shan. Initially, the western Tian Shan underwent a period of Triassic–early Jurassic fast-cooling and exhumation interpreted as a response to the collision of the Qiangtang block with the Eurasian margin. Subsequently a period of slow-cooling and denudation during the late Jurassic–Cretaceous was recorded, as the western margin of the Tian Shan experienced a

hiatus in reactivation. However, the major suture zones in the western Tian Shan still preserve a signal of late Jurassic–Cretaceous fast-cooling and reactivation, as a possible response to extensional tectonics on the Eurasian margin. Finally, much of the Mesozoic Tian Shan is overprinted by the distal effects of the India-Eurasia collision in the Cenzoic. The India-Eurasia collision, the latest and possibly the largest of the Gondwanan fragments to collide with the Eurasian continent, generated a thermal overprint along faults and generated most of the topography that we see today.

Using multiple middle to low temperature thermochronometers, this study attempted to unpack the complex and convoluted evolution of the world's largest intracontinental mountain range. Showing that it is possible to track the evolution, both spatially and temporally, of such a vast orogen from its ancestral foundation through to the more modern controls of continental growth. Furthermore, it has been possible to apply constraints and unpack the tectonic regimes that influence the growth of an intracontinental mountain range, providing an analogue for the definition of other intracontinetal tectonic settings throughout the globe.

Chapter 1

Introduction

1.1 Thesis Motivation

Understanding the tectonic evolution of our planet is one of the most fundamental questions in earth sciences. Our evolution on the planet Earth is influenced by interactions between tectonic plates, from controlling the macronutrient input to start complex life (e.g. Reinhard et al. 2017), to playing a major influence in our climate (e.g. Molnar & England 1990), even influencing the spread of trade, religion, and society (e.g. Frankopan 2015). The answer to these tectonic questions is stored in rocks that were formed over billions of years ago, that now comprise the present-day mountain ranges. Mountain ranges are formed in response to the current and past tectonic events, by analysing how rocks are exhumed in these ranges we are able to glean a better understanding regarding the tectonic evolution of our planet.

The classical view of the plate tectonic paradigm implies that the majority of mountain building occurs at the margins of tectonic plates (e.g. Molnar & Tapponnier 1975). Major ranges such as the Andes, and the Himalaya form along the boundaries between major tectonic plates. However, the existence of vast mountain ranges far from any modern plate boundary, such as the Tian Shan in Central Asia, raises questions on how these intracontinental systems fit within the tectonic paradigm. Intracontinental mountain ranges are often complex, as they developed during multiple phases of deformation in response to far-field stress propagated from the plate margins into the continental interior (e.g. Hendrix et al. 1992). The aim of this study is to elucidate the tectonic evolution of these intracontinental

systems by focusing on the growth of one of the world's largest mountain ranges, the Tian Shan within Central Asia. In contrast to the extensively studied central and eastern parts of the Tian Shan (e.g. Sobel, Oskin, Burbank & Mikolaichuk 2006, Jolivet et al. 2010, Glorie et al. 2011, De Grave et al. 2013, Macaulay et al. 2014, Nachtergaele et al. 2017, Bande et al. 2017a, De Pelsmaeker et al. 2018), constraints on the thermo-tectonic history of its westernmost extent remains elusive.

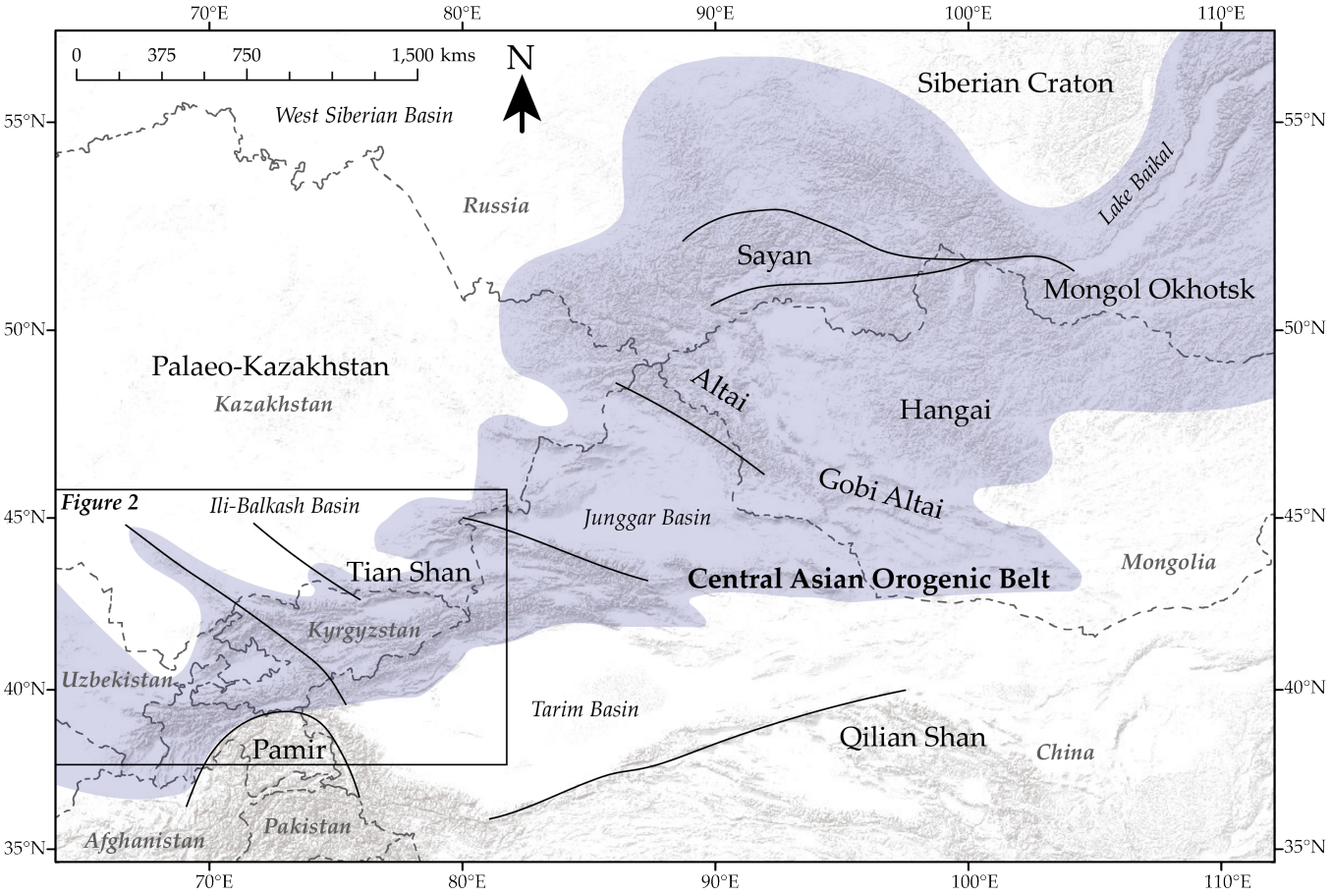

Figure 1.1: A topographic map of Central Asia. The Central Asian Orogenic Belt (CAOB) is outlined with blue shading and its various components are labelled. Black lines represent major regional faults.

1.2 Geological Background

The Tian Shan forms part of the world's largest intracontinental orogenic system: the Central Asian Orogenic Belt (CAOB, e.g. Cawood et al. 2009, Xiao et al. 2013). The CAOB stretches for over 5000 km, from Uzbekistan in the south-west, to the Baikal rift-zone at the Siberian Craton in the north-east (Figure 1.1). Abundant evidence for active tectonics (such as seismic data) underscores the CAOB as one of the world's most active intracontinental

orogenic systems (e.g. Hamburger et al. 1992, Yin & Harrison 2000, De Grave et al. 2007). The CAOB development initiated in the Neoproterozoic and grew during the Palaeozoic via the subsequent accretion of island arcs, ophiolites, oceanic islands, microcontinents, and accretionary wedges grew in a comparable style to the current, present-day evolution of the circum-Pacific (e.g. Windley et al. 2007, Xiao et al. 2013). The growth of this orogenic collage formed the structural architecture that the present-day mountain ranges are built upon, as well as generating numerous economic mineral deposits (e.g. Seltmann et al. 2011, Goldfarb et al. 2014, Kempe et al. 2016).

Of the mountain ranges that comprise the CAOB, the Tian Shan is one of the most prominent. Lying to the north of the Pamir, Himalayas, Tibet, and the Tarim Basin, the Tian Shan runs 2500 km from Uzebkistan in the west to Mongolia in the east, in excess of 400 km at its widest point, and hosting numerous peaks over 7000 m (Figure 1.2, e.g. Brookfield 2000, Sobel, Chen & Heermance 2006). While the Eurasian continent formed due to continental accretion during the Palaeozoic, much of the present-day topography is defined by the Cenozoic India-Eurasia collision, and the ongoing indentation associated with that collision (Molnar & Tapponnier 1975, 1977, Tapponnier & Molnar 1979, Peltzer & Tapponnier 1988). The India-Eurasia collision has been a major control on tectonics of Central Asia, generating lateral extrusion, crustal thickening, and intracontinental reactivation (De Grave et al. 2007). Not only influencing the tectonics, the impact of the India-Eurasia collision can be seen in Central Asia's climatic evolution. However, despite being the current and most obvious driver of intracontinental tectonics in the world, the India-Eurasia collision is far from the only tectonic process to deform the Eurasian interior.

The continental amalgamation of the northern segment of Eurasia was largely completed by the end of the Palaeozoic as a response to the closure of the Palaeo-Asian Ocean (PAO, e.g. Xiao et al. 2003, Windley et al. 2007). The PAO closure caused the ongoing continental accretion of Eurasia to jump southward in the Mesozoic and the Eurasian continent experienced intracontinental deformation controlled by the progressive closure of the Tethys Ocean that separated Eurasia and Gondwana. From the Late Triassic to the Early Cretaceous the southern margin of the newly amalgamated Eurasian continent experienced renewed collision of various island-arcs, terranes, and micro-continents which had rifted from Gondwana and

progressively accreted to Eurasia (Otto 1997, Garzanti 1999, Yin & Harrison 2000, De Grave et al. 2007). The continental collisions generated extensive deformation within the Central Asian interior, and in particular, the Tian Shan.

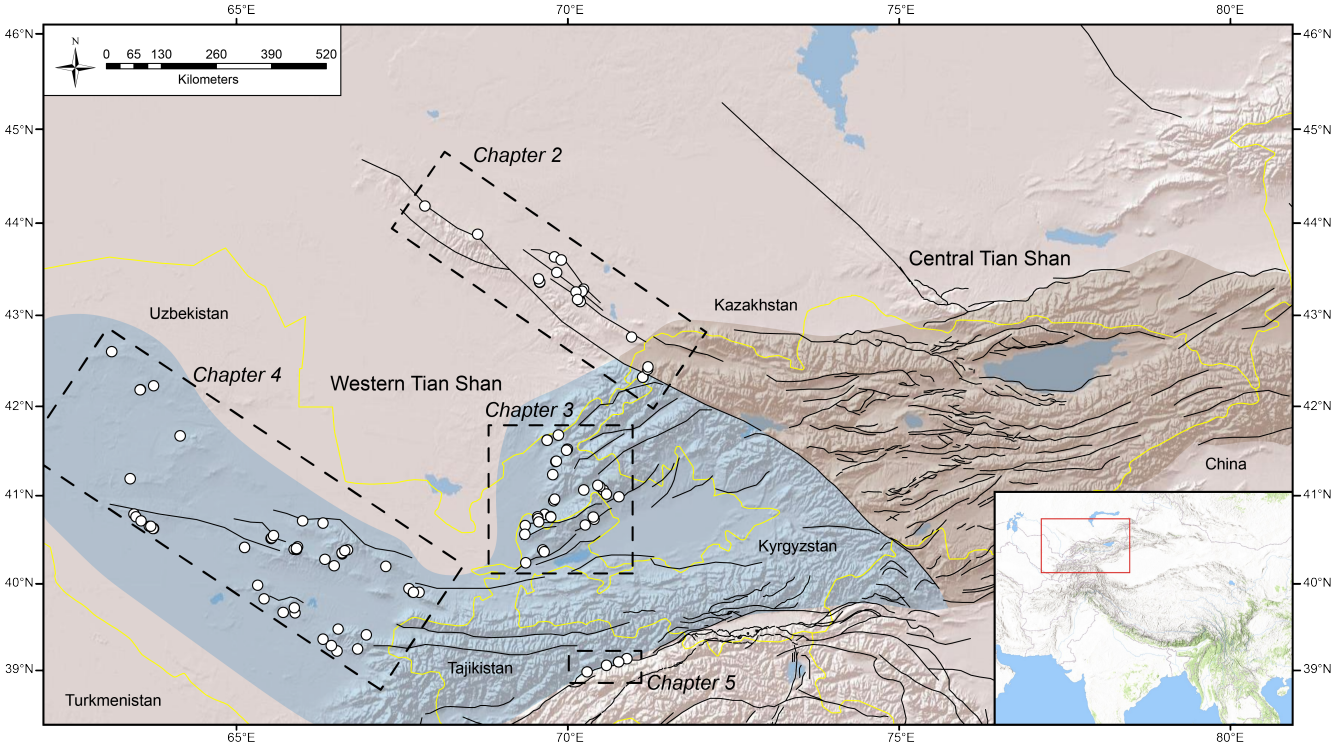

Figure 1.2: A topographic map of the Tian Shan outlining the divisions of the western, central, and eastern Tian Shan. White circles represent locations of samples taken in this study, while black lines represent regional faults. The samples are divided into the four study areas which comprise this thesis.

There have been numerous previous studies into the intracontinental orogen of the Tian Shan, using thermochronology to unpack the various periods of deformation and reactivation that spanned the Phanerozoic. Many of these studies have used low-temperature thermochronology in the central, eastern, and southern regions of the Tian Shan, identifying extensive Cenozoic reactivation along the fault zones, with preserved Mesozoic reactivation in uplifted cores and from samples taken from more northerly regions (e.g. Hendrix et al. 1992, Sobel & Dumitru 1997, Sobel & Arnaud 2000, Dumitru et al. 2001, De Grave et al. 2007, Glorie et al. 2010, Jolivet et al. 2010, Macaulay et al. 2014, Glorie & De Grave 2016). However, limited work has been done on the western-most margin of the Tian Shan, leaving a critical gap in our understanding of the Phanerozoic evolution of the Tian Shan. Using >100 basement samples taken from mountains and along major faults, this thesis aims to provide a continuous record of the deformation experienced by the western Tian Shan from

its amalgamation in the Palaeozoic, through to the ongoing indentation of the India-Eurasia collision, detailing periods of emplacement, exhumation, and fault-reactivation, as well as periods of tectonic stability.

1.3 Methods

The formation of mountainous topography is controlled by the underlying faults and structures. When a mountain is uplifted along a fault it brings rocks from deeper and hotter in the crust closer to the surface, as the uplifted mountain undergoes erosion the uplifted rocks are progressively exhumed, eventually cooling the rocks to surface temperatures. In an intracontinental setting, uplift and deformation along faults and structures is the most predominate form of cooling (e.g. Sobel & Strecker 2003), therefore, investigating the timing of cooling can assist in constraining timing and rates of uplift, exhumation, and mountain-building. In order to elucidate mountain-building in the intracontinental setting of the Tian Shan, this thesis employed five mid to low temperature thermochronometers to rocks sampled along major fault zones. The following section will briefly describe each technique.

1.3.1 Apatite Uranium-Lead (AUPb)

The apatite U-Pb method relies on the thermally activated volume diffusion of Pb within the crystal lattice of an apatite grain to provide information about its thermal history (Blackburn et al. 2011). Estimates of the closure temperature of the apatite U-Pb system range from 550-370°C temperature window (Chew & Donelick 2012, Thomson et al. 2012, Cochrane et al. 2014), although figures of 450-550°C are more typical (e.g. Schoene & Bowring 2007, Blackburn et al. 2011).

1.3.2 Zircon Fission Track (ZFT)

Zircon fission track thermochronology uses the number of fission tracks observed in the crystal lattice caused by the spontaneous decay of ^{238}U, compared to the amount of ^{238}U (ppm) remaining in the grain measured using Laser Ablation-Inductively Coupled Plasma Mass Spectrometry (LA-ICP-MS, e.g. Bernet & Garver 2005, Hasebe et al. 2009, Soares

et al. 2014). The ZFT thermochronometer constrains an effective annealing temperature of between ~180°C and ~240°C in natural systems (e.g. Tagami 2005, Bernet & Garver 2005).

1.3.3 Apatite and zircon (U-Th-Sm)/He (AHe and ZHe)

The (U-Th-Sm)/He thermochronometers are based on the diffusivity of ^{4}He. For apatite, the thermochronometer has a thermal sensitivity at 80-40°C, making it valuable for constraining the most recent thermal cooling event (Zeitler et al. 1987, Farley 2002). For zircon, the method records the thermal history at ~190-170°C (Reiners et al. 2002, Guenthner et al. 2013). The (U-Th-Sm)/He analyses for this study were undertaken at the John de Laeter Centre, Curtin University and followed the protocols described in Danišík et al. (2012,a).

1.3.4 Apatite Fission Track (AFT)

The apatite fission track method is based on the temperature dependent annealing of mineral lattice damage features, called 'fission tracks', that are created by the spontaneous decay of ^{238}U (Wagner & Van den haute 1992). The number of fission tracks are compared to the amount of ^{238}U (ppm) measured in the apatite grain using LA-ICP-MS. Fission tracks record the thermal history of a rock sample through the apatite partial annealing zone of ~120-60°C (APAZ, Green et al. 1986).

1.4 Thesis Outline

This thesis comprises of four chapters investigating the low-temperature thermochronology of the western Tian Shan. Three of these chapters have been journal articles (one published, one accepted for publication, and one in revision), and one is a manuscript that will shortly be submitted to a scientific journal. The overall goal of the thesis is to investigate the deformation and mountain-building process from an under-explored part of the Tian Shan, and to integrate the new results with existing thermochronological data to reveal a more complete picture of the low-temperature thermal history of the Tian Shan. The thesis chapters are organised both geographically and temporally, with the first chapter documenting the samples that are both taken the furthest north, as well as documenting the oldest thermochrono-

logical data. Chapters two and three step through the Mesozoic evolution of the central and western segments of the western Tian Shan, before finishing with the southern-most samples that record the youngest thermochronological ages and mark the boundary between the Pamir and the Tian Shan. The final chapter is a discussion of the shared trends and marked differences between the data sets, then comparing the trends identified in the western Tian Shan with that of published thermochronological data from the central, northern, and eastern Tian Shan.

Chapter One provides an introduction into the motivations and project goals behind the undertaking of this study. Providing an overview of the tectonic environment in which the Tian Shan evolved, and outlining where this project sits within the published literature. In addition, this chapter contains a brief description of each of the chapters contained within this thesis.

Chapter Two focuses on the northern-most extent of the western Tian Shan, the Karatau-Talas region in Kazakhstan and Kyrgyzstan. This chapter investigates the extent of deformation along a major north-west to south-east trending fault which dissect the Tian Shan, the Karatau-Talas Fergana fault. The obtained zircon and apatite fission track results reveal Permian–Early Triassic basement exhumation, followed by periods of Mesozoic reactivation in the Late Triassic–Early Jurassic, the Late Jurassic–Early Cretaceous, and limited deformation during the Cenozoic (in the high relief southern section of the study area). The thermo-tectonic history suggests that the Karatau-Talas Fergana fault acted as a major conduit for strain into the Eurasian interior from the late Palaeozoic to the present day.

Chapter Three details the low-temperature thermo-tectonic evolution of the Chatkal-Kurama terrane in eastern Uzbekistan and northern Tajikistan. Lying immediately south of the Karatau-Talas range, apatite fission track and (U-Th-Sm)/He results on samples from the Chatkal-Kurama terrane indicate rapid basement cooling via erosion in the Triassic transitioning into slow-cooling due to erosion and denudation during the Jurassic-Cretaceous, before a return to rapid basement cooling in the Cenozoic. The results suggest that the Talas Fergana Fault acted as a partition during the Jurassic–Cretaceous, since the Chatkal-Kurama terrane (to the east) experienced marine incursion by the Paratethys Sea, while the

central Tian Shan (to the west) experienced deformation at that time. The spatial distribution of apatite fission track ages (older to the north-west transitioning into younger in the south-east) suggest that the Chatkal-Kurama terrane experienced block rotation during the Cenozoic, with the south-eastern margin being progressively more deeply exhumed-compared to the north-west. This chapter is currently in revision for the journal Tectonics by *Gilby Jepson, Stijn Glorie, Dmitry Konopelko, Jack Gillespie, Martin Danišík, Rustam Mirkamalov, Yunus Mamadjanov, and Alan Collins* (2018).

Chapter Four focuses on the western-most extent of the Tian Shan, the Kyzylkum-Nurata segment in western Uzbekistan. The obtained fission track and (U-Th-Sm)/He thermochronological data suggest that this area underwent a multi-phase Mesozoic thermal history, starting with rapid Triassic and Late Jurassic-Early Cretaceous basement exhumation. This region lacks much of the Cenozoic overprint which has been identified elsewhere in the Tian Shan, providing a unique insight into the Cretaceous Uzbek Tian Shan. Thermal history reconstruction suggests that the Cretaceous Uzbek landscape was characterised by a series of parallel, linear mountain belts that formed along suture zones during fault reactivation, likely as a result of back-arc extension in the Tethys (associated with slab roll-back) during the Early Cretaceous. This chapter has been accepted for publication into the journal Gondwana Research by *Gilby Jepson, Stijn Glorie, Dmitry Konopelko, Rustam Mirkamalov, Martin Danišík, and Alan Collins* (2018).

Chapter Five investigates the thermo-tectonic evolution of the southern-most extent of the western Tian Shan, the boundary between the Tian Shan and the Pamirs, Tajikistan. A series of samples along the Vakhsh-Surkhob fault zone were analysed using apatite U-Pb and zircon (U-Th-Sm)/He thermochronometers, revealing a record of the Early Triassic formation of the Vakhsh-Surkhob fault and the Late Triassic reactivation as a response to the Qiangtang collision/Rushan Ocean closure. Apatite fission track and apatite (U-Th-Sm)/He results identify late Palaeogene reactivation of the Tian Shan-Pamir margin due to the India-Eurasia collision, as well as the late Miocene basement cooling which marks the onset of modern mountain building within the South Tian Shan that is ongoing today. This chapter has been published by *Gilby Jepson, Stijn Glorie, Dmitry Konopelko, Jack Gillespie, Martin Danišík, Noreen Evans, Yunus Mamadjanov, and Alan Collins* (2018) in *Terra Nova*,

doi: 10.1111/ter.12313.

Chapter Six is a discussion chapter, that integrates the insights into the tectonics of the western Tian Shan identified using low-temperature thermochronology, with the results that have been published in the central and eastern Tian Shan. The low-temperature thermochronology data compilation allows us to provide a more robust reconstruction of the regional thermo-tectonic history of the Tian Shan and better speculation on the mechanism that induced the more localised thermal events. This discussion chapter will lay the framework for a systematic review of low-temperature thermochronology data that could now be undertaken as many of the regional gaps in the Tian Shan have been filled.

Chapter 2

The Mesozoic low-temperature thermal evolution of the Karatau–Talas Range, Kazakhstan and Kyrgyzstan

Statement of Authorship

Title of Paper	The Mesozoic thermo-tectonic evolution of the Karatau–Talas Range, Kazakhstan and Kyrgyzstan
Publication Status	☐ Published ☐ Accepted for Publication ☐ Submitted for Publication ☑ Unpublished and Unsubmitted work written in manuscript style
Publication Details	Draft manuscript to be submitted for publication shortly.

Principal Author

Name of Principal Author (Candidate)	Gilby Jepson		
Contribution to the Paper	Sample collection, sample analysis, data interpretation, and principal author of paper.		
Overall percentage (%)	70		
Certification:	This paper reports on original research I conducted during the period of my Higher Degree by Research candidature and is not subject to any obligations or contractual agreements with a third party that would constrain its inclusion in this thesis. I am the primary author of this paper.		
Signature		Date	31/08/18

Co-Author Contributions

By signing the Statement of Authorship, each author certifies that:

i. the candidate's stated contribution to the publication is accurate (as detailed above);

ii. permission is granted for the candidate in include the publication in the thesis; and

iii. the sum of all co-author contributions is equal to 100% less the candidate's stated contribution.

Name of Co-Author	Stijn Glorie		
Contribution to the Paper	Sample collection, data interpretation, and thesis supervisor.		
Signature		Date	31/08/18

Name of Co-Author	Andrey Khudoley
Contribution to the Paper	Sample collection, data interpretation, figures, and geological background.

Signature		Date	31/08/18

Name of Co-Author	Sergey Malyshev		
Contribution to the Paper	Sample collection, data analysis, data interpretation, figures, and geological background.		
Signature		Date	31/08/18
Name of Co-Author	Alan Collins		
Contribution to the Paper	Data interpretation, secondary supervisor.		
Signature		Date	31/08/18

Please cut and paste additional co-author panels here as required.

Gilby Jepson, Stijn Glorie, Andre Khudoley, Sergey Malyshev, and Alan S. Collins

2.1 Introduction

The Central Asian Orogenic Belt (CAOB) is the worlds largest intracontinental orogen, stretching from Uzbekistan to Mongolia, and hosting steep and dramatic topography. The CAOB is a collage of tectonic accretion of Precambrian microcontinents, early Palaeozoic arc terranes, ophiolitic units, and accretionary wedges that amalgamated in the early and middle Palaeozoic (Windley et al. 2007, Xiao et al. 2012). The fingerprint of this accretion can be found in the detrital records of adjacent basins (e.g. Alexeiev et al. 2009, Brookfield 2000, Ren et al. 2011, Biske et al. 2013, Alexeiev et al. 2016, De Pelsmaeker et al. 2018, Song et al. 2018, Käßner et al. 2017a) and localised in the *in situ* topography (De Grave et al. 2011). However, the present day topography developed due to the Mesozoic and Cenozoic deformation, largely in response to distant tectonic events in the Tethys Ocean on the Eurasian margin (e.g. Hendrix et al. 1992, Dumitru et al. 2001, Sobel, Oskin, Burbank & Mikolaichuk 2006, De Grave et al. 2007, Glorie et al. 2011, Jepson et al. 2018a, Gillespie et al. 2017). It is this record, preserved away from the present day continental margin, that gives us insights into the growth of intra-continental mountain ranges not just in Central Asia, but globally.

Central Asia is dissected by a series of north-west to south-east trending strike-slip faults that run sub-parallel from the Kopet Dagh mountains in Turkmenistan, to the Har-Us Nuur mountains in western Mongolia (e.g. Rolland et al. 2013, Alexeiev et al. 2017). These faults represent a prominent geomorphological features which are related to Palaeozoic subduction-collision stages during the amalgamation of the ancestral Tian Shan (e.g. Sébastien et al. 2002, Laurent-Charvet et al. 2003, Allen et al. 2006, Alexeiev et al. 2009). As the E-W trending Mesozoic and Cenozoic deformation of the modern Tian Shan overprinted the ancestral Tian Shan, the NE-SW trending strike-slip faults acted as barriers and boundaries for strain, influencing the development of the modern Tian Shan (e.g. Laurent-Charvet et al. 2003, Allen et al. 2006, Nissen et al. 2009, Alexeiev et al. 2009, Bande et al. 2017b). Several geochronological and thermochronological studies have been performed on these strike-slip

faults, identifying a complicated and multi-stage deformation history, as the faults have been activated and reactivated throughout the Mesozoic and Cenozoic (e.g. Allen et al. 2001, Sébastien et al. 2002, Laurent-Charvet et al. 2003, Yuan et al. 2006, Charvet et al. 2007, Nissen et al. 2009, Glorie et al. 2012, Konopelko et al. 2013, Rolland et al. 2013, Bande et al. 2017b, Nachtergaele et al. 2017), indicating that this network of north-west to south-east trending faults are a major influence on the mountain building process in the Tian Shan from formation to the present day.

The NW-SE trending Karatau-Talas Fergana (KTF) fault is one of the largest and most active of these sub-parallel, strike-slip faults in the CAOB. The KTF Fault runs ~1500 km from the Tarim Basin (China) to South Kazakhstan, with a maximum displacement of ~200 km at the central part of the fault, and is a prominent geomorphological feature in the western Tian Shan (e.g Burtman 1975, 1980). Previous thermochronological studies, focusing on the high elevation south-eastern extent of the KTF Fault, have identified multiple episodes of deformation from the Carboniferous through to the Neogene (e.g. Huang et al. 2005, Sobel, Chen & Heermance 2006, Rolland et al. 2013, Konopelko et al. 2013, Bande et al. 2017b, Nachtergaele et al. 2017). However, little work has been done to constrain the extent of these deformation events in the north-western extent of the KTF, more specifically, in the Karatau Fault (KF) and the northern extent of the Talas-Fergana Fault (TFF, Figure 2.1). This study applies apatite and zircon fission track analysis to 20 Neoproterozoic to Permian sedimentary and granitoid samples from this area, aiming to decipher the timing of Palaeozoic and Mesozoic deformation along the KTF Fault. This study provides a key element in understanding the tectonic evolution of the western Tian Shan, as the presence of a series of NW–SE-trending structures throughout the Tian Shan such as the Irtysh Shear Zone, the Junggar Fault, the Kaindy-Atasu Fault, the Zhalair-Naiman Fault, and the Amu Dar'ya Fault, means that any constraints on the thermotectonic evolution of the Main Karatau Fault also has regional implications for Central Asia (e.g. Şengör et al. 1993, Allen et al. 2001, 2006).

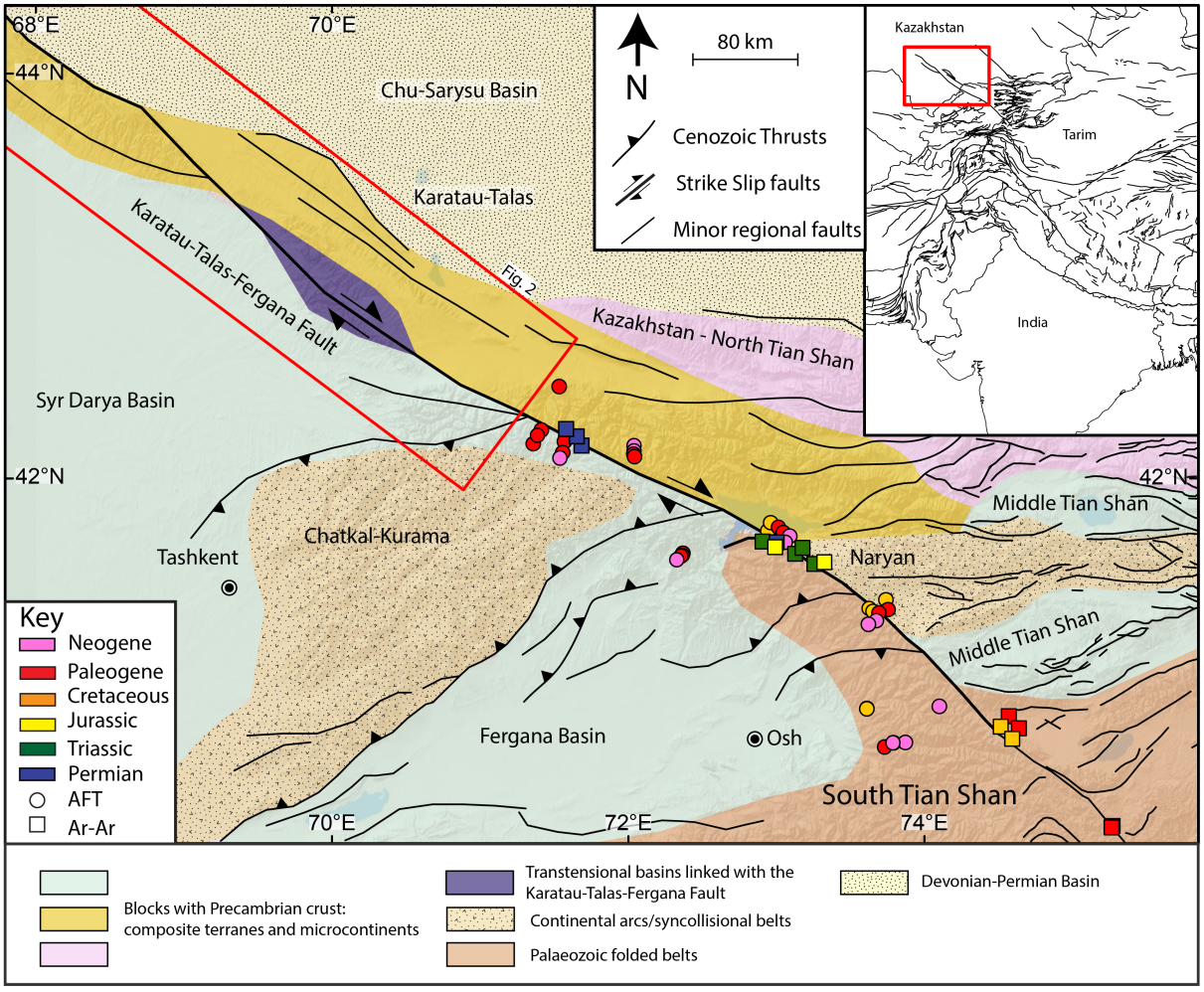

Figure 2.1: A tectonic map of southern Kazakhstan and the western Tian Shan (late Mesozoic and Cenozoic cover removed) modified from Rolland et al. (2013), Mohadjer et al. (2016). The Chatkal-Kurama represents a Carboniferous-Permian Continental arc/syncollisional belt, while Naryn is considered a Carboniferous Continental arc/syncollisional belt. Published thermochronological from along the Karatau Talas Fergana fault are included, with circles representing apatite fission track (AFT) data, and squares representing $^{40}Ar/^{39}Ar$ (Sobel & Arnaud 2000, Huang et al. 2005, Rolland et al. 2013, Konopelko et al. 2013, Bande et al. 2017b,c, Nachtergaele et al. 2017).

2.2 Tectonic Setting

2.2.1 Karatau and Talas Regions

The surface expression of the Karatau Fault, the Karatau range, is an elongate NW–SW-trending mountain range that lies on the north-eastern extent of the KTF Fault in South Kazakhstan (Figure 2.2). The Karatau range is bounded by the Chu Sarysu Basin to the north-east, and the Syr Dar'ya Basin to the south-west (Figure 2.1). The Karatau range is defined by a series of NW-SE trending faults that are parallel to sub-parallel of the KF (Figures 2.1 and 2.2). The continuation of the MKF and the Karatau range is the Talas-Fergana fault and the associated Talas range in Kyrgyzstan. The Talas range is defined by the TFF to the south-west, and the Central Talassian Thrust to the north-east (Figure 2.2, Khudoley 1993).

During the Neoproterozoic the Karatau region experienced the widespread deposition of shallow marine sediments, as well as minor amounts of tuffs which are interpreted to be indicative of a continental rift setting (Figure 2.2, Cook et al. 1991, Kröner et al. 2007, Alexeiev et al. 2009). The Early Palaeozoic structure of the Karatau region consists of north-west trending thrusts, which were generated synchronously with north-west trending folds (Cook et al. 1991, Alexeiev et al. 2009). The Devonian was characterised by a major transgression over Central Asia continuing the deposition of fluvial and shallow marine siliciclastic rocks, as well as the formation of carbonate platforms (Cook et al. 1991, Allen et al. 2001, Cook et al. 2002, Alexeiev et al. 2017). The Talas region experienced a similar series of sedimentation during the Neoproterozoic, with the deposition of submarine fan to shelf sediments with some carbonate units (Khudoley 1993, Voytenko & Khudoley 2012). The terrigenous and carbonate rocks of the Talas region underwent greenschist and amphibolite metamorphism during the Middle Ordovician (Khudoley 1993, Voytenko & Khudoley 2012). Sedimentation had largely ceased in both the Karatau and Talas regions by the Carboniferous due to the collision of various arcs and microcontinents (e.g. Allen et al. 2001).

2.2.2 Karatau-Talas-Fergana Fault

The Karatau Fault (KF) and the Talas-Fergana Fault (TFF) originated as a single structure in the Neoproterozoic - early Palaeozoic as a result of the accretion of various island arcs and micro-continents to the margin of the East European and Siberian cratons (Windley et al. 2007, Kröner et al. 2007, Alexeiev et al. 2009). This Proterozoic to Palaeozoic assemblage, known as Palaeo-Kazakhstan, formed the continental margin of the incipient Eurasian continent (Windley et al. 2007, Alexeiev et al. 2009). During the Palaeozoic, the progressive closure of the Turkestan Ocean to the south of Palaeo-Kazakhstan generated a subduction related margin in the Karatau-Talas region (Windley et al. 2007, Alexeiev et al. 2009, 2017). The subsequent closure of the Turkestan Ocean in the Permian-Triassic (~256-240 Ma) generated a series of regional NW-SE trending strike-slip faults such as the Djalair-Naiman, Central Kazakhstan, and Junggar, as well as the KTF Fault (Rolland et al. 2013, Konopelko et al. 2013). In the Middle to Late Palaeozoic the KTF Fault experienced three main deformation episodes: (1) a Late Carboniferous event as a result of the subduction of the Turkestan Ocean, (2) a Latest Permian to Triassic event due to the continental collision of the Tarim, Alai, and Karakum micro-continents to the Palaeo-Kazakhstan margin, and (3) a Triassic event caused by the ongoing indentation of the Karakum micro-continent into Palaeo-Kazakhstan (Windley et al. 2007, Alexeiev et al. 2009, Rolland et al. 2013, Konopelko et al. 2013).

Intracontinental deformation of Central Asia continued in the Mesozoic as a result of the closure of the Paleo-Tethys Ocean at the Eurasian margin (e.g. Xiao et al. 2013, Glorie & De Grave 2016, Jepson et al. 2018a, Song et al. 2018). The following progressive closure of the Tethys Ocean caused peri-Gondwanan fragments to accrete to the margin of Eurasia (De Grave et al. 2007, Jolivet et al. 2010, Glorie et al. 2010). Known collectively as the Cimmerian Orogeny, these events were dominated by the collision of the Qiangtang block in the Late Triassic–Early Jurassic, the Lhasa block in the Late Jurassic–Early Cretaceous, and the Karakoram and Kohistan-Ladakh arc in the Late Cretaceous (e.g. Sengör 1984, Hendrix et al. 1992, Kapp et al. 2007, Roger et al. 2010, Jolivet 2017, Nachtergaele et al. 2017, Gillespie et al. 2017). The Cimmerian Orogeny caused widespread deformation and reactivation basement structures in the Eurasian interior, generating much of the initial uplift

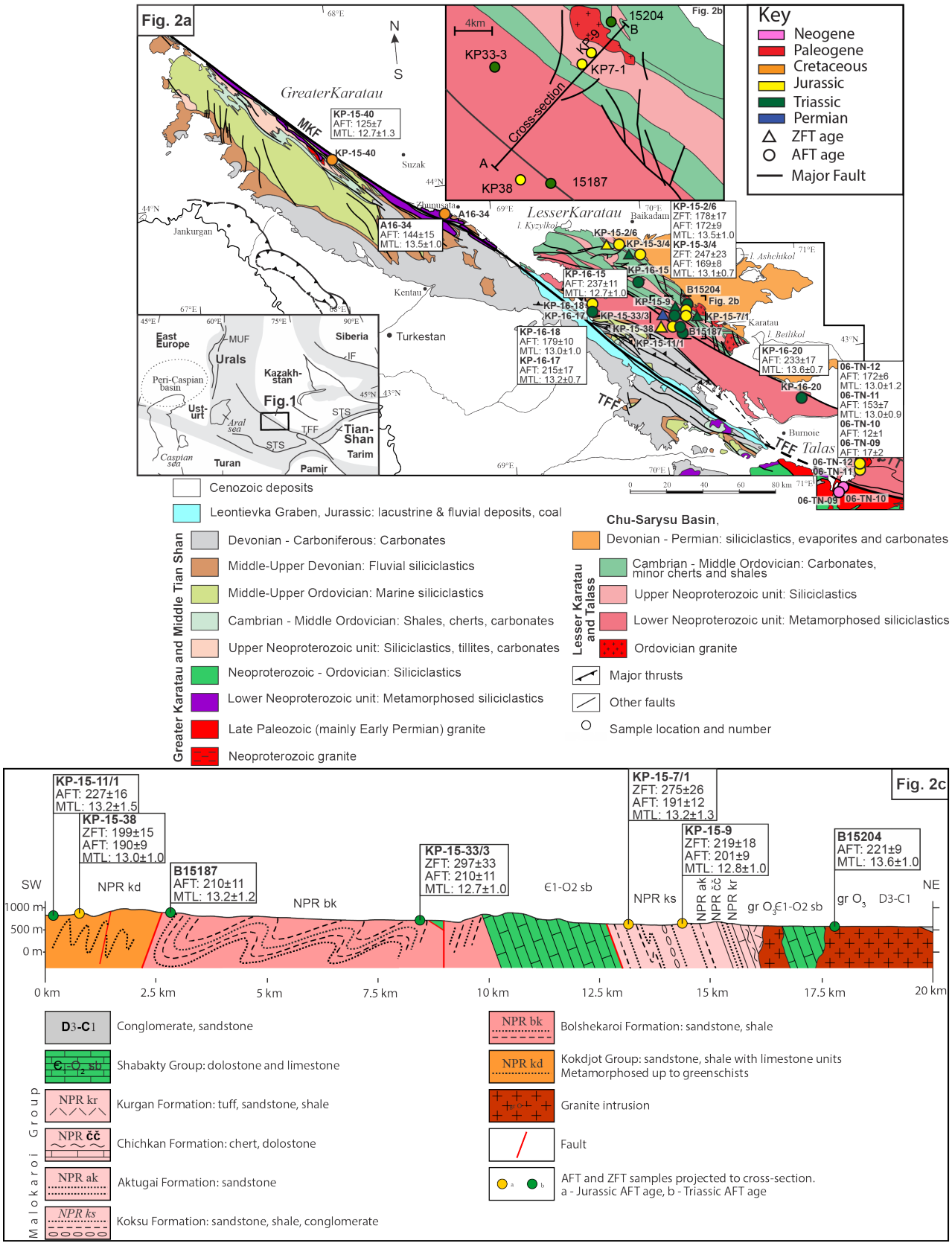

Figure 2.2: Tectonic map of the Karatau-Talas study area containing zircon fission track (ZFT), apatite fission track (AFT) ages in Ma, and the mean track length (MTL) in μm of samples.

seen in the modern-day Tian Shan today (e.g. Glorie et al. 2011, Sobel, Chen & Heermance 2006, Jolivet et al. 2010, De Grave et al. 2013, Jolivet et al. 2013). Along the KTF Fault, much of the deformation caused by these Mesozoic processes were expressed in the form of right-lateral displacement (Alexeiev et al. 2009, Konopelko et al. 2013, Rolland et al. 2013), indicating that the KTF Fault acted as a major conduit for intracontinental stress in Central Asia (Bande et al. 2017b, Nachtergaele et al. 2017, De Pelsmaeker et al. 2018, Jepson et al. 2018c).

The final closure of the Tethys Ocean in the Cenozoic brought about the India-Eurasia collision (e.g. Beck et al. 1995, Aitchison et al. 2007, Najman et al. 2010, van Hinsbergen et al. 2011). The deformation caused by the India-Eurasia collision exhuming the high elevations of the Himalaya, Tibet, and the Tian Shan (e.g. Allen et al. 2001, Dewey et al. 1989). Deformation caused by the India-Eurasia collision further away from the direct collision zone has been identified along reactivated basement structures throughout the paleo-Eurasian continent (e.g. Sobel, Chen & Heermance 2006, De Grave et al. 2007, Jolivet et al. 2010, Glorie et al. 2011, Macaulay et al. 2014, Bande et al. 2017b). Along the KTF Fault, the total displacement from the Permian to the Quaternary reaches 200 km, based on the offset of the Carboniferous South Tian Shan suture and related units (Burtman 1980). The majority of this vast displacement is found in the Talas-Fergana segment of the KTF Fault, whereas the Karatau section does not possess the same degree of displacement (Tapponnier & Molnar 1979). Therefore, it is hypothesised that the Karatau section preserves the pre-Cenozoic tectonic history of the KTF Fault without being overprinted by a later major tectonic event (Bande et al. 2017b, Allen et al. 2001).

2.3 Methodology

In this study, new thermochronological data for 20 Neoproterozoic to Permian sedimentary and granitoid rock samples from the Karatau and Talas ranges in Kazakhstan and Kyrgyzstan are presented (Figure 2.2). To these samples we applied two different thermochronological methods; (1) zircon fission track (partical annealing zone ~180–220°C, Zaun & Wagner 1985), and (2) apatite fission track (partial annealing zone ~120–60°C, Gleadow et al. 1986)

,in order to constrain the Mesozoic thermo-tectonic evolution Karatau and Talas ranges.

2.3.1 Zircon Fission Track Thermochronometry

Zircon grain mounts were obtained by standard sample processing techniques (Gleadow 2007). Zircon grains were embedded in Teflon sheets and etched in a NaOH-KOH eutectic melt at 220°C for 1.5-3 hours in order to account for the effects of radiation damage (Gleadow et al. 1976). The detection mica was etched in 48% HF for 20 min at 20°C. Samples were irradiated in the research reactor FRM II in Munich, Germany in the presence of a glass neutron dosimeter (CN1) with known uranium content together with a Fish River Canyon tuff zircon age standard. Area densities (tracks/cm^2) of spontaneous and induced tracks were measured with the Heidelberg FT-1 system. The system includes an optical microscope Leitz of 100x magnification, with a 3-axis microscope Autoscan stage, a high-resolution Peltier-cooled CCD colour Olympus® camera, and a high performing Windows® based computer system. To increase the precision of the stage movement each axis is equipped with an external laser controlled Sony® sensor (BL 55 RE). These sensors guarantee a deviation of less than 500 nm along a movement of 4-5 cm. The entire setup is controlled by the Autoscan® Software trackscan®. Area densities were counted by using a 160x objective. The presented ages are central ages and were calculated by applying the ζ-method after Hurford & Green (1982, 1983). The ζ-value of 123.5 (5.9) for CN1 (zircon) were gained using Fish Canyon zircon age standard. All ages and radial plots were calculated and drawn using computer code “TRACKKEY” (Dunkl 2002).

Generally, there are two general color series which are related to trace-element composition and increasing radiation damage: (a) common pink series; (b) yellow-brown series (Gordon Gastil et al. 1967). Accordingly, we assume that more brown grains are more metamict than pink ones and so it is related to more younger fission track ages (Garver & Kamp 2002). However, in this study, only single mounts were produced as only pink populations were determined (~180–220°C., Bernet & Garver 2005).

2.3.2 Apatite Fission Track Thermochronometry

Apatite grains were picked and mounted in epoxy resin, then polished to expose internal sections, and were subsequently chemically etched in a 5M HNO_3 solution for 20s at 20°C to reveal the natural spontaneous fission tracks (Gleadow et al. 2002). Fission track analysis was performed at The University of Adelaide using an Autoscan® system. The concentration of uranium (^{238}U) and chlorine (^{35}Cl) of each apatite grain was measured using Laser Ablation-Inductively Coupled Plasma-Mass Spectrometry. Data reduction was performed in Iolite® using the Trace Elements DRS (data reduction scheme, Paton et al. 2011). Instrumental drift correction was carried out using Madagascar apatite as an external standard, and elemental concentrations were calculated using ^{43}Ca as the internal standard (Thomson et al. 2012, Vermeesch 2017). Age calculation was carried out as described in Hasebe et al. (2004) and De Grave et al. (2012), using the Durango apatite (McDowell et al. 2005) to perform a zeta calibration (Vermeesch 2017). For a detailed methodology see Glorie et al. (2017) and Gillespie et al. (2017).

2.3.3 Thermal History Modelling

Thermal history models were produced for samples using their mean track length (MTL), ZFT ages, AFT ages, and confined track length distributions (Figure 2.3). The QTQt software (version 5.6.0) was applied, which uses Bayesian trans-dimensional Markov Chain Monte Carlo statistics to determine models for the cooling pathway of the sample (Gallagher 2012). An initial unconstrained run is performed to explore the statistical space, followed by adjustments to the search parameters or the addition of geological constraints where necessary. This approach follows the Bayesian philosophy of the software, which seeks to minimize the complexity of the model by statistical means. Many iterations ($>> 10,000$) are run to generate a range of models that create a probability distribution, from which individual models can be selected, including the maximum likelihood and "expected" (weighted mean) paths. The range of the general prior was set as t = AFT central age ± AFT central age, temperature = 70 ± 70°C. Acceptance rates for models were between 0.2 and 0.6 and birthdeath ratio was ~1. The annealing model from Ketcham et al. (2007) was used for fission track data with D_{par} as the kinetic parameter. More details on the modelling approach can

be found in Gallagher (2012) and Gillespie et al. (2017).

2.4 Results

In this study, zircon and apatite fission track thermochronology was performed on 20 basement samples from along the faults that comprise the KTF Fault. The samples from the Karatau-Talas region can be separated into three sample clusters based on regional proximity that run either along, or parallel to, the KTF Fault (Figure 2.2). The sample clusters are named after the regions in which they were sampled: (1) the Greater Karatau, (2) the Lesser Karatau, and (3) the Talas regions (Figure 2.2). Tables 1 and 2 summarise the ZFT and AFT data. Detailed tables and figures for all single-grain ZFT and AFT, mean track length (MTL) data, individual thermal history models, and modelling parameters are available in Figure 2.3 and the appendix files (Appendix files A, B, C, D, E, and F).

2.4.1 Apatite Fission Track

Table 2.1: Summary of apatite fission track data from the Karatau-Talas region: Lat is the north latitude, Long is the east longitude, Elev is elevation in metres a.s.l., n denotes the number of individual crystals dated, Age is the central age calculated for each sample in Ma, P Age is the pooled age of each sample in Ma, # is the number of confined tracks counted, MTL is the mean of measured confined tracks in μm and $\pm1\sigma$ is also in μm.

Sample	Lat	Long	Elev	n	Age$\pm1\sigma$	P Age$\pm1\sigma$	#	MTL	$\pm1\sigma$
Greater Karatau									
KP-15-40	44.168	67.913	575	32	124.6±6.8	115.2±13.9	63	12.7	1.3
A16-34	43.868	68.697	871	36	154.4±5.9	148.9±14.9	41	13.5	1.0
Lesser Karatau									
B15187	43.167	70.208	789	27	210±11	199.6±18.3	29	13.2	1.2
B15204	43.279	70.266	616	41	221.1±8.5	201.8±17.6	140	13.6	1.0
KP-15-2/6	43.628	69.836	439	18	172.1±8.9	169.1±15	62	13.5	1.0
KP-15-3/4	43.594	69.935	462	32	168.7±8.1	148.5±15	100	13.1	1.2
KP-15-7/1	43.250	69.238	397	31	184±12	176.4±15.9	100	13.2	1.3
KP-15-09	43.258	70.247	677	40	200.3±8.7	185.5±16.3	67	12.8	1.0
KP-15-11/1	43.145	70.216	861	20	227±16	214.5±24.3	18	13.2	1.4

KP-15-33/3	43.248	70.155	795	35	210±12	177.6±15.5	37	12.7	1.4
KP-15-38	43.170	70.180	1012	31	190.1±9.4	171±16.3	32	13.0	1.2
KP-16-15	43.458	69.869	584	33	236±11	228.6±24.6	26	12.7	1.0
KP-16-17	43.352	69.615	690	17	210±13	198.9±22.8	6	13.2	0.9
KP-16-18	43.356	69.616	753	21	179±10	164.4±17.9	11	13.0	1.0
KP-16-20	42.759	70.980	819	11	233±17	194.7±22.2	8	13.6	0.7
Talas									
06-TN-09	42.322	71.149	3030	41	15.4±1.8	16.1±2.1	-	-	-
06-TN-10	42.323	71.145	3237	43	11.1±1	11.2±1.1	-	-	-
06-TN-11	42.408	71.220	1949	41	163.1±8.9	141±18.5	14	13.0	0.9
06-TN-12	42.434	71.224	1748	42	162.5±7.1	175.5±22.1	28	13.0	1.2

Greater Karatau

The Greater Karatau region is the north-eastern extent of the Karatau-Talas study area. The Greater Karatau region comprises of two samples taken from directly along the Main Karatau Fault. Samples KP-15-40, and A16-34 produced AFT central ages of 124 ± 7 Ma and 144 ± 6 Ma, respectively. Sample KP-15-40 produced a relatively short MTL of 12.7 ± 1.3 μm, in contrast A16-34 yielded a long MTL of 13.5 ± 1.0 μm (Figure 2.2, 2.3, and Table 2.1).

Lesser Karatau

Of the samples collected in this study, the majority (14) were taken from the Lesser Karatau region, along faults and structures that run parallel or sub-parallel to the Main Karatau Fault (Figure 2.2). Seven of the 14 samples; B15187, B15204, KP-15-11/1, KP-15-33/3, KP-16-15, KP-16-17, and KP-16-20, produced Triassic AFT central ages of 210 ± 11 Ma, 221 ± 9 Ma, 227 ± 16 Ma, 210 ± 12 Ma, 237 ± 11 Ma, 215 ± 15 Ma, and 233 ± 17 Ma, respectively. The Triassic aged samples corresponded with largely with MTLs of 13.2± 1.2 μm, 13.6 ± 1.0 μm, 13.2 ± 1.4 μm, 12.7 ± 1.0 μm, 13.2 ± 0.9 μm, and 13.6 ± 0.7 μm, respectively. The samples KP-15-2/6, KP-15-3/4, KP-15-7/1, KP-15-9, KP-15-38, and KP-

16-18 of the Lesser Karatau region produced Jurassic AFT central ages of 172 ± 9 Ma, 169 ± 8 Ma, 191 ± 12 Ma, 201 ± 12 Ma, 190 ± 9 Ma, and 179 ± 10 Ma. The Jurassic AFT central ages corresponded with relatively long MTLs of 13.5 ± 1.0 μm, 13.1 ± 1.2 μm, 13.2 ± 1.3 μm, 12.8 ± 1.0 μm, 13.0 ± 1.2 μm, and 13.0 ± 1.0 μm, respectively (Figure 2.2, 2.3, and Table 2.1).

Talas

The continuation of the Main Karatau Fault into the Talas Fergana Fault occurs in the Talas region in north-eastern Kyrgyzstan (Khudoley 1993). Four samples were taken from along and to the east of the north-eastern Talas-Fergana Fault. The two fault samples, 06-TN-09 and 06-TN-10 both yielded similar Neogene ages of 17 ± 2 Ma and 12 ± 1 Ma. However, both samples yielded insufficient confined track lengths to produce a MTL. In the east, the two remaining samples 06-TN-11 and 06-TN-12 produced Jurassic AFT central ages of 153 ± 7 Ma and 172 ± 6 Ma, respectively. Samples 06-TN-11 and 06-TN-12 produced MTLs of 13.0 ± 0.9 μm and 13.0 ± 1.2 μm (Figure 2.2, 2.3, and Table 2.1).

2.4.2 Zircon Fission Track

Table 2.2: Zircon fission track data: n is the number of grains analysed per sample and ρ_s is the number of spontaneous tracks counted, ρ_D is the number of tracks in the dosimeter, ρ_i is the number of induced tracks, ^{238}U is the average concentration of uranium in ppm and χ^2 is the chi-squared value obtained for each sample.

Sample	n	$\rho_s \times 10^5 cm^{-2}$	$\rho_D \times 10^5 cm^{-2}$	$\rho_i \times 10^5 cm^{-2}$	^{238}U	χ^2	Age	$\pm 1\sigma$
KP-15-2/6	15	113.3	4.41	16.0	128.7	0.8	178.0	17.0
KP-15-3/3	25	109.7	4.41	12.1	121.9	1.0	247.2	23.2
KP-15-7/1	18	199.3	4.41	20.6	102.2	0.7	274.8	25.9
KP-15-09	21	118.0	4.41	14.2	148.4	1.0	218.8	18.2
KP-15-33/3	31	190.4	4.42	17.0	87.1	1.0	297.4	33.2
KP-15-38	25	131.5	4.42	17.9	115.4	0.9	199.2	15.1

Lesser Karatau

In the Lesser Karatau region six of the samples were selected for ZFT analysis, with all six samples passing the χ^2 test. Two of the samples, KP-15-7/1 and KP-15-33/3, produced Permian ZFT central ages of 275 ± 26 Ma and 297 ± 33 Ma. Two samples, KP-15-3/4

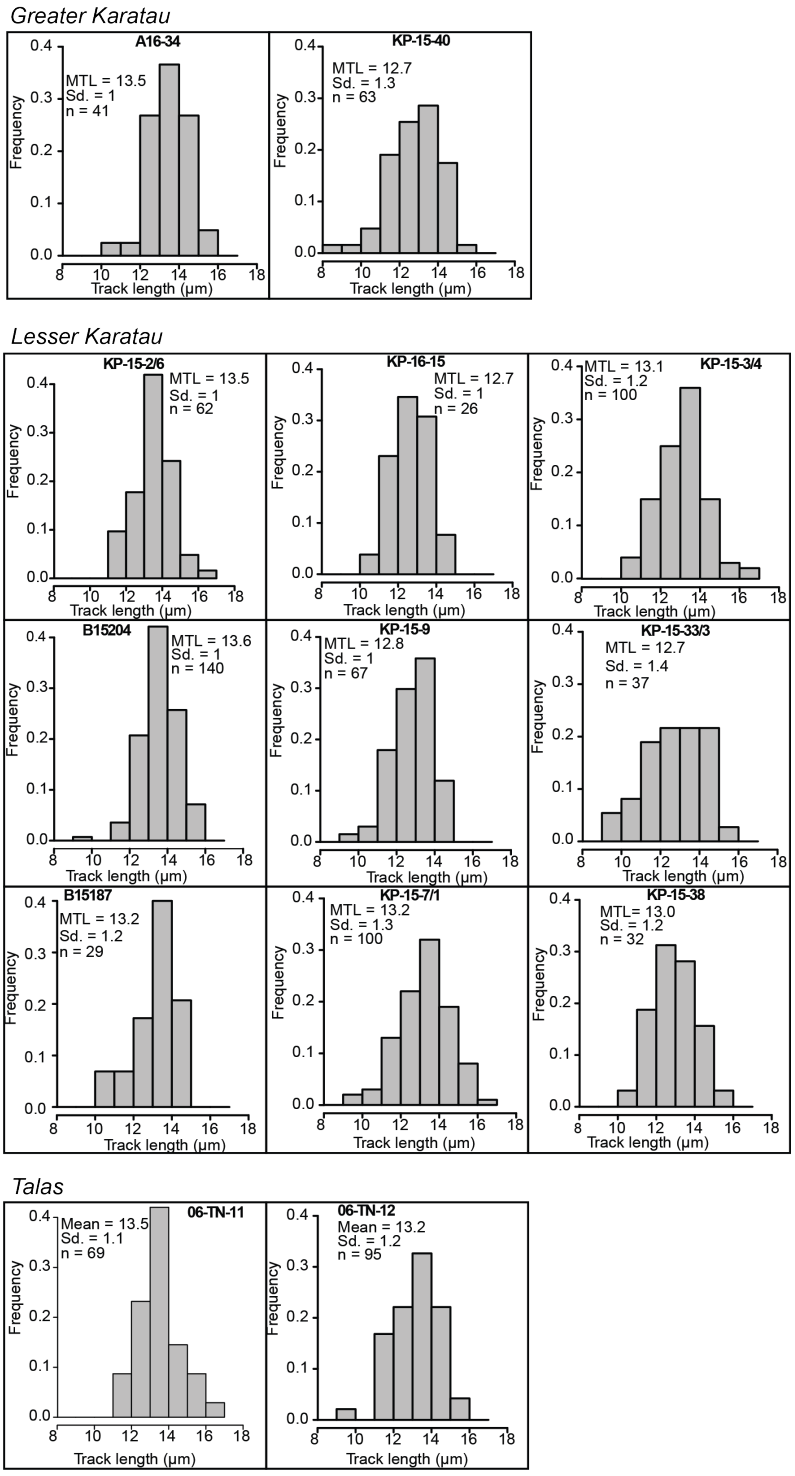

Figure 2.3: Histograms displaying the distribution of confined tracks in apatite measured for each sample in the Karatau-Talas region. MTL is the mean track length, Sd. is the standard deviation, and n is the number of confined track measured for each sample.

and KP-15-9 produced ZFT central ages of 247 ± 23 Ma, 219 ± 18 Ma, respectively. The remaining two samples, KP-15-2/6 and KP-15-38 produced Jurassic ZFT central ages of 178 ± 17 Ma and 199 ± 15 Ma, respectively (Figure 2.2 and Table 2.2).

2.4.3 Thermal History Modelling

Thermal history modelling was conducted on 12 samples that contained at least 25 confined tracks from the Karatau-Talas region (Figure 2.3), however models produced from samples with >50 confined tracks were considered less reliable. For all thermal history models, the AFT annealing model from Ketcham et al. (2007) was used. Zircon fission track data were integrated into thermal history models for their corresponding sample (Figure 2.4 and Table 2.2, Bernet & Garver 2005). Two of the AFT samples (KP-15-2/6 and KP-15-9) failed the χ^2 test for thermal history modelling, however, they displayed a close match between their ZFT and AFT central ages (within error, Table 1 and 2). Thus, modelling was performed on both samples, however, the expected model line is dashed to highlight its uncertainty (Figure 2.4). Additionally, thermal history modelling was performed for four samples (B15204, KP-15-7/1, KP-15-33/3, and KP-15-40) which failed the χ^2 test to provide additional constraints the thermo-tectonic history of the Karatau-Talas, these thermal models have also been dashed to highlight their uncertainty. Individual models, confined track distributions, and modelling parameters are available in Figure 2.3 and appendix Files C, D, E, and F (Flowers et al. 2015).

Both samples from the Greater Karatau region were modelled to show their thermal history. Sample A16-34 was taken from directly along the Main Karatau Fault, and displayed a relatively fast-cooling thermal history through the APAZ at ~160-150 Ma, while the less well constrained sample KP-15-40 showed a slower rate of basement cooling between ~140-120 Ma (Figure 2.4a).

Six samples were appropriate for thermal history modelling in the Lesser Karatau region. The thermal history models from Lesser Karatau show two distinct thermal history pathways. The first, identified by sample KP-16-15, indicates a slow-cooling middle Triassic thermal history, cooling through the APAZ from ~250-230 Ma. This is followed by a period of relatively fast cooling through both the combined ZFT partial annealing zone (ZPAZ) and

the APAZ (within error) at ~200 Ma shown by samples KP-15-9, KP-15-38, and to a lesser extent B15204 and KP-15-7/1. A brief hiatus in the basement cooling is experienced between ~190-160 Ma, before a return to fast basement cooling in the Late Jurassic, defined by samples KP-15-4/3 (both ZFT and AFT) and B15187, and further constrained by the less well defined sample KP-15-2/6 (Figure 2.4b).

Of the four samples from the Talas region, two were appropriate for thermal modelling. Neither samples (06-TN-09 and 06-TN-10) from the high elevation (>3000m) region of Talas, west of the Talas Fergana Fault, contained a sufficient number of confined tracks for thermal modelling. In the slightly lower elevation (~1800m), eastern side of the Talas Fergana Fault samples 06-TN-12 and 06-TN-11 both display relatively fast cooling in the mid Jurassic (~160 Ma, Figure 2.4c).

Thermal history modelling along the Main Karatau Fault determined two discrete fast basement-cooling periods. A period of rapid basement cooling during the Late Triassic–Early Jurassic, interrupted with a brief hiatus, where no basement-cooling is modelled to have occurred between ~190-160 Ma, before a return to fast basement cooling during the Late Jurassic–Early Cretaceous. The Late Jurassic–Early Cretaceous phase of rapid cooling is identified across all three sub-divisions in the Karatau-Talas region, suggesting that this event was more regional compared to the localisedLate Triassic–Early Jurassic period of rapid cooling identified in the Lesser Karatau(Figure 2.4).

2.5 Discussion

The combined ZFT and AFT results of this study points to a complex and punctuated Mesozoic tectonic evolution prior to the Cenozoic tectonics that dominate the Central Asian topography seen today. The low temperature thermochronometers identify two main phases of cooling and exhumation have been experienced by the Karatau-Talas region during the Palaeozoic–Mesozoic; the first (1) during the Late Permian–Early Triassic, with a period of tectonic stability during the Jurassic, before (2) a period of rapid cooling in the Late Triassic–Early Jurassic. The Karatau-Talas region is subsequently dominated by an absence in Late Cretaceous low-temperature thermochronological data, before the observation of

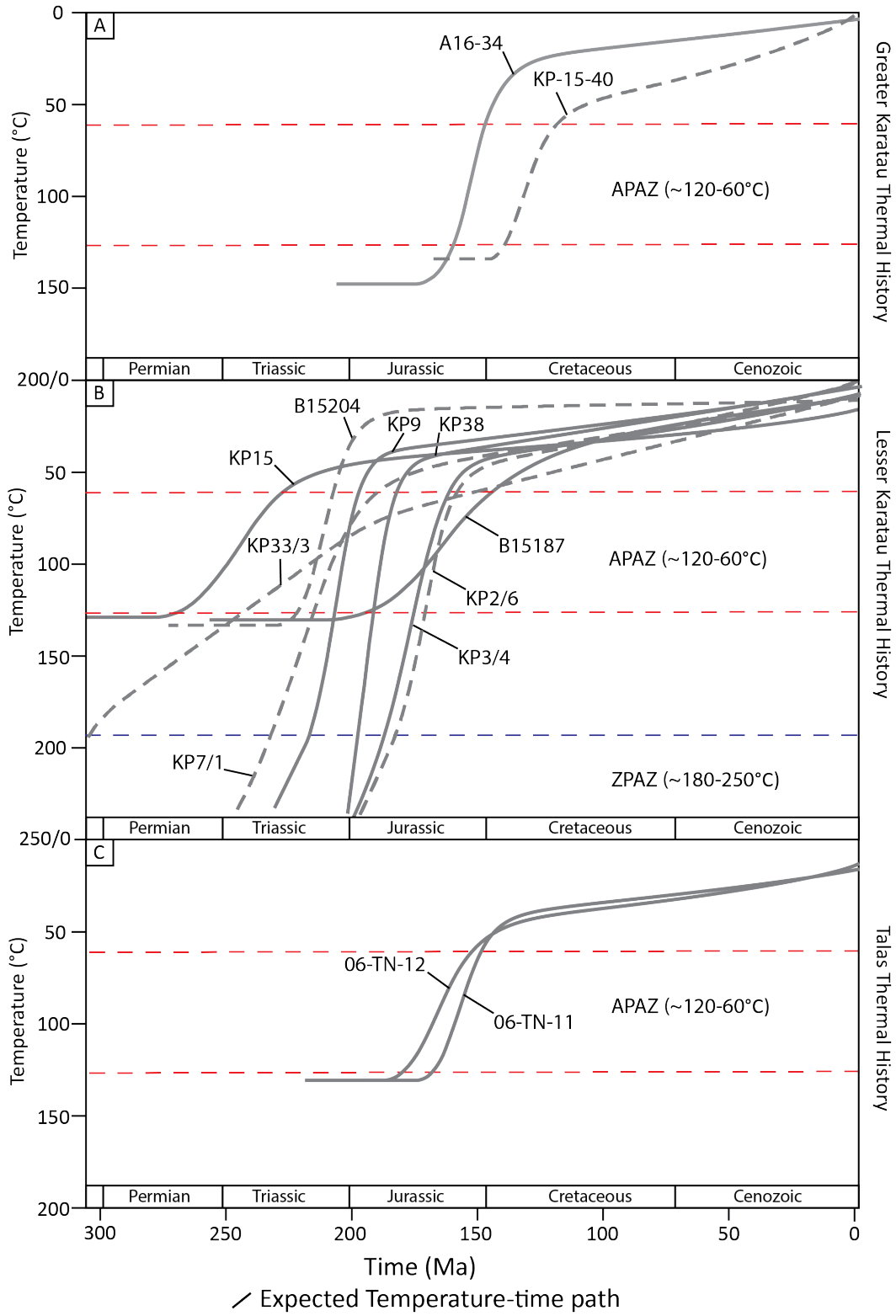

Figure 2.4: Plots displaying the modelled temperature-time paths for all samples within the Karatau-Talas region that yielded sufficient confined track data for modelling purposes (>25). Modelling was performed using QTQt Gallagher (2012), with the bold and dashed lines representing the expected temperature-time pathway modelled. Zircon fission track (ZFT) data was used to refine the thermal models where appropriate (see thermal model section). Bold lines represent thermal history models from samples which contained at least 25 confined tracks, with dashed lines representing thermal history models from samples which failed the χ^2 test, however, showed a close match between ZFT and apatite fission track ages. The dashed red lines represents the apatite partial annealing zone (APAZ) between 120°C and 60°C. For detailed individual thermal history models and modelling parameters see Figure 2.3 and Appendix File D).

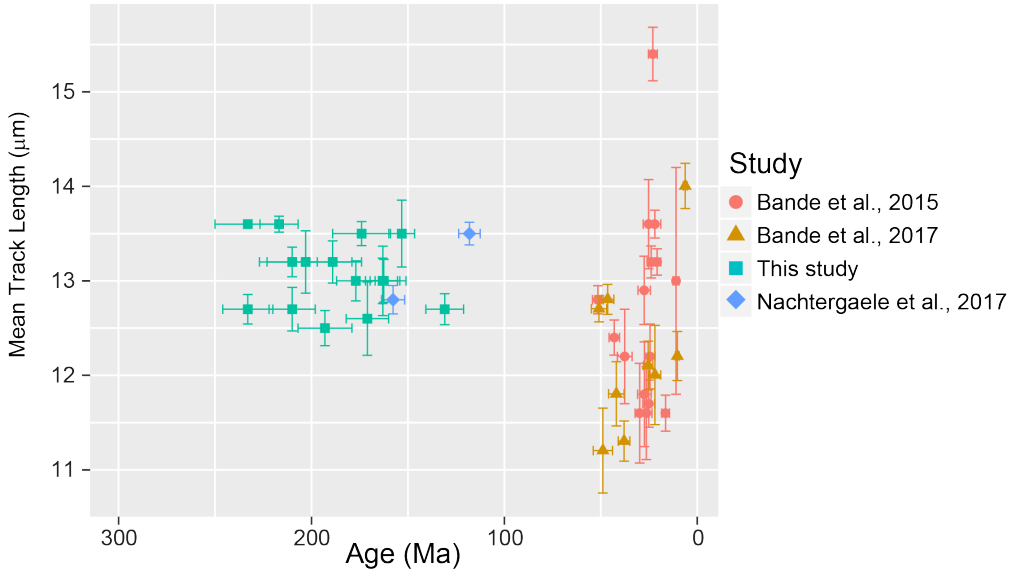

Figure 2.5: A comparison of Karatau-Talas Fergana (KTF) Fault thermochronological data: a "boomerang" demonstrating the relationship between AFT ages and MTL for a set of samples from a region which has likely experienced a multiple thermo-tectonic events (Green 1986, Gallagher & Brown 1997, Gallagher et al. 1998). The boomerang plot compares AFT data from the Karatau-Talas region with AFT data taken from along the KTF Fault (Bande et al. 2017b,c, Nachtergaele et al. 2017).

Miocene AFT ages in the high-elevation Talas range.

2.5.1 Carboniferous–Early Permian Amalgamation

The Carboniferous saw a series of major tectonic events that caused the formation of much of the Kazakhstan continent. The convergence of western Palaeo-Kazakhstan with East Europe along the Ust-yurt thrust, the closure of the Junggar Ocean, merging Palaeo-Kazakhstan and Siberia to the east, and the closure of the Turkestan Ocean to the south are all suggested to have occurred at ~335-315 Ma (Zonenshain et al. 1990, Filippova et al. 2001, Windley et al. 2007). Despite the regional tectonic upheaval, the Karatau-Talas region preserves no low-temperature thermochronological signal from the Carboniferous. However, in the Early Permian, the Neoproterozoic sample KP-15-33/3 records a ZFT age of 297 ± 33 Ma from one of the MKF sub-parallel faults in the Lesser Karatau. The ZFT age of sample KP-15-33/3 is within error of the Carboniferous $^{40}Ar/^{39}Ar$ age of 312 ± 4 Ma obtained along the TFF by Rolland et al. (2013).

Rolland et al. (2013) ascribes the presence of the Carboniferous $^{40}Ar/^{39}Ar$ age to the active, north-dipping subduction zone along the south-western margin of the Kazakhstan continent

transmitting stress along the KTF Fault (e.g. Burtman 1975, Allen et al. 2001, Alexeiev et al. 2009). As the ZFT age from the along strike sample KP-15-33/3 is within error of the Carboniferous activity of the TFF, it is likely that the Karatau MKF underwent a similar phase of cooling via exhumation due to movement along the TFF (Figure 2.1 and Figure 2.5). However, the large ZFT error range of KP-15-33/3 suggests that the Carboniferous deformation along the Karatau-Talas-Fergana fault was more limited in the Lesser Karatau, when compared to the Greater Karatau which experienced a far larger extent of late Carboniferous thrusting and folding (Allen et al. 2001, Alexeiev et al. 2009, 2017).

2.5.2 Late Permian–Early Triassic Compression

Two Neoproterozoic sandstone samples from the Lesser Karatau (KP-15-3/4 and KP-15-7/1) yielded Late Permian–Early Triassic ZFT ages (~270-240 Ma, Table ZFT). Both samples are found to the north-east of the Lesser Karatau on the margin of the Chu Sarysu Basin (Figure 2.2). Additionally, thermal history modelling from sample KP-16-15 shows a moderate rate of basement-cooling through the APAZ from ~250-230 Ma (Figure 2.4c). This indicates that the Lesser Karatau-Chu Sarysu Basin margin was exhumed through the zircon partial annealing zone, and to a lesser extent, the APAZ, around the Late Permian–Early Triassic (Figure 2.5 and 2.6).

During the Late Permian–Early Triassic, the Karatau-Talas region underwent a period of east-west shortening (Burtman 1980). The shortening is consistent with compression in the Ural collisional belt to the east of Kazakhstan, as well as the closure of the Paleo-Asian Ocean and the Tarim collision in the south (Windley et al. 2007, Xiao et al. 2009, Alexeiev et al. 2009, Glorie et al. 2010, De Grave et al. 2011, Macaulay et al. 2014, Glorie & De Grave 2016). In the Greater and Lesser Karatau, the east-west compression generated a series of north-south folds, as well as NE-SW strike slip faults, particularly along the margins of the Karatau region with both the Syr Darya and Chu Sarysu Basins (Burtman 1980, Allen et al. 2001, Alexeiev et al. 2009). Along the TFF, Rolland et al. (2013) and Konopelko et al. (2013) identified Late Permian–Early Triassic (~270-240 Ma) $^{40}Ar/^{39}Ar$ ages ascribed to the main phase of Permian dextral motion along the TFF.

The timing of the dextral motion along the TFF outlined by Rolland et al. (2013) and

Konopelko et al. (2013) coincides with the onset of the east-west compression identified by Alexeiev et al. (2009). The timing of both these events correlates with the ~270-240 Ma ZFT dates along the Lesser Karatau-Chu Sayrsu Basin, suggesting that the Late Permian–Early Triassic compression was major regional exhumation event that occur along the extent of the combined Karatau-Talas Fergana fault (Figure 2.6 Allen et al. 2006).

2.5.3 Triassic–Early Jurassic Exhumation

The Triassic–Early Jurassic (~220-190 Ma) saw a renewed drive in tectonic activity across the Tian Shan (e.g. Allen et al. 2001, De Grave et al. 2007, Xiao et al. 2009, Burtman 2010). The thermochronology of the Karatau-Talas region shows a distinct response to this regional tectonic activity. Thermal modelling from the Lesser Karatau of KP-15-38 and KP-15-9 show that the overlapping ZFT and AFT ages and long MTLs, which suggest that the Lesser Karatau underwent a period of rapid cooling in the Triassic–Early Jurassic (Figure 2.2c and Figure 2.4c). This is also illustrated by samples B15204, KP-16-20, KP-15-11/1, KP-15-33/3, and KP-16-17 which all display ~220-190 Ma AFT central ages (Table 1). Further illustrating that the Karatau, more specifically, the Lesser Karatau experienced a period of rapid, exhumation-driven basement-cooling (Figure 2.6).

Both Rolland et al. (2013) and Konopelko et al. (2013) identify Triassic to Early Jurassic (~220-180 Ma) $^{40}Ar/^{39}Ar$ ages, and suggest low-temperature ductile deformation and hydrothermal activity along the TFF as responsible for the resetting of the $^{40}Ar/^{39}Ar$ clock. While Allen et al. (2001) and Alexeiev et al. (2017) cite the formation of Early Jurassic pull apart basins such as the Leontiev Graben and the Yarkand-Fergana Basin as related to reactivation of the Karatau-Talas-Fergana fault (Figure 2.2). To the east of the KTF Fault several thermochronological and geochronological studies have identified the presence of a Triassic–Early Jurassic fast-cooling signal (Xiao et al. 2009, Glorie et al. 2010, De Grave et al. 2011, Macaulay et al. 2014, Glorie & De Grave 2016, De Pelsmaeker et al. 2018). To the west of the KTF Fault, the same signal is noted along the north-western margins of the Chatkal-Kurama and the Kyzylkum-Nurata terranes of the Middle and South Tian Shan, respectively (Jepson et al. 2018b,c). This regional deformation is attributed to the collision of the Qiangtang block, part of the Cimmerian units, transmitting stress from the Eurasian

margin along the Karatau-Talas-Fergana fault during the Late Triassic-Early Jurassic.

2.5.4 Late Jurassic–Early Cretaceous Reactivation

The Karatau-Talas region experienced a period of relative tectonic stability in the Middle Jurassic, with little notable exhumation. The stress that uplifted the Karatau in the Triassic–Early Jurassic and formed the Leontiev Graben gave way to continuing denudation of these newly uplifted ranges. During the Middle Jurassic a series of marine transgressions that took place, infilling the accommodation space generated during the Late Triassic–Early Jurassic (Allen et al. 2001, Alexeiev et al. 2017, De Pelsmaeker et al. 2018). In the Lesser Karatau, the thermal history model for sample KP-15-33/3 demonstrates this protracted cooling, likely as a response to denudation, from the Middle Jurassic through to the Early Cretaceous (Figure 2.4c and 2.6). In the mid to Late Jurassic the Karatau-Talas experienced a renewed pulse of cooling, with sample A16-34 from the Greater Karatau, samples 06-TN-11 and 06-TN-12 from the Talas region, as well sample KP-15-2/6 all show relatively fast cooling through the APAZ. Both samples A16-34, 06-TN-11, and 06-TN-12, were all taken from direct proximity to the Main Karatau Fault or the Talas Fergana Fault, suggesting that the extent of the Karatau-Talas-Fergana fault was reactivated during the Late Jurassic (Figure 2.1). The thermochronological results from the Karatau-Talas region indicate that the Middle Jurassic stability ended with a period of rapid cooling and exhumation in the Late Jurassic–Early Creataceous.

Several studies into the Tian Shan have found limited exhumation and fault activity during the Late Jurassic–Early Cretaceous, suggesting that the Tian Shan experienced a tectonic hiatus at this time (e.g. Macaulay et al. 2014, Käßner et al. 2017a, Bande et al. 2017c). While other authors have identified only minor Late Jurassic–Early Cretaceous reactivation along major faults, such as the Karatau-Talas-Fergana fault (Nachtergaele et al. 2017, De Pelsmaeker et al. 2018, Jepson et al. 2018b). However, in the south, the Tarim basin experienced fluvial Jurassic to Early Cretaceous deposition of sediments sourced from the Northern Pamir (e.g. Sobel 1999, Bershaw et al. 2012), suggesting a period of uplift and tectonism in the Pamir (Robinson 2015). In addition, Schwab et al. (2004) documented Late Jurassic cooling ages from the Central Pamir, suggesting a period of wide-spread Late

Jurassic–Early Cretaceous deformation. Previous studies into the thermo-tectonic evolution of the western Tian Shan have attributed recent (Miocene) exhumation along the KTF Fault as a response to the Cenozoic indentation of the Pamir (Sobel, Chen & Heermance 2006, Bande et al. 2017b, Nachtergaele et al. 2017). Therefore, it is likely that the Late Jurassic–Early Cretaceous basement-cooling and exhumation preserved in the north of the KTF Fault, was instigated by the tectonism experienced by the Pamir at this time being transmitted along the KTF Fault (Figure 2.6).

2.5.5 Late Cretaceous stability and Cenozoic Collision

In the middle to Late Cretaceous, the Tian Shan underwent a period of tectonic quiescence and stability in the Karatau-Talas region, with only one sample (KP-15-40) preserving a middle Cretaceous AFT age (124 ± 7 Ma) (Figure 2.2 and Table 2.1). The slow cooling of the Greater Karatau followed by an absence of Late Cretaceous–Palaeogene aged thermochronological data from both the Greater and Lesser Karatau suggest that the north-eastern extremity of the Tian Shan experienced a period of tectonic quiescence, similar to that which has been identified in the South and Middle Tian Shan (e.g. Macaulay et al. 2014, Käßner et al. 2017a, Bande et al. 2017c). In the south-western extent of the Talas-Fergana Fault, near the Tarim-Pamir contact, Sobel & Arnaud (2000) and Huang et al. (2005) identified the presence of Cretaceous $^{40}Ar/^{39}Ar$ ages. These ages were attributed to magmatism as a result of movement along the Talas Fergana Fault (Figure 2.1). This suggests that the Eurasian margin was still tectonically active during the Late Cretaceous, however the stresses generated were not causing a thermochronological impression on the Eurasian hinterland.

During the Palaeogene, the Eurasian continent underwent a period of rapid deformation as a result of the collision of India with Eurasia (Beck et al. 1995, Aitchison et al. 2007, Najman et al. 2010, van Hinsbergen et al. 2011). Resulting in reactivation and deformation of the ancestral Tian Shan, generating much of the modern topography that is present in Central Asia today. In the Karatau-Talas region the high-elevation samples in the Talas range (06-TN-09 and 06-TN-10), to the west of the Talas Fergana Fault, Kyrgyzstan host Miocene ages (Figure 2.2).

In the Middle and South Tian Shan, numerous studies have documented the thermochronological response to the India-Eurasia collision (e.g. Sobel, Oskin, Burbank & Mikolaichuk 2006, De Grave et al. 2012, Käßner et al. 2017b, Nachtergaele et al. 2017). The Kyrgyz Talas Fergana Fault has been particularly active in the Cenozoic, with much of the stress generated by the India-Eurasia collison, and subsequent Pamir indenters, transmitting the deformation along the TFF and and into the Eurasian interior (e.g. Bande et al. 2017b,c, Nachtergaele et al. 2017, De Pelsmaeker et al. 2018). The presence of young Miocene ages adjacent to Late Jurassic-Cretaceous ages (to the east if the TFF) in the Talas region show that the Karatau-Talas border represents the north-western most extent of the exhumation caused by the Cenozoic phase of collision (Figure 2.2 and Figure 2.5). Furthermore, indicating that the Palaeogene deformation generated by the India-Eurasia and the Pamir intenders collision is largely taken up by the high-elevation ranges in the Tian Shan, as the thermochronological response to the collision has not been exhumed to the surface along the Main Karatau Fault.

2.5.6 Regional Synthesis

As discussed above, the Karatau-Talas-Fergana fault is one of many north-west to south-east striking faults that dominate the Tian Shan topographic structure from the Kopet Dagh Ridge in the SW to the Sayans in the NE (Zonenshain et al. 1990, Şengör et al. 1993). Within the Tian Shan, many of these NW-SE trending structures host Cenozoic exhumation, indicating that these faults are major conduits for intracontinental stress from the Eurasian margin (e.g. De Grave et al. 2007). However, several of these major NW-SE regional faults, as well as major east-west structures, indicate Late Permian–Early Triassic deformation (Laurent-Charvet et al. 2003, de Jong et al. 2009, Wang et al. 2009, Rolland et al. 2013, Konopelko et al. 2013, De Pelsmaeker et al. 2015). The extent of this Late Permian–Early Triassic deformation is also recorded to the north of the Tian Shan, along major structures in the Urals and the West Siberian Basin (Hetzel & Glodny 2002, Buslov et al. 2003, Allen et al. 2006). These events suggest that the Eurasian continent underwent some degree of north-south compression and dextral shearing during the Late Permian–Early Triassic, indicating that the Eurasian edifice was amalgamated by the middle Permian (Rolland et al. 2013). The systematic timing of deformation and fault geometries recorded along the Karatau-Talas

Fergana Fault and across the Tian Shan suggest that the whole Eurasian edifice must have experienced a profound tectonic event at the end of the Permian, causing a large amount of deformation, to drive into the Eurasian interior along these structure-defining faults all through the Mesozoic, leaving a lasting impact that is defining the growth of Central Asia today.

In the Mesozoic, many of the NW-SE trending faults acted as conduits for the stress of the Cimmerian collisions on the Eurasian margin. Across many of the NW-SE trending structures comprise the framework of the Tian Shan, an array AFT ages have identified rapid uplift as a result of the intracontinental stresses occurring during the Mesozoic (e.g. Chen et al. 2006, Yuan et al. 2006, Zhiyong et al. 2011, De Grave et al. 2013, De Pelsmaeker et al. 2015). As a number of the NW-SE trending faults experienced a large degree of displacement during this time, which has been preserved till present day (Alexeiev et al. 2017). Thus, the intracontinental stresses that acted upon the newly formed continent during the Mesozoic were, and still remain the dominate control on the current geomorphology that is apparent today, and is preserved behind the major collision zones of the Himalaya and the Tian Shan.

2.6 Conclusion

In this study, we presented ZFT and AFT ages of 20 samples from along the Karatau-Talas region in Kazakhstan and Kyrgyzstan, in order to constrain the north-western extent of deformation in the Tian Shan. The low temperature thermochronometers identify two main phases of deformation along the Karatau-Talas Fergana Fault: (1) a Late Triassic–Early Jurassic reactivation and fast basement-cooling as a response to the Qiangtang collision on the Eurasian margin (~220-180 Ma), followed by a second (2) rapid, fault-hosted basement-cooling during the Late Jurassic–Early Cretaceous as a response to Pamir uplift and tectonism (~160-140 Ma). In addition, the Karatau-Talas region also preserves a minor signal related to the initiation of the fault in the Late Carboniferous–Early Permian post amalgamation of the Kazakhstan continent, as well as evidence of rapid cooling and deformation caused by the India-Eurasia collision in the Cenozoic. Thermochronological analysis of the Karatau-Talas region gives a more complete picture of the Mesozoic and Cenzoic tectonic evolution of the Tian Shan and Central Asia. Further emphasising the importance of under-

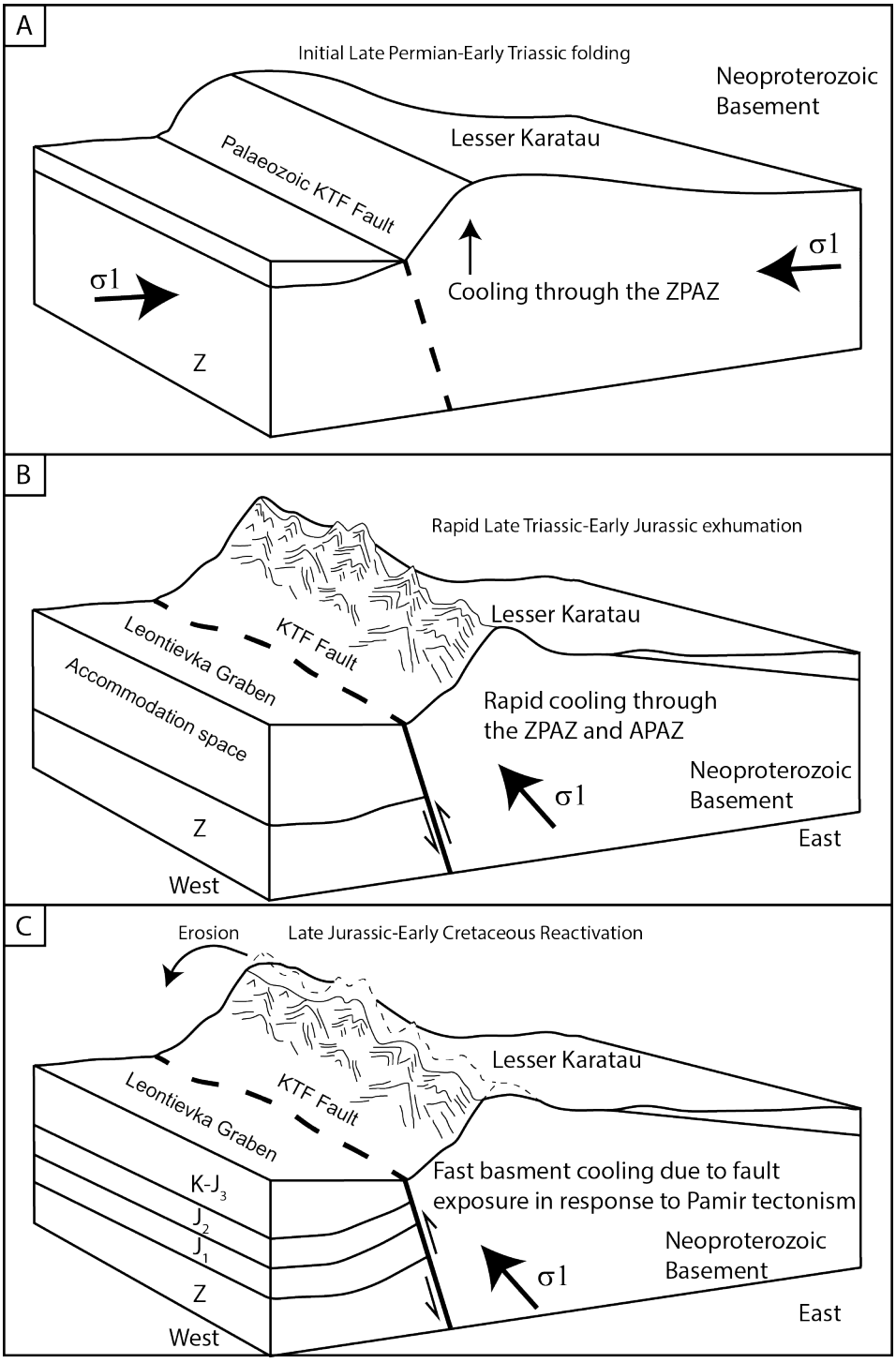

Figure 2.6: A schematic diagram highlighting the three main phases of deformation experienced by Karatau-Talas. A) Late Permian-Early Triassic folding due to east-west compression, B) Late Triassic-Early Jurassic uplift as a result of dextral movement along the Karatau-Talas Fergana (KTF) fault generating accommodation space in the Leontievka Graben and similar Early Jurassic pull-apart basins, and C) ongoing erosion of the Late Triassic-Early Jurassic uplift throughout the Jurassic followed by Late Jurassic-Early Cretaceous reactivation. Z is the Neoproterozoic, J_1 is the Early Jurassic, J_2 is the Middle Jurassic, J_3 is the Late Jurassic, and K is the Cretaceous.

standing the major geomorphological features in order to generate a model for the growth of an intracontinental tectonic setting.

Chapter 3

Low-temperature thermochronology of the Chatkal-Kurama terrane (Uzbekistan-Tajikistan): insights into the Meso-Cenozoic thermal history of the western Tian Shan

Statement of Authorship

Title of Paper	Low-temperature thermochronology of the Chatkal-Kurama terrane (Uzbekistan-Tajikistan): insights into the Meso-Cenozoic thermal history of the western Tian Shan
Publication Status	☐ Published ☐ Accepted for Publication ☑ Submitted for Publication ☐ Unpublished and Unsubmitted work written in manuscript style
Publication Details	Submitted to Tectonics

Principal Author

Name of Principal Author (Candidate)	Gilby Jepson		
Contribution to the Paper	Sample collection, sample analysis, data interpretation, and principal author of paper.		
Overall percentage (%)	70		
Certification:	This paper reports on original research I conducted during the period of my Higher Degree by Research candidature and is not subject to any obligations or contractual agreements with a third party that would constrain its inclusion in this thesis. I am the primary author of this paper.		
Signature		Date	31/08/18

Co-Author Contributions

By signing the Statement of Authorship, each author certifies that:

i. the candidate's stated contribution to the publication is accurate (as detailed above);

ii. permission is granted for the candidate in include the publication in the thesis; and

iii. the sum of all co-author contributions is equal to 100% less the candidate's stated contribution.

Name of Co-Author	Stijn Glorie		
Contribution to the Paper	Sample collection, data interpretation, and thesis supervisor.		
Signature		Date	31/08/18

Name of Co-Author	Dmitry Konopelko
Contribution to the Paper	Sample collection, data interpretation, and geological background.

Signature		Date	31/08/18

Name of Co-Author	Jack Gillespie		
Contribution to the Paper	Data interpretation		
Signature		Date	31/08/18
Name of Co-Author	Martin Danišík		
Contribution to the Paper	Data analysis, data interpretation, and methods.		
Signature		Date	31/08/18
Name of Co-Author	Rustam Mirkamalov		
Contribution to the Paper	Sample collection, data interpretation, and geological background.		
Signature		Date	31/08/18
Name of Co-Author	Yunus Mamadjanov		
Contribution to the Paper	Sample collection.		
Signature		Date	31/08/18

Name of Co-Author	Alan Collins		
Contribution to the Paper	Data interpretation, secondary supervisor.		
Signature		Date	31/08/18

Gilby Jepson, Stijn Glorie, Dmitry Konopelko, Jack Gillespie, Martin Danišík, Rustam Mirkamalov, Yunus Mamadjanov, and Alan S. Collins in submission to Tectonics

3.1 Introduction

Central Asia hosts one of the largest active intracontinental mountain belts in the world, the Tian Shan (Cawood et al. 2009). The Tian Shan is a vast mountain system that developed throughout the Mesozoic to Cenozoic as a response to tectonic forces at the distant Eurasian continental margins, and has long been studied to understand the far-field effects of continental collision (e.g. Allen et al. 1991, Hendrix et al. 1992, Jolivet et al. 2013). A number of studies have applied thermochronological techniques throughout the Tian Shan in order to constrain the timing and extent of intracontinental deformation (e.g. Sobel, Oskin, Burbank & Mikolaichuk 2006, De Grave et al. 2011, Glorie et al. 2011, Macaulay et al. 2014, Bande et al. 2017b, Glorie & De Grave 2016).

These studies demonstrated that, following the final closure of the Palaeo-Asian (or Turkestan) Ocean and amalgamation of the terranes in the late Palaeozoic, the Tian Shan experienced several major periods of cooling during the Mesozoic to Cenozoic. During the Mesozoic, distinct cooling events have been interpreted as related with exhumation in response to a number of Cimmerian collisions (e.g. the collisions of Qiangtang, Lhasa, and Karakorum with Eurasia, Dumitru et al. 2001, De Grave et al. 2013, Jolivet et al. 2013, De Pelsmaeker et al. 2015, Glorie & De Grave 2016, Käßner et al. 2017b, Gillespie et al. 2017). The subsequent Cenozoic collision of India with Eurasia not only generated the Himalayas and the uplift of the Tibetan plateau, but is also thought to have driven uplift and deformation in the Asian continental interior, including the Tian Shan and other intracontinental mountain ranges (e.g. Molnar & Tapponnier 1975, Clift et al. 2002, Bouilhol et al. 2013). Cenozoic cooling and exhumation is mainly recorded in close vicinity to major faults within the Tian Shan (e.g. Glorie et al. 2011, De Grave et al. 2012, Macaulay et al. 2014, Glorie & De Grave 2016, Bande et al. 2017b). While the thermochronology of most of the central Tian Shan (within Kyrgyzstan and China, to the east of the Talas Fergana Fault) has been extensively studied (Figure 3.1), such studies currently do not account for

the western-most expression of the Tian Shan. A recent study by Bande et al. (2017b) investigated the thermochronology of the Kyrgyz Chatkal ranges (Figure 3.1) and obtained mainly Cenozoic cooling ages (*ca.* 50-15 Ma), reflecting exhumation as a response to the indentation of the Pamir terrane. In this study, we apply low-temperature thermochronology to the Chatkal-Kurama terrane within western Uzbekistan and northern Tajikistan (west of the area studied by Bande et al. 2017b), plugging a critical gap in the thermochronological coverage of the region and developing a more complete picture of the thermal history of the western Tian Shan.

3.2 Geological Background

The ancestral Tian Shan formed in the late Palaeozoic during the closure of the Palaeo-Asian Ocean (PAO) and the subsequent collision of the Tarim Precambrian microcontinent with the southern margin of the early Palaeozoic Kazakhstan continent (e.g. Windley et al. 2007, Biske & Seltmann 2010, Xiao et al. 2013, Burtman 2015). The western part of the Tian Shan (within Tajikistan, Uzbekistan, Kyrgyzstan, and Kazakhstan) is traditionally subdivided into three major tectonic terranes: (1) the Northern Tian Shan, representing the deformed margin of the Palaeo-Kazakhstan microcontinent; (2) the Middle Tian Shan, composed of a Precambrian microcontinental sliver and a superimposed island-arc; and (3) the Southern Tian Shan, a late Palaeozoic fold-and-thrust belt (Figure 3.1, Biske & Seltmann 2010, Burtman 2015). These east-west trending linear terranes are cut by the north-west trending Talas-Fergana Fault with a total dextral offset of ~200 km (Figure 3.1, Burtman et al. 1996).

Our study area, the Chatkal-Kurama terrane, forms part of the Middle Tian Shan (MTS) that is exposed west of the Talas-Fergana Fault (TFF, Figure 3.1, e.g. Windley et al. 2007). The Chatkal-Kurama terrane formed due to the accretion of an island arc (locally known as the Chatkal Arc) onto the passive southern margin of the Palaeo-Kazakhstan during the late Ordovician (Alexeiev et al. 2016). This accretion caused the Chatkal arc to become the southern active margin of the Palaeo-Kazakhstan continent during the late Silurian – early Devonian, resulting in the generation of thick supra-subduction magmatic series (Konopelko

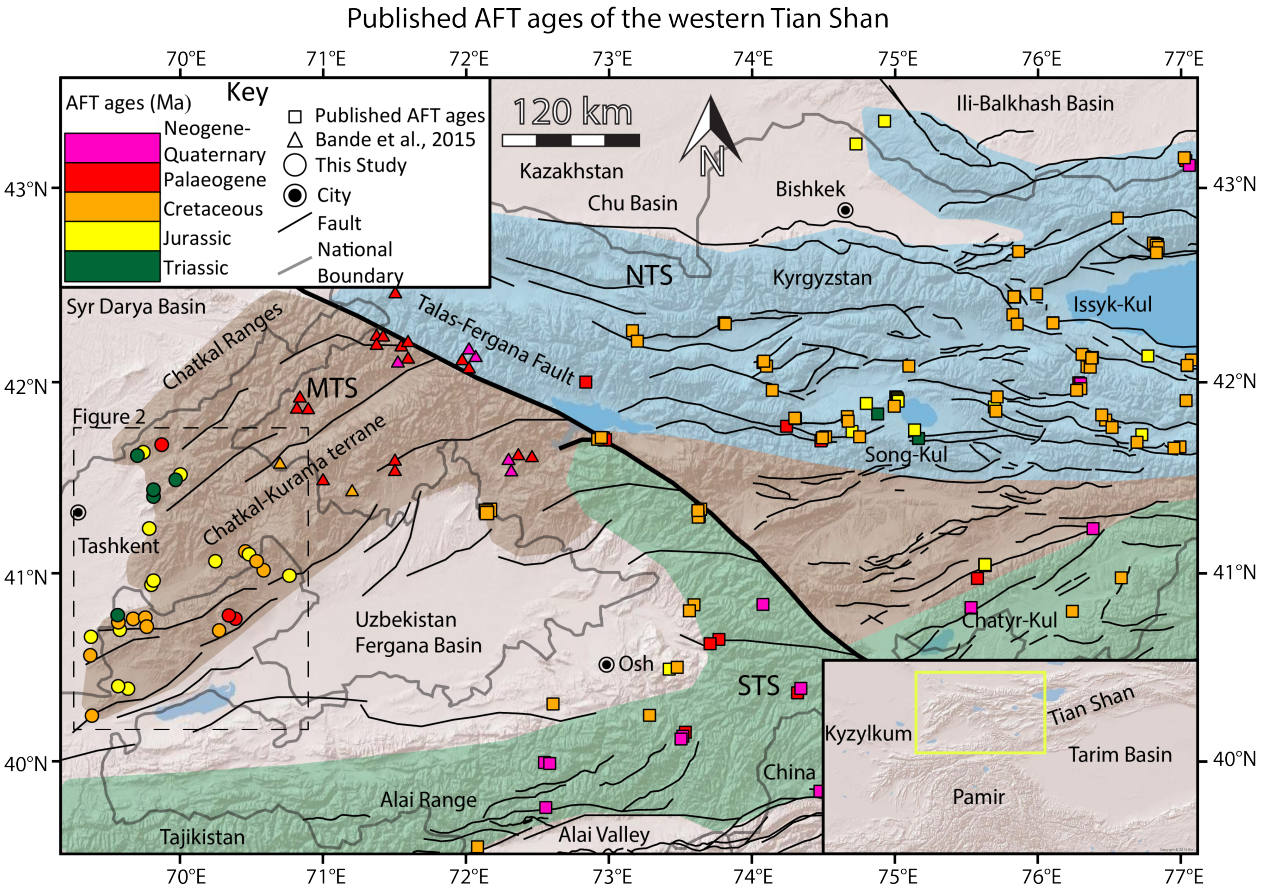

Figure 3.1: A shaded relief map of the western extent of the Tian Shan displaying published Mesozoic apatite fission track (AFT) ages for the region (colour coded following AFT central ages). Circle symbols represent sample location for data obtained in this study, triangles represent locations for data obtained by Bande et al. (2017b) (both to the west or in close proximity to the Talas-Fergana fault). Square symbols represent locations for published AFT ages from Sobel, Chen & Heermance (2006), Sobel, Oskin, Burbank & Mikolaichuk (2006), Glorie et al. (2010), De Grave et al. (2013), Macaulay et al. (2014), De Pelsmaeker et al. (2015), Käßner et al. (2017a), Bande et al. (2017c) and Nachtergaele et al. (2017). The Northern Tian Shan is denoted by NTS (shaded blue), the Middle Tian Shan by MTS (shaded brown), and the South Tian Shan by STS (shaded green).

et al. 2017a, Dolgopolova et al. 2017). During the Middle Devonian-early Carboniferous subduction halted and was followed by the deposition of carbonate sediments in a passive margin or transform fault environment, which were subsequently uplifted and eroded (Dolgopolova et al. 2017). Subduction under the southern margin of the Chatkal-Kurama terrane resumed in the early to middle Carboniferous, generating voluminous Andean-type intrusions and volcanics. This magmatic series, with ages in the range of *ca.* 320-300 Ma, comprise the majority of the Chatkal-Kurama terrane (Figure 3.2 Konopelko et al. 2017a, Dolgopolova et al. 2017). The subsequent closure of the Palaeo-Turkestan Ocean in the late Carboniferous resulted in voluminous, *ca.* 300-285 Ma post-collisional, granitoid magmatism during the Early Permian (Biske & Seltmann 2010, Seltmann et al. 2011, Konopelko et al. 2017a, Dolgopolova et al. 2017).

The Mesozoic history of the Tian Shan is dominated by deformation caused by the collision of Cimmerian continental fragments with the southern margin of Eurasia (e.g. De Grave et al. 2012, Käßner et al. 2017a). This period of Mesozoic deformation was initiated by the closure of the Palaeo-Asian Ocean (PAO) at the end of the Permian to the earliest Triassic (e.g. Xiao et al. 2009, Li et al. 2016). Subduction of the Palaeo-Tethys beneath Eurasia initiated in the Triassic, leading to the collision of the Qiangtang block to the southern Eurasian margin, which is thought to have induced extensive deformation to the Tian Shan (e.g. Ratschbacher et al. 2003, De Grave et al. 2011, Robinson 2015, Glorie & De Grave 2016). Subduction and accretion to the southern margin of Eurasia continued further south during the Jurassic and Early Cretaceous, culminating in the final closure of the Palaeo-Tethys Ocean (e.g. Kapp et al. 2007, Robinson 2015). Rapid Late Jurassic–Cretaceous cooling has been documented for the Kyrgyz Tian Shan (to the east of the TFF, e.g. De Grave et al. 2013, Nachtergaele et al. 2017). In contrast, the extent of Jurassic and Cretaceous cooling in the western-most Tian Shan (to the west of the TFF) is poorly defined. During the Late Jurassic–Early Cretaceous, coal deposits formed along the eastern margin of the Chatkal-Kurama terrane (Angren, Figure 3.2), suggesting a marine environment (Ahmedov 2000, Dill et al. 2008). To the south, the Fergana Basin (Figure 3.1), is characterised by basal sections of Jurassic conglomerate fining upward into Jurassic and Cretaceous sedimentary sequences, indicating that the Fergana Basin experienced marine incursions of the Paratethyan Sea

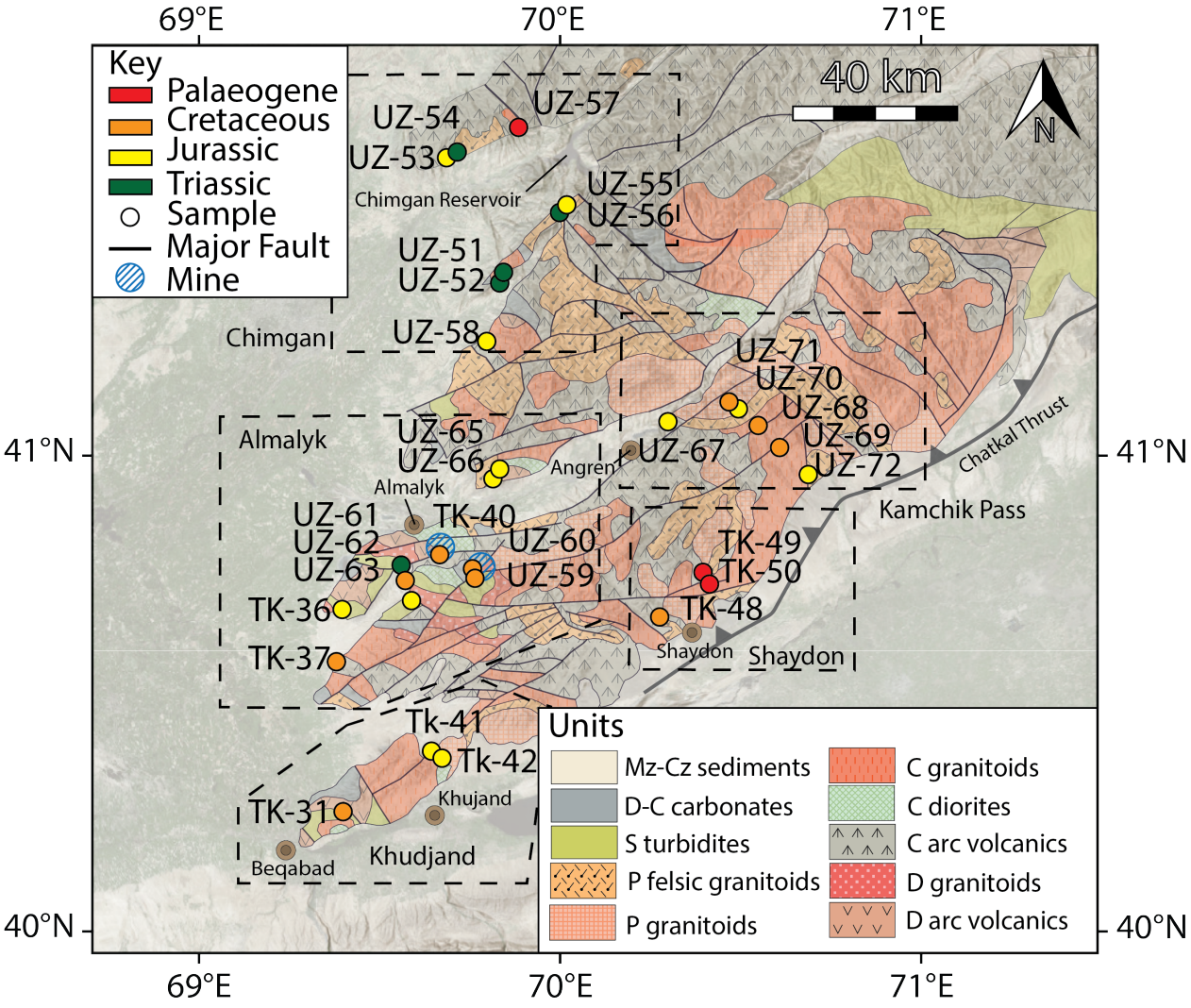

Figure 3.2: Geological map of the Chatkal-Kurama terrane modified from Dolgopolova et al. (2017). The map displays the locations for the apatite fission track (AFT) data obtained in this study. Sample symbols are colour coded following AFT central ages. A detailed summary of the AFT data is available in Appendix File G. *Mz* is the Mesozoic, *Cz* is the Cenozoic, *D* is Devonian, *C* is the Carboniferous, *S* is the Silurian, and *P* is the Permian.

(Burov & Molnar 1998, Bande et al. 2017b, De Pelsmaeker et al. 2018, Nachtergaele et al. 2017). Detailed analysis of the Late Cretaceous marine sediments suggested that the region was covered by a marine environment at least twice, once in the Turonian and again in the Maastrichtian (Ahmedov 2000).

During the Cenozoic, the Tian Shan experienced renewed deformation, generating much of the high relief that can be found today. Many authors have identified a dominant Cenozoic cooling signal within the Tian Shan, which is thought to be related with the India-Eurasia collision and subsequent Pamir indentations with the Eurasian margin (e.g. Molnar & Tapponnier 1975, Sobel, Chen & Heermance 2006, Aitchison et al. 2007, De Grave et al. 2007). In the western Tian Shan, previous studies have identified initiation of exhumation at *ca.* 30-20 Ma and accelerating of exhumation since *ca.* 15-10 Ma, which correlates with periods of Pamir convergence (e.g. Käßner et al. 2017b, Bande et al. 2017c, Jepson et al. 2018a).

3.3 Methodology

New thermochronological data for 30 granitoid rock samples from the western Tian Shan are presented (Figure 3.2). Three different thermochronological methods were applied; (1) zircon (U-Th-Sm)/He dating (closure temperature ~180°C; Reiners et al. 2002), (2) apatite fission track thermochronology (partial annealing zone ~120-60°C; Wagner & Van den haute 1992) and (3) apatite (U-Th-Sm)/He dating (closure temperature ~80-40°C, Zeitler et al. 1987).

3.3.1 Apatite fission track analysis (AFT)

The apatite fission track method is based on the temperature dependent annealing of mineral lattice damage features, known as 'fission tracks', that are created by the spontaneous decay of ^{238}U (Wagner & Van den haute 1992). Fission tracks record the thermal history of a rock sample through the apatite partial annealing zone (APAZ) of ~120-60°C (Green 1986). Apatite grains were picked and mounted in epoxy resin, then polished to expose internal sections, and were subsequently chemically etched in a 5M HNO_3 solution for 20s at 20°C to reveal the natural spontaneous fission tracks. Fission track analysis was performed at The

University of Adelaide using an Autoscan system. The concentration of uranium (^{238}U) and chlorine (^{35}Cl) of each apatite grain was measured using Laser Ablation-Inductively Coupled Plasma-Mass Spectrometry. Data reduction was performed in Iolite using the Trace Elements DRS (Paton et al. 2011). Instrumental drift correction was carried out using Madagascar apatite as an external standard, and elemental concentrations were calculated using ^{43}Ca as the internal standard. Age calculation was carried out as described in Hasebe et al. (2004) and De Grave et al. (2012), using the Durango apatite (McDowell et al. 2005) to perform a ζ-calibration (Vermeesch 2017). A duplicate sample was made for TK-50 and irradiated using californium (^{252}Cf) at The University of Melbourne in order to increase the likelihood of measuring a sufficient amount of confined tracks for thermal history reconstructions (Donelick & Miller 1991). For a detailed methodology see Glorie et al. (2017) and Gillespie et al. (2017).

3.3.2 Apatite and zircon (U-Th-Sm)/He

The (U-Th-Sm)/He thermochronometers are based on the diffusivity of ^{4}He. The thermal sensitivity for apatite helium (AHe) is 80-40°C, making it valuable for constraining the most recent thermal cooling event (Zeitler et al. 1987, Farley 2002). For zircon, the thermochronometer records the thermal history at ~190-170°C (Reiners et al. 2002, Guenthner et al. 2013). The (U-Th-Sm)/He analyses for this study were undertaken at the John de Laeter Centre, Curtin University and followed the protocols described in (Danišík et al. 2012).

Apatite and zircon crystals were hand-picked following the recommendations of Farley (2002), photographed and measured for physical dimensions, before being loaded in Pt (apatite) and Nb (zircon) microtubes. Helium (^{4}He) was extracted from apatite at ~900°C, under ultra-high vacuum using a diode laser and measured by isotope dilution on a Pfeiffer Prisma QMS-200 mass spectrometer. A "re-extract" was run after each sample to verify complete outgassing of the crystals. Helium gas results were corrected for blank, determined by heating empty microtubes using the same procedure. After the ^{4}He measurements, tubes containing the crystals were retrieved from the laser cell, spiked with ^{235}U and ^{230}Th and dissolved. Sample, blank, and spiked standard solutions were analysed by isotope dilution for ^{238}U and

^{232}Th, and by external calibration for ^{147}Sm on an Agilent 7500 ICP-MS. The total analytical uncertainty (TAU) was calculated as a square root of sum of squares of uncertainty on He and weighted uncertainties on U, Th, Sm and He measurements, and is typically <5% (1σ). The raw (U–Th-Sm)/He ages were corrected for alpha ejection (F_{T} correction) after Farley et al. (1996), whereby a homogenous distribution of U, Th and Sm was assumed for the crystals. Replicate analyses of internal standard Durango apatite (n=10) measured over the period of this study, yielded mean (U–Th–Sm)/He ages of 31.9 ± 1.9 Ma (1σ), consistent with the reference Durango (U–Th–Sm)/He age of 31.02 ± 1.01 Ma (McDowell et al. 2005). For the Fish Canyon zircon, we acquired 28.6 ± 0.8 Ma (n=10), which is in excellent agreement with the reference age of (Reiners 2005) at 28.3 ± 1.3 Ma.

3.3.3 Thermal History Modelling

Thermal history modelling was performed on a total of 24 samples, with a sufficient number of confined tracks (>10, although less tracks indicates less precision). The QTQt software (version 5.5.0) was applied, which uses Bayesian trans-dimensional Markov Chain Monte Carlo statistics to determine models for the cooling pathway of the sample (Gallagher 2012). Along with the confined track length, individual AFT, AHe, and ZHe ages were used in the modelling procedure. The concentration of ^{35}Cl was used as a kinetic parameter (Donelick et al. 2005). More details on the modelling approach can be found in (Gallagher 2012) and (Gillespie et al. 2017).

3.4 Results

For a systematic and thorough discussion, the results for the 30 samples in this study will be subdivided into five groups based on regional proximity to each other (Figure 3.2). The groups are named after nearby towns or mountain passes and will be discussed from north to south, and are as follows: (1) Chimgan, (2) Kamchik Pass, (3) Almalyk, (4) Shaydon, and (5) Khudjand (Figure 3.2). Tables 3.1 and 3.2 summarise the AFT and (U-Th-Sm)/He data. Detailed tables and figures for all single grain AFT, (U-Th-Sm)/He, mean track length (MTL) data and individual thermal history models are available in Appendix files G, H, I, J, K, and L.

Table 3.1: A summary table of the apatite fission track data(AFT): n is the number of grains analysed per sample and # of lengths is the number of confined track lengths idenfied in each sample. Elev is elevation in meters, age is the AFT central age in Ma, MTL is the mean track length in μ, and # is the number of confined tracks measured for each sample.

Sample	Lat	Long	Elev	n	Age	$\pm1\sigma$	#	MTL	$\pm1\sigma$
Chimgan									
UZ-51	41.391	69.857	1919	32	225.0	6.8	65	12.4	1.2
UZ-52	41.395	69.861	1769	5	235.0	20.0	-	-	-
UZ-53	41.629	69.725	1524	38	154.2	5.5	115	12.1	1.5
UZ-54	41.628	69.724	1109	37	207.2	4.4	170	12.4	1.1
UZ-55	41.528	70.024	1396	33	174.0	10.0	34	12.0	1.7
UZ-56	41.517	70.014	1909	34	218.9	6.3	64	12.7	1.3
UZ-57	41.684	69.894	1438	22	28.5	3.7	45	12.7	1.5
UZ-58	41.245	69.808	1207	31	171.3	7.5	31	12.7	1.6
Kamchick Pass									
UZ-67	41.072	70.271	1136	37	199.6	8.4	18	12.0	1.5
UZ-68	41.073	70.558	2139	27	135.0	12.0	24	11.8	1.1
UZ-69	41.027	70.609	1688	19	94.4	6.1	18	11.2	1.7
UZ-70	41.110	70.505	2061	27	156.0	15.0	13	11.4	1.2
UZ-71	41.125	70.479	1620	31	96.8	5.0	36	12.1	1.8
UZ-72	40.997	70.789	1530	41	167.0	12.0	63	12.1	1.4
Almalyk									
UZ-59	40.775	69.778	1041	31	100.0	9.1	27	11.7	1.6
UZ-60	40.768	69.781	1222	39	141.4	8.4	51	12.4	1.3
UZ-61	40.772	69.586	705	38	205.8	6.4	34	12.9	1.0
UZ-62	40.752	69.591	752	28	143.8	8.6	66	13.0	1.2
UZ-63	40.712	69.603	878	39	182.0	9.8	56	12.8	1.2
UZ-65	40.950	69.824	827	17	187.0	14.0	17	12.4	1.0
UZ-66	40.971	69.838	915	31	196.0	12.0	61	12.9	1.0
TK-36	40.674	69.401	540	28	183.0	11.0	63	13.1	0.9

TK-37	40.576	69.396	489	35	103.6	5.1	14	12.0	2.2
TK-40	40.799	69.690	864	14	116.1	5.5	-	-	-
Shaydon									
TK-48	40.678	70.292	1024	22	124.0	12.0	-	-	-
TK-49	40.746	70.426	1192	10	32.0	10.0	-	-	-
TK-50	40.768	70.410	1304	33	31.4	3.4	20	12.7	0.8
Khudjand									
TK-31	40.254	69.408	500	40	131.0	5.0	75	11.9	1.5
TK-41	40.397	69.660	633	34	163.9	4.8	99	13.3	1.1
TK-42	40.379	69.683	540	20	176.0	10.0	-	-	-

3.4.1 Chimgan region

Eight granitoid samples were collected in the southern Chatkal Mountains surrounding Chimgan reservoir, in the north of our study area (Figure 3.2). The majority of samples from the Chimgan region display a Triassic AFT central age. Samples UZ-52, UZ-54, and UZ-56 yield unimodal AFT ages of 235 ± 20 Ma, 207 ± 4 Ma, and 219 ± 6 Ma respectively (Table 3.1). Samples UZ-54 and UZ-56 produced mean track lengths (MTL) of 12.4 ± 1.1 μm and 12.7 ± 1.3 μm. Sample UZ-51 displays a slightly bimodal age distribution, with 80% of the single grain ages preserving a similar Triassic age (225 ± 7 Ma) and 20% of single grain ages recording a Palaeogene signal (*ca.* 52 ± 5 Ma, Appendix File G). Samples UZ-53, UZ-55, and UZ-58, which were sampled at slightly lower elevations (Table 3.1), yield ages of 155 ± 6 Ma, 174 ± 10 Ma, and 171 ± 8 Ma. Furthermore, they display reduced MTL values and broader confined track length distributions compared to the Triassic samples (Table 3.1 and Appendix File G). The most northerly sample (UZ-57), which was sampled in the Chatkal Ranges (an area of slightly higher relief; ~2000m, Figure 3.1), gave a younger AFT central age of 29 ± 4 Ma, with a MTL of 12.7 ± 1.5 μm (Table 3.1 and Appendix File G).

3.4.2 Kamchik Pass transect

A series of samples were taken over an elevation profile across Kamchik Pass across the eastern limb of the Chatkal-Kurama terrane (Figure 3.2). In total, six granitoid samples were taken with a minimum of ~150m vertical distance between neighbouring samples, and were grouped into the Kamchik Pass transect.

The AFT central ages from the Kamchik Pass samples can be separated into Jurassic and Cretaceous ages. Sample UZ-67, east of the main sample transect, produced an AFT central age of 200 ± 8 Ma and a MTL of 12.0 ± 1.5 μm. Samples UZ-70 and UZ-72 were taken at low elevations along the Kamchik pass transect and yielded Jurassic central ages of 156 ± 15 Ma and 167 ± 12 Ma (Figure 3.2). The MTL for the sample that produced a Middle Jurassic AFT age (UZ-72) is slightly longer compared to the Late Jurassic AFT sample (UZ-70) (Table 3.1 and Appendix File G). Samples UZ-68, UZ-69, and UZ-71 yielded Cretaceous AFT ages of 135 ± 12 Ma, 94 ± 6 Ma, and 97 ± 5 Ma, respectively (Table 3.1 and Figure 3.2). The three Cretaceous AFT age samples yielded, on average, shorter MTLs compared to the Jurassic AFT samples (Table 3.1 and Appendix File G). The samples along Kamchik Pass show no clear age-elevation relationship. Based on apatite quality, sample UZ-69 was selected for AHe analysis and yielded a Cenozoic AHe age of 13.5 ± 1.3 Ma, which is significantly younger than the AFT ages obtained for Kamchik Pass (Table 3.2 and Appendix File H).

Table 3.2: Mean zircon (U–Th–Sm)/He and apatite (U–Th–Sm)/He age and chemistry data. For single grain analysis, see Appendix File H. Concentrations of thorium, uranium and samarium in ng. He is the concentration of helium measured in ncc. Th/U is the ratio of thorium to uranium. Raw is the age before the F_{T} correction is made. F_{T} is the alpha-ejection correction parameter of Farley et al. (1996). Age is the Cor. age after applying the F_{T} correction. TAU is the total analytical uncertainty in (%).

Sample	^{232}Th±(%)	^{238}U±(%)	^{147}Sm±(%)	He±(%)	TAU	Th/U	Raw±1σ	F_{T}	Age±1σ
Zircon (U-Th-Sm)/He Data									
TK-42	1.132±1.4	2.683±1.9	0.002±18.2	53.137±1.0	2.0	0.5	159.5±3.2	0.70	229.0±6.2
TK-36	1.077±1.4	4.027±1.9	0.002±14.9	93.629±0.7	2.0	0.3	179.9±3.5	0.72	244.4±8.1
Apatite (U-Th-Sm)/He Data									
UZ-69	0.111±3.8	0.051±4.0	0.022±0.3	0.075±2.4	3.8	2.2	8.0±0.3	0.60	13.5±1.3
TK-50	0.119±3.9	0.067±4.1	0.041±0.2	0.175±2.2	4.0	1.8	12.7±0.5	0.69	18.2±1.2
TK-49	0.056±4.1	0.039±4.2	0.011±0.4	0.130±2.1	4.0	1.4	20.8±0.8	0.53	27.5±2.5
TK-41	0.143±5.2	0.067±5.3	0.021±0.4	1.000±2.6	4.9	2.3	69.1±3.5	0.65	125.8±6.3
TK-36	0.097±4.7	0.093±4.9	0.014±0.4	1.500±2.7	4.9	1.0	110.5±5.3	0.71	178.6±8.9

3.4.3 Almalyk region

Ten samples were taken from mineral deposit hosting regions surrounding the town of Almalyk (Figure 3.2). This includes two samples taken in close vicinity to the Sari-Cheku porphyry copper-gold deposit (UZ-59 and UZ-60), and one sample from just south of the Kalmakyr porphyry deposit (TK-40, Seltmann & Porter 2005).

The AFT central ages obtained for the ten samples produced one Late Triassic age, four Jurassic ages, and five Cretaceous ages. A Late Triassic AFT age was obtained for sample UZ-61 of 206 ± 6 Ma. The four Jurassic AFT ages are recorded by UZ-63, UZ-65, UZ-66, and TK-36, displaying ages of 182 ± 10 Ma, 187 ± 14 Ma, 196 ± 13 Ma, and 183 ± 11 Ma. The three samples that were taken near mineral deposits yielded Late Cretaceous ages. Samples TK-40, UZ-59, and UZ-60 gave AFT ages of 116 ± 6 Ma, 100 ± 9 Ma, and 141 ± 8 Ma. Away from the deposits, Cretaceous AFT ages were recorded for samples TK-37 and UZ-62, with central ages of 104 ± 5 Ma and 144 ± 9 Ma (Table 3.1 and Figure 3.2). Based on apatite and zircon quality, two samples were selected for AHe analysis and one sample was selected for ZHe analysis. Sample TK-40 produced an AHe age of 143 ± 7 Ma, which is slightly older than its AFT age of 116 ± 6 Ma. The AHe age for TK-36, calculated as 179 ± 9 Ma, is within error to its AFT age of 183 ± 11 Ma. Sample TK-36 was also selected for ZHe analysis yielded an age of 244 ± 8 Ma (Table 3.2). The Late Triassic–Early Jurassic samples of TK-36, UZ-61, UZ-63, UZ-65, and UZ-66 yielded, on average, longer MTLs when compared to the slightly shorter MTLs obtained by the Cretaceous samples UZ-59, UZ-60, and UZ-62 (Table 3.1 and Appendix File J).

3.4.4 Shaydon region

The Shaydon region consists of three samples that were taken near the village of Shaydon, Tajikistan (Figure 3.2). Sample TK-48 yielded a Cretaceous central age of 124 ± 12 Ma. Samples TK-49, and TK-50 both yielded consistent Palaeogene AFT ages of 32 ± 10 Ma, and 31 ± 3 Ma (Table 3.1). AHe analysis was performed on both Palaeogene AFT age samples. For sample TK-49, an Oligocene AHe age of 28 ± 3 Ma was obtained that is within error to its AFT age, and for sample TK-50, and a Miocene AHe age of 18 ± 1 Ma was obtained, which is slightly younger than its corresponding AFT age (Table 3.2). Sample TK-50 was

selected for ^{252}Cf irradiation to obtain a sufficient quantity of confined tracks, producing a MTL of 12.7 ± 0.8 μm (Table 3.1).

3.4.5 Khudjand region

The Khudjand region represents the most south-western extent of the Chatkal-Kurama terrane, from which three samples were taken (TK-41, TK-42, and TK-31). Samples TK-41, and TK-42 both yielded Jurassic AFT central ages of 164 ± 5 Ma and 176 ± 10 Ma. For sample TK-41, a MTL of 13.3 ± 1.1 μm was obtained. In contrast, sample TK-31, generated a Cretaceous AFT age of 131 ± 5 Ma and a shorter MTL of 11.9 ± 1.5 μm (Table 3.1). Based on apatite quality, sample TK-41 was selected for AHe analysis, producing a Cretaceous age of 126 ± 14 Ma that is slightly younger than its corresponding AFT age of 164 ± 5 Ma. Sample TK-42 was selected for ZHe analysis, yielding a Triassic age of 229 ± 6 Ma (Table 3.2).

3.4.6 Thermal history models

Thermal history models were produced for samples with a sufficient quantity of confined tracks (>10, Table 3.1 and Appendix File K). Of the 30 samples analysed in this study, 24 were suitable for thermal history modelling. Figure 3.3 displays all time-temperature models calculated for the Chatkal-Kurama terrane. Detailed individual thermal models for each sample and modelling parameters are available in Appendix File K and L.

The thermal history models in this study show a distinct relationship between samples with a similar AFT age and the rate of cooling for the thermal pathway obtained. The Triassic AFT age samples UZ-51, UZ-54, and UZ-56 from the Chimgan region and sample UZ-61 from the Almalyk region (green models in Figure 3.3) display rapid cooling through the APAZ during the Triassic (*ca.* 250-220 Ma) followed by a long period of thermal stability during most of the Mesozoic and Cenozoic. The Triassic-aged thermal history models for samples UZ-51 and UZ-54 show a return to the APAZ before a subsequent cooling pulse since *ca.* 25 Ma, however, this is not well pronounced in the models (Figure 3.3). The thermal history models for the Early Jurassic AFT age samples TK-36, UZ-63, UZ-65, and UZ-66 from the Almlyk region and sample TK-41 from the Khudjand region (yellow models in Figure 3.3)

show cooling through the APAZ during the latest Triassic–Early Jurassic (*ca.* 215-190 Ma). The Jurassic AFT samples display a similar thermal history to the models obtained for the Triassic AFT age samples, relatively fast cooling in the Early Jurassic, followed by thermal quiescence (or slight reheating) during most of the Late Jurassic–Palaeogene. Several samples were affected by renewed cooling since *ca.* 35 Ma. The Late Jurassic AFT samples UZ-53, UZ-55, and UZ-58 from the Chimgan region, and samples UZ-67, UZ-70, and UZ-72 from the Kamchik Pass all display very similar thermal history models to those obtained for the Lower Jurassic AFT samples. However, the initial cooling during the Jurassic through the APAZ was slower. The Cretaceous AFT age samples UZ-69, UZ-69, and UZ-71 from the Kamchik Pass, samples UZ-59, UZ-60, and UZ-62 from the Almalyk region, and sample TK-31 from the Khudjand region (orange models in Figure 3.3), display rather slow cooling and increased residence time in the APAZ during the Cretaceous, followed by a renewed onset of cooling since *ca.* 30 Ma. Finally, the two Cenozoic samples, UZ-57 from the Chimgan region, and TK-50 from the Shaydon region (red models in Figure 3) both display fast cooling through the APAZ since *ca.* 35 Ma (Figure 3.3 and Appendix File K). In summary, the thermal history models indicate rapid cooling during the Triassic–Early Jurassic (*ca.* 250-190 Ma), slow cooling or thermal quiescence during the Late Jurassic–Palaeogene and renewed cooling during the Neogene (*ca.* 35-25 Ma).

3.5 Interpretation and discussion

3.5.1 Thermochronological interpretations

The sample locations within the Chatkal-Kurama terrane range from the south-western margin of the terrane, near Khudjand, to the Uzbekistan-Kazakhstan border around the Chimgan reservoir in the north (Figure 3.2). Over this geographic extent, the obtained AFT ages display a clear younging trend from the north-west to the south-east. The oldest (Triassic) AFT ages from the Chatkal-Kurama terrane were obtained on the north-western margin. Towards the south-east, a mixture of Jurassic and Cretaceous AFT ages were obtained, with Cretaceous ages becoming more abundant further south and near the mineral deposits in the Almalyk region. The youngest AFT ages identified in this study were obtained

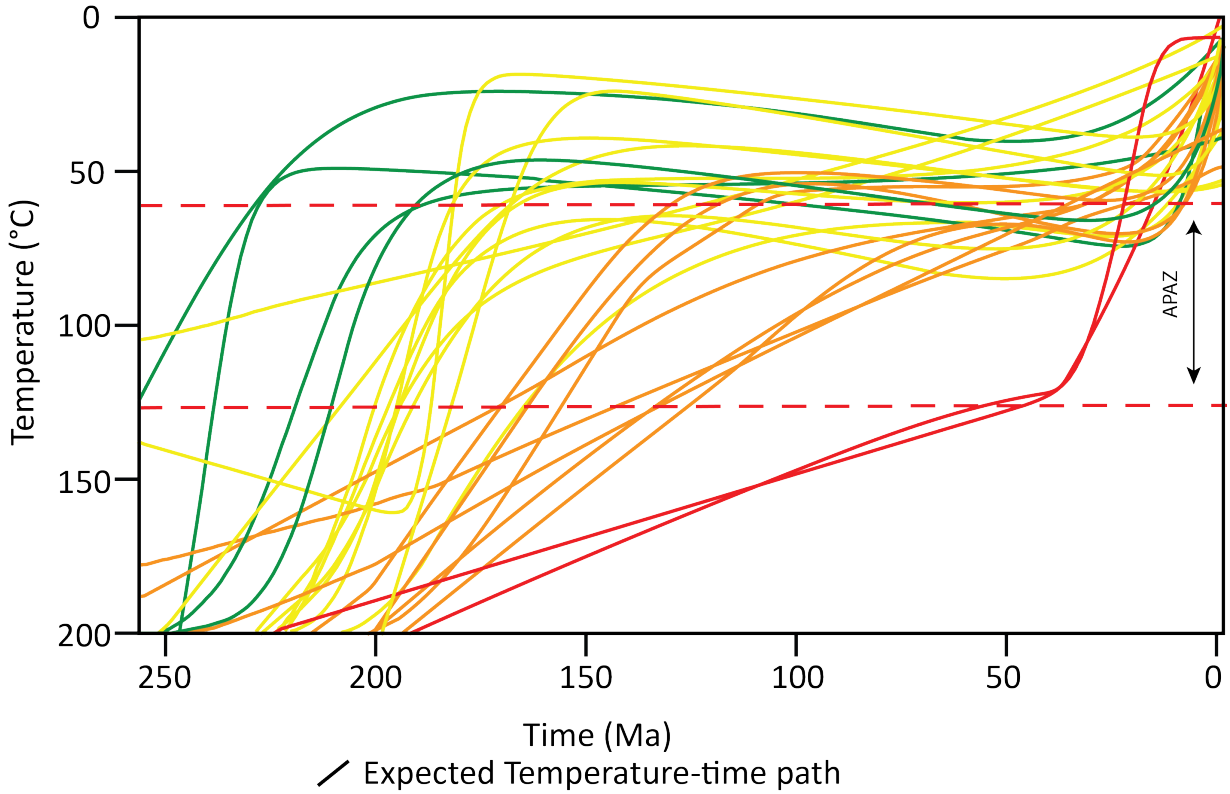

Figure 3.3: A plot displaying the modelled temperature-time paths for all samples within the Chatkal-Kurama terrane that yielded sufficient confined track data for modelling purposes. Modelling was performed using QTQt Gallagher (2012). Where available apatite and zircon (U-Th-Sm)/He data was incorporated into its respective thermal history model. The temperature-time path is coloured according to apatite fission track central age; green is Triassic, yellow is Jurassic, orange is Cretaceous, and red is Palaeogene. The red-dashed line represents the apatite partial annealing zone (APAZ). This figure demonstrates the relationship between Cretaceous apatite fission track age and increased residence time in the apatite partial annealing zone. Individual sample histograms and temperature-time plots are available in Appendix Files J and K, the used criteria for thermal modelling are tabulated in Appendix File L.

in the north of the study area (in the Chatkal Ranges) and in the south-east of the Chatkal-Kurama terrane, at the margin of the Fergana Basin (Figure 3.2).

As illustrated by the thermal history models (Figure 3.3), the Triassic and Early Jurassic AFT age samples cooled rapidly to the surface at that time and remained unaffected by any later thermal activity. The mid to Late Jurassic and Cretaceous AFT age samples underwent more protracted residence in the APAZ and partially record the subsequent Cenozoic cooling identified in the Cenozoic AFT age samples. This pattern can be illustrated by plotting the MTL values for each sample against their corresponding AFT central ages (Figure 3.4). In this plot, our new data from the Chatkal-Kurama terrane is combined with Bande et al. (2017b) from the adjoining Chatkal Ranges in western Kyrgyzstan, and display a characteristic 'boomerang' trend (Green et al. 1986, Gallagher 2012). The longer MTLs suggest faster cooling, while shorter MTLs reflect prolonged residence in the APAZ. The 'boomerang plot' demonstrates that the Triassic and Early Jurassic AFT ages are indicative of a significant thermal event at that time. The Late Jurassic and Cretaceous AFT ages correspond to shorter MTLs and are thus, slowly cooled APAZ residence ages. In the Late Palaeogene, the 'boomerang' begins to curve back up towards longer MTLs, suggesting the start of a second thermal event (Figure 3.4). The latter event is better exposed in the higher relief of the Chatkal Ranges (Figure 3.1, Bande et al. 2017b), but also the south-eastern margin on the Chatkal-Kurama terrane, along the Fergana basin margin.

The (U-Th-Sm)/He data obtained in this study further illustrate the two thermal events that were identified in the boomerang plot and thermal history models (during the Triassic and Late Palaeogene–Early Neogene, Figure 3.3 and Figure 3.4). The ZHe ages (*ca.* 250-225 Ma, TK-42 and TK-36) are in agreement with the Triassic AFT ages obtained from sample TK-42. Additionally, sample TK-36 yielded an Early Jurassic AHe age (*ca.* 180 Ma) that is within error to its corresponding AFT age (183 ± 11 Ma, Table 3.2 and Figure 3.4). These results strengthen the claim that the Chatkal-Kurama terrane underwent fast cooling during the Triassic–Early Jurassic. Sample TK-41 and TK-40 yielded scattered Late Jurassic–Cretaceous AHe ages which were significantly younger or older than their corresponding AFT age (163 ± 5 Ma), suggesting slow cooling at that time (Table 3.2 and Appendix File H). Late Palaeogene–Early Neogene AHe ages (*ca.* 28-14 Ma, UZ-69, TK-

49, and TK-50) chronologically match corresponding AFT ages (*ca.* 31 Ma), suggesting renewed cooling began during the Palaeogene, as illustrated by the thermal history models and boomerang plot (Figures 3.3 and 3.4, and Table 3.2).

The significant geographic younging trend throughout the Chatkal-Kurama terrane reflects the progressive influence of a Cenozoic thermal pulse from north-west to south-east. The north-western section of the Chatkal-Kurama terrane (excluding the Cenozoic AFT sample in the Chatkal Ranges) effectively represents a Triassic–Early Jurassic palaeo-surface while the Chatkal-Kurama terrane was, in our interpretation, progressively exhumed towards the south-east, during the Cenozoic. In addition, we suggest that the progressive exhumation to the south-east reflects a process of fault-block tilting. This Cenozoic tilting process exposed a deeper section of the thermal history of the Chatkal-Kurama terrane (that was at lower APAZ temperatures during the Cretaceous) in the south-east with respect to the north-west.

The Chatkal-Kurama terrane is bounded to the north-west by the Syrdarya Block, which represents a Mesoproterozoic to Neoproterozoic continental block, a part of the Kazakhstan palaeocontinent (Samygin & Burtman 2009, Dolgopolova et al. 2017, Konopelko et al. 2017b). To the south-east of the Chatkal-Kurama terrane, the Fergana Basin basement is a rigid piece of Palaeozoic crust (Figure 3.2, Burov & Molnar 1998). Both the Syrdarya Block and the Fergana basement are strong units within the Central Asian edifice that transmit stress from distant collisions at the Eurasian plate margins. The Chatkal-Kurama terrane is composed of weaker crust (e.g. volcanic arc) that is more easily deformed than the surrounding rigid block of the Fergana and Syrdarya blocks. Therefore, the crustal tilting can be explained by different crustal strengths in response to distant stresses. The north-east of the Chatkal-Kurama terrane was held in place along the margin of the Syrdarya Block, leading to the preservation of Triassic cooling ages, while the continental collisions on the southern Eurasian margin drove progressive tilting of the Chatkal-Kurama terrane, towards the Fergana basin margin, as demonstrated by the Cretaceous and Palaeogene AFT and AHe ages (Figure 3.2).

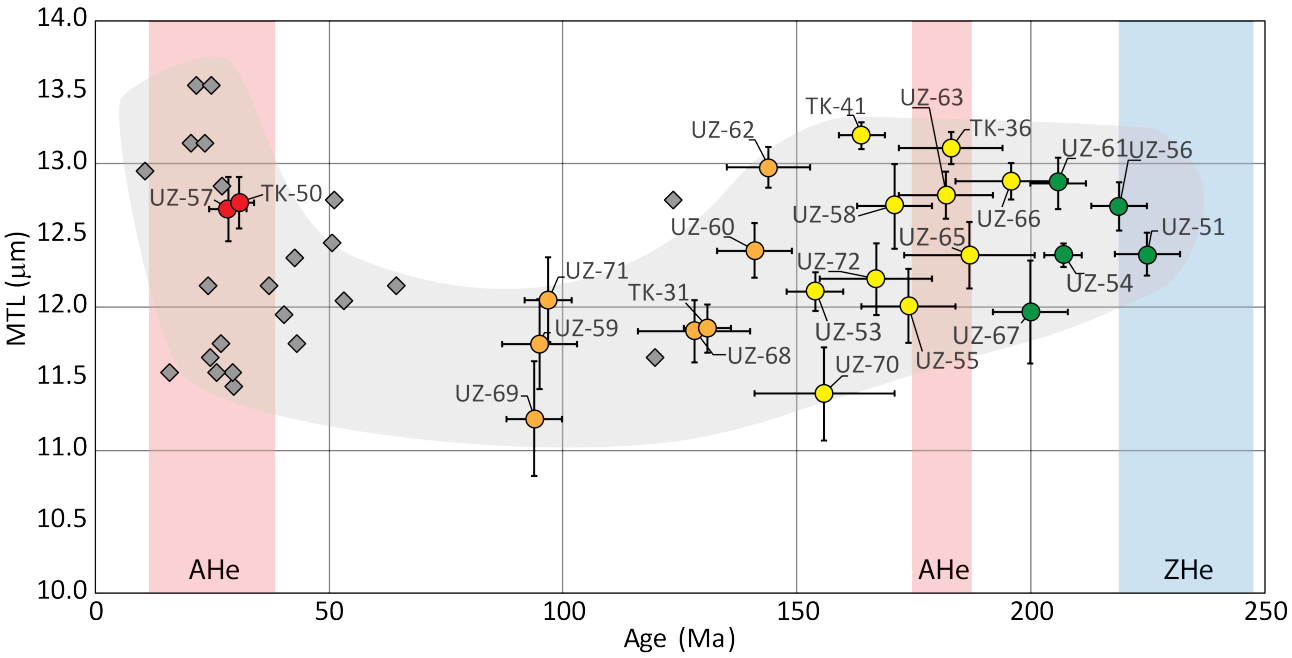

Figure 3.4: A 'boomerang' plot displaying apatite fission track (AFT) central age against mean track lengths (MTL). Circles denote AFT data obtained in this study, diamond symbols are data from (Bande et al. 2017b). Colour coding is the same as in previous figures and represents central AFT ages; green is Triassic, yellow is Jurassic, orange is Cretaceous, and red is Palaeogene. The x-axis error bars are the $\pm 1\sigma$ standard deviations, and the vertical error bars are standard errors of the mean. The red and blue shaded bars represent the age and $\pm 1\sigma$ uncertainties for the apatite helium (AHe), and zircon helium (ZHe) data obtained in this study, respectively. This plot highlights a period of fast cooling in the Triassic–Early Jurassic, followed by slow cooling in the Late Jurassic–Cretaceous, before showing a return to fast cooling in the Cenozoic.

3.5.2 Thermotectonic evolution of the Chatkal-Kurama terrane

Triassic–Early Jurassic

This study reports a Triassic–Early Jurassic fast cooling pulse experienced by the Chatkal-Kurama terrane (Figures 3.2, 3.3, 3.4, and Table 3.2). The oldest thermochronological ages obtained from the north-western margin of the Chatkal-Kurama terrane are the Triassic ZHe (245 and 229 Ma) and AFT ages (225 Ma) from samples TK-36, TK-42, and UZ-51 (Figure 3.4). In comparison, the youngest age of magmatism identified in the Chatkal-Kurama terrane is Permian (*ca.* 286 Ma, Konopelko et al. 2017a). Therefore, a direct thermal relationship between the Triassic AFT ages to post-magmatic cooling can be excluded.

Previous thermochronological studies in the Tian Shan ascribe Triassic–Early Jurassic AFT ages to the closure of the PAO in the Permian and the subsequent collision of the Qiangtang Block with the Eurasian margin (e.g. Xiao et al. 2009, Glorie et al. 2010, De Grave et al.

2011, Macaulay et al. 2014, Glorie & De Grave 2016). During this period samples along the north-western margin of the Chatkal-Kurama terrane were rapidly cooled to surface temperatures. Thus, we interpret the Triassic–Early Jurassic fast cooling signal in our data to be related with exhumation associated with the closure of the PAO and/or the Qiangtang convergence in the Triassic–Early Jurassic.

Late Jurassic–Cretaceous

In the Chatkal-Kurama terrane, our data are indicative of protracted residence in the APAZ during the Late Jurassic–Early Cretaceous, suggesting that the Chatkal-Kurama terrane experienced a period of steady, slow denudation and tectonic quiescence at that time (Figure 3.3). In the Late Jurassic–Cretaceous thermotectonic quiescence induced planation and punctuated marine incursions of the Paratethyan Sea (Burov & Molnar 1998, Bande et al. 2017a, De Pelsmaeker et al. 2018, Nachtergaele et al. 2017). These marine incursions deposited thick Jurassic and Cretaceous sedimentary sequences, conglomerates, and coal deposits (Ahmedov 2000, Dill et al. 2008).

Cenozoic

The presence of a Cenozoic fast cooling signal for the Chatkal-Kurama terrane (both in this study and Bande et al. (2017b)) is evident by overlapping ages for multiple thermochronometers (AFT and AHe), in combination with long MTLs and associated thermal history models (Figs. 3 and 4). Bande et al. (2017b) interprets this thermal event to deformation in the Chatkal-Kurama caused by the Cenozoic reactivation of the Talas-Fergana Fault (Sobel & Dumitru 1997). Similarly, the Cenozoic thermochronological ages identified in the south-eastern margin are likely in response to stresses from the reactivation of the Talas-Fergana Fault transmitting both along the TFF and the Fergana Basin into the Chatkal-Kurama terrane. The appearance of Palaeogene fast-cooling stands in contrast to the tectonic hiatus during the Late Jurassic to Miocene suggested by other thermochronological studies in the region (e.g. Käßner et al. 2017b). The Palaeogene sample in the north-eastern part of the Chatkal-Kurama Range (UZ-57) displays a similar thermal history to samples identified by Bande et al. (2017b), suggesting that this sample has been exhumed, likely inr esponse to deformation along the TFF, rather than preserving a Triassic-Jurassic AFT age, documented

Figure 5a: MTL vs AFT Age western Tian Shan

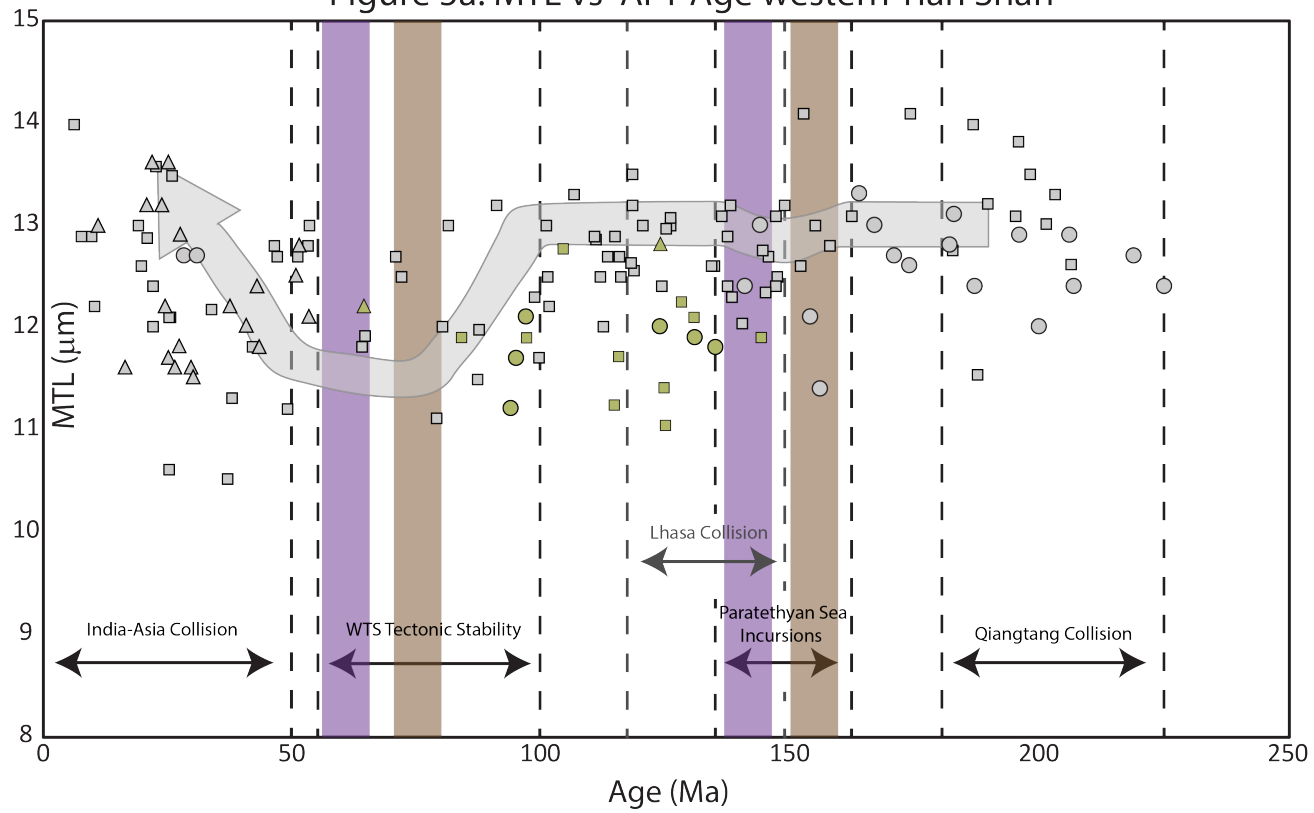

Figure 5b: Mesozoic Published MTLs

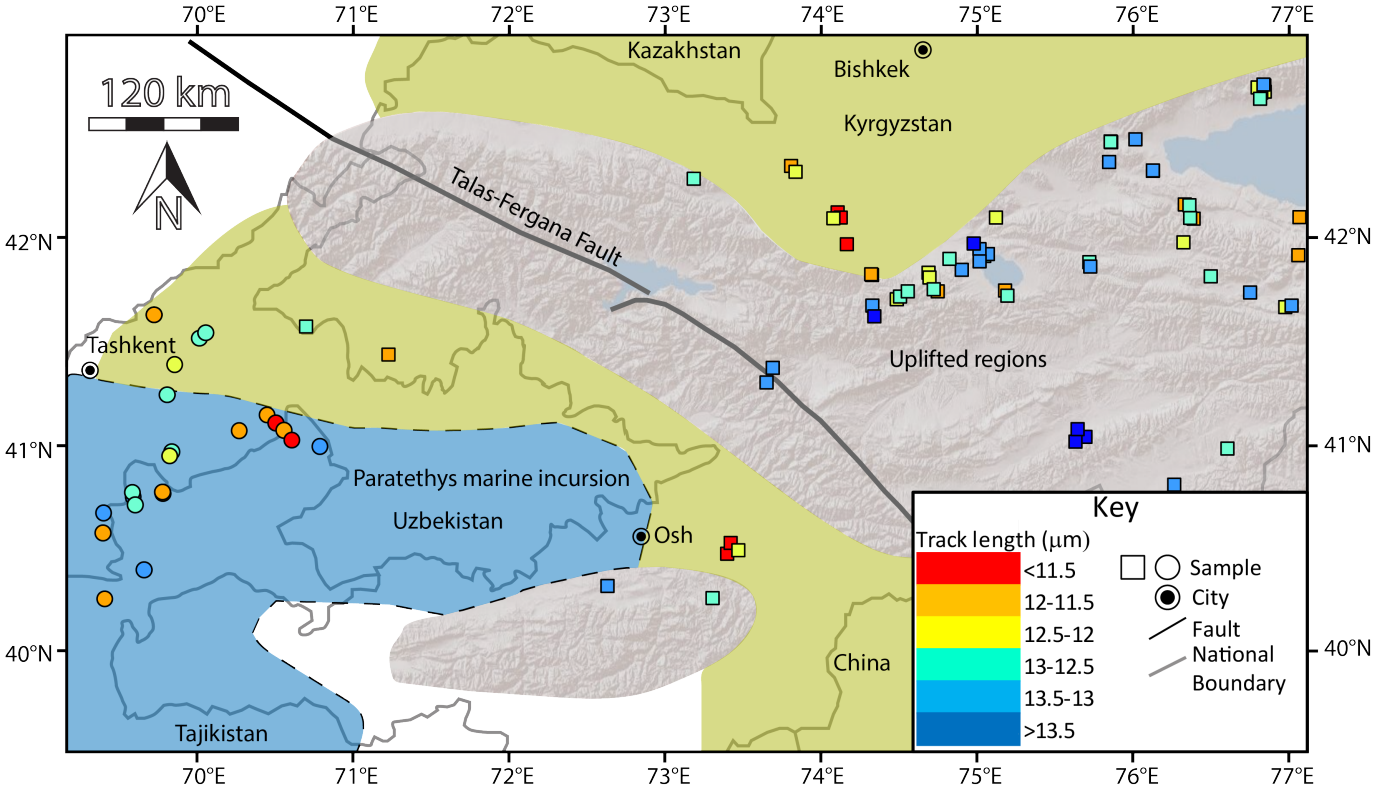

Figure 3.5: Caption next page

Figure 3.5: **Figure 3.5a:** A boomerang plot displaying apatite fission track (AFT) central age against mean track length (MTL) for the western Tian Shan. Circle symbols identify the samples obtained in this study, the triangles are from samples in (Bande et al. 2017b), and the squares represent data obtained from other published AFT data in the Tian Shan (Sobel, Chen & Heermance 2006, Glorie et al. 2010, De Grave et al. 2011, Glorie et al. 2011, De Grave et al. 2012, 2013, Thiede et al. 2013, Bande et al. 2017a, Käßner et al. 2017b, Bande et al. 2017c, Nachtergaele et al. 2017). The colour code of the symbols denotes they samples location in Figure 3.5b. Green coloured coded symbols identify samples that were assessed to lie in marine-mountain transition zone, grey colour coded symbols identify samples that lie in the regions that lie in the mountainous zone. The brown shaded bars represent periods of conglomerate formation experienced in the Tian Shan, the purple shaded bars represent periods of planation identified the Tian Shan, and the dashed lines represent major tectonic events that impacted the Mesozoic western Tian Shan. **Figure 3.5b:** A map of the western extent of the Tian Shan displaying the mean track length (MTL) of published Mesozoic apatite fission track (AFT) data for the region, modified from (De Pelsmaeker et al. 2018). The higher abundance of MTLs to the east of the Talas-Fergana Fault (TFF) is an indication that the Kyrgyz Tian Shan experienced a longer period of deformation and exhumation during the Mesozoic, when compared to the Chatkal-Kurama terrane to the west of the TFF. Blue regions represent areas of marine incursion during the Mesozoic, green regions represent areas of marine-mountain transition, and the grey regions represent areas that were uplifted in the Mesozoic (after De Pelsmaeker et al. 2018). Circles represent data obtained by this study. Published AFT data are represented by squares, obtained from; Glorie et al. (2010), De Grave et al. (2011), Glorie et al. (2011), De Grave et al. (2012), De Grave et al. (2013), Macaulay et al. (2014), and De Pelsmaeker et al. (2018).

by samples taken from the north-western margin with the Syr Darya Basin (UZ-53 and UZ-54, Figure 3.2). In the south-west of the Chatkal-Kurama, two samples with Palaeogene AFT ages (TK-49 and TK-50) occur along the Chatkal Thrust (Figure 3.2), along strike to Palaeogene AFT aged samples recorded by Bande et al. (2017b) (Figure 3.1). This suggests that deformation caused by the India-Eurasia collision in the Palaeogene must have affected the Eurasian interior, causing fault reactivation and block-rotation of the Chatkal-Kurama terrane driven by the Chatkal Thrust and the TFF (Figure 3.2, Burov & Molnar 1998, Bande et al. 2017b), exposing and cooling samples collected along the southern margin of this terrane through the APAZ. In addition, the Cenozoic reactivation of the Chatkal-Kurama terrane likely provided a source for the thick Cenozoic sedimentary sequences identified in the nearby Fergana Basin (Ahmedov 2000, Bande et al. 2017b, De Pelsmaeker et al. 2018).

Regional trends for the western Tian Shan

The following section aims to integrate the thermochronological results obtained for the Chatkal-Kurama into the greater western Tian Shan thermo-tectonic history. In this study,

we define the western Tian Shan as the section of the Tian Shan within the former Soviet Republics (Tajikistan, Uzbekistan, Kyrgyzstan, and Kazakhstan). The Mesozoic and Cenozoic thermo-tectonic evolution of the Chatkal-Kurama terrane is comparable to previous studies within the western Tian Shan (e.g. Sobel, Chen & Heermance 2006, Glorie et al. 2011, De Grave et al. 2013, Käßner et al. 2017a), demonstrating that the western Tian Shan underwent a cyclical tectonic evolution of deformation, quiescence, and reactivation as a result of strain propagation from the Eurasian margin into the Central Asian interior.

The relationship between the tectonic history of the Chatkal-Kurama terrane and the western Tian Shan is demonstrated in Figure 3.5. Figure 3.5a represents a boomerang plot for all AFT age and length data obtained in the western Tian Shan (latitudinal and longitudinal constraints were placed at 40.000°N and 77.140°E, respectively), allowing for a direct comparison between the AFT age and length data of the Chatkal-Kurama terrane (west of the TFF) and Kyrgyz western Tian Shan (east of the TFF). The plot shows that both the Chatkal-Kurama terrane and the western Kyrgyz Tian Shan both experienced a phase of fast cooling in the Triassic–Early Jurassic. However, while the Chatkal-Kurama terrane experienced a period of tectonic stability during the Late Jurassic–Cretaceous (low MTL values), the Kyrgyz western Tian Shan records prolonged fast cooling at that time (higher MTL values). From the Late Eocene–Early Oligocene, the western Tian Shan experienced the onset of renewed cooling as demonstrated by the increase in MTL values from corresponding Cenozoic AFT ages (Figure 3.5a).

The contrasting Mesozoic cooling histories on either side of the TFF are further explored in Figure 3.5b, which shows the geographical distribution of MTLs for the Mesozoic samples used in Figure 3.5a. The abundance of longer MTLs to the east of the TFF indicates that, during the Mesozoic, areas to the east of the Talas-Fergana fault experienced more rapid exhumation compared to the west (Figure 3.5b). Particularly in close vicinity to the TFF, new AFT results from the Kyrgyz Tian Shan are indicative of Late Jurassic–Early Cretaceous basement cooling and denudation at that time (Nachtergaele et al. 2017). To the west of the TFF, MTL values are lower, suggesting slow cooling and flattening of the pre-existing Mesozoic relief. Bande et al. (2017b) and De Pelsmaeker et al. (2018) suggest that during the Cretaceous much of the Chatkal-Kurama terrane was submerged by a marine incursion of the

Paratethys Sea, while the North Tian Shan remained tectonically active. In this model, the Talas-Fergana Fault partitions strain from the Eurasian margin into the area to the east of the fault, causing deformation, while leaving the Chatkal-Kurama terrane relatively undeformed. De Pelsmaeker et al. (2018) proposed a model for the palaeogeography of the western Tian Shan during the Late Jurassic–Early Cretaceous. The AFT data obtained in this study fits very well with this model and strengthen the hypothesis that the TFF acted as a topographic divide between the high eastern and low western Tian Shan during the Cretaceous. Figure 3.5b shows a slight modification to the model proposed by (De Pelsmaeker et al. 2018), by incorporating published AFT data from the western Tian Shan we show that the marine transition zone occured much closer to the major regional faults, to accommodate for the shorter MTLs near the northern margin of the Kyrgyz Tian Shan (Suusamyr valley, Glorie et al. 2010) and near the Kyrgyz Chatkal Ranges south-eastern piedmonts (Bande et al. 2017b). As shown, the regions that record relatively short MTLs were covered by the marine incursion of the Paratethys or are located within a transitional zone during the Late Jurassic–Early Cretaceous, while high relief maintained to the east of the TFF (Figure 3.5b).

Given the widespread occurrence of a Late Jurassic conglomerate deposits in the Tarim and Junggar basins, the fast, Late Jurassic cooling signal in the Kyrgyz Tian Shan is attributed to exhumation and denudation (Figure 3.5a Dumitru et al. 2001, Jolivet et al. 2013, Glorie & De Grave 2016). The contrast between slow cooling, tectonic stability in the Chatkal-Kurama terrane and fast cooling, tectonic activity in the Kyrgyz western Tian Shan (west of the TFF) continues through to the end of the early Cretaceous. During the late Cretaceous and early Palaeogene, the entire western Tian Shan records slow cooling or tectonic quiescence, leading to the development of widespread planation surfaces (e.g. Bazhenov et al. 1993, Burbank et al. 1999, Glorie et al. 2010, Jolivet et al. 2013).

The collision of India with Eurasia and the subsequent Pamir indentation during the Cenozoic marked the end of this period of tectonic stability (e.g. Schwab et al. 2004, Kapp et al. 2007). The stress from these Cenozoic collisions partitioned strain into the continental interior of Eurasia via major faults (Sobel, Chen & Heermance 2006, Glorie et al. 2010). These collisions continued to be the dominant control on the reactivation and exhumation that has been identified throughout the Tian Shan and the Chatkal-Kurama terrane in the Cenozoic

(Figure 3.5a, e.g. De Grave et al. 2012, Macaulay et al. 2014, Bande et al. 2017b, Käßner et al. 2017b, Bande et al. 2017c). Within our study area, fast Cenozoic cooling was revealed for the south-eastern margin of the Chatkal-Kurama terrane (Samples TK-49, TK-50, and UZ-69), which were induced by crustal tilting and fault reactivation. This observation is in good agreement with other studies that describe reactivation and deformation since *ca.* 30-20 Ma, with a significant increase across the Tian Shan in the last *ca.* 10 Ma (Sobel & Dumitru 1997, Sobel, Chen & Heermance 2006, Sobel, Oskin, Burbank & Mikolaichuk 2006, Glorie et al. 2010, De Grave et al. 2011, Glorie et al. 2011, De Grave et al. 2013, Macaulay et al. 2014, Käßner et al. 2017b, Bande et al. 2017c, Jepson et al. 2018a).

3.6 Conclusion

Based on the thermochronological results and modelling presented in this study, the following conclusions can be drawn for the thermotectonic evolution of the Chatkal-Kurama terrane:

- The Chatkal-Kurama terrane records fast cooling during the Triassic–Early Jurassic (*ca.* 225–180 Ma) as a result of the Palaeo-Asian Ocean and the Qiangtang collision at the Eurasian margin. Subsequently, slow cooling and tectonic quiescence prevailed during the Late Jurassic–Early Cretaceous, leading to widespread denudation and marine incursion of the Paratethys.

- Since the late Palaeogene (*ca.* 30 Ma), the Chatkal-Kurama terrane experienced reactivation and crustal tilting to the north-west, as a distant response to the collision of India and Eurasia and the subsequent Pamir indentation.

- Comparing our results with the neighbouring Kyrgyz western Tian Shan, the Talas-Fergana faults seemed to have acted as a structural divide, separating the low relief Chatkal-Kurama terrane from the high relief Kyrgyz Tian Shan during the late Mesozoic.

Chapter 4

Low-temperature thermo-tectonic evolution of the western Tian Shan, Uzbekistan

Statement of Authorship

Title of Paper	Low-temperature thermo-tectonic evolution of the western Tian Shan, Uzbekistan.
Publication Status	☐ Published ☐ Accepted for Publication ☑ Submitted for Publication ☐ Unpublished and Unsubmitted work written in manuscript style
Publication Details	Accepted to Gondwana Research

Principal Author

Name of Principal Author (Candidate)	Gilby Jepson		
Contribution to the Paper	Sample collection, sample analysis, data interpretation, and principal author of paper.		
Overall percentage (%)	60		
Certification:	This paper reports on original research I conducted during the period of my Higher Degree by Research candidature and is not subject to any obligations or contractual agreements with a third party that would constrain its inclusion in this thesis. I am the primary author of this paper.		
Signature		Date	31/08/18

Co-Author Contributions

By signing the Statement of Authorship, each author certifies that:

i. the candidate's stated contribution to the publication is accurate (as detailed above);

ii. permission is granted for the candidate in include the publication in the thesis; and

iii. the sum of all co-author contributions is equal to 100% less the candidate's stated contribution.

Name of Co-Author	Stijn Glorie		
Contribution to the Paper	Sample collection, data interpretation, and thesis supervisor.		
Signature		Date	31/08/18

Name of Co-Author	Dmitry Konopelko
Contribution to the Paper	Sample collection, data interpretation, and geological background.

Signature		Date	31/08/18

Name of Co-Author	Martin Danišík		
Contribution to the Paper	Data analysis, data interpretation, and methods.		
Signature		Date	31/08/18
Name of Co-Author	Rustam Mirkamalov		
Contribution to the Paper	Sample collection, data interpretation, and geological background.		
Signature		Date	31/08/18
Name of Co-Author	Alan Collins		
Contribution to the Paper	Data interpretation, secondary supervisor.		
Signature		Date	31/08/18

Gilby Jepson, Stijn Glorie, Dmitry Konopelko, Rustam Mirkamalov, Martin Danišík, and Alan S. Collins, in press Gondwana Research

4.1 Introduction

Central Asia hosts one of the world's largest active orogen, the intracontinental mountain range of the Tian Shan. The Tian Shan provides an excellent natural laboratory for investigating the impact of marginal tectonic processes on the continental interior. The Tian Shan is situated to the north of the active Cenozoic continental margin collisional orogenic belts of the Himalaya, Pamir, and Tibet, and south of the Palaeozoic orogens of Kazakhstan and Mongolia (Brookfield 2000, Alexeiev et al. 2009). The ancestral Tian Shan orogen formed during the Palaeozoic due to the accretion of several microcontinents and island arcs to the southern margin of Palaeo-Kazakhstan (Windley et al. 2007, Biske & Seltmann 2010, Xiao et al. 2013, Burtman 2015, Konopelko et al. 2017a). Throughout the Mesozoic and Cenozoic, progressive ocean closure along the southern margin of Eurasia generated regional deformation and the reactivation of existing structures (Bullen et al. 2001, 2003, De Grave et al. 2007, Glorie et al. 2010, 2011, Jepson et al. 2018a). As a result, these intracontinental structures in the Tian Shan have been the focus of many geo- and thermochronological studies in order to generate a model for the formation of the Tian Shan intracontinental orogenic system (e.g. Sobel & Dumitru 1997, Dumitru et al. 2001, Bullen et al. 2001, De Grave et al. 2007)

Previous thermochronological studies of the Tian Shan have identified several major periods of Mesozoic exhumation-related basement cooling, which have been interpreted to be related to exhumation in response to the collision of Cimmerian blocks with the southern Eurasian continental margin (e.g. Sobel, Oskin, Burbank & Mikolaichuk 2006, Glorie et al. 2011, De Grave et al. 2013, Macaulay et al. 2014, Glorie & De Grave 2016). In addition, thermochronometers have been successful in identifying the widespread presence of Cenozoic cooling, which has been interpreted as exhumation due to the ongoing India-Eurasia collision (e.g. Sobel, Chen & Heermance 2006, De Grave et al. 2012, Bande et al. 2017b, Käßner et al. 2017b, Nachtergaele et al. 2017, Jepson et al. 2018a). The majority of previous

thermochronological studies have focused on high relief areas within the core of the Tian Shan. However, there has been little work done on the eastern and western extremities of this vast mountain range. In this study we specifically target the westernmost extremity of the Tian Shan in Uzbekistan in order to provide constraints on the thermo-tectonic and landscape evolution of this largely unstudied, low relief segment of the Tian Shan. Filling this gap in the thermochronology allows for a more accurately constrained model on the tectonic evolution of the Tian Shan intracontinental system as a whole. In this study, we present new apatite fission track (AFT) and apatite (U-Th-Sm)/He (AHe) ages from the westernmost extent of the Tian Shan, termed the Kyzylkum-Nurata Segment of the South Tian Shan (Figure 4.1), specifically targeting the Gissar, Zeravshan, and South Tian Shan (STS) sutures in western Uzbekistan (Figure 4.3, Burtman 2015, Dolgopolova et al. 2017, Konopelko et al. 2017a).

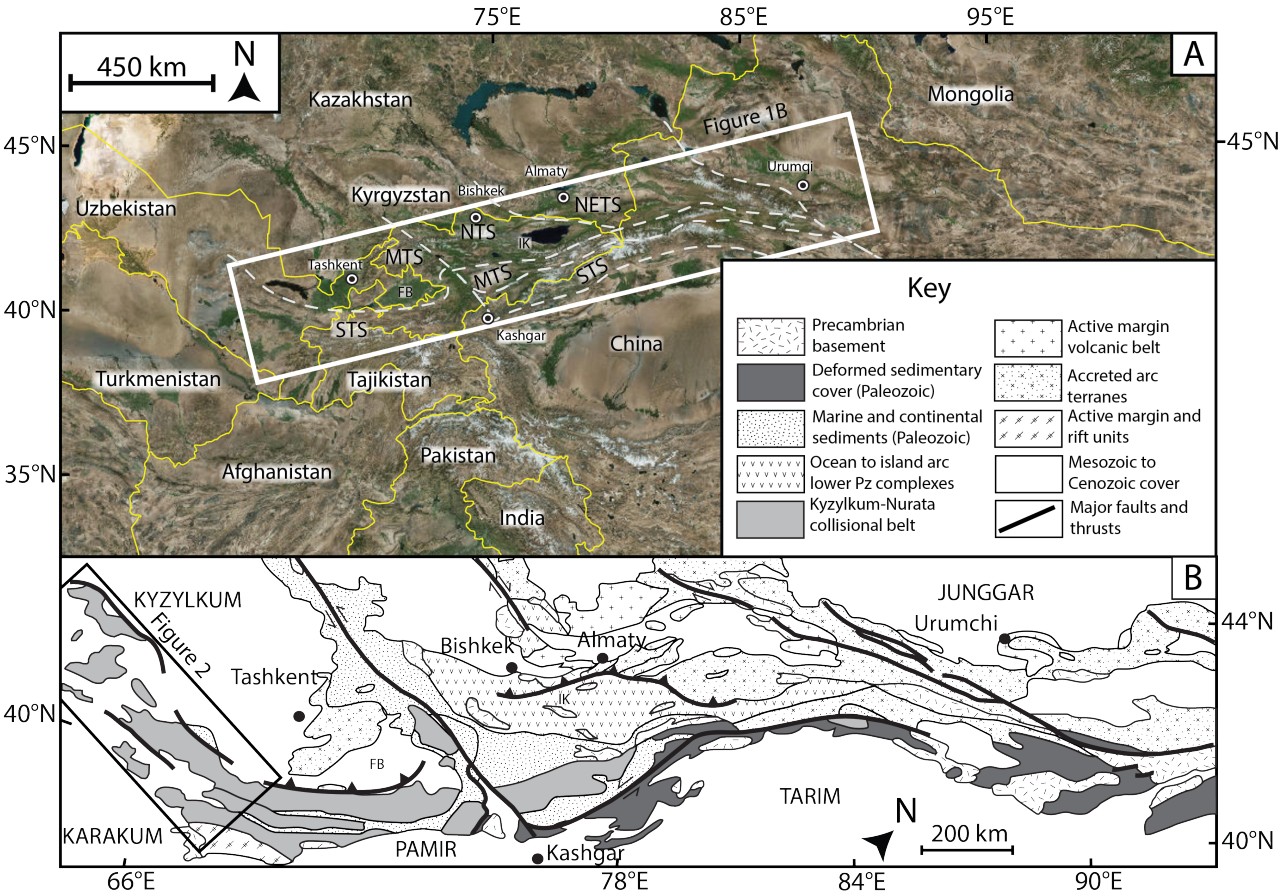

Figure 4.1: (a) Location map of the Tian Shan split into its main components; NETS is the north-eastern Tian Shan, NTS is the North Tian Shan, MTS is the Middle Tian Shan, and STS is the South Tian Shan (after Glorie et al. 2011). FB is the Fergana Basin, and IK is lake Issyk-Kul. (b) Simplified map of the Palaeozoic Tian Shan outlining study area (after Biske & Seltmann 2010).

4.2 Geological Background

The Uzbek western Tian Shan formed during the Palaeozoic, due to the collision between Precambrian microcontinents and island-arcs in the south with the Palaeozoic Kazakhstan continent to the north, as a response to the progressive closure of the Palaeo–Asian Ocean (Windley et al. 2007, Biske & Seltmann 2010, Xiao et al. 2013, Dolgopolova et al. 2017). The Tian Shan can be subdivided into three terranes: (1) the Northern Tian Shan (NTS), representing the deformed margin of the Palaeo-Kazakhstan microcontinent; (2) the Middle Tian Shan (MTS), comprised of Precambrian microcontinental slivers, such as the Karakum, and superimposed island-arcs, such as the Chatkal-Kurama; and (3) the Southern Tian Shan

(STS), a late Palaeozoic fold-and-thrust belt (Figure 4.1, Biske & Seltmann 2010, Burtman 2015, Konopelko et al. 2017a).

The STS is traditionally subdivided into four segments from west to east; the Kyzylkum-Nurata Segment, the Gissar Segment, the Alai Segment, and the Kokshaal Segment. Our study area, the Kyzylkum-Nurata Segment (Dolgopolova et al. 2017), is located in the westernmost extent of the South Tian Shan (STS, Figure 4.1). The Kyzylkum-Nurata Segment formed due to the closure of the Paleo-Asian Ocean in the Late Carboniferous, accreting the Kyzylkum-Alai terranes onto the Middle Tian Shan, generating the South Tian Shan fold belt (Burtman 2015, Konopelko et al. 2017a, Dolgopolova et al. 2017). Prior to the closure of the Paleo-Asian Ocean, the Kyzylkum-Alai terrane developed as the southern passive margin of the Paleo-Asian Ocean since the Neoproterozoic (Konopelko et al. 2015, Kempe et al. 2016, Dolgopolova et al. 2017). The Turkestan ocean closed in the Carboniferous-Permian, accreting the Kyzylkum-Alai terrane to the margin of the Middle Tian Shan which formed the South Tian Shan Suture, this accretion initiated the broadly synchronous closure of the Vashan and Gissar Basins, which had formed due to rifting in the Karakum continent further south (Figure 4.2). The closure of the Vashan Basin formed the Zeravshan suture (Figure 4.3, Dolgopolova et al. 2017), while the short-lived Gissar Basin was associated with rift and subduction related mamatism during the Carboniferous, and its closure resulted in the final amalgamation of the Gissar Segment to the South Tian Shan (Figure 4.2, Burtman 1975, Biske & Seltmann 2010, Seltmann et al. 2011, Konopelko et al. 2017a, 2018). The synchronous closure of the Vashan, Gissar, and Turkestan oceanic basins led to the emplacement of voluminous post-collisional granitoid magmatism (Figure 4.2, Biske & Seltmann 2010, Seltmann et al. 2011, Käßner et al. 2017a). The Late Palaeozoic ocean closure and collision resulted in the southward thrusting of carbonate platforms, forming a large nappe system (Dolgopolova et al. 2017). This oceanic closure was subsequently followed by a period of post-collisional granitoid magmatism throughout the Kyzylkum-Nurata Segment and the greater South Tian Shan during the early Permian (Konopelko et al. 2011, 2015, Kempe et al. 2016, Konopelko et al. 2017a, Dolgopolova et al. 2017). During the Late Permian–Early Triassic, the western Tian Shan experienced uplift and erosion resulting in a notable absence of Triassic sediments over such an extensive area (Figure 4.2, McCann 2016b).

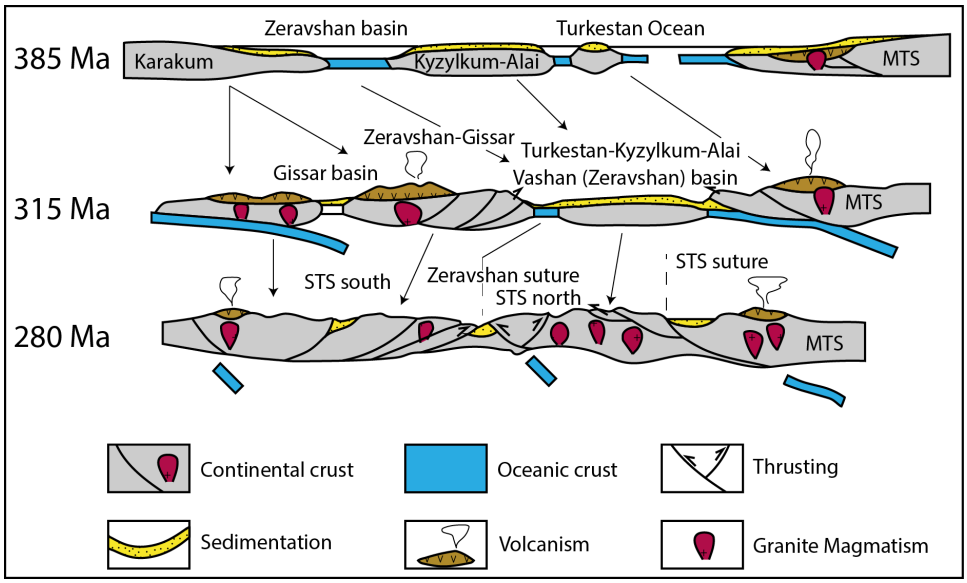

Figure 4.2: A schematic geodynamic model of the Palaeozoic western Tian Shan, modified after Dolgopolova et al. (2017)

During the Mesozoic, the South Tian Shan experienced punctuated episodes of deformation and reactivation (e.g. De Grave et al. 2007, Jolivet et al. 2010, 2013, De Grave et al. 2013). The closure of the Palaeo–Tethys Ocean during the Mesozoic initiated the accretion of Cimmerian continental fragments with the southern margin of Laurasia, causing widespread deformation (e.g. De Grave et al. 2007, Jolivet et al. 2010, Glorie et al. 2011, Xiao et al. 2013). Known collectively as the Cimmerian Orogeny, these events include the collisions of the Qiangtang block during the Late Triassic–Early Jurassic, the Lhasa block during the Late Jurassic–Early Cretaceous, and the Kohistan-Ladakh arc during the Late Cretaceous (e.g Yin & Harrison 2000, Angiolini et al. 2013, De Grave et al. 2013, Jolivet et al. 2013, Glorie & De Grave 2016, Käßner et al. 2017a). The series of collisions and other tectonic processes at the Tethyan margin are thought to have caused exhumation induced basement cooling within the Tian Shan and have been recorded using multi-chronometric methods (Glorie et al. 2010, Jolivet et al. 2010, De Grave et al. 2013, Jolivet et al. 2013, Gillespie et al. 2017). More specifically, the Tian Shan has been shown to have experienced two main deformation events in the Mesozoic. A rapid Triassic–Early Jurassic (~230–200 Ma) thermo-tectonic cooling that is recorded regionally throughout the Tian Shan and is thought to be related with the final closure of the Palaeo-Asian Ocean at ~250 Ma (Xiao et al. 2013) and/or the Qiangtang collision at ~180 Ma (e.g. Ratschbacher et al. 2003, Robinson 2015). Followed by a period of rapid cooling in the Cretaceous, recorded by samples taken in the

vicinity to relic suture-shear zones that dissect the Tian Shan (Figure 4.3, e.g. Glorie et al. 2010, De Grave et al. 2013, De Pelsmaeker et al. 2015, Nachtergaele et al. 2017). In contrast, away from the suture-shear zones, the Tian Shan as a whole experienced slow cooling and peneplanation during the Cretaceous period (Jolivet et al. 2010, Macaulay et al. 2014). The extent of this period of Cretaceous fault reactivation is particularly not well understood for the western Tian Shan and is the main target of this study.

The ongoing closure of the Neo-Tethys Ocean culminated in the collision of the continent of India with the southern margin of Eurasia during the Cenozoic (e.g. Beck et al. 1995, Aitchison et al. 2007, Najman et al. 2010, van Hinsbergen et al. 2011). The India-Eurasia collision caused widespread deformation and rapid exhumation in the Tian Shan (e.g. Sobel, Chen & Heermance 2006, De Grave et al. 2007, Jolivet et al. 2010, Macaulay et al. 2014, Bande et al. 2017b). In the South Tian Shan, previous studies have identified initiation of exhumation at ~30-20 Ma and accelerating of exhumation since ~15-10 Ma, which correlates with periods of Pamir convergence (e.g. De Grave et al. 2012, De Pelsmaeker et al. 2015, Käßner et al. 2017b, Rutte et al. 2017, Nachtergaele et al. 2017, Jepson et al. 2018a).

4.3 Methodology

In this study, new thermochronological data for 45 granitoid rock samples from the western extent of the South Tian Shan are presented (Figure 4.3). Two different thermochronological methods were applied; (1) apatite fission track (partial annealing zone ~120–60°C, Green et al. 1986), and (2) apatite (U-Th-Sm)/He dating (partial retention zone ~80–40°C, Zeitler et al. 1987).

4.3.1 Apatite Fission Track

The apatite fission track method (AFT) is based on the temperature dependent annealing of mineral lattice damage features, known as 'fission tracks', which are created by the spontaneous fission decay of ^{238}U (e.g. Fleischer et al. 1975, Wagner & Van den haute 1992, Gleadow et al. 2015). Fission tracks record the thermal history of a rock sample through the apatite partial annealing zone (APAZ) of ~120–60°C (Green et al. 1986). Apatite grains

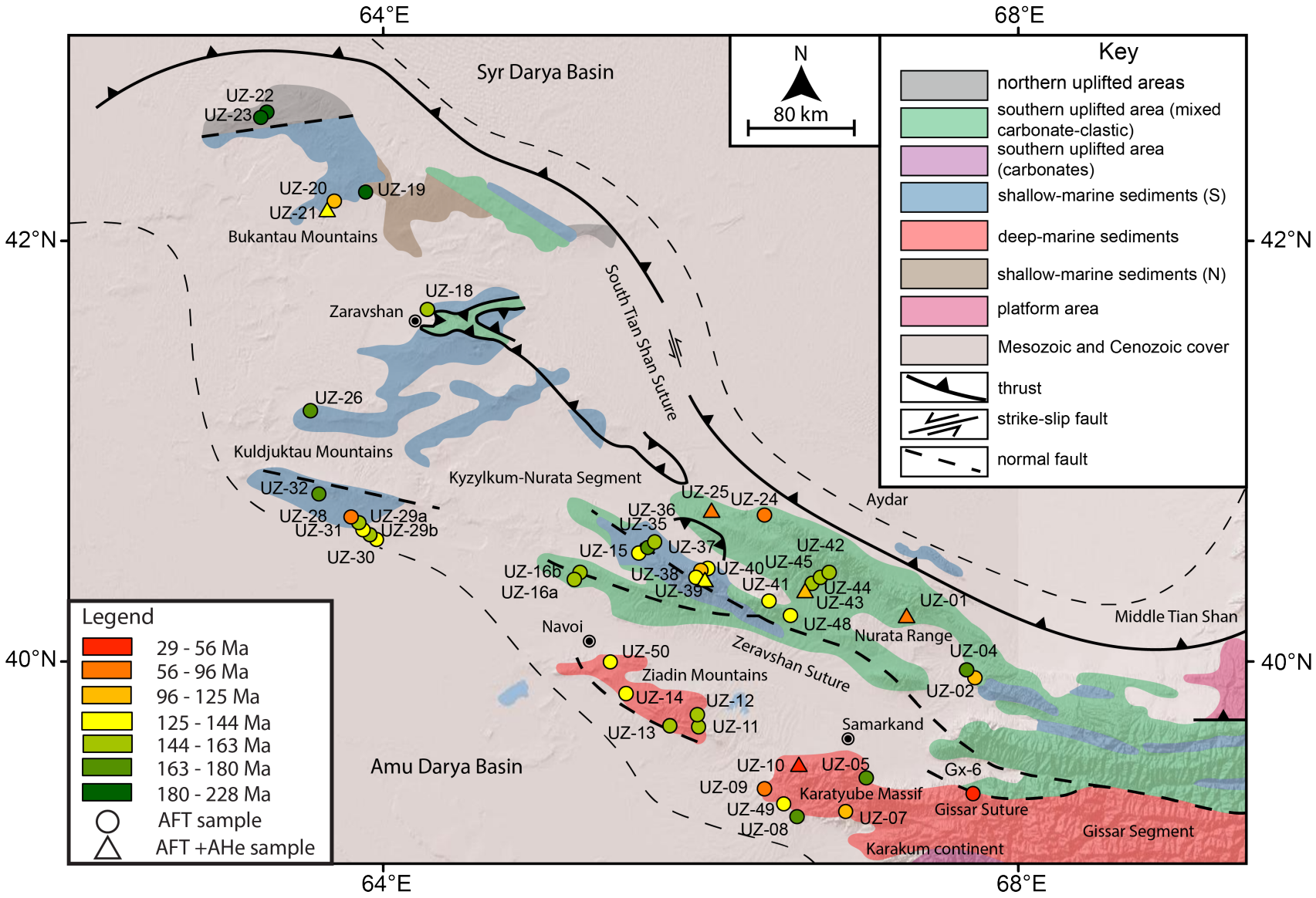

Figure 4.3: Structural units of the western segment of the Southern Tian Shan outlining the major Palaeozoic and Mesozoic structures (after Brookfield 2000). The map displays the locations and regional subdivisions for the apatite fission track (AFT) and apatite (U-Th-Sm)/He (AHe) data obtained in this study. Sample symbols are colour coded following AFT and AHe central ages.

were picked and mounted in epoxy resin, then polished to expose internal sections, and were subsequently chemically etched in a 5M HNO_3 solution for 20s at 20°C to reveal the natural spontaneous fission tracks (Gleadow et al. 2002). Fission track analysis was performed at The University of Adelaide using an Autoscan system. The concentration of uranium (^{238}U) and chlorine (^{35}Cl) of each apatite grain was measured using Laser Ablation-Inductively Coupled Plasma-Mass Spectrometry. Data reduction was performed in Iolite using the Trace Elements DRS (data reduction scheme, Paton et al. 2011). Instrumental drift correction was carried out using NIST610 as an external standard, and elemental concentrations were calculated using ^{43}Ca as the internal standard (Pearce et al. 1997, Vermeesch 2017). Age calculation was carried out as described in Hasebe et al. (2004) and De Grave et al. (2012), using the Durango apatite (McDowell et al. 2005) to perform a zeta calibration (Vermeesch 2017). For a detailed methodology see Glorie et al. (2017) and Gillespie et al. (2017).

4.3.2 Apatite (U-Th-Sm)/He

The (U-Th-Sm)/He thermochronometer is based on the accumulation and thermal diffusivity of radiogenic ^{4}He. Partial retention of He in apatite occurs between ~80–40°C making it valuable for constraining the most recent basement cooling event (Zeitler et al. 1987, Farley 2002). The apatite (U-Th-Sm)/He analyses for this study were undertaken at the John de Laeter Centre, Curtin University and followed the protocols described in Danišík et al. (2012).

Apatite crystals were hand-picked following the recommendations of Farley (2002), photographed and measured for physical dimensions, before being loaded in Pt microtubes. Helium (^{4}He) was extracted for apatite at ~900°C, under ultra-high vacuum using a diode laser and measured by isotope dilution on a Pfeiffer Prisma QMS-200 mass spectrometer. A "re-extract" was run after each sample to verify complete outgassing of the crystals. Helium gas results were corrected for blank, determined by heating empty microtubes using the same procedure. After the ^{4}He measurements, tubes containing the crystals were retrieved from the laser cell, spiked with ^{235}U and ^{230}Th and dissolved. Sample, blank, and spiked standard solutions were analysed by isotope dilution for ^{238}U and ^{232}Th, and by external calibration

for ^{147}Sm on an Agilent 7500 ICP-MS. The total analytical uncertainty (TAU) was calculated as a square root of sum of squares of uncertainty on He and weighted uncertainties on U, Th, Sm and He measurements, and is typically <5% (1σ). The raw (U–Th-Sm)/He ages were corrected for alpha ejection (Ft correction) after Farley et al. (1996), whereby a homogenous distribution of U, Th and Sm was assumed for the crystals. Replicate analyses of internal standard Durango apatite (n = 10) measured over the period of this study, yielded mean (U–Th–Sm)/He ages of 31.9 ± 1.9 Ma (1σ), consistent with the reference Durango (U–Th–Sm)/He age of 31.02 ± 1.01 Ma (McDowell et al. 2005).

4.3.3 Thermal History Modelling

Thermal history models were produced for samples using their mean track length (MTL), AFT ages, AHe ages, and confined track length distributions. The QTQt software (version 5.6.0) was applied, which uses Bayesian trans-dimensional Markov Chain Monte Carlo statistics to determine models for the cooling pathway of the sample (Gallagher 2012). An initial unconstrained run is performed to explore the statistical space, followed by adjustments to the search parameters or the addition of geological constraints where necessary. This approach follows the Bayesian philosophy of the software, which seeks to minimize the complexity of the model by statistical means. Many iterations ($>> 10,000$) are run to generate a range of models that create a probability distribution, from which individual models can be selected, including the maximum likelihood and "expected" (weighted mean) paths. The range of the general prior was set as t = AFT central age ± AFT central age, temperature = 70 ± 70°C. Acceptance rates for models were between 0.2 and 0.6 and birthdeath ratio was ~1. Spherical geometry and the radiation damage model of Gautheron et al. (2009) were used for modeling AHe data. The annealing model from Ketcham et al. (2007) was used for fission track data with D_{par} as the kinetic parameter. More details on the modelling approach can be found in Gallagher (2012) and Gillespie et al. (2017).

4.4 Results

The Kyzylkum-Nurata Segment hosts several relict suture zones, the South Tian Shan Suture, the Zeravshan suture, and the Gissar suture (Figure 4.3, Burtman 1975, Biske &

Seltmann 2010, Seltmann et al. 2011, Dolgopolova et al. 2017). In this study, forty-five granitoid samples were analysed from outcropping rocks along, and away from, the suture zones. The samples yielded a range of ages from Triassic to Palaeogene, from both AFT and AHe methods (Figure 4.3). For a more thorough description, samples have been subdivided into six geographical clusters of samples based on regional proximity to each other. The groups are named after the ranges or nearby features that they were sourced from: (1) the Bukantau Mountains, (2) the Kuldjuktau Mountains, (3) the Nurata Range, (4) Aydar, (5) the Ziadin Mountains, and (6) the Karatyube Massif (Figure 4.3). Mean track lengths are referred to their relative length following the outline established in Figure 4.5, with samples that produce MTLs 12.9-13.5 μm refered to as "long", MTLs of 12.6-12.8 μm are "moderate", and MTLs of 11.4-12.5 μm are refered to as "short". Tables 4.1 and 4.2 summarise the AFT and AHe data. Detailed tables and figures for all single-grain AFT, mean track length (MTL) data, individual thermal history models, and modelling parameters are available in Appendix files (Appendix files M, N, O, and P).

Table 4.1: Apatite fission track data: n is the number of grains analysed per sample and # of lengths is the number of confined track lengths identified in each sample. Age is the central age calculated for each sample, and P Age is the pooled age of each sample. Samples in italics represent samples with fewer than 40 confined tracks, and a represented as dashed lines in the thermal history modelling.

Sample	Lat	Long	Elev	*n*	Age±1σ	P Age±1σ	#	MTL	±1σ
Bukantau Mountains									
UZ-18	*41.676*	*64.278*	*370*	*5*	*154.0±12.0*	*151.4±13.0*	*8*	*12.8*	*0.9*
UZ-19	42.227	63.889	242	30	220.9±9.0	214.1±17.0	72	13.1	1.0
UZ-20	*42.184*	*63.691*	*256*	*29*	*127.8±6.7*	*111.8±9.6*	*33*	*12.5*	*0.9*
UZ-21	42.181	63.686	250	36	130.4±3.5	126.0±10.0	93	12.8	1.2
UZ-22	*42.599*	*63.264*	*405*	*40*	*209.7±7.9*	*202.3±18.4*	*20*	*12.8*	*1.0*
UZ-23	42.599	63.264	405	40	228.0±9.9	221.1±19.9	50	13.4	1.1
Kuldjuktau Mountains									
UZ-26	41.200	63.540	484	27	178.0±11.0	181.5±16.2	49	11.6	1.2
UZ-28	*40.666*	*63.825*	*310*	*13*	*92.0±12.0*	*98.1±9.0*	*37*	*11.9*	*1.1*
UZ-29a	40.640	63.887	310	37	125.0±3.9	129.4±11.8	53	12.9	1.3

UZ-29b	40.640	63.887	310	38	150.9±4.9	155.1±13.8	80	12.7	0.9
UZ-30	40.642	63.878	312	38	136.6±3.9	138.9±12.5	48	12.3	1.3
UZ-31	*40.665*	*63.846*	*322*	*35*	*153.8±7.6*	*152.3±10.2*	*31*	*12.5*	*1.1*
UZ-32	*40.802*	*63.594*	*409*	*28*	*180.0±9.5*	*178.4±17.8*	*33*	*12.2*	*1.0*

Aydar

UZ-01	40.214	67.334	1092	33	83.2±6.0	84.7±6.9	46	12.4	1.8
UZ-24	*40.701*	*66.402*	*418*	*39*	*92.0±4.8*	*85.1±7.5*	*35*	*12.5*	*1.2*
UZ-25	40.724	66.099	455	35	92.6±3.8	93.4±8.3	94	12.6	1.1

Nurata Range

UZ-02	*39.921*	*67.728*	*1012*	*28*	*114.5±9.2*	*133.1±12.6*	*35*	*13.5*	*1.3*
UZ-04	39.959	67.677	820	26	176.1±7.0	162.8±8.8	94	12.5	1.1
UZ-42	40.400	66.765	1019	31	151.7±8.5	148.8±14.1	82	12.6	1.2
UZ-43	*40.357*	*66.686*	*1050*	*34*	*112.1±4.6*	*107.6±6.9*	*37*	*13.1*	*1.1*
UZ-44	40.366	66.684	1095	42	152.0±8.4	136.0±19.5	46	13.0	1.1
UZ-45	*40.390*	*66.725*	*1291*	*43*	*149.0±7.4*	*140.6±13.4*	*22*	*13.0*	*1.2*
UZ-15	*40.530*	*65.628*	*578*	*40*	*139.7±6.9*	*131.4±11.2*	*35*	*13.0*	*1.3*
UZ-16a	40.428	65.239	572	39	152.0±9.6	141.6±12.3	66	12.8	1.1
UZ-16b	*40.428*	*65.239*	*572*	*37*	*163.3±8.0*	*156.3±13.6*	*35*	*12.4*	*1.0*
UZ-35	40.539	65.641	585	36	177.0±12.0	166.7±16.3	89	12.5	1.1
UZ-36	*40.560*	*65.669*	*506*	*38*	*160.0±10.0*	*152.7±13.6*	*38*	*13.0*	*1.3*
UZ-37	40.433	66.025	805	29	143.9±7.3	142.3±13.2	70	12.6	1.4
UZ-38	*40.404*	*65.970*	*1498*	*35*	*138.6±9.2*	*132.6±12.4*	*26*	*12.8*	*1.0*
UZ-39	40.401	66.005	1240	35	115.6±7.8	94.8±7.8	104	12.9	1.2
UZ-40	*40.417*	*66.005*	*1023*	*39*	*109.8±5.2*	*110.2±9.8*	*26*	*13.0*	*1.1*
UZ-41	*40.291*	*66.430*	*1125*	*42*	*131.1±5.4*	*133.8±12.0*	*35*	*12.9*	*1.0*
UZ-48	40.220	66.565	1009	33	134.1±9.6	140.0±9.4	44	12.9	1.1

Ziadin Mountains

UZ-11	39.683	65.988	559	38	156.0±7.7	139.1±12.5	95	13	0.9
UZ-12	39.742	65.978	708	41	154.2±6.3	150.3±12.8	55	13.2	1.1
UZ-13	39.689	65.807	572	29	150.9±6.6	139.1±8.4	44	12.3	1.0

UZ-14	*39.845*	*65.528*	*472*	*32*	*132.8±6.1*	*127.5±10.6*	*16*	*12.9*	*0.9*
UZ-50	39.997	65.431	615	27	141.4±6.6	129.1±11.0	144	13.2	1.0
Karatyube Massif									
UZ-05	*39.435*	*67.043*	*923*	*31*	*177.0±11.0*	*167.5±10.4*	*37*	*12.7*	*1.0*
UZ-07	39.271	66.914	1206	41	124.2±3.4	121.6±6.1	71	12.5	1.2
UZ-08	*39.247*	*66.608*	*724*	*37*	*177.0±11.0*	*159.8±11.9*	*33*	*12.1*	*1.1*
UZ-09	*39.382*	*66.401*	*682*	*11*	*96.6±7.8*	*84.5±8.4*	*18*	*12.2*	*1.5*
UZ-10	39.499	66.628	911	29	56.1±4.0	52.8±5.9	93	12	1.5
UZ-49	39.309	66.524	890	36	130.3±4.4	126.4±7.5	66	12.4	1.4
GX-6	39.360	67.717	1752	36	29.5±1.8	30.0±2.4	-	-	-

4.4.1 Apatite Fission Track

Bukantau Mountains

The Bukantau Mountains is the northern-most extent of the Kyzylkum-Nurata Segment and lies directly on the margin of the Syr-Darya Block, and hosts the Teskuduk ophiolite complex of the South Tien Shan (Figure 4.3, Brookfield 2000, Dolgopolova et al. 2017). The Bukantau Mountains yielded the oldest AFT ages of all samples of the Kyzylkum-Nurata Segment, with the north-eastern samples UZ-19, UZ-22, and UZ-23 producing AFT central ages of 221 ± 9 Ma, 210 ± 8 Ma, and 228 ± 10 Ma, respectively. The samples of Triassic AFT age corresponded with long to moderate MTLs of 13.1 ± 1.0 μm, 12.8 ± 1.0 μm, 13.4 ± 1.1 μm, respectively. In the south-west of the Bukantau Mountains, samples UZ-18, UZ-20, and UZ-21 yield Jurassic and Cretaceous AFT ages of 154 ± 12 Ma, 124 ± 7 Ma, and 130 ± 4 Ma, and moderate MTLs of 12.8 ± 0.9 μm, 12.5 ± 0.9 μm, and 12.8 ± 1.2 μm, respectively (Figure 4.3, 4.5, and Table 4.1).

Kuldjuktau Mountains

The Kuldjuktau Mountains is the south-western most extent of both the Gissar and Zeravshan sutures, and represents the last set of outcrops of the South Tian Shan North of the

Amu Darya Basin (Figure 4.3, Burtman 2000, McCann 2016a). Samples from the Kuldjuktau Mountains yielded Jurassic and Cretaceous AFT central ages. North of the Kuldjuktau Mountains, in the southern Tamdy mountains, sample UZ-26 yielded a Jurassic AFT central age of 178 ± 11 Ma, with a MTL of 11.6 ± 1.2 μm. The remaining samples formed a transect across several minor faults (Figure 4.5). Samples UZ-29b, UZ-31, UZ-32 yielded Jurassic AFT central ages of 151 ± 5 Ma, 154 ± 8 Ma, and 180 ± 10 Ma, respectively. The samples of Jurassic AFT age produced moderate to short MTLs of 12.7 ± 0.9 μm, 12.5 ± 1.1 μm, and 12.2 ± 1.0 μm, respectively. Samples UZ-28, UZ-29a, and UZ-30 yielded Cretaceous AFT central ages of 92 ± 12 Ma, 125 ± 4 Ma, and 137 ± 4 Ma, respectively. The Cretaceous-aged samples yielded both long and short MTLs of 11.9 ± 1.1 μm, 12.9 ± 1.3 μm, and 12.3 ± 1.3 μm, respectively Figure 4.3, 4.5 and Table 4.1).

Nurata Range

The Nurata Range is the main segment of the South Tian Shan Suture that crops out within Uzbekistan, which extends to the Turkistan-Alai Suture in Kyrgyzstan (De Grave et al. 2012, Dolgopolova et al. 2017). The Nurata Range can be further divided into two subsets, the northern Nurata Range and the southern Nurata Range (Figure 4.3). In this study, four samples were taken along a transect in the core of the northern Nurata Range, and two samples from its extent into the Nurata-Turkestan-Alai region (Figure 4.1). The northern Nurata Range transect strikes from north-east (UZ-42) to south-west (UZ-43). Samples UZ-42, UZ-45, and UZ-44 yielded Jurassic AFT central ages of 152 ± 9 Ma, 155 ± 7 Ma, 152 ± 8 Ma, receptively. From the same transect, UZ-43 yielded a Cretaceous central age of 112 ± 5 Ma. The transect yielded long to moderate MTLs of 12.6 ± 1.2 μm, 13.0 ± 1.2 μm, and 13.0 ± 1.1 μm, respectively for the Jurassic samples, and 13.1 ± 1.1 μm for the Cretaceous samples. In the Turkestan-Alai segment, sample UZ-04 yielded a Jurassic AFT central age of 176 ± 7 Ma, and sample UZ-02 yielded a Cretaceous AFT central age of 115 ± 9 Ma, with MTLs of 13.5 ± 1.3 μm and 12.5 ± 1.1 μm, respectively (Figure 4.3, 4.5 and Table 4.1).

The southern section of the Nurata Range represents the inferred western extent of the Zeravshan suture, which formed due to the closure of the Vashan basin in the late Palaeozoic

(Dolgopolova et al. 2017). Three samples were taken along the north-western extent, two samples were taken from the south-western extent, two samples were taken from the eastern extent, and one vertical profile of four samples were obtained from the core of the southern Nurata Range (Figure 4.3). Across the north-western extent, sample UZ-36, UZ-35, and UZ-15 produced AFT central ages of 160 ± 10 Ma, 177 ± 12 Ma, and 140 ± 7 Ma, with long to moderate MTLs of 13.0 ± 1.3 μm, 12.5 ± 1.1 μm, and 13.0 ± 1.3 μm, respectively. The two samples, UZ-16a and UZ-16b, from the south-western extent, yielded indistinguishable Jurassic AFT central ages of 152 ± 10 Ma and 163 ± 8 Ma, respectively. Samples UZ-16a and UZ-16b produced MTLs of 12.8 ± 1.1 μm and 12.4 ± 1.0 μm, respectively. The vertical profile in the core of the southern Nurata Range consists of four samples, from ~800m to ~1500m with a ~200m sample interval, with all samples returning Cretaceous AFT central ages and relatively long MTLs. At the base of the profile, sample UZ-37 (840m) yielded an age of 144 ± 7 Ma, sample UZ-40 (1010m) yielded an age of 140 ± 7 Ma, sample UZ-39 (1235m) yielded a major age peak of 116 ± 8 Ma, and sample UZ-38 (1520m) yielded an age of 139 ± 9 Ma. All four samples along the vertical profile returned similar long to moderate MTLs of 12.6 ± 1.4 μm, 13.0 ± 1.1 μm, 12.9 ± 1.2 μm, and 12.8 ± 1.0 μm, respectively. To the east of the southern Nurata Range, both UZ-41 and UZ-48 yielded Cretaceous AFT central ages of 131 ± 5 Ma and 134 ± 10 Ma, respectively, with these samples producing MTLs of 12.9 ± 1.0 μm and 12.9 ± 1.1 μm, respectively (Figure 4.3, 4.5 and Table 4.1).

Aydar

Samples from along the northern margin of the Nurata Range and the southern margin of the Aydar lake yield markedly different AFT ages compared to the rest of the Nurata Range (Figure 4.3). Three samples were collected from the boundary between the Nurata Range and the Aydar lake, samples UZ-25, UZ-24, and UZ-01. Samples UZ-25 and UZ-24 produced Cretaceous AFT central ages of 92 ± 5 Ma and 93 ± 4 Ma and moderate to short MTLs of 12.5 ± 1.2 μm and 12.6 ± 1.1 μm, respectively. To the east, sample UZ- 01 yielded a Cretaceous AFT central age of 83 ± 6 Ma and a MTL of 12.4 ± 1.8 μm (Figure 4.3, 4.5 and Table 4.1).

Ziadin Mountains

The Ziadin Mountains is the inferred western continuation of the Gissar suture outcropping in Uzbekistan, between the Kuldjuktau Mountains to the north-west and the Karatyube Massif to the south-east (Dolgopolova et al. 2017). Five samples were taken from the Ziadin Mountains along the Gissar suture. The three eastern samples, UZ-11, UZ-12, and UZ-13, all yielded similar Jurassic AFT central ages of 156 ± 8 Ma, 154 ± 6 Ma, and 151 ± 7 Ma, respectively. The samples of Jurassic age produced MTLs of 13.0 ± 0.9 μm, MTL of 13.2 ± 1.1 μm, and 12.3 ± 1.0 μm, respectively. The two western samples UZ-14 and UZ-50 both yielded Cretaceous AFT central ages of 133 ± 6 Ma, and 141 ± 7 Ma and long MTLs of 12.9 ± 0.9 μm and 13.2 ± 1.0 μm, respectively (Figure 4.3, 4.5 and Table 4.1).

Karatyube Massif

The large Karatybe Massif is located on the western termination of the Gissar range mountain range that largely crops out in Tajikistan (Konopelko et al. 2017a). The seven samples from the Karatyube Massif yielded a range of ages over the Mesozoic and Cenozoic, two produced Jurassic AFT central ages, three produced Cretaceous AFT central ages, and two produced Palaeogene AFT central ages. Samples UZ-05 and UZ-08 yielded identical ages of 177 ± 11 Ma, and both samples produced moderate to short MTLs of 12.7 ± 1.0 μm and 12.1 ± 1.1 μm, respectively. Three samples yielded a Cretaceous AFT central age; UZ-07, UZ-09, and UZ-49 yielded ages of 124 ± 3 Ma, 97 ± 8 Ma, and 130 ± 4 Ma, respectively. The Cretaceous ages were associated with short MTLs of 12.5 ± 1.2 μm, 12.2 ± 1.5 μm, and 12.4 ± 1.4 μm, respectively. The two Palaeogene AFT central ages identified in the Karatyube Massif are the youngest basement AFT ages for the entire Kyzylkum-Nurata Segment. Sample UZ-10 yielded an AFT central age of 56 ± 4 Ma, and sample Gx-6 yielded an age of 30 ± 2 Ma. Sample UZ-10 displayed a short MTL of 12.0 ± 1.5 μm. Sample Gx-6, despite being irradiated with ^{252}Cf to increase the number of confined tracks, did not produce enough tracks to produce a reliable MTL and length distribution (Figure 4.3, 4.5 and Table 4.1).

4.4.2 Apatite (U-Th-Sm)/He

Table 4.2: Apatite (U-Th-Sm)/He age and chemistry data. ^{232}Th, ^{238}U, and ^{147}Sm concentrations are in ng, He is the concentration of helium measured in ncc, Th/U is the ratio of thorium to uranium. Raw is the age before the *Ft* correction is made. *Ft* is the alpha-ejection correction parameter of Farley et al. (1996). Age is the age after applying the *Ft* correction, eU is the effective uranium concentration, and TAU is the total analytical uncertainty. Samples in italics represent grains that were excluded due to inclusions or poor quality.

Apatite (U-Th-Sm)/He data

Sample	^{232}Th	±(%)	^{238}U	±(%)	^{147}Sm	±(%)	He±(%)	TAU	eU	Th/U	Raw±1σ	F_T	Age±1σ
UZ-01-1	0.041	5.7	0.028	5.8	0.011	0.9	0.198±1.0	4.7	1.46	53.71	43.1±2.0	0.51	84.3±9.3
UZ-01-2	0.056	4.1	0.034	4.2	0.016	1.2	0.355±1.1	3.4	1.63	32.26	60.8±2.1	0.66	91.9±5.6
UZ-01-3	0.058	5.7	0.037	5.9	0.014	0.8	0.294±0.7	4.6	1.54	49.53	47.1±2.2	0.58	81.0±8.9
UZ-01-4	0.133	4.0	0.085	4.2	0.026	0.8	0.733±0.7	3.4	1.56	64.61	51.5±1.7	0.65	79.2±4.8
UZ-01-5	*0.085*	*4.0*	*0.055*	*4.2*	*0.022*	*0.4*	*0.607±0.8*	*3.4*	*1.52*	*55.73*	*65.6±2.2*	*0.64*	*103.2±6.2*
											UZ-01 Age±1σ= 84.1±7.1		
UZ-10-1	0.032	5.7	0.029	5.8	0.009	1.1	0.101±1.6	5.0	1.08	36.94	22.5±1.1	0.59	38.4±4.3
UZ-10-2	0.107	4.0	0.082	4.2	0.021	0.5	0.275±1.2	3.6	1.29	80.38	20.9±0.7	0.58	36.3±3.8
UZ-10-3	0.042	5.7	0.035	5.8	0.009	0.9	0.084±1.8	5.1	1.19	58.31	15.5±0.8	0.65	23.9±1.7
UZ-10-4	0.067	4.0	0.045	4.2	0.013	0.8	0.144±1.7	3.7	1.48	73.24	19.5±0.7	0.65	29.9±1.9
UZ-10-5	0.097	5.7	0.079	5.8	0.019	0.5	0.325±1.0	4.8	1.22	85.18	26.2±1.3	0.70	37.6±2.6
UZ-10-6	0.096	4.0	0.114	4.2	0.026	0.5	0.328±1.0	3.7	0.83	52.71	19.7±0.7	0.75	26.3±1.6
UZ-10-7	0.073	5.7	0.060	5.8	0.015	0.7	0.153±1.2	4.8	1.21	77.92	16.2±0.8	0.59	27.6±3.1
UZ-10-8	0.099	4.0	0.073	4.2	0.020	0.6	0.196±1.0	3.5	1.35	74.97	16.7±0.6	0.64	26.2±1.6

UZ-10 Age±1σ= 30.8±2.6

UZ-21-1	0.019	4.1	0.093	4.2	0.020	0.7	1.189±0.7	4.1	0.20	53.52	99.4±4.1	0.75	132.5±8.6
UZ-21-2	0.025	5.7	0.123	5.8	0.034	0.6	1.440±0.7	5.6	0.20	49.13	90.5±5.1	0.73	123.7±9.3
UZ-21-3	*0.069*	*12.8*	*0.720*	*5.8*	*0.062*	*0.6*	*13.131±0.7*	*5.7*	*0.10*	*137.53*	*144.6±8.3*	*0.80*	*180.1±13.7*
UZ-21-4	*0.043*	*14.8*	*0.193*	*4.2*	*0.036*	*0.6*	*4.621±0.8*	*4.1*	*0.22*	*70.10*	*183.6±7.5*	*0.75*	*244.6±15.8*
UZ-21-5	*0.024*	*14.2*	*0.077*	*5.8*	*0.018*	*0.7*	*1.290±0.9*	*5.5*	*0.31*	*48.91*	*126.3±6.9*	*0.71*	*179.1±13.3*
UZ-21-6	*0.007*	*6.7*	*0.052*	*4.2*	*0.012*	*0.6*	*0.892±0.9*	*4.2*	*0.13*	*52.87*	*135.8±5.7*	*0.69*	*195.7±12.8*

UZ-21 Age±1σ= 128.1±8.9

UZ-25-1	0.005	5.8	0.018	5.8	0.005	1.1	0.143±1.4	5.7	0.27	29.54	60.5±3.4	0.61	98.8±7.5
UZ-25-2	0.005	5.8	0.092	5.8	0.011	0.8	0.749±0.9	5.8	0.06	57.68	65.5±3.8	0.71	91.8±7.0
UZ-25-3	0.010	5.8	0.018	5.8	0.008	0.9	0.144±1.3	5.3	0.57	15.28	59.1±3.2	0.68	86.6±6.3
UZ-25-4	0.007	4.4	0.056	4.2	0.007	0.9	0.451±0.8	4.2	0.13	53.11	64±2.7	0.63	101.6±6.6
UZ-25-5	*0.009*	*4.3*	*0.095*	*4.2*	*0.020*	*0.5*	*1.028±0.8*	*4.2*	*0.10*	*35.33*	*85.9±3.6*	*0.75*	*114.8±7.5*
UZ-25-6	*0.015*	*4.1*	*0.099*	*4.2*	*0.022*	*0.6*	*1.089±0.7*	*4.1*	*0.15*	*32.61*	*86.7±3.6*	*0.74*	*117.0±7.6*
UZ-25-7	*0.037*	*5.7*	*0.039*	*5.8*	*0.011*	*0.6*	*0.765±0.8*	*4.9*	*0.96*	*17.76*	*130.2±6.4*	*0.74*	*176.4±12.4*
UZ-25-8	*0.016*	*4.1*	*0.064*	*4.2*	*0.009*	*0.9*	*0.730±0.7*	*4.0*	*0.26*	*50.75*	*88.2±3.5*	*0.66*	*134.5±8.6*

UZ-25 Age±1σ= 94.7±6.9

UZ-39-1	0.015	5.7	0.721	5.8	0.035	0.5	9.921±0.6	5.8	0.02	192.65	111.4±6.5	0.78	142.8±11.0
UZ-39-2	0.013	4.2	0.394	4.2	0.021	0.6	5.436±0.8	4.2	0.03	159.96	111.3±4.7	0.73	151.9±10.0

UZ-39-3	0.021	5.7	0.328	5.8	0.024	0.6	4.640±0.6	5.8	0.06	140.20	113.2±6.5	0.76	148.3±11.3
UZ-39-4	0.027	4.1	0.329	4.2	0.032	0.6	4.169±0.7	4.2	0.08	86.84	101.1±4.2	0.78	129.3±8.4
UZ-39-5	0.020	5.7	0.298	5.8	0.034	0.6	4.200±0.7	5.8	0.06	66.99	112.7±6.5	0.73	154.1±11.8
UZ-39-6	0.028	4.1	0.509	4.2	0.054	0.6	5.899±0.6	4.2	0.05	83.86	93.1±3.9	0.82	114.0±7.4
UZ-39-7	*0.008*	*5.7*	*0.202*	*5.8*	*0.013*	*0.5*	*4.691±0.7*	*5.8*	*0.04*	*115.60*	*185.4±10.7*	*0.71*	*262.9±20.1*

UZ-39 Age±1σ= 140.9±10.0

UZ-43-1	0.062	5.7	0.069	5.8	0.009	0.6	0.988±0.8	5.0	0.89	31.85	96.1±4.8	0.75	128.1±9.0
UZ-43-2	0.059	4.1	0.047	4.2	0.015	0.7	0.582±0.8	3.5	1.23	44.56	77.8±2.7	0.69	112.4±6.8
UZ-43-3	0.171	5.7	0.142	5.8	0.054	0.4	1.928±0.7	4.7	1.19	101.75	86.3±4.1	0.71	122.4±8.4
UZ-43-4	0.041	4.1	0.043	4.2	0.015	0.7	0.477±0.8	3.6	0.97	40.10	74.4±2.7	0.65	113.9±7.0
UZ-43-5	*0.048*	*5.7*	*0.045*	*5.8*	*0.020*	*0.6*	*0.333±1.1*	*4.9*	*1.06*	*33.62*	*48.1±2.4*	*0.67*	*71.6±5.0*
UZ-43-6	*0.202*	*4.0*	*0.137*	*4.2*	*0.046*	*0.5*	*2.406±0.8*	*3.4*	*1.47*	*89.85*	*106.0±3.6*	*0.73*	*144.8±8.7*

UZ-43 Age±1σ= 119.2±7.8

Six samples were selected for AHe analysis (Table 4.2). Samples that produced young AFT ages and relatively long MTLs were prioritised in order to better constrain the Cretaceous–Cenozoic phase of cooling experienced by the Kyzylkum-Nurata Segment. In the Bukantau Mountains, sample UZ-21 yielded a Cretaceous AHe age of 128 ± 9 Ma, which overlaps with the AFT central age from sample UZ-21 of 130 ± 4 Ma (Table 4.1 and 4.2). For the Nurata Range, one sample was selected from the northern area and one sample was selected from the southern area. Sample UZ-43 yielded an AHe age of 119 ± 8 Ma, which is within error with its respective AFT age (AFT central age of 112 ± 5 Ma, Table 4.1 and 4.2). In the southern Nurata Range, sample UZ-39 produced an AHe age of 141 ± 10 Ma with significant single-grain age scatter. Compared to the AFT age for this sample (99 Ma central age, 116 Ma oldest age peak), the AHe age is significantly older. This discrepancy may be explained by the anomalously high eU (effective uranium, Table 4.2). However, the AHe age is in excellent agreement with the other samples in the vertical profile (AFT age range ~140–110 Ma, Table 4.1 and 4.2, Appendix File M). Two samples from the Aydar – Nurata Range margin were selected for AHe analysis; UZ-01 (AFT central age of 83 ± 6 Ma) yielded an AHe age of 84 ± 7 and UZ-25 (AFT central age of 93 ± 4 Ma) yielded an AHe age of 95 ± 7 Ma. Both AHe ages from the Aydar area were thus, in excellent agreement with their respective AFT age (Table 4.1 and 4.2). Sample UZ-10 (AFT central age of 56 ± 4 Ma) from the Karatyube Massif yielded an AHe age of 31 ± 3 Ma (Table 4.1). Although, the ages produced by the AFT and AHe thermochronometers do not overlap, the presence of a young ~30 Ma AHe age combined with the regionally proximal ~30 Ma AFT central age for sample Gx-6, does suggest the presence of a Eocene–Oligocene cooling signal in the south-eastern end of the Kyzylkum-Nurata Segment (Figure 4.3 and Table 4.2).

4.4.3 Thermal History Modelling

Thermal history modelling was conducted for thirty-nine samples. Models that are based on less than 40 confined tracks are thought to be less accurate and are, therefore, drawn as dashed lines in the thermal history modelling figures (Figure 4.4 and Table 4.1). All models were constrained to start at temperatures greater than the APAZ (>120°C ± 20°C). For all samples the AFT annealing model Ketcham et al. (2007) was used. In addition,

apatite helium data were integrated into relevant thermal models, using the He radiation damage model of Gautheron et al. (2009). Individual models, confined track distributions, and modelling parameters are available in Figure 4.4 and Appendix Files O, and P (following Flowers et al. 2015).

The thermal models produced two distinct Mesozoic and Cenozoic thermal histories. The six regions identified in the results can, therefore, be further subdivided into two tectonic groups with discrete thermal evolutions. The first group can be identified by samples that were taken in close proximity to relict suture zones, comprising of the the Nurata Range and the Ziadin Mountains. The second group is identified by samples that were taken from regions that were distal to the main suture zones, the Kuldjuktau Mountains, the Bukantau Mountains, the Aydar area, and the Karatyube Massif (Figure 4.4).

Tectonic Group One: Near Major Structures

For the Nurata Range, sixteen samples were modelled (five from the northern and eleven from the southern range). Samples UZ-43 and UZ-39 were constrained using additional AHe data (Table 4.2). The models show rapid cooling in the Late Triassic–Early Jurassic (~210–180 Ma), slower cooling in the Jurassic (~180–150 Ma), faster cooling in the Late Jurassic–Early Cretaceous (~150–120 Ma), and slow cooling in the middle to Late Cretaceous (~120-100 Ma, Figure 4.4a). Five thermal history models were obtained from the Ziadin Mountains in southern Uzbekistan. No additional constraints were placed on any of the five thermal history models. All five thermal history models identified relatively rapid cooling during the Late Jurassic–Early Cretaceous (~160–130 Ma). The thermal evolution for the regions that comprise Tectonic Group One preserve two pulses of relatively rapid cooling during (1) the Late Triassic–Early Jurassic (~210–180 Ma) and (2) the Late Jurassic–Early Cretaceous (~160–130 Ma, Figure 4.4).

Tectonic Group Two

Thermal history modelling was performed on seven samples from the Kuldjuktau Mountains. There were no AHe or additional data, all seven models were allowed to run unconstrained. The Kuldjuktau Mountains displays a broad range of thermal histories dominated by slow

cooling throughout the Mesozoic from ~220 Ma to ~110 Ma. However, one sample displays a variation from the theme of slow cooling, UZ-29b, which shows rapid cooling at ~170 Ma (Figure 4.4c).

For the Aydar region, thermal history models were produced for all three samples. Two of the three samples had corresponding AHe data which was used by each respective model (Table 4.2 and Appendix File O and P). All three samples produced Late Cretaceous AFT ages, with two samples modelling relatively fast cooling through the APAZ at ~110–90 Ma. In contrast, sample UZ-01 displays protracted cooling throughout the Late Cretaceous (Figure 4.4d).

Thermal history modelling was performed on five samples from the Karatyube Massif, with one sample modelled with its respective AHe data. The four thermal history models without AHe constraints all produced slow cooling thermal histories, entering the upper APAZ in the Early Jurassic and cooling to below the APAZ in the mid-Cretaceous. Two samples which produced thermal histories with an extended residence in the APAZ during the Late Jurassic–Early Cretaceous (Figure 4.4e). The Palaeogene sample, UZ-10, demonstrates a relatively rapid rate of cooling at ~50 Ma. After exiting the APAZ, sample UZ-10 shows a deviation in its thermal history model, constrained by the AHe data obtained for that sample at ~30 Ma, before cooling to surface temperatures at ~15 Ma (Figure 4.4e and 4.5, and Appendix File O).

Five samples from the Bukantau Mountains were suitable for modelling. Four of the five thermal history models were run without additional AHe constraints, with one sample constrained by Cretaceous AHe data (UZ-21). The thermal history models for the Bukantau Mountains record a dominant rapid Triassic cooling signal (~220–200 Ma) while also displaying a period of rapid cooling in the Late Jurassic (~140 Ma), and a period of relatively slow cooling in the Late Cretaceous (~110 Ma, Figure 4.4f).

The thermal evolution for the regions that comprise Tectonic Group Two is generally defined by slow cooling throughout the Jurassic and Cretaceous–early Palaeogene, excluding a few samples which demonstrate faster cooling. In addition, the thermal model for one sample (UZ-10), shows evidence for renewed cooling in the late Palaeogene (Figure 4.4c, 4.4d, 4.4e,

and 4.4f).

4.5 Interpretation and Discussion

The results of this study reveal that the Kyzylkum-Nurata Segment, and the relict suture zones that it hosts, underwent a multi-phase cooling history during the Mesozoic and Cenozoic.

4.5.1 Mesozoic and Cenozoic Thermal History and Control of the Suture Zones

The Kyzylkum-Nurata Segment is dominated by three relict suture zones, the South Tian Shan Suture in the north, the Zeravshan suture in the centre, and the Gissar suture to the south (Figure 4.5, Burtman 1975, Konopelko et al. 2017a). These three sutures are the dominant control on the current topography of the Kyzylkum-Nurata Segment, as most of the ranges and outcropping rocks either lie on, or along strike of, each of the suture zones (Figure 4.5, Dolgopolova et al. 2017). In order to evaluate the control of these suture zones on the Mesozoic topography, Figure 4.5 was produced to plot the geospatial location of the confined track MTL for each analysed samples. Longer MTL values correspond to faster cooling (as shown in the thermal history models of Figure 4.4) and show a close relationship with the samples in close vicinity to the sutures (Figure 4.5).

The Nurata Range strikes along the Zeravshan suture and is dominated by long MTLs and fast cooling during the Late Jurassic–Early Cretaceous. In contrast, the Kuldjuktau Mountains, which is located to the south of the western extent of the Zeravshan suture, is characterised by mostly slow cooling during the Late Jurassic–Early Cretaceous and exhibits associated short MTLs (Figures 4.4 and 4.5). This pattern suggests that the Nurata Range was exhumed in the Early Cretaceous, controlled by the reactivation of the Zeravshan suture. At the northern slopes of the Nurata Range, in the Aydar region, the thermal history models show a mixture between relatively fast, Late Cretaceous cooling, and slow, protracted cooling (Figure 4.4d). Here, the AFT ages are younger (Late Cretaceous) and the associated MTLs are shorter on average and show broad distributions (Figures 4.3 and 4.5). This suggests

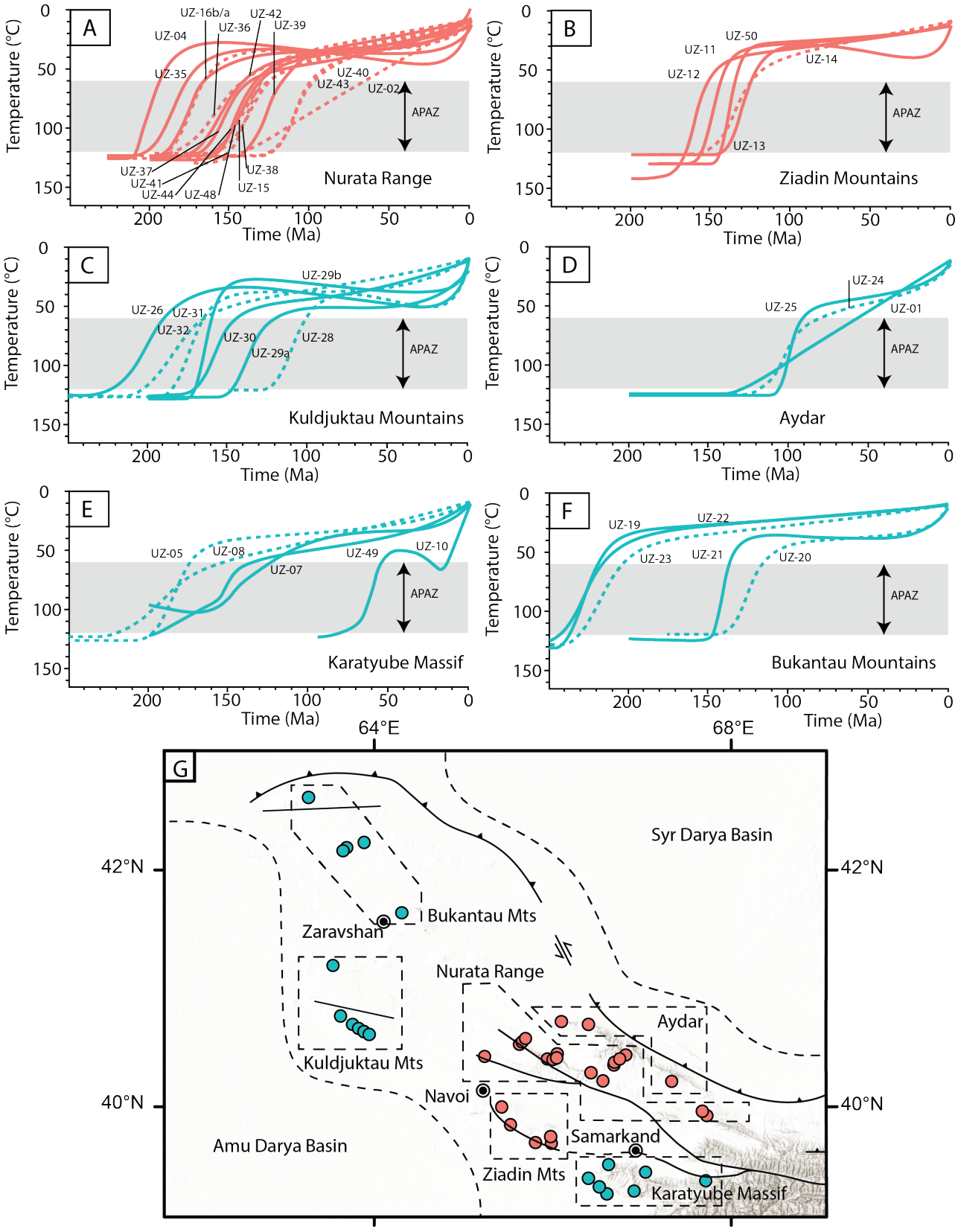

Figure 4.4: Caption next page

Figure 4.4: Plots displaying the modelled temperature-time paths for all samples within the Kyzylkum-Nurata Segment that yielded sufficient confined track data for modelling purposes (>40). Modelling was performed using QTQt Gallagher (2012), with the bold and dashed lines representing the expected temperature-time pathway modelled. Apatite (U-Th-Sm)/He data was used to refine the thermal models where appropriate (see thermal model section). The thermal history models are grouped in their corresponding region; with associated sample location inset (g). Bold lines represent thermal history models from samples which contained at least 40 confined tracks, with dashed lines representing thermal history models from samples which contained between 40 and 25 confined tracks. The grey bar represents the apatite partial annealing zone (APAZ) between 120°C and 60°C. For detailed individual thermal history models and modelling parameters see Appendix File O and P)

that the AFT ages of the Aydar region may represent mixing ages between two thermal events that are not clearly identified by the thermal history modelling. The Aydar samples are in relatively close vicinity to the South Tian Shan Suture, which has been reactivated in the Cenozoic (e.g. Glorie et al. 2011, Käßner et al. 2017b), and therefore, the AFT ages may have been affected by this reactivation event.

The Bukantau Mountains preserve Early Triassic rapid cooling in the north-east and rapid Early Cretaceous cooling the south-west, suggesting that the Cretaceous fault reactivation seen in the Nurata Range also affected the Bukantau Mountains (Figures 4.3, 4.4, and 4.5). However, given that Early Triassic AFT cooling ages are preserved in the region, the oldest preserved cooling signal identified in the Kyzylkum-Nurata Segment, the area would have not been extensively affected by the Cretaceous deformation and exhumation.

In the south of the Kyzylkum-Nurata Segment, along the Gissar suture, there is a section displaying fast cooling (Ziadin Mountains), and a section displaying slow cooling (Karatyube Massif, Figure 4.5). In more detail, samples taken from along a granitoid pluton to the south of the Gissar suture (UZ-08, UZ-09, and UZ-49) display a mixed series of ages from Jurassic to Late Cretaceous along with slow cooling models and relatively short MTLs (Figures 4.3, 4.4, and 4.5). In contrast, samples taken to the north of the Gissar suture, within the Ziadin Mountains, display fast cooling during the Early Cretaceous and associated with long MTLs (Figures 4.4 and 4.5). The differential record of cooling ages on either side of the suture suggests that the suture was reactivated in the Early Cretaceous, leading to the rapidly cooled AFT ages and long MTLs observed in the Ziadin Mountains. Within the suture and

particularly in the high relief areas of the Karatyube Massif, Palaeogene AFT and AHe ages, and fast cooling models were obtained, suggesting that the eastern extent of the suture was reactivated during the Cenozoic (Figure 4.5).

In summary, the Kyzylkum-Nurata Segment records a clear spatial relationship between MTLs and their associated thermal history models, and proximity to a major suture zone. Samples that were taken from ranges and outcrops that lie directly along the suture zones display a different thermal history from samples that were taken from the suture zone peripheries (Figure 4.4). This implies that the main NW–SE striking suture zones were reactivated during the Early Cretaceous. Therefore, the Early Cretaceous topography was likely characterised by a series of linear NW-SE striking ridges that built on the reactivated fault zones.

4.5.2 AFT Age-Confined Track Length Plot

In order to further distinguish periods of tectonic reactivation and exhumation (fast cooling) from periods of erosion and peneplanation (slow cooling), the mean track length for each sample was plotted against its respective age (Figure 4.6). Called a "boomerang plot", this plot demonstrates the relationship between AFT ages and MTL for a set of samples from a region which has likely experienced a multiple thermo-tectonic events (Green 1986, Gallagher & Brown 1997, Gallagher et al. 1998). In such a plot for the Kyzylkum-Nurata Segment, a characteristic "boomerang" trend can be identified, the descending segment defined by comprise Tectonic Group Two samples with Triassic-Early Jurassic AFT ages and the ascending segment defined by published data from the proximal, high elevation (>2km) region of the Gissar Range (Käßner et al. 2017b).

In more detail, Tectonic Group Two demonstrates that the Kyzylkum-Nurata Segment experienced a partial 'boomerang' in the Mesozoic, beginning with fast cooling in the Late Triassic–Early Jurassic (~220–180 Ma), followed by a protracted period of thermal stability, defined by short MTLs, from the Early Jurassic to the Late Cretaceous (~200-50 Ma, blue symbols in Figure 4.6). Within this period of thermal stability, the data is rather scattered by may hint to a gentle increase of MTLs and cooling rate during the Early Cretaceous. The fast-cooling Cenozoic AFT data from the Gissar Range, identified by Käßner et al. (2017b),

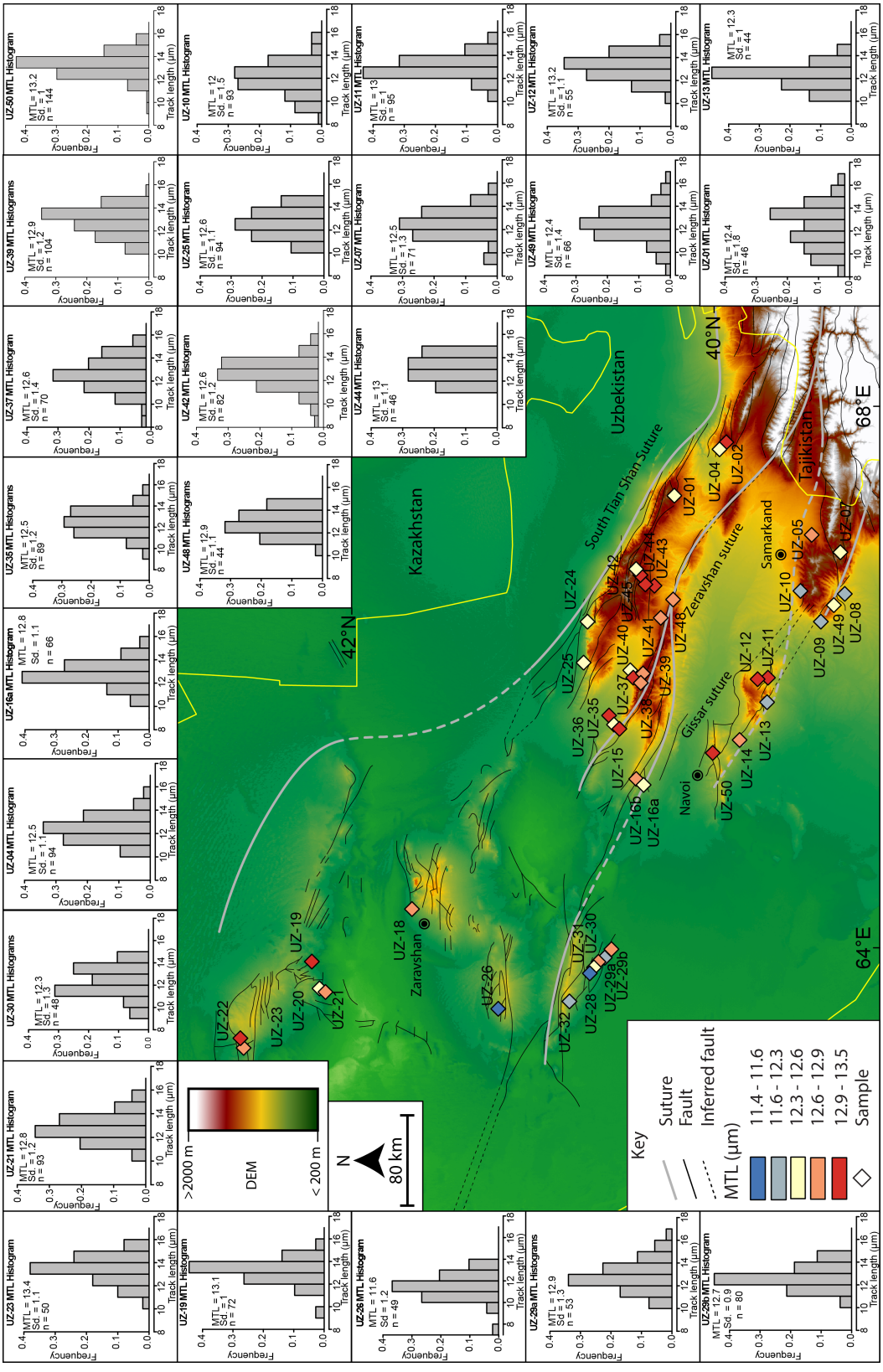

Figure 4.5: Digital elevation map (DEM) of the Kyzylkum-Nurata Segment outlining both the major faults and major sutures (from Survey 2012, Dolgopolova et al. 2017), as well as confined track histograms for modelled samples. The map displays the mean track length (MTL) in μm obtained for each sample with red representing long MTLs, and blue representing short MTLs. In the histograms, Sd. is the standard deviation in μm, and n is the number of confined tracks measured for that sample.

compliments the Mesozoic data obtained in this study, defining the Cenozoic segment to complete the Mesozoic–Cenozoic MTL boomerang (~50–5 Ma, black symbols in Figure 4.6).

In contrast to the complete boomerang recorded by Tectonic Group Two and the published data (Käßner et al. 2017b), samples from Tectonic Group One record a distinct period of rapid cooling during the Late Jurassic–Early Cretaceous (~160–130 Ma, red symbols in Figure 4.6). The samples that comprise Tectonic Group One were sampled either directly or proximal to the major structures of the South Tian Shan and Zeravshan sutures, further highlighting that these suture zones were affected by a secondary phase of exhumation that is only slightly recorded further away from these structures (Figure 4.5 and 4.6).

The interpretation of two discrete thermo-tectonic histories for the Kyzylkum-Nurata Segment can also be identified when comparing the sample elevation to its relative AFT age (Figure 4.7). The age-elevation plot reveals a clear trend of increasing AFT ages with increasing elevation (Figure 4.7). The oldest samples (Triassic) in the Kyzylkum-Nurata Segment are found at the lowest elevation (~200 m). The relationship between age and elevation for Group One and Two diverge in the Jurassic–Cretaceous. In this time period, samples from Group Two (away from the sutures) show significant scatter and a large variation in AFT age at a given elevation, implying slow cooling and thus, a prolonged residence in the APAZ. In contrast, samples from Group One show a strong linear trend of increasing age with elevation during the Late Jurassic–Early Cretaceous.

Combined, both Tectonic Group One and Two chart the thermal evolution of the Kyzylkum-Nurata Segment (Figure 4.6). Although classified as Tectonic Group One, the Bukantau Mountains along the Southern Tian Shan Suture displays a similarity to both Tectonic Group One and Two. The Bukantau Mountains hosts low relief and old ages, synonymous with the regions that define Tectonic Group Two. However, it also hosts fast, suture zone cooling that is characteristic of the regions that comprise Tectonic Group One. As this region shows similarities of both groups, it is reasonable to suggest that the Bukantau Mountains hosts the thermo-tectonic relic of the ancestral Tian Shan which the modern Tian Shan is built upon. Away from the main suture zones, in low-relief areas, the Kyzylkum-Nurata Segment records slow cooling and erosion throughout the Mesozoic, since the Late Triassic (~220 Ma). In the main suture zone, a second phase of rapid uplift and fast cooling has been

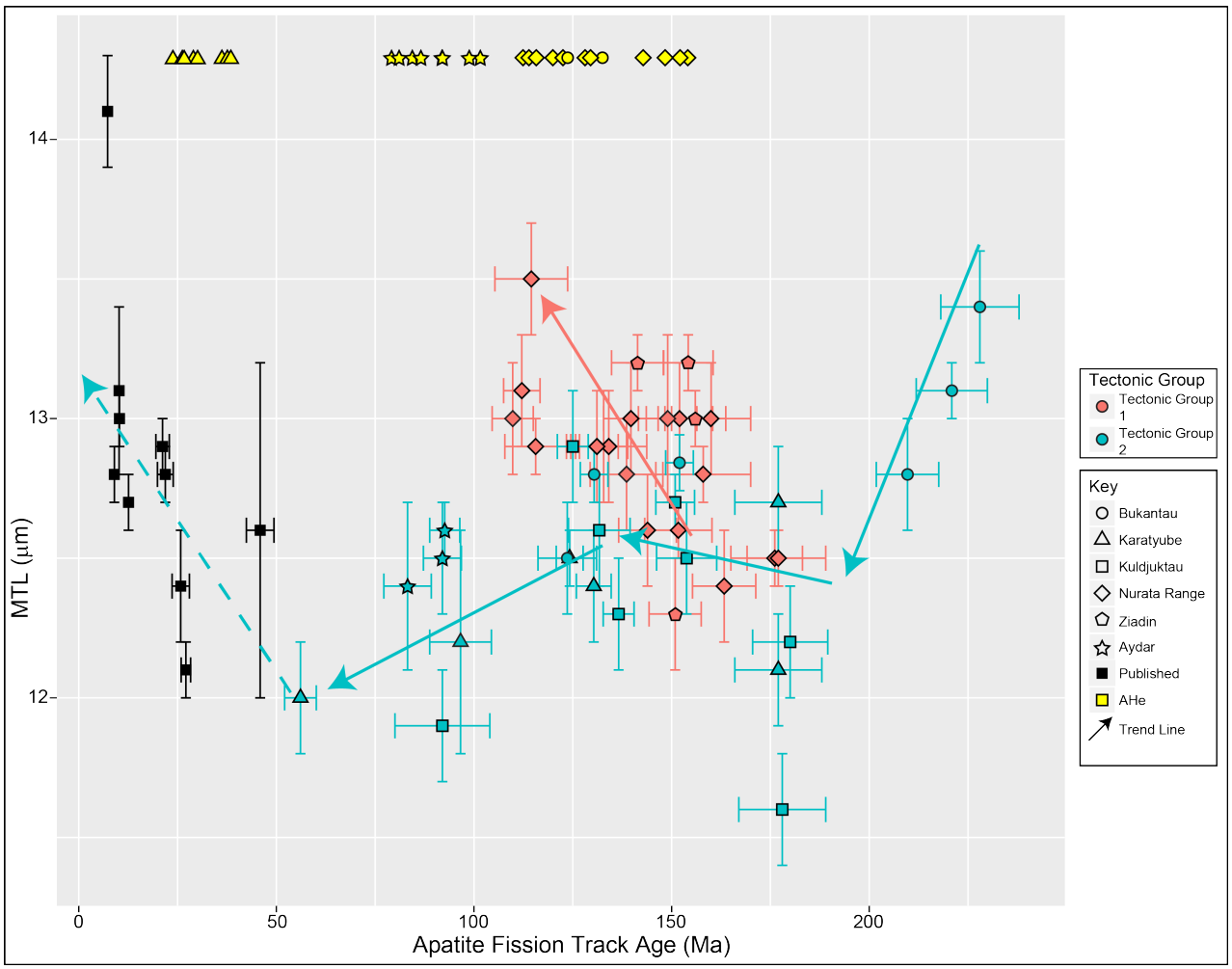

Figure 4.6: A 'boomerang' plot displaying apatite fission track (AFT) central age, and apatite (U-Th-Sm)/He (AHe) ages against mean track lengths (MTL, Table 4.1 and 4.2). Red filled symbols represent samples that correspond to Tectonic Group One and blue filled symbols represent samples that correspond to Tectonic Group Two. Black filled samples are AFT and MTL data obtained from the nearby Gissar Range (Käßner et al. 2017b). The solid arrows outline the thermal pathways defined in this study, and the dashed arrows outline a thermal pathway inferred from this study and the data from Käßner et al. (2017b).

identified in the Early Cretaceous, overprinting the ancestral Tian Shan thermal history of regional slow cooling (Figure 4.4 and 4.5, De Grave et al. 2012). Finally, the Karatyube Massif and Aydar regions of the Kyzylkum-Nurata Segment host samples that document the transition between the Jurassic–Cretaceous thermal history, and the rapid Cenozoic deformation identified elsewhere in the South Tian Shan (Figure 4.6).

4.5.3 Thermotectonic evolution of the Kyzylkum-Nurata Region

Triassic Exhumation

The Kyzylkum-Nurata Segment, hosts three samples which produced a Triassic AFT central age. All three are located in the north-western region of the Bukantau Mountains on the margin of the Syr Darya Basin (Figure 4.3). The three samples yielded central ages of ~230-210 Ma, and were associated with relatively long MTLs and thermal history models showing fast cooling (Figure 4.4). A recent study by Dolgopolova et al. (2017) into the emplacement age and origin of the Kyzylkum-Nurata Segment magmatism, found that all granitoid samples (including a sample from the same region in the Bukantau Mountains) exhibited Permian ages of ~293–273 Ma. The difference in the zircon uranium-lead (ZrUPb) age and the fast cooling, Triassic AFT central ages, suggest that following emplacement, the Kyzylkum-Nurata Segment experienced steady, post-emplacement magmatic cooling. A similar relationship between the Triassic Tian Shan thermochronology and the Syr Darya block has also been found in the Chatkal-Kurama range in the western Tian Shan, with fast cooling Triassic AFT ages identified on the Chatkal-Kurama–Syr Darya margin (Jepson et al., in review).

Previous thermchonological studies in the Tian Shan ascribe Triassic–Early Jurassic AFT ages to the closure of the Turkestan Ocean in the Permian and the subsequent collision of the Qiangtang Block with the Eurasian margin (e.g. Xiao et al. 2009, Glorie et al. 2010, De Grave et al. 2011, Macaulay et al. 2014, Glorie & De Grave 2016). During this period, samples from along the north-western margin of the Kyzylkum-Nurata Segment were rapidly cooled to surface temperatures (Figure 4.4c). Thus, we interpret the Triassic fast cooling signal in our data to be related with exhumation associated with the closure of the Turkestan Ocean and/or the Qiangtang convergence in the Triassic–Early Jurassic.

Jurassic–Cretaceous Regional Tectonic Stability and Peneplanation

The Jurassic-Cretaceous thermo-tectonic evolution of the Kyzylkum-Nurata Segment is defined by two discrete trends outlined by the “boomerang plot” (Figure 4.6); one profile demonstrating thermo-tectonic stability, and one profile demonstrating an increased basement cooling via exhumation. The samples that comprise Tectonic Group Two record a

regional trend of tectonic stability and pleneplanation.

A series of samples from across the Kyzylkum-Nurata Segment yielded Early to Middle Jurassic AFT central ages (Figure 4.2). The Early to Middle Jurassic AFT ages were largely associated with low MTLs, and the associated thermal history models showing slow cooling (Figures 4.4 and 4.5). These data are indicative of protracted residence in the APAZ, suggesting a period of steady, slow denudation and tectonic quiescence at that time. A recent study into the lowest part of the Mesozoic cover of the Kyzylkum-Nurata Segment by McCann (2016b) identified the presence of Lower Jurassic alluvial-fan, river valley, lagoonal, and shallow marine sedimentation (distinct absence of Triassic sedimentation). The source of the sedimentation is assessed as derived from the weathering and erosion of the recently uplifted Kyzylkum-Nurata Segment (McCann 2016b). This conclusion fits with the Triassic exhumation identified in this study, indicating that the Triassic exhumation provided the source that underwent subsequent erosion and sedimentary deposition in the Kyzylkum-Nurata Segment during the Jurassic.

During the Jurassic, the greater western Tian Shan experienced periodic marine incursions by the Paratethys Sea into the Amu Darya, Tajik, Fergana, and Tarim basins (Bosboom et al. 2011, 2014, Bande et al. 2017b, De Pelsmaeker et al. 2018). The series of marine incursions by the Paratethys Sea to the western Tian Shan indicates that there was a period of tectonic stability, erosion, and sedimentation experienced by the Kyzylkum-Nurata Segment during the Jurassic (Figure 4.7).

Localised Late Jurassic to Early Cretaceous Exhumation

In contrast to the regional tectonic stability, defined by samples from Tectonic Group Two, samples taken in vicinity of the faults (Tectonic Group One) record rapid basement cooling and exhumation during the Late Jurassic–Early Cretaceous. During the Late Jurassic–Early Cretaceous, the sutures of the Kyzylkum-Nurata Segment underwent a period of exhumation, deformation, and mountain building. This period of deformation and reactivation is evidenced by samples with overlapping closure temperatures, long MTLs, and rapid cooling thermal history models (Figure 4.6). Recent thermochronological studies on the basement of the proximal Gissar Range by Käßner et al. (2017b) and Käßner et al. (2017a) also iden-

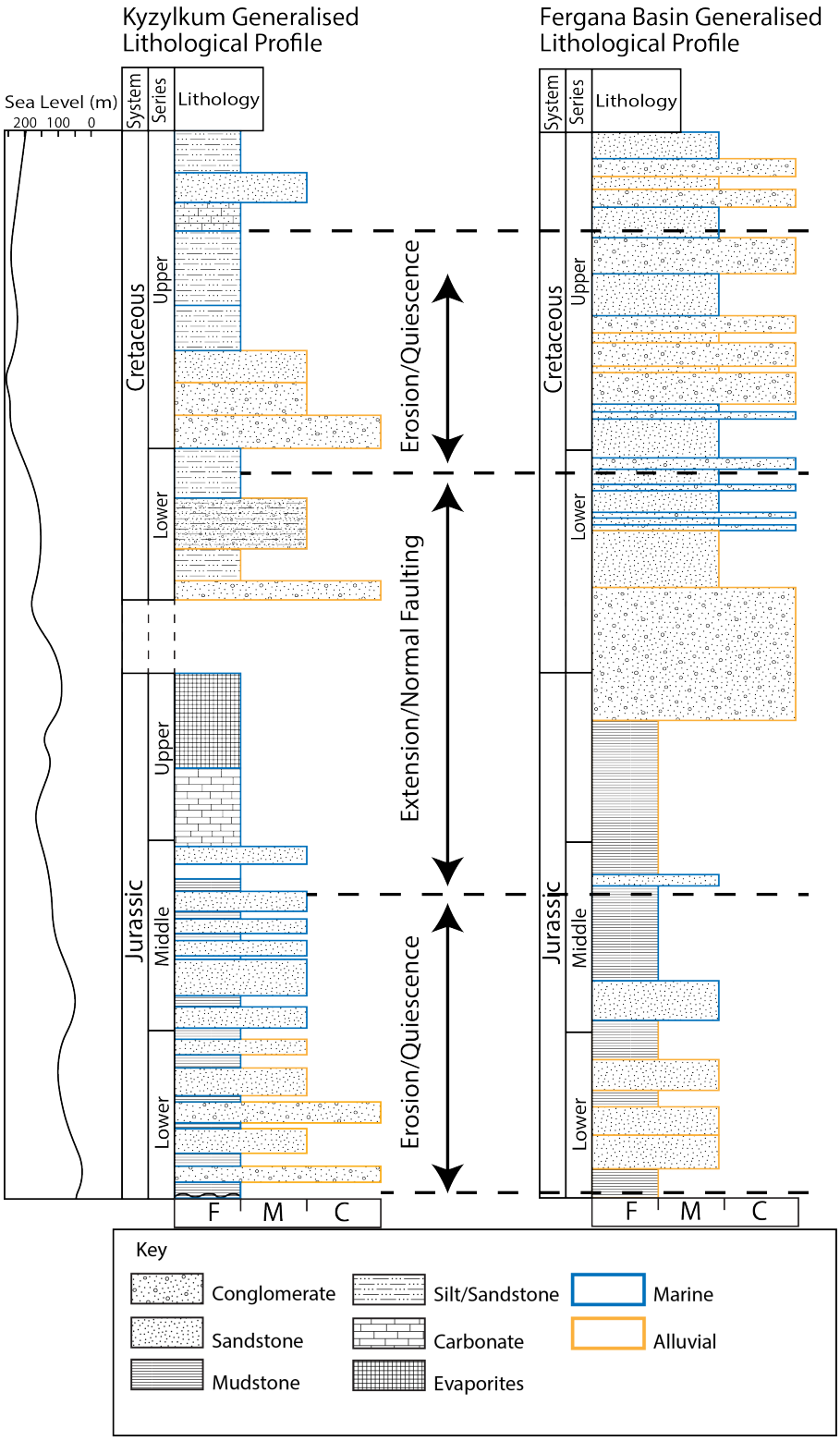

Figure 4.7: Generalised lithological profiles for both the Kyzylkum (McCann 2016a,b), and the nearby Fergana Basin (De Pelsmaeker et al. 2018), as well as the global eustasy for the Jurassic and Cretaceous (Haq et al. 1987). Compared against the relationship between the apatite fission track (AFT) age and mean track length (MTL) of samples from the Kyzylkum-Nurata Segment in order to identify periods of uplift, erosion, and tectonic stability. Sediment grain size is defined by fine (F), medium (M), or coarse (C).

tified the presence of a Late Jurassic–Early Cretaceous cooling signal, however, this signal was largely obscured due to a prolific Cenozoic thermal overprint (e.g. Bande et al. 2017b, Käßner et al. 2017b,a, Jepson et al. 2018a). The basement outcrops in the Kyzylkum-Nurata Segment preserve this Cretaceous cooling event, as the faults and ranges have been sheltered from the major impacts of subsequent Mesozoic–Cenozoic collisions, further evidenced work by De Pelsmaeker et al. (2018) and Jepson et al., (in review) indicating that Talas-Fergana Fault (Figure 4.1) acted as a barrier to the strain that was being experienced by the Tian Shan east of the Talas-Fergana Fault.

The Mesozoic sedimentary record in the Kyzylkum desert identified by McCann (2016a,b) and simplified in Figure 4.7, shows a period of marine incursion depositing a carbonate layer, transitioning into a salt dominated layer, before a distinct hiatus and subsequent coarse clastic sedimentation at the start of the Early Cretaceous. The marine sediment transition and unconformity could represent a response to exhumation along the Kyzylkum-Nurata Segment, leading to a lack of sedimentation during the Early Cretaceous. At the same time, in the Fergana Basin, thick packages of coarse alluvial sediments were being deposited, indicating that some of the coarse sediment preserved in the Fergana Basin could have been sourced from the exhumed Kyzylkum-Nurata Segment (Figure 4.7).

To the east of the Kyzylkum-Nurata Segment, in the Kyrgyz Tian Shan, other geo- and thermochronological studies have identified Late Jurassic–Early Cretaceous exhumation. Nachtergaele et al. (2017) and De Pelsmaeker et al. (2018) found that the areas to the east of the Talas–Fergana fault underwent rapid Early Cretaceous basement cooling, and that the fault acted as a structural divide between the Cretaceous exhumed Tian Shan to the east and the Paratethys Ocean to the west. The Late Jurassic–Early Cretaceous thermochronological signal has previously been interpreted as a relic of the Cimmearan collisions that drove much of the deformation in the Middle Tian Shan (De Grave et al. 2007, Glorie & De Grave 2016, Käßner et al. 2017a, Nachtergaele et al. 2017). Given that the exhumation at the time was solely focused on suture zones within the Kyzylkum-Nurata Segment, it may be more likely that the suture zones were reactivated by an extensional tectonic event. Stockli et al. (2002) demonstrated that extension and associated rapid footwall exhumation can result in (tilted) sections where samples record rapid localised cooling, without the need

for voluminous denudation. Recent geodynamic models by Hall (2012) and Zahirovic et al. (2016) have suggested that the southern Eurasia margin was undergoing slab rollback related extension during the mid-Cretaceous (~155 Ma), which could have been a possible mechanism for footwall exhumation and basement cooling identified in the sampled suture zones. Therefore, we envisage the Cretaceous Tian Shan landscape and deformation style to be comparable to the present-day Basin and Range province in the south-western USA.

Late Cretaceous to Early Palaeogene Tectonic Stability and Denudation

From the mid Cretaceous to the early Palaeogene, the low-temperature thermochronology of the Kyzylkum-Nurata Segment shows a decline in fast cooling and exhumation, and thus, transitioning into a period of slow cooling and erosion, with distinct absence of thermochronology data from ~80–50 Ma (Figure 4.6). Similarly, in the Gissar Range, Käßner et al. (2017b) also identifies a period of Late Jurassic to Oligocene quiescence from ~150 to 25 Ma.

McCann (2016a) identified the presence of Cretaceous sedimentation from the Albian to the Maastrichian in fluvial and shallow marine environments indicative of a coastal-marine transitional zone. During the Late Cretaceous the Kyzylkum-Nurata Segment experienced coastline change due to major marine incursions, with much of the material for sedimentation coming from the Late Jurassic-Early Cretaceous exhumed regions in the Kyzylkum-Nurata Segment (Figure 4.7). The sedimentary evidence, in conjunction with the thermochronological data provided in this paper, suggest that the Kyzylkum-Nurata Segment experienced a period of erosion and denudation causing sedimentation during the Late Cretaceous–early Palaeogene (McCann 2016a).

The Late Cretaceous stability is contrasted by samples of the Aydar region, close to the South Tian Shan suture, which display over-lapping AFT and AHe thermochronometers (Figure 4.5 and 4.6, Tables 4.1 and 4.2). McCann (2016a) found that the northern and southern extents experienced a phase of terrestrial sedimentation during the Upper Cretaceous. The terrestrial sedimentation and over-lapping thermochronometers implies that the margins of the Northern Nurata Range experienced some degree of exhumation during the Late Cretaceous. Although, it is likely that the Cretaceous AFT and AHe ages represent mixing

ages between the Early Cretaceous and late Palaeogene thermal events.

Palaeogene Reactivation

During the Palaeogene, the Eurasian continent was redeformed as a result of the collision of India with Eurasia (e.g. Beck et al. 1995, Aitchison et al. 2007, Najman et al. 2010, van Hinsbergen et al. 2011). In the Kyzylkum-Nurata Segment we identify only a minor thermochronological response to this collision in the Karatyube Massif, proximal to the high elevation Gissar Range (Figure 4.3). In addition, it is possible that the presence of mixing ages in the Aydar region may also be an indicator of Palaeogene thermal activity, as explained above. Given the lack of relief within the Kyzylkum-Nurata Segment, the thermo-tectonic response to the India–Eurasia collision has not been exhumed to the surface yet.

In the South Tian Shan, numerous thermochronological studies report Palaeogene and Neogene ages that correspond with the collision and ongoing indenture of the Indian continent with Eurasia (Sobel, Chen & Heermance 2006, De Grave et al. 2012, Bande et al. 2017b, Käßner et al. 2017b, Nachtergaele et al. 2017, Jepson et al. 2018a). Since only a slight Palaeogene thermochronological signal can be identified in the Kyzylkum-Nurata Segment, it is likely that much of the exhuming strain and deformation produced by the India–Eurasia collision is partitioned away from the western margin of the South Tian Shan and into the core of the Tian Shan.

4.5.4 Conclusion

In this study we presented low-temperature apatite thermochronological analysis of forty-five samples from the western segment of the Southern Tian Shan, the Kyzylkum-Nurata Segment, in order to track its thermo-tectonic evolution through the Mesozoic–Cenozoic. The Kyzylkum-Nurata Segment experienced a phase of fast basement cooling and exhumation in the Triassic that is interpreted as a response to the closure of the Palaeo-Asian Ocean. During the Jurassic and Cretaceous, the study area experienced regional slow cooling. However, the major suture zones that dissect the Kyzylkum-Nurata Segment record rapid cooling during the Late Jurassic–Early Cretaceous, coincident with increased sedimentation in the Kyzylkum and Fergana Basins. We interpret this event of fault reactivation to be related

with footwall exhumation as a response to extensional tectonics in the Tethys Ocean. In the Late Cretaceous, the Kyzylkum-Nurata Segment experienced a second phase of marine incursion, erosion, and slow cooling until the early Palaeogene. Finally, in the Palaeogene, the Kyzylkum-Nurata Segment records minor evidence for cooling and exhumation due to the collision of India with the Eurasian margin.

This study has revealed that the western segment of the South Tian Shan has experienced a different thermo-tectonic evolution when compared to its core, where thermo-tectonic evolution of the South Tian Shan has been overprinted via rapid Cenozoic exhumation. The western segment preserves a detailed archive of the Mesozoic tectonic activity that Eurasia experienced prior to the India–Eurasia collision.

Chapter 5

Thermochronological insights into the structural contact between the Tian Shan and Pamirs, Tajikistan

Statement of Authorship

Title of Paper	Thermochronological insights into the structural contact between the Tian Shan and Pamirs, Tajikistan
Publication Status	☑ Published ☐ Accepted for Publication ☐ Submitted for Publication ☐ Unpublished and Unsubmitted work written in manuscript style
Publication Details	Published in Terra Nova

Principal Author

Name of Principal Author (Candidate)	Gilby Jepson		
Contribution to the Paper	Sample collection, sample analysis, data interpretation, and principal author of paper.		
Overall percentage (%)	70		
Certification:	This paper reports on original research I conducted during the period of my Higher Degree by Research candidature and is not subject to any obligations or contractual agreements with a third party that would constrain its inclusion in this thesis. I am the primary author of this paper.		
Signature		Date	31/08/18

Co-Author Contributions

By signing the Statement of Authorship, each author certifies that:

i. the candidate's stated contribution to the publication is accurate (as detailed above);

ii. permission is granted for the candidate in include the publication in the thesis; and

iii. the sum of all co-author contributions is equal to 100% less the candidate's stated contribution.

Name of Co-Author	Stijn Glorie		
Contribution to the Paper	Sample collection, data interpretation, and thesis supervisor.		
Signature		Date	31/08/18

Name of Co-Author	Dmitry Konopelko
Contribution to the Paper	Sample collection, data interpretation, and geological background.

Signature		Date	31/08/18
Name of Co-Author	Jack Gillespie		
Contribution to the Paper	Data interpretation		
Signature		Date	31/08/18
Name of Co-Author	Martin Danišík		
Contribution to the Paper	Data analysis, data interpretation, and methods.		
Signature		Date	31/08/18
Name of Co-Author	Noreen Evans		
Contribution to the Paper	Data analysis, data interpretation, and methods.		
Signature		Date	31/08/18
Name of Co-Author	Yunus Mamadjanov		
Contribution to the Paper	Sample collection.		
Signature		Date	31/08/18
Name of Co-Author	Alan Collins		
Contribution to the Paper	Data interpretation, secondary supervisor.		
Signature		Date	31/08/18

Please cut and paste additional co-author panels here as required.

Published by Gilby Jepson, Stijn Glorie, Dmitry Konopelko, Jack Gillespie, Martin Danišík, Noreen Evans, Yunus Mamadjanov, and Alan S. Collins (2018) in , 'Thermochronological insights into the structural contact between the Tian Shan and Pamirs, Tajikistan', Terra Nova 30(2), 95-104, doi : 10.1111/*ter*.12313

5.1 Introduction

The Tian Shan is the world's largest intracontinental deformation zone and has experienced a periodic exhumation history since the late Palaeozoic in response to tectonic events at the southern Eurasian Plate margins (e.g. Windley et al. 1990, Bullen et al. 2001, De Grave et al. 2007). The exact timing of the thermal events that affected the Tian Shan throughout the Meso-Cenozoic is difficult to constrain, because older events can be overprinted or completely erased by subsequent events. Dating the discrete thermal events within modern mountainous regions such as the South Tian Shan (STS) requires (1) the use of multi-method thermochronology, (2) sufficient exposure of vertical sampling profiles and/or (3) targeting major faults (e.g. De Grave et al. 2011, Macaulay et al. 2014, Glorie & De Grave 2016). The latter is particularly relevant for the Tian Shan as several authors have demonstrated that Cenozoic deformation within the Tian Shan was focused along pre-existing basement structures (Molnar & Tapponnier 1975).

In this study, we target the structural contact between the STS and the northern Pamir Mountains (Pamirs). Through the application of (1) apatite U/Pb dating (closure temperature ~550-350°C Cherniak et al. 1991), (2) zircon (U–Th–Sm)/He dating (closure temperature ~180°C, Reiners et al. 2002), (3) apatite fission track thermochronology (partial annealing zone ~120–60°C, Wagner et al. 1992) and (4) apatite U–Th–Sm/He dating (partial annealing zone ~80–40°C, Zeitler et al. 1987), we aim to provide insights into the thermotectonic history of the STS and the western Central Asian Orogenic Belt in general.

5.2 Geological Background

The structural contact between the Tian Shan and Pamirs is characterised by a series of thrust faults, known as the Vakhsh-Surkhob fault zone (e.g. Hamburger et al. 1992, Burtman

& Molnar 1993) or Vakhsh thrust system (Schurr et al. 2014). The South Tian Shan (STS), to the north of the Vakhsh-Surkhob fault zone, formed as a result of the closure of the Palaeo-Turkestan Ocean during the late Carboniferous (e.g. Windley et al. 1990, Hamburger et al. 1992, Burtman & Molnar 1993, Konopelko et al. 2015, 2017a). The Pamirs, south of the fault zone, represent a complex Mesozoic collisional structure indented and thrust to the north during Meso-Cenozoic times (Figure 5.1, e.g. Burtman 2000, Sobel et al. 2013, Stübner et al. 2013, Robinson 2015). The Tian Shan experienced the far-field effects of oceanic closures and terrane accretion of peri-Gondwanan fragments to the southern Eurasian margin during the Permian to Palaeogene (e.g. Brookfield 2000, De Grave et al. 2013, Glorie & De Grave 2016).

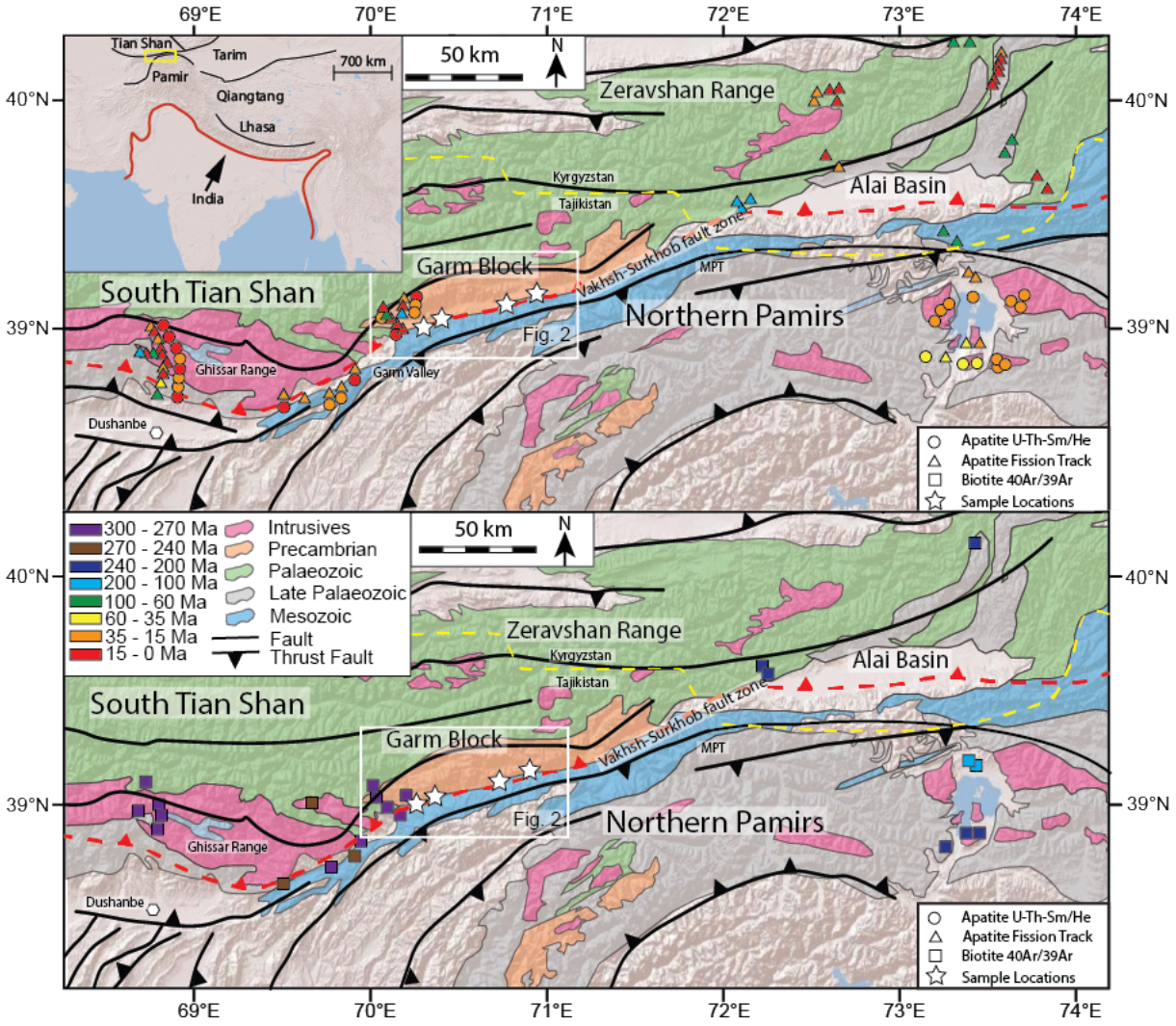

Figure 5.1: Geological map of the South Tian Shan and Pamirs modified after Vlasov et al. (1991) with published thermochronological data (Amidon & Hynek 2010, De Grave et al. 2012, Bande et al. 2017b,c, Käßner et al. 2017a,b). The MPT = Main Pamir Thrust, and the red dashed line represents the Vakhsh-Surkhob fault zone. Ages of thermochronological data are shown by the colour scale, depicted in the inset. The yellow line represents the border between Tajikistan and Kyrgyzstan

The most prominent of these tectonic events were (1) the final closure of the Palaeo-Asian Ocean (PAO) from the Carboniferous until the end of the Permian (e.g. Li et al., 2016; Xiao et al., 2009), (2) the collision of the Qiangtang block in the Triassic (e.g. Ratschbacher et al. 2003, Robinson 2015), (3) the collision of the Lhasa block and the closure of the Rushan Ocean in the Jurassic (e.g. Schwab et al. 2004, Kapp et al. 2007), and (4) the Palaeogene collision of India with Eurasia (e.g. Rowley 1996).

Thermochronological studies have previously determined that the Tian Shan experienced abundant exhumation during the Mesozoic, related to the Qiangtang and, to a lesser extent, the Lhasa collisions (e.g. Jolivet et al. 2007, De Grave et al. 2011, 2013). Cenozoic thermochronological ages (~25–20 Ma and 10–3 Ma) have been reported in areas of high relief and along major fault zones, demonstrating local topographic development since the late Oligocene (Hendrix et al. 1992, Sobel, Oskin, Burbank & Mikolaichuk 2006, Glorie et al. 2011, Macaulay et al. 2014, Glorie & De Grave 2016). In contrast, Käßner et al. (2017a,b) recently concluded that the western STS experienced tectonic quiescence between 150 and 15 Ma (Figure 5.1). This study targets a major structural contact, aiming to distinguish between these models and to refine the thermal history of the STS.

5.3 Samples and Methods

Six samples were taken from granitoids, migmatite leucosomes and gneisses (with late Carboniferous–early Permian zircon U/Pb ages; Konopelko et al. 2015) from STS exposure along the Surkhob river valley (Figure 5.2). In this valley, the south-verging Surkhob fault marks the northern edge of the Vakhsh-Surkhob fault zone and represents a back-thrust to the regional north-verging orogenic polarity (e.g. Hamburger et al. 1992, Burtman & Molnar 1993). The samples were analysed using apatite U-Pb, apatite fission track and zircon and apatite (U–Th–Sm)/He methods.

Apatite fission track ages and chemical compositions are presented on radial plots (Vermeesch 2009). Apatite chemistry, in particular variability in chlorine concentration (^{35}Cl), is known to influence the annealing properties of fission tracks (Green et al. 1986). Hendriks & Redfield (2005) suggested that uranium (^{238}U) may also enhance annealing. In this study, we measured both Cl and U concentrations using laser ablation–inductively coupled plasma–mass spectrometry and discuss their relevance in the context of fission track annealing. For the determination of Cl values, we followed the protocol outlined in Chew et al. (2014). Fission track lengths were obtained after ^{252}Cf irradiation (Donelick & Miller 1991). Thermal history modelling was conducted in QTQt using Cl as the kinetic parameter. Detailed methodology is given in Data S1.

5.4 Results

Detailed methods, single-grain apatite uranium-lead, apatite fission track, zircon and apatite (U-Th-Sm)/He, and thermal modelling constraint data are available in Appendix Files Q, R, S, T, and U.

5.4.1 Apatite U/Pb results

Apatite U/Pb analysis was applied to three samples (Gm-21, Gm-17 and Gm-16) (Figure 5.2). The three samples yielded similar ^{207}Pb corrected weighted average ^{206}Pb/^{283}U ages of 251 ± 3 Ma, 252 ± 7 Ma and 252 ± 5 Ma (Figure 5.3; Table 5.1; Appendix File R). Given the consistency of the obtained apatite U/Pb results, the three samples were pooled to produce a weighted mean apatite U/Pb age of 251 ± 2 Ma (Figure 5.3). This age constrains the timing of cooling below ~550-350°C along the STS–Pamirs border to the Permian–Triassic boundary.

5.4.2 Apatite fission track results

Apatite fission track (AFT) thermochronology was applied to six samples from along the Vakhsh-Surkhob fault zone (Figure 5.2). Individual radial plots of AFT ages were produced for samples Gm-21, Gm-19 and Gm-11. Samples Gm-15, Gm-16 and Gm-17 were taken from different rock samples at the same locality, to exclude any compositional control on the obtained ages. Given that the three samples show similar AFT ages, they are pooled into a single radial plot (Figure 5.4). Sample Gm-21 produced a central age of 22 ± 2 Ma, Gm-19 produced a central age of 10 ± 1 Ma, samples Gm-15, Gm-16 and Gm-17 gave a combined central age of 10 ± 1 Ma, and Gm-11 produced a central age of 9 ± 2 Ma (Figure 5.4). The results for each sample are detailed in Table 5.2, Figure 5.4 and Appendix File S. For several samples (particularly Gm-15, Gm-16, Gm-17 and Gm-19), a bimodality in single grain AFT ages is detected that correlates with different U concentrations. Based on this bimodality, two principal age components can be defined: (1) an Oligocene–early Miocene (~30–20 Ma) population that is best preserved in the west (sample Gm-21), and (2) a late Miocene (~10 Ma) population that is best preserved in the east (all other samples; Figure 5.4). Given the large variation in U concentrations between samples, the relationship between age and

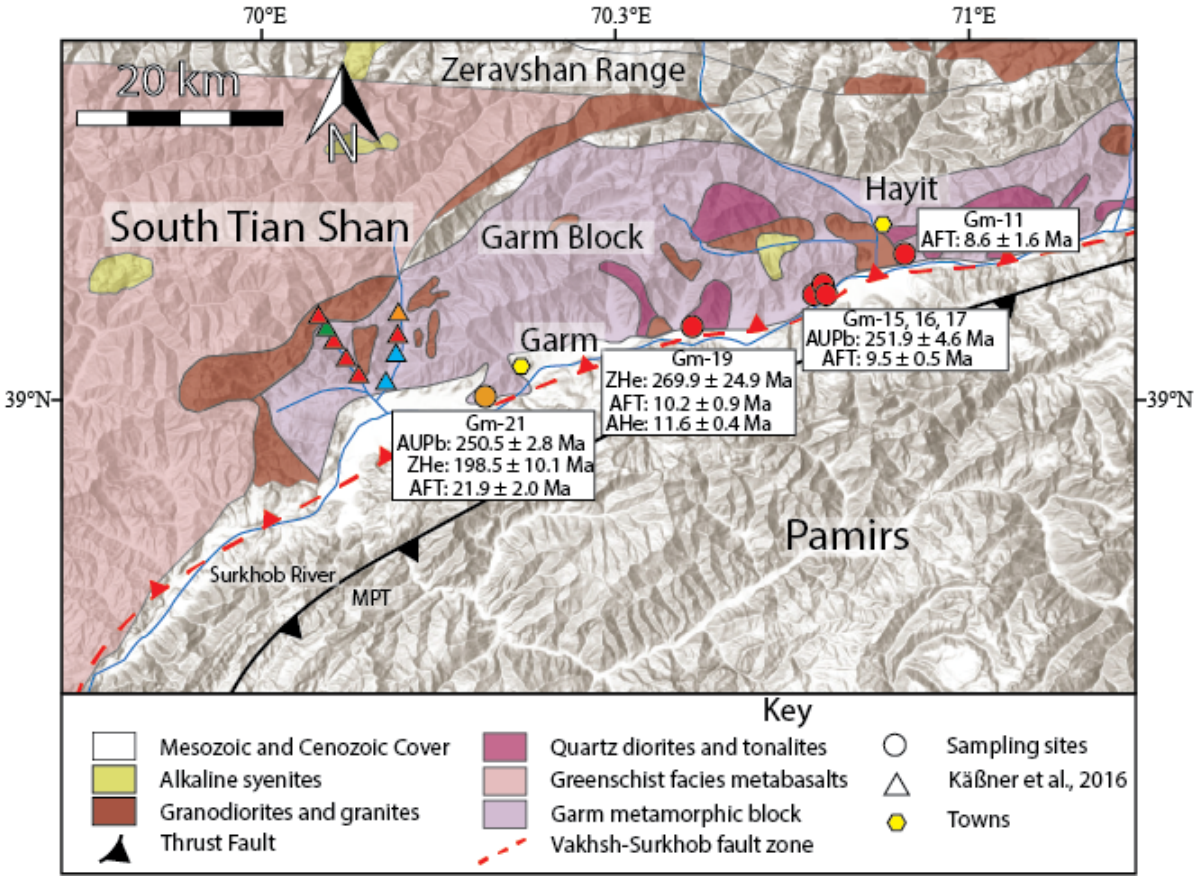

Figure 5.2: Schematic geological map of the study area along the Vakhsh-Surkhob fault zone, Tajikistan (modified after Konopelko et al. 2015). For each sample, a summary of the apatite U/Pb (AUPb), zircon (U–Th–Sm)/He (ZHe), apatite fission track (AFT, central ages) and apatite (U–Th–Sm)/He (AHe, corrected mean ages) results is given. The MPT = Main Pamir Thrust; triangles represent AFT data from Käßner et al. (2017b). The colour key for the sample ages is given in Figure 5.1

U is demonstrated in the individual radial plots. Correlations with Cl concentrations are rather modest and only become apparent in a pooled radial plot (Figure 5.4). The AFT length results show a narrow distribution (1.2 μm standard deviation) and long (14.1 μm) mean track length (MTL) for the eastern samples and broader (1.4–2.4 μm) distributions centred around shorter MTLs (12.8–13.1 μm) for the western samples (Figure 5.4). These length data suggest a longer residence in the partial annealing zone for samples in the west compared with the east.

5.4.3 Apatite and zircon (U–Th–Sm)/He results

Apatite (U–Th–Sm)/He (AHe) analysis was carried out on 7 grains from sample Gm-19, producing four consistent single grain ages with a mean age of 11.6 Ma ± 0.9 Ma (Table 5.3; Appendix File T). This AHe age correlates with the ~10 Ma AFT age peak, indicating a period of rapid cooling along the Vakhsh-Surkhob fault zone. Three other single grain AHe ages were largely consistent and produced a mean AHe age of 23.7 ± 1.6 Ma (Table 5.3; Appendix File T). The meaning of the ~24 Ma AHe age is uncertain and could indicate the presence of undetected, He-bearing inclusions (Table 5.3, Appendix File T, Ehlers & Farley 2003, Danišík et al. 2017). However, the remarkable consistency between both AFT and AHe populations likely indicates that some apatite grains (partially) preserve different cooling steps in the thermal history of the fault (e.g. Glorie & De Grave 2016).

Table 5.1: Apatite U/Pb data. n is the number of analyses performed on each sample. Each value refers to a weighted mean. A table showing the individual analyses can be found in Appendix File R

Sample	n	$^{207}Pb/^{235}U$	$\pm1\sigma$	$^{206}Pb/^{238}U$	$\pm1\sigma$	$^{207}Pb/^{206}Pb$	$\pm1\sigma$	Age (Ma)	$\pm1\sigma$
Gm-16	25	2.4	0.25	0.06	0.002	0.3	0.02	251.9	4.6
Gm-17	19	9.9	1.1	0.11	0.008	0.6	0.02	251.9	7.4
Gm-21	15	1.2	0.06	0.05	0.001	0.2	0.01	250.5	2.8

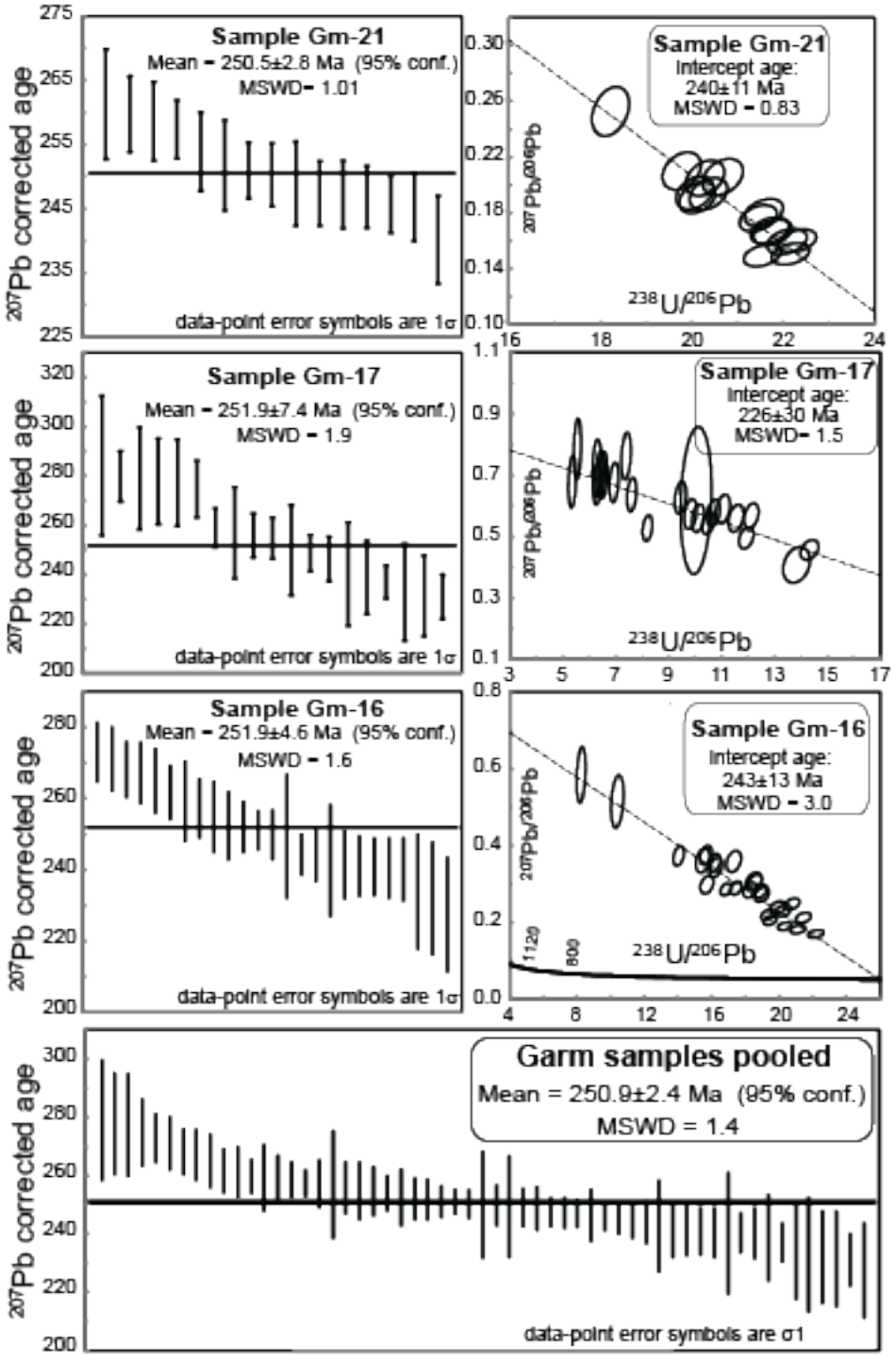

Figure 5.3: Tera-Wasserburg plots and ^{207}Pb corrected weighted average $^{206}Pb/^{238}U$ age rank plots for samples Gm-21, Gm-19 and Gm-16, along the VakhshSurkhob fault zone, Tajikistan

Table 5.2: Apatite fission track data and chemistry: ρ_s is the density of spontaneous tracks within the region of interest and is expressed as 10^5 tracks/cm^2. n is the number of grains analysed per sample. N_s is the total number of counted spontaneous tracks per sample. ^{238}U is the average concentration in ppm of uranium 238 measured in each grain. ^{35}Cl is the average concentration in ppm of chlorine 35 measured in each grain; concentrations were obtained using laser ablation–inductively coupled plasma–mass spectrometry (LA-ICP-MS). Dpar is the average length of spontaneous track etch pits in μm. t is the AFT central age for each sample in Ma. Single grain data are available in Appendix File S.

Sample	Long	Lat	ρ_s	$\pm1\sigma$	n	N_s	^{238}U	$\pm1\sigma$	^{35}Cl	$\pm1\sigma$	Dpar	$\pm1\sigma$	t	$\pm1\sigma$
Gm-11	39.161	70.907	0.6	0.1	13	33	18.7	2.7	830.0	460.0	1.2	0.4	8.6	1.6
Gm-15	39.121	70.785	3.5	0.3	18	334	77.3	5.7	891.7	351.7	1.5	0.3	12.7	2.0
Gm-16	39.121	70.785	3.4	0.3	30	372	123.1	6.9	1260.0	534.0	1.4	0.3	7.3	0.5
Gm-17	39.122	70.786	1	0.1	25	161	22.4	0.8	1292.2	460	1.2	0.4	12	1
Gm-19	39.082	70.609	33.7	0.4	33	1852	73.7	5.4	2836.3	903.7	1.8	0.5	10.2	0.9
Gm-21	39.006	70.317	17.9	1.4	20	966	204.3	11.2	3232.5	737	1.7	0.7	21.9	2

Table 5.3: Mean zircon (U–Th–Sm)/He and apatite (U–Th–Sm)/He age and chemistry data. For single grain analysis, see Appendix File T. Concentrations of thorium, uranium and samarium in ng. He is the concentration of helium measured in ncc. Th/U is the ratio of thorium to uranium. Raw is the age before the FT correction is made. F_{T} is the alpha-ejection correction parameter of Farley et al. (1996). Age is the age after applying the F_{T} correction. TAU is the total analytical uncertainty in %, and eU is the effective uranium (Guenthner et al. 2013). The apatite U–Th–Sm/He data for Gm-19 were subdivided into two age populations, discussed in the text.

Sample	^{232}Th±(%)	^{238}U±(%)	^{147}Sm±(%)	He±(%)	TAU	eU	Th/U	Raw	±1σ	F_{T}	Cor. age±1σ
Zircon (U-Th-Sm)/He data											
Gm-19	0.668±1.6	2.333±2.0	0.004±15.7	64.308±0.8	2.0	2.5	0.3	205.7	4.2	0.77	269.9±24.9
Gm-21	0.573±1.4	3.944±1.9	0.002±17.4	69.295±1.0	2.1	4.1	0.2	138.9	2.9	0.70	198.5±10.1
Apatite (U-Th-Sm)/He data											
Gm-19 (1)	0.005±5.1	0.191±5.0	0.015±0.4	0.204±2.8	5.8	0.2	0.1	7.6	0.4	0.65	11.6±0.9
Gm-19 (2)	0.003±9.2	0.056±3.9	0.011±0.3	0.102±1.7	4.2	0.1	0.1	15.6	0.7	0.65	23.7±1.6

Zircon (U–Th–Sm)/He (ZHe) analysis was performed on samples Gm-21 and Gm-19, with four single grain ages produced for each sample (Table 5.3, Appendix File T). Sample Gm-21 yielded consistent single grain ages and a weighted mean age of 199 ± 10 Ma, while sample Gm-19 produced more variable single grain ages. The youngest single grain ZHe age for Gm-19 (197 ± 13 Ma) matches well with the mean ZHe age for Gm-21 (199 ± 10 Ma, Appendix File T). The other single grain ages exceed the zircon U–Pb age obtained for the rock (281 ± 16 and 301 ± 17 Ma, Konopelko et al. 2015), due to radiation damage (Guenthner et al. 2013, Danišík et al. 2017).

5.4.4 Thermal history reconstruction

QTQt thermal history models were obtained for samples Gm-21, Gm-19 and Gm-15, Gm-16 and Gm-17 (pooled) using AFT and AHe data, where available, and with Cl as a kinetic parameter (Figure 5.4 Gallagher 2012). The modelling parameters are outlined in Appendix File U (Flowers et al. 2015). The models for Gm- 21 and Gm-19 (Figure 5.5) indicate that cooling along the Vakhsh-Surkhob fault zone initiated prior to ~25 Ma and ~19 Ma, respectively. Both models show a secondary thermal event (re-entry to the APAZ) at ~10–5 Ma. In the east, the thermal model for pooled samples Gm-15, Gm-16 and Gm-17 shows enhanced cooling to subsurface temperatures at ~10 Ma (Figure 5.5). Hence, the models suggest two phases of fast cooling during the Oligocene–early Miocene and late Miocene, consistent with the AFT age populations defined above.

5.5 Discussion

The results constrain the thermal history of the sampled rocks along the STS–Pamirs boundary from ~500°C to surface temperatures. The following section discusses the results, in order of time and closure temperature of the applied thermochronometers.

5.5.1 Permian–Triassic

This study reports Permian–Triassic boundary apatite uranium lead (AUPb) ages that are significantly younger than the late Carboniferous–early Permian zircon crystallisation U/Pb

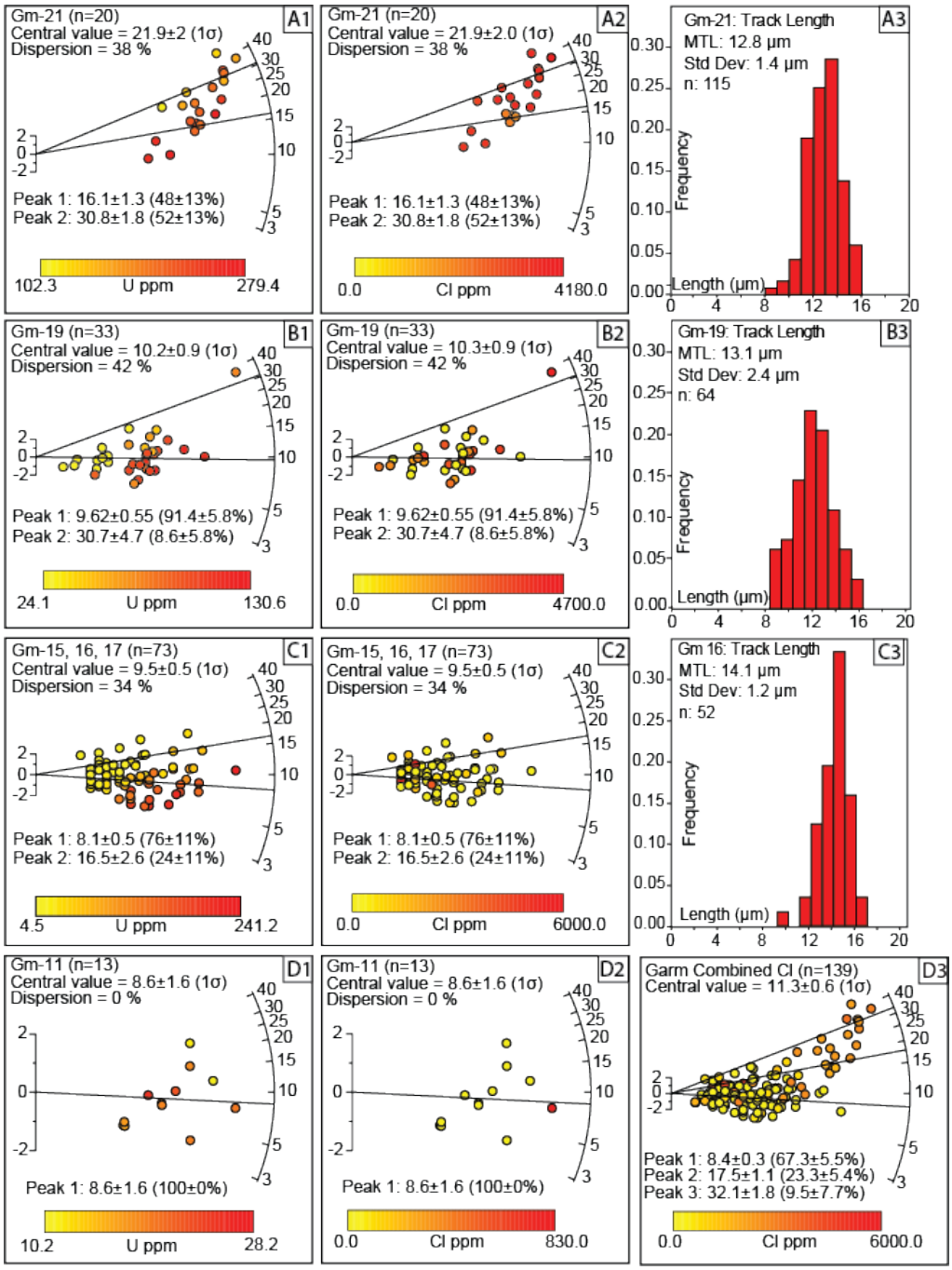

Figure 5.4: Radial plots detailing the single grain apatite fission track ages in relation to uranium (U, left column) and chlorine (Cl, central column) concentrations and associated confined fission track length histograms (right column) obtained for the study area. Radial plots were obtained using the automatic mixture modelling software RadialPlotter (Vermeesch 2009). The intersections of the radial lines with the peripheral axes indicate age peaks discerned by RadialPlotter (Vermeesch 2009). Grain colour shading on the circular symbols represents the U and Cl content (in ppm) for each single grain counted. The pooled radial plot displays a trend of older single grain ages corresponding to higher Cl concentrations and vice versa. In the track length histograms (right column), MTL is the mean track length (μm), n is the total number of confined tracks identified, and Std Dev is the standard deviation.

ages obtained for the same rocks (292 ± 2 and 290 ± 2 Ma, Konopelko et al. 2015). We interpret the AUPb ages to be related to orogenic crustal thickening and post-collisional magmatism following the closure of the PAO at the end of the Permian (~255-251 Xiao et al. 2009, Li et al. 2016). Käßner et al. (2017b) report a compilation of mica K–Ar and ^{40}Ar–^{39}Ar data obtained to the west of our study area (Figure 5.1), peaking at ~256–237 Ma. Hence, our data support Käßner et al. (2017b); Käßner et al. (2017a) who suggested a widespread thermal response to late Permian orogensis within the Pamirs and STS.

Two major events affected the study region during the late Triassic–early Jurassic: the Rushan Ocean closure and the Qiangtang collision. The closure of the Rushan Ocean has been constrained to ~210–160 Ma (Schwab et al. 2004, Angiolini et al. 2013). The Qiangtang collision with Eurasia is thought to have occurred at ~230–200 Ma (e.g. Ratschbacher et al. 2003, Robinson 2015). The far-field effects of the Qiangtang collision have been recognised elsewhere within the Tian Shan using several thermochronometers (De Grave et al. 2011, 2012, Macaulay et al. 2014, Glorie & De Grave 2016). The 199 ± 10 Ma ZHe mean age presented in this study can, therefore, be related to exhumation after the closure of the Rushan Ocean and/or the Qiangtang collision.

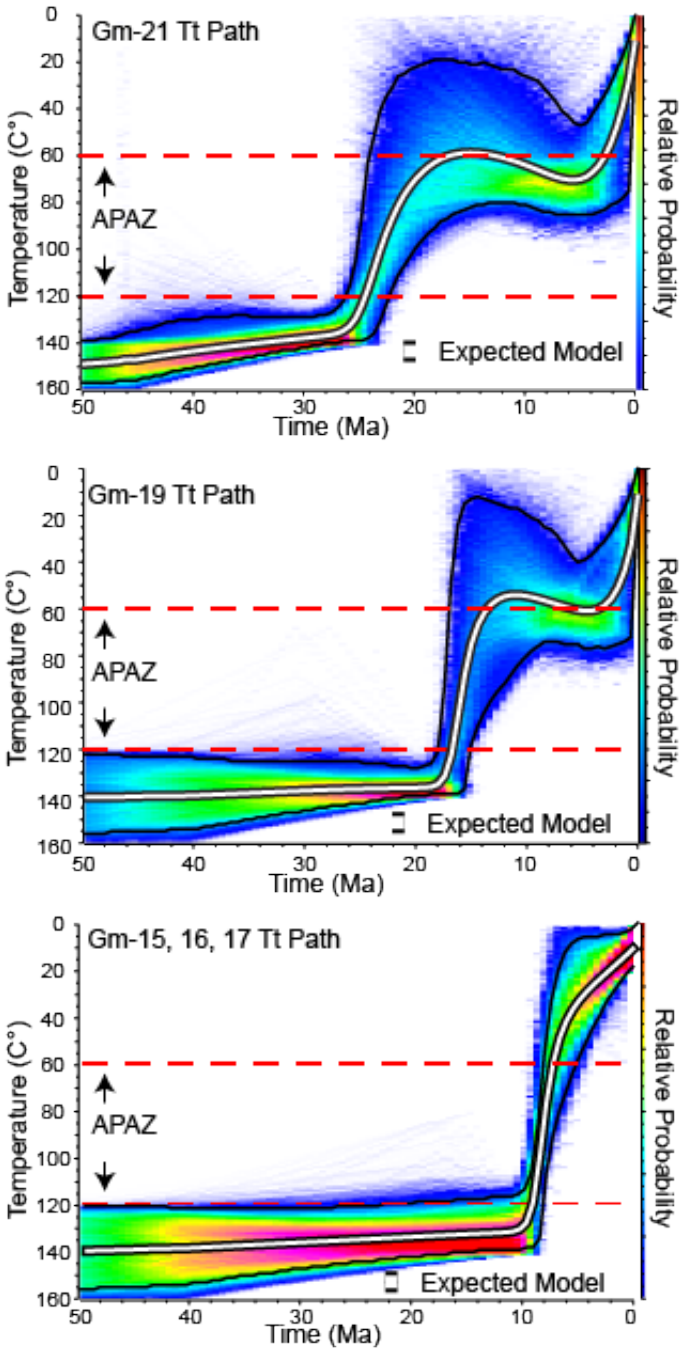

Figure 5.5: QTQt models (Gallagher 2012) for the Cenozoic low temperature (<120°C) thermal history of the Vakhsh-Surkhob fault zone, Tajikistan. The modelling output shows all possible models in time–temperature space as a function of their probability, with warmer colours being more probable. The black and white line represents the "QTQt expected" model and therefore constrains the most likely time–temperature path for each sample. Plots were generated using Cl as a kinetic parameter for annealing in apatite. Modelling parameters are given in Appendix File U.

5.5.2 Palaeogene–Neogene cooling

During the Palaeogene–Neogene, Central Asia was affected by distant tectonics related to the closure of the Tethys Ocean and the subsequent collision of India with Eurasia (e.g. De Grave

et al. 2007). The AFT data obtained in this study record two cooling events that initiated at ~25 Ma and ~10 Ma. The ~25 Ma age corresponds to abundant Oligocene–Miocene AFT ages for major faults within the STS, including in the nearby Ghissar and Garm regions (Figure 5.1, Sobel, Oskin, Burbank & Mikolaichuk 2006, De Grave et al. 2011, Glorie et al. 2011, Käßner et al. 2017b, Bande et al. 2017b). We therefore interpret the ~25 Ma cooling signal to be related to deformation focused along the Vakhsh-Surkhob fault zone.

The ~10 Ma AFT/AHe cooling signal confirms recent data by Käßner et al. (2017b) and Carrapa et al. (2014), suggesting a phase of rapid cooling during the late Miocene. This cooling event is thought to be related to the northward motion of the Pamirs (Cao et al. 2013, Thiede et al. 2013, Käßner et al. 2017b), which induced deformation and intense mountain building throughout the entire Tian Shan (e.g. Abdrakhmatov et al. 1996). Given the similarity of our ~10 Ma cooling signal in the Vakhsh-Surkhob fault zone to data from Käßner et al. (2017b) for samples just north of the fault zone (Figure 5.2), we suggest that thrusting along the Vakhsh-Surkhob fault zone and Main Pamir Thrust initiated extensive exhumation of the Tian Shan basement at that time Käßner et al. (2017b).

The Vakhsh-Surkhob fault zone provides a unique record of two separate Cenozoic cooling periods. The western segment partially preserves an initial ~25 Ma cooling event and records a relatively lower exhumation level. We interpret this 25 Ma cooling event to represent the timing of initial thrusting along the Vakhsh-Surkhob fault zone. The eastern segment records 10 Ma cooling ages and therefore more extensive (up to several kilometres) exhumation at that time. Our data refutes the model of tectonic quiescence until ~15 Ma for the south-western Tian Shan, proposed by Käßner et al. (2017b) and suggests a two-phase exhumation since ~25 Ma, supporting e.g. Sobel, Oskin, Burbank & Mikolaichuk (2006), Glorie et al. (2011), and Glorie & De Grave (2016).

5.6 Conclusion

Multi-method thermochronology along the Vakhsh-Surkhob fault zone has revealed a model for the thermotectonic history of the southernmost Tian Shan. In our model, a phase of late

Permian orogenic crustal thickening, related to the final PAO closure, induced cooling along the Pamir–Tian Shan terrane boundary at ~251 Ma. This event was subsequently influenced by the Qiangtang collision and/or Rushan Ocean closure at ~200 Ma as constrained by our ZHe data. The Vakhsh-Surkhob fault zone records two pulses of Cenozoic deformation. A first tectonic pulse at ~25 Ma, related to the far-field response to the India–Eurasia collision, exhumed the sampled rock units to shallow crustal levels (De Grave et al. 2007). A second pulse induced cooling at ~10 Ma due to the advancing Pamirs. The Cenozoic thermal history is differentially preserved along the Vakhsh-Surkhob fault zone, reflecting different crustal exposure levels and deeper exhumation to the east.

Chapter 6

Discussion and Conclusions

6.1 The Thermo-Tectonic Evolution of the Western Tian Shan

As outlined in the above five chapters that comprise this thesis, the Tian Shan is one of the world's largest currently active intracontinental orogenic zones. As a result of this, much of the current research on the uplift of the Tian Shan has been on the high altitude, central segments of the Tian Shan, particularly in the Kyrgyz and Chinese Tian Shan. Despite the relevance of focusing on the high altitude ranges of the Tian Shan, the presence of extensive Cenozoic thermo-tectonic overprints in such regions hinders a rigorous evaluation of the Mesozoic thermal history of the Tian Shan. In contrast, the samples that comprise this thesis have focused on the western-most extent of the Tian Shan in Uzbekistan, Tajikistan, Kyrgyzstan, and Kazakhstan in order to provide a more detailed investigation into the tectonic evolution of the (western) Tian Shan. Over 100 basement samples from major faults, sutures, and ranges were analysed using the middle to low temperature thermochronometers of apatite uranium-lead (AUPb), zircon fission track (ZFT), zircon (U-Th-Sm)/He (ZHe), apatite fission track (AFT), and apatite (U-Th-Sm)/He (AHe).

The aim of this thesis was to provide a continuous record of the thermo-tectonic evolution of the western Tian Shan, from its amalgamation in the late Palaeozoic, through the deformation caused by incremental tectonic processes in the Tethys during the Mesozoic, up to the Cenozoic overprint caused by the India-Eurasia collision and its ongoing indentation.

The previous four chapters have implemented the latest multi-method thermochronological techniques, regional geology, and published interpretations. By integrating the data from this thesis with previously published low-temperature thermochronological data, this discussion chapter aims to provide a holistic and chronological interpretation regarding the low-temperature tectonic evolution of the Tian Shan.

6.1.1 Late Palaeozoic

Much of the Eurasian continent was amalgamated during the Palaeozoic, from *ca.* 540 Ma until *ca.* 250 Ma (e.g. Windley et al. 1990, 2007). The formation of the Central Asian Orogenic Belt (CAOB), followed an archipelago-type (Indonesian) model with the progressive amalgamation of island-arcs and continental ribbons to the East European Craton and the Siberian Craton (e.g. Filippova et al. 2001, Windley et al. 2007). The Tian Shan is subdivided into three tectonic components reflecting the accretion of Central Asia; the North Tian Shan (NTS), the Middle Tian Shan (MTS), and the South Tian Shan (STS, e.g. Allen et al. 1993, Carroll et al. 1995). Initially, the NTS formed as a response to the closure of the Tersky Ocean and the assembly of Palaeo-Kazakhstan (e.g. Filippova et al. 2001, Konopelko et al. 2008, Alexeiev et al. 2009, Xiao et al. 2013). The formation of the Palaeo-Kazakhstan continent generated an active margin which experienced further growth during the Silurian and Devonian, as a response to the periodic accretions brought by the northward subduction of the Turkestan ocean (Konopelko et al. 2008, Glorie et al. 2011). The MTS represents a microcontinental sliver, as well as a superimposed island-arc which accreted onto the passive southern margin of the newly formed NTS during the late Ordovician (Biske & Seltmann 2010, Alexeiev et al. 2016). During the Middle Devonian–Early Carboniferous subduction halted, and the region experienced passive margin sedimentation (Dolgopolova et al. 2017). Subduction resumed under the southern margin of the MTS in the early to mid Carboniferous, with the progressive closure of the Turkestan Ocean generating voluminous Andean-type intrusions and volcanics (Konopelko et al. 2017a). The closure of the Turkestan Ocean during the Late Carboniferous to Early Permian caused the accretion of the Tarim microcontionent to the southern Palaeo-Kazakhstan margin, forming the STS (e.g. Biske & Seltmann 2010, Glorie et al. 2011). The amalgamation of the Tarim microcontinent to

the central and eastern Tian Shan caused the Palaeo-Kazakhstan subduction zone to jump south to the margin between the newly formed Eurasian continent and the Palaeotethys (e.g. Filippova et al. 2001, De Grave et al. 2007, Dolgopolova et al. 2017).

In the northern extent of the western Tian Shan, along the Palaeo-Kazakhstan margin, the closure of the Paleo-Asian Ocean was heralded by the formation of a series of large north-west to south-east trending strike-slip faults across the Tian Shan, such as the Talas-Fergana Fault, that can still be identified in the present day geomorphology (e.g. Burtman 1980, Allen et al. 2006, Charvet et al. 2007). The impact of this event is recorded by both zircon fission track (ZFT) and apatite fission track (AFT) thermochronology in the northern-most study area, the Karatau-Talas-Fergana (KTF) Fault, as well as in $^{40}Ar/^{39}Ar$ dates obtained from granites along the middle Kyrgyz extent of the KTF Fault (Konopelko et al. 2013, Rolland et al. 2013). In addition to the KTF Fault, the other regional north-west to south-east trending strike-slip faults, such as the Djalair-Naiman, Junggar, and Irtysh faults record Late Permian–Early Triassic $^{40}Ar/^{39}Ar$ suggesting deformation at this time (Laurent-Charvet et al. 2003, de Jong et al. 2009, Wang et al. 2009). Away from the major regional north-west to south-east trending strike-slip faults, Triassic AFT central ages are identified at the north-eastern margins of both the Chatkal-Kurama range and the Kyzylkum-Nurata Segment (Chapter 2 and 3), with the Early Triassic AFT ages associated with fast basement cooling. Along the southern-most contact between the western Tian Shan and the Pamir in the Garm Valley, the Late Permian–Early Triassic zircon and apatite U-Pb ages obtained represent both the crystallisation and cooling via exhumation of collisional magmas emplaced along the southern margin of the Tian Shan due to the PAO closure (Chapter 4, Konopelko et al. 2015, Käßner et al. 2017a). To the east, the trend of Late Permian–Early Triassic zircon crystallisation ages continues, trending to the southern margin of the central Tian Shan (Hegner et al. 2010, Macaulay et al. 2014, De Pelsmaeker et al. 2015, 2018).

The abundance of Late Permian–Early Triassic magmatic crystallisation ages throughout the Tian Shan suggests that closure of the PAO formed much of the Tian Shan that is currently exposed today (Filippova et al. 2001, Windley et al. 2007, Xiao et al. 2013, Konopelko et al. 2017a). The volume of magmatism pre-PAO closure suggests that the Tian Shan experienced conditions analogous to an Andean-type margin (e.g. Windley et al. 2007, Seltmann

et al. 2011, Jolivet et al. 2013, Xiao et al. 2013). From an Andean-type margin pre-PAO closure, the Tian Shan transitioned into a more Alpine-type setting with the closure of the PAO and the collision of Palaeo-Kazakhstan the Tarim microcontinent (Xiao et al. 2003, Jolivet et al. 2010, 2013, Xiao et al. 2013). Under the new continent-continent collisional regime, the Tian Shan experienced intense deformation, generating many of the east-west trending sutures currently observed today, as well as reactivating the north-west to south-east trending faults that dissect the east-west topography (e.g. Laurent-Charvet et al. 2003, Allen et al. 2006, Alexeiev et al. 2009, Jolivet et al. 2013, Rolland et al. 2013). The extent of deformation is still recorded in the fringes of the Tian Shan, more specifically, by the fast-cooling AFT and ZFT ages from the western-most study areas identified in this thesis (Chapters 1, 2, and 3). As we are still able to identify remnants of this period, preserved in low-altitude, basin-margin regions, suggests that the Late Permian–Early Triassic collision resulted in extensive deformation, generating many of the structures that can be still seen in the present day (e.g. Allen et al. 2006, De Grave et al. 2007, Glorie & De Grave 2016).

6.1.2 Late Triassic–Early Jurassic

The closure of the PAO marked the final amalgamation of the Palaeozoic Tian Shan (e.g. Windley et al. 2007, Xiao et al. 2013). The continental collision of the Tarim microcontinent towards Palaeo-Kazakhstan resulted in the Tian Shan shifting from a marginal collisional zone, to a region dominated by intracontinental deformation (Hendrix et al. 1992, Dumitru et al. 2001, Sobel, Oskin, Burbank & Mikolaichuk 2006, De Grave et al. 2007, Jolivet et al. 2010, Glorie et al. 2011). The change from a collisional margin to and intracontinental deformation zone did not mark the end of deformation experienced by the Tian Shan. In the western Tian Shan, deformation continued unabated, however, rather than being extensive across the broader Tian Shan, the Triassic deformation was focused around pre-existing major structures formed during the Palaeozoic. This is particularly evident along the series of north-west to south-east trending strike-slip faults such as the KTF Fault.

During the Triassic and into the Early Jurassic, the KTF Fault remained an active structure, transmitting strain from the newly formed subduction zone along the southern Eurasian margin where the Palaeotethys developed (Filippova et al. 2001, Glorie et al. 2010,

Käßner et al. 2017a). In the western Tian Shan, this thesis identified a series of Triassic–Early Jurassic fast-cooling AFT thermal history models in the Karatau, Chatkal-Kurama, and Kyzylkum regions (Chapters 1, 2, and 3). Both the Kyzylkum-Nurata Segment and the Chatkal-Kurama terrane display progressively slower AFT thermal history models from the Late Triassic through the Early Jurassic, suggesting that the western Tian Shan was experiencing a progressively slower rates of exhumation.

In contrast, there is continued uplift exhumation along the along the KTF Fault, with Early Jurassic fast-cooling AFT thermal models obtained from the Karatau Ranges (Chapter 1), as well as Early Jurassic $^{40}Ar/^{39}Ar$ dates (*ca. 190 Ma* Konopelko et al. 2013, Rolland et al. 2013). To the east of the KTF Fault, in the central Tian Shan, small pockets of Late Triassic–Early Jurassic AFT ages have been identified along the uplifted plateaus such as the Song-Kul and Issyk-Kul lakes (De Grave et al. 2011, 2013, Macaulay et al. 2014, Nachtergaele et al. 2017). These preserved regions are also associated with relatively fast cooling rates; suggesting that both the western Tian Shan and central Tian Shan experienced continued rapid exhumation. The preservation of rapid cooling throughout the western central Tian Shan suggests that exhumation was regional and fast during Late Triassic–Early Cretaceous. The proposed mechanism of the deformation experienced in the central Tian Shan was the collision of the peri-Gondwanan Qiangtang block to the Eurasian margin (*ca.* 230–200 Ma) on the Eurasian margin (e.g. Bullen et al. 2001, Sobel, Oskin, Burbank & Mikolaichuk 2006, De Grave et al. 2007, 2011, Jolivet et al. 2013, Glorie & De Grave 2016). To the west, the closure of the Rushan Ocean between the central and southern Pamir also generated extensive deformation, and is another possible mechanism for the rapid exhumation experienced in the western and central Tian Shan (Chapter 4, Schwab et al. 2004, Angiolini et al. 2013).

6.1.3 Late Jurassic–Early Cretaceous

Following the Qiantang collision, the Tian Shan experienced two different thermo-tectonic evolution pathways: The central Tian Shan underwent punctuated deformation and exhumation characterized by a period of fault reactivation, in response to distant tectonics along the Eurasian margin. In contrast, the western Tian Shan experienced increasingly slower rates of denudation indicating tectonic stability.

Central Tian Shan Exhumation

The closure of the Palaeotethys Ocean caused the southern Eurasian margin to jump southward, initiating the subduction of the Mesotethys Ocean (e.g. Roger et al. 2010, Jolivet 2017). Subsequently the Tian Shan experienced a period of punctuated exhumation via denudation of the terrane uplifted by the prior Qiangtang collision (e.g. De Grave et al. 2007, Glorie et al. 2010, Glorie & De Grave 2016). The Early Cretaceous punctuated deformation and denudation is contemporaneous with the deposition of sedimentary sequences in the Junggar and Tarim basins (Hendrix 2000, De Grave et al. 2007), as well as hosting periods of conglomerate deposition and development of planation surfaces (Jolivet et al. 2013). The deposition of conglomerates suggests that the central Tian Shan, which was reactivated and uplifted during the Late Triassic–Early Jurassic Qiangtang collision, experienced an extensive rate of erosion during the Late Jurassic–Early Cretaceous. However, the preservation of peneplanation surfaces suggest that differential exhumation was experienced by the central Tian Shan (De Grave et al. 2007, Glorie et al. 2010, Jolivet et al. 2013). In addition to extensive exhumation, the central Tian Shan is also suggested to have experienced renewed deformation in response to the Lhasa collision-accretion event to the southern Eurasian margin, potentially triggering further exhumation in the central Tian Shan (e.g. Schwab et al. 2004, Robinson et al. 2004, Robinson 2015, De Pelsmaeker et al. 2018)

Western Tian Shan Tectonic Stability

In contrast to the continued rapid exhumation in response to erosion in the central Tian Shan, the western Tian Shan saw a continued period of tectonic stability and erosion. Apatite fission track data from both the Chatkal-Kurama and the Kyzylkum-Nurata regions demonstrate steadily decreasing rates of cooling from the Late Jurassic through to the Early Cretaceous (Chapters 2 and 3). Published AFT data from the southern and eastern margins of the western Tian Shan also identify slow-cooling regions related to tectonic stability (Bullen et al. 2003, Sobel, Chen & Heermance 2006, Macaulay et al. 2014, Käßner et al. 2017b, Bande et al. 2017c). The postulation of a middle to late Mesozoic tectonic quiescence in the western Tian Shan is further evidenced by the deposition of Late Jurassic–Early Cretaceous marine sediments in the Kyzylkum segment and Fergana Basin due to

the incursion of the Paratethyan Sea (Bosboom et al. 2011, McCann 2016a,b, Bande et al. 2017a, De Pelsmaeker et al. 2018). In the both the Kyzylkum segment and Fergana Basin, sediment sources are suggested to be derived from terrestrial sources (McCann 2016a,b, Bande et al. 2017a, De Pelsmaeker et al. 2018), contemporaneous with the slow-cooling Late Jurassic–Early Cretaceous AFT thermal history models identified in this thesis. The presence of terrestrial detritus suggests that some segments of the western Tian Shan, such as the Chatkal-Kurama terrane and the linear ridges of the Kyzylkum segment remained elevated above the Paratethyan Sea and continued minor erosion (Chapters 2 and 3).

Despite geological, thermochronological, and biostratigraphical data, providing constraints that the western Tian Shan experienced tectonic stability for most of the middle to late Mesozoic, this thesis presents evidence that suggests regions of fast basement-cooling. Along major faults and sutures in both the Kyzylkum segment and the Karatau-Talas region, fast-cooling Late Jurassic–Early Cretaceous AFT thermal history models indicate that some degree of exhumation was still experienced by the Tian Shan. In the Kyzylkum-Nurata segment (Chapter 3), the fast-cooling Late Jurassic–Early Cretaceous AFT ages are exclusively found in reactivated sutures, relic structures from the Palaeozoic amalgamation of the Tian Shan. This thesis has suggested that the Early Cretaceous western Tian Shan was formed by extensional tectonics, where fault reactivation records rapid cooling by footwall exhumation. The extensional setting hypothesis is supported by recent geodynamic (Gplate) models that suggest that Central Asia was under extension during the middle Cretaceous (Hall 2012, Zahirovic et al. 2016). This thesis has suggested that, as the pattern of Early Cretaceous AFT ages and associated thermal history models are concentrated along major Palaeozoic sutures, the Cretaceous western Tian Shan landscape and deformation style to be comparable to the present-day Basin and Range Province in the south-western USA (Stockli et al. 2002). In the Karatau-Talas region, several samples directly along the KTF record rapid-cooling Late Jurassic–Early Cretaceous AFT thermal history models (Chapter 1). Although, temporally and thermochronologically similar to the proposed extension model suggested for the western Tian Shan, the Karatau-Talas region does not provide any geological evidence for Late Jurassic–Early Cretaceous extension (Khudoley 1993, Allen et al. 2001). During the Late Jurassic–Early Cretaceous, the eastern Tian Shan was experiencing

the initial, far-field accretion of the Lhasa terrane to the southern Eurasian margin which caused extensive deformation and exhumation in the eastern Tian Shan (Hendrix et al. 1992, Sobel 1999, Hendrix 2000, Li et al. 2004). However, Jolivet (2017) noted the absence of Late Jurassic–Early Cretaceous reactivation along the Altyn-Tagh Fault, closer to the proposed Lhasa terrane accretion. South of the western Tian Shan, the deformation and shortening was being experienced in the Southern Pamir during the Late Jurassic–Early Cretaceous recorded by Late Jurassic thermochronological cooling ages from the Rushan-Pshart zone (Robinson et al. 2004, Schwab et al. 2004, Robinson 2015). Cenozoic reactivation of the KTF Fault is often closely linked with the tectonics of the Pamir (Sobel, Oskin, Burbank & Mikolaichuk 2006, Macaulay et al. 2013, Bande et al. 2017a), therefore, this thesis suggests that the tectonism in the Pamir as a possible mechanism for reactivation along the KTF Fault, which caused the contemporaneous fast-cooling Late Jurassic AFT thermal history models still preserved along the Karatau Fault in the Karatau-Talas region (Chapter 1).

6.1.4 Late Cretaceous–Early Palaeogene

During the Late Cretaceous–Early Palaeogene, the majority of the Tian Shan experienced tectonic stability and quiescence (Sobel, Chen & Heermance 2006, De Grave et al. 2007, Macaulay et al. 2013, Bosboom et al. 2015). However, in some localised regions the Tian Shan experienced continued deformation and exhumation, as a response to the collision-accretion of the Kohistan-Dras island-arc in Pakistan during the Middle to Late Cretaceous (e.g. Searle 1991, Jolivet et al. 2010, 2013, Glorie & De Grave 2016). In the western Tian Shan, the thermochronology compiled by this thesis has documented a regionally extensive period of tectonic stability, with a limited number of AFT ages recording slow Late Cretaceous thermal history models scattered throughout the western Tian Shan (Chapter 2 and 3). The Late Cretaceous–Early Palaeogene slow-cooling identified in this thesis is in agreement with the hypothesis of tectonic quiescence experienced by the western and central Tian Shan, with many of the previous studies have suggested that the temporal extent of this period of tectonic stability has been continuous from *ca.* 150–50 Ma (e.g. Macaulay et al. 2013, Käßner et al. 2017b, Bande et al. 2017c). However, the extensive thermo-tectonic results compiled by this thesis demonstrate that the tectonic stability of western Tian Shan was

less extensive and confined to the Late Cretaceous–Early Palaeogene. Despite the regional proximity of the Kohistan-Dras island-arc, just south of the western Tian Shan, there is no record of a pronounced thermochronological response via deformation of the Kohistan-Dras collision during the Late Cretaceous–Early Palaeogene. However, previous studies have identified Kohistan-Dras collision as an instigator of exhumation in the central and eastern Tian Shan (e.g. Jolivet et al. 2010, Glorie & De Grave 2016). The absence of more proximal exhumation suggests that either strain was partitioned from the collisional margin along major structures into the central and eastern Tian Shan, or that there was not enough strain in order to exhume the rocks through the APAZ to expose the thermal signature. Regardless of the driver behind reactivation in the eastern and central Tian Shan, the western Tian Shan remained tectonically stable with marine incursions up until the India-Eurasia collision (Bosboom et al. 2011, 2014, 2015, McCann 2016a).

6.1.5 Late Palaeogene–Neogene

The Cenozoic tectonic evolution of Eurasia was defined by the collision between India and Asia. Initiating in the Palaeogene, the timing of the initial India-Asia collision has remained unclear, with both a direct *ca.* 50 Ma (e.g. Rowley 1996), and a two-stage 'hard' (*ca.* 50 Ma) and 'soft' (*ca.* 30 Ma, e.g. van Hinsbergen et al. 2012, Bouilhol et al. 2013) collision being suggested. In the Tian Shan, the India-Asia collision caused intense deformation, reactivating many pre-existing structures from both the Palaeozoic amalgamation and subsequent intracontinental deformation (e.g. Molnar & Tapponnier 1975).

In the central Tian Shan, the impact of the India-Asia collision was not identified until much later than the hypothesised *ca.* 50 Ma onset. Along major structures in the northern extent of the central Tian Shan, low-temperature thermochronometers have identified two major periods of deformation during the Eocene-Oligocene and the Miocene (e.g. De Grave et al. 2007). The Eocene-Oligocene event occurred between *ca.* 25-16 Ma, reactivating pre-existing structures and crustal weaknesses leading to an increase in the rate of exhumation. In the Miocene the central Tian Shan experienced a second event between *ca.* 15-5 Ma, which again saw an increase in exhumation rates and mountain building (Sobel, Oskin, Burbank & Mikolaichuk 2006, Glorie et al. 2010, 2011, De Grave et al. 2012, Macaulay et al. 2013, 2014,

Nachtergaele et al. 2017). The cause of both the Eocene-Oligocene and Miocene has been cited to be a response to collapse of Tibet (*ca.* 25-16 Ma), and India's continued indentation into Asia (*ca.* 15-5 Ma, e.g. Sobel, Chen & Heermance 2006, De Grave et al. 2007, Molnar & Stock 2009, Glorie & De Grave 2016).

In the western Tian Shan, a similar period of deformation and exhumation was being experienced during the Cenozoic. The stress from the India-Asia collision reactivated major structures such as the KTF Fault, as well as east-west trending Palaeozoic sutures such as the Gissar and Zeravshan sutures to the south. Along the KTF Fault, several thermochronological studies have documented a similar two-stage exhumation of the western Tian Shan, as rapidly cooling thermochronological ages identified in close proximity highlight an increased rate of exhumation for both a *ca.* 25-16 Ma and a *ca.* 15-5 Ma (Huang et al. 2005, Sobel et al. 2006a, Bande et al. 2017b, Nachtergaele et al. 2017). In the northern-most high-altitude Talas ranges, west of the KTF Fault, this thesis also identified Miocene AFT ages, in agreement with the previous studies along the KTF Fault (Chapter 1). Similarly, along the southern margin of the western Tian Shan with the Pamir, a series of rapidly cooled AFT and AHe thermal history models have been identified during both the Eocene-Oligocene and the Miocene (Chapter 4, De Grave et al. 2012, Yang et al. 2014, Käßner et al. 2017b, Bande et al. 2017c). However, despite the unanimous geological and thermochronological evidence regarding the India-Asia collision along the major structures of the southern and eastern margins of the western Tian Shan, the Kyzylkum-Nurata, Chatkal-Kurama, and the Karatau-Talas regions, remain relatively untouched. Only along the Chatkal Fault, in the Chatkal-Kurama terrane is there evidence for rapid late Palaeogene reactivation (block-tilting in response to the northward movement of the Fergana Basin). The limited presence of late Palaeogene exhumation in the central and western-most regions of the western Tian Shan suggests that strain from the India-Asia collision and subsequent Pamir indentation is being transmitted away from the western Tian Shan, and in to the central Tian Shan along major structures (such as the KTF Fault). The trend of strain from marginal collisions being partitioned in to the central Tian Shan during the Cenozoic India-Asia collision follows a similar trend to that which was identified in the Mesozoic. The difference in deformation may be in response to the difference rheology, with strain preferentially partitioning to the

weaker rocks of an accretionary complex (i.e. the Middle Tian Shan), over the stronger rocks that comprise the margins of cratons such as the Syr Darya Basin (western Tian Shan). The absence of Cenozoic deformation and exhumation in the western Tian Shan has preserved much of the Mesozoic tectonic record, providing us with a unique opportunity to provide a complete record of the Mesozoic–Cenozoic Tian Shan.

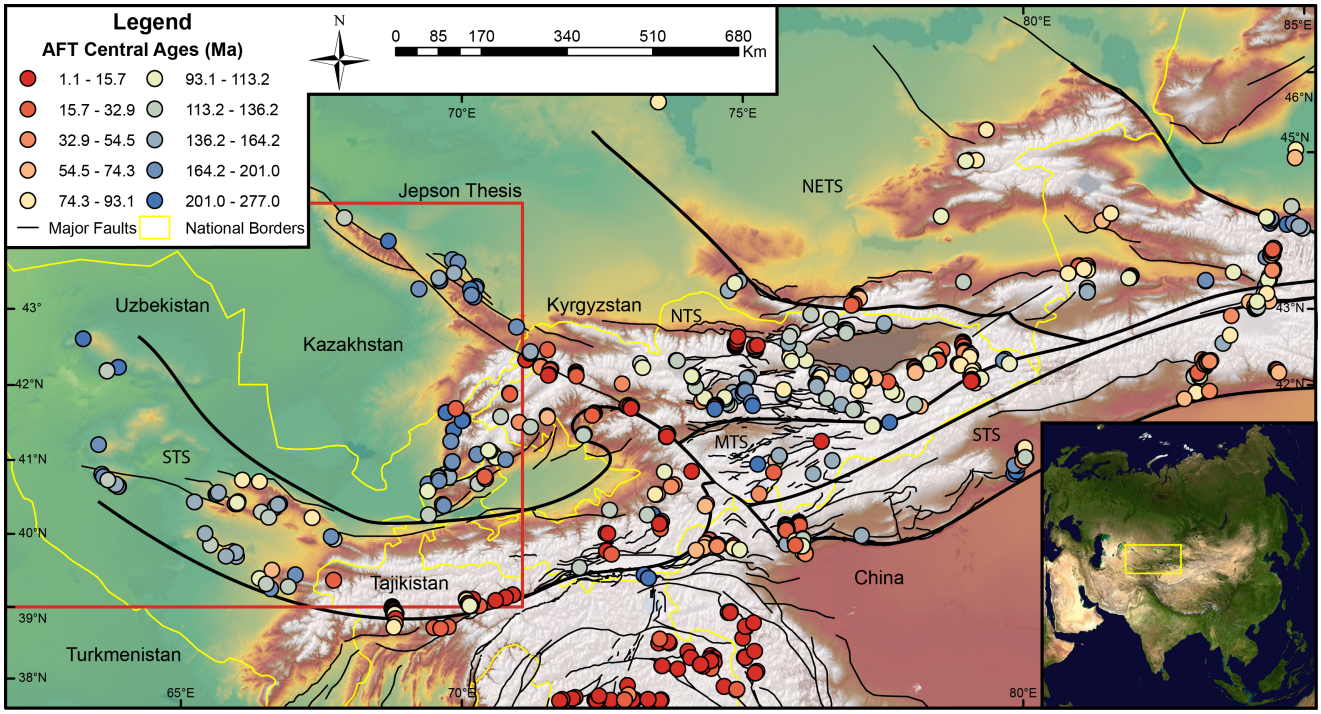

Figure 6.1: A digital elevation map of the Tian Shan outlining major structures and all published basement apatite fission track (AFT) data (Chen et al. 2006, Dumitru et al. 2001, Sobel, Chen & Heermance 2006, Sobel, Oskin, Burbank & Mikolaichuk 2006, De Grave et al. 2007, Glorie et al. 2010, 2011, De Grave et al. 2011, 2012, Stübner et al. 2013, Thiede et al. 2013, Yang et al. 2013, De Grave et al. 2013, Macaulay et al. 2013, 2014, De Pelsmaeker et al. 2015, Käßner et al. 2017b,a, Bande et al. 2017b,a, Rutte et al. 2017, Bande et al. 2017c, Nachtergaele et al. 2017). NTS is the North Tian Shan, MTS is the Middle Tian Shan, and STS is the South Tian Shan.

6.1.6 Summary

This thesis provides a representative thermochronological record of the Mesozoic to Cenozoic tectonic evolution of the western Tian Shan. Previous studies have investigated the high-elevation ranges along major structures in the Kyrgyz and Chinese Tian Shan, documenting the dominant Cenozoic overprint in response to the India-Asia collision. As a result, only minor patches of inherited Mesozoic cores were preserved, leaving behind an incomplete record to be investigated. The above thesis has sought to compile a more complete

thermo-tectonic evolution detailing the late Paleozoic, Mesozoic, and Cenozoic events preserved along the margins of the Tian Shan. The new low-temperature thermochronological data outline a punctuated deformation history for the western Tian Shan from amalgamation through to present-day. The ancestral Tian Shan formed in the Late Palaeozoic during the Palaeo-Asian (Turkestan) Ocean, resulting in widespread deformation generating the east-west topographic fabric of the Tian Shan and reactivating the large strike-slip faults such as the KTF Fault. In the western Tian Shan the PAO closure is recorded by Late Permian–Early Triassic (*ca.* 260-240 Ma) folding along the Karatau-Talas-Fergana Fault, causing the exhumation of Neoproterozoic sediments through the AFT and ZFT partial annealing zones. Following the PAO closure, the subduction zone jumped south to the Eurasian margin, the Tian Shan began its evolution as an intracontinental mountain range. During the Triassic, the Tian Shan underwent rapid exhumation generated by the PAO closure, marked by rapid cooling AFT and ZFT ages until the Late Triassic. In the Late Triassic–Early Jurassic (*ca.* 200-180 Ma), the Qiangtang block collided with the Eurasian margin, in the western Tian Shan this collision can be identified by rapidly exhumed AFT and ZFT ages preserved along the marginal structures of the north-western extent of the Tian Shan. The Late Triassic–Early Jurassic deformation and exhumation gave way to tectonic stability during the Middle to Late Jurassic, identified by gradually decreasing basement-cooling rates in the Kuratau-Talas, Chatkal-Kurama, and Kyzylkum-Nurata regions. During the Late Jurassic–Early Cretaceous (*ca.* 160-120 Ma), the western Tian Shan saw a divergence in tectonic evolutions. Parts of the western Tian Shan, such as the Chatkal-Kurama terrane and portions of the Kyzylkum-Nurata segment that were distal from the major regional sutures continued to experience decreasing rates of basement cooling in response to slowing rates of erosion. In contrast, samples taken along major structures and regional sutures, such as the Gissar and Zeravshan sutures in the Kyzylkum-Nurata, and the KTF Fault in the Karatau-Talas, identify a period rapid basement-cooling and exhumation. This thesis suggests two possible mechanisms for the rapid, major structure-based exhumation the western Tian Shan. The first mechanism, stress transmitted from the contemporaneous tectonism being experienced by Southern Pamir on the Eurasian margin, of particular influence would be the KTF Fault, as it lies directly north of the Pamir. Another source of rapid basement-cooling in the western

Tian Shan during the Late Jurassic–Early Cretaceous is footwall exhumation as a response to extensional tectonics in the Tethys Ocean, of particular relevance in the Kyzlkum-Nurata segment. During the Late Cretaceous–Early Palaeogene (*ca.* 100-40 Ma) the entire western Tian Shan experienced a period of extended tectonic stability with slow basement cooling rates obtained for thermochronological samples in this thesis, as well as the published literature in the central Tian Shan. Finally, in the Eocene–Oligocene, Eurasia experienced the far-field effects of the India-Asia collision, generating extensive deformation and exhumation through-out the Tian Shan. More specifically, the western Tian Shan underwent two stages of exhumation identified by low-temperature thermochronology; an initial period of exhumation from *ca.* 25-16 Ma in response to the India-Asia collision, followed by a second period of deformation and exhumation *ca.* 15-5 Ma as a response to the continued indentation of India and the Pamir into Asia. The majority of stress from the ongoing India-Asia collision was transmitted away from the western Tian Shan into the central and eastern Tian Shan, preventing the Cenozoic exhumation overprint and allowing this thesis to fully investigate the complete Mesozoic-Cenozoic thermo-tectonic evolution of the western Tian Shan (Kazakhstan, Kyrgyzstan, Uzbekistan, and Tajikistan).

6.1.7 Future Research

In this thesis I have attempted to provide a complete thermo-tectonic evolution of the western Tian Shan by investigating the cooling rate of granitoid or basement rocks through the earth's crust. This is by no means an exhaustive study of Central Asian tectonics, however, it does provide important constraints that will be valuable in understanding not only the intracontinental orogenics of Central Asia, but assisting in our understanding of the tectonic evolution of the earth. As with any study, this thesis has raised more questions than it has answered, and I would like to outline some of the important problems that are still left outstanding.

Central Asian Basement Spatiotemporal Evolution

This study attempted to fill outstanding gaps in the thermo-tectonic evolution of the Tian Shan, there are still several regions where more thermo-tectonic constraints would be of

immense value. Along the border between central and eastern Tian Shan there are extensive mountains ranges that remain thermo-tectonically under-explored, these ranges connect the Tian Shan to the south-west, with the Altai range in the north-east. The further exploration of the Tian Shan-Alai ranges would help confirm or modify the hypotheses put forward by this study, assisting in our understanding of the Palaeozoic-Mesozoic tectonics of the Tian Shan.

As well as the distal eastern margin of the Tian Shan, more thermochronological basement work should be applied to the nearby Zeravshan and Gissar ranges. In these remote, and difficult to access ranges along the southern margin of the Fergana Basin exists the boundary between the Mesozoic and Cenozoic expressions of the Tian Shan. Data from the southern South Tian Shan-Fergana Basin margin would shed light on when and why deformation from the India-Asia collision was partitioned away from the western Tian Shan.

Central Asian Detrital Thermochronological and Geochronological Evolution

Published work on the detrital evolution of the Tian Shan has been invaluable in improving the tectonic constraints of this thesis. However, there still remains numerous intramontane basins within the Tian Shan that archive the tectonic and climate evolution of the world's largest continent. Relating the source, timing, and deposition rates of the sedimentary basins throughout the Tian Shan allow for the distinction between periods of tectonic uplift, exhumation, and stability in response to marginal forcing. Many of these sedimentary basins lie along major structures, such as the KTF Fault, linking the shared evolution of the individual basins would provide evidence for shared growth. As well as relating basins within in the Tian Shan, further investigation into the sedimentary evolution of the major basins that lie on the margin of the Tian Shan, such as the Syr Darya, Chu Sarysu, and Junggar basins would provide insights into the Palaeozoic, Mesozoic, and Cenozoic erosion rates and deformation of the Tian Shan.

Tectonic Models, Erosion Rates, and Climate

Deciphering the interplay between mountain building and climate change remains one of the greatest outstanding questions. This thesis, like numerous studies before it, investigated the thermo-tectonic evolution of the mountains that currently dominate the Central Asian

topography. With the addition of both the western and eastern margins of the Tian Shan, the coverage of thermochronological studies is becoming thorough enough to produce a 1st order model detailing the timing and rates of exhumation throughout the Tian Shan. A complete tectonic model for the Tian Shan, coupled with a detailed sedimentary analysis of the intramontane basins would allow researchers to constrain sources and volumes of deposition for both the Mesozoic and Cenozoic. Integrating rates of uplift, exhumation, erosion, and sedimentation with climatic proxies for Central Asia would greatly improve our understanding of the iteration between plate tectonics and the environmental evolution of earth.

Appendix A

Karatau-Talas AFT Single Grain Data

Supplemtary File 1: Apatite fission track data and chemical data for the Karatau-Talas region (Chapter 1): ρ_s is the density of spontaneous tracks within the region of interest and is expressed as 10^5 tracks/cm^2. N_s is the total number of counted spontaneous tracks per sample. ^{238}U is the average concentration in ppm of uranium 238 measured in each grain. ^{35}Cl is the average concentration in ppm of chlorine 35 measured in each grain; concentrations were obtained using laser ablation–inductively coupled plasma–mass spectrometry (LA-ICP-MS). BLOD is below limits of detection, and thus, could not provide a concentration value and was not used in calculating sample concentration averages. Dpar is the length of spontaneous track etch pits in μm. t is the AFT single grain age for each sample in Ma.

Sample	ρ_s	N_s	^{238}U	$\pm1\sigma$	^{35}Cl	$\pm1\sigma$	Dpar	$\pm1\sigma$	t	$\pm1\sigma$
B15187-1	5.8	36	3.6	0.3	2990	600	1.8	1.2	319.0	60.2
B15187-2	11.1	35	12.5	0.7	BLOD	BLOD	1.7	0.4	178.9	32.4
B15187-3	19.1	77	24.3	1.3	BLOD	BLOD	1.3	0.5	158.2	20.8
B15187-5	5.0	13	3.4	0.2	9300	2000	1.8	0.3	294.0	83.8
B15187-6	6.8	23	8.8	0.5	BLOD	BLOD	0.9	0.2	155.2	33.9
B15187-7	2.9	8	3.8	0.3	1160	490	1.4	0.5	155.8	56.6
B15187-8	37.7	149	31.7	1.4	1180	520	1.5	0.3	239.3	24.1
B15187-9	3.5	11	3.6	0.2	3680	530	1.6	0.3	198.7	61.4
B15187-10	6.1	25	4.3	0.3	4710	650	1.4	0.4	287.9	61.6
B15187-11	13.6	45	11.0	0.6	2130	990	1.3	0.3	250.0	40.8
B15187-12	9.6	34	10.9	0.6	2560	700	2.1	0.7	177.6	32.6

B15187-13	5.1	24	5.0	0.3	10590	880	2.0	0.3	209.0	44.8
B15187-15	7.2	11	8.9	0.5	3870	460	1.0	0.2	162.5	50.2
B15187-16	14.0	41	16.4	0.8	3500	630	1.4	0.8	172.0	29.0
B15187-17	11.8	32	9.0	0.5	6210	720	1.9	1.0	263.8	50.3
B15187-18	4.5	11	4.7	0.5	BLOD	BLOD	1.3	0.2	194.3	61.9
B15187-19	20.7	69	17.0	0.8	BLOD	BLOD	1.5	0.4	244.5	33.0
B15187-20	8.5	26	5.6	0.4	2000	620	0.7	0.2	305.7	65.0
B15187-21	5.7	26	7.0	0.4	BLOD	BLOD	1.1	0.4	163.9	33.9
B15187-22	3.7	16	4.0	0.3	BLOD	BLOD	1.0	0.6	185.9	48.8
B15187-23	3.1	8	2.7	0.2	2930	610	2.9	0.8	230.6	83.8
B15187-24	15.0	46	19.3	1.1	2500	640	1.4	0.4	156.6	25.5
B15187-25	3.0	5	2.5	0.2	21100	2900	1.6	0.2	244.2	110.9
B15187-26	5.2	10	4.9	0.3	5430	620	1.5	0.1	210.4	67.9
B15187-27	2.6	8	2.3	0.2	BLOD	BLOD	0.9	0.2	224.8	82.5
B15204-1	21.3	75	25.9	1.1	7520	790	1.8	0.3	165.6	21.4
B15204-2	17.3	55	13.9	0.7	8480	760	2.1	0.5	249.3	37.3
B15204-3	16.7	39	10.3	0.5	10060	790	2.1	0.5	326.7	56.0
B15204-4	24.2	39	19.0	1.0	7540	860	1.8	0.2	256.1	44.3
B15204-5	11.3	47	10.1	0.7	9000	1200	1.9	0.3	224.0	37.0
B15204-6	11.1	40	9.0	0.5	8560	710	1.7	0.4	248.7	42.7
B15204-7	24.0	102	28.8	1.3	7000	730	1.8	0.3	167.7	19.4
B15204-8	37.6	102	45.0	2.9	7880	810	2.0	0.7	167.8	20.9
B15204-9	16.8	69	11.1	0.6	9610	840	1.8	0.4	302.9	41.3
B15204-10	27.9	72	18.1	1.2	7030	710	1.8	0.5	310.2	43.6
B15204-11	20.1	69	12.7	0.7	7220	740	2.0	0.5	317.8	43.8
B15204-12	8.8	36	9.2	0.5	7820	770	1.9	0.4	191.0	34.5
B15204-13	11.3	52	8.8	0.6	9340	860	2.0	0.5	258.0	40.8
B15204-14	8.7	37	8.9	0.5	8740	650	1.9	0.3	196.4	34.6
B15204-15	9.1	41	12.4	0.6	8280	660	1.7	0.4	147.1	24.9
B15204-16	33.5	145	31.2	1.3	8200	1000	2.1	0.5	215.8	21.7

B15204-17	4.6	25	4.7	0.2	7600	740	1.6	0.4	196.8	41.3
B15204-18	16.6	70	12.3	0.7	9520	910	2.0	0.4	271.7	37.4
B15204-19	9.4	47	6.6	0.5	9480	920	2.2	0.4	289.6	48.4
B15204-20	18.5	72	18.8	1.0	8700	760	1.5	0.9	197.7	26.5
B15204-21	13.1	44	19.0	1.1	7470	790	1.9	0.3	138.4	23.0
B15204-22	9.7	40	8.9	0.7	8600	760	1.9	0.3	219.0	39.2
B15204-23	6.5	31	4.5	0.2	8280	770	1.4	0.5	289.9	55.4
B15204-24	15.9	46	16.9	1.1	8100	1000	1.7	0.4	189.7	31.4
B15204-25	20.5	85	18.7	1.0	9060	750	1.8	0.4	220.8	28.0
B15204-26	9.6	52	6.3	0.5	10400	1000	1.9	0.2	303.4	48.9
B15204-27	13.1	55	10.1	0.5	9020	800	1.8	0.4	261.2	39.1
B15204-28	13.4	53	13.9	0.8	8420	900	1.9	0.9	194.0	29.8
B15204-29	19.6	67	18.0	1.0	6060	710	1.8	0.3	218.7	30.4
B15204-30	21.8	86	20.0	1.5	11290	950	1.9	0.3	219.1	30.0
B15204-31	26.3	158	35.1	1.5	9690	720	1.9	0.4	150.4	14.8
B15204-32	14.4	48	11.9	0.7	8990	830	1.9	0.3	243.4	38.9
B15204-33	10.3	49	12.6	0.9	8630	840	1.9	0.3	163.9	27.0
B15204-34	16.5	79	10.9	0.6	9230	820	1.9	0.3	305.6	39.8
B15204-35	15.6	85	9.5	0.8	9600	870	1.8	0.3	328.5	47.0
B15204-36	7.9	46	5.5	0.4	10230	870	1.7	0.3	292.0	48.3
B15204-37	10.8	34	11.5	0.8	10130	980	2.2	0.5	188.7	35.7
B15204-38	22.8	72	28.3	1.5	6610	800	1.8	0.3	161.8	21.8
B15204-39	23.8	115	28.0	1.6	9800	1100	1.9	0.6	171.2	19.9
B15204-40	20.4	76	20.5	1.1	7720	750	1.8	0.4	200.4	26.5
B15204-41	11.4	59	10.9	0.8	9150	880	1.9	0.3	210.6	32.1
A16-34-1	20.2	67	15.1	1.0	1130	160	1.4	0.2	263.2	38.5
A16-34-2	13.7	21	20.4	1.8	1520	190	1.3	0.4	131.8	31.6
A16-34-3	18.6	35	23.1	1.4	1960	200	1.8	0.8	158.4	29.4
A16-34-4	27.7	31	49.2	2.9	1860	200	1.6	0.4	110.6	21.5
A16-34-5	20.6	43	29.2	1.4	3180	240	2.1	0.9	139.0	23.1

A16-34-6	27.8	28	25.3	2.2	5200	1400	1.4	0.2	216.0	46.0
A16-34-7	16.9	40	27.9	1.5	2110	180	1.4	0.2	119.2	20.7
A16-34-8	22.8	66	21.1	0.9	1870	190	1.3	0.2	213.1	29.3
A16-34-9	24.5	37	26.2	1.8	2010	210	1.5	0.5	183.8	33.8
A16-34-10	24.6	56	26.7	1.3	3080	260	1.5	0.4	181.4	27.1
A16-34-11	26.9	31	38.5	2.1	2410	240	1.4	0.3	137.5	26.6
A16-34-12	18.4	44	20.5	1.4	2180	270	1.4	0.2	176.5	30.3
A16-34-13	15.6	37	23.1	1.2	2300	170	1.3	0.3	133.1	23.8
A16-34-14	11.5	33	20.5	1.2	2440	250	1.4	0.2	110.4	20.9
A16-34-15	26.5	46	30.5	1.6	1840	220	1.5	0.2	170.8	27.9
A16-34-16	18.8	60	20.6	1.1	2740	230	1.3	0.2	179.1	26.4
A16-34-17	7.4	10	11.4	0.5	900	150	1.2	0.3	127.7	41.2
A16-34-18	20.9	29	22.7	1.8	1650	210	1.3	0.3	180.6	37.4
A16-34-19	2.7	4	9.8	0.6	7500	520	1.3	0.2	54.2	27.4
A16-34-20	4.9	9	7.2	0.5	980	150	1.5	0.1	134.7	46.2
A16-34-21	32.2	59	37.1	1.7	1560	240	1.6	0.3	170.6	24.8
A16-34-22	11.2	16	18.4	0.8	1760	230	1.5	0.2	119.0	30.7
A16-34-23	17.1	49	30.7	1.6	1980	200	1.4	0.3	109.6	17.4
A16-34-24	18.0	49	14.8	1.0	2010	230	1.6	0.2	238.7	39.3
A16-34-25	13.9	43	21.1	1.3	1670	150	1.5	0.3	129.8	22.2
A16-34-26	18.0	51	19.5	1.1	1550	200	1.5	0.3	181.6	28.7
A16-34-27	19.2	50	26.6	1.7	1770	210	1.4	0.2	141.9	23.0
A16-34-28	28.1	58	42.4	2.3	2430	240	1.4	0.3	130.2	19.5
A16-34-29	23.4	40	25.5	1.3	3170	250	1.4	0.3	180.3	31.1
A16-34-30	13.7	26	14.5	0.7	2020	320	1.0	0.2	185.5	38.5
A16-34-31	18.8	47	38.6	2.4	3030	280	1.5	0.4	95.8	15.8
A16-34-32	7.2	8	11.4	0.7	1980	210	1.1	0.3	124.1	44.9
A16-34-33	6.1	12	11.8	0.8	1560	200	0.9	0.2	102.7	30.9
A16-34-34	17.7	25	26.1	1.5	1920	310	1.2	0.3	133.1	28.4
A16-34-35	25.6	38	26.4	1.4	2260	210	1.5	0.5	190.7	33.7

A16-34-36	29.5	93	41.3	3.2	3190	490	1.3	0.3	140.5	19.3
KP-15-2/6-1	27.0	123	30.7	1.8	4350	510	2.9	0.8	176.6	20.2
KP-15-2/6-2	24.0	83	29.5	1.3	1630	460	2.8	0.6	163.6	20.4
KP-15-2/6-3	17.7	72	25.0	1.1	1420	550	2.9	0.5	142.2	18.7
KP-15-2/6-4	4.8	30	5.8	0.3	1440	540	2.0	2.1	165.5	32.3
KP-15-2/6-5	16.2	49	15.7	0.8	1410	470	2.8	0.6	208.3	32.5
KP-15-2/6-6	12.3	55	19.1	1.0	BLOD	BLOD	2.9	0.6	129.6	19.4
KP-15-2/6-7	8.0	29	11.2	0.6	BLOD	BLOD	3.1	0.6	144.7	28.4
KP-15-2/6-8	10.0	37	11.2	0.6	BLOD	BLOD	2.9	0.3	179.8	31.8
KP-15-2/6-9	5.7	19	4.5	0.2	2510	490	3.4	0.3	252.6	60.0
KP-15-2/6-10	3.5	23	2.8	0.2	3720	530	3.4	0.5	248.5	55.0
KP-15-2/6-11	13.9	61	13.8	0.8	4720	570	2.4	1.2	201.8	29.4
KP-15-2/6-12	16.0	79	15.4	1.0	1450	440	3.1	0.5	209.9	28.2
KP-15-2/6-13	13.1	37	12.2	0.6	3010	480	3.1	0.3	216.8	38.2
KP-15-2/6-14	15.3	61	19.1	0.8	3020	420	3.4	0.7	160.9	22.6
KP-15-2/6-15	7.7	16	13.8	0.8	1300	490	2.7	0.5	112.9	29.3
KP-15-2/6-16	19.2	51	18.0	0.9	2080	500	2.9	0.5	215.2	33.0
KP-15-2/6-17	17.0	46	30.7	1.6	1340	370	2.4	0.5	111.6	18.0
KP-15-2/6-18	3.0	5	6.0	0.8	13200	2500	2.1	0.5	99.6	46.5
KP-15-3/4-1	12.6	31	18.9	1.3	17600	4600	2.3	1.2	134.1	26.3
KP-15-3/4-2	1.7	4	2.5	0.2	6650	870	1.6	0.2	133.7	67.6
KP-15-3/4-3	1.4	3	1.9	0.1	5370	730	1.5	0.2	144.7	84.4
KP-15-3/4-4	3.6	13	3.5	0.2	3390	630	1.4	0.7	205.9	59.2
KP-15-3/4-5	6.1	21	5.2	0.4	1300	550	1.0	0.3	238.0	55.3
KP-15-3/4-6	24.4	57	32.9	5.4	330000	76000	1.3	0.4	148.9	31.9
KP-15-3/4-7	1.5	6	1.8	0.1	5120	540	2.1	0.4	167.0	69.6
KP-15-3/4-8	3.0	14	1.8	0.1	4150	550	2.1	0.4	331.9	92.8
KP-15-3/4-9	1.8	7	2.4	0.2	4330	790	1.8	0.2	153.0	58.9
KP-15-3/4-10	2.3	9	3.0	0.2	1060	540	1.5	0.5	154.5	52.7
KP-15-3/4-11	4.5	12	5.9	0.4	4810	640	1.1	0.1	153.7	46.1

KP-15-3/4-12	6.6	24	7.3	0.4	5200	770	1.6	0.4	181.2	39.2
KP-15-3/4-13	3.2	13	3.5	0.2	4370	660	1.7	0.7	186.0	53.5
KP-15-3/4-14	2.0	8	3.3	0.2	7560	720	2.0	0.5	124.9	45.2
KP-15-3/4-15	21.9	68	30.9	1.7	2530	550	1.7	0.6	142.4	19.7
KP-15-3/4-16	3.2	10	3.4	0.2	3200	590	1.5	0.3	190.8	62.3
KP-15-3/4-17	2.4	9	1.4	0.1	4340	730	1.5	0.5	331.6	113.2
KP-15-3/4-18	0.9	2	1.0	0.1	2930	490	1.5	0.5	182.4	129.8
KP-15-3/4-19	2.5	10	2.2	0.2	2230	470	1.6	0.2	237.3	77.9
KP-15-3/4-20	11.7	41	18.8	0.9	BLOD	BLOD	1.2	0.4	125.0	21.0
KP-15-3/4-21	11.5	28	13.7	0.7	1070	540	1.2	0.3	169.7	33.9
KP-15-3/4-22	11.0	24	12.5	0.9	1720	600	0.9	0.3	177.6	38.9
KP-15-3/4-23	2.9	14	2.4	0.2	1600	550	0.8	0.4	245.9	68.7
KP-15-3/4-24	12.5	40	12.1	1.0	BLOD	BLOD	1.2	0.2	207.8	37.6
KP-15-3/4-25	5.9	27	5.9	0.4	3740	690	1.9	1.2	202.5	42.1
KP-15-3/4-26	6.0	16	5.6	0.4	6200	1500	1.7	0.2	215.4	56.6
KP-15-3/4-27	12.3	30	16.0	1.0	8200	1800	1.3	0.7	153.9	30.2
KP-15-3/4-28	1.2	4	1.3	0.1	2100	450	2.2	0.7	181.3	92.2
KP-15-3/4-29	1.3	3	2.4	0.2	2600	500	1.5	0.0	111.3	64.8
KP-15-3/4-30	28.7	51	47.0	3.3	BLOD	BLOD	1.2	0.2	122.6	19.8
KP-15-3/4-31	31.4	91	43.7	2.1	BLOD	BLOD	1.3	0.4	144.3	17.5
KP-15-3/4-32	4.5	9	5.2	0.3	4560	570	1.6	0.9	175.1	59.4
KP-15-7/1-1	18.4	87	10.2	0.7	1050	600	1.4	0.3	362.7	49.0
KP-15-7/1-2	26.7	63	40.2	2.1	2080	560	1.5	0.3	133.7	19.0
KP-15-7/1-3	17.5	41	24.2	1.1	2620	630	1.6	0.2	145.8	24.4
KP-15-7/1-4	1.5	5	1.5	0.1	920	490	1.5	0.5	209.0	94.9
KP-15-7/1-5	13.0	82	13.0	0.8	1210	500	1.5	0.3	200.8	26.5
KP-15-7/1-6	4.7	29	5.0	0.3	1800	490	1.0	0.2	190.4	37.7
KP-15-7/1-7	3.3	12	8.3	0.4	1240	580	1.4	0.1	81.0	23.9
KP-15-7/1-8	24.0	113	18.4	1.2	BLOD	BLOD	1.2	0.2	262.1	31.7
KP-15-7/1-9	18.1	35	21.3	1.2	2200	460	1.2	0.6	171.2	31.2

KP-15-7/1-10	11.8	40	11.4	0.5	2920	610	1.5	0.4	207.5	34.8
KP-15-7/1-11	1.8	8	2.8	0.2	7030	640	1.7	0.1	132.2	47.7
KP-15-7/1-12	17.2	53	31.5	1.9	2060	460	1.9	0.3	110.0	17.0
KP-15-7/1-13	10.0	35	6.2	0.4	880	540	1.9	0.4	324.7	59.2
KP-15-7/1-14	7.5	69	6.2	0.4	3280	490	2.1	0.4	244.4	35.3
KP-15-7/1-15	26.1	95	14.2	0.9	BLOD	BLOD	1.9	0.7	370.9	46.7
KP-15-7/1-16	13.0	80	8.9	0.6	BLOD	BLOD	1.2	0.4	295.0	40.4
KP-15-7/1-17	0.9	6	2.5	0.1	BLOD	BLOD	1.1	0.2	70.1	28.9
KP-15-7/1-18	3.2	14	1.9	0.2	1650	600	0.9	0.3	348.3	98.7
KP-15-7/1-19	24.1	54	23.3	1.3	2570	580	1.2	0.3	208.1	31.6
KP-15-7/1-20	8.3	27	8.1	0.5	BLOD	BLOD	1.3	0.5	204.8	42.3
KP-15-7/1-21	5.3	30	3.5	0.2	BLOD	BLOD	1.5	0.3	304.6	60.0
KP-15-7/1-22	7.3	57	10.9	0.5	BLOD	BLOD	1.5	0.3	135.1	19.8
KP-15-7/1-23	2.4	23	2.1	0.2	BLOD	BLOD	2.0	0.9	230.8	52.8
KP-15-7/1-24	25.2	91	38.2	1.9	BLOD	BLOD	1.3	0.3	132.4	16.2
KP-15-7/1-25	6.6	26	10.5	0.7	1700	460	1.0	0.3	125.7	26.5
KP-15-7/1-26	4.2	11	4.1	0.2	1100	460	1.2	0.4	202.6	62.4
KP-15-7/1-27	10.6	57	10.8	0.6	1770	630	1.5	0.4	196.5	29.0
KP-15-7/1-28	4.0	19	4.9	0.3	BLOD	BLOD	1.0	0.1	164.3	39.5
KP-15-7/1-29	1.6	5	2.5	0.2	BLOD	BLOD	1.5	0.6	129.5	59.0
KP-15-7/1-30	16.1	108	13.5	0.7	1040	450	1.1	0.3	239.2	27.6
KP-15-7/1-31	2.0	10	3.6	0.2	1230	510	1.0	0.3	112.6	36.5
hline KP-15-9-1	18.9	68	17.6	0.7	860	440	1.5	0.3	215.4	28.7
KP-15-9-2	23.8	103	37.2	1.6	1080	500	1.5	0.3	128.7	14.7
KP-15-9-3	4.3	24	3.4	0.2	1220	430	1.3	0.3	255.6	55.4
KP-15-9-4	8.8	34	5.2	0.4	3960	690	1.7	0.2	341.9	65.2
KP-15-9-5	5.5	29	6.4	0.3	4890	590	1.5	0.3	172.7	33.9
KP-15-9-6	4.3	22	5.9	0.3	1100	510	1.9	1.1	144.7	32.4
KP-15-9-7	11.1	50	10.9	0.7	BLOD	BLOD	1.5	0.2	206.3	32.9
KP-15-9-8	15.6	65	14.7	0.8	1910	500	1.4	0.4	214.2	30.4

KP-15-9-9	5.5	23	3.7	0.2	1110	400	1.6	0.3	299.4	65.4
KP-15-9-10	5.4	28	3.4	0.2	3500	490	1.3	0.2	321.1	64.2
KP-15-9-11	6.8	47	8.5	0.5	1480	600	1.5	0.2	160.6	25.7
KP-15-9-12	13.2	45	17.7	0.7	2670	540	1.4	0.3	149.8	23.8
KP-15-9-13	11.5	52	14.3	0.9	1040	560	1.3	0.3	162.0	25.2
KP-15-9-14	8.0	42	9.8	0.6	930	450	1.8	0.5	165.5	28.2
KP-15-9-15	5.8	39	6.4	0.4	1720	530	1.4	0.2	182.0	32.4
KP-15-9-16	0.7	3	0.7	0.1	1600	400	1.3	0.4	199.5	116.6
KP-15-9-17	13.3	66	11.3	0.6	2150	490	1.5	0.3	236.5	33.0
KP-15-9-18	6.4	22	8.4	0.6	1140	520	1.0	0.1	155.1	35.1
KP-15-9-19	8.5	31	10.4	0.5	3470	590	1.4	0.2	164.2	31.2
KP-15-9-20	5.0	23	11.5	0.7	BLOD	BLOD	1.3	0.3	87.1	19.2
KP-15-9-21	1.0	4	1.8	0.2	1170	550	1.5	0.4	107.5	55.1
KP-15-9-22	10.8	55	10.6	0.5	1480	490	1.6	0.2	205.9	30.2
KP-15-9-23	29.1	79	24.9	1.3	BLOD	BLOD	1.5	0.3	234.7	30.5
KP-15-9-24	30.6	114	45.8	1.9	1870	440	1.6	0.4	134.2	14.7
KP-15-9-25	28.0	147	28.3	1.7	BLOD	BLOD	1.3	0.3	198.8	21.7
KP-15-9-26	19.7	75	20.7	1.9	2440	540	1.5	0.2	191.6	29.2
KP-15-9-27	12.9	62	14.1	0.8	3740	600	1.6	0.5	184.1	26.4
KP-15-9-28	24.4	106	19.7	1.1	3140	600	1.4	0.3	249.2	29.5
KP-15-9-29	3.1	14	5.1	0.3	BLOD	BLOD	0.9	0.4	123.2	34.0
KP-15-9-30	6.0	24	4.7	0.3	2570	650	1.4	0.2	259.4	55.8
KP-15-9-31	3.8	21	2.5	0.2	BLOD	BLOD	1.6	0.2	303.0	70.2
KP-15-9-32	2.6	14	3.1	0.2	1820	530	1.4	0.3	166.4	46.1
KP-15-9-33	11.3	45	11.8	0.5	BLOD	BLOD	1.0	0.2	192.1	30.9
KP-15-9-34	3.4	15	2.4	0.2	940	430	1.0	0.3	292.6	78.9
KP-15-9-35	10.7	44	8.4	0.4	1100	490	1.2	0.3	255.8	41.9
KP-15-9-36	16.3	92	21.8	1.1	2410	520	1.4	0.4	150.1	18.3
KP-15-9-37	5.0	25	3.8	0.2	2020	550	1.4	0.3	264.3	56.3
KP-15-9-38	11.6	40	9.8	0.5	1840	630	1.3	0.3	237.0	40.6

KP-15-9-39	2.5	17	3.1	0.2	7000	630	1.7	0.2	164.2	42.2
KP-15-9-40	26.9	121	18.1	1.7	2140	430	1.4	0.3	298.5	40.7
KP-15-11/1-1	3.1	9	3.9	0.4	760	400	1.9	0.5	160.8	56.3
KP-15-11/1-2	4.2	21	2.7	0.2	1460	510	1.4	0.4	305.3	70.3
KP-15-11/1-3	7.4	23	4.5	0.3	1010	450	1.5	0.3	325.1	71.9
KP-15-11/1-4	1.7	4	2.7	0.2	BLOD	BLOD	1.4	0.5	121.0	61.5
KP-15-11/1-5	4.5	14	3.2	0.7	880	440	1.7	0.2	283.1	96.5
KP-15-11/1-6	1.2	5	1.6	0.1	1180	480	1.0	0.3	152.6	69.5
KP-15-11/1-7	1.5	6	2.7	0.2	2180	440	1.4	0.3	115.7	47.9
KP-15-11/1-8	3.3	16	4.4	0.3	2220	630	1.1	0.2	148.2	38.6
KP-15-11/1-9	5.3	23	3.6	0.2	2000	480	1.8	0.3	288.8	63.5
KP-15-11/1-10	1.8	4	2.3	0.2	1670	450	1.6	0.0	158.5	81.1
KP-15-11/1-11	1.9	13	2.6	0.2	1470	490	1.2	0.4	146.0	42.1
KP-15-11/1-12	4.6	16	3.3	0.3	2600	800	2.3	0.9	274.9	72.8
KP-15-11/1-13	1.0	3	1.9	0.2	1300	580	1.5	0.3	104.7	61.3
KP-15-11/1-14	4.3	12	3.1	0.2	2150	520	1.2	0.6	272.2	80.8
KP-15-11/1-15	2.7	12	3.1	0.2	BLOD	BLOD	1.5	0.5	173.0	51.9
KP-15-11/1-16	2.7	7	2.2	0.4	3200	720	3.2	0.8	245.2	102.7
KP-15-11/1-17	3.4	10	2.6	0.2	2360	590	2.2	1.2	261.0	85.3
KP-15-11/1-18	3.1	7	1.7	0.4	1450	480	1.5	0.6	371.9	161.4
KP-15-11/1-19	5.0	15	3.0	0.2	2200	520	2.1	0.2	331.2	89.0
KP-15-11/1-20	20.3	84	18.8	1.0	11100	2500	1.8	0.4	213.5	27.2
KP-16-15-1	1.4	2	1.9	0.1	590	170	1.4	0.0	147.9	105.2
KP-16-15-2	37.9	100	30.4	1.5	710	190	1.4	0.3	245.3	29.6
KP-16-15-3	18.7	31	13.8	0.9	2220	290	1.6	0.4	266.4	52.2
KP-16-15-4	2.9	7	3.9	0.3	650	200	1.0	0.1	146.7	56.8
KP-16-15-5	32.1	68	24.1	1.5	840	180	1.5	0.3	261.7	37.7
KP-16-15-6	2.3	6	4.7	0.6	500	150	0.7	0.1	96.0	41.1
KP-16-15-7	0.5	2	0.7	0.1	1570	280	1.5	0.2	134.3	96.1
KP-16-15-8	10.6	28	10.4	0.7	2540	240	1.4	0.1	199.6	40.9

KP-16-15-9	25.5	50	23.1	1.4	2750	270	1.4	0.2	217.0	34.9
KP-16-15-10	12.1	27	7.9	0.5	1540	260	1.3	0.4	301.5	63.0
KP-16-15-11	13.2	37	7.0	0.4	880	210	1.3	0.3	372.6	67.5
KP-16-15-12	1.8	6	1.8	0.1	1570	210	1.3	0.2	191.3	79.5
KP-16-15-13	18.8	51	19.7	3.2	BLOD	BLOD	1.2	0.3	187.6	41.2
KP-16-15-14	13.6	34	13.2	0.8	800	210	1.4	0.2	202.6	37.9
KP-16-15-15	6.1	12	6.6	0.4	1770	210	1.7	0.2	181.5	54.1
KP-16-15-16	5.4	24	6.3	0.3	810	160	1.2	0.2	169.0	36.5
KP-16-15-17	3.0	7	2.1	0.1	1510	190	1.1	0.1	280.4	108.2
KP-16-15-18	10.0	33	9.2	0.5	2340	240	1.3	0.2	213.0	40.0
KP-16-15-19	1.8	2	2.8	0.2	930	190	1.4	0.3	124.4	88.5
KP-16-15-20	3.3	8	2.4	0.2	730	210	1.3	0.2	274.3	101.4
KP-16-15-21	6.1	19	5.4	0.3	610	150	1.1	0.2	219.8	53.2
KP-16-15-22	12.9	28	9.6	0.7	2650	290	1.4	0.4	265.6	55.2
KP-16-15-23	12.0	20	10.5	0.7	2550	320	1.4	0.4	224.4	53.2
KP-16-15-24	4.2	14	5.3	0.3	620	210	1.1	0.3	157.3	43.8
KP-16-15-25	16.7	25	9.7	0.6	2790	290	1.4	0.2	337.1	72.1
KP-16-15-26	20.3	34	11.5	0.7	2120	270	1.1	0.2	346.7	65.4
KP-16-15-27	6.5	13	5.0	0.3	3100	310	1.5	0.1	256.2	73.5
KP-16-15-28	19.6	26	16.2	0.8	1360	210	1.5	0.7	237.4	49.1
KP-16-15-29	26.1	46	14.3	0.7	3060	290	1.4	0.2	360.5	58.7
KP-16-15-30	11.3	34	10.1	0.7	2740	310	1.4	0.2	219.9	41.5
KP-16-15-31	13.4	30	15.9	0.8	1280	210	1.4	0.2	165.3	32.1
KP-16-15-32	12.4	27	10.7	0.7	1290	250	1.3	0.1	227.8	47.2
KP-16-17-1	7.6	14	8.4	0.6	3150	220	1.3	0.1	179.8	50.6
KP-16-17-2	8.8	22	6.8	0.5	1020	150	1.2	0.2	255.0	58.7
KP-16-17-3	2.4	4	2.6	0.2	2420	260	1.1	0.1	180.1	91.2
KP-16-17-4	7.6	16	5.2	0.3	2480	400	1.6	0.1	285.9	74.4
KP-16-17-5	10.6	16	14.4	0.9	1340	210	1.1	0.2	144.7	37.9
KP-16-17-6	6.2	18	4.3	0.3	390	130	1.3	0.1	286.0	71.7

KP-16-17-7	4.7	6	10.7	0.7	610	140	1.2	0.5	86.7	36.1
KP-16-17-8	6.3	9	7.1	0.5	2100	220	1.3	0.6	173.5	59.4
KP-16-17-9	12.6	21	8.8	0.5	2660	230	1.6	0.4	280.1	64.2
KP-16-17-10	6.1	18	6.4	0.4	650	130	1.0	0.2	188.5	46.8
KP-16-17-11	4.4	13	4.3	0.3	1970	230	1.5	0.4	201.6	58.0
KP-16-17-12	9.5	13	8.8	0.4	630	160	1.3	0.4	210.9	60.2
KP-16-17-13	29.9	48	26.0	1.4	400	160	1.7	0.6	226.0	36.3
KP-16-17-14	5.0	5	4.4	0.4	1590	240	1.6	0.5	221.7	101.4
KP-16-17-15	55.5	68	59.5	3.8	910	150	1.3	0.4	183.3	26.5
KP-16-17-16	7.6	8	5.5	0.4	1790	190	1.5	0.2	274.3	99.5
KP-16-17-17	3.5	2	3.1	0.2	2320	720	1.2	0.0	222.0	157.9
KP-16-18-1	12.5	29	15.1	0.9	460	160	1.1	0.2	162.9	32.6
KP-16-18-2	3.1	9	3.4	0.2	3020	250	2.0	0.2	183.7	63.0
KP-16-18-3	11.3	28	12.9	1.0	960	180	1.5	0.5	171.4	35.7
KP-16-18-4	11.8	27	18.3	1.5	1100	270	1.3	0.3	126.5	27.1
KP-16-18-5	2.3	4	6.2	0.3	520	140	1.1	0.0	73.9	37.3
KP-16-18-6	12.9	22	11.0	0.6	3940	300	1.4	0.4	231.2	52.1
KP-16-18-7	11.9	25	31.2	1.6	440	120	1.2	0.2	75.1	15.9
KP-16-18-8	16.4	41	17.5	1.3	420	210	1.2	0.2	183.7	32.9
KP-16-18-9	8.6	34	7.6	0.5	1460	220	1.5	0.2	223.0	42.4
KP-16-18-10	7.6	22	5.9	0.3	2900	200	1.7	0.6	253.4	57.0
KP-16-18-11	6.3	15	7.7	0.5	680	150	1.3	0.2	161.4	43.4
KP-16-18-12	20.7	69	18.7	1.1	1640	200	1.5	0.3	217.1	30.8
KP-16-18-13	10.6	27	11.5	0.7	610	190	1.3	0.2	181.8	37.8
KP-16-18-14	17.8	47	14.3	1.1	870	190	1.2	0.2	244.7	41.9
KP-16-18-15	7.8	18	6.6	0.3	1940	210	1.7	0.4	235.2	57.8
KP-16-18-16	17.5	39	26.2	1.5	1680	190	1.2	0.3	131.0	23.1
KP-16-18-17	4.9	14	8.6	0.6	1300	220	1.4	0.5	112.5	31.5
KP-16-18-18	15.8	25	23.7	1.7	970	200	1.3	0.3	130.8	28.4
KP-16-18-19	2.5	6	3.6	0.3	330	110	1.1	0.2	136.9	57.2

KP-16-18-20	16.5	36	35.2	2.1	810	180	1.5	0.2	91.9	16.8
KP-16-18-21	24.7	49	26.9	1.5	1200	160	1.3	0.3	180.8	29.0
KP-15-33/3-1	11.4	58	11.7	0.7	BLOD	BLOD	1.3	0.4	197.2	29.6
KP-15-33/3-2	1.1	8	0.9	0.1	7060	660	1.9	0.5	241.1	87.9
KP-15-33/3-3	5.6	21	4.9	0.3	2140	630	1.4	0.4	230.1	52.8
KP-15-33/3-4	12.4	41	11.6	0.6	BLOD	BLOD	1.4	0.4	214.9	36.1
KP-15-33/3-5	5.0	26	4.0	0.2	10600	1100	1.9	0.4	255.9	52.9
KP-15-33/3-6	1.2	10	0.9	0.1	BLOD	BLOD	2.6	0.6	294.6	97.3
KP-15-33/3-7	6.0	20	5.1	0.3	10360	920	2.0	0.4	234.0	54.6
KP-15-33/3-8	1.3	7	0.9	0.1	8280	900	2.5	0.7	290.9	112.6
KP-15-33/3-9	3.1	21	2.1	0.1	BLOD	BLOD	1.4	0.4	298.9	69.2
KP-15-33/3-10	2.4	16	2.7	0.2	4130	600	2.0	0.5	174.7	46.2
KP-15-33/3-11	6.7	17	7.7	0.5	1290	600	1.6	0.2	173.7	43.9
KP-15-33/3-12	28.7	140	42.4	2.0	BLOD	BLOD	1.1	0.4	136.2	14.2
KP-15-33/3-13	6.8	33	12.3	0.7	BLOD	BLOD	1.5	0.5	111.6	20.7
KP-15-33/3-14	2.7	13	2.5	0.2	8540	770	1.5	0.5	221.6	65.1
KP-15-33/3-15	45.9	144	56.6	2.4	940	480	1.5	1.0	163.0	16.5
KP-15-33/3-16	5.4	30	5.0	0.3	9610	900	1.8	0.3	219.9	43.3
KP-15-33/3-17	1.7	9	2.4	0.2	2890	510	2.7	2.3	141.2	48.3
KP-15-33/3-18	5.5	33	6.3	0.4	BLOD	BLOD	1.4	0.2	175.1	32.9
KP-15-33/3-19	4.8	22	3.4	0.2	9100	1100	2.1	0.8	287.7	64.9
KP-15-33/3-20	7.0	41	4.0	0.3	8460	840	1.9	0.5	351.2	62.6
KP-15-33/3-21	4.3	13	4.0	0.2	13500	1100	1.9	0.3	219.3	62.3
KP-15-33/3-22	1.7	12	1.1	0.1	6730	690	1.9	0.2	308.7	92.6
KP-15-33/3-23	6.2	35	10.1	0.5	BLOD	BLOD	1.6	1.0	123.0	22.3
KP-15-33/3-24	0.6	3	1.0	0.1	5020	580	0.7	0.1	118.5	69.3
KP-15-33/3-25	14.2	61	11.1	0.5	2280	640	1.4	0.3	256.8	36.2
KP-15-33/3-26	4.2	28	2.7	0.2	8380	870	2.3	1.3	311.8	63.9
KP-15-33/3-27	7.1	43	4.7	0.3	8650	960	2.1	1.0	301.6	50.7
KP-15-33/3-28	6.6	30	5.8	0.3	BLOD	BLOD	1.1	0.2	226.4	43.8

KP-15-33/3-29	31.6	104	41.8	2.0	BLOD	BLOD	1.1	0.5	151.8	17.6
KP-15-33/3-30	4.5	19	5.4	0.3	8310	870	2.1	0.6	168.5	40.2
KP-15-33/3-31	24.1	159	29.8	1.4	BLOD	BLOD	1.5	0.6	162.9	16.3
KP-15-33/3-32	1.0	7	1.6	0.2	5470	650	1.6	0.2	133.4	53.4
KP-15-33/3-33	6.3	27	4.0	0.2	7940	730	1.7	0.4	318.6	65.0
KP-15-33/3-34	4.2	13	3.4	0.2	8720	890	2.2	0.3	249.5	71.4
KP-15-33/3-35	6.0	28	3.8	0.3	11290	920	2.0	0.5	313.2	63.8
KP-15-38-1	9.9	54	11.7	0.7	BLOD	BLOD	1.3	0.5	168.1	26.0
KP-15-38-2	4.0	18	2.8	0.2	1340	440	1.0	0.4	288.0	70.8
KP-15-38-3	2.2	11	1.9	0.1	1630	390	1.2	0.6	234.3	72.8
KP-15-38-4	3.7	20	3.5	0.2	3430	610	1.1	0.4	211.1	50.1
KP-15-38-5	2.3	10	3.3	0.2	830	460	1.1	0.4	138.0	44.9
KP-15-38-6	2.7	8	4.1	0.3	1490	420	1.1	0.2	130.9	47.4
KP-15-38-7	3.6	15	4.8	0.2	2850	540	1.4	0.5	148.1	39.4
KP-15-38-8	2.2	9	1.6	0.1	3090	400	1.2	0.4	281.5	95.9
KP-15-38-9	1.5	7	1.1	0.1	2150	440	1.2	0.6	271.3	105.7
KP-15-38-10	4.4	22	4.0	0.3	1110	420	1.1	0.5	221.0	50.4
KP-15-38-11	13.8	34	11.8	1.0	44000	11000	1.2	0.5	232.2	45.3
KP-15-38-12	3.4	13	2.6	0.2	3530	500	1.2	0.4	253.5	72.7
KP-15-38-13	14.2	63	23.3	1.4	1020	460	1.1	0.2	120.7	17.5
KP-15-38-14	1.6	5	1.3	0.1	2220	380	1.5	0.5	240.6	109.4
KP-15-38-15	1.8	9	1.9	0.2	1990	350	1.2	0.4	195.3	67.4
KP-15-38-16	10.6	54	9.4	0.5	730	440	0.9	0.3	224.2	33.7
KP-15-38-17	1.6	7	2.4	0.2	BLOD	BLOD	1.3	0.5	131.5	50.7
KP-15-38-18	3.1	13	4.2	0.3	1460	530	1.2	0.4	147.3	42.4
KP-15-38-19	3.2	14	2.8	0.2	4390	440	1.3	0.5	228.0	64.0
KP-15-38-20	4.5	17	5.6	0.3	720	400	1.2	0.3	160.2	40.2
KP-15-38-21	1.5	7	1.3	0.1	7080	810	1.0	0.1	231.3	90.2
KP-15-38-22	26.9	105	30.2	1.8	6870	740	1.1	0.3	176.3	21.3
KP-15-38-23	5.4	20	9.8	0.7	1810	590	1.4	0.5	108.6	25.9

KP-15-38-24	2.2	15	1.7	0.1	740	400	0.8	0.4	252.8	68.7
KP-15-38-25	20.2	87	21.9	1.1	750	330	1.1	0.2	183.2	22.8
KP-15-38-26	13.7	53	16.2	0.9	BLOD	BLOD	1.2	0.3	168.5	26.0
KP-15-38-27	2.2	8	3.0	0.2	2000	420	1.5	0.5	146.5	53.1
KP-15-38-28	1.5	7	2.1	0.2	BLOD	BLOD	1.1	0.4	136.6	53.6
KP-15-38-29	21.3	62	17.3	0.9	BLOD	BLOD	1.2	0.5	243.9	35.0
KP-15-40-1	28.8	188	51.5	2.6	1380	340	2.0	0.5	110.7	10.7
KP-15-40-2	5.1	44	7.6	0.5	640	350	2.5	1.0	133.9	22.3
KP-15-40-3	6.0	27	6.7	0.4	BLOD	BLOD	1.5	0.4	179.4	36.7
KP-15-40-4	7.5	27	18.4	1.3	950	370	1.5	0.5	80.6	16.8
KP-15-40-5	3.7	19	5.7	0.4	740	340	1.9	0.7	129.9	31.3
KP-15-40-6	4.7	21	4.0	0.2	820	370	1.5	0.4	230.5	52.6
KP-15-40-7	7.3	49	14.0	0.7	BLOD	BLOD	1.6	0.3	104.1	16.2
KP-15-40-8	7.8	32	10.0	0.6	BLOD	BLOD	1.6	0.3	153.4	29.2
KP-15-40-9	10.9	57	19.0	1.1	BLOD	BLOD	1.9	0.4	113.6	17.0
KP-15-40-10	8.1	33	23.6	1.1	BLOD	BLOD	1.8	0.7	68.4	12.6
KP-15-40-11	5.0	21	7.8	0.4	BLOD	BLOD	1.9	0.3	127.6	29.1
KP-15-40-12	9.8	55	14.1	0.7	2540	440	2.4	0.9	138.2	20.7
KP-15-40-13	8.2	20	20.3	1.1	1280	510	1.8	0.2	79.7	18.6
KP-15-40-14	20.6	57	39.2	1.9	BLOD	BLOD	1.7	0.3	104.3	15.3
KP-15-40-15	3.9	17	7.9	0.6	1140	420	1.5	0.5	98.2	25.1
KP-15-40-16	13.1	70	14.6	1.0	BLOD	BLOD	1.7	0.5	177.2	25.4
KP-15-40-17	5.6	24	16.4	0.9	770	350	1.7	0.2	67.9	14.6
KP-15-40-18	14.5	53	20.7	1.1	BLOD	BLOD	1.7	0.3	138.7	21.1
KP-15-40-19	5.5	23	13.1	0.7	BLOD	BLOD	1.7	0.4	83.8	18.4
KP-15-40-20	5.4	39	5.4	0.5	BLOD	BLOD	1.6	0.3	199.1	37.7
KP-15-40-21	7.0	38	10.3	0.8	BLOD	BLOD	1.6	0.3	135.4	24.8
KP-15-40-22	5.2	41	7.9	0.4	BLOD	BLOD	1.6	0.5	129.8	22.1
KP-15-40-23	4.5	37	5.3	0.4	BLOD	BLOD	1.7	0.4	166.7	30.9
KP-15-40-24	3.6	19	5.2	0.3	BLOD	BLOD	1.7	0.3	136.0	32.6

KP-15-40-25	1.9	8	4.4	0.3	1070	440	1.6	0.5	84.9	30.7
KP-15-40-26	6.6	28	5.4	0.3	730	390	1.7	0.4	243.9	49.4
KP-15-40-27	13.7	43	25.0	1.3	BLOD	BLOD	1.7	0.4	108.5	18.0
KP-15-40-28	26.2	139	47.6	2.2	2020	460	1.6	0.3	109.2	11.4
KP-15-40-29	4.9	23	5.1	0.3	BLOD	BLOD	1.7	0.3	189.8	42.0
KP-15-40-30	4.7	26	8.3	0.5	BLOD	BLOD	1.8	0.3	113.4	23.9
KP-15-40-31	5.0	26	6.9	0.4	BLOD	BLOD	1.3	0.4	143.0	30.0
KP-15-40-32	2.3	15	4.9	0.4	BLOD	BLOD	1.4	0.2	93.4	25.3
06TN09-1	0.2	2	13.5	0.7	BLOD	BLOD	1.5	0.5	3.1	2.2
06TN09-2	1.3	6	11.8	0.6	BLOD	BLOD	1.3	0.2	21.7	9.0
06TN09-3	3.2	14	15.0	0.8	870	400	1.5	0.2	41.8	11.5
06TN09-4	1.7	8	36.8	2.5	BLOD	BLOD	1.2	0.3	9.4	3.4
06TN09-5	0.6	5	9.6	0.6	1130	400	1.4	0.2	12.0	5.4
06TN09-6	0.4	2	13.8	0.9	890	400	0.8	0.3	5.3	3.8
06TN09-7	4.5	25	15.8	1.0	BLOD	BLOD	1.3	0.4	56.6	12.0
06TN09-8	2.4	8	16.0	1.1	BLOD	BLOD	1.0	0.3	29.3	10.6
06TN09-9	4.1	19	18.6	1.4	BLOD	BLOD	1.3	0.2	43.2	10.6
06TN09-10	0.6	3	14.6	0.8	770	360	1.1	0.2	8.5	4.9
06TN09-11	2.1	8	19.1	0.8	700	340	1.3	0.3	22.0	7.9
06TN09-12	2.9	17	25.3	1.7	BLOD	BLOD	1.4	0.3	22.8	5.8
06TN09-13	4.1	15	19.7	1.0	BLOD	BLOD	1.2	0.3	41.4	11.0
06TN09-14	1.4	5	20.4	1.1	BLOD	BLOD	1.6	0.6	13.4	6.0
06TN09-15	0.9	5	21.2	1.1	BLOD	BLOD	1.4	0.3	8.7	3.9
06TN09-16	0.6	3	18.7	1.0	BLOD	BLOD	0.5	0.2	6.6	3.8
06TN09-17	0.6	5	14.0	0.7	BLOD	BLOD	1.3	0.4	9.2	4.1
06TN09-18	1.1	9	24.4	1.4	BLOD	BLOD	1.6	0.2	9.2	3.1
06TN09-19	1.9	7	23.5	1.2	900	490	1.5	0.2	16.1	6.2
06TN09-20	2.2	14	17.6	1.0	BLOD	BLOD	1.2	0.2	24.3	6.7
06TN09-21	0.7	3	19.5	0.9	BLOD	BLOD	1.6	0.3	7.4	4.3
06TN09-22	1.5	7	26.2	1.3	BLOD	BLOD	1.5	0.3	11.6	4.5

06TN09-23	2.3	18	24.6	1.4	BLOD	BLOD	1.5	0.2	18.6	4.6
06TN09-24	1.4	9	21.9	1.5	770	370	0.9	0.3	12.7	4.4
06TN09-25	1.8	12	27.8	1.6	BLOD	BLOD	1.5	0.3	12.9	3.8
06TN09-26	0.9	5	23.8	1.4	BLOD	BLOD	2.0	0.0	7.6	3.4
06TN09-27	1.7	9	12.4	0.8	BLOD	BLOD	1.4	0.2	26.7	9.1
06TN09-28	1.5	9	30.5	1.4	BLOD	BLOD	1.6	0.7	10.1	3.4
06TN09-29	0.2	1	21.3	1.2	BLOD	BLOD	1.6	0.2	2.1	2.1
06TN09-30	0.8	3	16.7	0.8	BLOD	BLOD	1.7	0.4	10.0	5.8
06TN09-31	0.7	3	20.0	1.0	BLOD	BLOD	1.8	0.3	7.0	4.0
06TN09-32	1.3	11	22.0	0.9	BLOD	BLOD	1.5	0.4	11.8	3.6
06TN09-33	0.9	3	19.0	1.0	810	330	1.8	0.4	9.9	5.7
06TN09-34	1.3	6	30.5	1.8	BLOD	BLOD	1.4	0.4	8.4	3.5
06TN09-35	0.8	4	13.3	0.9	BLOD	BLOD	1.4	0.2	12.1	6.1
06TN09-36	0.9	4	19.5	1.1	920	350	1.4	0.4	9.6	4.8
06TN09-37	0.3	1	14.3	1.3	1330	460	1.6	0.3	4.0	4.0
06TN09-38	3.7	21	15.0	0.8	1260	470	1.0	0.2	49.3	11.2
06TN09-39	1.6	8	17.0	0.9	1330	370	1.4	0.1	19.1	6.9
06TN09-40	6.3	29	21.1	1.3	820	440	1.2	0.4	59.0	11.8
06TN09-41	2.2	7	24.4	1.3	830	370	1.6	0.3	17.5	6.7
06TN10-1	0.7	5	17.8	1.0	920	490	1.5	0.1	7.8	3.5
06TN10-2	1.9	9	24.6	1.3	BLOD	BLOD	0.8	0.1	15.3	5.2
06TN10-3	0.9	4	17.7	1.1	1270	450	1.5	0.3	9.7	4.9
06TN10-4	1.6	12	30.8	1.7	BLOD	BLOD	2.1	0.2	10.2	3.0
06TN10-5	0.9	8	24.9	1.7	BLOD	BLOD	1.8	0.7	7.4	2.7
06TN10-6	0.9	9	12.1	0.7	BLOD	BLOD	2.2	0.3	15.0	5.1
06TN10-7	1.0	8	25.1	1.5	BLOD	BLOD	1.6	0.4	8.1	2.9
06TN10-8	0.6	3	12.1	0.6	BLOD	BLOD	1.2	0.2	9.6	5.6
06TN10-9	0.3	3	11.8	0.6	1670	480	2.3	0.5	4.6	2.7
06TN10-10	1.4	12	14.0	0.8	BLOD	BLOD	2.1	0.2	20.4	6.0
06TN10-11	1.9	16	23.6	1.3	BLOD	BLOD	1.5	0.1	16.3	4.2

06TN10-12	0.8	9	15.2	1.0	BLOD	BLOD	1.5	0.3	10.7	3.7
06TN10-13	4.6	44	27.9	1.5	BLOD	BLOD	1.5	0.3	33.0	5.4
06TN10-14	0.3	2	15.4	1.0	BLOD	BLOD	1.5	0.4	3.9	2.8
06TN10-15	0.6	3	35.1	3.7	990	540	1.6	0.2	3.6	2.1
06TN10-16	1.3	8	15.8	0.9	1050	430	1.2	0.3	16.4	5.9
06TN10-17	1.1	10	36.5	2.2	990	440	1.9	1.8	5.8	1.9
06TN10-18	1.9	21	25.4	1.3	1600	420	1.9	1.0	14.7	3.4
06TN10-19	1.1	9	16.1	0.7	1500	380	0.8	0.1	14.0	4.8
06TN10-20	0.8	4	17.5	1.0	1500	450	1.6	0.5	9.2	4.7
06TN10-21	0.8	6	43.5	2.2	1450	490	1.7	0.3	3.6	1.5
06TN10-22	1.5	11	14.5	0.9	BLOD	BLOD	1.1	0.3	20.6	6.4
06TN10-23	1.1	12	35.7	2.1	BLOD	BLOD	1.5	0.4	6.3	1.9
06TN10-24	1.2	10	40.3	2.3	1140	460	1.3	0.1	6.0	1.9
06TN10-25	1.6	9	28.0	1.6	BLOD	BLOD	1.4	0.2	11.4	3.9
06TN10-26	0.4	4	11.4	0.6	970	470	1.9	0.0	7.8	3.9
06TN10-27	1.7	12	20.2	1.4	BLOD	BLOD	1.4	0.5	16.9	5.1
06TN10-28	0.7	5	22.8	1.4	BLOD	BLOD	1.9	0.4	6.1	2.7
06TN10-29	1.0	10	7.0	0.5	840	520	1.4	0.4	28.6	9.3
06TN10-30	1.7	16	28.2	2.1	1090	510	2.0	0.2	11.8	3.1
06TN10-31	1.5	9	29.4	1.4	BLOD	BLOD	1.7	0.3	10.0	3.4
06TN10-32	1.4	10	25.2	1.5	1750	510	1.8	0.5	11.1	3.6
06TN10-33	0.2	2	13.6	0.7	BLOD	BLOD	1.2	0.2	2.6	1.8
06TN10-34	1.0	9	28.1	1.5	BLOD	BLOD	2.2	0.6	7.0	2.4
06TN10-35	0.8	8	25.2	1.4	1520	430	1.9	0.2	6.4	2.3
06TN10-36	2.1	14	29.3	2.5	740	510	1.6	0.2	14.3	4.1
06TN10-37	2.2	15	16.0	0.8	1330	480	1.9	0.0	27.0	7.2
06TN10-38	1.1	9	21.0	1.3	830	400	1.4	0.2	10.6	3.6
06TN10-39	0.6	4	23.7	1.4	BLOD	BLOD	1.8	0.2	5.1	2.6
06TN10-40	0.8	7	14.6	1.1	1490	500	1.6	0.5	10.9	4.2
06TN10-41	1.6	16	22.9	1.0	BLOD	BLOD	2.0	0.2	13.7	3.5

06TN10-42	3.6	30	24.0	1.2	BLOD	BLOD	1.6	0.5	30.1	5.8
06TN10-43	0.8	11	9.7	0.6	1150	390	1.5	0.5	15.6	4.8
06TN11-1	2.6	21	2.9	0.2	BLOD	BLOD	2.5	0.3	174.1	40.0
06TN11-2	1.6	11	2.8	0.2	BLOD	BLOD	2.2	0.7	112.9	35.0
06TN11-3	3.1	18	2.4	0.2	BLOD	BLOD	2.6	0.9	257.1	64.1
06TN11-4	1.6	14	3.8	0.5	BLOD	BLOD	2.3	0.8	82.1	24.2
06TN11-5	2.7	21	2.4	0.2	BLOD	BLOD	1.7	0.7	225.4	52.5
06TN11-6	2.3	22	3.4	0.3	930	540	2.3	0.8	133.9	30.6
06TN11-7	2.9	20	2.3	0.2	BLOD	BLOD	2.2	0.6	245.0	57.8
06TN11-8	2.8	18	3.0	0.2	1280	450	2.4	0.4	183.0	45.4
06TN11-9	6.8	25	15.3	9.8	BLOD	BLOD	2.3	0.5	88.1	59.2
06TN11-10	1.4	8	2.6	0.2	BLOD	BLOD	1.5	0.5	110.6	40.0
06TN11-11	1.4	8	3.4	0.2	BLOD	BLOD	2.4	0.6	84.3	30.5
06TN11-12	2.8	19	3.2	0.2	BLOD	BLOD	2.7	0.3	176.1	42.3
06TN11-13	2.3	16	3.2	0.2	940	470	1.6	0.3	144.5	38.0
06TN11-14	2.2	17	2.3	0.2	BLOD	BLOD	3.2	0.7	183.5	46.6
06TN11-15	3.3	28	3.4	0.2	BLOD	BLOD	2.4	0.6	189.0	38.0
06TN11-16	2.5	15	2.5	0.2	BLOD	BLOD	2.2	0.7	198.5	54.6
06TN11-17	1.9	15	2.9	0.3	BLOD	BLOD	2.0	0.6	127.3	35.1
06TN11-18	2.3	10	2.2	0.1	BLOD	BLOD	1.0	0.6	206.1	67.0
06TN11-19	3.5	19	2.7	0.2	BLOD	BLOD	2.4	0.7	264.2	64.0
06TN11-20	2.4	14	2.2	0.2	BLOD	BLOD	2.7	0.5	220.3	62.6
06TN11-21	2.7	18	3.8	0.2	BLOD	BLOD	2.7	0.2	138.5	33.9
06TN11-22	2.0	16	2.7	0.2	BLOD	BLOD	2.5	0.1	142.6	37.3
06TN11-23	2.6	14	5.0	0.3	BLOD	BLOD	2.7	0.1	103.1	28.7
06TN11-24	2.1	13	3.7	0.3	BLOD	BLOD	2.2	0.9	111.1	32.1
06TN11-25	2.6	17	3.5	0.2	BLOD	BLOD	2.8	0.6	148.3	37.7
06TN11-26	1.6	16	2.1	0.2	BLOD	BLOD	2.4	0.5	152.2	40.2
06TN11-27	1.7	12	2.4	0.2	BLOD	BLOD	1.9	0.1	140.1	42.0
06TN11-28	1.2	6	3.0	0.3	BLOD	BLOD	2.6	0.4	78.0	32.7

06TN11-29	2.2	21	3.2	0.3	BLOD	BLOD	2.1	0.6	132.7	31.4
06TN11-30	2.1	20	3.8	0.3	BLOD	BLOD	2.6	0.6	110.7	26.6
06TN11-31	2.5	9	2.9	0.2	BLOD	BLOD	2.3	0.2	167.2	57.7
06TN11-32	1.6	11	2.4	0.2	BLOD	BLOD	2.3	0.3	131.0	40.6
06TN11-33	2.1	13	2.5	0.2	BLOD	BLOD	2.4	0.7	165.2	47.8
06TN11-34	1.3	10	2.8	0.2	BLOD	BLOD	2.6	0.1	92.4	30.1
06TN11-35	2.3	15	3.1	0.2	BLOD	BLOD	2.2	0.4	149.0	40.4
06TN11-36	1.5	12	2.7	0.2	BLOD	BLOD	2.7	0.7	108.5	33.0
06TN11-37	1.8	14	2.8	0.2	BLOD	BLOD	1.9	0.5	128.7	35.7
06TN11-38	2.7	21	2.9	0.2	BLOD	BLOD	2.2	0.5	184.8	42.2
06TN11-39	1.9	8	2.6	0.2	BLOD	BLOD	2.2	0.2	144.7	52.4
06TN11-40	2.6	17	3.3	0.2	BLOD	BLOD	2.3	0.3	159.8	40.6
06TN11-41	2.6	13	3.8	0.2	BLOD	BLOD	1.7	0.8	138.4	39.5
06TN12-1	3.2	31	3.6	0.2	BLOD	BLOD	2.4	0.2	161.3	33.2
06TN12-2	3.9	25	3.4	0.2	BLOD	BLOD	2.0	0.4	211.8	47.1
06TN12-3	4.7	25	3.4	0.3	BLOD	BLOD	1.7	0.4	255.2	58.1
06TN12-4	2.3	17	2.4	0.2	BLOD	BLOD	2.0	0.2	180.9	47.5
06TN12-5	6.5	54	6.3	0.3	BLOD	BLOD	1.7	0.7	187.5	30.8
06TN12-6	3.6	18	2.9	0.2	BLOD	BLOD	2.0	0.3	228.1	59.2
06TN12-7	4.0	31	3.0	0.2	BLOD	BLOD	1.8	0.3	239.3	49.6
06TN12-8	2.8	19	2.5	0.2	BLOD	BLOD	1.7	0.2	201.3	50.4
06TN12-9	2.9	18	3.3	0.2	BLOD	BLOD	1.8	0.2	160.7	40.9
06TN12-10	1.7	12	3.4	0.2	BLOD	BLOD	1.5	0.5	90.7	27.7
06TN12-11	3.4	24	3.5	0.2	BLOD	BLOD	1.7	0.1	176.0	40.2
06TN12-12	2.6	18	2.6	0.2	BLOD	BLOD	1.8	0.3	181.7	47.1
06TN12-13	3.9	30	3.2	0.2	BLOD	BLOD	1.9	0.5	222.2	46.5
06TN12-14	2.0	10	3.4	0.2	BLOD	BLOD	1.6	0.2	109.0	36.2
06TN12-15	4.4	31	3.0	0.2	BLOD	BLOD	1.5	0.4	264.5	54.6
06TN12-16	3.6	26	3.7	0.3	BLOD	BLOD	1.6	0.5	173.7	38.6
06TN12-17	4.4	39	4.2	0.2	BLOD	BLOD	2.1	0.3	192.1	35.6

06TN12-18	2.4	14	3.1	0.2	BLOD	BLOD	1.9	0.2	139.3	39.7
06TN12-19	3.4	20	3.3	0.2	BLOD	BLOD	2.2	0.3	189.8	46.8
06TN12-20	3.9	28	4.9	0.3	BLOD	BLOD	1.8	0.4	145.1	30.9
06TN12-21	1.7	13	3.0	0.3	BLOD	BLOD	2.4	0.3	104.2	31.4
06TN12-22	2.0	17	2.6	0.2	BLOD	BLOD	2.5	0.3	139.6	37.0
06TN12-23	2.7	13	3.9	0.3	BLOD	BLOD	2.3	0.3	125.6	37.2
06TN12-24	9.8	52	9.4	0.6	BLOD	BLOD	2.2	0.5	191.0	32.3
06TN12-25	4.1	26	3.0	0.2	BLOD	BLOD	2.3	0.5	252.0	56.0
06TN12-26	1.7	12	2.6	0.2	BLOD	BLOD	2.8	2.2	117.2	36.0
06TN12-27	1.3	7	3.0	0.2	BLOD	BLOD	2.5	0.7	77.3	30.2
06TN12-28	2.1	12	2.5	0.2	BLOD	BLOD	1.7	0.6	151.4	46.4
06TN12-29	2.5	21	3.6	0.2	BLOD	BLOD	2.6	0.6	126.8	30.2
06TN12-30	2.1	14	2.7	0.2	BLOD	BLOD	2.0	0.5	141.7	40.4
06TN12-31	4.9	28	5.3	0.4	BLOD	BLOD	2.6	0.5	168.5	36.2
06TN12-32	1.9	11	3.1	0.2	BLOD	BLOD	2.6	0.2	111.2	35.3
06TN12-33	7.2	44	8.2	0.5	BLOD	BLOD	2.6	0.4	160.2	28.5
06TN12-34	2.5	22	3.2	0.2	BLOD	BLOD	2.5	0.4	143.6	34.4
06TN12-35	2.1	21	3.2	0.2	BLOD	BLOD	2.8	0.3	122.7	29.7
06TN12-36	5.0	40	6.0	0.3	BLOD	BLOD	2.3	0.5	152.1	28.0
06TN12-37	2.3	13	2.5	0.2	BLOD	BLOD	2.4	0.6	168.6	49.7
06TN12-38	3.4	19	2.7	0.2	BLOD	BLOD	2.2	0.5	228.7	58.1
06TN12-39	4.3	26	6.2	0.4	BLOD	BLOD	2.0	0.5	126.4	28.1
06TN12-40	3.0	33	3.6	0.2	BLOD	BLOD	2.4	0.2	153.5	31.0
06TN12-41	3.0	24	3.6	0.2	BLOD	BLOD	2.2	0.4	153.0	34.8
06TN12-42	7.0	44	5.7	0.4	BLOD	BLOD	1.2	0.6	224.4	40.9

Appendix B

Karatau-Talas ZFT Single Grain Data

Supplemtary File 2: Single grain zircon fission track data for the Karatau-Talas region (Chapter 1): n is the number of grains analysed per sample and ρ_s is the number of spontaneous tracks counted, Area is the area counted in μm^2, ρ_D is the number of tracks in the dosimeter, ρ_i is the number of induced tracks, χ^2 is the chi-squared value obtained for each sample, and ^{238}U is the concentration of ^{238}U in ppm.

Sample	N_s	N_i	Area	$\rho_s \times 10^5$	$\rho_D \times 10^5$	$\rho_i \times 10^5$	Age$\pm 1\sigma$(Ma)	^{238}U
KP-15-38-1	86	10	635.44	135.339	4.42	15.737	230.61±77.86	112.94
KP-15-38-2	43	6	566.68	75.881	4.42	10.588	192.74±84.52	75.99
KP-15-38-3	140	9	1281.19	109.273	4.42	7.025	411.27±142.84	50.41
KP-15-38-4	64	7	490.04	130.602	4.42	14.285	244.89±98.22	102.51
KP-15-38-5	141	19	1064.07	132.51	4.42	17.856	199.48±49.71	128.15
KP-15-38-6	80	14	468.17	170.878	4.42	29.904	154.14±45.28	214.61
KP-15-38-7	100	15	680.5	146.951	4.42	22.043	179.48±50.46	158.19
KP-15-38-8	75	16	1292.64	58.021	4.42	12.378	126.72±35.44	88.83
KP-15-38-9	146	23	686.73	212.602	4.42	33.492	171.01±39.26	240.36
KP-15-38-10	160	15	1062.08	150.648	4.42	14.123	284.82±78.15	101.36
KP-15-38-11	167	25	2048.6	81.519	4.42	12.203	179.83±39.55	87.58
KP-15-38-12	72	10	428.03	168.213	4.42	23.363	193.62±66.02	167.67
KP-15-38-13	101	17	928.55	108.772	4.42	18.308	160.19±42.71	131.39
KP-15-38-14	128	13	916.69	139.633	4.42	14.181	263.35±77.72	101.77
KP-15-38-15	95	15	1022.36	92.922	4.42	14.672	170.62±48.13	105.29
KP-15-38-16	69	9	717.98	96.103	4.42	12.535	205.98±73.68	89.96

KP-15-38-17	83	11	668.43	124.172	4.42	16.456	202.77±65.81	118.1
KP-15-38-18	81	10	480.01	168.746	4.42	20.833	217.42±73.64	149.51
KP-15-38-19	86	15	899.61	95.597	4.42	16.674	154.65±43.92	119.66
KP-15-38-20	95	18	539.01	176.249	4.42	33.395	142.50±37.28	239.66
KP-15-38-21	90	9	573.68	156.882	4.42	15.688	267.38±94.38	112.59
KP-15-38-22	63	10	623.68	101.013	4.42	16.034	169.74±58.37	115.07
KP-15-38-23	96	9	786.03	122.133	4.42	11.45	284.82±100.25	82.17
KP-15-38-24	120	16	841.9	142.535	4.42	19.005	201.57±54.54	136.39
KP-15-38-25	117	16	611.98	191.183	4.42	26.145	196.60±53.27	187.63
KP-15-33/3-1	61	5	250.29	243.717	4.42	19.977	324.74±151.89	143.37
KP-15-33/3-2	69	7	327.61	210.616	4.42	21.367	263.64±105.36	153.34
KP-15-33/3-3	84	8	326	257.669	4.42	24.54	280.46±104.67	176.11
KP-15-33/3-4	60	6	321.23	186.782	4.42	18.678	267.38±115.22	134.05
KP-15-33/3-5	66	7	242	272.727	4.42	28.926	252.4±101.08	207.59
KP-15-33/3-6	64	6	346.39	184.763	4.42	17.322	284.82±122.39	124.31
KP-15-33/3-7	64	4	387.5	165.161	4.42	10.323	422.64±218.79	74.08
KP-15-33/3-8	54	4	362.06	149.147	4.42	11.048	358.40±186.54	79.29
KP-15-33/3-9	104	10	399.55	260.293	4.42	25.028	277.85±92.98	179.62
KP-15-33/3-10	62	6	602.64	102.881	4.42	9.956	276.10±118.81	71.45
KP-15-33/3-11	89	9	352.44	252.525	4.42	25.536	264.47±93.4	183.26
KP-15-33/3-12	61	5	346.38	176.107	4.42	14.435	324.74±151.89	103.59
KP-15-33/3-13	40	4	114.17	350.355	4.42	35.035	267.38±140.82	251.44
KP-15-33/3-14	50	5	477.51	104.71	4.42	10.471	267.38±126.09	75.15
KP-15-33/3-15	125	10	830.99	150.423	4.42	12.034	332.53±110.47	86.36
KP-15-33/3-16	151	12	508.35	297.039	4.42	23.606	334.69±101.7	169.41
KP-15-33/3-17	104	10	402.88	258.141	4.42	24.821	278.46±93.19	177.73
KP-15-33/3-18	173	9	776.69	222.74	4.42	11.588	505.60±174.61	82.97
KP-15-33/3-19	43	4	219.98	195.472	4.42	18.183	287.63±151	130.2
KP-15-33/3-20	181	13	891.27	203.081	4.42	14.586	370.13±107.8	104.44
KP-15-33/3-21	75	8	534.14	140.413	4.42	14.977	251.55±94.36	107.24

KP-15-33/3-22	52	5	517.55	100.473	4.42	9.661	278.46±131.08	69.18
KP-15-33/3-23	38	4	231.44	164.189	4.42	17.283	254.83±134.53	123.75
KP-15-33/3-24	73	6	425.09	171.728	4.42	14.115	324.59±138.76	101.07
KP-15-33/3-25	38	4	277.54	136.917	4.42	14.412	254.83±134.53	103.2
KP-15-33/3-26	85	7	378.94	224.31	4.42	18.473	323.97±128.37	132.27
KP-15-33/3-27	128	10	743.04	172.265	4.42	13.458	341.05±113.21	96.37
KP-15-33/3-28	40	4	483.99	82.646	4.42	8.265	267.97±141.13	59.18
KP-15-33/3-29	64	6	492.72	129.891	4.42	12.177	285.45±122.66	87.19
KP-15-33/3-30	89	7	688.52	129.263	4.42	10.167	338.82±134.02	72.8
KP-15-33/3-31	123	10	595.1	206.688	4.42	16.804	328.06±109.05	120.32
KP-15-9-1	104	18	901.57	115.354	4.41	19.965	155.49±40.41	143.61
KP-15-9-2	73	10	941.43	77.542	4.41	10.622	195.84±66.72	76.4
KP-15-9-3	74	11	675.68	109.519	4.41	16.28	180.68±59.05	117.1
KP-15-9-4	123	15	1236.68	99.46	4.41	12.129	219.57±61.00	87.24
KP-15-9-5	115	19	1022.86	112.43	4.41	18.575	162.79±41.09	133.61
KP-15-9-6	164	17	941.32	174.223	4.41	18.06	257.56±66.81	129.9
KP-15-9-7	94	12	860.73	109.21	4.41	13.942	209.91±65.15	100.28
KP-15-9-8	42	6	587.37	71.505	4.41	10.215	187.90±82.52	73.48
KP-15-9-9	82	9	964.09	85.054	4.41	9.335	243.51±86.33	67.15
KP-15-9-10	108	16	669.67	161.273	4.41	23.892	181.29±49.36	171.85
KP-15-9-11	108	11	1787.8	60.409	4.41	6.153	262.03±83.91	44.26
KP-15-9-12	93	14	801.74	115.998	4.41	17.462	178.45±51.89	125.6
KP-15-9-13	117	12	507.06	230.742	4.41	23.666	260.25±79.90	170.23
KP-15-9-14	49	5	451.37	108.558	4.41	11.077	261.56±123.45	79.68
KP-15-9-15	92	11	438.56	209.777	4.41	25.082	223.88±72.25	180.41
KP-15-9-16	85	10	1297.74	65.498	4.41	7.706	227.47±76.85	55.43
KP-15-9-17	37	5	623.34	59.358	4.41	8.021	198.48±95.06	57.7
KP-15-9-18	221	23	1406.81	157.093	4.41	16.349	256.55±57.58	117.6
KP-15-9-19	28	2	350.47	79.893	4.41	5.707	370.48±271.77	41.05
KP-15-9-20	67	5	369.62	181.267	4.41	13.527	355.04±165.5	97.3

KP-15-9-21	126	14	1335.79	94.326	4.41	10.481	240.60±68.79	75.39
KP-15-7/1-1	47	6	181.45	259.025	4.41	33.067	209.91±91.57	237.85
KP-15-7/1-2	58	13	289.59	200.283	4.41	44.891	120.39±37.41	322.9
KP-15-7/1-3	85	9	452.8	187.721	4.41	19.876	252.25±89.27	142.97
KP-15-7/1-4	39	8	450.86	86.501	4.41	17.744	131.44±51.41	127.63
KP-15-7/1-5	76	6	342.86	221.665	4.41	17.5	336.10±143.46	125.87
KP-15-7/1-6	106	10	535.61	197.905	4.41	18.67	282.45±94.44	134.29
KP-15-7/1-7	161	8	950.66	169.356	4.41	8.415	526.11±192.29	60.53
KP-15-7/1-8	71	4	535.24	132.651	4.41	7.473	466.21±240.65	53.75
KP-15-7/1-9	82	9	379.74	215.937	4.41	23.7	243.51±86.33	170.47
KP-15-7/1-10	120	8	401.37	298.976	4.41	19.932	396.15±145.93	143.37
KP-15-7/1-11	71	8	182.99	387.999	4.41	43.718	237.32±89.26	314.46
KP-15-7/1-12	64	7	815.28	78.501	4.41	8.586	244.35±98.00	61.76
KP-15-7/1-13	124	12	416.4	297.791	4.41	28.818	275.49±84.36	207.29
KP-15-7/1-14	27	3	101.5	266.01	4.41	29.557	240.60±146.89	212.6
KP-15-7/1-15	71	6	356.72	199.036	4.41	16.82	314.52±134.59	120.98
KP-15-7/1-16	78	6	396.58	196.682	4.41	15.129	344.72±147	108.82
KP-15-7/1-17	124	12	803.3	154.363	4.41	14.938	275.49±84.36	107.45
KP-15-7/1-18	233	19	1079.96	215.749	4.41	17.593	325.66±79.3	126.55
KP-15-7/1-19	117	15	955.34	122.469	4.41	15.701	209.03±58.22	112.94
KP-15-7/1-20	66	7	671.68	98.261	4.41	10.422	251.84±100.85	74.96
KP-15-3/4-1	87	11	534.19	162.863	4.41	20.592	211.91±68.59	148.12
KP-15-3/4-2	31	6	299.7	103.437	4.41	20.02	139.22±62.46	144
KP-15-3/4-3	82	12	662.18	123.833	4.41	18.122	183.49±57.41	130.35
KP-15-3/4-4	37	4	754.41	49.045	4.41	5.302	247.16±130.64	38.14
KP-15-3/4-5	51	9	1032.13	49.412	4.41	8.72	152.53±55.65	62.72
KP-15-3/4-6	53	6	744.02	71.235	4.41	8.064	236.22±102.4	58.01
KP-15-3/4-7	126	13	628.86	200.363	4.41	20.672	258.74±76.42	148.69
KP-15-3/4-8	74	10	445.15	166.236	4.41	22.464	198.48±67.57	161.58
KP-15-3/4-9	64	8	366.14	174.797	4.41	21.85	214.30±81.04	157.16

KP-15-3/4-10	90	8	748.71	120.207	4.41	10.685	299.37±111.41	76.86
KP-15-3/4-11	72	3	519.88	138.493	4.41	5.771	622.66±368.16	41.51
KP-15-3/4-12	54	6	1017.3	53.082	4.41	5.898	240.60±104.2	42.42
KP-15-3/4-13	74	7	888.96	83.243	4.41	7.874	281.70±112.24	56.64
KP-15-3/4-14	59	6	665.39	88.67	4.41	9.017	262.43±113.18	64.86
KP-15-3/4-15	25	3	292.3	85.529	4.41	10.263	223.08±136.74	73.82
KP-15-3/4-16	61	5	873.72	69.816	4.41	5.723	324.03±151.55	41.16
KP-15-3/4-17	57	4	761.17	74.885	4.41	5.255	376.91±195.82	37.8
KP-15-3/4-18	106	10	819.06	129.417	4.41	12.209	282.45±94.44	87.82
KP-15-3/4-19	59	4	673.58	87.592	4.41	5.938	389.74±202.26	42.71
KP-15-3/4-20	67	6	475.84	140.804	4.41	12.609	297.20±127.47	90.7
KP-15-3/4-21	71	11	454.7	156.147	4.41	24.192	173.46±56.84	174.01
KP-15-3/4-22	59	7	692.74	85.169	4.41	10.105	225.59±90.85	72.68
KP-15-3/4-23	25	2	225.81	110.713	4.41	8.857	331.79±244.35	63.71
KP-15-3/4-24	53	5	532.19	99.588	4.41	9.395	282.45±132.85	67.58
KP-15-3/4-25	54	6	454.27	118.872	4.41	13.208	240.60±104.2	95
KP-15-2/6-1	98	12	1639.37	59.779	4.41	7.32	218.69±67.73	52.65
KP-15-2/6-2	70	11	1581.35	44.266	4.41	6.956	171.05±56.1	50.03
KP-15-2/6-3	79	18	1452.08	54.405	4.41	12.396	118.45±31.47	89.16
KP-15-2/6-4	25	4	621.4	40.232	4.41	6.437	168.03±90.86	46.3
KP-15-2/6-5	90	14	1339.12	67.208	4.41	10.455	172.77±50.34	75.2
KP-15-2/6-6	51	12	353.78	144.157	4.41	33.919	114.74±37.23	243.98
KP-15-2/6-7	44	5	328.29	134.028	4.41	15.23	235.35±111.66	109.55
KP-15-2/6-8	35	7	396.57	88.257	4.41	17.651	134.77±56.19	126.96
KP-15-2/6-9	121	17	646.07	187.286	4.41	26.313	191.01±50.34	189.27
KP-15-2/6-10	66	7	380.4	173.502	4.41	18.402	251.84±100.85	132.36
KP-15-2/6-11	52	5	370.02	140.533	4.41	13.513	277.23±130.51	97.2
KP-15-2/6-12	46	4	423.06	108.732	4.41	9.455	305.87±160.14	68.01
KP-15-2/6-13	46	4	378.94	121.391	4.41	10.556	305.87±160.14	75.93
KP-15-2/6-14	54	9	286.3	188.613	4.41	31.436	161.39±58.64	226.11

KP-15-2/6-15	43	6	291.54	147.493	4.41	20.58	192.31±84.33	148.03

Appendix C

Karatau-Talas AFT Radial Plots

Supplementary File 3a: Single grain apatite fission track data for samples taken from the Karatau-Talas region plotted using Vermeesch (2009). Single grain ages are coloured according to their respective uranium 238 (U) measurements.

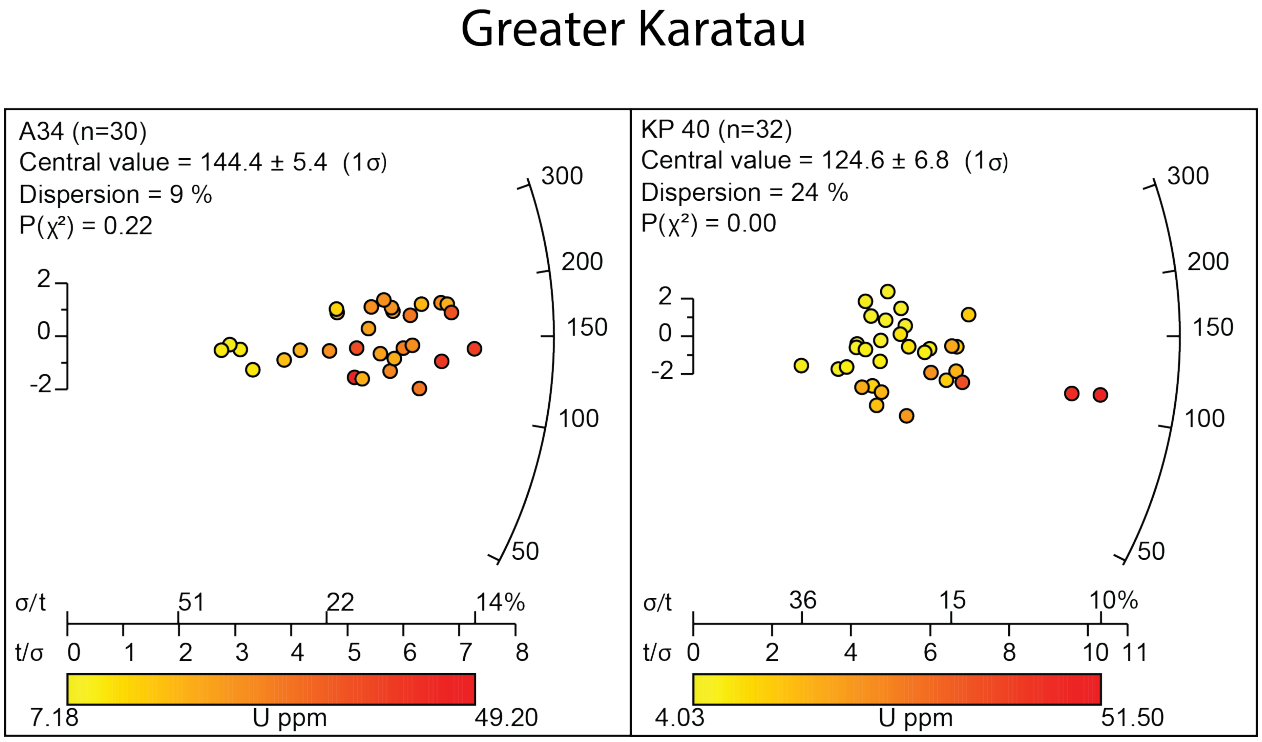

Supplementary File 3b

Lesser Karatau (a)

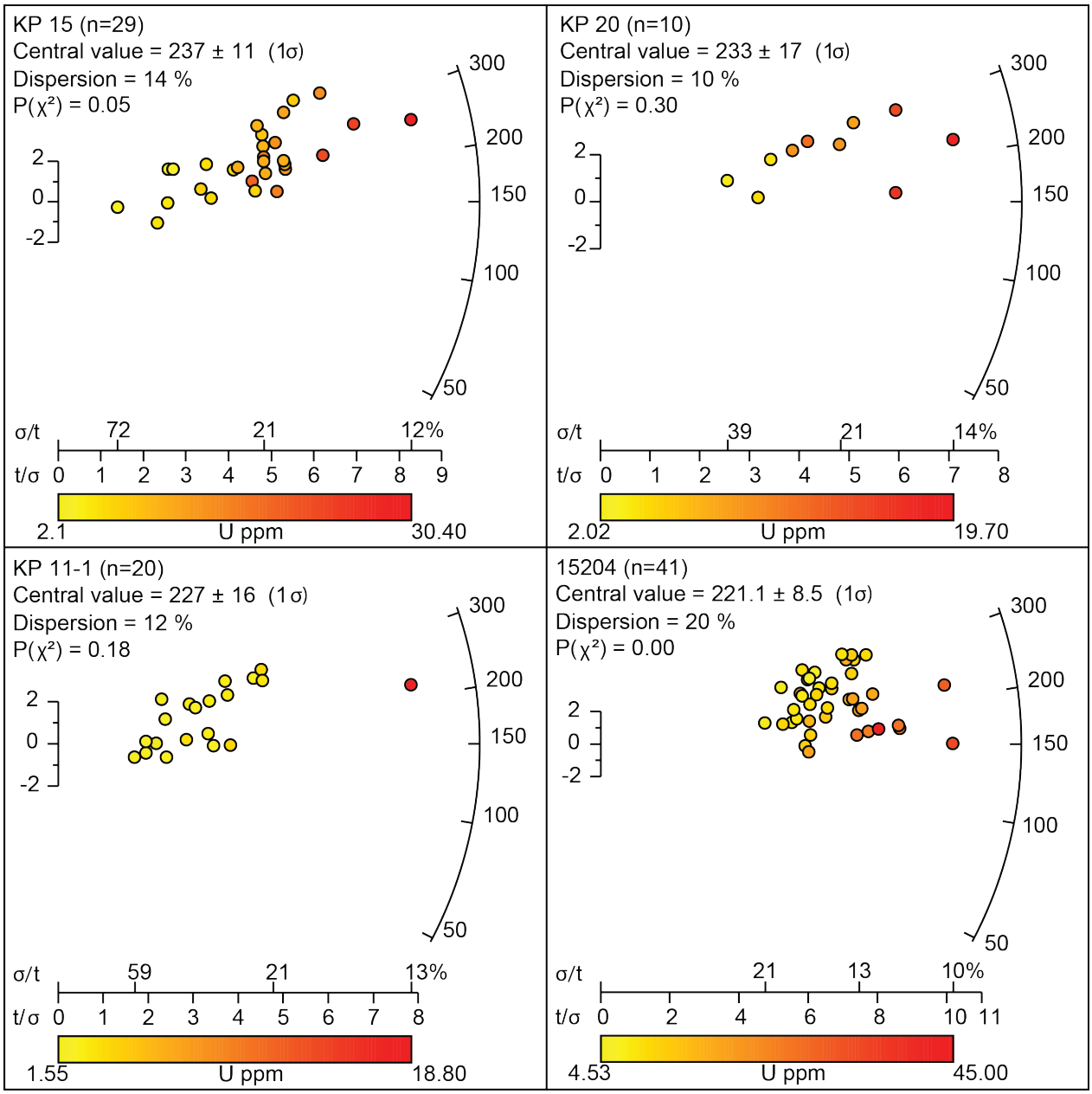

Supplementary File 3c

Lesser Karatau (b)

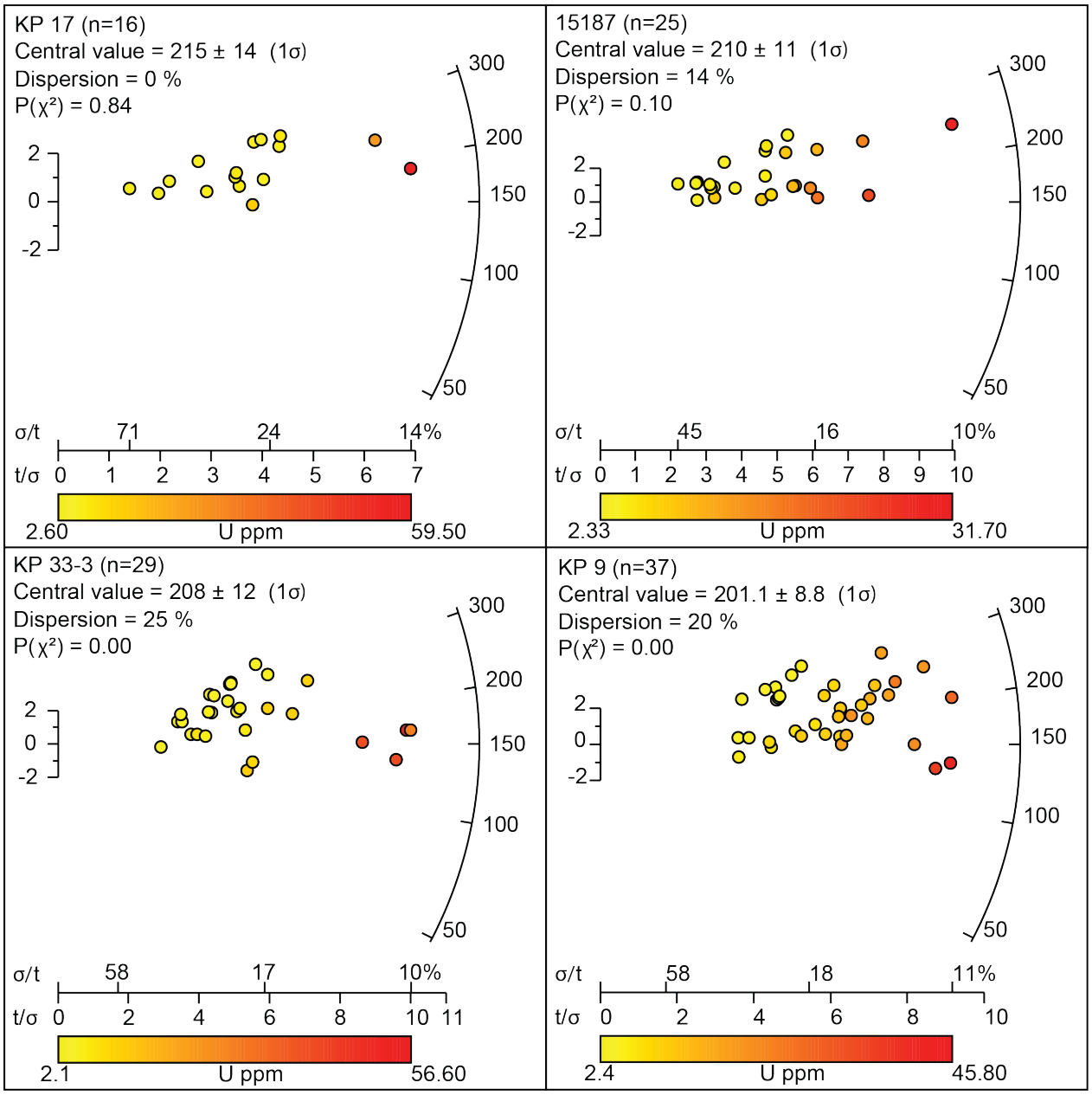

Supplementary File 3d

Lesser Karatau (c)

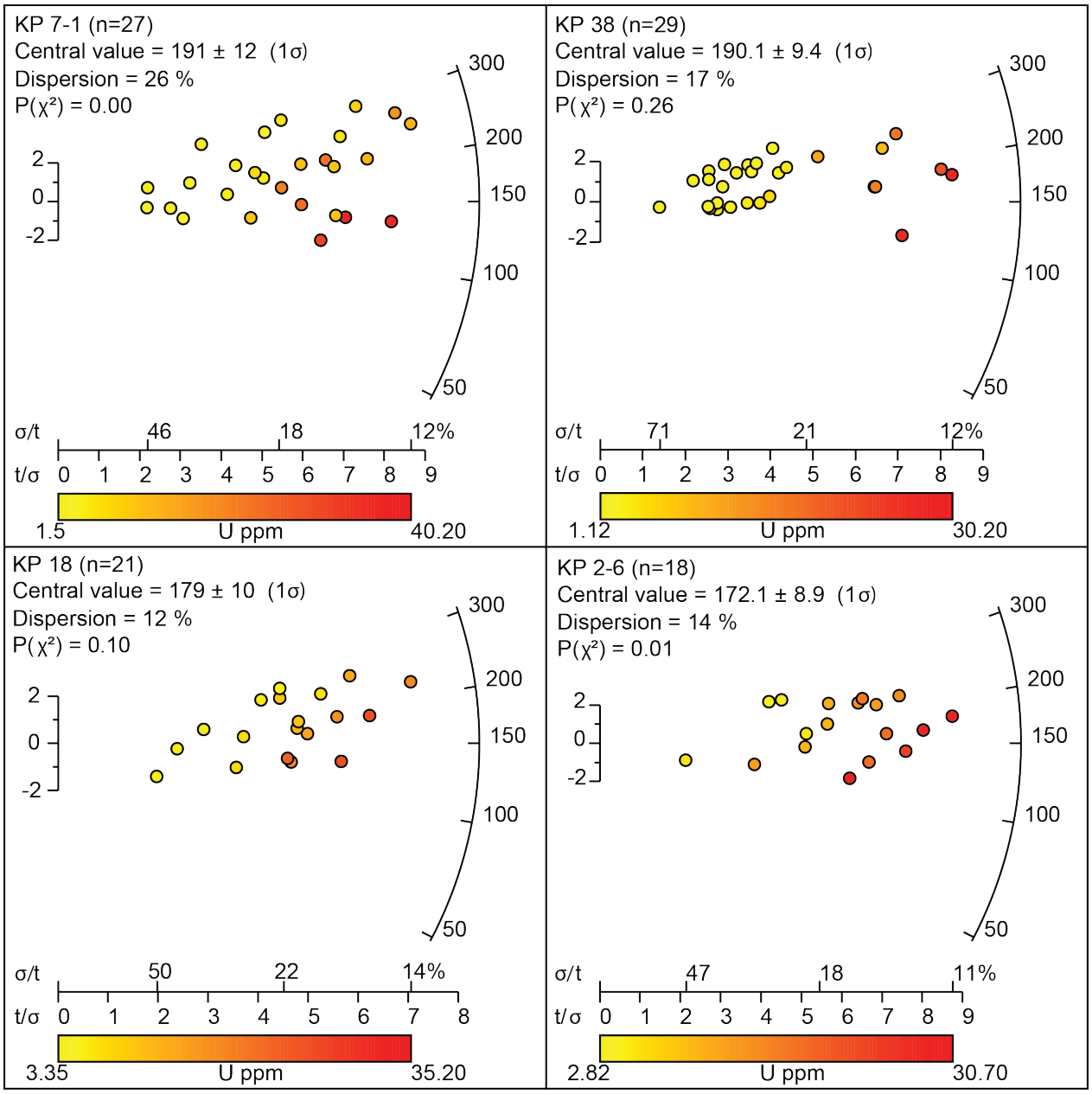

Supplementary File 3e

Lesser Karatau (d)

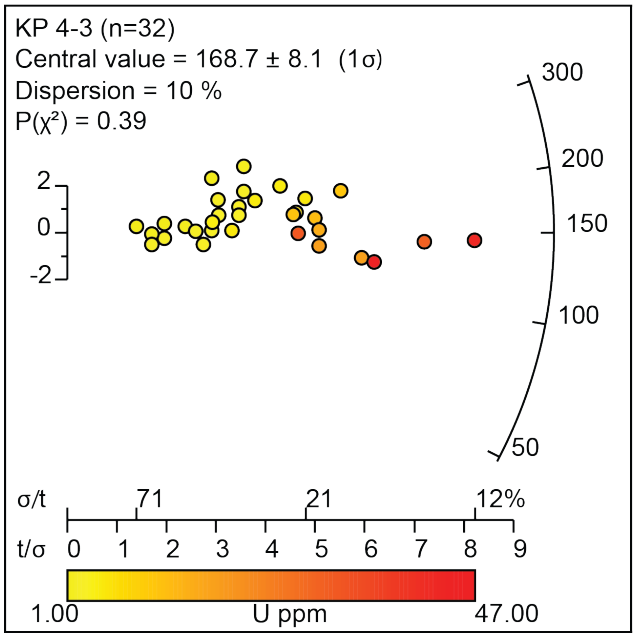

Supplementary File 3f

Talas Range (a)

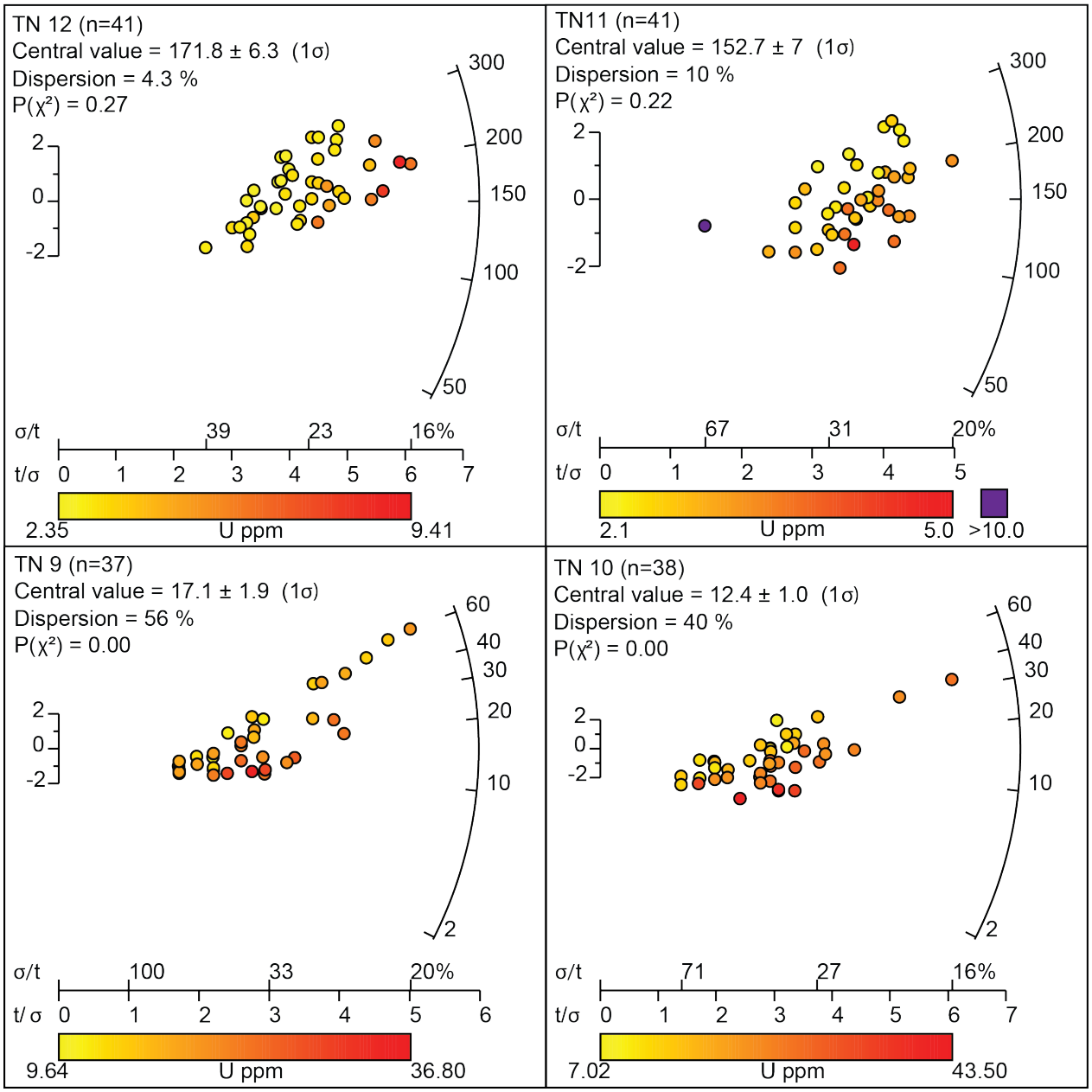

Appendix D

Karatau-Talas ZFT Radial Plots

Supplementary File 4a: Single grain Zircon fission track data for samples taken from the Karatau-Talas region plotted using Vermeesch (2009). Single grain ages are coloured according to their respective uranium 238 (U) measurements.

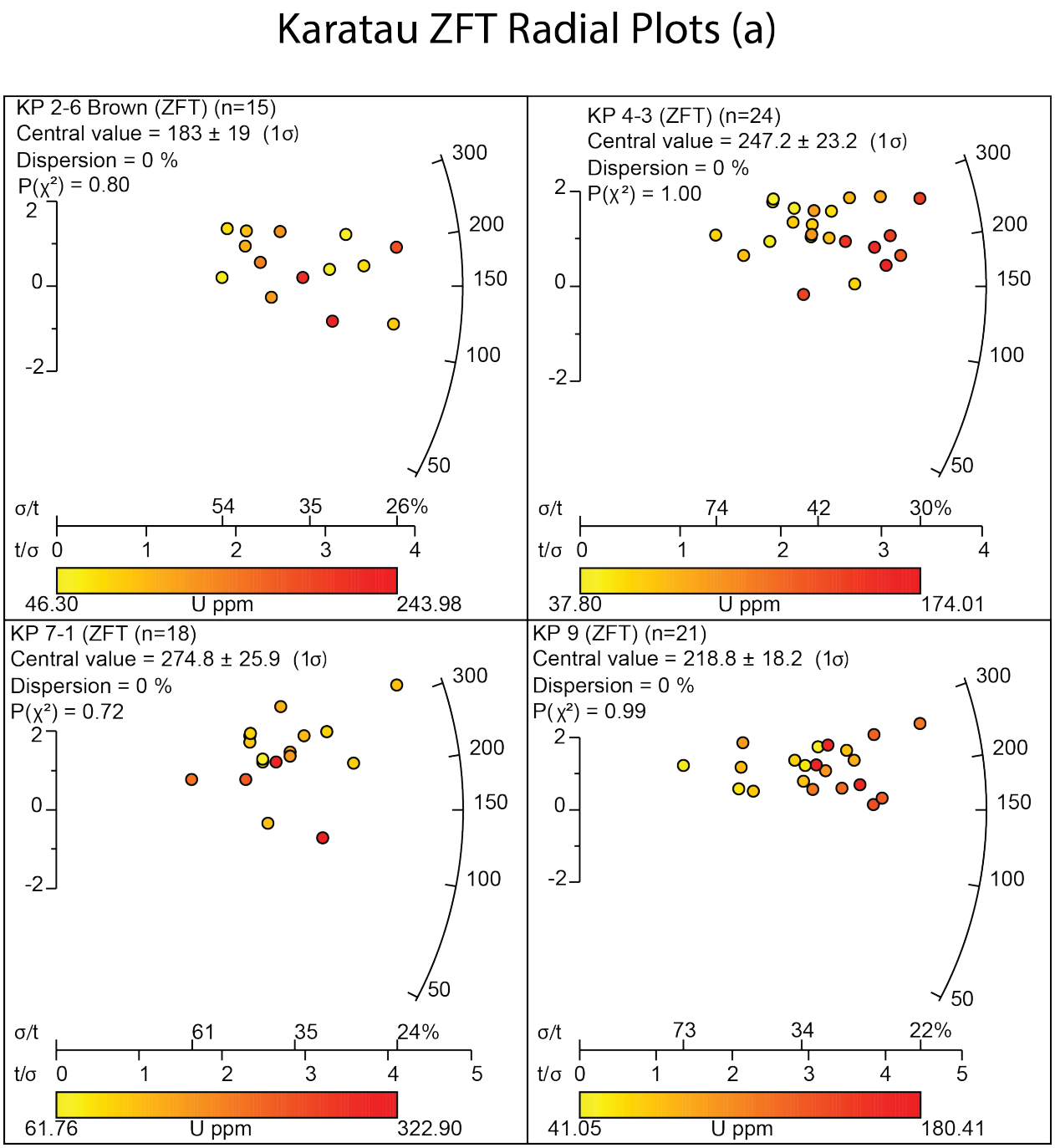

Supplementary File 4b

Karatau ZFT Radial Plots (b)

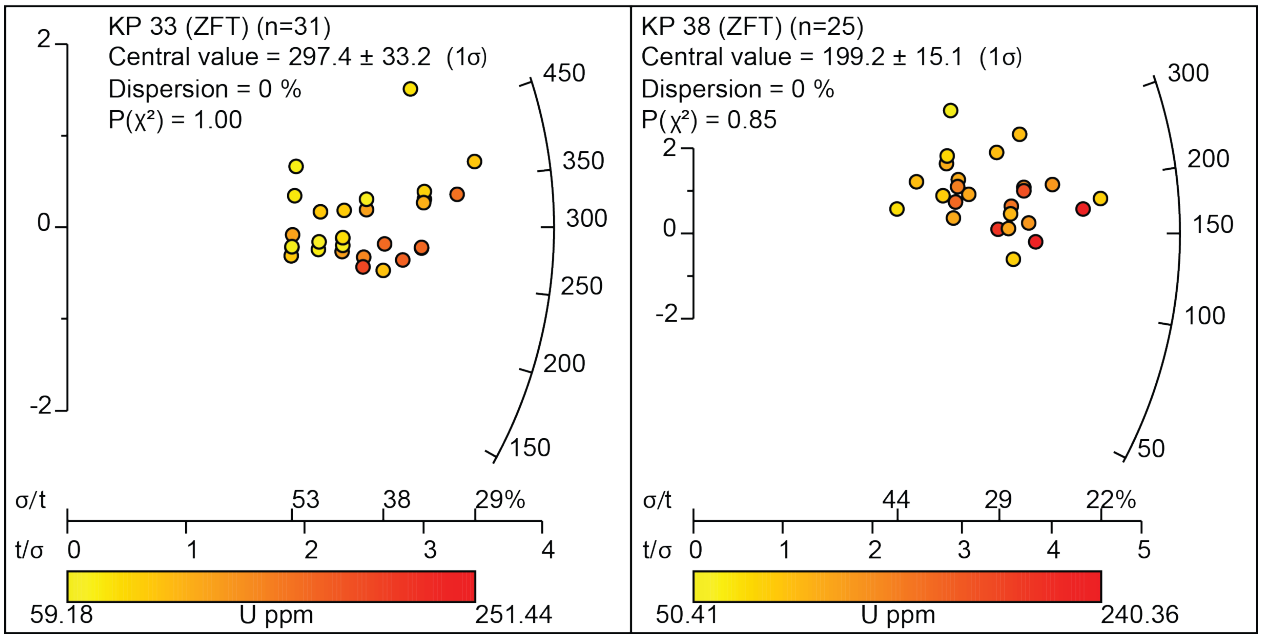

Appendix E

Karatau-Talas Thermal History Models

Supplementary File 5a: Individual time-temperature plots for each sample modelled using Gallagher (2012). For modelling parameters see Supplementary File 7.

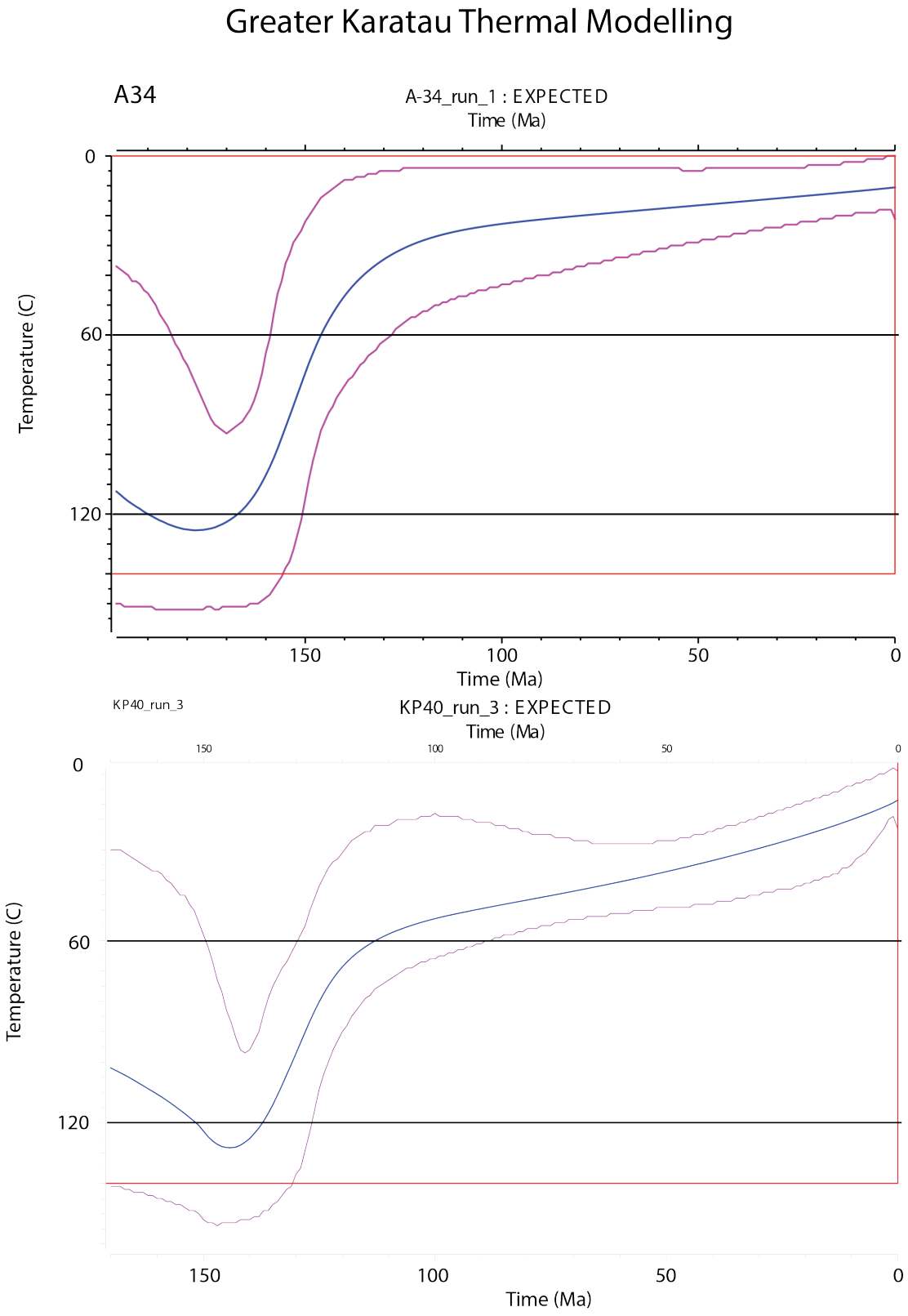

Supplementary File 5b

Lesser Karatau Thermal Modelling (a)

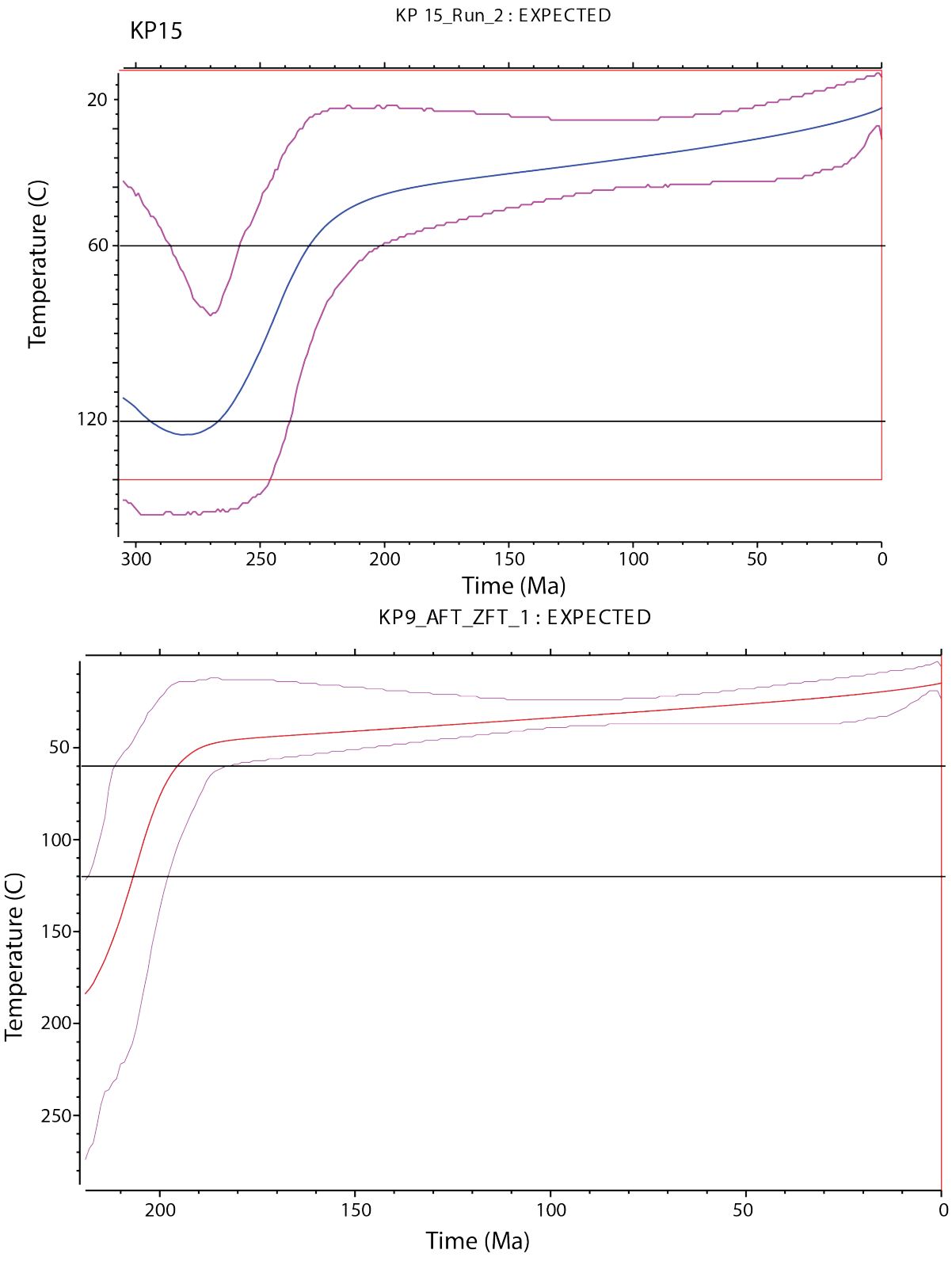

Supplementary File 5c

Lesser Karatau Thermal Modelling (b)

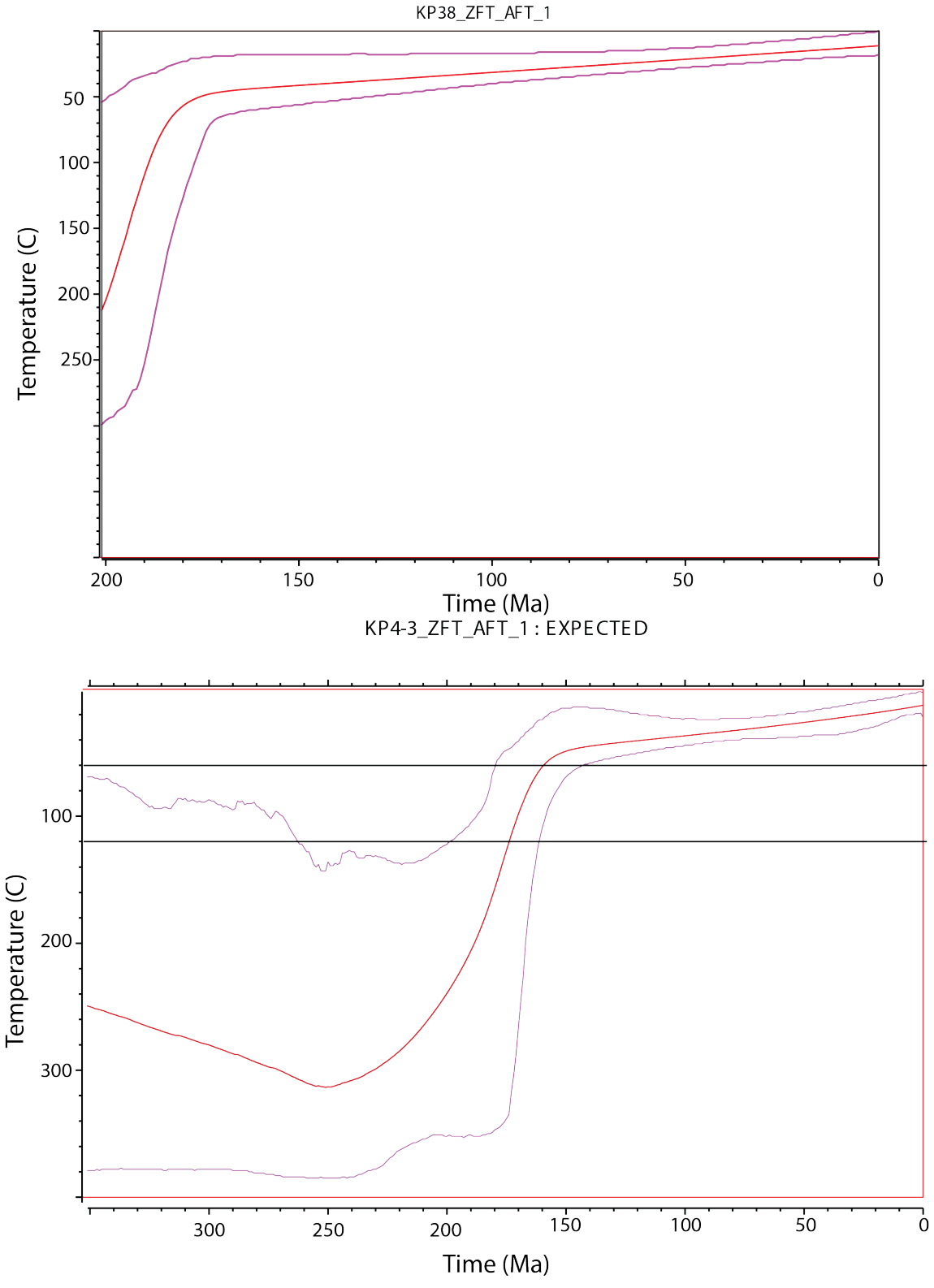

Supplementary File 5d

Lesser Karatau Thermal Modelling (c)

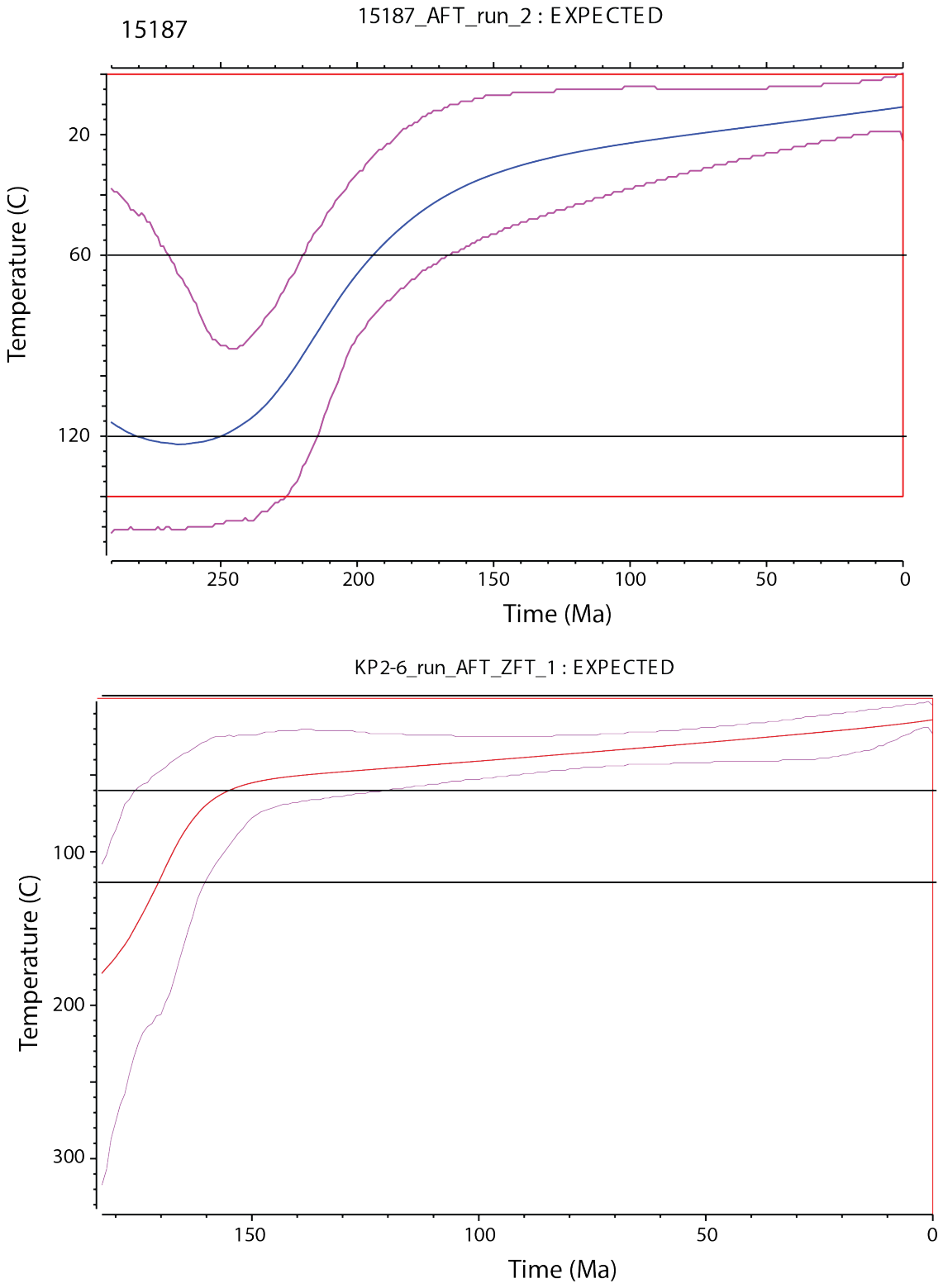

Supplementary File 5e

Lesser Karatau Thermal Modelling (d)

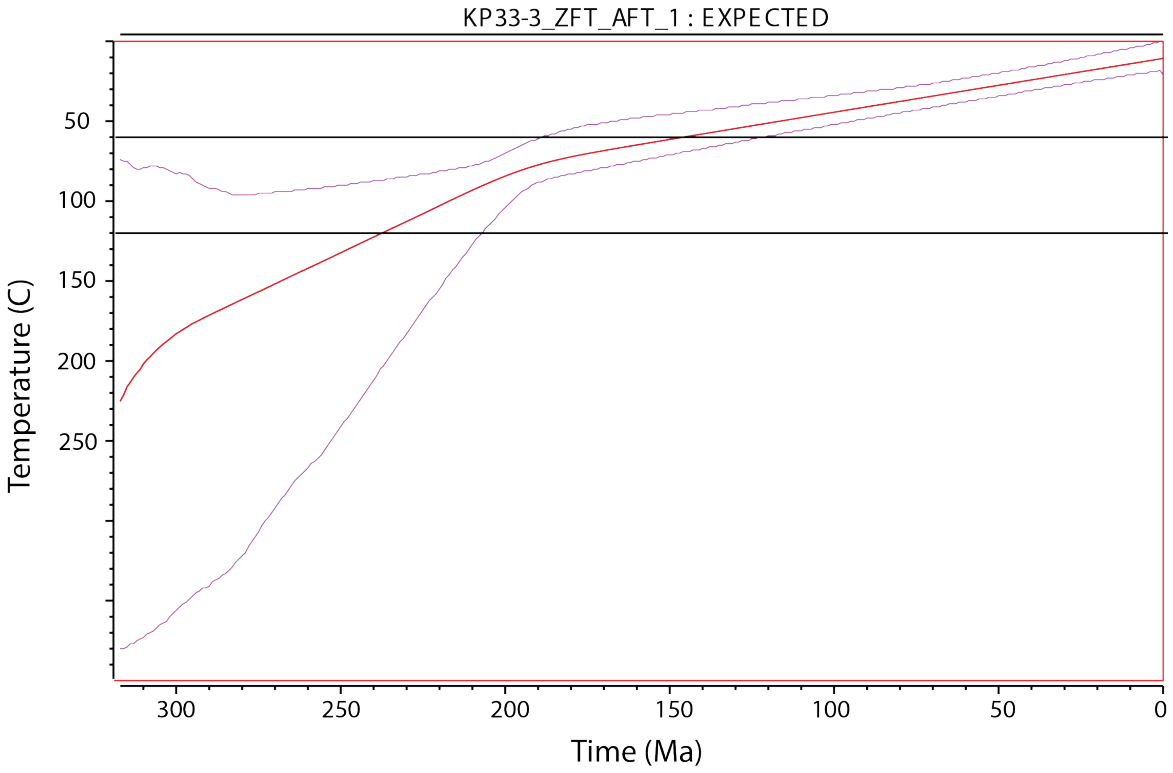

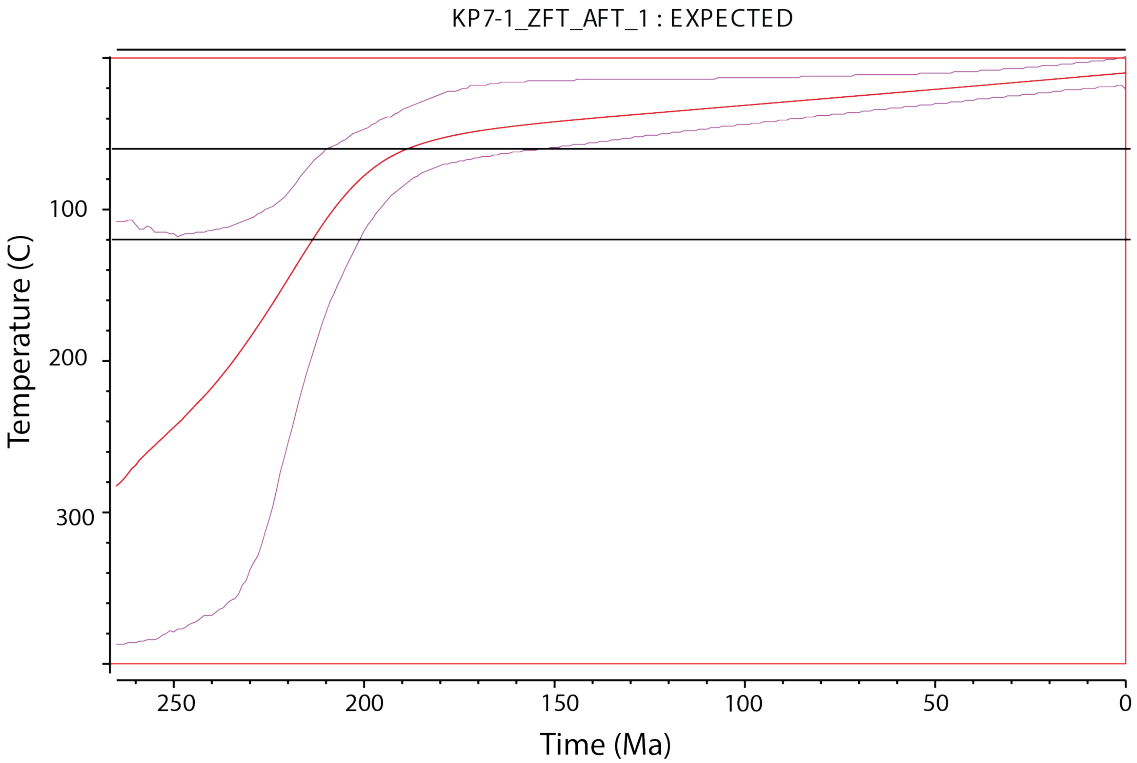

Supplementary File 5f

Lesser Karatau Thermal Modelling (e)

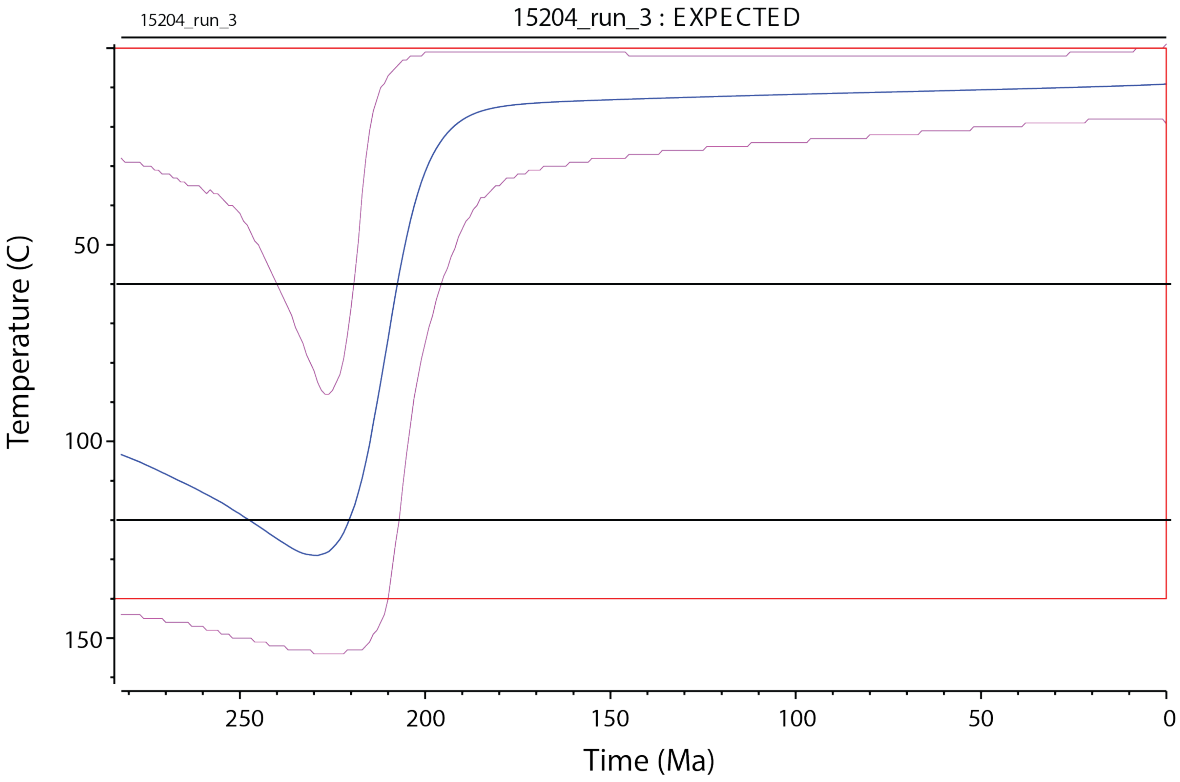

Supplementary File 5g

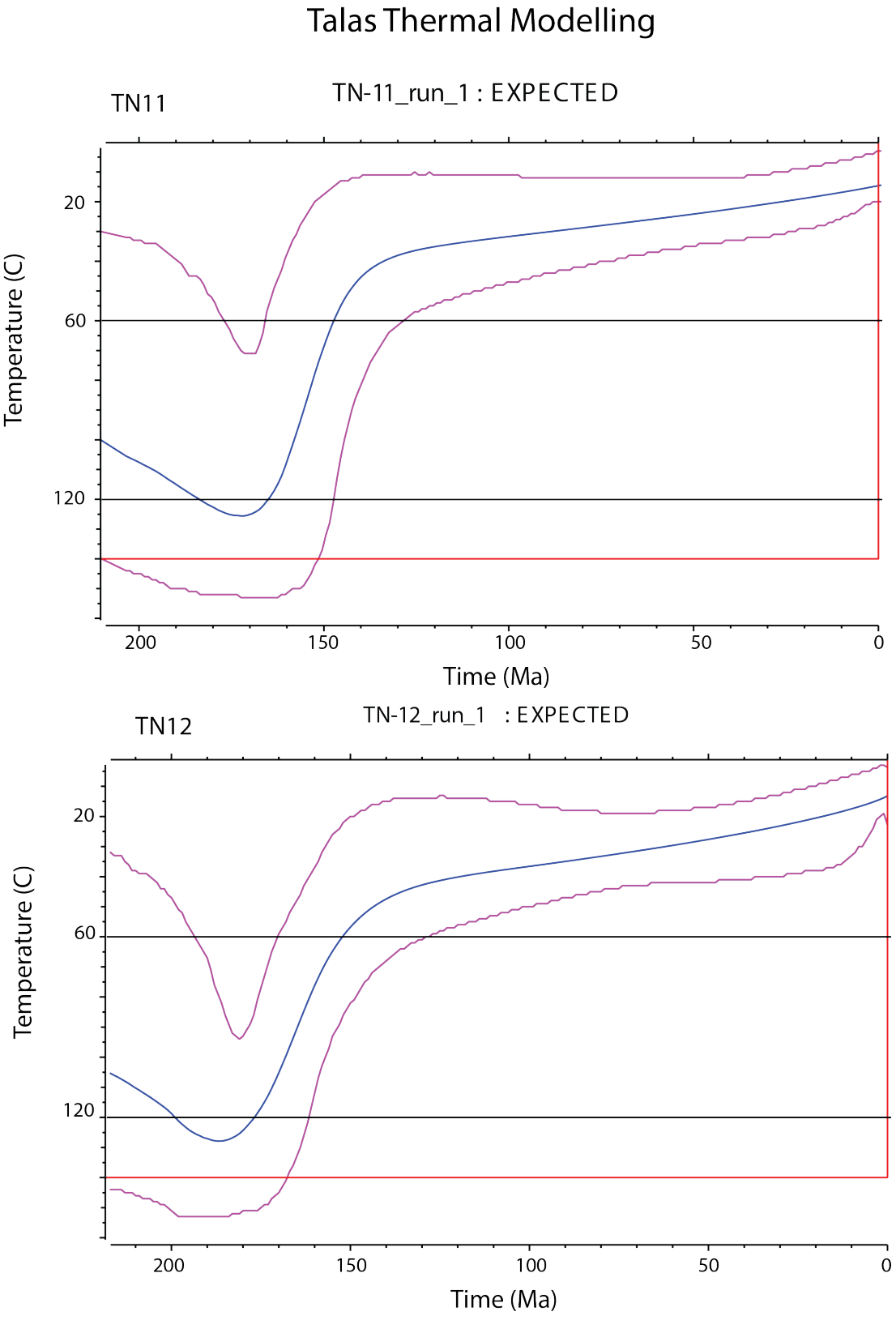

Appendix F

Karatau-Talas Thermal History Modelling Constraints

Thermal history modelling parameters following Flowers et al. (2015).

Supplementary File 7: Thermal history model input table for simulations of the Karatau-Talas, Kazakhstan and Kyrgyzstan, based on framework established by Flowers et al. (2015)

1. Thermochronologic Data

Samples and data used in simulations

Simulation inputs			Data Source	All data
Sample Region	AFT	ZFT		
Greater Karatau				
A34	×		Supplementary File 1 and 5	yes
Lesser Karatau				
KP15	×		Supplementary File 1 and 5	yes
KP9	×	×	Supplementary File 1, 2, and 5	yes
KP38	×	×	Supplementary File 1, 2, and 5	yes
KP4-3	×	×	Supplementary File 1, 2, and 5	yes
15187	×		Supplementary File 1 and 5	yes
KP2-6	×	×	Supplementary File 1, 2, and 5	yes
Talas				
TN-11	×		Supplementary File 1 and 5	yes
TN-12	×		Supplementary File 1 and 5	yes

Data treatment, uncertainties, and other relevant constraints

ZFT Data

ZFT dates (Ma): Box constraints on the models (ZFT central age ± 1σ) were from Supplementary File 2 , 4, and 5

Error (Ma) applied in modeling: error of 1σ was used from Supplementary file 4

AFT data

Dpar (µm): From Supplementary file 1

Lengths: Length data for all samples is available in Supplementary File 5

Initial mean track length: 16.3 µm

Track length reduction standard: 0.893

2. Additional geological information

Assumption	Explaination and data source
As all the samples were Neoproterozoic basement and there was no evidence for re-heating. Samples we assumed to have come from depth through the APAZ	

3. System- and model-specific parameters

He radiation damage model : Flowers et al. 2009

FT annealing model : Ketcham et al. 2007

FT c-axis projection : Not used

Modeling code : QTQt 5.6.0 PC

Statistical fitting criteria : Default QTQt values

MCMC Parameters : Burn-in = 200,000, Post-burn-in = 200,000

Appendix G

Chatkal-Kurama AFT Single Grain Data

Supplemtary File 1: Apatite fission track data and chemistry: ρ_s is the density of spontaneous tracks within the region of interest and is expressed as 10^5 tracks/cm^2. N_s is the total number of counted spontaneous tracks per sample. ^{238}U is the average concentration in ppm of uranium 238 measured in each grain. ^{35}Cl is the average concentration in ppm of chlorine 35 measured in each grain; concentrations were obtained using laser ablation–inductively coupled plasma–mass spectrometry (LA-ICP-MS). BLOD is below limits of detection, and thus, could not provide a concentration value and was not used in calculating sample concentration averages. Dpar is the length of spontaneous track etch pits in μm. t is the AFT single grain age for each sample in Ma.

Sample	ρ_s	N_s	^{238}U	$\pm1\sigma$	^{35}Cl	$\pm1\sigma$	Dpar	$\pm1\sigma$	t	$\pm1\sigma$
UZ-51-1	10.9	29	6.8	0.5	2390	380	3.3	0.7	223.6	45.0
UZ-51-2	8.2	17	9.4	1.2	2700	500	3.1	0.5	191.1	52.4
UZ-51-3	47.5	160	64.1	4.4	9820	670	3.4	0.4	161.6	16.9
UZ-51-4	13.4	53	16.5	1.1	2850	490	2.1	0.2	176.8	27.0
UZ-51-5	10.3	31	8.9	0.5	3150	430	2.2	1.3	251.6	47.1
UZ-51-6	12.0	36	12.5	0.8	3930	320	2.6	0.6	208.7	37.4
UZ-51-7	4.7	15	6.8	0.5	3280	750	2.9	0.3	151.6	40.9
UZ-51-8	58.4	185	63.3	5.7	11190	680	2.0	0.2	200.6	23.3
UZ-51-9	6.3	14	9.3	0.7	3120	450	1.5	0.2	148.5	41.2
UZ-51-10	13.2	34	9.4	0.4	4680	550	3.2	0.3	301.4	53.0
UZ-51-11	49.8	130	46.8	2.5	11710	820	3.9	0.5	231.0	23.7

UZ-51-12	50.1	154	60.0	4.2	10960	770	2.0	1.1	182.1	19.4
UZ-51-13	20.1	87	13.6	0.7	2120	430	2.3	1.0	318.4	38.1
UZ-51-14	24.3	82	17.4	1.0	5090	550	1.2	0.1	301.6	37.3
UZ-51-15	3.5	7	9.0	0.4	4540	760	3.0	0.4	84.8	32.2
UZ-51-16	6.4	19	5.4	0.3	3410	590	3.0	0.3	256.6	61.0
UZ-51-17	19.8	81	17.9	0.9	4420	500	2.5	0.9	239.4	29.3
UZ-51-18	40.8	169	36.6	1.9	4520	430	1.4	0.4	241.9	22.4
UZ-51-19	5.7	18	8.2	0.4	4890	530	1.7	0.7	152.4	36.8
UZ-51-20	28.0	53	12.6	0.6	1070	440	1.7	0.8	271.1	39.7
UZ-51-21	7.4	18	42.8	2.3	5930	460	2.2	0.9	38.1	9.2
UZ-51-22	13.7	23	4.9	0.3	6540	420	2.5	0.8	271.5	59.1
UZ-51-23	5.6	17	18.4	2.3	4280	520	2.2	0.7	67.0	18.3
UZ-51-24	10.8	16	6.7	0.4	4530	530	2.2	0.5	215.9	55.8
UZ-51-25	17.9	26	8.1	0.6	4680	440	2.4	0.5	138.9	29.2
UZ-51-26	9.1	21	6.5	0.4	4340	770	2.0	0.8	300.1	68.3
UZ-51-27	15.5	30	32.4	2.0	6350	550	2.0	0.7	85.0	16.4
UZ-51-28	41.1	105	32.8	2.3	17300	1000	1.7	0.6	271.6	32.6
UZ-51-29	4.2	11	39.6	2.2	15230	890	2.1	0.7	23.4	7.2
UZ-51-30	9.7	24	34.1	2.4	16990	890	2.1	0.7	62.4	13.5
UZ-51-31	4.2	9	55.9	3.1	17900	1300	2.0	1.0	16.8	5.7
UZ-51-32	8.3	8	5.3	0.3	3670	900	1.8	0.7	226.9	80.9
UZ-52-1	13.3	43	12.4	0.6	1220	270	1.8	1.0	223.0	35.5
UZ-52-2	24.4	13	10.3	0.6	2800	520	1.4	0.4	255.6	72.3
UZ-52-3	23.6	31	16.9	1.1	2240	450	1.6	0.6	233.6	44.6
UZ-52-5	12.9	48	7.8	0.5	2570	490	2.0	0.9	252.4	39.4
UZ-52-6	13.1	14	13.7	1.0	10320	630	1.7	0.5	206.4	57.1
UZ-53-1	16.8	161	29.8	2.0	17810	920	3.3	0.7	120.0	12.4
UZ-53-2	25.4	95	40.4	2.6	14590	740	3.1	0.5	137.6	16.7
UZ-53-3	29.7	101	91.1	5.8	17290	870	3.4	0.4	71.5	8.4
UZ-53-4	17.9	77	32.9	1.8	4830	500	2.1	0.2	119.1	15.1

UZ-53-5	28.5	105	46.6	2.4	19770	750	2.2	1.3	133.6	14.7
UZ-53-6	29.8	135	33.8	1.8	19500	1000	2.6	0.6	191.9	19.4
UZ-53-7	31.6	91	51.1	2.8	17000	1100	2.9	0.3	135.0	16.0
UZ-53-8	21.4	49	38.4	2.5	17040	970	2.0	0.2	121.8	19.1
UZ-53-9	32.6	85	40.6	2.6	16100	1100	1.5	0.2	175.1	22.1
UZ-53-10	29.3	57	44.2	2.4	18600	1100	3.2	0.3	144.9	20.7
UZ-53-11	37.8	109	56.6	2.1	22100	1300	3.9	0.5	145.9	15.0
UZ-53-12	33.2	61	37.2	2.1	23900	1000	2.0	1.1	194.0	27.1
UZ-53-13	32.8	139	55.7	3.6	22300	1100	2.3	1.0	128.7	13.7
UZ-53-14	34.5	57	48.7	3.4	21700	1200	1.2	0.1	154.6	23.1
UZ-53-15	27.4	136	42.9	1.9	24800	1300	3.0	0.4	139.3	13.4
UZ-53-16	24.7	58	46.8	2.9	22900	1300	3.0	0.3	115.7	16.8
UZ-53-17	32.5	74	50.6	2.5	16770	900	2.5	0.9	140.3	17.7
UZ-53-18	35.9	93	40.9	2.6	25000	1900	3.0	0.9	191.3	23.3
UZ-53-19	27.2	169	27.2	2.1	26700	1400	2.9	0.5	217.2	23.7
UZ-53-20	27.5	69	33.7	1.6	23200	1100	2.4	0.7	177.8	23.0
UZ-53-21	25.0	82	33.5	1.8	23700	1100	1.2	0.1	162.9	20.0
UZ-53-22	31.3	96	39.4	2.2	31500	1500	2.7	0.7	172.9	20.1
UZ-53-23	34.8	158	41.3	2.5	28600	2000	2.7	0.7	183.3	18.3
UZ-53-24	33.1	121	31.0	2.2	27800	1500	3.2	0.8	231.6	26.7
UZ-53-25	33.6	58	38.9	1.7	31200	2100	4.0	0.4	188.2	26.0
UZ-53-26	26.4	92	37.4	2.1	22600	1400	2.4	0.7	153.8	18.2
UZ-53-27	29.4	83	37.4	2.0	33100	1800	2.3	0.5	171.4	20.9
UZ-53-28	29.9	69	49.7	3.6	36900	2300	1.8	0.2	131.5	18.5
UZ-53-29	27.2	57	44.6	2.6	27900	1800	1.9	0.2	133.5	19.3
UZ-53-30	30.6	116	42.0	2.8	29600	1900	2.9	0.6	158.8	18.2
UZ-53-31	28.1	131	27.5	1.3	47800	2700	2.9	0.4	221.7	22.0
UZ-53-32	33.8	79	42.5	2.4	45400	2400	2.8	0.7	173.2	21.8
UZ-53-33	24.5	62	35.6	1.7	32000	2400	2.9	0.7	150.2	20.4
UZ-53-34	27.7	102	39.9	2.2	47500	2500	3.0	0.5	151.5	17.2

UZ-53-35	34.9	79	44.9	3.0	51400	2700	3.0	0.4	169.3	22.2
UZ-53-36	36.1	86	50.1	3.7	47600	2400	2.8	0.8	157.5	20.6
UZ-53-37	29.8	90	36.1	2.5	48700	3000	2.9	0.6	180.1	22.7
UZ-53-38	26.6	63	45.9	3.4	69800	2900	2.6	0.6	127.0	18.6
UZ-54-1	49.7	126	30.3	1.7	8350	500	2.0	0.7	213.0	22.4
UZ-54-2	38.6	105	36.0	2.8	12740	520	2.3	0.9	194.8	24.3
UZ-54-3	48.6	116	41.0	2.4	13840	420	2.2	0.7	215.0	23.6
UZ-54-4	48.0	202	39.7	2.5	9740	400	2.0	0.8	219.2	20.7
UZ-54-5	36.7	79	32.6	1.7	16250	460	2.3	0.6	204.7	25.4
UZ-54-6	46.8	169	36.9	2.6	8170	460	1.9	0.6	230.0	24.0
UZ-54-7	63.7	223	46.0	3.2	9650	440	1.7	0.7	215.4	20.8
UZ-54-8	76.0	201	108.2	9.7	1600	170	1.7	0.8	128.3	14.6
UZ-54-9	46.0	124	35.0	2.5	10270	460	2.2	0.9	238.1	27.3
UZ-54-10	46.9	182	39.6	2.5	14410	340	2.5	0.8	214.9	20.9
UZ-54-11	42.2	181	31.3	2.0	10560	420	2.2	0.7	244.3	24.0
UZ-54-12	35.3	100	30.0	1.5	13160	630	2.2	0.5	213.3	23.8
UZ-54-13	35.5	113	31.9	1.6	13280	430	2.4	0.5	202.1	21.5
UZ-54-14	50.1	162	45.1	4.1	13120	730	2.0	0.8	201.8	24.2
UZ-54-15	41.6	217	34.8	2.3	13540	700	2.0	0.7	216.7	20.5
UZ-54-16	40.7	139	31.1	1.3	6360	650	1.7	0.6	236.9	22.4
UZ-54-17	53.0	186	38.7	2.4	5410	380	2.1	0.7	247.9	23.8
UZ-54-18	35.4	103	38.4	2.6	6250	260	2.1	0.7	167.8	20.1
UZ-54-19	35.0	100	38.8	3.6	2910	210	2.0	1.0	164.4	22.4
UZ-54-20	45.5	115	41.7	4.1	9430	460	1.8	0.7	198.3	26.9
UZ-54-21	32.1	226	27.9	1.7	8690	390	2.0	0.5	208.6	18.8
UZ-54-22	61.3	235	66.8	5.7	13600	650	2.1	0.7	167.2	18.0
UZ-54-23	60.4	203	42.0	2.6	11390	640	2.1	0.6	209.5	19.6
UZ-54-24	37.4	144	32.3	2.5	12660	470	2.3	0.7	210.2	23.9
UZ-54-25	40.4	210	38.1	2.8	13320	590	2.1	0.5	192.8	19.4
UZ-54-26	41.4	175	33.6	3.1	7480	450	2.0	0.9	223.5	26.7

UZ-54-27	48.0	237	49.1	4.0	8010	590	1.9	0.6	178.0	18.5
UZ-54-28	46.4	170	35.7	2.9	10540	550	2.2	0.7	235.5	26.3
UZ-54-29	41.0	113	32.6	2.8	15110	850	2.3	0.5	228.1	29.1
UZ-54-30	37.7	140	32.6	2.1	9250	430	2.2	0.6	210.1	22.3
UZ-54-31	49.3	156	28.7	2.3	10570	750	2.2	0.6	235.7	26.7
UZ-54-32	43.6	144	36.3	3.4	9510	640	1.9	0.7	182.8	22.9
UZ-54-33	46.8	137	38.4	2.8	13720	590	2.2	0.6	220.9	24.8
UZ-54-34	35.1	154	33.3	2.4	6670	510	2.1	0.7	191.4	20.7
UZ-54-35	43.1	125	33.8	2.5	10660	710	2.1	0.6	231.3	26.8
UZ-54-36	37.0	80	30.6	1.9	7370	330	2.4	0.7	219.2	28.0
UZ-54-37	29.0	76	32.5	2.3	2470	310	1.8	0.7	162.5	21.9
UZ-55-1	3.5	9	7.7	0.6	510	120	2.1	0.7	83.3	28.5
UZ-55-2	26.7	105	35.2	2.8	9260	180	2.1	0.6	138.3	17.4
UZ-55-3	11.0	20	8.9	0.5	600	160	2.3	0.7	224.8	52.0
UZ-55-4	16.0	58	10.4	0.8	BLOD	BLOD	2.1	0.5	277.7	42.0
UZ-55-5	4.8	11	6.8	0.4	580	180	2.0	0.9	129.5	39.8
UZ-55-6	6.1	13	6.4	0.5	640	220	1.9	0.6	175.9	50.4
UZ-55-7	4.7	12	5.2	0.4	450	170	2.2	0.7	163.2	48.6
UZ-55-8	10.1	29	10.5	0.6	530	160	2.3	0.5	175.0	33.8
UZ-55-9	16.5	28	19.2	1.7	500	120	2.2	0.6	156.9	32.8
UZ-55-10	7.9	19	12.6	0.8	770	180	2.2	0.6	114.5	27.2
UZ-55-11	15.8	43	11.1	0.9	510	180	1.8	0.6	258.1	44.4
UZ-55-12	3.7	7	4.1	0.3	510	160	1.5	0.5	164.1	63.0
UZ-55-13	10.4	17	12.1	1.2	630	140	1.6	0.6	156.8	41.1
UZ-55-14	3.7	9	7.2	0.5	610	120	1.7	0.6	96.0	32.6
UZ-55-15	8.6	11	9.2	0.6	530	160	1.5	0.7	171.3	53.0
UZ-55-16	13.9	34	12.0	0.8	630	190	1.9	0.7	209.4	38.5
UZ-55-17	11.7	21	10.4	0.9	760	210	1.6	0.6	204.3	48.0
UZ-55-18	12.0	45	13.2	0.7	600	140	1.6	0.5	165.8	26.3
UZ-55-19	9.9	12	9.4	0.6	450	150	1.5	0.6	192.0	56.6

UZ-55-20	12.7	22	14.4	0.9	560	140	1.6	0.5	161.0	35.7
UZ-55-21	6.8	32	8.0	0.5	470	170	1.7	0.6	156.1	29.4
UZ-55-22	22.7	67	15.9	1.2	650	130	1.3	0.5	258.3	37.1
UZ-55-23	20.3	87	39.6	2.5	BLOD	BLOD	1.7	0.5	93.9	11.7
UZ-55-24	10.4	36	12.2	0.9	370	220	1.6	0.6	155.2	28.4
UZ-55-25	13.4	69	10.1	1.0	490	150	1.5	0.5	239.7	37.4
UZ-55-26	11.2	27	11.3	0.7	600	120	1.7	0.6	179.8	36.2
UZ-55-27	13.5	53	9.5	1.0	620	210	1.5	0.7	257.0	44.3
UZ-55-28	9.4	24	14.2	0.7	760	180	2.3	0.5	121.6	25.5
UZ-55-29	13.1	17	8.8	0.7	660	150	2.2	0.6	268.2	68.9
UZ-55-30	10.6	58	6.7	0.6	BLOD	BLOD	2.2	0.6	287.4	44.5
UZ-55-31	10.4	13	22.5	9.0	BLOD	BLOD	1.8	0.6	84.5	41.1
UZ-55-32	9.5	22	12.2	0.6	650	170	1.5	0.5	141.8	31.1
UZ-55-33	11.4	18	13.6	0.6	490	170	1.8	0.6	153.1	36.7
UZ-56-1	11.9	27	11.0	1.2	1660	220	1.8	0.6	224.8	49.7
UZ-56-2	11.5	22	7.3	0.5	680	220	1.5	0.5	324.4	72.0
UZ-56-3	5.1	10	6.0	0.3	750	130	1.6	0.6	179.2	57.5
UZ-56-4	4.5	9	5.1	0.3	16200	5500	1.7	0.6	187.4	63.7
UZ-56-5	43.1	88	36.3	1.9	5210	420	1.5	0.7	246.4	29.3
UZ-56-6	15.1	29	12.5	1.0	1090	240	2.3	0.5	250.8	50.7
UZ-56-7	41.4	103	36.6	2.4	12660	570	2.2	0.6	235.4	27.9
UZ-56-8	14.7	31	14.9	0.7	820	330	2.2	0.6	205.7	38.3
UZ-56-9	28.8	53	36.9	2.5	9770	680	1.8	0.6	163.1	25.0
UZ-56-10	38.1	91	30.5	2.5	11900	350	1.5	0.5	258.9	34.4
UZ-56-11	43.8	83	35.3	1.9	11840	380	1.6	0.6	257.3	31.5
UZ-56-12	8.4	13	7.9	0.4	700	210	1.7	0.6	220.0	62.2
UZ-56-13	13.7	24	11.5	0.7	760	200	1.5	0.7	247.9	52.6
UZ-56-14	16.7	34	23.5	1.6	BLOD	BLOD	1.9	0.7	148.8	27.4
UZ-56-15	44.3	269	43.6	3.5	13540	420	1.6	0.6	211.6	21.3
UZ-56-16	44.2	116	39.8	2.6	12290	600	1.6	0.5	230.9	26.2

UZ-56-17	11.8	37	10.4	0.6	4020	310	1.5	0.6	235.9	40.9
UZ-56-18	13.8	42	9.6	0.5	310	190	2.3	0.6	298.7	48.9
UZ-56-19	35.5	98	48.9	2.3	11250	460	2.0	0.5	187.9	20.9
UZ-56-20	37.9	110	32.8	2.3	10070	330	1.6	0.6	239.8	28.4
UZ-56-21	48.9	143	39.9	2.7	11200	480	1.5	0.5	254.1	27.3
UZ-56-22	61.4	112	57.5	2.4	10170	350	1.9	0.4	222.2	22.9
UZ-56-23	2.0	4	3.3	0.2	510	200	2.0	0.4	127.4	64.1
UZ-56-24	59.5	201	52.7	3.1	10970	410	1.8	0.5	234.8	21.6
UZ-56-25	54.5	125	63.0	3.1	12410	640	1.7	0.6	180.7	18.4
UZ-56-26	7.8	19	7.6	0.5	720	170	2.0	1.0	215.9	51.3
UZ-56-27	45.6	78	47.8	2.0	11380	400	2.0	0.7	198.9	24.0
UZ-56-28	7.6	14	12.8	0.7	BLOD	BLOD	1.9	0.8	124.8	34.0
UZ-56-29	10.3	30	13.4	0.7	730	180	1.9	0.8	161.0	30.5
UZ-56-30	13.9	40	14.0	1.4	540	180	2.9	1.0	207.1	38.7
UZ-56-31	22.2	159	46.5	3.0	12790	490	2.3	0.3	245.3	25.1
UZ-56-32	54.9	19	8.8	1.6	BLOD	BLOD	2.1	0.5	180.1	52.7
UZ-56-33	7.6	19	7.4	0.7	700	230	1.5	0.5	249.3	61.5
UZ-56-34	8.9	64	25.5	1.7	510	230	1.6	0.6	173.5	24.6
UZ-57-1	7.5	11	40.9	3.3	4380	740	1.3	0.5	15.5	4.8
UZ-57-2	12.2	10	36.4	2.3	8140	740	1.7	0.5	29.3	9.5
UZ-57-3	1.9	2	36.9	2.9	2540	270	1.4	0.6	6.6	4.7
UZ-57-4	7.0	13	60.1	3.2	5630	270	1.8	0.6	16.2	4.6
UZ-57-5	14.7	9	33.7	2.8	6250	640	1.5	0.5	29.0	10.0
UZ-57-6	18.5	23	81.5	7.3	4590	320	1.6	0.6	15.3	3.5
UZ-57-7	12.2	27	79.0	13.0	7930	240	1.7	0.6	14.2	3.6
UZ-57-8	12.6	20	45.4	2.2	5170	300	1.5	0.7	32.4	7.4
UZ-57-9	17.8	24	24.2	1.6	10700	370	1.9	0.7	72.1	15.5
UZ-57-10	17.8	20	40.9	4.3	8200	270	1.6	0.6	29.6	7.3
UZ-57-11	12.8	31	41.9	2.8	8260	440	1.6	0.5	36.0	6.9
UZ-57-12	9.7	15	62.5	2.9	6190	290	1.5	0.6	16.9	4.4

UZ-57-13	16.8	26	60.7	3.9	8090	570	1.6	0.5	23.3	4.8
UZ-57-14	31.8	31	42.3	2.5	9340	390	1.7	0.6	79.6	15.0
UZ-57-15	9.4	11	68.6	8.9	8010	510	1.3	0.5	17.1	5.6
UZ-57-16	22.1	20	44.5	3.4	9750	800	1.7	0.5	28.2	6.7
UZ-57-17	26.3	17	116.5	7.3	7000	410	1.6	0.6	16.6	4.2
UZ-57-18	17.8	16	19.8	1.0	11990	320	1.5	0.5	67.1	17.1
UZ-57-19	1.8	1	5.8	0.8	670	230	1.0	0.6	19.3	19.4
UZ-57-20	26.7	32	37.9	3.2	13590	700	1.9	0.6	72.0	14.1
UZ-57-21	9.8	9	23.5	1.5	10300	380	1.3	0.3	35.5	12.1
UZ-57-22	26.0	33	40.8	4.0	10160	560	1.6	0.7	39.7	7.9
UZ-58-1	8.3	26	4.8	0.3	7400	270	2.0	0.4	247.7	50.4
UZ-58-2	10.0	33	6.7	0.4	8710	470	2.0	0.7	226.8	41.5
UZ-58-3	5.2	24	6.7	0.3	8580	360	2.3	0.6	133.9	28.0
UZ-58-4	12.5	45	14.9	1.2	6430	300	2.3	0.6	143.7	24.4
UZ-58-5	6.8	12	6.0	0.4	9450	340	2.0	0.5	195.0	58.0
UZ-58-6	6.1	18	5.6	0.5	7650	400	1.6	0.5	188.3	47.3
UZ-58-7	11.2	15	10.5	0.7	8570	440	1.5	0.6	182.7	48.8
UZ-58-8	6.5	22	6.2	0.4	8180	350	1.6	0.5	178.9	39.9
UZ-58-9	8.5	27	7.7	0.5	9280	390	1.7	0.6	188.3	38.3
UZ-58-10	12.0	23	11.0	0.9	7680	430	1.6	0.6	184.4	41.1
UZ-58-11	4.1	14	6.6	0.6	7680	390	1.5	0.5	108.2	30.7
UZ-58-12	11.4	22	11.0	0.7	7430	360	1.9	0.4	177.9	39.6
UZ-58-13	9.7	17	7.0	0.7	8010	440	2.0	0.4	233.3	60.9
UZ-58-14	6.6	10	8.0	0.5	8310	460	1.8	0.5	142.5	45.9
UZ-58-15	8.8	24	7.5	0.5	8740	360	1.7	0.6	199.5	42.5
UZ-58-16	4.0	9	7.0	0.4	8650	380	3.1	0.5	98.3	33.3
UZ-58-17	7.1	13	11.1	0.7	7920	490	2.7	0.7	110.6	31.5
UZ-58-18	4.7	10	7.7	0.7	8030	330	1.5	0.4	106.2	34.9
UZ-58-19	7.7	28	6.6	0.6	8140	360	1.4	0.6	199.7	41.9
UZ-58-20	11.9	59	9.1	0.9	8130	380	2.2	0.8	221.9	36.0

UZ-58-21	7.1	18	7.0	0.4	7120	310	1.7	0.6	172.5	41.7
UZ-58-22	10.8	30	9.9	0.5	7180	330	1.9	0.5	186.5	35.5
UZ-58-23	11.1	27	9.0	0.8	8370	330	1.4	0.5	208.2	43.9
UZ-58-24	10.3	24	13.9	1.4	6970	340	1.9	0.9	127.3	29.0
UZ-58-25	5.0	12	5.6	0.3	8390	340	1.6	0.6	154.1	45.4
UZ-58-26	9.2	15	8.1	0.4	7320	440	1.1	0.3	194.7	51.2
UZ-58-27	7.5	16	11.4	1.4	6700	380	1.9	0.5	112.0	31.2
UZ-58-28	12.1	23	10.8	0.9	10810	550	2.2	0.6	190.9	43.1
UZ-58-29	10.7	19	15.7	1.0	6970	370	1.8	0.4	116.7	27.8
UZ-58-30	9.4	11	8.4	0.9	7250	460	2.0	0.3	190.8	61.0
UZ-58-31	11.6	24	14.7	1.5	8940	330	2.0	0.8	135.0	30.8
UZ-59-1	5.2	12	18.9	1.1	4460	280	1.8	0.7	50.5	14.9
UZ-59-2	12.6	30	20.3	1.1	4980	230	2.3	0.7	113.7	21.7
UZ-59-3	13.1	34	19.6	1.5	4760	330	1.9	0.8	122.4	23.0
UZ-59-4	5.5	14	11.7	0.7	5150	310	2.1	0.4	86.3	23.6
UZ-59-5	11.2	30	26.3	2.0	3950	230	1.9	0.6	77.8	15.4
UZ-59-6	17.1	25	27.0	1.7	4130	230	2.0	0.4	115.9	24.3
UZ-59-7	17.2	59	23.8	1.7	4290	350	2.0	0.7	132.0	19.6
UZ-59-8	11.4	31	15.1	0.7	5270	270	2.3	0.6	138.1	25.7
UZ-59-9	18.8	51	34.1	2.9	5250	250	2.3	0.6	100.7	16.5
UZ-59-10	23.6	61	23.7	2.4	4970	360	2.0	0.5	181.4	29.6
UZ-59-11	6.8	17	11.0	1.0	3900	480	1.6	0.6	113.5	29.4
UZ-59-12	9.3	19	15.6	1.8	5510	280	1.5	0.5	108.9	28.0
UZ-59-13	31.9	72	26.3	1.9	5120	380	1.9	0.4	220.2	30.4
UZ-59-14	5.5	11	19.9	1.0	5250	240	2.0	0.4	50.7	15.5
UZ-59-15	11.7	32	25.7	1.6	4800	230	1.8	0.5	83.8	15.7
UZ-59-16	8.1	19	29.1	2.2	2380	160	1.7	0.6	51.3	12.4
UZ-59-17	5.4	11	6.6	0.5	4560	250	2.0	1.0	149.2	46.1
UZ-59-18	24.6	38	21.4	1.6	5150	300	2.0	0.7	208.5	37.3
UZ-59-19	12.5	43	12.9	0.8	4920	310	1.9	0.8	177.0	29.3

UZ-59-20	11.2	20	25.7	1.5	5050	300	1.9	0.8	79.6	18.4
UZ-59-21	7.4	16	24.6	1.7	4330	260	2.9	1.0	55.1	14.3
UZ-59-22	13.5	32	21.0	2.0	5230	410	2.3	0.3	117.9	23.7
UZ-59-23	18.4	38	45.0	2.6	5760	340	2.1	0.5	75.0	12.9
UZ-59-24	6.2	12	12.4	1.0	5140	280	3.1	0.5	91.4	27.4
UZ-59-25	5.2	12	5.1	0.4	4410	220	2.7	0.7	187.1	55.5
UZ-59-26	11.2	32	53.7	3.3	5110	330	1.5	0.4	38.3	7.2
UZ-59-27	4.5	14	11.9	0.7	4120	170	1.4	0.6	69.1	19.0
UZ-59-28	7.0	10	32.7	4.3	4450	270	2.0	1.0	39.2	13.4
UZ-59-29	14.4	20	35.2	2.6	5060	260	2.6	0.8	74.8	17.6
UZ-59-30	11.5	30	34.0	2.9	5300	290	1.8	0.4	62.0	12.5
UZ-59-31	48.7	72	34.0	3.2	5300	340	1.7	0.6	259.1	39.1
UZ-60-1	20.3	103	19.8	1.5	6630	320	2.2	0.6	186.8	23.2
UZ-60-2	3.2	11	3.5	0.2	2050	150	2.1	0.3	167.7	51.6
UZ-60-3	13.8	37	16.3	1.0	5250	260	2.4	0.5	154.7	27.1
UZ-60-4	20.8	56	16.0	1.1	5340	300	1.9	0.6	235.8	35.4
UZ-60-5	23.3	86	28.4	2.3	5000	200	1.9	0.4	149.4	20.2
UZ-60-6	17.2	74	23.4	2.3	5550	380	2.2	0.8	134.4	20.5
UZ-60-7	25.0	119	26.9	2.0	5180	220	1.7	0.6	169.3	20.0
UZ-60-8	16.5	58	19.9	1.1	3080	220	1.9	0.5	150.8	21.5
UZ-60-9	18.1	54	27.8	1.8	3050	140	1.4	0.5	118.9	17.9
UZ-60-10	19.0	55	32.6	1.9	2810	280	1.6	0.4	106.5	15.7
UZ-60-11	13.9	49	16.5	1.0	4370	270	2.1	0.7	153.6	23.7
UZ-60-12	19.2	75	21.8	1.5	4260	290	1.5	0.6	160.1	21.5
UZ-60-13	16.3	32	28.7	2.1	4330	260	2.0	0.5	103.7	19.8
UZ-60-14	11.8	35	18.3	1.9	3410	370	2.0	0.7	117.8	23.4
UZ-60-15	16.1	49	20.3	1.8	4620	220	2.3	1.4	144.9	24.4
UZ-60-16	15.6	26	17.4	1.4	6430	290	1.5	0.5	163.5	34.7
UZ-60-17	12.2	71	17.9	1.2	4970	240	1.6	0.7	124.4	17.0
UZ-60-18	9.9	40	12.5	1.0	3840	190	1.3	0.6	145.4	25.6

UZ-60-19	8.7	45	10.7	0.8	2010	190	1.4	0.5	148.5	25.0
UZ-60-20	21.4	41	18.0	1.0	5280	350	1.8	0.8	215.7	35.8
UZ-60-21	17.1	65	19.1	1.6	5090	240	1.7	0.5	163.2	24.4
UZ-60-22	15.7	39	18.9	1.4	5030	260	1.9	0.7	151.7	26.8
UZ-60-23	18.9	59	39.7	2.4	3260	220	2.3	0.8	87.4	12.5
UZ-60-24	11.1	32	20.0	1.2	5300	290	2.6	0.7	101.5	18.9
UZ-60-25	19.5	29	35.9	2.5	2230	200	2.4	1.0	99.5	19.7
UZ-60-26	16.3	42	22.2	1.6	4630	260	2.1	0.9	134.0	22.8
UZ-60-27	11.5	47	9.3	0.9	3880	270	2.4	0.8	224.8	39.8
UZ-60-28	4.4	26	6.9	0.6	1830	210	1.9	1.0	115.6	24.6
UZ-60-29	12.5	37	18.0	1.0	5950	430	2.3	0.7	126.6	21.9
UZ-60-30	11.9	32	26.2	2.5	4090	170	1.6	0.7	83.3	16.7
UZ-60-31	18.4	43	28.1	1.6	5020	240	1.9	0.8	119.7	19.5
UZ-60-32	17.0	35	17.1	1.1	5290	230	1.8	0.7	181.1	32.7
UZ-60-33	24.0	60	31.1	2.1	3170	250	1.9	0.9	140.7	20.5
UZ-60-34	24.7	52	38.6	2.9	4230	290	1.6	0.6	117.1	18.5
UZ-60-35	14.2	36	20.2	1.3	5200	230	1.6	0.5	128.4	22.9
UZ-60-36	5.0	12	6.2	0.6	7750	400	1.7	0.6	148.9	45.5
UZ-61-1	12.0	57	8.6	0.9	4740	560	1.8	0.4	218.8	37.5
UZ-61-2	18.3	99	17.2	1.7	5260	780	2.4	0.6	191.7	27.0
UZ-61-3	7.8	40	5.2	0.8	5160	840	1.9	0.4	220.4	47.1
UZ-61-4	8.3	32	9.0	0.8	5710	850	2.0	0.4	168.4	33.7
UZ-61-5	5.8	40	3.7	0.6	4680	710	1.7	0.5	226.9	49.1
UZ-61-6	15.9	112	15.4	1.8	5940	800	1.8	0.5	187.9	28.2
UZ-61-7	10.1	81	9.6	1.2	6550	710	2.0	0.4	191.8	32.1
UZ-61-8	10.9	56	9.1	0.8	4540	440	2.2	0.4	218.9	35.5
UZ-61-9	9.6	36	6.1	0.5	6630	750	1.7	0.4	215.0	39.8
UZ-61-10	10.3	72	11.0	1.0	4200	990	1.5	0.7	169.5	25.0
UZ-61-11	8.6	28	7.1	0.9	5650	410	2.1	0.5	178.0	40.0
UZ-61-12	8.0	27	5.8	0.9	4990	600	2.2	0.3	222.4	54.1

UZ-61-13	5.6	39	4.3	0.6	4720	830	2.1	0.3	229.4	49.3
UZ-61-14	11.9	49	12.6	1.8	4910	760	1.1	0.3	171.4	34.6
UZ-61-15	21.4	78	8.5	1.3	5960	860	1.9	0.5	313.0	59.6
UZ-61-16	17.5	80	11.6	1.6	7280	740	2.2	0.6	224.9	39.9
UZ-61-17	42.2	198	45.9	3.1	3810	400	1.8	0.4	167.6	16.4
UZ-61-18	17.5	59	12.6	1.0	4330	230	2.0	0.3	250.7	38.1
UZ-61-19	9.9	84	8.1	0.9	4350	590	2.0	0.8	223.2	33.8
UZ-61-20	25.7	229	31.8	2.5	4350	400	1.9	0.4	147.3	15.1
UZ-61-21	12.6	54	7.0	0.6	5060	500	1.9	0.5	252.1	40.2
UZ-61-22	7.7	60	7.1	0.7	4930	430	2.7	0.6	196.9	32.3
UZ-61-23	8.7	70	7.2	0.7	4370	420	2.7	1.2	217.8	33.5
UZ-61-24	7.1	42	5.7	0.6	4110	400	2.4	0.4	224.9	41.5
UZ-61-25	33.8	152	26.6	3.1	4360	660	2.2	0.6	215.2	30.6
UZ-61-26	7.8	48	7.3	1.0	3980	850	2.1	0.6	195.4	38.0
UZ-61-27	13.1	43	7.1	0.5	4730	560	2.2	0.9	258.6	43.3
UZ-61-28	30.0	110	18.7	2.7	4420	470	2.1	0.4	214.5	37.1
UZ-61-29	16.5	37	7.2	0.9	4580	580	2.5	0.8	324.7	66.8
UZ-61-30	15.3	55	9.9	2.0	4910	760	1.7	0.3	226.5	55.0
UZ-61-31	7.0	29	6.9	0.6	5780	630	1.5	0.5	185.2	38.3
UZ-61-32	5.5	25	4.5	0.6	5430	870	1.7	0.4	223.8	54.4
UZ-61-33	17.9	70	11.0	0.9	4880	480	2.1	1.0	250.2	36.5
UZ-61-34	21.3	115	19.8	2.0	5100	630	2.1	0.4	195.9	26.9
UZ-61-35	15.5	73	13.0	1.7	7600	1000	1.8	0.5	215.9	37.9
UZ-61-36	15.3	58	14.8	2.1	8600	2400	1.8	0.6	188.4	36.4
UZ-61-37	9.2	19	6.4	0.6	6140	510	1.9	0.4	176.0	43.8
UZ-61-38	8.4	31	8.1	1.1	7200	840	1.7	0.6	153.7	34.6
UZ-62-1	19.0	45	11.3	1.0	5200	220	2.1	0.5	200.4	34.6
UZ-62-2	21.6	193	14.0	0.6	5080	160	2.1	0.6	219.8	18.3
UZ-62-3	21.7	150	21.4	1.6	4720	270	2.3	0.6	184.7	20.4
UZ-62-4	14.2	100	15.2	1.3	4810	280	2.3	0.8	169.6	22.3

UZ-62-5	15.1	67	14.8	1.4	5060	380	2.3	0.5	185.9	28.7
UZ-62-6	14.9	74	15.6	1.3	5330	190	2.0	0.6	173.3	24.8
UZ-62-7	20.0	116	18.2	1.1	5100	220	2.3	0.4	199.3	22.1
UZ-62-8	11.4	52	9.4	1.1	4190	310	2.3	0.5	220.2	39.9
UZ-62-9	17.4	84	14.9	2.1	4660	440	2.1	0.6	211.6	37.7
UZ-62-10	19.2	96	22.2	2.7	4530	200	2.4	0.7	157.5	25.0
UZ-62-11	22.7	120	21.7	1.7	4520	210	2.1	0.8	190.4	22.9
UZ-62-12	17.3	89	14.7	1.3	4880	180	1.8	0.5	213.3	29.4
UZ-62-13	16.8	99	21.3	1.7	4850	280	2.3	0.5	144.0	18.5
UZ-62-14	18.6	110	21.6	2.5	4390	310	2.3	0.3	156.6	23.5
UZ-62-15	15.5	85	20.3	2.7	4430	300	2.4	0.4	138.9	23.8
UZ-62-16	14.9	51	24.3	2.6	4120	420	1.7	0.8	112.5	19.8
UZ-62-17	18.9	71	24.1	2.0	4370	290	2.1	0.4	142.9	20.7
UZ-62-18	19.1	92	23.9	2.4	3940	270	2.3	0.8	145.7	21.1
UZ-62-19	17.2	75	22.0	1.7	4060	210	2.2	0.4	142.8	19.8
UZ-62-20	23.0	116	38.6	2.8	3850	250	1.9	0.6	108.8	12.8
UZ-62-21	13.1	56	19.2	1.2	3780	160	2.2	0.4	124.5	18.4
UZ-62-22	13.5	28	27.6	1.6	4050	180	2.0	0.3	89.8	17.8
UZ-62-23	17.4	60	28.5	2.4	2810	150	1.9	0.5	110.0	17.0
UZ-62-24	16.6	76	33.4	1.8	3400	190	2.2	0.3	90.8	11.5
UZ-62-25	9.9	52	14.4	1.3	3810	280	2.4	0.2	125.8	20.8
UZ-62-26	17.8	70	33.8	2.5	3430	130	2.3	0.6	96.3	13.5
UZ-62-27	29.2	131	74.9	6.2	1490	190	2.1	0.4	71.5	8.6
UZ-62-28	18.0	57	38.9	3.0	4230	220	2.2	0.6	85.0	13.0
UZ-63-1	9.0	58	10.6	0.6	660	92	1.9	0.7	154.3	21.9
UZ-63-2	10.4	29	9.5	0.7	730	140	1.7	0.5	198.0	39.7
UZ-63-3	6.4	20	12.3	0.7	800	160	1.7	0.8	95.5	21.9
UZ-63-4	9.5	19	14.8	0.9	710	160	1.6	0.3	117.3	27.8
UZ-63-5	10.9	52	14.2	1.3	1640	230	1.6	0.7	140.6	23.4
UZ-63-6	23.5	88	14.7	0.7	680	180	1.8	0.5	260.4	30.6

UZ-63-7	16.1	89	13.7	0.8	1070	170	1.8	0.6	212.3	25.8
UZ-63-8	9.9	39	12.2	0.6	670	130	1.8	0.4	147.2	24.6
UZ-63-9	8.8	44	10.5	0.6	1890	220	1.4	0.4	154.0	25.1
UZ-63-10	15.8	48	16.2	1.4	1480	170	1.8	0.6	178.0	29.9
UZ-63-11	10.2	44	9.7	0.7	1100	190	1.8	0.5	190.2	31.6
UZ-63-12	7.7	61	12.3	0.8	630	160	1.8	0.8	114.5	16.5
UZ-63-13	9.0	33	14.0	0.8	550	140	2.0	0.6	116.8	21.5
UZ-63-14	8.7	68	13.2	1.0	1130	170	1.5	0.5	119.9	17.1
UZ-63-15	8.2	84	10.6	0.7	1230	180	1.3	0.4	141.1	17.9
UZ-63-16	11.0	43	11.2	0.7	400	160	1.7	0.4	179.1	29.3
UZ-63-17	12.4	55	10.1	1.0	820	200	1.6	0.5	223.1	37.3
UZ-63-18	15.5	62	13.0	0.7	1010	190	1.5	0.7	215.3	29.9
UZ-63-19	12.7	51	8.1	1.1	860	150	1.7	0.5	282.0	55.0
UZ-63-20	11.5	61	12.3	0.8	630	130	1.6	0.5	170.1	24.4
UZ-63-21	13.8	54	7.3	0.4	1120	150	1.5	0.4	302.5	44.1
UZ-63-22	10.6	31	6.4	0.5	910	160	1.8	0.3	256.7	50.3
UZ-63-23	7.6	26	5.6	0.3	500	120	2.3	0.2	243.9	49.9
UZ-63-24	10.4	48	10.0	0.8	650	200	1.6	0.3	187.8	31.2
UZ-63-25	8.2	59	5.5	0.6	490	130	1.3	0.4	272.0	45.4
UZ-63-26	9.6	55	8.5	0.5	1000	150	1.5	0.5	205.9	30.3
UZ-63-27	13.1	102	7.4	0.4	1440	160	1.6	0.6	318.3	36.3
UZ-63-28	9.2	23	12.7	1.1	990	200	1.8	0.4	132.5	29.9
UZ-63-29	7.9	55	10.5	0.7	1640	160	1.6	0.5	138.2	20.7
UZ-63-30	15.6	105	12.8	0.8	580	160	2.1	0.8	221.1	26.0
UZ-63-31	11.1	66	7.4	0.4	627	95	1.6	0.4	268.6	35.4
UZ-63-32	13.3	69	8.1	0.6	700	130	1.6	0.4	295.3	41.5
UZ-63-33	13.7	144	12.3	1.6	1540	130	1.6	0.4	201.6	31.1
UZ-63-34	13.0	64	13.6	0.8	430	140	1.8	0.3	173.7	23.9
UZ-63-35	10.3	45	6.3	0.4	1110	140	1.8	0.5	294.3	47.7
UZ-63-36	5.9	22	11.3	0.5	640	180	1.9	0.7	95.4	20.7

UZ-63-37	8.1	27	8.7	0.6	370	170	1.7	0.3	169.4	34.6
UZ-63-38	9.3	42	11.5	0.8	410	140	2.3	1.0	146.8	25.0
UZ-63-39	5.9	22	12.6	0.7	830	130	1.7	0.5	86.1	18.9
UZ-65-1	8.3	13	9.0	0.5	877	92	1.1	53.2	166.9	47.0
UZ-65-2	13.8	43	9.0	0.4	9540	310	1.8	0.7	276.6	43.6
UZ-65-3	4.2	9	5.4	0.3	2350	300	1.4	0.7	141.0	47.7
UZ-65-4	2.7	11	3.7	0.3	1420	120	1.4	0.5	132.3	40.9
UZ-65-5	7.6	20	8.3	0.3	6760	160	1.2	0.5	166.2	37.7
UZ-65-6	11.4	14	5.1	0.4	1030	120	1.5	0.6	313.3	86.9
UZ-65-7	4.9	18	5.0	0.3	2590	140	1.8	0.6	178.4	43.5
UZ-65-8	17.2	164	23.6	1.3	389	95	1.4	0.3	133.1	12.7
UZ-65-9	2.3	9	2.3	0.1	1336	96	1.3	0.5	179.0	60.4
UZ-65-10	34.2	94	27.7	1.2	2680	120	2.1	0.8	223.9	25.1
UZ-65-11	10.9	31	7.2	0.4	7190	290	2.3	0.5	234.9	44.2
UZ-65-12	7.6	33	5.6	0.2	6680	240	1.7	0.7	245.3	43.8
UZ-65-13	4.4	13	3.3	0.2	1807	97	1.7	0.7	242.4	68.2
UZ-65-14	4.9	8	7.7	0.5	1620	130	1.3	0.8	115.4	41.6
UZ-65-15	7.3	25	10.2	0.6	1350	110	1.6	0.5	130.3	27.1
UZ-65-16	10.9	25	15.0	1.3	690	150	1.8	0.5	132.8	28.9
UZ-65-17	22.7	29	13.8	0.9	651	95	1.6	0.3	239.8	47.4
UZ-66-1	12.5	21	18.3	1.6	2360	240	2.9	0.5	142.4	33.5
UZ-66-2	12.2	46	24.5	1.7	1700	180	2.6	1.0	104.5	17.0
UZ-66-3	18.2	73	15.9	1.2	2270	240	2.7	0.6	237.3	33.0
UZ-66-4	24.0	69	18.0	1.2	2620	220	2.3	0.8	275.9	38.0
UZ-66-5	24.0	64	13.5	0.9	2420	200	2.5	0.6	297.3	42.4
UZ-66-6	17.5	99	12.5	1.0	2340	330	2.8	0.5	289.1	37.1
UZ-66-7	8.5	29	9.4	0.8	2030	230	2.7	0.3	188.5	38.1
UZ-66-8	14.4	53	17.6	1.3	2360	170	2.2	0.6	170.7	26.6
UZ-66-9	12.4	28	5.6	0.5	2080	340	2.8	0.4	356.8	73.6
UZ-66-10	11.8	39	27.9	2.1	1620	180	2.5	1.0	89.2	15.8

UZ-66-11	12.7	37	18.6	1.6	1820	200	2.4	0.5	142.5	26.4
UZ-66-12	20.2	54	15.8	1.1	2330	220	2.4	0.4	265.6	40.6
UZ-66-13	7.6	18	8.2	0.6	2870	290	2.7	1.0	193.9	48.1
UZ-66-14	7.1	29	17.7	1.5	2010	250	2.1	0.4	84.8	17.3
UZ-66-15	20.1	62	30.0	1.8	1870	200	2.4	0.6	140.0	19.7
UZ-66-16	11.3	16	5.7	0.4	1970	140	1.9	0.5	275.9	71.3
UZ-66-17	21.0	95	17.4	1.0	2680	210	2.3	0.5	250.4	29.4
UZ-66-18	6.8	22	7.4	0.4	2000	200	1.5	0.5	192.2	42.3
UZ-66-19	18.3	76	19.5	1.4	1740	260	2.6	0.5	195.4	26.4
UZ-66-20	15.0	61	18.3	1.6	2700	150	2.7	0.7	170.9	26.5
UZ-66-21	12.8	63	14.1	1.7	2140	270	2.7	0.7	189.8	33.1
UZ-66-22	13.7	44	20.8	1.5	2330	280	2.4	0.4	138.2	23.1
UZ-66-23	21.5	62	11.5	1.2	1960	260	2.4	0.3	295.4	48.6
UZ-66-24	15.6	24	8.3	0.7	2790	320	2.6	0.2	267.4	58.5
UZ-66-25	17.0	50	15.4	1.0	1820	280	2.4	0.4	228.8	35.6
UZ-66-26	18.7	56	24.4	1.5	2360	230	2.9	0.7	160.5	23.6
UZ-66-27	19.7	51	18.6	1.4	1870	290	2.5	0.7	220.0	35.0
UZ-66-28	16.0	36	18.1	1.3	2100	220	2.3	0.3	184.6	33.5
UZ-66-29	14.4	43	11.8	1.0	1400	230	2.6	0.6	253.6	43.9
UZ-66-30	14.0	39	18.2	1.4	2620	210	2.4	0.5	160.2	28.5
UZ-66-31	19.3	41	17.5	1.8	2090	250	2.3	0.7	229.1	42.8
UZ-67-1	4.0	14	2.7	0.1	1130	170	2.1	0.3	309.1	84.0
UZ-67-2	10.3	39	10.8	0.6	1240	310	1.5	0.4	199.4	33.9
UZ-67-3	1.8	3	3.8	0.3	1350	220	1.5	0.2	102.7	59.9
UZ-67-4	11.4	43	10.8	1.1	1410	200	1.7	0.2	218.8	40.1
UZ-67-5	12.6	36	12.3	0.7	1240	180	2.4	0.7	213.3	37.6
UZ-67-6	7.6	28	7.5	0.6	1440	290	1.9	0.3	208.6	42.3
UZ-67-7	9.6	54	10.7	0.5	1570	290	1.7	0.3	187.2	26.8
UZ-67-8	5.5	14	7.1	0.6	1300	240	2.2	0.2	162.7	45.3
UZ-67-9	6.1	38	4.5	0.3	970	210	2.0	0.4	252.1	44.2

UZ-67-10	10.8	35	9.1	0.9	1020	330	2.2	0.3	248.1	48.2
UZ-67-11	4.1	14	5.4	0.3	1300	200	1.8	0.2	157.3	42.9
UZ-67-12	11.5	89	9.0	0.6	1120	260	2.0	0.3	263.0	32.4
UZ-67-13	8.1	40	8.3	0.7	1730	270	1.9	0.3	202.1	36.0
UZ-67-14	5.9	31	5.7	0.3	920	180	1.9	0.3	215.2	40.0
UZ-67-15	14.2	45	21.3	1.2	1010	290	1.9	0.4	139.9	22.3
UZ-67-16	4.9	28	3.8	0.2	1610	210	1.9	0.5	269.4	53.1
UZ-67-17	6.3	33	5.9	0.5	1520	210	1.9	0.3	224.6	43.3
UZ-67-18	8.1	31	9.2	0.4	1290	150	1.6	0.4	183.8	34.1
UZ-67-19	9.9	28	6.0	0.6	1190	180	2.5	0.8	308.0	64.6
UZ-67-20	6.4	24	7.8	0.3	950	140	2.7	0.6	171.0	35.7
UZ-67-21	12.5	61	12.8	0.6	1080	230	2.1	0.3	203.4	27.7
UZ-67-22	11.4	39	15.9	1.0	1320	300	2.2	0.6	150.0	25.7
UZ-67-23	10.5	37	23.9	2.9	1390	200	2.6	0.7	91.9	18.8
UZ-67-24	8.5	24	11.8	0.6	1180	220	1.7	0.5	150.0	31.7
UZ-67-25	13.0	24	13.7	0.8	1140	180	1.5	0.2	197.8	41.8
UZ-67-26	13.7	31	12.9	0.6	1120	180	2.1	0.7	221.6	41.0
UZ-67-27	5.2	9	6.6	0.4	1350	170	2.2	0.3	165.3	56.2
UZ-67-28	11.4	37	9.7	0.8	1060	200	1.4	0.5	243.0	45.1
UZ-67-29	8.0	18	5.9	0.4	1360	270	2.7	0.4	282.1	68.7
UZ-67-30	12.7	29	14.8	0.9	1290	200	2.2	0.5	179.2	34.8
UZ-67-31	2.9	7	4.7	0.3	990	280	2.3	0.7	129.2	49.3
UZ-67-32	5.3	12	6.8	0.3	1290	200	2.2	0.7	162.0	47.3
UZ-67-33	5.7	14	3.6	0.3	1060	200	1.9	0.2	287.3	79.5
UZ-67-34	9.1	23	9.0	0.6	1540	230	2.2	0.3	200.6	43.8
UZ-67-35	3.2	7	4.3	0.3	3910	290	2.5	0.4	153.5	59.0
UZ-67-36	6.5	16	5.8	0.4	1210	220	2.2	0.2	233.8	60.9
UZ-67-37	3.9	12	6.2	0.3	940	140	2.0	0.2	130.6	38.4
UZ-68-1	15.1	22	50.1	3.6	1420	280	1.6	0.3	63.5	14.3
UZ-68-2	3.0	4	2.8	0.1	1560	240	1.5	0.5	223.9	112.4

UZ-68-3	5.0	9	15.5	1.1	3970	320	2.7	0.5	68.0	23.2
UZ-68-4	5.0	8	7.8	0.5	1940	270	1.1	0.4	136.0	48.8
UZ-68-5	4.8	11	7.2	0.3	2050	280	2.0	0.1	140.5	42.8
UZ-68-6	4.3	11	5.1	0.3	2190	200	1.9	0.7	177.9	55.0
UZ-68-7	11.3	26	15.4	1.2	5850	390	1.7	0.4	153.7	32.4
UZ-68-8	10.9	32	8.0	0.6	1160	260	1.5	0.3	282.5	54.8
UZ-68-9	13.9	44	17.0	0.9	1900	230	1.7	0.4	169.8	27.1
UZ-68-10	3.6	11	6.6	0.5	2030	300	1.2	0.2	115.5	35.7
UZ-68-11	1.7	3	5.2	0.4	1490	230	2.1	0.0	69.4	40.4
UZ-68-12	8.3	15	8.1	0.6	2210	330	2.3	0.9	212.5	57.2
UZ-68-13	44.4	74	83.0	13.0	2430	280	1.8	0.6	112.2	21.9
UZ-68-14	4.3	9	3.7	0.2	2220	290	1.7	0.2	238.8	80.3
UZ-68-15	1.9	4	5.9	0.3	1960	280	2.2	0.3	67.5	33.9
UZ-68-16	3.2	6	4.2	0.3	21100	9900	1.5	0.6	159.7	66.1
UZ-68-17	12.2	20	26.9	1.6	2550	290	1.8	0.4	94.8	21.9
UZ-68-18	0.8	2	4.8	0.3	2270	280	1.6	0.3	34.3	24.4
UZ-68-19	1.7	2	4.9	0.3	1850	330	1.7	0.5	74.6	53.0
UZ-68-20	4.1	7	3.9	0.3	1480	240	1.4	0.3	222.1	85.3
UZ-68-21	5.6	8	5.5	0.2	8700	2900	1.6	0.4	214.8	76.5
UZ-68-22	2.3	4	5.3	0.5	2290	430	2.3	0.8	91.2	46.5
UZ-68-23	1.8	2	3.3	0.2	2310	240	1.4	0.5	110.4	78.3
UZ-68-24	0.7	1	4.5	0.2	1880	260	0.5	0.4	30.5	30.6
UZ-68-25	12.8	21	22.0	1.5	3490	310	1.5	0.7	121.8	27.8
UZ-68-26	6.7	11	10.4	0.8	8100	3400	1.5	0.8	135.4	42.0
UZ-68-27	31.6	71	42.9	3.9	4740	340	1.9	0.4	154.1	23.0
UZ-69-1	4.0	5	13.9	0.9	4600	370	1.9	0.2	60.7	27.4
UZ-69-2	10.1	10	25.0	1.7	4430	300	1.6	0.9	85.1	27.5
UZ-69-3	3.5	6	22.5	1.9	8830	440	2.2	0.6	32.5	13.6
UZ-69-4	6.6	14	12.8	0.6	5170	430	1.5	0.5	108.2	29.4
UZ-69-5	6.5	12	22.9	1.1	5270	450	1.6	0.5	59.6	17.4

UZ-69-6	5.8	13	17.4	1.0	5430	310	1.8	0.3	70.4	19.9
UZ-69-7	18.2	10	13.2	0.7	6130	390	1.6	0.3	144.2	46.2
UZ-69-8	2.3	4	11.7	0.7	6710	470	1.7	0.5	40.6	20.5
UZ-69-9	10.2	31	21.5	1.3	6400	390	1.4	0.3	99.6	18.9
UZ-69-10	7.1	13	13.0	1.0	5910	360	1.6	0.4	114.8	33.0
UZ-69-11	6.0	9	10.5	0.5	5580	290	2.0	0.1	120.5	40.6
UZ-69-12	18.1	19	15.8	1.1	6620	330	2.3	0.4	157.1	37.7
UZ-69-13	11.5	14	16.5	1.0	6320	300	0.6	0.1	102.6	28.1
UZ-69-14	11.0	10	12.2	0.9	5570	390	1.8	0.6	99.1	32.3
UZ-69-15	12.3	13	18.1	1.1	4770	360	2.2	0.6	109.2	31.0
UZ-69-16	9.3	11	16.8	0.7	5590	390	1.9	0.7	91.9	28.0
UZ-69-17	9.4	17	16.3	1.1	5270	470	1.5	0.5	102.9	25.9
UZ-69-18	9.8	23	23.2	1.7	4870	390	2.0	0.2	81.4	18.0
UZ-69-19	14.5	21	24.9	2.1	5770	450	1.5	0.2	91.6	21.4
UZ-70-1	4.8	12	3.6	0.3	630	190	1.4	0.6	272.9	81.4
UZ-70-2	2.2	3	6.5	0.4	600	240	1.5	0.2	71.0	41.2
UZ-70-3	6.6	18	5.1	0.3	790	190	2.3	0.4	271.4	66.5
UZ-70-4	3.2	11	7.8	0.3	910	240	2.0	0.1	86.1	26.2
UZ-70-5	4.9	10	12.7	1.0	620	210	2.3	0.4	80.4	26.2
UZ-70-6	2.0	3	6.6	0.5	25900	9200	0.6	0.1	63.1	36.7
UZ-70-7	6.9	17	7.1	0.6	2270	710	1.8	0.6	203.2	52.6
UZ-70-8	13.2	26	11.0	0.6	4170	280	2.2	0.6	247.7	50.5
UZ-70-9	3.4	10	4.0	0.3	BLOD	BLOD	1.9	0.7	179.2	58.4
UZ-70-10	1.8	2	5.1	0.3	BLOD	BLOD	1.5	0.5	73.3	52.0
UZ-70-11	8.5	19	8.8	0.5	BLOD	BLOD	2.0	0.2	200.4	47.5
UZ-70-12	6.4	19	6.1	0.3	450	240	1.8	0.6	217.8	51.0
UZ-70-13	3.4	7	5.1	0.5	830	550	2.2	0.1	141.8	55.7
UZ-70-14	4.9	22	4.1	0.2	640	220	1.9	0.7	249.9	54.5
UZ-70-15	2.9	4	8.2	0.3	590	270	2.3	0.2	73.0	36.6
UZ-70-16	3.3	4	6.0	0.4	2400	1600	3.4	0.8	114.3	57.5

UZ-70-17	2.3	3	3.9	0.4	590	190	2.0	0.5	120.2	70.5
UZ-70-18	7.0	19	5.3	0.4	790	260	2.1	0.3	270.7	64.7
UZ-70-19	16.5	30	30.6	2.1	7670	600	2.6	0.8	113.3	22.1
UZ-70-20	11.0	23	13.9	0.9	3770	290	2.1	0.3	164.9	36.0
UZ-70-21	3.0	6	3.3	0.2	610	180	1.6	0.4	187.2	77.1
UZ-70-22	4.7	6	4.4	0.4	470	220	3.6	0.8	222.0	92.5
UZ-70-23	6.9	14	6.9	0.4	BLOD	BLOD	1.9	0.6	209.5	57.2
UZ-70-24	5.3	11	22.4	2.5	BLOD	BLOD	1.9	0.5	49.5	15.9
UZ-70-25	13.6	21	26.4	1.7	5420	600	2.4	0.7	107.8	24.5
UZ-70-26	5.9	7	4.0	0.3	6430	930	1.6	0.6	302.3	116.5
UZ-70-27	1.8	3	5.1	0.5	62300	5000	1.1	0.5	74.2	43.3
UZ-71-1	12.1	55	46.0	3.8	5380	680	1.8	0.4	53.8	7.2
UZ-71-2	5.8	7	12.0	2.1	1560	220	1.4	0.5	48.3	18.3
UZ-71-3	8.7	21	17.0	2.0	BLOD	BLOD	1.6	0.5	107.0	23.3
UZ-71-4	23.8	42	40.0	1.7	540	360	1.1	0.4	106.5	16.4
UZ-71-5	22.9	41	38.0	1.7	5180	290	1.9	0.2	110.5	17.3
UZ-71-6	9.2	32	29.0	3.2	500	180	1.6	0.9	59.7	10.6
UZ-71-7	36.2	127	86.0	2.4	11160	360	2.2	0.6	105.9	9.4
UZ-71-8	4.8	20	12.0	2.5	560	210	1.5	0.5	114.0	25.5
UZ-71-9	13.7	24	21.0	1.5	400	160	1.6	0.5	126.9	25.9
UZ-71-10	20.8	74	49.0	2.4	2580	360	1.8	0.3	109.0	12.7
UZ-71-11	6.2	18	12.0	1.9	800	160	1.4	0.2	132.5	31.2
UZ-71-12	20.5	41	35.0	1.7	BLOD	BLOD	1.2	0.3	116.4	18.2
UZ-71-13	3.7	11	7.0	1.9	630	230	1.5	0.6	140.9	42.5
UZ-71-14	3.5	12	10.0	2.9	770	330	1.0	0.2	71.6	20.7
UZ-71-15	6.2	17	13.0	2.1	720	190	1.4	0.2	106.2	25.8
UZ-71-16	17.6	31	29.0	1.7	2260	290	1.5	0.3	110.2	19.8
UZ-71-17	9.0	37	24.0	2.7	720	250	1.5	0.4	98.0	16.1
UZ-71-18	13.3	43	33.0	2.5	5170	360	1.6	0.3	89.6	13.7
UZ-71-19	18.7	65	47.0	2.5	2090	540	1.3	0.6	93.9	11.6

UZ-71-20	14.5	71	54.0	3.7	580	210	1.2	0.3	60.5	7.2
UZ-71-21	4.3	19	12.0	2.8	960	220	1.4	0.1	97.0	22.2
UZ-71-22	6.4	33	18.0	2.8	2350	260	1.5	0.2	110.1	19.2
UZ-71-23	22.6	51	39.0	1.7	34000	11000	1.9	0.3	128.7	18.0
UZ-71-24	5.1	16	13.0	2.5	1110	250	1.3	0.2	82.4	20.6
UZ-71-25	33.8	72	55.0	1.6	2610	220	1.6	0.4	136.9	16.1
UZ-71-26	7.0	17	12.0	1.7	BLOD	BLOD	1.2	0.2	141.1	34.2
UZ-71-27	3.5	11	8.0	2.3	810	240	1.5	0.6	103.7	31.3
UZ-71-28	14.3	54	45.0	3.2	11900	5500	1.4	0.6	65.0	8.9
UZ-71-29	2.1	7	5.0	2.4	2550	500	1.8	0.7	101.5	38.4
UZ-71-30	4.1	18	12.0	2.9	1040	260	1.4	0.1	87.2	20.6
UZ-71-31	3.1	8	7.0	2.2	1090	270	1.5	0.4	87.6	31.0
UZ-72-1	9.1	20	10.7	0.9	3000	940	0.9	0.2	201.8	48.2
UZ-72-2	7.1	23	6.4	0.4	1140	410	1.2	0.3	259.2	55.9
UZ-72-3	5.0	15	5.3	0.3	1670	560	1.4	0.7	224.8	59.2
UZ-72-4	4.8	19	6.1	0.3	970	580	1.0	0.2	185.0	43.6
UZ-72-5	50.1	145	89.3	6.1	BLOD	BLOD	1.2	0.3	132.8	14.3
UZ-72-6	6.3	18	9.2	0.6	BLOD	BLOD	1.4	0.7	162.0	39.8
UZ-72-7	7.8	33	8.1	0.5	1220	730	1.3	0.4	225.7	41.7
UZ-72-8	5.4	14	17.0	1.3	BLOD	BLOD	1.0	0.2	75.1	20.9
UZ-72-9	23.3	57	15.1	1.0	BLOD	BLOD	1.1	0.2	358.2	53.0
UZ-72-10	20.3	24	19.9	1.3	1440	610	1.1	0.2	239.6	51.4
UZ-72-11	4.9	14	9.1	0.5	1220	520	0.8	0.4	127.2	34.7
UZ-72-12	13.3	34	23.4	1.0	1680	610	1.0	0.2	134.8	23.8
UZ-72-13	5.6	21	13.0	0.7	1270	500	1.4	0.4	103.1	23.3
UZ-72-14	4.1	8	5.0	0.4	1300	550	1.1	0.2	194.3	70.0
UZ-72-15	2.6	7	5.4	0.3	1190	600	0.9	0.1	114.0	43.7
UZ-72-16	7.6	24	15.7	0.8	BLOD	BLOD	0.9	0.2	115.2	24.3
UZ-72-17	10.1	18	13.6	0.6	BLOD	BLOD	1.1	0.4	175.5	42.1
UZ-72-18	42.8	77	68.9	3.9	1530	490	1.3	0.4	146.7	18.7

UZ-72-19	4.8	13	9.9	0.4	1410	500	0.9	0.0	114.4	32.1
UZ-72-20	11.8	32	25.2	2.1	BLOD	BLOD	1.1	0.3	110.7	21.6
UZ-72-21	2.8	5	6.3	0.5	BLOD	BLOD	1.5	0.2	104.5	47.4
UZ-72-22	1.4	3	6.4	0.4	1670	540	1.2	0.3	52.8	30.7
UZ-72-23	9.2	20	6.3	0.3	BLOD	BLOD	1.1	0.3	337.8	77.6
UZ-72-24	4.5	7	10.9	0.6	BLOD	BLOD	0.8	0.2	98.3	37.5
UZ-72-25	5.7	12	4.5	0.3	1120	410	1.2	0.2	296.3	87.6
UZ-72-26	6.5	10	8.2	0.6	9000	2700	0.8	0.0	188.4	60.9
UZ-72-27	6.7	23	5.8	0.3	BLOD	BLOD	1.0	0.4	268.7	57.6
UZ-72-28	10.8	28	8.2	0.5	BLOD	BLOD	1.2	0.5	307.8	61.2
UZ-72-29	24.8	47	24.9	1.4	BLOD	BLOD	1.3	0.4	233.7	36.5
UZ-72-30	5.9	13	15.8	0.6	BLOD	BLOD	1.4	0.2	88.5	24.8
UZ-72-31	6.0	24	5.6	0.3	BLOD	BLOD	1.1	0.2	249.5	53.0
UZ-72-32	3.2	7	5.8	0.3	BLOD	BLOD	1.2	0.4	129.5	49.3
UZ-72-33	12.9	16	43.7	2.2	BLOD	BLOD	1.1	0.3	70.0	17.8
UZ-72-34	4.9	7	16.1	2.1	BLOD	BLOD	1.0	0.2	72.0	28.8
UZ-72-35	6.2	13	4.0	0.2	1410	450	0.9	0.2	359.5	101.6
UZ-72-36	4.4	12	7.6	0.4	1230	420	1.1	0.1	135.9	39.9
UZ-72-37	9.0	42	8.8	0.5	800	560	1.1	0.3	241.3	39.4
UZ-72-38	7.3	12	6.1	0.3	1520	540	1.3	0.2	279.7	82.1
UZ-72-39	2.2	8	6.8	0.4	1620	420	1.1	0.2	75.3	27.0
UZ-72-40	19.8	34	37.3	2.0	1120	420	1.2	0.5	125.5	22.5
UZ-72-41	4.6	14	4.9	0.3	1160	440	1.2	0.3	223.6	61.5
TK-31-1	89.2	191	115.7	8.7	3570	720	1.6	0.4	152.7	15.9
TK-31-2	63.3	342	109.4	7.0	3980	540	1.7	0.6	114.9	9.6
TK-31-3	94.1	462	92.2	4.8	3780	410	1.5	0.5	201.3	14.1
TK-31-4	79.4	295	86.2	6.0	2860	440	1.4	0.5	182.0	16.5
TK-31-5	88.7	176	194.0	12.0	3690	530	1.5	0.5	91.0	8.9
TK-31-6	73.0	209	128.1	8.6	3510	690	1.4	0.4	113.2	10.9
TK-31-7	106.0	299	248.0	15.0	3300	610	1.8	0.7	85.1	7.1

TK-31-8	100.0	292	140.4	9.9	4670	560	1.5	0.4	141.7	13.0
TK-31-9	58.7	201	113.7	6.3	3560	660	1.5	0.5	102.7	9.2
TK-31-10	100.0	987	226.0	18.0	4090	710	1.5	0.5	88.4	7.6
TK-31-11	106.0	436	204.0	12.0	3100	490	1.6	0.6	103.6	7.9
TK-31-12	98.6	371	126.1	6.6	3630	460	1.6	0.6	154.8	11.4
TK-31-13	119.0	874	220.0	13.0	4380	780	1.7	0.6	107.2	7.3
TK-31-14	51.3	189	58.4	3.3	3130	550	1.2	0.5	173.7	16.0
TK-31-15	57.8	340	104.4	5.4	3580	600	1.4	0.5	109.9	8.2
TK-31-16	103.0	347	183.0	11.0	2840	510	1.7	0.6	112.3	9.0
TK-31-17	81.0	197	111.8	6.0	3120	530	1.4	0.5	143.6	12.8
TK-31-18	125.0	456	256.0	19.0	3720	780	1.6	0.6	97.0	8.5
TK-31-19	66.3	773	97.0	6.6	3370	630	1.4	0.5	135.4	10.4
TK-31-20	85.8	305	160.8	9.7	3440	520	1.6	0.5	106.1	8.8
TK-31-21	119.0	469	185.7	9.9	2820	480	1.5	0.5	127.4	9.0
TK-31-22	79.1	405	104.0	14.0	3040	530	1.5	0.5	150.6	21.6
TK-31-23	90.4	365	120.6	7.6	3620	550	1.4	0.5	148.4	12.2
TK-31-24	92.5	363	178.0	14.0	4060	750	1.6	0.5	103.3	9.8
TK-31-25	106.0	375	160.0	11.0	3890	420	1.8	0.6	131.8	11.3
TK-31-26	86.8	513	133.1	8.7	3980	480	1.5	0.5	129.4	10.2
TK-31-27	126.0	474	187.0	11.0	2870	650	1.6	0.5	133.7	10.0
TK-31-28	78.5	185	88.9	8.1	2810	620	1.5	0.4	174.5	20.4
TK-31-29	100.0	264	114.5	8.6	3620	470	1.7	0.6	172.6	16.8
TK-31-30	103.0	429	160.7	8.9	3180	440	1.6	0.5	126.5	9.3
TK-31-31	80.7	236	145.1	7.3	3150	460	1.6	0.5	110.4	9.1
TK-31-32	104.0	453	145.0	11.0	3550	430	1.6	0.6	142.2	12.7
TK-31-33	97.5	504	121.3	9.6	3150	670	1.5	0.5	159.1	14.4
TK-31-34	90.6	462	109.8	6.8	3500	510	1.4	0.5	163.2	12.6
TK-31-35	82.5	535	129.8	8.6	2850	650	1.5	0.6	126.1	10.0
TK-31-36	99.6	767	144.9	7.4	3730	560	1.6	0.6	136.2	8.5
TK-31-37	109.0	540	126.3	9.6	2610	460	1.7	0.6	170.1	14.9

TK-31-38	89.5	396	93.4	7.2	3610	570	1.4	0.5	189.1	17.4
TK-31-39	97.2	251	170.0	14.0	3210	400	1.2	0.4	113.6	11.8
TK-31-40	87.4	603	103.8	5.1	3030	550	1.7	0.5	166.6	10.6
TK-36-1	29.6	244	23.8	1.6	1750	350	1.2	0.3	244.4	22.7
TK-36-2	10.5	60	7.9	1.0	1480	420	1.3	0.3	260.1	46.1
TK-36-3	19.2	143	13.3	0.7	1050	410	1.4	0.3	283.1	28.1
TK-36-4	23.0	291	25.0	1.7	1260	450	1.2	0.3	183.2	16.4
TK-36-5	13.6	35	11.4	0.6	870	450	1.5	0.2	234.4	41.3
TK-36-6	14.4	209	24.6	1.8	960	400	1.0	0.2	116.4	11.7
TK-36-7	28.1	95	16.1	0.8	1090	500	1.1	0.3	339.5	38.9
TK-36-8	19.5	115	22.8	1.8	830	600	1.2	0.3	169.2	20.7
TK-36-9	15.4	50	18.1	0.9	1360	400	1.4	0.3	168.3	25.4
TK-36-10	9.3	76	10.8	1.1	1400	540	1.2	0.4	170.8	26.2
TK-36-11	16.0	70	20.2	2.1	0	0	1.3	0.2	157.0	24.9
TK-36-12	10.7	85	9.0	0.7	0	0	1.2	0.3	233.0	31.3
TK-36-13	18.8	145	26.9	1.3	830	580	1.3	0.4	138.3	13.3
TK-36-14	12.3	62	11.6	0.6	870	350	1.2	0.3	210.0	28.6
TK-36-15	24.4	149	16.9	1.0	1110	350	1.3	0.3	282.8	28.1
TK-36-16	11.5	102	15.3	0.8	1680	390	1.2	0.4	149.4	16.7
TK-36-17	7.9	54	15.1	1.3	0	0	1.1	0.4	104.4	16.8
TK-36-18	16.5	170	34.1	2.2	1070	280	0.9	0.2	96.2	9.6
TK-36-19	28.5	133	22.1	2.2	0	0	1.2	0.3	253.2	33.4
TK-36-20	10.7	95	17.5	1.3	1650	350	1.1	0.2	121.0	15.3
TK-36-21	13.3	54	12.7	1.0	2090	790	1.1	0.2	206.3	32.2
TK-36-22	25.8	185	40.4	2.0	1440	440	1.0	0.3	126.7	11.2
TK-36-23	10.4	108	13.2	1.1	1290	600	1.1	0.2	156.3	19.9
TK-36-24	12.0	99	14.6	0.8	950	480	1.0	0.2	162.5	18.7
TK-36-25	11.8	61	11.8	0.8	0	0	1.4	0.2	198.0	28.5
TK-36-26	14.5	96	13.9	1.2	940	560	1.2	0.4	206.0	27.5
TK-36-27	17.9	156	20.3	1.0	1400	450	1.2	0.3	174.6	16.4

TK-36-28	9.7	25	7.9	0.3	1710	520	1.1	0.3	241.8	49.3
TK-37-1	26.2	71	27.4	2.2	5460	440	1.0	0.2	181.0	25.9
TK-37-2	17.8	45	22.0	1.8	5530	670	1.1	0.3	159.7	27.2
TK-37-3	19.7	107	31.4	2.1	2860	470	1.2	0.3	124.4	14.6
TK-37-4	20.5	50	30.0	1.7	4820	660	1.4	0.3	135.3	20.6
TK-37-5	15.5	38	43.7	3.1	5120	630	1.2	0.4	70.6	12.5
TK-37-6	12.7	61	24.1	1.5	4030	730	1.3	0.2	104.5	14.9
TK-37-7	9.4	34	26.0	1.7	3280	700	1.2	0.3	71.9	13.2
TK-37-8	12.1	29	32.1	1.9	6820	710	1.6	0.5	74.9	14.6
TK-37-9	14.1	41	26.1	1.4	5130	690	1.6	0.6	106.9	17.7
TK-37-10	14.9	34	26.3	2.7	2830	540	1.5	0.5	112.3	22.4
TK-37-11	11.0	39	22.4	1.8	3630	580	1.5	0.5	98.0	17.6
TK-37-12	14.6	58	18.9	1.1	3500	640	1.9	0.8	152.7	21.9
TK-37-13	17.2	63	27.5	1.9	3650	630	2.4	1.0	123.8	17.8
TK-37-14	17.6	37	31.6	1.7	2260	460	2.4	0.6	110.6	19.1
TK-37-15	21.1	90	23.9	2.0	4310	340	2.3	0.7	174.4	23.5
TK-37-16	14.5	46	30.9	2.1	2790	720	2.0	1.0	93.2	15.1
TK-37-17	14.2	87	26.5	1.5	2840	510	2.4	0.7	106.6	12.9
TK-37-18	13.6	41	22.2	1.6	3470	650	2.4	0.6	121.7	20.9
TK-37-19	11.1	48	16.4	1.3	3540	390	2.3	0.6	133.7	22.0
TK-37-20	11.4	94	25.6	1.6	4490	580	2.2	0.6	88.9	10.7
TK-37-21	14.2	32	30.1	1.9	3480	630	2.5	0.7	94.1	17.7
TK-37-22	17.7	32	34.7	3.8	5010	670	2.2	0.7	101.2	21.0
TK-37-23	8.5	36	28.9	1.4	2850	580	2.4	0.9	65.9	11.4
TK-37-24	17.8	74	23.1	1.3	3040	500	2.2	0.8	152.3	19.7
TK-37-25	11.4	46	31.9	1.9	2550	400	1.6	0.6	71.0	11.3
TK-37-26	8.6	45	24.5	2.0	2690	690	1.5	0.5	69.8	11.9
TK-37-27	8.6	25	31.1	1.9	4240	640	1.5	0.5	76.7	16.0
TK-37-28	8.3	45	21.6	1.5	3840	550	1.9	0.8	76.2	12.5
TK-37-29	10.1	25	17.9	0.9	2860	380	2.4	1.0	112.2	23.1

TK-37-30	9.3	41	27.0	1.8	2440	630	2.4	0.6	69.0	11.7
TK-37-31	15.4	69	25.3	2.1	1990	460	2.3	0.7	120.7	17.6
TK-37-32	13.1	97	24.7	1.5	2800	390	1.5	0.5	105.3	12.5
TK-37-33	12.4	41	25.2	1.6	4110	410	1.9	0.8	98.0	16.5
TK-37-34	10.7	46	17.7	1.0	1930	380	2.4	1.0	119.8	18.9
TK-37-35	7.0	80	26.4	2.2	4400	760	2.4	0.6	65.6	9.1
TK-40-1	2.1	49	29.6	3.0	BLOD	BLOD	1.1	0.2	164.0	23.7
TK-40-2	8.8	80	26.4	2.6	BLOD	BLOD	1.2	0.3	309.4	44.0
TK-40-3	2.3	67	30.7	3.1	BLOD	BLOD	1.3	0.5	129.1	16.0
TK-40-4	8.3	88	32.5	3.3	BLOD	BLOD	1.1	0.6	185.7	25.1
TK-40-5	7.0	61	36.3	3.6	BLOD	BLOD	1.2	0.4	173.4	25.3
TK-40-6	1.2	55	33.2	3.3	BLOD	BLOD	1.6	0.5	117.7	15.9
TK-40-7	2.0	132	27.8	2.8	BLOD	BLOD	1.5	0.2	118.1	10.5
TK-40-8	2.3	63	33.7	3.4	BLOD	BLOD	1.7	0.4	132.5	17.0
TK-40-9	1.9	91	31.2	3.1	BLOD	BLOD	1.2	0.7	115.1	12.3
TK-40-10	2.4	43	26.0	2.6	BLOD	BLOD	1.3	0.4	85.9	13.3
TK-40-11	1.7	63	36.7	3.7	BLOD	BLOD	1.4	0.2	106.8	13.6
TK-40-12	2.7	55	38.6	3.9	BLOD	BLOD	1.6	0.3	98.5	13.5
TK-40-13	1.9	83	26.8	2.7	BLOD	BLOD	1.5	0.5	120.3	13.4
TK-40-14	1.8	49	33.9	3.4	BLOD	BLOD	1.7	0.4	100.0	14.4
TK-40-15	1.9	63	31.9	3.2	BLOD	BLOD	1.4	0.1	163.0	20.8
TK-40-16	2.5	51	33.0	3.3	BLOD	BLOD	2.0	0.2	106.8	15.2
TK-40-17	2.2	23	32.6	3.3	BLOD	BLOD	1.1	0.8	70.4	14.8
TK-41-1	33.5	266	49.0	2.5	9970	590	2.4	0.9	121.0	9.7
TK-41-2	29.3	104	26.4	1.2	12890	710	1.9	0.3	179.4	19.4
TK-41-3	25.3	63	21.6	1.1	11450	610	2.8	0.8	184.6	25.1
TK-41-4	30.6	156	29.2	1.9	11700	620	2.0	0.6	181.2	18.7
TK-41-5	34.4	260	29.9	1.7	8890	470	1.9	0.8	204.2	17.2
TK-41-6	19.6	68	37.1	2.0	10190	650	2.4	1.0	105.0	13.9
TK-41-7	38.0	162	45.1	2.1	9730	720	2.4	0.6	166.6	15.2

TK-41-8	27.5	178	31.2	1.3	9130	520	2.3	0.7	174.4	15.0
TK-41-9	25.9	129	34.1	1.6	11090	590	2.0	1.0	150.3	15.0
TK-41-10	28.5	231	31.3	1.9	8930	820	2.4	0.7	179.9	16.1
TK-41-11	24.5	142	26.9	1.6	12200	550	2.4	0.6	179.8	18.5
TK-41-12	24.0	117	26.6	1.0	11450	530	2.3	0.6	178.1	17.8
TK-41-13	26.8	153	22.2	1.3	5290	470	2.2	0.6	206.7	20.6
TK-41-14	29.6	133	30.5	1.7	13050	750	2.5	0.7	191.8	19.8
TK-41-15	33.5	229	37.7	1.5	14950	980	2.2	0.7	175.5	13.5
TK-41-16	29.5	307	34.8	2.4	10150	860	2.4	0.9	167.6	15.0
TK-41-17	18.7	97	22.7	1.3	10700	510	2.2	0.8	162.9	19.0
TK-41-18	15.3	78	20.9	1.1	11990	830	2.4	0.5	145.0	18.1
TK-41-19	30.7	130	29.0	1.9	10990	850	1.8	0.3	208.5	22.8
TK-41-20	35.3	216	36.5	2.4	10870	720	2.3	0.6	190.7	18.0
TK-41-21	31.1	104	29.9	2.2	12410	930	1.9	0.0	205.2	25.2
TK-41-22	29.8	171	33.7	2.4	12800	1000	2.9	1.3	175.0	18.3
TK-41-23	25.4	138	27.8	1.3	13260	820	2.2	0.4	180.8	17.6
TK-41-24	30.5	163	40.1	2.6	11880	750	2.1	0.8	150.5	15.3
TK-41-25	16.6	66	20.5	1.5	6740	570	2.2	0.6	160.1	22.9
TK-41-26	22.8	133	27.3	2.0	9950	930	2.2	1.2	164.9	18.7
TK-41-27	5.7	25	7.8	0.4	10110	940	1.5	0.7	143.6	29.6
TK-41-28	34.7	139	39.2	2.7	14110	820	2.4	0.7	174.8	19.1
TK-41-29	19.3	78	31.9	2.1	11590	850	3.1	0.1	120.3	15.8
TK-41-30	21.8	138	27.8	1.9	13200	1200	2.3	0.6	155.3	17.0
TK-41-31	18.6	77	32.6	1.6	13000	950	1.6	0.8	113.6	14.1
TK-41-32	30.8	150	42.0	2.0	13310	990	2.3	0.5	145.3	13.7
TK-41-33	39.2	139	53.2	3.5	12340	840	2.2	0.6	146.0	15.7
TK-41-34	14.7	59	26.4	1.7	15400	980	3.4	0.8	110.7	16.1
TK-48-1	6.3	47	6.2	0.3	930	93	1.0	0.2	197.9	30.5
TK-48-2	6.6	50	7.1	0.4	BLOD	BLOD	1.2	0.3	184.4	28.0
TK-48-3	7.3	31	11.9	0.7	BLOD	BLOD	1.0	0.2	121.8	23.1

TK-48-4	5.0	24	5.9	0.3	1170	117	0.9	0.2	167.3	35.1
TK-48-5	8.4	93	26.5	1.2	1300	130	1.1	0.3	62.9	7.1
TK-48-6	7.5	47	6.6	0.4	BLOD	BLOD	1.0	0.3	222.3	35.1
TK-48-7	2.3	21	8.2	0.4	BLOD	BLOD	0.8	0.3	54.9	12.2
TK-48-8	5.1	29	5.7	0.3	1690	169	1.1	0.2	175.5	34.1
TK-48-9	6.1	25	25.8	1.2	BLOD	BLOD	1.2	0.4	47.3	9.7
TK-48-10	6.3	49	12.0	0.8	BLOD	BLOD	1.1	0.2	104.4	16.4
TK-48-11	7.5	35	7.8	0.5	1140	114	1.3	0.3	191.2	34.7
TK-48-12	5.2	33	6.3	0.3	BLOD	BLOD	1.1	0.2	162.9	29.7
TK-48-13	5.5	13	5.4	0.2	2740	274	1.0	0.2	201.1	56.5
TK-48-14	4.9	14	8.9	0.4	BLOD	BLOD	1.0	0.2	108.4	29.3
TK-48-15	6.6	34	7.0	0.4	1030	103	1.0	0.2	187.1	34.0
TK-48-16	4.2	18	9.9	0.6	BLOD	BLOD	0.9	0.3	85.1	20.7
TK-48-17	9.0	65	8.2	0.4	BLOD	BLOD	1.0	0.2	216.6	29.0
TK-48-18	5.5	43	15.6	0.8	1170	117	1.1	0.2	70.4	11.3
TK-48-19	7.0	34	9.9	0.4	1270	127	1.0	0.2	139.8	24.7
TK-48-20	5.2	17	11.6	0.4	1050	105	1.0	0.2	89.2	21.9
TK-48-21	4.4	31	8.9	0.5	BLOD	BLOD	1.2	0.4	97.3	18.4
TK-48-22	6.7	42	13.6	0.6	1210	121	1.0	0.3	98.4	15.8
TK-49-1	1.7	4	5.9	0.3	570	310	1.4	0.8	40.4	20.3
TK-49-2	1.6	4	5.6	0.3	BLOD	BLOD	0.7	0.0	28.3	14.2
TK-49-3	5.8	34	15.3	0.9	BLOD	BLOD	1.0	0.2	114.5	20.8
TK-49-4	2.6	5	34.7	7.3	211000	29000	1.0	0.5	11.5	5.7
TK-49-5	3.4	2	7.8	0.5	BLOD	BLOD	0.8	0.2	49.3	35.0
TK-49-6	3.2	12	4.1	0.3	BLOD	BLOD	0.9	0.1	131.2	39.1
TK-49-7	3.4	7	16.0	1.3	BLOD	BLOD	1.1	0.3	49.5	19.1
TK-49-8	9.6	13	59.6	3.4	BLOD	BLOD	1.1	0.2	9.2	2.6
TK-49-9	2.8	6	14.8	0.8	BLOD	BLOD	1.1	0.2	26.5	10.9
TK-49-10	2.0	8	61.0	3.2	BLOD	BLOD	0.1	0.2	7.3	2.6
TK-50-1	1.4	7	12.0	0.8	1180	380	0.6	0.0	21.4	8.2

TK-50-2	1.0	3	11.9	1.1	1750	680	1.3	0.1	17.4	10.2
TK-50-3	0.4	1	6.3	0.6	1370	290	2.0	0.2	11.6	11.7
TK-50-4	0.9	2	20.7	1.8	BLOD	BLOD	1.5	0.3	8.8	6.3
TK-50-5	1.6	4	4.6	0.3	1160	430	1.0	0.1	68.6	34.5
TK-50-6	0.3	1	5.4	0.4	BLOD	BLOD	1.2	0.4	11.0	11.0
TK-50-7	1.6	8	21.1	1.5	1640	390	1.5	0.4	15.1	5.5
TK-50-8	2.3	5	10.7	1.1	BLOD	BLOD	1.3	0.6	42.3	19.4
TK-50-9	2.7	11	17.9	1.3	1760	370	0.7	0.5	30.6	9.5
TK-50-10	1.8	11	8.5	0.4	1620	370	1.7	0.9	42.4	12.9
TK-50-11	2.8	4	14.7	1.4	2090	470	1.2	0.1	38.1	19.4
TK-50-12	2.8	10	8.2	0.5	2340	670	1.1	0.2	65.7	21.1
TK-50-13	0.6	1	12.1	0.8	1100	350	1.5	0.3	10.2	10.2
TK-50-14	1.5	5	10.4	0.8	1050	560	1.8	0.1	27.8	12.6
TK-50-15	1.8	12	4.8	0.3	1310	390	1.3	0.5	73.7	21.8
TK-50-16	1.3	5	7.9	0.4	BLOD	BLOD	1.2	0.6	32.5	14.6
TK-50-17	0.9	5	6.0	0.4	2050	380	1.2	0.2	29.0	13.1
TK-50-18	2.2	6	15.4	1.0	1350	640	0.8	0.3	28.9	11.9
TK-50-19	2.3	8	9.4	0.6	1760	360	1.1	0.4	48.3	17.4
TK-50-20	1.4	5	6.1	0.4	1280	450	1.1	0.3	46.2	20.8
TK-50-21	1.4	4	12.6	0.7	1620	480	1.2	0.2	22.4	11.3
TK-50-22	0.7	1	9.0	0.5	1100	520	1.1	0.1	14.7	14.7
TK-50-23	0.8	2	25.0	2.2	1520	590	1.3	0.5	6.6	4.7
TK-50-24	0.5	1	7.5	0.6	2340	320	1.7	0.4	13.8	13.8
TK-50-25	3.0	12	17.2	1.1	1700	480	1.2	0.3	34.3	10.1
TK-50-26	0.7	2	6.6	0.4	1350	500	1.4	0.4	22.5	16.0
TK-50-27	2.3	4	6.8	0.4	2300	410	0.7	0.6	66.9	33.7
TK-50-28	3.2	11	12.5	0.8	1500	380	1.1	0.4	50.9	15.7
TK-50-29	3.6	15	10.8	0.7	2320	520	1.3	0.5	65.7	17.5
TK-50-30	0.9	2	8.9	0.5	910	400	1.3	0.4	19.5	13.9
TK-50-31	2.8	5	20.1	2.4	1380	440	1.4	0.5	28.1	13.0

TK-50-32	0.2	1	10.9	1.1	1560	500	1.4	0.4	4.1	4.1
TK-50-33	0.5	2	7.4	0.4	1480	370	1.3	0.2	12.9	9.1

Appendix H

Chatkal-Kurama Helium Data

Single grain zircon (U–Th–Sm)/He and apatite (U–Th–Sm)/He age and chemistry data. For single grain analysis, see Table 2. Concentrations of thorium, uranium and samarium in ng. He is the concentration of helium measured in ncc. Th/U is the ratio of thorium to uranium. Raw age is the age before the F_T correction is made. F_T is the alpha-ejection correction parameter of Farley et al. (1996). Cor. age is the age after applying the F_T correction, and TAU is the total analytical uncertainty.

Sample	^{232}Th	±(%)	^{238}U	±(%)	^{147}Sm	±(%)	He	±(%)	TAU(%)	Th/U	Raw age	±1σ	F_T	Cor. age	±1σ
Zircon (U-Th-Sm)/He Data															
TK-42-1	0.555	1.4	1.212	1.9	0.002	26.1	28.120	1.8	2.5	0.45	169.6	4.2	0.64	265.7	13.5
TK-42-2	1.408	1.4	4.501	2.0	0.003	2.0	68.269	0.7	2.0	0.31	115.0	2.3	0.71	161.6	8.8
TK-42-3	1.033	1.4	1.586	1.9	0.001	27.5	46.088	0.6	1.8	0.65	203.5	3.6	0.72	281.7	15.4
TK-42-4	1.530	1.4	3.434	1.9	0.003	17.2	70.073	0.8	1.9	0.44	149.9	2.9	0.72	206.9	11.5
TK-36-1	2.347	1.4	7.770	2.0	0.005	6.6	179.440	0.7	2.0	0.30	174.5	3.5	0.80	216.9	13.4
TK-36-2	0.924	1.4	2.900	1.9	0.002	21.7	71.820	0.6	1.9	0.32	186.2	3.5	0.73	256.6	14.2
TK-36-3	1.022	1.4	4.638	1.9	0.001	4.9	109.085	0.6	1.9	0.22	180.8	3.5	0.70	256.6	13.8
TK-36-4	0.753	1.4	3.496	1.9	0.001	11.9	73.653	0.6	1.9	0.21	162.4	3.1	0.66	247.4	23.6
Apatite (U-Th-Sm)/He Data															
TK-40-1	0.620	5.7	0.253	5.8	0.076	0.3	4.001	8.6	9.6	2.43	81.8	7.8	0.75	156.0	12.6
TK-40-2	0.242	4.0	0.112	4.3	0.030	0.3	1.759	6.2	6.9	2.16	85.1	5.9	0.67	127.3	10.4
TK-40-3	0.717	5.7	0.290	5.9	0.081	0.4	6.295	4.5	6.2	2.46	111.8	6.9	0.76	146.4	12.7
TK-41-1	0.211	5.7	0.079	5.8	0.030	0.4	1.524	3.5	5.5	2.63	96.3	5.3	0.72	133.3	10.2
TK-41-2	0.046	4.1	0.017	4.2	0.012	0.4	0.110	3.4	4.6	2.71	32.3	1.5	0.56	57.9	3.1

TK-41-3	0.173	5.7	0.104	5.9	0.021	0.4	1.399	0.9	4.6	1.65	78.7	3.6	0.67	118.4	7.6
TK-36-1	0.127	4.0	0.123	4.2	0.016	0.3	1.075	3.8	5.2	1.03	57.5	3.0	0.75	76.9	5.9
TK-36-2	0.118	5.7	0.089	5.9	0.017	0.4	1.775	1.5	4.9	1.31	123.2	6.0	0.62	197.9	12.3
TK-36-3	0.071	4.1	0.079	4.2	0.014	0.4	1.591	2.8	4.5	0.90	135.2	6.1	0.70	192.8	21.2
TK-36-4	0.088	4.1	0.092	4.2	0.014	0.4	1.737	1.5	3.8	0.96	125.2	4.8	0.73	170.6	19.1
TK-36-5	0.080	5.7	0.083	5.8	0.010	0.4	1.386	3.8	6.2	0.96	111.2	6.9	0.73	153.3	18.7
UZ-69-1	0.052	3.3	0.022	3.5	0.012	0.4	0.038	2.7	3.7	2.37	9.1	0.3	0.55	16.7	1.8
UZ-69-2	0.081	4.6	0.042	4.7	0.017	0.3	0.055	2.2	4.2	1.90	7.4	0.3	0.55	13.4	1.4
UZ-69-3	0.173	3.3	0.085	3.5	0.033	0.3	0.141	1.1	2.8	2.02	9.2	0.3	0.72	12.8	0.7
UZ-69-4	0.111	3.3	0.051	3.5	0.022	0.3	0.075	2.4	3.5	2.16	8.0	0.3	0.51	15.7	1.7
UZ-69-5	0.140	4.6	0.056	4.7	0.027	0.3	0.066	3.5	4.9	2.51	6.1	0.3	0.66	9.2	0.6
TK-50-1	0.242	3.3	0.138	3.5	0.077	0.2	0.475	5.1	5.7	1.74	19.9	1.1	0.74	27.0	2.1
TK-50-2	0.078	4.6	0.043	4.7	0.029	0.3	0.075	1.2	3.8	1.78	9.9	0.4	0.70	14.1	0.9
TK-50-3	0.090	4.6	0.058	4.7	0.029	0.2	0.084	1.1	3.8	1.55	8.6	0.3	0.69	12.5	0.8
TK-50-4	0.065	3.3	0.029	3.5	0.030	0.3	0.066	1.3	2.9	2.23	12.3	0.4	0.64	19.2	1.1
TK-49-1	0.030	4.6	0.022	4.7	0.007	0.4	0.046	3.2	4.9	1.33	12.9	0.6	0.54	24.1	2.7
TK-49-2	0.023	3.3	0.014	3.5	0.006	0.4	0.035	1.5	3.1	1.56	14.2	0.4	0.47	30.6	3.2
TK-49-3	0.089	4.6	0.054	4.7	0.014	0.4	0.068	1.4	3.9	1.66	7.5	0.3	0.54	13.8	1.5
TK-49-4	0.112	3.3	0.083	3.5	0.024	0.3	0.374	3.3	4.3	1.34	28.0	1.2	0.68	41.4	2.7

Appendix I

Chatkal-Kurama AFT Radial Plots

1 Single grain apatite fission track data for samples taken from the Chatkal-Kurama terrane plotted using Vermeesch (2009). Single grain ages are coloured according to their respective chlorine (Cl) measurements, or uranium (U) measurements.

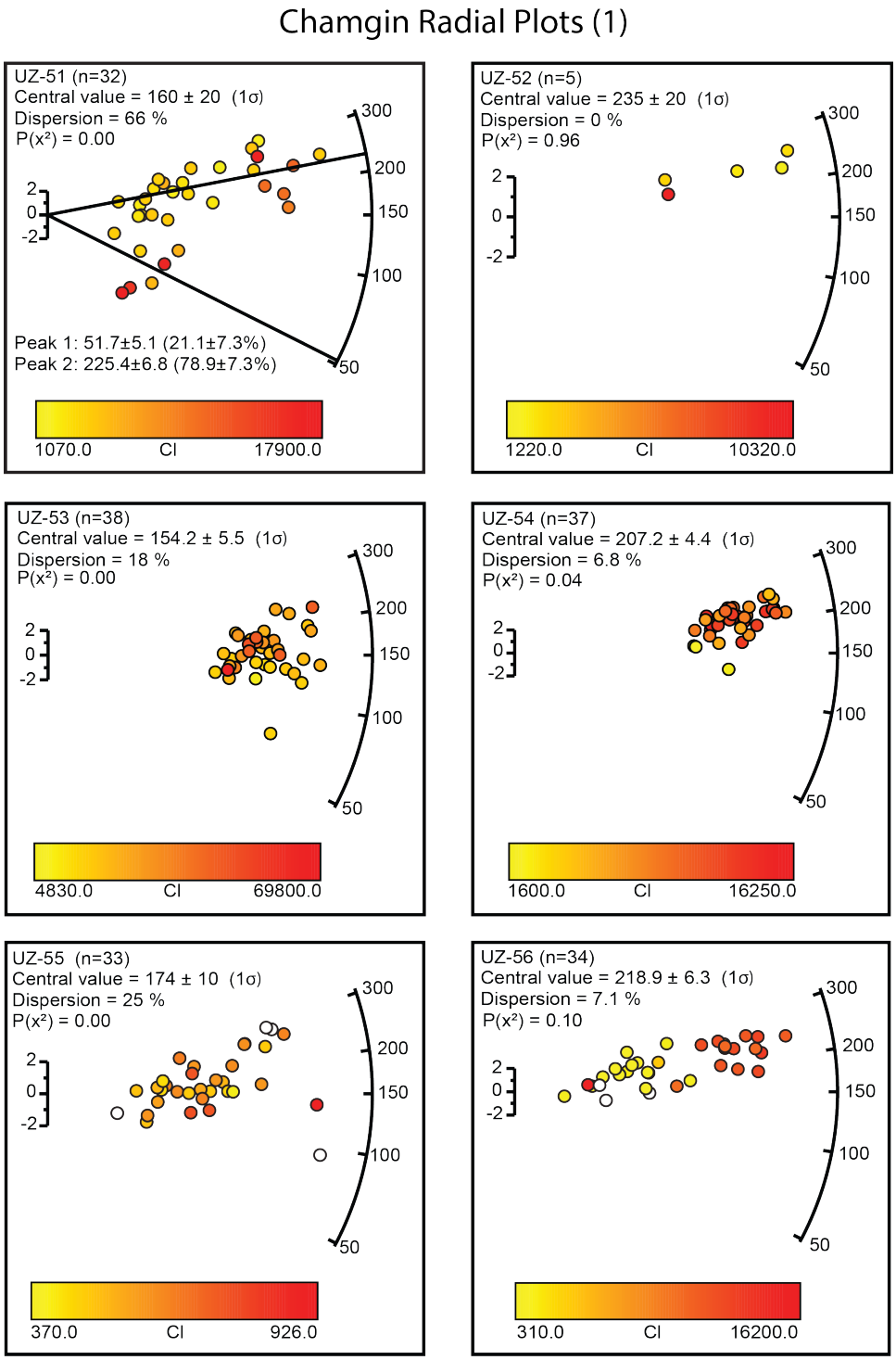

2

Chamgin Radial Plots (2)

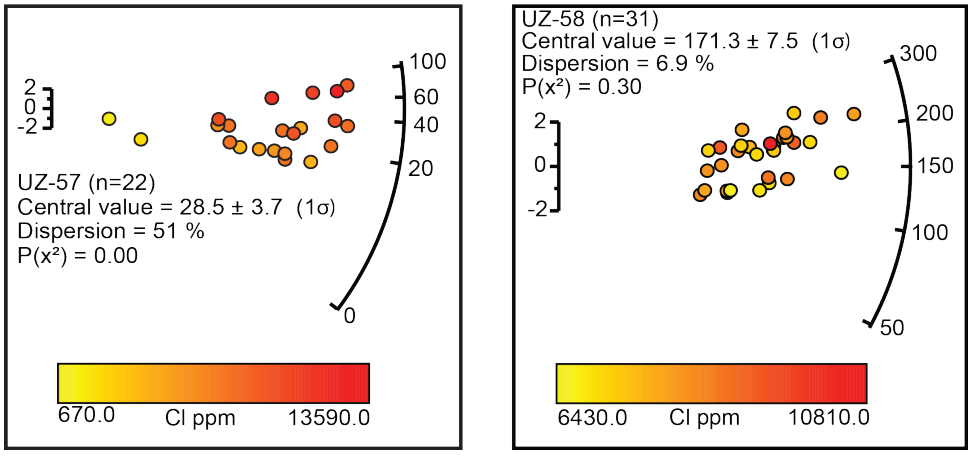

3

Kamchik Pass Radial Plots

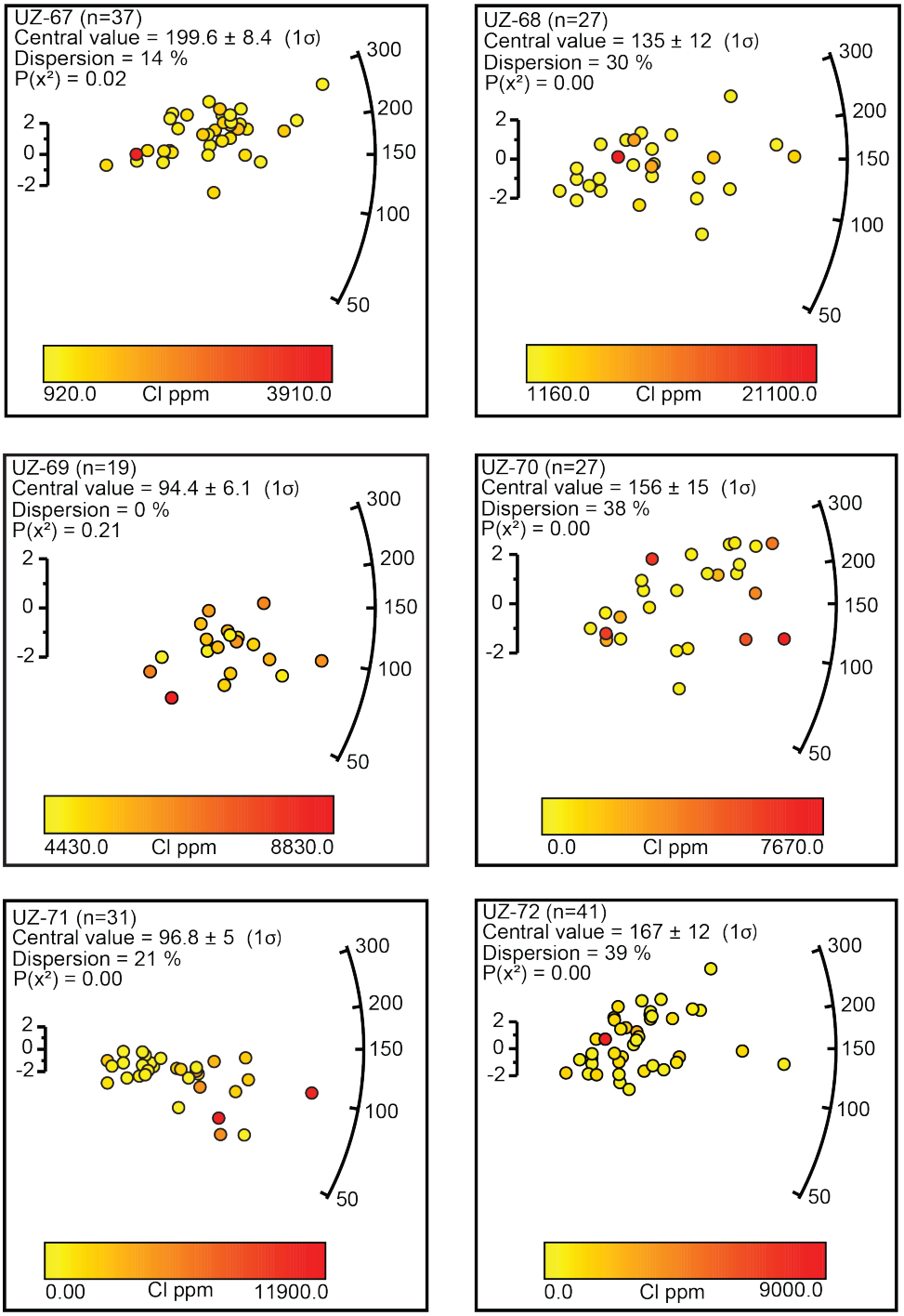

4

Almalyk Radial Plots (1)

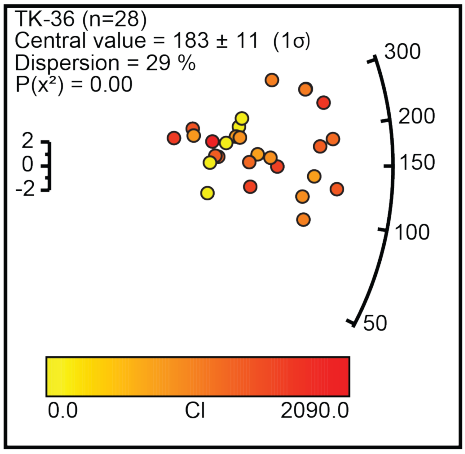

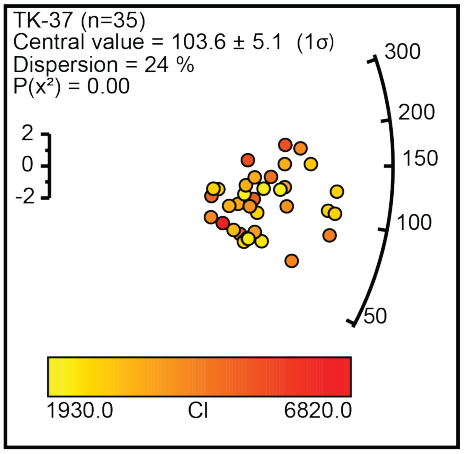

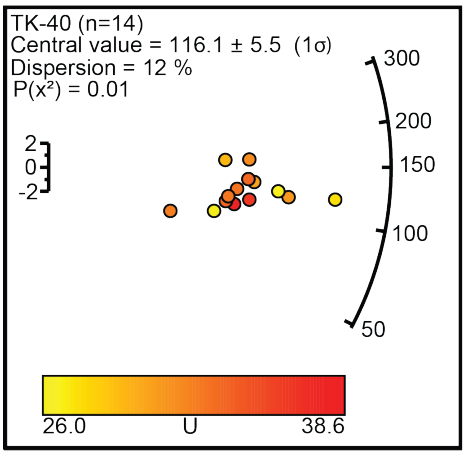

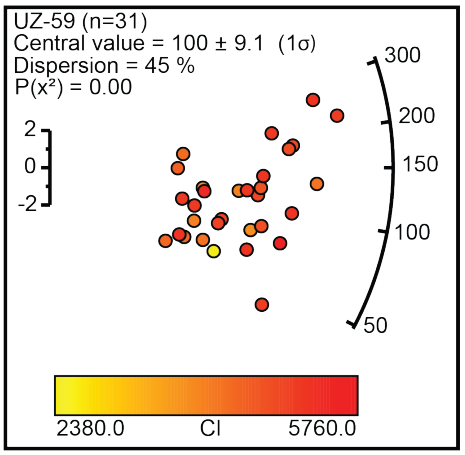

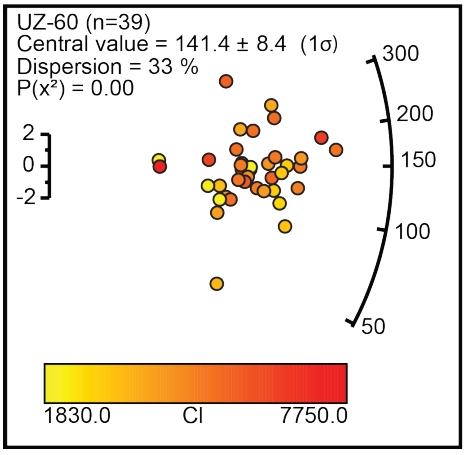

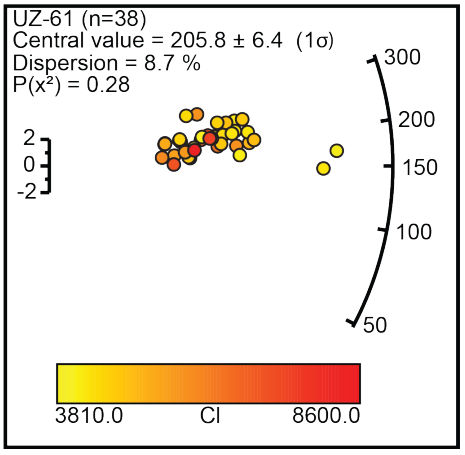

5

Almalyk Radial Plots (2)

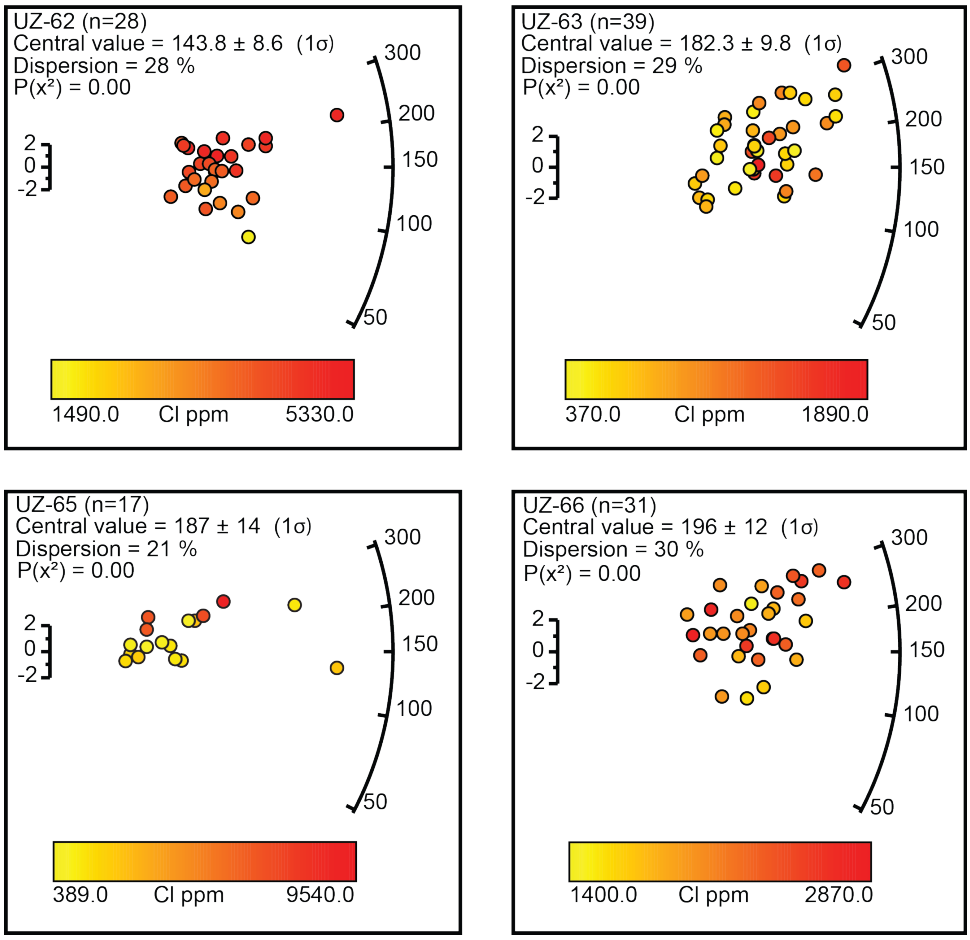

6

Shaydon Radial Plots

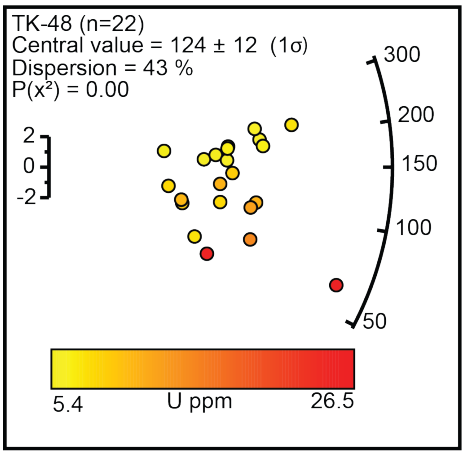

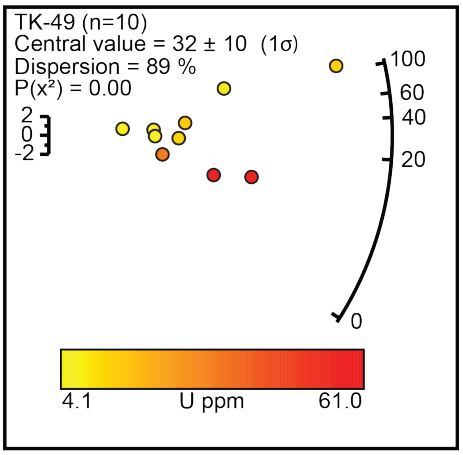

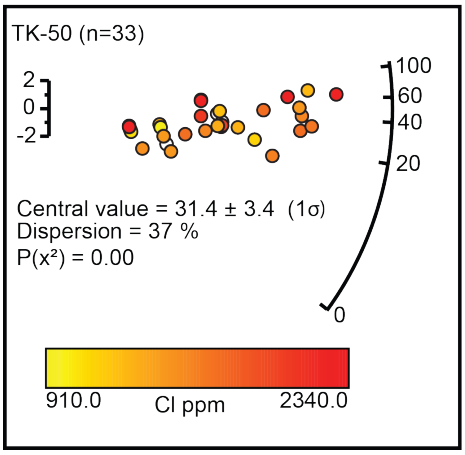

7

Shaydon Radial Plots

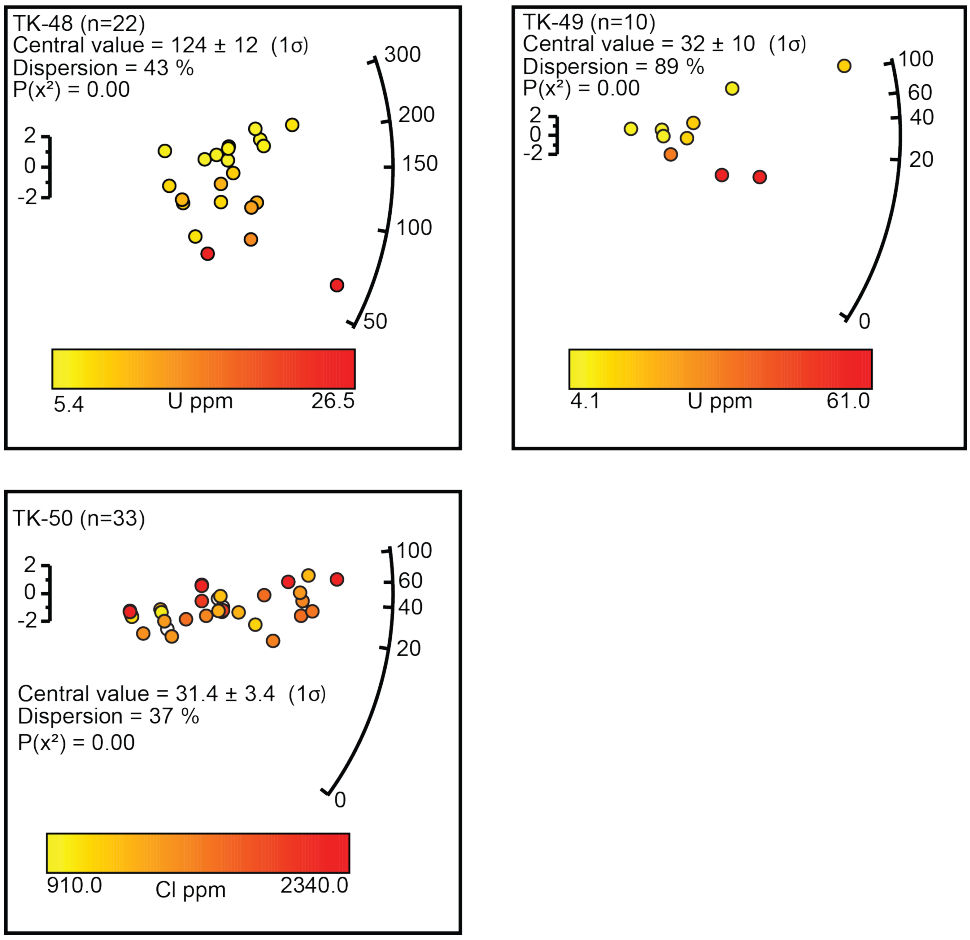

Appendix J

Chatkal-Kurama MTL Histograms

1 Confined fission track length histograms for each sample in the Chatkal-Kurama region.

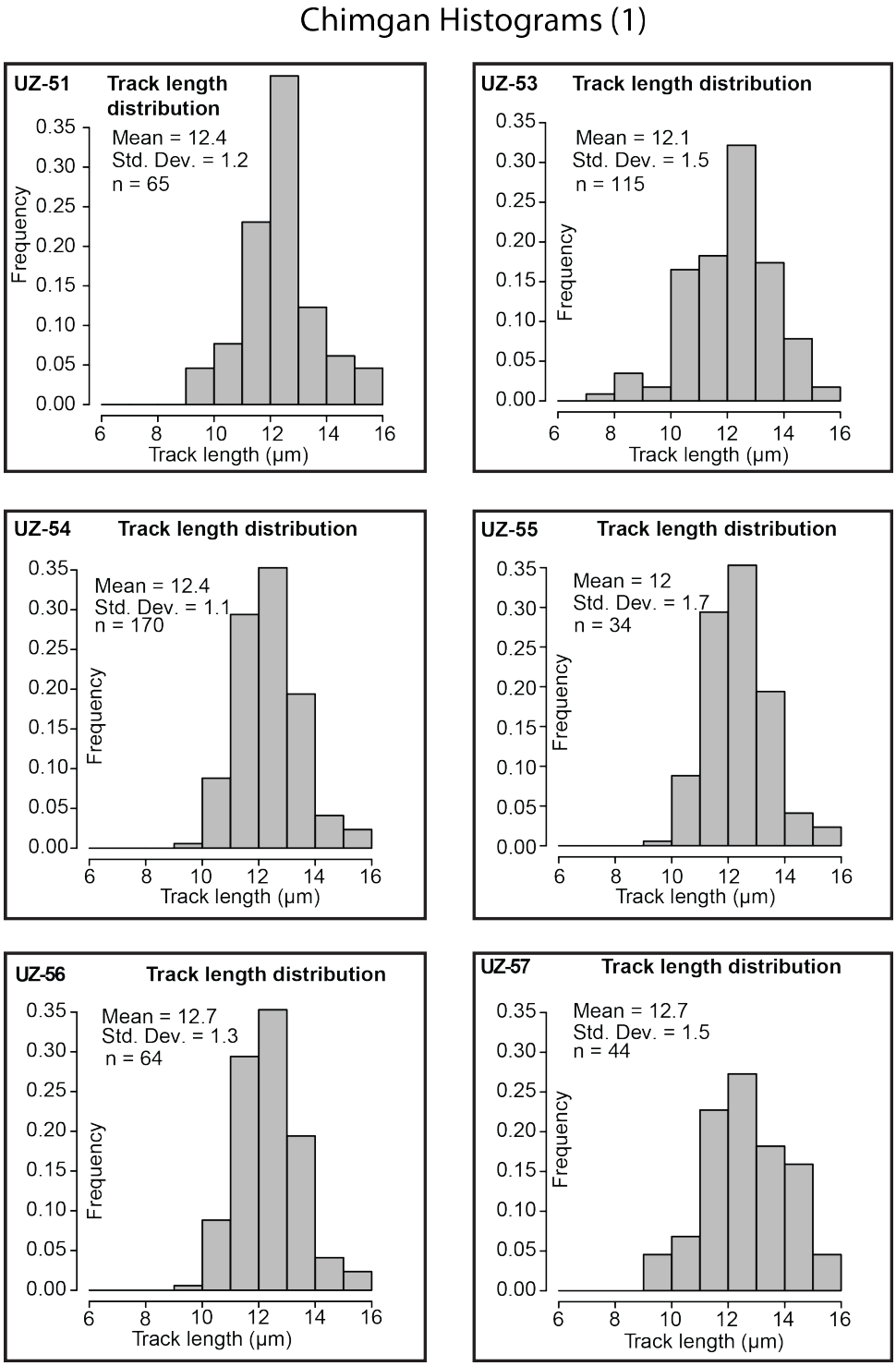

2

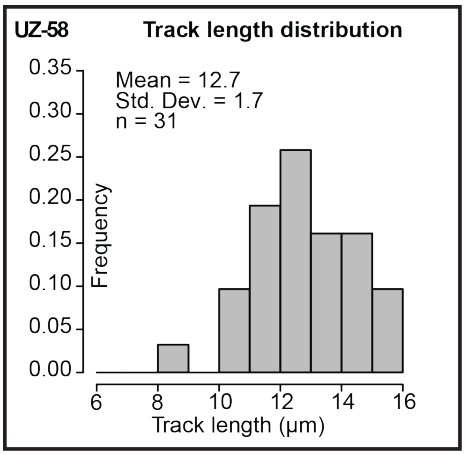
UZ-58
Track length distribution
Mean = 12.7
Std. Dev. = 1.7
n = 31
Frequency
0.35
0.30
0.25
0.20
0.15
0.10
0.05
0.00
6
8
10
12
14
16
Track length (μm)

3

Kamchik Pass Histograms

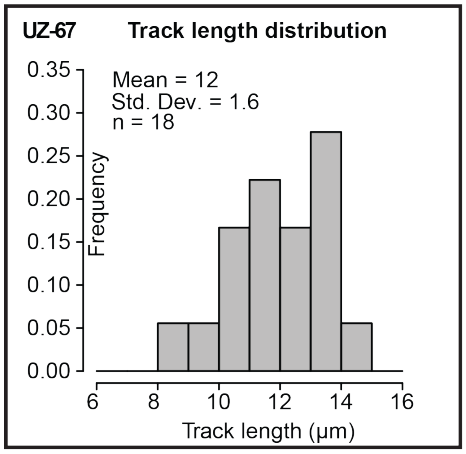

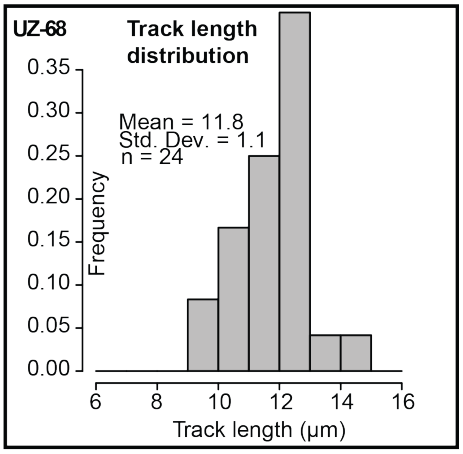

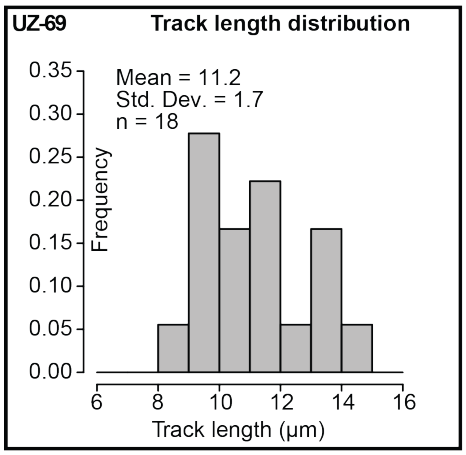

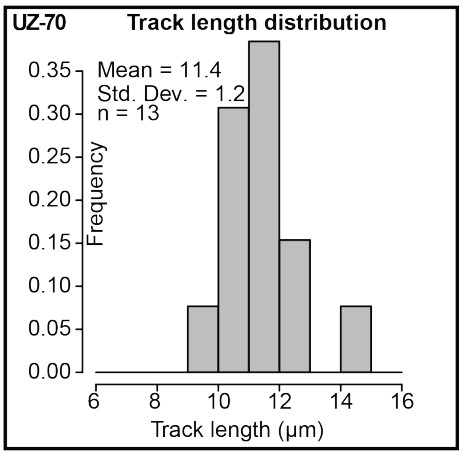

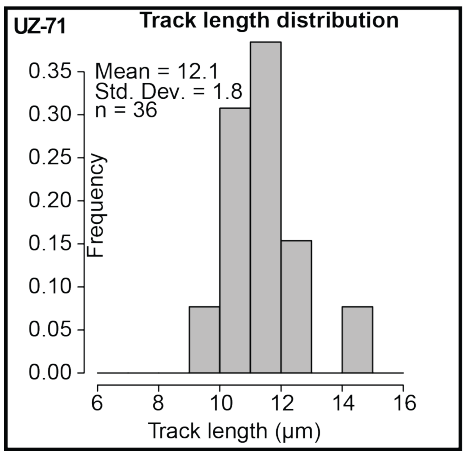

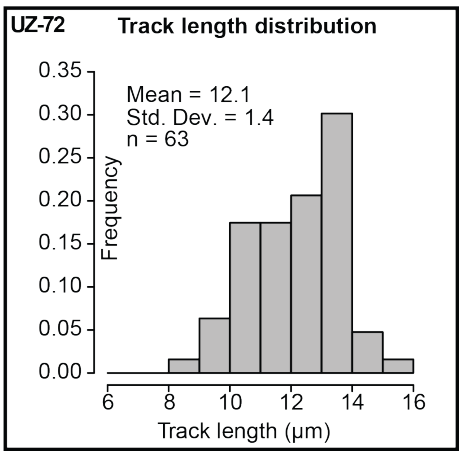

4

Almalyk Histograms (1)

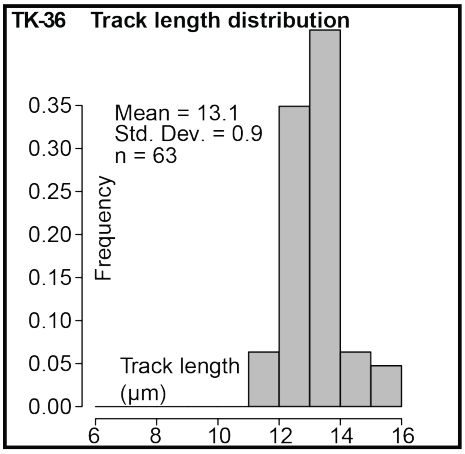

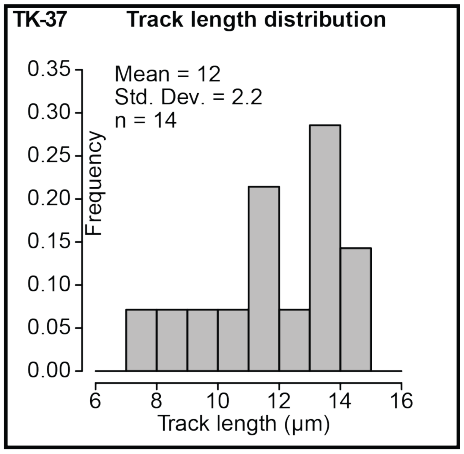

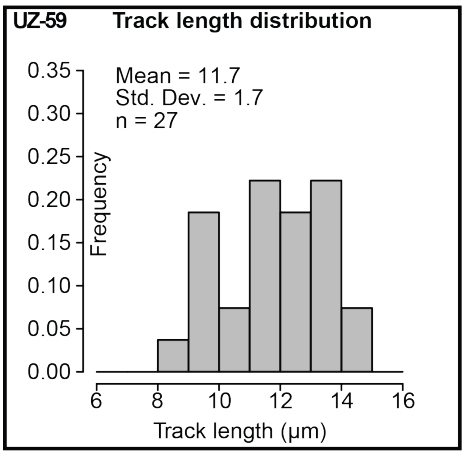

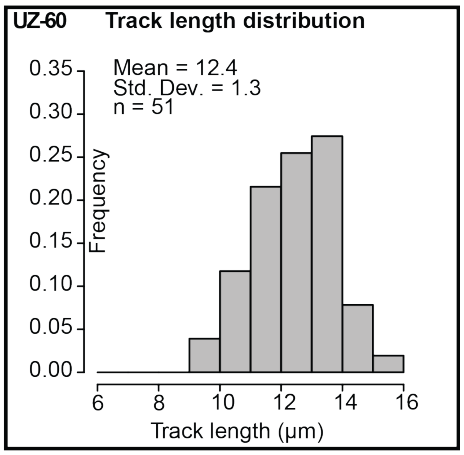

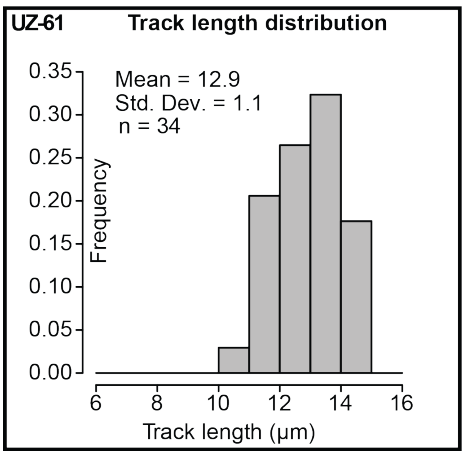

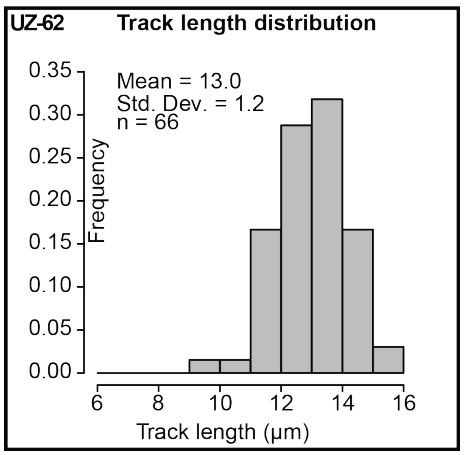

5

Almalyk Histograms (2)

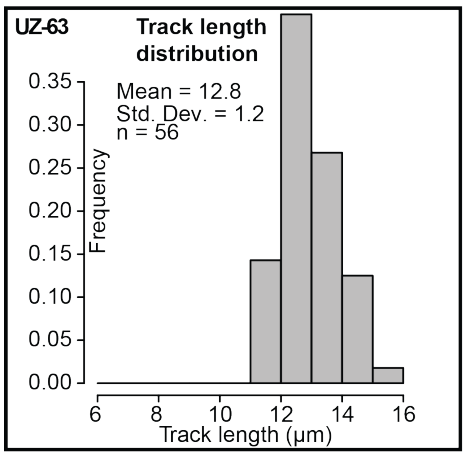

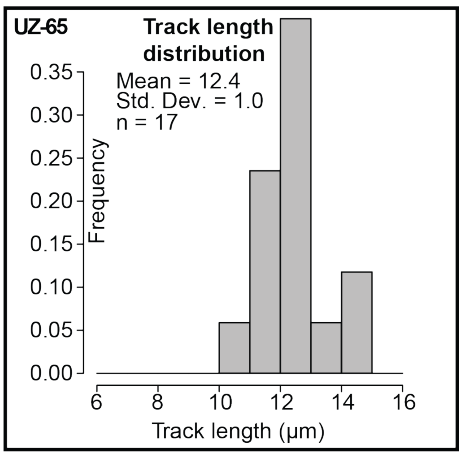

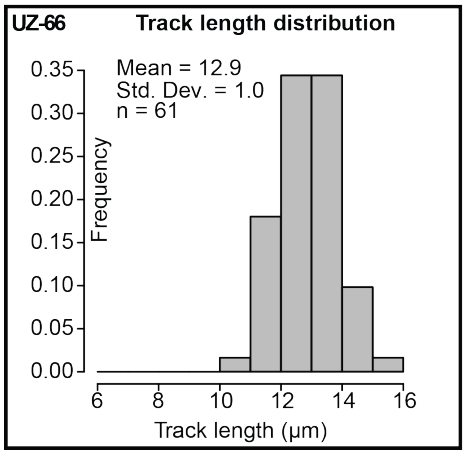

6

Shaydon Histograms

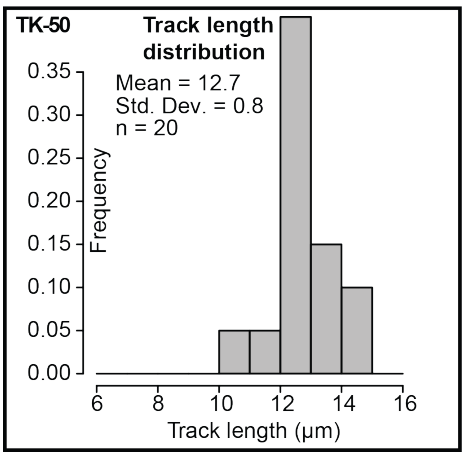

7

Khujand Histograms

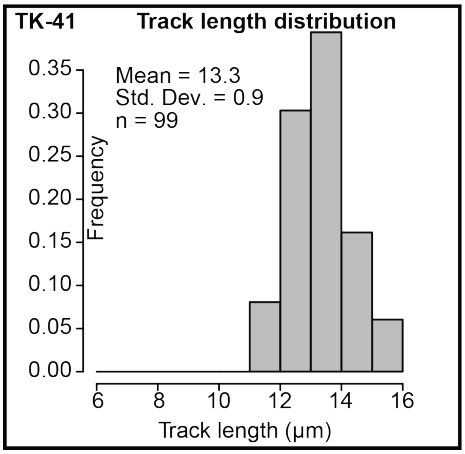

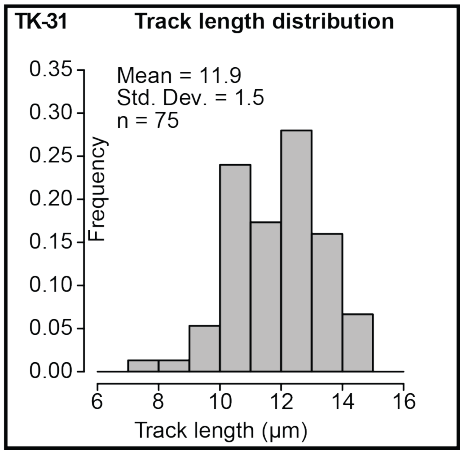

Appendix K

Chatkal-Kurama Thermal History Models

1 Individual time-temperature plots for each sample modelled using Gallagher (2012). For modelling parameters see Supplementary File 6.

Chimgan Temperature-Time Models (1)

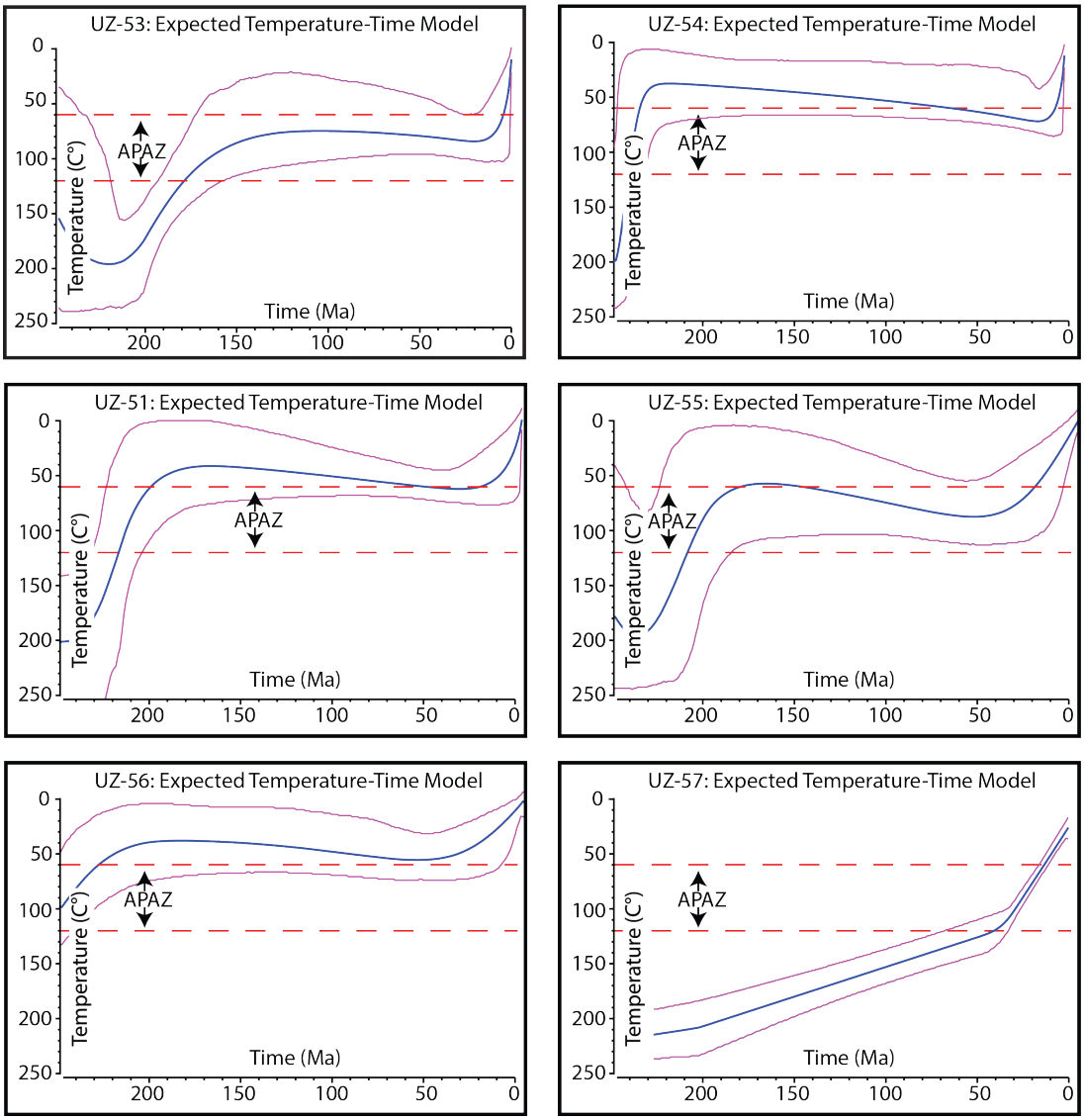

2

Chimgan Temperature-Time Models (2)

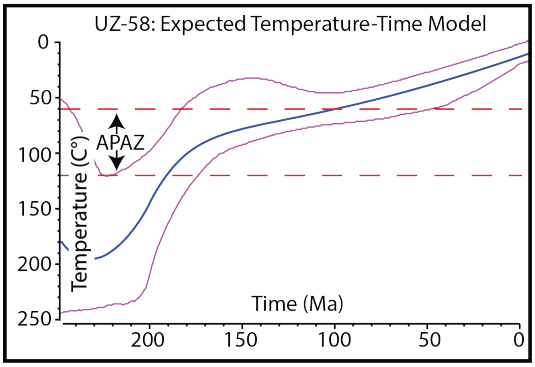

3

Kamchik Pass Temperature-Time Models

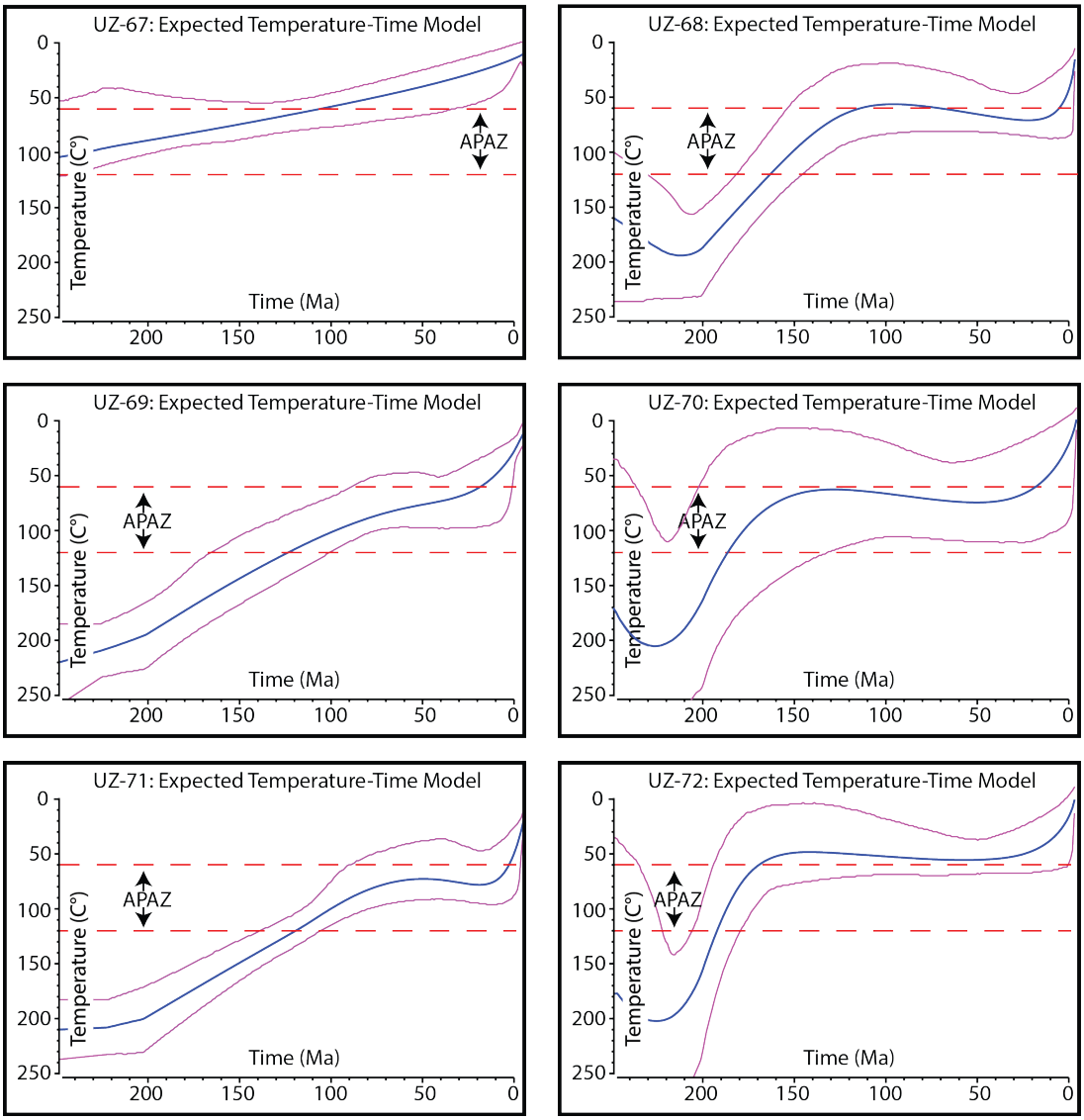

4

Almalyk Temperature-Time Models (1)

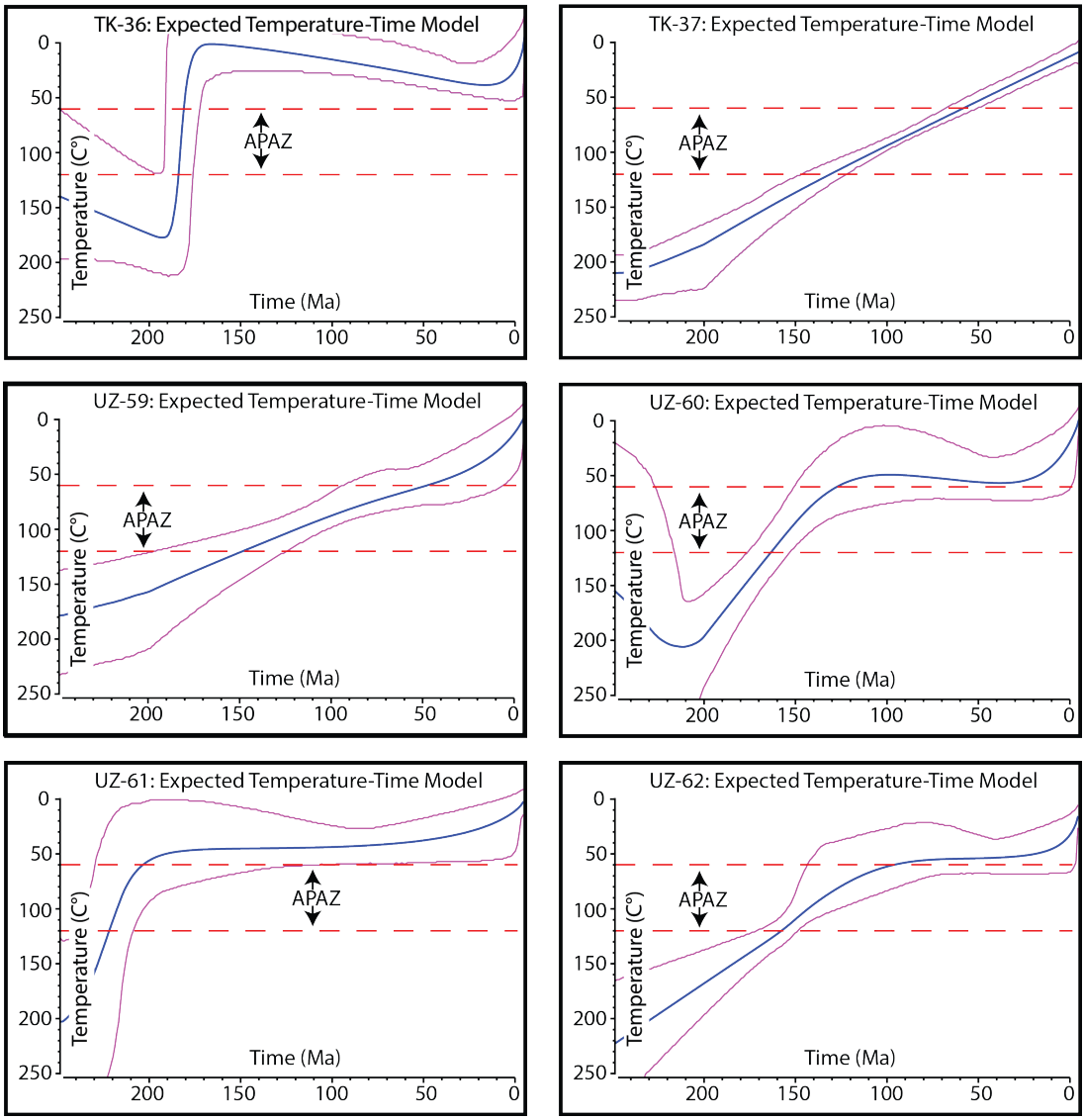

5

Almalyk Temperature-Time Models (2)

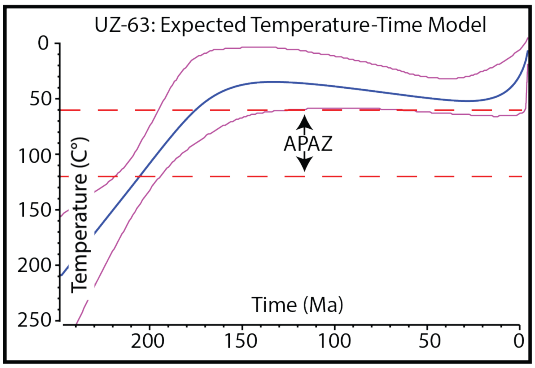

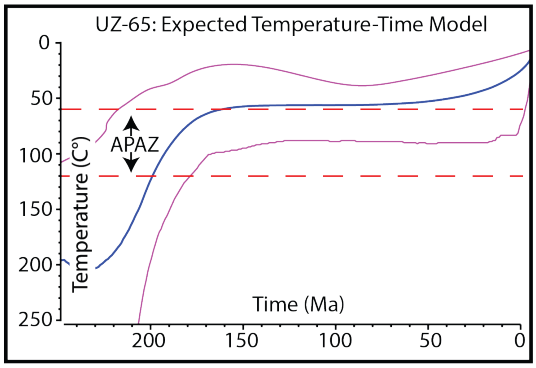

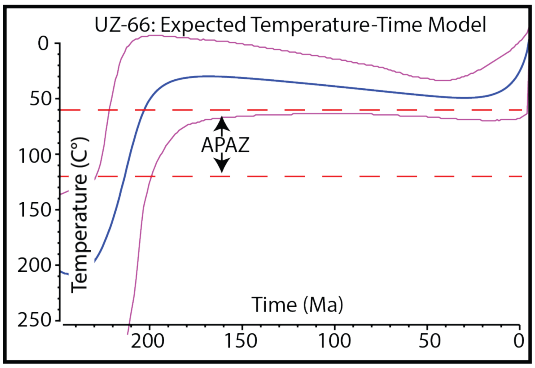

6

Shaydon Temperature-Time Models

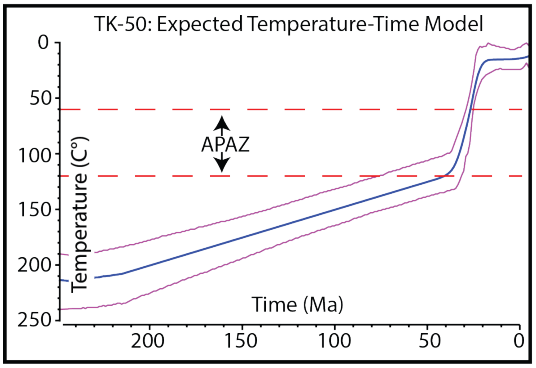

7

Khujand Temperature-Time Models

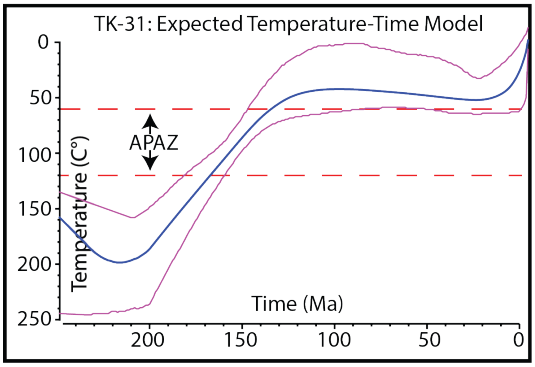

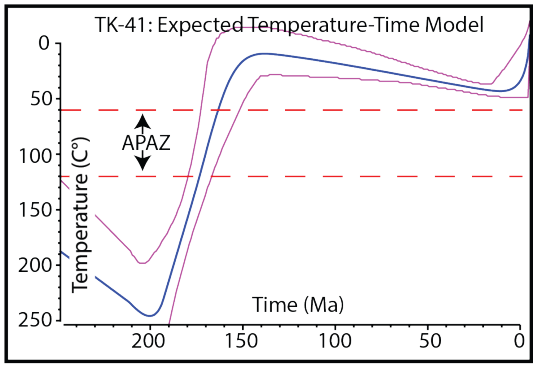

Appendix L

Chatkal-Kurama Thermal Modelling Constraints

Supplementary File 6: Thermal history model input table for simulations of the Chatkal-Kurama terrane, Uzbekistan and Tajikistan, based on framework established by Flowers et al. (2015)

1. Thermochronologic Data

Samples and data used in simulations

Simulation inputs				Data Source	All data needed for modeling published?
Sample Region	AHe	AFT	ZHe		
Chimgan					
UZ-53		×		Supplementary File 1	yes
UZ-54		x		Supplementary File 1	yes
UZ-55		x		Supplementary File 1	yes
UZ-56		x		Supplementary File 1	yes
UZ-57		x		Supplementary File 1	yes
UZ-58		x			
Kamchik Pass					
UZ-67		×		Supplementary File 1	yes
UZ-68		×		Supplementary File 1	yes
UZ-69	x	x		Supplementary File 1 and 2	yes
UZ-70		x		Supplementary File 1	yes
UZ-71		x		Supplementary File 1	yes
UZ-72		x		Supplementary File 1	yes
Almalyk					
TK-36	×	x	x	Supplementary file 1 and 2	yes
TK-37		×		Supplementary File 1	yes
UZ-57		×		Supplementary File 1	yes
UZ-60		×		Supplementary File 1	yes
UZ-61		×		Supplementary File 1	yes
UZ-62		×		Supplementary File 1	yes
UZ-63		×		Supplementary File 1	yes
UZ-65		×		Supplementary File 1	yes
UZ-66		×		Supplementary File 1	yes
Shaydon					
TK-50	x	x		Supplementary file 1 and 2	yes
Khujand					
TK-31		x		Supplementary File 1	yes
TK-41	x	×		Supplementary file 1 and 2	yes

Data treatment, uncertainties, and other relevant constraints

AHe Data

He dates (Ma): Single grain AHe ages were from Supplementary File 2 modelled individually

Error (Ma) applied in modeling: error of 1σ was used from Supplementary file 1

r (μm): Equivalent spherical radius of each grain

ZHe Data

He dates (Ma): Single grain ZHe ages were from Supplementary file 2 modelled individually

Error (Ma) applied in modeling: error of 1σ was used from Supplementary file 2

r (μm): Equivalent spherical radius of each grain

AFT data

Cl wt%: From Supplementary file 1

Lengths: Length data for all samples is available in Supplementary File 4

Initial mean track length: 16.3 µm

Track length reduction standard: 0.893

2. Additional geological information

Assumption	Explaination and data source
As all the samples were granitoid and there was no evidence for re-heating. Samples were assumed to have come from >120°C through the APAZ	

3. System- and model-specific parameters

He radiation damage model : Flowers et al. 2009

FT annealing model : Ketcham et al. 2007

FT c-axis projection : Not used

Modeling code : QTQt 5.6.0 PC

Statistical fitting criteria : Default QTQt values

MCMC Parameters : Burn-in = 200,000, Post-burn-in = 200,000

tT path characteristics : Not indicated

Appendix M

Kyzylkum-Nurata AFT Single Grain Data

Apatite fission track data and chemical data: ρ_s is the density of spontaneous tracks within the region of interest and is expressed as 10^5 tracks/cm^2. N_s is the total number of counted spontaneous tracks per sample. ^{238}U is the average concentration in ppm of uranium 238 measured in each grain. ^{35}Cl is the average concentration in ppm of chlorine 35 measured in each grain; concentrations were obtained using laser ablation–inductively coupled plasma–mass spectrometry (LA-ICP-MS). BLOD is below limits of detection, and thus, could not provide a concentration value and was not used in calculating sample concentration averages. Dpar is the length of spontaneous track etch pits in μm. t is the AFT single grain age for each sample in Ma.

Sample	ρ_s	N_s	^{238}U	$\pm1\sigma$	^{35}Cl	$\pm1\sigma$	Dpar	$\pm1\sigma$	t	$\pm1\sigma$
UZ-01-1	13.9	40	26.9	1.5	1820	110	1.7	0.5	107.5	19.6
UZ-01-2	3.3	10	26.1	2.3	10500	5500	2.0	0.1	26.3	8.8
UZ-01-3	3.5	7	21.6	2.4	2270	300	2.2	0.5	33.2	13.3
UZ-01-4	7.6	20	29.0	2.3	11900	4500	2.3	0.9	54.3	13.5
UZ-01-5	11.7	29	23.8	2.4	2400	140	2.5	1.1	102.0	22.8
UZ-01-6	13.4	72	30.3	1.6	29400	8800	2.1	1.0	91.9	13.6
UZ-01-7	13.3	50	31.9	1.8	1840	140	1.9	0.3	86.4	14.6
UZ-01-8	12.0	23	18.9	1.0	2350	140	2.4	0.2	131.5	29.8
UZ-01-9	3.2	10	16.8	1.3	6500	1800	1.9	0.5	39.1	13.0
UZ-01-10	12.2	53	33.0	2.4	2250	150	1.9	0.3	76.6	13.1
UZ-01-11	15.1	25	17.6	1.6	1740	150	2.0	0.6	177.6	41.1

UZ-01-12	13.2	42	17.2	3.2	2310	180	2.1	0.7	159.7	40.3
UZ-01-13	15.5	78	25.8	2.4	2240	150	2.1	0.9	124.8	20.4
UZ-01-14	7.7	21	36.0	2.4	2690	620	1.7	0.3	44.2	10.6
UZ-01-15	10.3	34	32.9	2.1	5600	2100	1.9	0.5	64.9	12.8
UZ-01-16	16.6	66	29.8	1.8	2390	340	1.9	0.4	115.7	17.9
UZ-01-17	5.7	15	23.4	1.4	15400	5100	1.7	0.6	50.4	13.8
UZ-01-18	12.6	37	36.0	2.9	2040	130	1.8	0.3	72.3	14.2
UZ-01-19	4.4	21	11.8	0.7	2360	130	2.1	0.7	77.4	18.3
UZ-01-20	6.0	15	19.3	1.2	2950	220	3.0	2.0	64.0	17.6
UZ-01-21	28.7	54	101.3	7.6	198000	29000	2.0	0.6	58.7	10.1
UZ-01-22	15.1	25	30.3	2.6	1890	160	2.1	0.6	103.5	23.7
UZ-01-23	15.2	19	19.7	1.2	7200	3100	2.6	1.3	159.6	39.6
UZ-01-24	13.7	41	37.6	3.3	5300	2100	1.6	0.3	75.7	14.6
UZ-01-25	12.2	70	25.6	2.4	1750	110	1.6	0.3	98.7	16.6
UZ-01-26	14.8	44	39.9	3.7	11900	5600	1.7	0.3	76.8	14.7
UZ-01-27	9.0	42	30.6	2.4	1560	130	1.8	0.3	61.3	11.5
UZ-01-28	16.5	57	21.3	1.4	1910	200	1.7	0.3	160.2	26.3
UZ-01-29	11.3	25	14.4	1.0	1910	150	1.8	0.4	162.5	36.3
UZ-01-30	16.3	59	36.7	2.7	2940	180	2.1	0.4	92.2	15.3
UZ-01-31	5.9	14	24.6	1.8	11400	4200	2.0	0.7	49.6	14.2
UZ-01-32	13.9	53	38.0	2.8	3250	230	2.1	0.3	75.9	13.0
UZ-01-33	11.4	48	33.4	2.1	2340	190	1.9	0.3	70.5	12.2
UZ-02-1	0.5	1	1.5	0.1	1800	120	3.1	0.7	68.5	68.8
UZ-02-2	23.3	81	38.5	2.1	970	290	2.3	0.8	125.6	18.0
UZ-02-3	0.6	1	1.6	0.1	1740	120	2.9	0.5	71.3	71.7
UZ-02-4	0.6	1	2.2	0.3	2660	680	2.9	0.5	55.4	56.1
UZ-02-5	1.4	4	2.6	0.2	1340	130	2.9	0.5	108.4	55.4
UZ-02-6	1.4	2	3.3	0.2	40100	5600	1.7	0.5	89.2	63.7
UZ-02-7	0.4	1	2.3	0.1	2030	150	4.1	0.7	36.3	36.5
UZ-02-8	2.7	5	2.4	0.2	3030	880	5.8	0.4	234.1	107.5

UZ-02-9	0.9	3	1.7	0.1	1890	120	1.9	0.6	110.7	64.6
UZ-02-10	0.9	4	1.9	0.1	1216	98	2.5	1.1	103.4	52.5
UZ-02-11	1.0	2	2.0	0.1	1550	170	1.9	0.6	100.5	71.7
UZ-02-12	0.9	2	3.7	0.3	16000	11000	1.9	0.6	52.6	37.6
UZ-02-13	1.0	2	2.0	0.1	1810	120	1.9	0.6	107.0	76.3
UZ-02-14	1.0	3	2.1	0.1	1520	130	3.4	0.3	100.3	58.7
UZ-02-15	13.5	65	24.8	1.9	516	93	2.5	0.5	113.1	18.4
UZ-02-16	2.2	4	3.0	0.2	2430	270	2.9	0.2	148.5	75.9
UZ-02-17	19.9	81	33.8	4.2	22000	16000	2.4	0.7	122.2	22.2
UZ-02-18	1.0	4	2.5	0.2	30900	7600	1.9	0.6	87.1	44.4
UZ-02-19	0.9	2	2.4	0.1	1170	140	2.6	0.6	82.2	58.5
UZ-02-20	1.1	5	1.9	0.1	1870	260	3.0	0.1	123.7	56.3
UZ-02-21	2.4	5	2.2	0.1	1390	150	2.2	0.3	231.3	105.9
UZ-02-22	1.1	2	1.9	0.1	2350	180	3.4	0.3	116.4	83.0
UZ-02-23	1.2	3	2.2	0.2	1770	120	3.2	0.2	115.2	67.5
UZ-02-24	3.1	6	2.0	0.1	3230	200	2.9	0.2	329.6	138.3
UZ-02-25	2.1	3	3.7	0.2	18300	7200	3.0	0.8	117.6	68.7
UZ-02-26	18.1	28	17.6	1.3	520	130	2.2	0.3	212.7	45.8
UZ-02-27	0.7	2	2.0	0.2	1910	140	2.4	0.2	77.8	55.6
UZ-02-28	1.5	4	2.4	0.3	9400	4900	3.4	0.3	125.6	65.6
UZ-02-29	3.2	5	2.5	0.1	30000	11000	2.3	0.5	270.7	123.3
UZ-02-30	1.3	3	2.6	0.2	3080	320	2.1	0.5	102.3	60.1
UZ-02-31	1.2	3	2.2	0.1	2730	450	2.1	0.5	110.5	64.5
UZ-02-32	6.6	18	20.1	1.3	540	130	2.8	0.2	68.3	17.4
UZ-04-1	24.8	100	27.2	1.2	3140	290	2.0	0.3	199.4	23.7
UZ-04-2	38.8	105	37.6	1.7	5370	460	2.0	0.3	225.6	26.4
UZ-04-3	26.7	97	46.2	2.1	6030	410	2.0	0.3	126.5	15.3
UZ-04-4	32.3	170	34.6	1.6	5390	430	2.0	0.3	204.1	20.6
UZ-04-5	4.0	16	5.9	0.4	24500	3600	1.7	0.3	149.8	39.2
UZ-04-6	25.1	83	32.8	1.2	6260	460	1.7	0.3	167.8	20.9

UZ-04-7	7.0	24	9.6	0.5	3410	500	1.7	0.2	159.4	34.6
UZ-04-8	27.4	67	35.6	1.4	5520	400	1.9	0.3	168.5	23.0
UZ-04-9	41.2	57	46.0	2.2	8820	580	1.4	0.2	196.2	29.1
UZ-04-10	30.6	81	28.6	1.3	4020	320	1.9	0.3	234.0	30.1
UZ-04-11	15.8	35	35.8	2.3	25600	6600	2.2	0.3	96.5	18.0
UZ-04-12	29.4	70	36.0	1.5	3120	330	1.8	0.3	178.5	24.1
UZ-04-13	44.1	95	51.4	2.1	6140	380	1.8	0.2	187.8	22.5
UZ-04-14	27.7	58	39.7	1.9	6130	500	1.8	0.4	152.6	22.5
UZ-04-15	18.1	34	16.3	1.2	530	250	1.5	0.3	243.3	46.8
UZ-04-16	5.0	18	9.6	0.4	BLOD	BLOD	1.3	0.4	113.0	27.6
UZ-04-17	28.0	76	30.7	1.3	5520	390	1.9	0.2	199.3	26.1
UZ-04-18	28.4	74	30.7	1.4	6040	440	1.8	0.3	202.3	27.0
UZ-04-19	30.5	49	34.0	1.6	6470	490	2.1	0.3	196.1	30.9
UZ-04-20	34.9	100	39.2	2.3	8000	540	2.1	0.3	194.7	24.3
UZ-04-21	27.5	102	36.4	1.6	5770	460	2.0	0.2	165.6	19.5
UZ-04-22	23.8	39	51.2	3.1	5520	920	1.7	0.1	101.7	18.1
UZ-04-23	42.0	79	58.2	3.3	5860	500	1.9	0.3	158.0	21.2
UZ-04-24	29.9	126	38.0	1.6	6520	380	2.1	0.2	172.2	18.8
UZ-04-25	19.9	73	25.4	1.2	3610	360	1.8	0.3	171.7	23.1
UZ-04-26	31.2	143	31.9	2.1	6450	500	2.2	0.3	213.8	24.8
UZ-05-1	10.6	28	10.6	0.6	BLOD	BLOD	1.8	0.1	207.9	41.5
UZ-05-2	17.3	17	19.7	1.0	1510	430	2.1	0.8	183.3	45.9
UZ-05-3	58.3	114	98.2	4.0	900	340	1.8	0.4	124.0	13.5
UZ-05-4	22.7	61	20.9	0.8	620	300	1.9	0.2	226.5	31.4
UZ-05-5	6.9	7	11.7	0.8	19000	4100	1.6	0.0	123.5	47.7
UZ-05-6	27.6	60	33.3	1.6	1070	330	1.7	0.4	173.5	24.8
UZ-05-7	14.5	49	9.3	0.4	780	330	1.2	0.3	326.1	50.0
UZ-05-8	10.9	23	22.7	2.3	2840	790	1.3	0.1	100.5	23.6
UZ-05-9	20.9	21	18.8	1.3	1660	350	1.2	0.3	232.1	53.8
UZ-05-10	9.4	28	6.5	0.3	840	380	1.3	0.2	302.8	60.3

UZ-05-11	31.1	71	37.8	1.8	4700	1200	1.3	0.3	171.8	22.9
UZ-05-12	27.1	60	44.8	1.4	1350	360	1.3	0.4	126.4	17.4
UZ-05-13	14.8	37	14.3	0.9	1160	320	1.3	0.5	216.2	38.9
UZ-05-14	4.2	12	12.0	0.4	710	330	1.0	0.1	73.3	21.5
UZ-05-15	13.6	40	21.9	1.3	BLOD	BLOD	1.1	0.2	130.1	22.5
UZ-05-16	25.2	40	29.7	1.4	BLOD	BLOD	1.2	0.3	177.4	30.0
UZ-05-17	26.4	74	17.9	1.2	BLOD	BLOD	1.2	0.3	308.7	43.0
UZ-05-18	18.6	33	14.4	0.7	970	310	1.5	0.5	270.0	50.0
UZ-05-19	8.9	27	11.3	0.5	860	300	1.2	0.2	165.4	33.2
UZ-05-20	9.6	35	17.3	1.2	870	350	2.2	0.3	116.0	21.6
UZ-05-21	6.4	29	7.6	0.5	BLOD	BLOD	2.2	0.6	176.7	35.1
UZ-05-22	3.6	15	4.5	0.3	BLOD	BLOD	1.2	0.3	169.2	45.1
UZ-05-23	9.5	51	13.1	0.7	1090	400	2.3	0.7	151.7	23.6
UZ-05-24	17.2	23	35.6	3.4	6500	2200	2.7	0.3	100.8	23.4
UZ-05-25	19.1	48	18.7	1.4	990	350	2.1	0.7	213.6	35.6
UZ-05-26	12.4	49	13.3	0.7	BLOD	BLOD	1.5	0.2	194.0	30.5
UZ-05-27	6.1	28	10.5	0.6	BLOD	BLOD	1.6	0.3	122.0	24.4
UZ-05-28	19.6	48	21.4	1.8	BLOD	BLOD	1.6	0.3	191.1	32.7
UZ-05-29	14.7	41	12.8	0.8	27400	2300	1.1	0.2	238.9	41.2
UZ-05-30	11.3	21	14.7	0.6	BLOD	BLOD	1.8	0.6	161.4	36.4
UZ-05-31	17.4	32	16.1	1.2	830	240	1.6	0.2	226.0	44.2
UZ-07-1	20.6	74	40.7	1.3	BLOD	BLOD	1.2	0.3	105.6	13.3
UZ-07-2	23.8	63	32.4	1.1	480	310	1.2	0.3	153.3	20.8
UZ-07-3	13.7	50	33.8	1.3	BLOD	BLOD	1.1	0.2	84.5	12.8
UZ-07-4	18.2	73	29.5	1.5	BLOD	BLOD	0.9	0.2	129.2	17.2
UZ-07-5	19.7	68	44.4	1.5	BLOD	BLOD	0.9	0.2	92.8	12.2
UZ-07-6	19.3	94	30.2	1.4	BLOD	BLOD	1.1	0.2	133.7	15.9
UZ-07-7	27.7	61	43.7	1.8	600	280	1.2	0.2	132.3	18.5
UZ-07-8	14.6	56	32.0	1.6	850	290	1.1	0.2	95.4	14.1
UZ-07-9	15.1	63	25.5	1.2	BLOD	BLOD	1.4	0.3	123.6	17.3

UZ-07-10	2.4	12	2.5	0.2	9190	760	1.5	0.2	199.7	60.3
UZ-07-11	27.6	114	38.3	1.7	550	320	1.7	0.3	150.6	16.6
UZ-07-12	20.0	83	33.0	1.8	2260	470	1.1	0.3	126.6	16.2
UZ-07-13	40.5	169	61.6	2.2	4800	1600	1.4	0.3	137.5	12.7
UZ-07-14	11.2	53	19.2	0.8	BLOD	BLOD	0.8	0.2	121.8	18.1
UZ-07-15	26.7	91	42.8	2.1	BLOD	BLOD	1.5	0.2	130.4	15.9
UZ-07-16	14.8	53	17.7	0.7	830	280	1.2	0.2	174.2	25.8
UZ-07-17	19.1	93	32.6	1.4	BLOD	BLOD	1.3	0.3	122.6	14.5
UZ-07-18	23.8	81	39.5	1.5	BLOD	BLOD	1.1	0.3	125.7	15.5
UZ-07-19	24.3	100	37.8	1.4	520	240	1.0	0.3	134.5	15.2
UZ-07-20	19.9	78	31.6	1.0	690	270	1.0	0.2	131.6	16.2
UZ-07-21	13.4	57	32.4	1.4	BLOD	BLOD	0.9	0.2	86.1	12.4
UZ-07-22	15.7	78	21.5	0.7	BLOD	BLOD	1.2	0.3	152.9	19.0
UZ-07-23	3.9	19	4.5	0.2	1710	340	1.2	0.2	183.5	43.4
UZ-07-24	24.5	126	40.7	1.6	640	300	1.1	0.3	125.7	13.1
UZ-07-25	19.6	80	24.5	1.1	640	270	1.0	0.3	166.9	21.1
UZ-07-26	26.6	107	46.5	2.6	BLOD	BLOD	1.0	0.2	119.7	14.1
UZ-07-27	24.7	93	50.1	3.3	BLOD	BLOD	1.2	0.2	102.9	13.2
UZ-07-28	22.4	81	38.2	1.7	BLOD	BLOD	1.0	0.3	122.3	15.3
UZ-07-29	21.5	100	39.7	1.6	BLOD	BLOD	1.3	0.4	113.4	12.9
UZ-07-30	13.4	63	28.2	1.5	BLOD	BLOD	1.3	0.3	99.3	14.1
UZ-07-31	15.5	74	22.9	0.9	BLOD	BLOD	1.4	0.3	141.4	18.2
UZ-07-32	24.1	91	43.6	1.7	520	250	1.2	0.3	115.5	13.6
UZ-07-33	25.1	106	44.0	2.2	BLOD	BLOD	1.1	0.2	119.2	13.8
UZ-07-34	19.5	86	40.9	1.7	BLOD	BLOD	1.2	0.3	99.8	12.1
UZ-07-35	25.3	78	49.4	2.7	540	320	1.2	0.2	107.1	14.0
UZ-07-36	22.5	113	30.4	2.0	BLOD	BLOD	1.5	0.3	154.9	18.7
UZ-07-37	20.5	44	38.2	2.0	1630	330	1.3	0.3	112.4	18.4
UZ-07-38	23.2	74	49.5	2.2	BLOD	BLOD	1.1	0.6	98.0	12.7
UZ-07-39	21.7	97	22.9	3.4	275000	39000	1.1	0.3	198.1	36.4

UZ-07-40	19.9	94	38.1	2.0	BLOD	BLOD	1.2	0.2	109.2	13.3
UZ-07-41	21.1	62	32.3	1.2	BLOD	BLOD	1.2	0.2	136.6	18.8
UZ-08-1	6.5	20	7.8	0.3	720	270	0.8	0.3	174.7	40.2
UZ-08-2	5.1	15	4.5	0.3	670	340	0.9	0.1	235.0	63.7
UZ-08-3	9.2	8	10.4	0.6	2360	770	0.8	0.2	185.8	66.9
UZ-08-4	22.1	37	46.0	2.2	1060	310	1.6	0.5	100.5	17.6
UZ-08-5	45.8	49	79.3	4.9	1680	380	1.5	0.4	120.7	19.3
UZ-08-6	4.2	7	4.0	0.3	970	270	1.6	0.6	218.0	84.2
UZ-08-7	8.7	10	15.2	1.0	128000	18000	1.2	0.5	119.6	38.8
UZ-08-8	3.5	18	2.9	0.1	610	350	1.8	0.6	255.1	62.1
UZ-08-9	5.4	4	9.6	0.6	2530	560	1.6	0.5	117.7	59.5
UZ-08-10	4.8	10	4.0	0.4	1110	340	1.7	0.3	254.2	84.0
UZ-08-11	6.8	15	5.0	0.4	3300	1400	1.6	0.3	283.2	76.6
UZ-08-12	7.6	17	6.8	0.5	41400	7500	1.6	0.1	233.7	60.0
UZ-08-13	3.5	14	3.3	0.2	610	270	1.2	0.2	223.7	61.8
UZ-08-14	7.9	19	12.1	0.9	83000	14000	1.2	0.4	135.7	33.2
UZ-08-15	4.7	12	8.6	0.7	75000	15000	0.7	0.2	114.9	34.6
UZ-08-16	2.8	14	3.9	0.3	720	250	1.4	0.3	150.7	41.9
UZ-08-17	8.6	20	7.1	0.4	940	310	1.3	0.3	252.0	59.2
UZ-08-18	3.0	6	5.9	0.3	4300	1700	1.4	0.3	105.7	43.6
UZ-08-19	6.1	8	5.6	0.3	660	250	1.2	0.2	229.0	82.1
UZ-08-20	3.0	10	3.5	0.2	600	240	1.5	0.2	182.6	59.0
UZ-08-21	9.6	10	6.1	0.4	920	280	1.5	0.2	331.9	108.4
UZ-08-22	12.9	32	12.3	0.8	BLOD	BLOD	1.5	0.2	219.3	42.1
UZ-08-23	15.5	15	14.4	2.2	2390	630	1.4	0.4	225.6	68.2
UZ-08-24	4.0	7	3.8	0.2	490	250	1.2	0.1	222.7	85.2
UZ-08-25	7.9	11	7.4	0.5	620	260	1.3	0.3	222.3	69.0
UZ-08-26	2.8	15	4.6	0.3	660	280	1.7	0.5	126.6	33.7
UZ-08-27	5.8	12	5.3	0.3	6100	1200	1.8	0.1	228.1	67.3
UZ-08-28	2.2	3	11.0	0.9	1630	330	1.5	0.3	41.3	24.2

UZ-08-29	5.1	20	5.8	0.3	BLOD	BLOD	1.7	0.5	182.3	42.1
UZ-08-30	6.1	21	5.3	0.2	BLOD	BLOD	1.8	0.1	241.9	54.5
UZ-08-31	7.9	16	8.8	0.5	23000	5300	1.8	0.3	188.5	48.6
UZ-08-32	8.1	29	8.7	0.4	BLOD	BLOD	1.4	0.3	194.4	37.6
UZ-08-33	5.0	8	13.3	0.8	700	280	1.9	0.2	77.7	28.0
UZ-08-34	2.7	4	4.0	0.3	490	250	1.4	0.4	137.4	69.5
UZ-08-35	11.3	14	7.8	0.5	590	270	1.3	0.3	301.1	83.8
UZ-08-36	5.7	11	13.9	0.7	BLOD	BLOD	1.4	0.2	85.3	26.3
UZ-08-37	6.0	6	12.5	1.1	950	340	1.3	0.3	100.9	42.3
UZ-09-1	53.2	37	74.4	3.3	930	240	2.2	0.5	149.4	26.0
UZ-09-2	31.2	39	77.8	4.1	BLOD	BLOD	1.8	0.6	83.7	14.5
UZ-09-3	16.5	33	24.6	1.1	740	260	2.0	0.3	139.8	25.7
UZ-09-4	17.4	28	56.9	3.5	14100	8700	1.5	0.3	63.8	12.9
UZ-09-5	30.5	40	66.8	2.4	890	290	2.7	0.7	95.6	15.9
UZ-09-6	47.4	37	120.8	8.8	33600	7700	2.0	0.6	82.0	15.1
UZ-09-7	52.3	75	141.4	5.3	810	280	1.3	0.4	77.4	9.8
UZ-09-8	40.6	49	161.0	10.0	BLOD	BLOD	1.5	0.3	52.6	8.4
UZ-09-9	50.3	30	114.4	7.7	770	390	2.6	0.5	91.9	18.2
UZ-09-10	33.4	29	97.7	6.1	66000	19000	2.0	0.2	71.4	14.2
UZ-09-11	42.3	48	79.4	5.7	760	290	1.8	0.6	111.3	18.4
UZ-09-12	5.3	32	8.1	0.4	670	290	1.6	0.4	136.6	25.6
UZ-10-1	3.8	13	21.1	1.4	BLOD	BLOD	1.0	0.2	37.4	10.7
UZ-10-2	3.3	11	19.1	1.2	690	330	1.1	0.3	35.7	11.1
UZ-10-3	11.2	30	26.8	1.8	560	320	1.2	0.2	87.5	17.3
UZ-10-4	3.2	7	12.0	0.9	4540	720	1.0	0.3	55.8	21.6
UZ-10-5	3.3	13	9.4	0.4	760	270	0.9	0.2	74.4	21.1
UZ-10-6	5.1	13	9.6	0.4	BLOD	BLOD	1.6	0.5	109.8	31.1
UZ-10-7	4.7	15	20.9	1.3	630	320	1.2	0.3	47.0	12.6
UZ-10-8	3.5	9	13.8	0.8	BLOD	BLOD	1.5	0.5	53.3	18.1
UZ-10-9	2.0	7	9.7	0.4	BLOD	BLOD	0.8	0.1	43.4	16.6

UZ-10-10	2.8	9	10.3	0.5	BLOD	BLOD	1.1	0.2	57.4	19.5
UZ-10-11	4.4	14	20.6	1.4	1160	330	1.4	0.4	44.9	12.5
UZ-10-12	3.8	12	8.2	0.4	640	260	1.3	0.3	96.8	28.6
UZ-10-13	4.1	17	9.9	0.6	BLOD	BLOD	0.9	0.3	86.2	21.8
UZ-10-14	6.7	11	18.1	1.6	750	290	0.8	0.2	77.7	24.6
UZ-10-15	4.2	8	18.0	1.8	1140	400	1.3	0.2	48.8	18.0
UZ-10-16	1.0	2	5.1	0.3	740	300	0.2	0.2	40.8	28.9
UZ-10-17	4.7	18	17.9	2.4	BLOD	BLOD	1.3	0.3	54.7	15.0
UZ-10-18	1.6	8	8.6	0.5	BLOD	BLOD	1.3	0.4	38.1	13.7
UZ-10-19	1.6	3	37.0	4.6	89000	43000	1.3	0.4	8.8	5.2
UZ-10-20	4.6	19	13.8	0.8	BLOD	BLOD	1.7	0.5	69.3	16.7
UZ-10-21	3.5	18	11.2	0.7	560	270	1.2	0.3	65.3	16.1
UZ-10-22	1.3	4	10.2	0.5	950	330	1.1	0.4	27.5	13.8
UZ-10-23	2.2	6	7.4	0.4	BLOD	BLOD	1.0	0.2	61.9	25.6
UZ-10-24	5.1	27	17.1	0.8	560	250	1.4	0.4	62.5	12.6
UZ-10-25	3.7	13	11.3	0.8	BLOD	BLOD	1.2	0.1	67.8	19.5
UZ-10-26	1.4	5	10.2	0.6	460	250	1.3	0.1	28.6	12.9
UZ-10-27	1.7	6	11.9	0.6	BLOD	BLOD	1.2	0.3	29.3	12.1
UZ-10-28	5.1	18	15.3	1.2	770	330	1.3	0.2	69.4	17.4
UZ-10-29	2.9	9	19.6	1.6	650	300	1.4	0.1	31.2	10.8
UZ-11-1	10.2	24	11.1	0.6	BLOD	BLOD	1.2	0.2	192.6	41.5
UZ-11-2	14.8	30	14.3	0.6	550	300	1.0	0.2	216.6	41.5
UZ-11-3	8.5	26	12.9	0.7	750	340	1.3	0.2	136.9	28.4
UZ-11-4	22.4	24	47.9	9.1	BLOD	BLOD	1.0	0.2	97.7	27.5
UZ-11-5	13.4	44	12.1	0.5	BLOD	BLOD	1.1	0.2	231.7	37.1
UZ-11-6	19.1	32	15.3	0.9	14300	4400	1.6	0.2	261.2	49.7
UZ-11-7	7.9	34	11.7	0.6	660	310	0.9	0.2	141.7	25.8
UZ-11-8	19.1	33	32.3	1.4	BLOD	BLOD	1.2	0.2	123.8	22.7
UZ-11-9	4.6	21	5.3	0.4	BLOD	BLOD	1.1	0.2	183.7	42.8
UZ-11-10	28.2	50	50.2	1.7	810	320	1.1	0.2	117.3	17.6

UZ-11-11	11.7	14	13.6	0.5	BLOD	BLOD	1.3	0.1	179.6	49.0
UZ-11-12	7.6	14	9.5	0.5	BLOD	BLOD	1.2	0.1	167.4	45.9
UZ-11-13	10.8	18	14.2	0.6	BLOD	BLOD	0.9	0.2	159.1	38.6
UZ-11-14	7.1	8	22.4	2.7	930	320	1.1	0.3	65.9	24.7
UZ-11-15	24.7	43	25.3	1.8	BLOD	BLOD	1.0	0.2	204.2	35.2
UZ-11-16	8.3	18	16.8	1.6	BLOD	BLOD	1.1	0.2	103.3	26.6
UZ-11-17	66.2	105	161.3	5.4	730	310	1.2	0.2	85.7	9.4
UZ-11-18	13.3	55	13.4	1.0	BLOD	BLOD	1.2	0.2	206.1	32.5
UZ-11-19	54.2	90	92.9	2.7	1300	430	1.2	0.2	121.9	14.1
UZ-11-20	5.1	16	4.0	0.2	720	360	1.2	0.3	266.5	68.5
UZ-11-21	14.9	33	14.0	0.7	BLOD	BLOD	0.9	0.1	221.2	40.8
UZ-11-22	33.1	62	52.2	2.0	BLOD	BLOD	1.1	0.2	132.6	18.3
UZ-11-23	61.4	61	95.6	3.5	610	320	1.3	0.2	134.3	18.6
UZ-11-24	44.2	54	63.4	3.7	BLOD	BLOD	1.1	0.2	145.6	22.2
UZ-11-25	26.0	56	42.0	1.1	850	370	1.1	0.2	129.6	18.3
UZ-11-26	14.0	36	13.3	0.6	BLOD	BLOD	1.1	0.2	220.0	38.9
UZ-11-27	31.1	56	42.2	2.1	BLOD	BLOD	1.1	0.2	153.9	22.7
UZ-11-28	37.3	50	51.7	2.1	BLOD	BLOD	1.2	0.2	150.9	22.9
UZ-11-29	6.6	16	13.4	0.8	700	360	1.2	0.2	103.4	26.9
UZ-11-30	25.8	60	37.5	1.8	BLOD	BLOD	1.1	0.2	143.6	20.5
UZ-11-31	10.1	25	12.1	0.6	BLOD	BLOD	1.2	0.3	173.0	36.3
UZ-11-32	11.9	43	22.1	1.5	BLOD	BLOD	1.0	0.2	112.9	19.3
UZ-11-33	15.9	38	13.4	0.5	580	300	1.1	0.2	248.4	42.5
UZ-11-34	11.5	31	13.4	0.6	BLOD	BLOD	1.0	0.3	179.6	34.0
UZ-11-35	2.3	5	65.9	5.5	BLOD	BLOD	1.0	0.3	7.3	3.3
UZ-11-36	20.2	63	47.9	3.5	3700	1600	1.1	0.2	88.3	13.3
UZ-11-37	9.4	17	11.1	0.5	850	380	1.1	0.1	176.4	44.0
UZ-11-38	10.7	51	13.1	0.5	670	340	1.3	0.3	171.4	25.8
UZ-11-39	12.7	18	18.6	0.8	BLOD	BLOD	1.0	0.2	142.9	34.6
UZ-11-40	16.0	21	14.7	0.7	BLOD	BLOD	1.2	0.2	227.6	51.4

UZ-12-1	14.7	47	15.9	0.8	410	180	1.3	0.3	197.7	31.2
UZ-12-2	13.9	24	29.2	1.4	930	240	1.7	0.2	101.6	21.6
UZ-12-3	11.8	35	15.6	0.8	BLOD	BLOD	1.6	0.1	161.8	29.1
UZ-12-4	13.9	23	14.7	0.6	BLOD	BLOD	1.5	0.2	201.2	43.4
UZ-12-5	23.4	68	30.8	1.8	BLOD	BLOD	1.5	0.3	162.7	22.7
UZ-12-6	23.0	53	22.6	1.1	490	240	1.4	0.3	217.3	32.7
UZ-12-7	9.6	19	15.6	0.7	BLOD	BLOD	1.3	0.2	131.7	31.2
UZ-12-8	15.4	22	18.7	0.6	400	210	1.5	0.2	175.8	38.4
UZ-12-9	8.9	26	14.8	0.7	BLOD	BLOD	1.4	0.1	128.5	26.5
UZ-12-10	35.2	69	50.1	2.9	BLOD	BLOD	1.5	0.3	150.0	20.8
UZ-12-11	26.8	61	51.1	2.3	BLOD	BLOD	1.4	0.2	112.0	15.8
UZ-12-12	15.0	32	17.2	0.8	BLOD	BLOD	1.4	0.3	187.1	34.8
UZ-12-13	20.2	34	41.8	3.0	BLOD	BLOD	1.7	0.2	103.5	19.6
UZ-12-14	13.0	31	12.4	0.6	BLOD	BLOD	1.6	0.2	223.6	42.2
UZ-12-15	13.4	28	16.0	0.8	490	160	1.6	0.3	179.1	35.5
UZ-12-16	6.8	21	9.7	0.6	BLOD	BLOD	1.4	0.4	150.6	34.7
UZ-12-17	28.9	61	32.5	2.5	390	260	1.5	0.3	190.0	29.3
UZ-12-18	29.7	39	47.6	2.0	620	250	1.4	0.3	133.3	22.6
UZ-12-19	8.9	16	16.8	0.8	530	180	1.6	0.2	113.1	29.0
UZ-12-20	8.8	17	11.1	0.6	BLOD	BLOD	1.6	0.2	169.2	42.4
UZ-12-21	8.0	23	30.9	2.4	1050	210	1.4	0.3	55.0	12.4
UZ-12-22	8.0	19	14.9	0.7	BLOD	BLOD	1.6	0.2	114.3	27.1
UZ-12-23	23.5	64	21.0	1.0	BLOD	BLOD	1.2	0.3	239.0	33.0
UZ-12-24	13.6	53	16.5	0.7	BLOD	BLOD	1.6	0.5	176.2	26.2
UZ-12-25	10.4	23	16.0	0.6	BLOD	BLOD	1.5	0.3	138.4	29.8
UZ-12-26	19.4	53	35.7	1.8	BLOD	BLOD	1.7	0.3	116.0	17.5
UZ-12-27	8.8	16	22.7	0.8	BLOD	BLOD	1.2	0.3	83.4	21.3
UZ-12-28	27.3	65	31.6	3.6	BLOD	BLOD	1.7	0.3	184.9	31.9
UZ-12-29	12.0	44	17.4	1.0	540	240	1.3	0.4	147.9	24.4
UZ-12-30	14.7	43	15.1	0.8	BLOD	BLOD	1.3	0.3	207.0	34.1

UZ-12-31	7.8	21	15.8	1.2	680	250	1.5	0.3	106.0	24.8
UZ-12-32	13.6	29	19.1	1.0	BLOD	BLOD	1.3	0.2	152.7	30.0
UZ-12-33	11.5	41	24.5	1.5	450	210	1.6	0.2	100.5	17.3
UZ-12-34	17.0	55	16.4	0.8	450	310	1.5	0.2	221.8	32.8
UZ-12-35	7.5	21	13.3	0.6	4140	400	1.5	0.2	119.4	27.0
UZ-12-36	27.6	66	39.2	1.8	BLOD	BLOD	1.5	0.4	150.4	20.5
UZ-12-37	16.3	50	18.5	1.3	1750	400	1.3	0.3	187.9	30.5
UZ-12-38	9.6	32	14.4	0.6	930	230	1.4	0.5	142.0	26.3
UZ-12-39	24.3	61	14.7	0.5	BLOD	BLOD	1.3	0.3	353.6	48.5
UZ-12-40	12.8	63	19.2	0.9	BLOD	BLOD	1.4	0.3	141.7	19.7
UZ-12-41	10.8	30	13.1	0.5	BLOD	BLOD	1.5	0.3	177.2	33.7
UZ-12-42	15.7	49	15.9	0.8	BLOD	BLOD	1.4	0.3	211.6	32.8
UZ-12-43	7.9	23	17.5	1.0	BLOD	BLOD	1.6	0.4	96.6	21.2
UZ-13-1	13.6	32	38.6	2.0	BLOD	BLOD	1.1	0.2	75.2	14.1
UZ-13-2	12.4	36	36.7	1.6	BLOD	BLOD	1.0	0.3	72.1	12.7
UZ-13-3	18.6	55	26.0	1.3	640	310	1.0	0.2	153.2	22.8
UZ-13-4	6.7	22	5.6	0.3	BLOD	BLOD	1.2	0.2	256.4	57.1
UZ-13-5	0.7	1	0.6	0.0	BLOD	BLOD	1.5	0.5	279.2	280.2
UZ-13-6	22.0	67	21.8	0.7	BLOD	BLOD	1.1	0.2	215.8	28.3
UZ-13-7	41.2	78	134.0	11.0	BLOD	BLOD	1.1	0.3	65.7	9.5
UZ-13-8	13.2	44	19.6	1.0	BLOD	BLOD	1.1	0.2	144.1	23.5
UZ-13-9	11.1	11	27.2	1.1	600	370	1.2	0.2	87.4	26.8
UZ-13-10	15.5	23	32.9	1.3	BLOD	BLOD	1.1	0.2	100.9	21.7
UZ-13-11	12.7	24	154.0	14.0	BLOD	BLOD	0.9	0.2	17.6	4.0
UZ-13-12	24.6	64	35.0	1.8	BLOD	BLOD	1.2	0.3	150.0	21.0
UZ-13-13	9.6	9	32.6	1.4	580	280	1.2	0.2	63.0	21.3
UZ-13-14	15.8	55	36.0	1.8	BLOD	BLOD	1.1	0.3	94.0	14.0
UZ-13-15	15.3	25	30.8	1.2	BLOD	BLOD	1.5	0.6	105.9	21.9
UZ-13-16	27.0	58	40.3	1.6	960	320	1.2	0.2	143.4	20.4
UZ-13-17	3.4	6	3.2	0.2	BLOD	BLOD	1.0	0.2	227.1	93.8

UZ-13-18	31.5	64	34.3	1.4	2850	370	1.2	0.4	196.3	26.8
UZ-13-19	18.8	22	23.0	1.4	BLOD	BLOD	1.0	0.3	174.8	39.3
UZ-13-20	14.9	48	22.8	1.1	BLOD	BLOD	0.9	0.3	139.3	21.8
UZ-13-21	9.5	42	12.0	0.8	BLOD	BLOD	0.9	0.2	168.6	28.9
UZ-13-22	5.7	9	15.2	1.4	BLOD	BLOD	1.0	0.3	80.8	28.1
UZ-13-23	17.9	30	34.4	2.8	790	320	1.2	0.3	111.4	22.6
UZ-13-24	24.6	49	32.7	1.9	BLOD	BLOD	1.3	0.3	160.5	25.5
UZ-13-25	26.4	44	22.5	1.6	890	420	1.1	0.3	251.2	42.9
UZ-13-26	30.6	48	30.8	2.2	BLOD	BLOD	1.3	0.4	212.5	35.1
UZ-13-27	18.9	55	29.4	1.4	BLOD	BLOD	1.1	0.3	137.3	20.3
UZ-13-28	11.0	26	12.5	0.6	BLOD	BLOD	1.3	0.2	188.2	38.5
UZ-13-29	11.2	19	16.5	0.7	BLOD	BLOD	1.0	0.3	145.9	34.4
UZ-13-30	23.5	53	28.9	1.2	BLOD	BLOD	1.2	0.2	173.7	25.8
UZ-13-31	18.1	36	26.8	1.1	BLOD	BLOD	1.1	0.3	144.7	25.4
UZ-13-32	7.5	13	14.3	0.8	BLOD	BLOD	1.3	0.2	111.5	31.8
UZ-13-33	18.7	21	33.5	1.7	1130	320	0.9	0.2	119.1	27.1
UZ-13-34	11.1	9	20.5	1.1	BLOD	BLOD	1.7	0.2	115.3	39.2
UZ-13-35	15.5	47	30.3	3.2	BLOD	BLOD	1.2	0.2	109.2	20.1
UZ-13-36	27.2	29	50.7	2.2	BLOD	BLOD	1.0	0.3	114.8	22.3
UZ-13-37	17.3	38	28.9	1.3	BLOD	BLOD	1.3	0.2	128.3	22.1
UZ-13-38	29.8	41	52.5	3.2	BLOD	BLOD	1.1	0.2	121.4	20.9
UZ-13-39	13.5	40	36.8	1.4	BLOD	BLOD	1.1	0.2	78.7	13.1
UZ-13-40	10.1	30	12.6	0.6	BLOD	BLOD	1.2	0.2	172.1	33.0
UZ-14-1	16.2	86	23.9	1.0	BLOD	BLOD	1.1	0.2	125.2	15.2
UZ-14-2	9.3	30	11.3	0.5	BLOD	BLOD	1.0	0.2	153.3	29.4
UZ-14-3	4.8	38	4.9	0.3	BLOD	BLOD	1.1	0.2	179.6	31.4
UZ-14-4	8.3	35	9.9	1.5	BLOD	BLOD	0.9	0.2	155.2	35.7
UZ-14-5	5.2	28	9.3	0.5	BLOD	BLOD	1.2	0.3	104.3	20.7
UZ-14-6	13.4	53	21.3	1.1	BLOD	BLOD	1.1	0.5	116.5	17.7
UZ-14-7	11.6	67	17.1	0.8	BLOD	BLOD	0.9	0.2	125.9	17.1

UZ-14-8	16.5	77	14.6	0.6	BLOD	BLOD	0.9	0.2	209.3	26.4
UZ-14-9	26.2	111	42.7	1.5	BLOD	BLOD	1.0	0.2	113.6	12.3
UZ-14-10	3.1	11	6.8	0.3	BLOD	BLOD	0.8	0.2	85.4	26.2
UZ-14-11	9.3	32	12.3	0.6	BLOD	BLOD	1.0	0.2	140.2	26.2
UZ-14-12	13.1	51	25.8	1.3	BLOD	BLOD	1.1	0.1	93.7	14.4
UZ-14-13	13.4	62	21.7	1.2	BLOD	BLOD	1.0	0.3	114.4	16.4
UZ-14-14	5.2	35	11.6	0.5	BLOD	BLOD	1.4	0.2	82.1	14.7
UZ-14-15	10.9	48	16.1	0.7	BLOD	BLOD	1.1	0.2	125.1	19.4
UZ-14-16	14.5	43	20.0	1.1	1230	400	1.0	0.2	134.0	22.3
UZ-14-17	11.5	48	27.0	1.2	1520	630	1.0	0.2	78.6	12.2
UZ-14-18	17.4	55	24.2	0.9	1650	620	1.0	0.4	133.0	19.3
UZ-14-19	11.3	32	11.7	0.5	10700	820	1.0	0.2	177.6	33.0
UZ-14-20	7.6	28	10.6	0.8	9400	1400	1.1	0.2	131.3	27.0
UZ-14-21	11.2	42	10.9	0.6	960	450	1.0	0.2	188.9	32.0
UZ-14-22	4.5	20	7.2	0.5	1020	570	0.8	0.1	116.1	27.6
UZ-14-23	8.9	37	8.5	0.4	BLOD	BLOD	1.5	0.3	194.2	33.7
UZ-14-24	8.4	50	11.2	0.5	BLOD	BLOD	0.8	0.2	139.0	21.2
UZ-14-25	9.8	40	9.3	0.5	3900	1100	1.1	0.2	195.3	33.3
UZ-14-26	14.7	56	22.1	1.3	BLOD	BLOD	1.0	0.3	123.2	18.6
UZ-14-27	17.7	84	17.3	0.9	BLOD	BLOD	0.9	0.2	189.9	23.9
UZ-14-28	12.8	65	17.9	1.0	BLOD	BLOD	1.4	0.4	132.3	18.5
UZ-14-29	15.0	60	26.2	1.0	BLOD	BLOD	1.1	0.1	105.9	14.8
UZ-14-30	16.2	63	16.4	0.7	BLOD	BLOD	0.9	0.2	181.9	25.3
UZ-14-31	10.0	45	16.1	0.8	BLOD	BLOD	1.0	0.3	115.6	18.7
UZ-14-32	8.5	28	15.4	0.8	BLOD	BLOD	1.0	0.2	101.9	20.3
UZ-15-1	4.0	37	5.6	0.3	BLOD	BLOD	1.5	0.4	131.0	23.0
UZ-15-2	15.9	62	28.4	1.9	BLOD	BLOD	1.6	0.7	103.8	15.4
UZ-15-3	7.5	43	6.5	0.4	BLOD	BLOD	1.5	0.4	212.8	35.4
UZ-15-4	11.1	34	14.5	0.7	BLOD	BLOD	3.3	0.0	141.6	25.8
UZ-15-5	10.4	37	8.6	0.5	BLOD	BLOD	1.6	0.4	223.5	39.9

UZ-15-6	6.2	24	8.9	0.5	BLOD	BLOD	1.2	0.4	127.9	27.4
UZ-15-7	3.7	10	7.1	0.3	BLOD	BLOD	1.8	0.2	97.6	31.3
UZ-15-8	15.5	49	17.7	0.9	BLOD	BLOD	1.7	0.2	162.3	25.3
UZ-15-9	18.3	66	35.3	1.9	BLOD	BLOD	1.7	0.4	95.9	13.4
UZ-15-10	16.4	50	26.1	1.1	BLOD	BLOD	1.2	0.6	116.4	17.7
UZ-15-11	10.5	26	15.2	0.6	BLOD	BLOD	1.0	0.4	127.8	26.1
UZ-15-12	5.1	13	7.1	0.4	BLOD	BLOD	1.1	0.2	134.3	38.4
UZ-15-13	8.3	32	7.7	0.5	BLOD	BLOD	1.6	0.6	200.5	38.4
UZ-15-14	17.2	53	23.8	1.4	BLOD	BLOD	1.7	0.4	134.0	20.7
UZ-15-15	4.8	41	7.4	0.4	BLOD	BLOD	1.4	0.2	121.6	20.5
UZ-15-16	8.9	39	7.3	0.6	BLOD	BLOD	1.4	0.5	224.9	40.7
UZ-15-17	9.3	55	5.5	0.3	BLOD	BLOD	1.6	0.4	313.5	46.9
UZ-15-18	6.8	32	9.1	0.5	BLOD	BLOD	1.6	0.3	137.3	25.9
UZ-15-19	4.8	18	8.8	0.5	BLOD	BLOD	1.6	0.3	102.2	25.0
UZ-15-20	3.9	17	6.1	0.5	BLOD	BLOD	1.9	0.4	118.2	30.3
UZ-15-21	8.7	36	13.1	0.8	BLOD	BLOD	1.5	0.1	122.2	22.1
UZ-15-22	3.9	23	7.5	0.5	2600	1100	1.2	0.2	96.1	21.2
UZ-15-23	17.1	48	32.6	1.6	BLOD	BLOD	0.9	0.4	97.2	15.3
UZ-15-24	9.4	46	7.7	0.4	16500	2700	1.3	0.2	224.1	35.6
UZ-15-25	6.0	32	10.3	0.5	BLOD	BLOD	1.2	0.7	108.6	20.3
UZ-15-26	4.8	20	5.9	0.3	BLOD	BLOD	1.6	0.3	151.4	35.1
UZ-15-27	4.4	13	4.3	0.3	BLOD	BLOD	1.6	0.2	191.2	55.1
UZ-15-28	6.0	28	8.6	0.4	690	390	1.5	0.2	129.9	25.8
UZ-15-29	10.3	24	13.5	0.7	BLOD	BLOD	1.4	0.1	141.5	30.3
UZ-15-30	16.1	36	16.0	0.7	BLOD	BLOD	2.1	0.7	186.4	32.9
UZ-15-31	6.9	35	7.2	0.3	BLOD	BLOD	1.4	0.4	179.1	31.8
UZ-15-32	15.6	62	29.3	1.4	BLOD	BLOD	1.7	0.2	98.2	13.8
UZ-15-33	5.4	24	6.5	0.4	BLOD	BLOD	NA	0.0	154.2	33.2
UZ-15-34	9.7	52	9.8	0.5	BLOD	BLOD	1.6	0.2	183.0	27.9
UZ-15-35	5.2	23	8.2	0.5	BLOD	BLOD	0.8	0.0	116.6	25.5

UZ-15-36	5.6	21	7.6	0.4	BLOD	BLOD	1.5	0.1	135.6	31.0
UZ-15-37	12.5	52	24.3	1.1	BLOD	BLOD	1.4	0.1	95.5	14.4
UZ-15-38	12.3	35	14.9	0.8	BLOD	BLOD	1.6	0.4	152.5	27.7
UZ-15-39	3.6	11	6.3	0.4	BLOD	BLOD	NA	0.0	105.4	32.6
UZ-15-40	7.9	35	13.8	0.6	BLOD	BLOD	1.6	0.2	105.2	18.8
UZ-16a-1	20.5	54	17.8	0.9	650	220	1.4	0.3	246.8	37.1
UZ-16a-2	34.8	47	43.6	1.9	BLOD	BLOD	1.2	0.2	170.4	26.7
UZ-16a-3	32.3	37	127.0	7.8	BLOD	BLOD	0.9	0.3	54.3	9.7
UZ-16a-4	6.7	9	6.5	0.3	BLOD	BLOD	0.9	0.2	219.1	74.4
UZ-16a-5	44.5	76	120.6	6.1	BLOD	BLOD	1.1	0.4	78.8	10.3
UZ-16a-6	36.5	83	27.8	1.2	BLOD	BLOD	1.3	0.2	280.5	34.7
UZ-16a-7	45.4	53	60.2	2.7	BLOD	BLOD	1.4	0.4	161.1	24.0
UZ-16a-8	10.1	25	24.5	3.1	21400	4600	0.9	0.2	87.7	21.0
UZ-16a-9	16.1	44	23.2	1.1	BLOD	BLOD	1.2	0.2	148.5	24.1
UZ-16a-10	32.4	70	44.5	2.5	BLOD	BLOD	1.1	0.4	155.5	21.3
UZ-16a-11	18.6	40	33.8	2.0	BLOD	BLOD	1.5	0.4	117.8	20.4
UZ-16a-12	38.6	72	64.6	4.3	BLOD	BLOD	1.7	0.3	127.6	17.9
UZ-16a-13	28.4	37	47.3	1.7	BLOD	BLOD	1.1	0.2	128.2	22.1
UZ-16a-14	30.2	72	37.0	1.7	BLOD	BLOD	1.3	0.3	174.4	23.0
UZ-16a-15	46.6	47	33.1	1.8	BLOD	BLOD	1.4	0.3	301.0	48.2
UZ-16a-16	17.3	24	21.6	1.6	3040	350	2.6	0.1	171.6	37.8
UZ-16a-17	25.3	13	59.2	5.6	660	280	1.5	0.4	91.5	27.0
UZ-16a-18	19.2	16	58.1	2.8	BLOD	BLOD	1.1	0.2	70.6	18.2
UZ-16a-19	32.6	63	45.7	2.6	BLOD	BLOD	1.2	0.3	152.3	21.8
UZ-16a-20	22.7	49	32.0	1.2	BLOD	BLOD	1.6	0.1	151.6	23.1
UZ-16a-21	39.5	47	59.9	3.2	BLOD	BLOD	1.4	0.5	140.8	22.5
UZ-16a-22	15.9	45	17.3	1.0	1380	220	1.5	0.2	196.4	32.2
UZ-16a-23	10.1	26	15.3	0.8	6400	2500	0.8	0.0	141.5	29.2
UZ-16a-24	39.6	50	46.6	4.2	BLOD	BLOD	1.1	0.2	181.8	31.2
UZ-16a-25	39.4	96	22.4	1.2	BLOD	BLOD	1.2	0.3	375.9	45.6

UZ-16a-26	40.4	124	40.6	2.1	600	220	1.2	0.2	212.5	23.4
UZ-16a-27	5.8	15	4.9	0.2	BLOD	BLOD	0.7	0.2	252.0	66.9
UZ-16a-28	28.2	63	56.0	2.5	620	250	1.1	0.4	107.7	15.0
UZ-16a-29	11.0	21	18.4	1.0	BLOD	BLOD	1.2	0.3	127.9	29.1
UZ-16a-30	13.6	54	3.5	0.4	1580	500	1.4	0.3	828.4	150.1
UZ-16a-31	13.1	22	36.3	1.8	BLOD	BLOD	1.3	0.3	76.9	17.1
UZ-16a-32	44.4	98	57.7	2.9	BLOD	BLOD	1.1	0.3	164.4	19.5
UZ-16a-33	14.8	32	23.8	1.1	BLOD	BLOD	1.0	0.2	132.5	24.7
UZ-16a-34	26.4	58	49.7	3.3	3300	1400	1.2	0.2	113.5	17.2
UZ-16a-35	4.4	16	5.1	0.2	BLOD	BLOD	1.6	0.7	185.2	47.4
UZ-16a-36	5.5	23	5.8	0.3	1320	410	1.4	0.3	203.0	43.9
UZ-16a-37	17.9	45	20.2	1.1	2430	450	1.7	0.3	189.9	31.0
UZ-16a-38	46.5	69	72.4	5.5	BLOD	BLOD	1.4	0.4	137.4	20.2
UZ-16a-39	25.4	67	33.6	2.1	BLOD	BLOD	1.3	0.4	161.5	23.0
UZ-16a-40	9.3	44	17.8	0.9	BLOD	BLOD	0.8	0.2	111.6	18.2
UZ-16a-41	40.2	59	40.4	2.3	BLOD	BLOD	1.4	0.4	212.9	31.3
UZ-18-1	32.9	67	41.2	2.1	1050	250	1.4	0.5	170.5	23.4
UZ-18-2	10.6	21	14.1	0.8	1590	340	1.1	0.2	161.6	36.8
UZ-18-3	12.8	22	25.1	1.2	BLOD	BLOD	1.0	0.2	109.0	24.2
UZ-18-4	9.5	19	14.5	0.5	BLOD	BLOD	1.2	0.3	139.7	32.8
UZ-18-5	38.9	76	51.9	2.6	17800	3900	1.2	0.3	160.1	20.9
UZ-19-1	15.5	20	21.9	0.9	1610	300	1.8	0.7	151.2	34.9
UZ-19-2	35.6	92	53.3	2.6	3210	440	1.7	0.2	142.7	17.3
UZ-19-3	55.2	69	56.8	4.9	3860	510	1.9	0.4	207.6	31.7
UZ-19-4	36.4	87	29.5	1.6	4170	530	1.7	0.4	264.0	33.2
UZ-19-5	21.0	61	26.8	1.1	3420	430	1.7	0.2	167.6	23.4
UZ-19-6	37.3	65	36.5	2.1	4070	440	1.7	0.3	218.2	30.9
UZ-19-7	51.1	85	62.1	2.1	3390	400	1.7	0.3	175.8	21.0
UZ-19-8	37.9	77	31.8	1.4	2940	320	1.2	0.2	254.9	32.6
UZ-19-9	35.7	123	44.7	1.8	3160	360	1.9	0.4	170.5	18.0

UZ-19-10	36.2	75	33.1	1.1	2330	450	1.6	0.3	233.6	29.4
UZ-19-11	43.0	121	43.4	2.5	19900	1100	1.9	0.6	211.6	24.1
UZ-19-12	63.2	64	50.8	2.4	2760	390	1.3	0.4	265.9	36.9
UZ-19-13	32.4	44	41.6	2.0	3160	430	1.8	0.9	166.4	27.1
UZ-19-14	48.4	118	41.0	1.8	2710	420	1.7	0.4	252.4	27.4
UZ-19-15	51.6	65	53.4	2.2	2350	390	1.6	1.3	206.7	28.1
UZ-19-16	31.2	37	20.3	2.5	2490	520	2.2	1.0	328.9	68.7
UZ-19-17	8.1	16	5.2	0.3	860	340	1.6	0.4	333.5	86.1
UZ-19-18	30.3	39	34.9	1.9	4310	550	1.6	0.4	185.7	32.2
UZ-19-19	46.1	41	36.5	1.8	2450	350	1.6	0.2	270.1	45.4
UZ-19-20	72.1	57	35.6	1.5	2260	400	1.4	0.3	433.2	62.3
UZ-19-21	48.8	61	51.6	2.1	2470	340	1.6	0.2	202.1	28.2
UZ-19-22	32.7	58	30.2	1.2	2980	300	1.7	0.6	231.3	32.9
UZ-19-23	23.5	43	21.9	1.3	1850	340	1.6	0.5	229.2	38.5
UZ-19-24	48.4	90	41.3	1.7	2650	310	1.7	0.4	250.4	29.8
UZ-19-25	58.8	83	77.6	3.0	2370	230	1.9	0.4	161.9	19.8
UZ-19-26	44.0	84	41.9	2.6	2310	350	1.7	0.3	224.4	29.4
UZ-19-27	22.9	61	28.1	1.5	1910	350	1.6	0.3	174.3	25.0
UZ-19-28	45.9	52	33.7	1.6	2260	310	1.7	0.3	290.9	44.0
UZ-19-29	55.2	84	37.5	1.9	1790	310	1.6	0.4	314.8	39.6
UZ-19-30	46.0	70	35.6	1.1	2490	250	1.6	0.7	276.0	35.6
UZ-19-31	36.9	50	26.4	0.9	2280	280	1.4	0.5	298.1	44.7
UZ-20-1	11.7	23	22.9	1.2	BLOD	BLOD	1.8	0.3	94.7	20.7
UZ-20-2	22.0	74	26.9	1.4	BLOD	BLOD	1.8	0.4	150.9	20.1
UZ-20-3	11.8	58	13.6	0.6	1120	330	2.3	0.8	160.9	23.0
UZ-20-4	16.8	79	31.0	1.5	BLOD	BLOD	1.6	0.4	100.5	12.9
UZ-20-5	8.4	14	14.5	0.7	BLOD	BLOD	1.5	0.4	107.3	29.5
UZ-20-6	14.8	67	17.2	0.7	BLOD	BLOD	2.1	0.6	159.6	21.3
UZ-20-7	13.3	25	11.2	0.7	BLOD	BLOD	2.2	0.3	219.8	46.5
UZ-20-8	38.5	76	82.7	4.5	BLOD	BLOD	1.9	0.5	86.2	11.4

UZ-20-9	17.6	46	28.9	2.4	BLOD	BLOD	1.6	0.5	112.9	19.6
UZ-20-10	26.3	74	38.7	2.1	BLOD	BLOD	1.8	0.7	125.5	16.8
UZ-20-11	15.9	69	14.2	0.8	BLOD	BLOD	1.9	0.3	207.8	28.9
UZ-20-12	24.0	76	26.9	1.6	BLOD	BLOD	2.0	0.4	165.0	22.2
UZ-20-13	9.0	25	19.3	1.1	BLOD	BLOD	1.4	0.7	86.3	18.2
UZ-20-14	15.2	52	26.7	1.5	BLOD	BLOD	1.8	0.4	105.3	16.3
UZ-20-15	23.6	99	31.0	2.1	BLOD	BLOD	2.1	0.5	141.1	17.9
UZ-20-16	10.4	26	17.0	1.1	BLOD	BLOD	2.2	0.2	113.3	23.8
UZ-20-17	10.6	37	10.9	0.6	BLOD	BLOD	2.8	0.3	179.1	31.6
UZ-20-18	10.1	36	24.0	1.1	BLOD	BLOD	2.8	0.3	77.6	13.7
UZ-20-19	18.2	57	24.1	1.4	BLOD	BLOD	2.5	0.6	139.4	20.8
UZ-20-20	11.2	41	13.6	0.7	BLOD	BLOD	2.3	0.8	152.4	25.7
UZ-20-21	26.6	75	47.7	2.6	1170	460	2.4	0.7	103.2	13.7
UZ-20-22	11.8	29	11.1	0.7	BLOD	BLOD	2.0	0.5	195.8	39.1
UZ-20-23	9.8	50	16.6	0.8	BLOD	BLOD	1.2	0.2	109.6	17.0
UZ-20-24	25.7	84	55.7	2.6	1020	430	0.9	0.2	85.5	10.6
UZ-20-25	34.6	120	52.6	3.1	930	460	1.4	0.6	121.7	14.0
UZ-20-26	10.2	38	17.6	0.9	BLOD	BLOD	1.3	0.6	107.0	18.7
UZ-20-27	18.3	44	26.3	1.6	BLOD	BLOD	1.9	0.3	128.6	21.5
UZ-20-28	17.3	57	15.5	1.0	BLOD	BLOD	1.4	0.5	206.9	31.3
UZ-20-29	27.0	50	44.9	2.5	BLOD	BLOD	1.6	0.3	111.2	17.4
UZ-21-1	23.7	113	28.5	1.1	BLOD	BLOD	2.1	0.4	154.0	16.7
UZ-21-2	22.7	64	34.6	1.6	BLOD	BLOD	1.6	0.6	121.1	16.8
UZ-21-3	44.8	183	76.6	3.9	BLOD	BLOD	2.0	0.4	108.3	10.6
UZ-21-4	21.0	97	31.8	1.6	BLOD	BLOD	1.8	0.3	122.0	14.6
UZ-21-5	25.1	102	35.3	1.4	BLOD	BLOD	1.6	0.4	131.6	14.9
UZ-21-6	30.7	85	37.1	1.4	BLOD	BLOD	1.8	0.8	152.8	18.5
UZ-21-7	29.5	161	35.5	1.2	BLOD	BLOD	2.0	0.4	153.9	14.4
UZ-21-8	16.8	70	25.8	1.5	1920	730	2.1	0.4	120.6	16.7
UZ-21-9	20.2	44	33.2	1.6	BLOD	BLOD	1.3	0.5	112.4	18.3

UZ-21-10	23.8	68	34.0	1.4	BLOD	BLOD	1.9	0.7	129.6	17.3
UZ-21-11	25.9	85	46.2	1.6	BLOD	BLOD	1.5	0.5	103.5	12.4
UZ-21-12	22.6	97	30.4	1.3	BLOD	BLOD	1.7	0.7	137.8	16.1
UZ-21-13	23.4	102	23.3	1.2	BLOD	BLOD	2.0	0.8	185.5	21.9
UZ-21-14	31.6	118	52.9	2.5	BLOD	BLOD	2.1	0.6	110.5	12.2
UZ-21-15	26.4	98	33.7	1.4	700	460	2.3	0.5	145.0	16.8
UZ-21-16	25.4	100	37.2	2.3	BLOD	BLOD	2.1	0.7	126.4	15.6
UZ-21-17	24.4	162	35.7	1.3	BLOD	BLOD	2.1	1.2	126.3	11.9
UZ-21-18	26.6	121	30.0	1.8	3400	1000	1.8	0.4	164.1	18.9
UZ-21-19	30.4	100	51.8	2.3	870	400	2.0	0.6	108.5	12.6
UZ-21-20	45.7	120	84.8	2.8	BLOD	BLOD	1.5	0.5	99.8	10.4
UZ-21-21	24.3	110	38.5	1.8	BLOD	BLOD	2.0	1.0	116.9	13.2
UZ-21-22	42.9	105	71.9	4.8	BLOD	BLOD	1.8	0.7	110.3	13.7
UZ-21-23	30.2	73	34.7	1.7	BLOD	BLOD	1.7	0.4	160.7	21.3
UZ-21-24	25.7	119	36.4	1.6	720	370	1.7	0.3	130.6	14.2
UZ-21-25	29.2	168	54.3	2.7	BLOD	BLOD	2.0	0.5	99.6	9.9
UZ-21-26	25.1	103	31.2	1.5	BLOD	BLOD	1.8	0.9	148.7	17.3
UZ-21-27	30.1	110	34.3	1.5	BLOD	BLOD	1.1	0.3	162.5	18.1
UZ-21-28	21.1	75	25.4	0.9	BLOD	BLOD	1.4	0.5	153.2	19.3
UZ-21-29	24.6	68	34.6	1.6	BLOD	BLOD	1.2	0.4	131.6	17.8
UZ-21-30	23.9	71	32.7	1.4	BLOD	BLOD	1.2	0.5	135.0	17.8
UZ-21-31	21.8	61	33.9	1.5	BLOD	BLOD	1.9	0.3	119.0	16.7
UZ-21-32	24.1	89	31.9	1.7	BLOD	BLOD	1.6	0.7	139.8	17.4
UZ-21-33	20.4	100	31.2	1.5	690	370	2.2	0.5	120.9	14.2
UZ-21-34	25.2	95	32.6	1.6	BLOD	BLOD	2.1	0.5	143.0	17.2
UZ-21-35	26.3	86	42.6	1.9	BLOD	BLOD	2.1	0.6	114.2	14.0
UZ-21-36	30.5	92	36.6	2.5	BLOD	BLOD	2.1	0.3	154.1	20.1
UZ-22-1	5.1	33	3.6	0.2	780	380	1.5	0.3	265.3	50.0
UZ-22-2	7.2	22	8.5	0.5	BLOD	BLOD	0.6	0.0	157.1	35.4
UZ-22-3	8.3	39	6.2	0.3	740	290	1.5	0.3	250.2	43.3

UZ-22-4	4.6	18	6.5	0.4	990	420	2.2	0.2	130.5	32.1
UZ-22-5	5.7	24	6.8	0.3	1010	390	1.8	0.3	156.2	33.0
UZ-22-6	3.6	16	3.9	0.2	1030	370	1.6	0.3	168.7	43.9
UZ-22-7	3.7	13	4.3	0.2	BLOD	BLOD	2.3	0.5	159.7	45.3
UZ-22-8	6.2	24	5.4	0.4	1370	480	2.5	0.3	212.1	46.4
UZ-22-9	6.3	27	7.3	0.6	1090	450	2.0	0.1	160.5	34.0
UZ-22-10	5.2	19	3.9	0.3	1080	490	1.9	0.5	242.2	58.9
UZ-22-11	7.8	27	5.2	0.3	BLOD	BLOD	1.6	0.3	279.5	57.8
UZ-22-12	5.7	32	5.3	0.3	2150	520	2.1	0.2	201.2	38.5
UZ-22-13	4.5	13	4.8	0.3	BLOD	BLOD	1.3	0.4	176.7	50.6
UZ-22-14	7.2	34	6.4	0.3	BLOD	BLOD	1.7	0.3	206.8	37.6
UZ-22-15	5.1	17	5.2	0.3	990	440	1.6	0.2	182.8	46.0
UZ-22-16	7.6	25	6.2	0.3	890	420	2.3	0.7	229.3	48.0
UZ-22-17	5.0	22	4.0	0.3	BLOD	BLOD	1.0	0.2	232.0	52.5
UZ-22-18	3.8	22	3.9	0.2	1770	490	2.2	0.8	178.7	40.0
UZ-22-19	6.8	40	5.7	0.4	1290	500	2.0	0.5	219.6	38.7
UZ-22-20	6.0	36	4.4	0.3	BLOD	BLOD	1.9	0.3	249.1	44.8
UZ-22-21	8.6	34	6.2	0.3	BLOD	BLOD	1.8	0.2	256.1	47.0
UZ-22-22	11.3	35	10.1	0.7	1130	600	2.5	0.3	208.5	38.7
UZ-22-23	6.6	25	4.6	0.3	1780	500	2.1	0.3	267.0	56.3
UZ-22-24	5.3	27	5.2	0.4	990	400	2.0	0.4	188.2	39.4
UZ-22-25	5.3	28	4.8	0.2	1140	410	1.4	0.5	203.0	39.9
UZ-22-26	4.3	21	5.3	0.2	BLOD	BLOD	1.5	0.3	148.4	33.4
UZ-22-27	6.0	39	7.1	0.5	BLOD	BLOD	1.5	0.2	157.5	28.0
UZ-22-28	3.2	29	3.5	0.2	1710	370	1.5	0.4	169.2	33.5
UZ-22-29	6.9	29	6.1	0.3	BLOD	BLOD	2.1	0.9	211.6	41.1
UZ-22-30	7.8	23	4.3	0.2	BLOD	BLOD	1.8	0.2	338.1	73.9
UZ-22-31	9.6	31	6.9	0.3	1100	370	1.8	0.2	257.6	48.8
UZ-22-32	11.7	46	9.8	0.6	1110	450	1.5	0.4	220.2	36.0
UZ-22-33	7.5	47	6.9	0.3	1110	410	1.5	1.0	200.3	31.6

UZ-22-34	9.6	43	5.3	0.3	BLOD	BLOD	1.4	0.9	337.1	57.0
UZ-22-35	3.5	25	5.0	0.4	1290	500	1.7	0.1	131.0	28.2
UZ-22-36	8.3	27	4.4	0.3	BLOD	BLOD	1.5	0.4	349.0	71.3
UZ-22-37	6.5	21	6.2	0.4	BLOD	BLOD	1.9	0.4	194.4	44.6
UZ-22-38	3.2	18	3.4	0.3	106000	18000	2.4	0.3	174.7	44.5
UZ-22-39	4.2	20	4.6	0.2	860	430	1.9	0.3	171.1	39.7
UZ-22-40	4.4	27	3.6	0.3	1170	370	1.1	0.3	225.5	47.1
UZ-23-1	5.3	37	4.2	0.2	2510	440	1.9	0.3	233.0	40.9
UZ-23-2	7.3	25	7.4	0.4	2220	460	2.0	0.3	183.2	38.3
UZ-23-3	3.5	21	4.1	0.2	1820	500	1.7	0.3	157.9	36.2
UZ-23-4	7.4	49	4.7	0.3	2540	450	1.9	0.4	288.2	45.4
UZ-23-5	7.7	33	5.6	0.4	1750	450	1.9	1.1	254.3	48.3
UZ-23-6	9.1	38	6.4	0.3	1680	460	1.7	0.2	264.7	46.1
UZ-23-7	5.2	34	3.7	0.2	2200	460	1.6	0.3	263.7	49.4
UZ-23-8	6.9	38	5.1	0.3	3070	560	1.7	0.4	254.1	45.1
UZ-23-9	8.1	28	6.5	0.4	1370	460	1.8	0.4	229.6	46.0
UZ-23-10	8.4	40	4.4	0.2	2280	480	1.8	0.2	351.8	60.3
UZ-23-11	3.4	16	4.0	0.3	2830	690	1.9	0.3	157.8	41.2
UZ-23-12	5.5	20	4.9	0.3	1850	420	1.8	0.2	211.2	49.4
UZ-23-13	5.1	21	3.9	0.2	1730	460	1.9	0.3	242.5	55.6
UZ-23-14	7.5	29	5.9	0.3	1750	470	2.1	0.5	237.5	46.5
UZ-23-15	7.3	30	4.4	0.3	2240	430	2.2	0.3	305.5	59.9
UZ-23-16	6.0	35	3.7	0.2	1920	510	2.0	0.4	299.0	54.7
UZ-23-17	5.3	21	4.8	0.4	2020	460	1.7	0.3	205.1	48.1
UZ-23-18	4.4	20	4.0	0.2	2060	400	2.2	0.2	207.7	48.5
UZ-23-19	5.8	30	4.6	0.3	2590	450	2.4	0.7	233.6	45.4
UZ-23-20	5.2	17	5.4	0.3	2250	490	2.3	0.3	180.2	45.3
UZ-23-21	3.5	29	4.4	0.3	2060	380	1.5	0.2	143.9	28.7
UZ-23-22	7.3	44	3.8	0.2	2380	530	2.0	0.4	354.0	58.1
UZ-23-23	6.5	33	4.4	0.2	1870	440	2.1	0.2	276.1	51.1

UZ-23-24	3.3	19	4.7	0.5	2060	480	2.3	0.2	128.6	33.2
UZ-23-25	3.0	17	5.1	0.3	2340	440	2.6	0.2	109.7	27.8
UZ-23-26	3.6	21	4.0	0.2	2120	430	2.4	0.3	167.4	37.8
UZ-23-27	11.0	66	10.2	0.6	2330	430	1.9	0.5	200.0	28.0
UZ-23-28	11.1	42	5.3	0.3	2420	430	1.8	0.6	388.2	66.3
UZ-23-29	4.3	18	3.5	0.2	2010	410	2.2	0.3	226.4	55.6
UZ-23-30	5.3	28	3.4	0.2	2150	500	2.1	0.2	292.4	58.3
UZ-23-31	6.6	43	4.8	0.3	2280	450	1.9	0.3	253.8	42.2
UZ-23-32	2.7	18	3.1	0.2	2020	560	2.1	0.3	163.4	40.0
UZ-23-33	5.1	33	6.0	0.4	2360	500	1.8	0.3	160.0	30.2
UZ-23-34	4.0	25	3.5	0.2	2370	430	1.2	0.3	213.3	45.3
UZ-23-35	4.1	25	4.0	0.2	2210	400	2.0	0.3	188.8	39.4
UZ-23-36	7.7	23	6.3	0.3	2280	470	1.6	0.3	227.5	49.5
UZ-23-37	6.2	31	6.3	0.4	2090	500	1.3	0.2	183.1	35.6
UZ-23-38	9.3	40	9.0	0.4	2260	500	1.6	0.2	190.5	32.1
UZ-23-39	5.7	33	4.1	0.3	1820	470	1.8	0.2	254.9	48.2
UZ-23-40	7.0	38	3.8	0.2	1930	490	1.3	0.4	338.2	59.9
UZ-24-1	2.5	11	11.4	0.5	BLOD	BLOD	1.3	0.2	47.5	14.6
UZ-24-2	8.2	35	12.3	0.5	BLOD	BLOD	1.4	0.2	142.8	25.5
UZ-24-3	9.0	12	17.5	1.1	BLOD	BLOD	1.3	0.1	110.3	32.9
UZ-24-4	7.4	26	13.3	0.6	3900	1700	1.0	0.2	118.9	24.3
UZ-24-5	11.2	20	20.0	1.0	BLOD	BLOD	1.7	0.2	119.9	27.8
UZ-24-6	10.4	23	24.6	1.5	780	360	1.6	0.6	90.5	19.9
UZ-24-7	5.8	22	14.7	0.7	BLOD	BLOD	2.0	0.3	84.3	18.6
UZ-24-8	8.2	11	23.1	1.0	BLOD	BLOD	1.9	0.4	75.8	23.3
UZ-24-9	10.4	36	14.7	0.8	BLOD	BLOD	1.9	0.3	150.4	26.8
UZ-24-10	12.4	34	44.2	1.9	BLOD	BLOD	2.3	0.3	59.8	10.8
UZ-24-11	9.9	19	19.4	0.8	BLOD	BLOD	2.5	0.2	108.9	25.7
UZ-24-12	20.6	74	60.6	2.2	610	290	2.3	0.4	72.7	9.3
UZ-24-13	2.7	5	7.9	0.4	BLOD	BLOD	2.1	0.2	73.1	33.0

UZ-24-14	7.3	15	22.7	1.2	BLOD	BLOD	2.4	0.3	68.6	18.3
UZ-24-15	5.1	12	9.6	0.4	BLOD	BLOD	1.9	0.4	113.8	33.4
UZ-24-16	7.0	8	11.5	0.5	BLOD	BLOD	2.1	0.3	129.7	46.5
UZ-24-17	6.9	14	18.3	0.9	BLOD	BLOD	2.2	0.2	81.1	22.2
UZ-24-18	4.7	6	13.6	0.5	BLOD	BLOD	1.5	0.2	74.1	30.5
UZ-24-19	8.2	37	14.4	0.7	BLOD	BLOD	2.4	0.4	120.8	21.3
UZ-24-20	11.5	15	41.4	3.6	BLOD	BLOD	2.0	0.6	59.2	16.3
UZ-24-21	16.2	51	43.8	7.7	BLOD	BLOD	2.0	0.4	79.0	18.0
UZ-24-22	9.7	32	21.0	1.2	BLOD	BLOD	2.3	0.2	98.6	18.7
UZ-24-23	11.8	23	27.2	1.4	BLOD	BLOD	2.4	0.4	92.4	20.2
UZ-24-24	10.2	46	24.9	1.0	BLOD	BLOD	2.8	0.3	87.3	13.7
UZ-24-25	15.0	60	33.4	1.6	BLOD	BLOD	2.3	0.4	95.9	13.7
UZ-24-26	9.9	52	28.7	1.6	BLOD	BLOD	2.3	0.4	73.7	11.4
UZ-24-27	10.5	36	16.4	0.6	BLOD	BLOD	2.4	0.6	137.1	24.0
UZ-24-28	3.4	12	8.4	0.5	630	280	2.2	0.2	86.2	25.6
UZ-24-29	7.1	15	16.2	0.6	BLOD	BLOD	1.9	0.2	94.1	24.8
UZ-24-30	3.7	8	9.7	0.5	BLOD	BLOD	1.9	0.7	81.9	29.5
UZ-24-31	8.9	56	30.1	2.0	630	330	1.3	0.2	63.0	9.7
UZ-24-32	12.7	38	26.7	1.3	BLOD	BLOD	1.4	0.2	101.8	17.7
UZ-24-33	4.7	15	5.4	0.3	BLOD	BLOD	1.1	0.2	186.6	49.6
UZ-24-34	25.4	113	82.6	4.5	BLOD	BLOD	1.4	0.4	65.8	7.6
UZ-24-35	3.0	8	5.5	0.3	BLOD	BLOD	1.3	0.2	118.4	42.5
UZ-25-1	9.7	12	21.5	1.0	BLOD	BLOD	0.9	0.1	93.6	27.6
UZ-25-2	10.7	27	23.9	1.3	BLOD	BLOD	1.2	0.5	92.4	18.9
UZ-25-3	6.6	24	5.9	0.3	BLOD	BLOD	1.0	0.2	231.1	49.1
UZ-25-4	13.6	29	21.4	0.8	490	210	0.9	0.2	131.1	25.4
UZ-25-5	8.0	21	18.8	1.5	BLOD	BLOD	0.8	0.1	88.1	20.8
UZ-25-6	4.2	9	18.4	0.8	BLOD	BLOD	0.6	0.1	46.8	15.9
UZ-25-7	12.1	28	24.0	1.0	BLOD	BLOD	0.9	0.1	104.5	20.7
UZ-25-8	9.7	32	15.6	0.8	420	190	1.3	0.5	128.3	24.3

UZ-25-9	16.2	47	32.7	1.5	BLOD	BLOD	1.4	0.4	102.4	16.2
UZ-25-10	7.9	24	15.3	0.8	620	380	0.8	0.2	107.3	23.0
UZ-25-11	3.2	5	9.2	0.5	810	190	1.6	0.2	73.4	33.2
UZ-25-12	7.7	21	21.3	1.2	510	220	1.4	0.2	75.2	17.2
UZ-25-13	2.9	8	4.3	0.2	BLOD	BLOD	1.0	0.2	138.3	49.7
UZ-25-14	9.6	25	23.4	1.0	BLOD	BLOD	0.9	0.2	84.4	17.6
UZ-25-15	2.9	7	11.3	0.5	BLOD	BLOD	0.9	0.1	53.5	20.5
UZ-25-16	16.0	58	34.0	1.6	BLOD	BLOD	1.0	0.3	97.5	14.2
UZ-25-17	12.0	55	26.7	1.1	BLOD	BLOD	1.1	0.3	93.2	13.7
UZ-25-18	15.7	50	35.2	1.7	BLOD	BLOD	1.3	0.2	92.4	14.3
UZ-25-19	12.2	48	25.9	0.9	BLOD	BLOD	1.0	0.3	97.5	15.0
UZ-25-20	13.4	39	29.6	1.1	BLOD	BLOD	1.0	0.1	93.7	15.9
UZ-25-21	26.1	107	50.6	2.1	BLOD	BLOD	1.1	0.2	106.6	12.1
UZ-25-22	17.7	69	39.7	1.9	BLOD	BLOD	0.9	0.2	91.9	12.5
UZ-25-23	28.0	68	47.2	1.6	570	210	1.0	0.2	122.8	16.3
UZ-25-24	12.0	57	31.3	1.2	BLOD	BLOD	1.0	0.2	78.9	11.4
UZ-25-25	15.1	47	36.7	1.8	BLOD	BLOD	0.9	0.2	84.9	13.5
UZ-25-26	9.9	40	17.0	0.8	BLOD	BLOD	1.1	0.2	120.5	20.5
UZ-25-27	14.4	77	25.3	1.1	BLOD	BLOD	0.9	0.2	117.9	15.2
UZ-25-28	9.2	44	37.0	3.2	BLOD	BLOD	1.0	0.2	51.5	9.2
UZ-25-29	8.8	36	18.9	0.9	390	200	0.8	0.2	96.2	17.2
UZ-25-30	4.1	17	13.0	1.0	BLOD	BLOD	0.7	0.2	65.8	16.9
UZ-25-31	12.3	40	14.7	1.0	BLOD	BLOD	1.1	0.6	172.7	30.6
UZ-25-32	13.9	74	37.0	1.5	BLOD	BLOD	0.8	0.1	77.8	10.1
UZ-25-33	17.2	40	58.4	3.0	BLOD	BLOD	1.1	0.2	60.7	10.4
UZ-25-34	8.5	23	26.4	1.9	BLOD	BLOD	1.5	0.3	66.3	14.9
UZ-25-35	8.6	29	16.6	0.7	BLOD	BLOD	0.8	0.1	107.9	21.0
UZ-25-36	24.0	100	75.3	4.7	310	180	1.0	0.4	65.8	8.2
UZ-25-37	18.3	61	29.1	1.3	BLOD	BLOD	1.2	0.3	130.3	18.5
UZ-25-38	30.2	103	63.2	3.1	BLOD	BLOD	1.3	0.3	98.9	11.6

UZ-25-39	10.2	32	29.9	1.6	530	190	0.9	0.2	70.6	13.4
UZ-25-40	8.5	24	22.9	1.0	460	210	0.9	0.2	76.2	16.2
UZ-26-1	41.0	16.61	13.7	0.7	BLOD	BLOD	1.2	0.3	238.7	39.3
UZ-26-2	61.0	11.44	14.0	1.0	BLOD	BLOD	1.4	0.4	162.2	23.6
UZ-26-3	37.0	12.13	9.1	0.5	BLOD	BLOD	1.3	0.3	261.6	45.7
UZ-26-4	82.0	50	13.4	1.1	BLOD	BLOD	1.4	0.3	257.1	50.8
UZ-26-5	49.0	18.23	13.4	0.9	BLOD	BLOD	1.3	0.4	283.9	40.3
UZ-26-6	50.0	15.35	37.0	4.4	BLOD	BLOD	1.3	0.4	98.0	18.2
UZ-26-7	169.0	50.34	15.1	2.1	BLOD	BLOD	1.3	0.4	200.5	39.8
UZ-26-8	34.0	8.661	44.8	4.0	BLOD	BLOD	1.3	0.5	221.3	26.1
UZ-26-9	98.0	28.7	12.2	1.0	BLOD	BLOD	1.4	0.3	140.7	26.7
UZ-26-10	75.0	13.06	15.4	1.2	63900	7400	1.3	0.3	164.2	26.3
UZ-26-11	22.0	8.116	15.0	0.9	22600	3600	1.2	0.2	172.1	22.3
UZ-26-12	51.0	17.75	10.4	0.9	10700	1900	1.1	0.2	154.5	35.3
UZ-26-13	37.0	9.623	21.7	2.8	10800	1700	1.5	0.6	161.9	30.8
UZ-26-14	40.0	24.53	15.0	1.2	6980	580	1.1	0.3	127.3	23.3
UZ-26-15	45.0	19.04	17.8	2.0	6510	990	1.2	0.4	270.5	52.5
UZ-26-16	69.0	22.46	28.5	2.8	3840	610	1.2	0.4	132.5	23.7
UZ-26-17	16.0	8.692	19.6	2.4	1550	320	1.5	0.5	225.6	38.7
UZ-26-18	40.0	8.935	13.3	1.0	2070	310	1.1	0.3	129.8	33.8
UZ-26-19	12.0	7.158	17.5	1.4	1380	230	1.0	0.3	101.5	18.0
UZ-26-20	39.0	14.85	9.9	0.6	1200	250	1.2	0.4	142.8	42.1
UZ-26-21	49.0	26.52	19.3	1.5	940	150	1.3	0.5	152.4	27.1
UZ-26-22	22.0	9.731	17.5	1.3	660	230	0.5	0.2	296.6	47.8
UZ-26-23	29.0	19.1	12.8	0.7	820	170	1.2	0.2	150.7	33.1
UZ-26-24	83.0	33.63	28.0	2.0	550	180	1.5	0.3	135.3	26.9
UZ-26-25	28.0	26.11	42.6	2.6	BLOD	BLOD	1.1	0.3	156.3	19.6
UZ-26-26	59.0	14.08	16.2	1.1	960	130	1.5	0.4	171.9	25.2
UZ-26-27	55.0	29.31	14.3	0.9	700	160	1.2	0.3	284.2	49.1
UZ-28-1	138.0	34.15	72.0	8.0	BLOD	BLOD	1.1	0.3	71.6	10.0

UZ-28-2	83.0	21.68	34.1	1.5	BLOD	BLOD	1.2	0.2	126.1	14.9
UZ-28-3	32.0	14.67	61.8	4.8	BLOD	BLOD	1.3	0.4	47.4	9.1
UZ-28-4	12.0	1.999	8.1	0.5	BLOD	BLOD	1.2	0.1	73.5	21.7
UZ-28-5	38.0	9.19	15.5	1.4	BLOD	BLOD	1.1	0.3	117.7	21.9
UZ-28-6	34.0	11.52	17.4	1.3	BLOD	BLOD	1.2	0.2	131.3	24.6
UZ-28-7	14.0	4.844	19.8	3.0	10700	1900	1.2	0.2	48.8	15.0
UZ-28-8	37.0	10.44	28.9	1.8	10800	1700	1.2	0.4	72.0	12.7
UZ-28-9	54.0	16.61	28.3	2.1	6980	580	1.2	0.2	116.5	18.1
UZ-28-10	65.0	17.41	37.1	2.8	3840	610	1.4	0.3	93.4	13.6
UZ-28-11	85.0	17.96	22.3	2.0	1550	320	1.2	0.2	159.4	22.4
UZ-28-12	92.0	14.4	15.5	0.9	940	150	1.3	0.2	183.2	22.1
UZ-28-13	14.0	3.821	12.5	0.9	820	170	1.1	0.3	39.0	10.8
UZ-29a-1	18.2	61	17.2	0.7	630	210	3.4	1.1	218.4	30.8
UZ-29a-2	22.3	27	45.3	2.6	670	240	3.5	1.0	101.8	20.9
UZ-29a-3	23.7	69	47.7	3.2	540	220	3.2	1.8	102.8	14.8
UZ-29a-4	16.4	28	20.1	1.6	690	220	3.7	1.5	168.7	35.3
UZ-29a-5	1.6	4	3.4	0.2	540	190	0.6	0.1	99.2	50.1
UZ-29a-6	33.2	60	42.8	1.9	590	200	3.2	3.1	160.4	22.9
UZ-29a-7	21.8	37	46.8	2.6	BLOD	BLOD	3.9	0.5	96.3	17.2
UZ-29a-8	13.0	28	24.2	1.3	BLOD	BLOD	4.3	1.4	111.1	22.3
UZ-29a-9	20.8	50	41.2	1.9	490	260	3.8	0.9	104.6	16.1
UZ-29a-10	29.2	72	43.1	2.1	450	250	3.1	1.2	140.2	18.8
UZ-29a-11	9.2	28	17.1	0.8	BLOD	BLOD	1.6	0.2	111.6	22.2
UZ-29a-12	23.6	45	37.0	1.9	1420	290	5.2	1.7	131.8	21.5
UZ-29a-13	3.0	9	7.0	0.4	BLOD	BLOD	1.5	0.2	90.2	30.7
UZ-29a-14	26.0	80	48.6	2.5	1220	280	3.7	0.4	110.6	14.4
UZ-29a-15	19.5	52	44.8	2.9	BLOD	BLOD	4.2	1.8	90.1	14.3
UZ-29a-16	22.7	54	50.1	4.0	10800	2000	2.2	0.4	93.7	15.3
UZ-29a-17	36.2	125	67.2	3.9	1340	280	3.2	1.1	111.3	12.7
UZ-29a-18	30.4	141	21.2	1.0	BLOD	BLOD	3.2	0.5	296.0	31.1

UZ-29a-19	13.2	24	23.0	1.7	820	310	3.0	0.4	119.0	26.3
UZ-29a-20	21.4	77	42.4	2.2	BLOD	BLOD	2.7	1.4	104.3	13.7
UZ-29a-21	29.0	72	48.6	2.9	BLOD	BLOD	2.0	0.7	123.4	17.1
UZ-29a-22	22.3	44	42.5	2.3	1470	500	3.2	1.8	108.6	18.0
UZ-29a-23	22.4	88	40.6	2.1	880	320	4.4	1.5	113.8	14.3
UZ-29a-24	23.2	56	40.1	1.6	BLOD	BLOD	5.6	1.2	119.5	17.4
UZ-29a-25	24.3	78	37.7	1.8	BLOD	BLOD	3.7	1.9	133.3	17.3
UZ-29a-26	20.0	38	40.7	3.4	BLOD	BLOD	3.9	0.6	101.5	19.0
UZ-29a-27	23.7	93	38.2	2.0	660	310	4.3	1.3	128.2	15.8
UZ-29a-28	21.4	41	40.7	2.4	BLOD	BLOD	2.2	0.5	108.6	18.7
UZ-29a-29	23.9	95	36.9	1.6	950	320	3.9	0.8	133.6	15.9
UZ-29a-30	23.5	46	38.5	2.1	BLOD	BLOD	3.1	0.9	126.1	20.5
UZ-29a-31	31.2	71	34.6	1.7	BLOD	BLOD	1.1	0.2	186.3	25.1
UZ-29a-32	26.7	70	39.8	2.0	1270	430	1.8	0.6	138.5	18.9
UZ-29a-33	25.4	83	44.7	2.0	BLOD	BLOD	2.8	0.5	117.7	14.8
UZ-29a-34	21.6	41	36.3	1.7	1130	460	3.2	1.0	123.0	20.7
UZ-29a-35	20.8	97	32.2	1.5	1120	400	3.8	1.0	133.7	15.9
UZ-29a-36	26.1	81	44.9	2.6	BLOD	BLOD	3.6	0.8	120.3	15.9
UZ-29a-37	27.1	62	34.2	1.9	3630	900	3.8	0.7	163.8	23.7
UZ-29b-1	5.1	18	4.7	0.2	750	330	1.3	0.3	224.2	54.8
UZ-29b-2	28.1	43	40.2	2.3	6800	1800	1.2	0.2	144.5	24.3
UZ-29b-3	32.5	165	37.6	1.7	1430	340	1.8	0.5	178.8	17.7
UZ-29b-4	20.9	35	37.7	1.5	BLOD	BLOD	2.0	0.6	114.6	20.5
UZ-29b-5	32.5	52	39.9	1.8	690	310	2.1	0.2	168.4	25.5
UZ-29b-6	27.9	99	60.9	3.2	BLOD	BLOD	1.8	0.4	94.8	11.4
UZ-29b-7	26.7	62	40.8	2.3	BLOD	BLOD	1.9	0.4	135.4	19.6
UZ-29b-8	32.4	106	39.6	2.1	BLOD	BLOD	1.6	0.3	169.2	20.0
UZ-29b-9	27.0	72	38.0	2.1	1470	340	2.1	0.7	147.1	20.1
UZ-29b-10	28.0	46	38.4	2.0	1210	330	2.3	0.2	150.8	24.4
UZ-29b-11	23.3	63	38.1	1.5	BLOD	BLOD	1.7	0.4	126.7	17.5

UZ-29b-12	22.3	59	36.7	1.5	BLOD	BLOD	1.9	0.5	125.6	17.9
UZ-29b-13	32.8	99	50.0	2.4	810	340	1.5	0.4	135.8	16.1
UZ-29b-14	27.0	60	38.3	1.9	1240	280	1.2	0.3	145.5	21.0
UZ-29b-15	38.6	91	40.7	1.7	930	270	1.4	0.2	196.1	23.6
UZ-29b-16	23.2	38	35.3	1.5	BLOD	BLOD	1.4	0.4	135.7	23.4
UZ-29b-17	40.1	133	33.0	1.8	940	310	1.3	0.3	251.0	27.7
UZ-29b-18	18.9	39	30.2	1.5	BLOD	BLOD	1.5	0.4	129.6	22.4
UZ-29b-19	26.8	78	41.0	2.6	1270	320	1.5	0.2	135.1	18.4
UZ-29b-20	26.8	78	38.2	2.1	BLOD	BLOD	1.6	0.4	145.3	19.2
UZ-29b-21	34.3	110	38.6	2.5	BLOD	BLOD	1.4	0.5	183.6	22.5
UZ-29b-22	39.8	99	48.2	2.2	1100	410	2.1	0.8	170.6	20.1
UZ-29b-23	36.1	123	50.1	3.3	BLOD	BLOD	1.6	0.4	149.0	17.7
UZ-29b-24	25.0	64	29.6	1.4	BLOD	BLOD	2.2	0.2	174.8	24.5
UZ-29b-25	28.9	57	40.5	2.3	4320	920	1.6	0.3	147.6	22.1
UZ-29b-26	30.6	45	37.7	1.7	BLOD	BLOD	2.4	0.6	167.8	27.0
UZ-29b-27	32.9	92	46.4	3.0	990	330	2.7	0.5	146.8	19.0
UZ-29b-28	27.6	70	43.7	2.7	1120	270	2.7	0.3	130.6	18.4
UZ-29b-29	30.2	89	43.3	1.9	BLOD	BLOD	2.3	0.4	144.0	17.6
UZ-29b-30	34.5	86	39.7	2.6	1070	350	2.2	0.4	179.7	23.9
UZ-29b-31	24.5	88	22.6	1.3	BLOD	BLOD	2.2	0.5	224.1	28.7
UZ-29b-32	29.3	68	48.6	2.2	BLOD	BLOD	1.8	0.4	124.4	16.9
UZ-29b-33	28.5	87	34.4	1.5	1680	330	2.1	0.4	171.5	21.1
UZ-29b-34	28.2	82	38.3	1.8	BLOD	BLOD	1.9	0.4	152.0	19.3
UZ-29b-35	28.6	87	44.1	2.1	1200	280	2.2	0.5	134.2	16.7
UZ-29b-36	32.9	138	38.8	1.7	1760	320	2.1	0.7	175.5	18.3
UZ-29b-37	23.1	78	38.9	2.4	BLOD	BLOD	1.3	0.3	122.9	16.6
UZ-29b-38	28.7	63	39.4	1.9	BLOD	BLOD	1.3	0.4	150.7	21.3
UZ-29b-39	19.3	41	40.4	2.2	BLOD	BLOD	1.6	0.6	98.9	16.9
UZ-30-1	24.3	68	36.8	1.7	BLOD	BLOD	2.0	0.4	136.7	18.6
UZ-30-2	18.5	40	36.3	3.0	1020	520	1.7	0.4	105.3	19.3

UZ-30-3	28.2	53	41.2	2.4	BLOD	BLOD	1.8	0.3	141.6	21.9
UZ-30-4	25.2	78	35.9	1.8	540	230	1.9	0.5	144.9	18.9
UZ-30-5	19.4	21	37.9	2.0	BLOD	BLOD	1.2	0.4	105.6	24.1
UZ-30-6	24.7	56	50.9	2.8	BLOD	BLOD	1.5	0.5	100.3	15.1
UZ-30-7	32.7	60	46.0	2.2	BLOD	BLOD	1.5	0.2	146.8	21.1
UZ-30-8	24.4	76	36.7	1.6	BLOD	BLOD	1.5	0.3	137.2	17.8
UZ-30-9	7.4	22	10.0	0.5	BLOD	BLOD	1.2	0.2	153.1	34.2
UZ-30-10	28.3	60	38.1	1.7	BLOD	BLOD	1.6	0.3	153.5	21.9
UZ-30-11	24.0	70	37.3	2.4	BLOD	BLOD	1.5	0.3	133.0	18.9
UZ-30-12	28.5	62	39.8	2.1	650	270	1.5	0.2	148.2	21.3
UZ-30-13	30.2	110	38.1	1.7	BLOD	BLOD	1.5	0.3	164.1	18.6
UZ-30-14	20.7	40	33.8	1.8	600	260	1.7	0.3	126.6	21.8
UZ-30-15	32.2	78	46.4	2.0	BLOD	BLOD	1.4	0.4	143.3	18.4
UZ-30-16	21.9	45	20.9	1.1	BLOD	BLOD	1.4	0.2	216.6	35.4
UZ-30-17	29.8	94	40.6	1.7	BLOD	BLOD	1.8	0.3	151.8	18.0
UZ-30-18	28.1	70	24.1	1.1	BLOD	BLOD	2.0	0.4	240.6	32.4
UZ-30-19	4.1	8	7.6	0.5	BLOD	BLOD	1.5	0.5	110.8	40.2
UZ-30-20	20.2	48	33.2	1.8	660	300	1.5	0.5	126.0	20.1
UZ-30-21	32.0	87	34.5	2.0	18500	4200	1.7	0.4	191.8	24.7
UZ-30-22	32.0	99	33.5	1.6	BLOD	BLOD	1.6	0.3	197.2	23.4
UZ-30-23	27.3	70	55.9	3.4	BLOD	BLOD	1.6	0.3	100.8	14.1
UZ-30-24	23.2	71	37.1	1.9	BLOD	BLOD	2.1	0.6	129.5	17.6
UZ-30-25	28.6	62	41.3	3.6	3400	1100	1.9	0.4	143.1	22.8
UZ-30-26	2.6	18	3.9	0.2	1460	410	1.4	0.6	141.1	34.7
UZ-30-27	26.0	98	40.1	2.7	1340	650	1.5	0.4	134.0	17.2
UZ-30-28	25.4	116	37.1	1.6	BLOD	BLOD	1.4	0.5	141.4	15.6
UZ-30-29	14.9	39	35.5	1.7	BLOD	BLOD	1.2	0.2	87.0	15.0
UZ-30-30	20.5	92	34.5	1.4	1040	390	1.6	0.5	122.7	14.6
UZ-30-31	32.7	110	59.8	2.6	BLOD	BLOD	1.5	0.3	113.0	12.7
UZ-30-32	23.3	67	40.4	2.0	BLOD	BLOD	1.5	0.6	119.0	16.4

UZ-30-33	29.1	81	44.3	1.7	1080	490	2.0	0.4	135.7	16.9
UZ-30-34	28.3	57	54.1	3.1	870	460	2.5	0.4	108.2	16.2
UZ-30-35	28.9	50	37.2	2.6	BLOD	BLOD	1.9	0.3	160.6	26.2
UZ-30-36	31.4	73	44.2	3.1	4400	1400	1.7	0.5	146.9	20.9
UZ-30-37	25.3	56	34.7	1.5	1070	560	1.5	0.3	150.9	22.1
UZ-30-38	30.4	46	40.2	1.7	BLOD	BLOD	1.6	0.3	156.1	24.8
UZ-30-39	19.9	37	36.3	2.0	BLOD	BLOD	1.5	0.3	113.1	20.2
UZ-30-40	28.9	85	37.7	1.9	BLOD	BLOD	1.3	0.3	158.3	20.0
UZ-31-1	12.0	31	9.3	0.6	BLOD	BLOD	1.3	0.2	267.7	51.9
UZ-31-2	23.3	25	41.5	1.8	1050	320	1.5	0.4	116.2	24.3
UZ-31-3	12.8	18	21.5	1.0	710	300	1.4	0.2	123.4	30.1
UZ-31-4	16.3	56	21.1	1.0	640	300	1.3	0.2	160.0	23.6
UZ-31-5	11.7	28	7.5	0.5	BLOD	BLOD	1.1	0.2	323.3	65.5
UZ-31-6	2.8	6	4.4	0.2	BLOD	BLOD	1.1	0.2	129.6	53.6
UZ-31-7	17.3	29	29.0	1.7	600	340	1.3	0.2	123.5	24.6
UZ-31-8	15.4	27	21.1	1.0	590	310	1.6	0.4	151.3	30.6
UZ-31-9	12.3	36	15.6	1.1	4100	1700	1.3	0.3	163.3	30.3
UZ-31-10	2.5	3	4.4	0.2	730	320	1.3	0.2	118.8	69.0
UZ-31-11	6.0	17	8.0	0.4	500	260	1.5	0.2	156.3	39.3
UZ-31-12	19.9	53	32.3	6.0	1140	540	1.3	0.3	127.4	29.9
UZ-31-13	22.0	43	37.7	2.3	1190	430	1.6	0.3	120.4	20.4
UZ-31-14	9.5	11	18.3	1.0	630	240	1.4	0.3	107.4	33.2
UZ-31-15	21.1	47	30.0	1.1	BLOD	BLOD	1.2	0.3	145.1	22.6
UZ-31-16	14.0	42	14.0	0.6	900	240	1.1	0.3	206.3	34.0
UZ-31-17	11.7	32	8.8	0.6	BLOD	BLOD	1.0	0.2	275.4	53.0
UZ-31-18	21.1	96	17.9	0.9	2660	350	1.8	0.2	244.2	29.7
UZ-31-19	4.0	14	4.4	0.3	630	310	1.0	0.2	189.4	52.7
UZ-31-20	23.2	60	22.2	1.3	600	280	1.4	0.2	216.2	31.9
UZ-31-21	17.8	35	24.2	1.4	BLOD	BLOD	1.0	0.3	152.4	28.0
UZ-31-22	6.8	8	12.7	0.9	770	230	1.2	0.2	111.8	40.5

UZ-31-23	21.4	71	20.7	1.3	BLOD	BLOD	1.2	0.3	213.3	30.0
UZ-31-24	31.1	102	68.8	2.8	BLOD	BLOD	1.4	0.3	93.4	10.7
UZ-31-25	10.6	50	17.2	0.7	BLOD	BLOD	1.0	0.2	126.9	19.5
UZ-31-26	12.4	44	12.9	0.7	590	230	1.2	0.3	198.4	32.7
UZ-31-27	30.2	80	31.0	2.5	1650	980	1.0	0.3	201.1	28.9
UZ-31-28	3.4	6	4.8	0.3	450	220	1.6	0.2	148.6	61.8
UZ-31-29	9.6	20	9.3	0.5	740	270	1.0	0.2	211.7	49.6
UZ-31-30	6.3	28	8.2	0.5	BLOD	BLOD	1.2	0.3	159.1	32.1
UZ-31-31	7.1	11	13.1	0.9	BLOD	BLOD	1.0	0.3	111.4	34.8
UZ-31-32	1.8	9	4.1	0.3	BLOD	BLOD	1.5	0.2	91.4	31.2
UZ-31-33	9.6	36	11.0	0.6	BLOD	BLOD	0.9	0.2	179.9	32.4
UZ-31-34	12.4	44	10.8	0.7	BLOD	BLOD	1.2	0.2	235.5	39.8
UZ-31-35	11.8	15	20.8	1.4	BLOD	BLOD	1.1	0.2	116.8	31.5
UZ-31-36	17.5	42	22.2	2.1	BLOD	BLOD	1.3	0.3	162.7	30.2
UZ-31-37	12.3	28	18.0	0.8	BLOD	BLOD	1.2	0.2	140.8	28.0
UZ-31-38	8.7	10	5.8	0.4	300	140	1.7	0.2	306.3	99.5
UZ-31-39	11.9	45	22.4	1.2	460	220	1.4	0.2	109.7	18.0
UZ-32-1	6.8	17	5.9	0.3	BLOD	BLOD	1.1	0.5	237.9	59.9
UZ-32-2	7.5	12	9.2	0.7	1110	280	2.1	0.2	170.1	51.3
UZ-32-3	8.5	10	11.0	0.7	BLOD	BLOD	1.9	0.8	159.5	52.0
UZ-32-4	14.9	12	17.8	1.0	BLOD	BLOD	1.4	0.8	172.7	51.3
UZ-32-5	12.0	16	12.0	0.6	BLOD	BLOD	2.3	0.4	207.8	53.7
UZ-32-6	7.6	22	9.0	0.4	BLOD	BLOD	1.1	0.3	174.5	38.7
UZ-32-7	10.2	10	12.9	1.0	BLOD	BLOD	1.8	0.2	163.4	53.6
UZ-32-8	9.4	19	9.6	0.5	BLOD	BLOD	1.7	0.3	201.2	48.2
UZ-32-9	7.5	20	12.3	0.7	BLOD	BLOD	2.4	0.1	125.6	29.4
UZ-32-10	6.4	13	11.5	0.7	BLOD	BLOD	2.1	0.1	115.4	33.0
UZ-32-11	3.9	5	9.2	0.4	BLOD	BLOD	2.2	0.3	88.2	39.8
UZ-32-12	18.8	35	15.1	0.9	BLOD	BLOD	1.5	0.4	258.3	47.5
UZ-32-13	11.2	20	14.4	0.6	BLOD	BLOD	2.0	0.6	161.6	37.4

UZ-32-14	18.6	15	16.5	0.9	680	240	1.8	0.1	232.7	62.1
UZ-32-15	14.9	51	16.5	0.8	BLOD	BLOD	1.7	0.3	187.4	28.8
UZ-32-16	8.8	35	6.8	0.4	2480	350	1.6	0.3	269.1	50.0
UZ-32-17	20.3	38	25.2	1.3	BLOD	BLOD	2.0	0.3	166.1	29.1
UZ-32-18	14.8	30	13.9	0.6	2250	340	2.7	0.3	219.7	42.1
UZ-32-19	29.2	42	19.5	1.0	BLOD	BLOD	1.9	0.3	310.0	52.0
UZ-32-20	11.5	13	15.9	0.9	BLOD	BLOD	1.6	0.4	148.7	42.5
UZ-32-21	7.7	11	10.0	0.6	21200	4900	1.4	0.6	160.9	49.9
UZ-32-22	13.1	16	23.6	2.9	BLOD	BLOD	1.6	0.5	115.1	32.4
UZ-32-23	9.0	19	22.0	1.3	BLOD	BLOD	1.9	0.5	84.4	20.3
UZ-32-24	17.0	48	28.1	1.4	BLOD	BLOD	1.5	0.4	124.7	19.7
UZ-32-25	7.6	11	8.0	0.5	BLOD	BLOD	1.6	0.9	198.1	61.4
UZ-32-26	9.1	12	14.7	1.0	BLOD	BLOD	1.3	0.0	127.4	38.2
UZ-32-27	6.5	11	10.5	0.5	BLOD	BLOD	1.6	0.3	128.8	39.6
UZ-32-28	9.5	13	9.3	0.5	BLOD	BLOD	2.0	0.2	212.7	60.9
UZ-32-29	8.5	18	6.8	0.3	BLOD	BLOD	2.2	0.1	255.9	62.5
UZ-32-30	9.8	10	7.5	0.4	BLOD	BLOD	1.0	0.2	268.9	87.0
UZ-32-31	10.7	11	14.0	0.7	BLOD	BLOD	1.4	0.3	158.2	48.9
UZ-35-1	17.1	42	12.9	0.8	BLOD	BLOD	1.1	0.3	300.0	51.9
UZ-35-2	12.2	18	9.9	0.9	BLOD	BLOD	1.4	0.3	278.6	71.8
UZ-35-3	16.2	35	16.4	0.6	BLOD	BLOD	1.4	0.5	223.3	40.2
UZ-35-4	6.0	16	7.0	0.4	660	280	1.5	0.6	193.2	50.7
UZ-35-5	8.8	9	9.3	0.6	BLOD	BLOD	1.3	0.2	214.7	73.7
UZ-35-6	6.7	16	10.2	0.5	500	310	1.2	0.3	150.5	39.2
UZ-35-7	5.8	16	6.1	0.3	610	220	1.1	0.1	216.3	56.4
UZ-35-8	11.5	32	10.4	0.5	780	270	1.1	0.2	251.3	47.8
UZ-35-9	5.1	5	3.7	0.3	1100	320	1.2	0.0	315.4	143.5
UZ-35-10	3.6	7	8.6	0.5	700	350	0.9	0.3	94.1	36.3
UZ-35-11	9.2	20	9.3	0.6	BLOD	BLOD	1.1	0.2	223.1	53.1
UZ-35-12	13.6	24	24.3	1.1	BLOD	BLOD	1.0	0.2	126.5	27.2

UZ-35-13	10.7	20	10.2	0.5	790	320	0.6	0.1	239.1	56.0
UZ-35-14	5.7	17	9.6	0.5	BLOD	BLOD	0.8	0.2	136.1	34.4
UZ-35-15	6.5	14	11.4	0.6	BLOD	BLOD	0.9	0.2	128.5	35.6
UZ-35-16	5.0	12	7.1	0.5	BLOD	BLOD	1.2	0.7	160.7	48.2
UZ-35-17	8.2	27	8.4	0.5	BLOD	BLOD	1.2	0.5	223.4	46.2
UZ-35-18	13.1	42	21.9	0.9	BLOD	BLOD	1.0	0.2	135.0	22.5
UZ-35-19	2.7	9	6.3	0.5	BLOD	BLOD	0.9	0.3	97.0	33.6
UZ-35-20	10.5	43	27.0	1.5	890	450	1.0	0.2	88.3	15.0
UZ-35-21	9.4	29	14.3	0.7	BLOD	BLOD	1.2	0.2	149.9	29.8
UZ-35-22	7.6	33	8.9	0.5	BLOD	BLOD	1.0	0.2	191.7	36.4
UZ-35-23	7.4	16	7.1	0.4	1760	600	1.0	0.2	235.7	61.2
UZ-35-24	5.1	8	6.6	0.4	BLOD	BLOD	1.3	0.2	176.9	64.1
UZ-35-25	18.0	49	22.5	1.1	BLOD	BLOD	1.3	0.3	181.5	28.8
UZ-35-26	9.2	26	8.9	0.4	BLOD	BLOD	1.3	0.3	235.5	49.0
UZ-35-27	8.4	38	15.5	1.0	BLOD	BLOD	1.2	0.1	123.2	22.3
UZ-35-28	5.8	17	10.6	0.4	BLOD	BLOD	1.1	0.3	123.4	30.9
UZ-35-29	14.2	38	9.3	0.5	8130	860	1.0	0.3	343.8	60.7
UZ-35-30	15.8	24	15.2	1.3	BLOD	BLOD	1.0	0.3	235.6	53.4
UZ-35-31	12.9	39	8.6	0.4	BLOD	BLOD	1.1	0.2	337.3	59.0
UZ-35-32	8.5	23	18.1	0.9	BLOD	BLOD	1.8	0.4	107.2	23.5
UZ-35-33	16.2	46	16.8	1.1	BLOD	BLOD	1.2	0.2	218.3	36.8
UZ-35-34	11.5	31	25.7	1.5	BLOD	BLOD	1.3	0.1	101.3	19.8
UZ-35-35	8.0	22	13.0	0.6	BLOD	BLOD	1.3	0.2	138.5	31.0
UZ-35-36	5.3	13	11.8	0.6	BLOD	BLOD	1.3	0.3	100.7	28.8
UZ-36-1	6.2	22	5.9	0.3	BLOD	BLOD	1.2	0.2	230.9	51.3
UZ-36-2	4.5	18	5.1	0.3	BLOD	BLOD	1.1	0.2	198.0	48.3
UZ-36-3	3.6	17	4.7	0.3	660	320	1.2	0.3	168.0	43.0
UZ-36-4	5.4	18	11.4	0.8	98000	15000	1.5	0.1	104.2	25.8
UZ-36-5	4.7	23	6.9	0.4	810	310	1.0	0.2	151.2	33.2
UZ-36-6	3.3	14	4.5	0.2	850	410	1.2	0.2	159.4	43.6

UZ-36-7	5.0	23	5.2	0.3	BLOD	BLOD	1.0	0.2	213.8	46.5
UZ-36-8	4.4	15	6.6	0.4	BLOD	BLOD	0.7	0.2	146.3	39.0
UZ-36-9	4.4	16	12.5	1.0	BLOD	BLOD	1.2	0.2	78.4	20.8
UZ-36-10	6.3	19	15.6	0.8	BLOD	BLOD	1.2	0.2	89.1	21.2
UZ-36-11	14.7	51	15.6	0.8	BLOD	BLOD	1.5	0.6	208.1	32.0
UZ-36-12	7.7	35	7.6	0.3	BLOD	BLOD	1.4	0.2	223.9	39.7
UZ-36-13	4.3	19	8.5	0.3	BLOD	BLOD	1.2	0.3	113.0	26.7
UZ-36-14	7.5	21	4.4	0.2	BLOD	BLOD	1.3	0.4	375.2	85.6
UZ-36-15	7.7	28	15.5	1.2	BLOD	BLOD	1.3	0.2	109.2	22.7
UZ-36-16	7.0	26	5.7	0.4	670	280	1.2	0.2	272.5	58.0
UZ-36-17	12.6	44	28.4	1.5	BLOD	BLOD	1.5	0.2	97.8	16.1
UZ-36-18	4.3	18	6.0	0.3	BLOD	BLOD	1.4	0.3	157.6	38.2
UZ-36-19	12.2	39	10.4	0.6	BLOD	BLOD	1.4	0.3	257.8	44.8
UZ-36-20	19.0	80	34.7	1.5	BLOD	BLOD	1.3	0.1	120.9	15.2
UZ-36-21	11.9	45	26.5	1.2	BLOD	BLOD	1.2	0.3	99.5	16.0
UZ-36-22	10.2	32	22.7	1.2	BLOD	BLOD	1.5	0.7	99.2	18.7
UZ-36-23	15.1	44	32.8	1.5	590	240	1.3	0.4	101.9	16.5
UZ-36-24	5.4	23	5.0	0.2	3470	800	1.2	0.2	242.6	52.8
UZ-36-25	4.2	26	6.7	0.4	1690	610	1.2	0.3	138.3	28.7
UZ-36-26	5.0	18	5.0	0.3	590	170	1.2	0.4	220.8	54.1
UZ-36-27	3.8	19	6.1	0.3	420	190	1.1	0.3	136.9	32.3
UZ-36-28	3.2	11	7.9	0.6	8300	1700	1.5	0.3	88.4	27.6
UZ-36-29	8.0	30	9.3	0.7	BLOD	BLOD	1.1	0.3	190.7	38.0
UZ-36-30	5.8	25	6.1	0.4	400	190	1.2	0.3	209.1	44.2
UZ-36-31	6.4	25	7.3	0.4	BLOD	BLOD	1.1	0.2	191.7	40.2
UZ-36-32	4.0	19	5.7	0.3	390	180	1.2	0.3	155.4	36.9
UZ-36-33	11.2	62	7.2	0.4	BLOD	BLOD	1.2	0.2	341.9	48.6
UZ-36-34	1.2	7	3.2	0.2	410	170	1.5	0.3	80.4	30.9
UZ-36-35	5.5	25	6.1	0.4	350	210	1.3	0.2	198.7	42.0
UZ-36-36	3.1	12	5.0	0.3	370	170	1.2	0.2	139.0	41.3

UZ-36-37	5.1	14	7.1	0.4	460	190	1.1	0.2	158.8	43.7
UZ-36-38	6.5	16	6.1	0.3	BLOD	BLOD	1.1	0.2	235.0	60.6
UZ-37-1	28.0	74	47.6	2.2	2680	640	1.2	0.2	130.1	17.0
UZ-37-2	16.2	34	27.5	1.1	880	270	1.2	0.2	130.5	23.5
UZ-37-3	21.7	43	29.4	1.4	930	230	1.3	0.3	163.2	26.8
UZ-37-4	28.4	42	58.0	7.3	3000	1600	1.3	0.3	108.1	21.9
UZ-37-5	26.5	43	29.6	1.3	1430	260	1.3	0.3	197.9	32.3
UZ-37-6	15.8	60	24.7	1.5	1280	240	1.2	0.2	141.7	20.9
UZ-37-7	14.1	46	24.7	1.5	1080	300	1.3	0.2	126.6	20.8
UZ-37-8	23.4	81	32.2	1.8	850	330	1.3	0.2	160.8	20.9
UZ-37-9	14.1	25	21.3	0.8	BLOD	BLOD	1.1	0.2	146.2	30.3
UZ-37-10	27.0	71	59.4	2.5	1200	450	1.4	0.2	100.3	13.2
UZ-37-11	20.7	57	36.0	1.6	620	330	1.6	0.4	127.4	18.5
UZ-37-12	25.0	40	44.1	1.5	1070	330	1.3	0.3	125.2	20.8
UZ-37-13	20.8	29	17.7	0.8	1320	290	1.3	0.3	258.6	50.4
UZ-37-14	37.9	57	52.0	3.3	810	300	1.4	0.3	161.3	24.5
UZ-37-15	33.2	28	48.5	2.3	1170	250	1.5	0.3	151.5	30.1
UZ-37-16	43.2	53	80.2	4.9	38000	15000	1.3	0.4	119.2	18.5
UZ-37-17	19.9	33	23.4	1.3	730	240	1.3	0.3	188.3	35.2
UZ-37-18	11.5	16	23.8	1.5	1150	290	1.4	0.2	106.6	27.8
UZ-37-19	17.1	27	62.5	3.4	780	310	1.2	0.2	60.6	12.3
UZ-37-20	16.2	48	14.5	1.0	1060	240	1.1	0.2	247.7	40.4
UZ-37-21	24.3	46	22.9	1.0	1070	260	1.5	0.2	235.1	37.2
UZ-37-22	26.2	59	42.9	6.3	14000	10000	1.2	0.3	135.2	27.0
UZ-37-23	6.3	20	10.6	0.6	1830	260	1.2	0.2	131.9	30.8
UZ-37-24	33.2	57	88.6	4.1	1300	310	1.2	0.2	82.8	12.0
UZ-37-25	19.9	13	30.2	1.2	850	300	1.2	0.4	145.8	41.2
UZ-37-26	13.9	20	20.4	1.2	1170	350	1.4	0.2	150.7	35.3
UZ-37-27	28.4	40	53.6	2.5	1260	350	1.3	0.4	117.2	19.8
UZ-37-28	15.5	30	30.9	1.5	1580	270	1.5	0.6	111.1	21.4

UZ-37-29	16.8	25	34.3	1.7	1240	310	1.3	0.2	108.3	22.7
UZ-37-30	26.3	22	41.6	2.4	1120	260	1.3	0.2	139.6	31.3
UZ-37-31	22.5	31	80.0	41.0	1040000	290000	1.2	0.3	62.0	33.8
UZ-37-32	20.5	38	36.6	2.7	22300	3700	1.3	0.2	123.8	22.6
UZ-38-1	4.6	27	6.0	0.3	BLOD	BLOD	1.0	0.2	172.0	35.0
UZ-38-2	3.8	12	10.8	0.5	BLOD	BLOD	1.3	0.5	78.3	23.1
UZ-38-3	4.7	13	6.0	0.2	BLOD	BLOD	1.0	0.1	172.4	48.7
UZ-38-4	9.1	46	11.0	0.8	BLOD	BLOD	1.2	0.2	181.7	30.4
UZ-38-5	7.5	17	14.0	0.9	BLOD	BLOD	1.3	0.1	118.3	29.9
UZ-38-6	1.2	8	2.8	0.2	BLOD	BLOD	1.1	0.3	96.6	34.8
UZ-38-7	8.4	34	13.7	0.7	BLOD	BLOD	1.3	0.3	135.6	24.7
UZ-38-8	6.9	24	15.0	0.7	BLOD	BLOD	0.9	0.2	102.1	21.7
UZ-38-9	12.1	27	24.6	1.0	BLOD	BLOD	1.0	0.2	108.4	21.7
UZ-38-10	12.6	61	18.8	1.6	BLOD	BLOD	1.3	0.4	147.8	23.4
UZ-38-11	9.9	21	8.2	0.5	BLOD	BLOD	1.8	0.4	266.2	61.2
UZ-38-12	6.5	15	4.7	0.3	BLOD	BLOD	0.8	0.1	305.3	81.5
UZ-38-13	38.0	45	98.6	4.8	1180	430	1.0	0.2	85.1	13.7
UZ-38-14	4.8	9	8.1	0.6	BLOD	BLOD	1.3	0.3	129.6	44.5
UZ-38-15	8.3	32	11.6	0.4	BLOD	BLOD	0.9	0.2	158.0	29.1
UZ-38-16	1.0	2	1.8	0.2	BLOD	BLOD	1.6	0.1	126.3	90.1
UZ-38-17	5.2	8	12.7	0.9	BLOD	BLOD	0.8	0.2	90.3	32.8
UZ-38-18	1.5	5	2.8	0.2	BLOD	BLOD	1.8	1.8	122.2	55.5
UZ-38-19	1.9	5	4.7	0.3	BLOD	BLOD	1.0	0.3	88.8	40.3
UZ-38-20	23.2	54	43.8	2.1	BLOD	BLOD	1.1	0.2	117.0	17.5
UZ-38-21	2.7	8	3.0	0.2	BLOD	BLOD	1.2	0.4	200.8	72.5
UZ-38-22	2.2	3	6.8	0.3	BLOD	BLOD	0.8	0.2	71.2	41.3
UZ-38-23	6.8	25	11.6	0.6	BLOD	BLOD	1.0	0.2	129.9	27.3
UZ-38-24	17.1	40	16.8	0.8	BLOD	BLOD	1.3	0.2	225.1	38.1
UZ-38-25	2.3	3	13.5	0.8	BLOD	BLOD	1.2	0.3	37.7	21.9
UZ-38-26	2.5	3	2.7	0.2	1310	430	0.7	0.3	207.2	120.6

UZ-38-27	28.0	74	51.6	3.0	1010	370	1.2	0.3	119.8	16.2
UZ-38-28	2.7	8	4.1	0.3	690	350	1.2	0.4	141.9	51.3
UZ-38-29	7.7	19	16.6	0.8	BLOD	BLOD	1.0	0.2	102.7	24.4
UZ-38-30	1.7	4	3.2	0.2	BLOD	BLOD	0.9	0.0	119.0	60.3
UZ-38-31	12.7	14	19.4	0.9	BLOD	BLOD	0.7	0.1	144.2	39.5
UZ-38-32	6.5	15	4.8	0.3	BLOD	BLOD	0.8	0.4	300.9	80.9
UZ-38-33	4.7	9	6.0	0.3	BLOD	BLOD	0.9	0.1	170.8	58.0
UZ-38-34	2.5	10	2.0	0.2	BLOD	BLOD	1.0	0.2	270.8	91.6
UZ-38-35	13.4	32	33.1	2.1	BLOD	BLOD	0.9	0.3	89.4	17.1
UZ-39-1	26.4	75	40.6	2.5	BLOD	BLOD	1.3	0.2	143.8	19.6
UZ-39-2	2.3	11	5.1	0.3	BLOD	BLOD	1.2	0.6	99.8	30.8
UZ-39-3	37.2	117	94.4	5.1	BLOD	BLOD	1.5	0.3	87.2	9.9
UZ-39-4	18.9	76	44.4	2.3	BLOD	BLOD	1.5	0.3	94.2	12.4
UZ-39-5	20.9	75	34.4	1.4	BLOD	BLOD	1.5	0.2	134.2	17.2
UZ-39-6	34.1	126	53.0	2.9	1030	380	1.6	0.5	142.2	15.8
UZ-39-7	41.5	143	79.3	3.3	BLOD	BLOD	1.6	0.3	115.8	11.7
UZ-39-8	47.4	109	141.6	4.9	BLOD	BLOD	1.5	0.2	74.0	8.1
UZ-39-9	11.0	48	22.9	1.1	BLOD	BLOD	1.4	0.2	106.0	16.6
UZ-39-10	17.3	43	36.3	1.7	BLOD	BLOD	1.4	0.4	105.4	17.3
UZ-39-11	37.6	89	72.7	2.3	BLOD	BLOD	1.5	0.4	114.4	13.4
UZ-39-12	18.8	50	101.4	3.5	830	350	1.5	0.2	40.9	6.2
UZ-39-13	23.2	75	99.0	6.9	19500	6600	1.8	0.2	51.8	7.3
UZ-39-14	15.4	66	34.2	1.9	BLOD	BLOD	1.6	0.2	99.7	14.0
UZ-39-15	34.3	99	87.7	3.1	BLOD	BLOD	1.7	0.3	86.5	9.8
UZ-39-16	14.7	75	27.1	1.7	BLOD	BLOD	1.6	0.2	120.0	16.4
UZ-39-17	26.2	91	51.2	2.7	BLOD	BLOD	1.1	0.2	113.3	14.0
UZ-39-18	31.5	102	31.9	1.8	BLOD	BLOD	1.4	0.3	218.0	26.2
UZ-39-19	17.0	89	39.6	2.0	660	390	1.8	0.2	95.0	11.7
UZ-39-20	11.2	28	35.3	1.8	BLOD	BLOD	1.4	0.3	69.9	13.9
UZ-39-21	23.8	81	56.2	4.4	BLOD	BLOD	1.1	0.2	93.4	13.2

UZ-39-22	2.8	10	72.5	3.3	BLOD	BLOD	1.0	0.3	8.6	2.8
UZ-39-23	7.3	36	65.7	2.4	760	290	1.2	0.2	24.4	4.3
UZ-39-24	5.3	33	12.9	0.6	BLOD	BLOD	1.1	0.2	90.7	16.8
UZ-39-25	34.5	134	152.8	7.2	800	330	1.4	0.3	50.0	5.3
UZ-39-26	24.1	142	91.8	4.3	BLOD	BLOD	1.3	0.2	58.1	6.0
UZ-39-27	34.4	121	53.1	3.6	660	340	1.3	0.3	143.1	17.1
UZ-39-28	27.8	136	34.3	1.6	BLOD	BLOD	1.6	0.6	178.9	18.8
UZ-39-29	12.2	61	126.1	8.0	BLOD	BLOD	1.5	0.3	21.3	3.2
UZ-39-30	14.9	49	32.9	1.5	BLOD	BLOD	1.4	0.3	100.1	15.5
UZ-39-31	6.5	36	16.0	0.7	BLOD	BLOD	1.1	0.3	90.2	15.9
UZ-39-32	48.4	261	158.7	7.4	BLOD	BLOD	1.5	0.4	67.4	5.8
UZ-39-33	20.8	74	44.7	2.0	850	350	1.6	0.5	102.8	13.4
UZ-39-34	17.3	66	35.0	1.4	980	350	1.3	0.2	109.5	14.8
UZ-39-35	42.3	174	85.3	3.8	BLOD	BLOD	1.5	0.3	109.7	10.5
UZ-39-36	31.0	182	62.0	2.6	BLOD	BLOD	1.3	0.4	110.5	10.3
UZ-39-37	15.7	78	25.6	1.2	BLOD	BLOD	1.3	0.2	135.5	17.4
UZ-39-38	27.1	113	57.0	2.6	BLOD	BLOD	1.4	0.2	105.2	11.7
UZ-40-1	12.2	45	39.3	2.0	BLOD	BLOD	1.3	0.3	68.6	11.1
UZ-40-2	14.3	15	13.9	1.1	1230	360	1.4	0.9	227.0	61.9
UZ-40-3	12.4	36	24.0	1.8	BLOD	BLOD	1.2	0.2	114.0	21.3
UZ-40-4	7.4	8	9.4	0.5	4700	1100	1.3	0.2	172.8	62.3
UZ-40-5	8.0	14	9.6	0.5	BLOD	BLOD	1.2	0.1	182.8	50.3
UZ-40-6	4.2	6	8.8	0.5	BLOD	BLOD	1.3	0.2	105.1	43.4
UZ-40-7	9.5	15	28.9	1.3	730	310	1.2	0.5	72.7	19.3
UZ-40-8	14.0	27	28.6	1.7	BLOD	BLOD	1.5	0.3	107.8	22.1
UZ-40-9	8.2	26	10.2	0.4	810	300	1.2	0.2	177.1	36.2
UZ-40-10	7.2	25	10.8	0.6	BLOD	BLOD	1.4	0.3	148.1	31.1
UZ-40-11	12.6	27	24.9	1.1	800	240	1.5	0.6	111.8	22.5
UZ-40-12	8.7	21	20.2	1.2	BLOD	BLOD	1.5	0.9	95.5	21.9
UZ-40-13	5.5	14	14.5	0.7	670	210	1.3	0.2	83.1	22.8

UZ-40-14	7.6	21	14.5	0.7	BLOD	BLOD	1.2	0.2	116.6	26.5
UZ-40-15	12.1	24	26.7	1.4	510	200	1.3	0.3	100.0	21.4
UZ-40-16	15.3	57	29.9	1.7	BLOD	BLOD	1.5	0.4	113.4	16.9
UZ-40-17	2.8	9	2.9	0.2	BLOD	BLOD	1.3	0.2	216.2	73.7
UZ-40-18	8.3	22	12.3	0.7	BLOD	BLOD	1.6	0.3	148.3	33.1
UZ-40-19	13.3	39	34.0	2.3	420	230	1.1	0.1	86.2	15.3
UZ-40-20	11.4	37	24.0	1.2	450	230	1.4	0.5	105.0	18.5
UZ-40-21	12.0	33	23.0	1.2	430	220	1.3	0.4	115.2	21.4
UZ-40-22	7.0	27	10.6	0.8	BLOD	BLOD	1.4	0.2	147.3	31.1
UZ-40-23	10.6	41	25.9	1.2	430	220	1.4	0.3	90.4	15.1
UZ-40-24	8.2	24	21.3	1.2	BLOD	BLOD	1.4	0.2	84.6	18.2
UZ-40-25	3.6	23	15.1	0.7	810	210	1.2	0.3	52.0	11.3
UZ-40-26	10.7	28	20.8	0.9	540	230	1.4	0.2	113.8	22.5
UZ-40-27	6.0	11	12.1	1.0	BLOD	BLOD	1.1	0.1	110.3	34.7
UZ-40-28	4.1	26	6.8	0.3	BLOD	BLOD	1.4	1.0	135.4	27.9
UZ-40-29	6.8	26	14.6	0.8	430	190	1.0	0.3	102.7	21.2
UZ-40-30	12.0	26	23.0	1.1	BLOD	BLOD	1.1	0.2	115.4	23.7
UZ-40-31	10.1	28	19.2	1.0	400	180	1.3	0.2	116.3	23.2
UZ-40-32	7.4	32	14.6	0.7	360	170	1.1	0.3	112.7	21.1
UZ-40-33	4.3	8	7.1	0.4	BLOD	BLOD	1.3	0.2	132.2	47.5
UZ-40-34	7.7	22	21.6	1.0	BLOD	BLOD	1.0	0.1	78.6	17.4
UZ-40-35	20.2	40	61.6	2.1	BLOD	BLOD	1.2	0.2	72.6	12.1
UZ-40-36	8.6	36	12.0	0.5	BLOD	BLOD	1.0	0.2	158.8	28.1
UZ-40-37	3.7	6	11.0	0.7	BLOD	BLOD	1.2	0.1	74.6	30.9
UZ-40-38	7.5	12	14.1	0.9	BLOD	BLOD	NA	0.0	118.1	35.3
UZ-40-39	7.2	20	15.4	0.6	BLOD	BLOD	1.3	0.2	103.7	23.9
UZ-41-1	17.1	68	22.0	1.4	1150	290	1.6	0.3	171.5	24.4
UZ-41-2	13.9	43	32.8	2.2	1050	270	2.0	0.6	93.8	16.0
UZ-41-3	15.9	59	29.1	1.4	1300	350	1.3	0.2	120.4	17.3
UZ-41-4	21.6	42	29.6	1.6	750	250	1.5	0.3	161.6	27.1

UZ-41-5	19.3	46	33.8	1.7	1340	250	1.6	0.4	125.9	20.2
UZ-41-6	24.9	51	44.4	1.9	1060	240	1.5	0.3	124.1	18.8
UZ-41-7	18.8	74	34.0	1.6	1110	220	1.7	0.3	122.1	16.0
UZ-41-8	10.8	14	23.9	1.2	1440	270	1.5	0.3	99.6	27.4
UZ-41-9	9.5	11	20.9	0.9	1060	250	1.8	0.1	100.2	30.7
UZ-41-10	18.6	50	17.1	1.0	970	270	1.5	0.3	240.6	38.0
UZ-41-11	11.4	45	18.0	1.2	940	270	1.6	0.5	139.9	23.5
UZ-41-12	15.5	31	33.4	2.2	1070	250	1.3	0.3	102.5	20.0
UZ-41-13	12.9	35	25.2	1.3	1270	250	1.6	0.2	113.2	20.5
UZ-41-14	9.6	15	22.1	1.0	1080	190	1.6	0.3	96.1	25.4
UZ-41-15	17.5	26	33.7	1.5	1060	230	1.4	0.3	114.6	23.5
UZ-41-16	18.1	26	47.4	3.4	13700	3200	1.4	0.2	84.5	17.9
UZ-41-17	12.8	21	27.2	1.2	740	210	1.5	0.4	103.7	23.4
UZ-41-18	23.6	63	29.3	1.8	1070	270	1.3	0.2	177.7	25.8
UZ-41-19	10.2	30	16.9	0.9	1320	300	1.4	0.3	133.5	25.9
UZ-41-20	20.6	41	35.5	1.8	1390	250	1.6	0.6	128.4	21.6
UZ-41-21	21.9	34	30.5	1.1	1350	220	1.6	0.2	158.9	28.5
UZ-41-22	11.7	31	30.5	3.1	3600	1300	1.6	0.5	84.9	17.8
UZ-41-23	17.9	40	31.4	1.6	1050	270	1.5	0.3	126.0	21.5
UZ-41-24	14.9	39	11.4	0.5	1630	280	1.7	0.5	289.8	49.2
UZ-41-25	20.2	44	35.5	1.4	1740	250	1.6	0.3	125.9	20.2
UZ-41-26	16.7	23	32.6	1.3	1130	250	1.6	0.4	113.3	24.4
UZ-41-27	15.7	22	27.1	1.4	1190	230	1.6	0.3	127.7	28.4
UZ-41-28	21.1	44	53.2	2.9	800	260	1.7	0.2	87.9	14.5
UZ-41-29	13.9	33	19.9	1.7	1410	310	1.4	0.3	154.1	30.5
UZ-41-30	11.0	25	14.7	0.6	1030	240	1.6	0.3	165.6	34.5
UZ-41-31	18.9	58	33.5	1.6	1000	210	1.3	0.3	124.9	18.1
UZ-41-32	11.4	26	24.6	1.2	890	250	1.2	0.3	102.2	21.0
UZ-41-33	15.1	48	23.3	1.2	1260	220	1.9	0.3	143.5	22.7
UZ-41-34	16.4	41	15.7	0.9	1010	210	1.6	0.5	230.5	39.2

UZ-41-35	27.4	45	29.6	1.1	1370	230	1.4	0.3	204.3	32.4
UZ-41-36	17.8	41	26.1	1.1	800	220	1.4	0.2	150.8	25.1
UZ-41-37	9.1	21	9.3	0.8	1380	250	0.8	0.2	215.3	50.8
UZ-41-38	14.7	42	19.7	1.1	1130	210	1.5	0.3	164.6	27.7
UZ-41-39	15.3	21	38.2	1.9	930	230	1.6	0.3	88.6	20.1
UZ-41-40	16.7	39	33.4	1.8	1020	190	1.5	0.2	110.3	19.1
UZ-41-41	17.4	31	36.0	1.4	690	210	1.4	0.2	107.0	20.1
UZ-41-42	17.9	41	26.0	1.7	41600	9300	1.4	0.3	151.9	26.4
UZ-41-43	9.6	24	19.9	4.0	20000	15000	1.3	0.3	107.1	31.0
UZ-42-1	4.6	11	5.3	0.3	BLOD	BLOD	0.5	0.2	191.7	59.0
UZ-42-2	1.9	2	8.4	0.5	BLOD	BLOD	1.1	0.4	51.0	36.3
UZ-42-3	6.8	8	6.5	0.4	640	190	1.3	0.3	229.5	82.9
UZ-42-4	6.1	14	7.1	0.5	BLOD	BLOD	1.2	0.1	190.4	53.1
UZ-42-5	4.0	4	7.5	0.5	BLOD	BLOD	1.5	0.2	119.2	60.3
UZ-42-6	4.4	16	11.2	0.6	BLOD	BLOD	0.9	0.2	87.7	22.7
UZ-42-7	3.9	7	14.4	0.8	BLOD	BLOD	1.0	0.1	60.5	23.2
UZ-42-8	8.1	33	26.6	1.3	BLOD	BLOD	1.0	0.2	67.5	12.5
UZ-42-9	10.5	33	21.1	0.9	BLOD	BLOD	1.2	0.2	109.8	20.1
UZ-42-10	4.4	11	9.8	0.6	BLOD	BLOD	1.0	0.1	99.2	30.7
UZ-42-11	3.5	16	5.7	0.4	BLOD	BLOD	1.0	0.1	135.2	35.2
UZ-42-12	8.1	16	6.7	0.3	1430	530	1.1	0.2	269.5	69.5
UZ-42-13	2.6	5	3.5	0.2	BLOD	BLOD	1.0	0.1	163.2	73.6
UZ-42-14	5.7	26	10.0	0.4	BLOD	BLOD	1.3	0.4	127.3	26.0
UZ-42-15	5.8	19	9.3	0.5	BLOD	BLOD	0.7	0.2	137.3	32.6
UZ-42-16	2.4	9	4.7	0.3	BLOD	BLOD	0.6	0.1	114.3	38.9
UZ-42-17	6.6	16	8.6	0.4	BLOD	BLOD	1.1	0.2	169.7	43.8
UZ-42-18	4.5	14	9.4	0.4	BLOD	BLOD	1.1	0.2	107.0	29.2
UZ-42-19	6.7	31	11.4	0.7	BLOD	BLOD	1.1	0.2	130.2	25.2
UZ-42-20	9.3	21	9.7	0.7	BLOD	BLOD	1.2	0.2	212.3	49.8
UZ-42-21	8.4	19	18.6	1.4	BLOD	BLOD	1.5	0.2	99.5	24.3

UZ-42-22	14.6	34	19.3	0.8	BLOD	BLOD	1.1	0.5	167.1	30.2
UZ-42-23	5.5	23	10.5	0.6	BLOD	BLOD	1.0	0.3	115.8	25.4
UZ-42-24	3.1	5	5.4	0.3	BLOD	BLOD	1.0	0.6	128.5	58.1
UZ-42-25	7.2	14	8.3	0.5	BLOD	BLOD	1.3	0.2	192.0	53.0
UZ-42-26	3.5	10	4.4	0.3	BLOD	BLOD	1.2	0.2	178.2	57.8
UZ-42-27	11.0	26	18.5	1.0	BLOD	BLOD	0.8	0.2	131.0	27.1
UZ-42-28	5.7	17	7.3	0.3	BLOD	BLOD	1.0	0.3	172.5	43.1
UZ-42-29	6.2	8	8.9	0.5	BLOD	BLOD	1.0	0.5	152.1	54.7
UZ-42-30	7.4	13	9.0	0.6	BLOD	BLOD	1.2	0.1	182.6	52.4
UZ-42-31	14.1	37	21.6	1.0	BLOD	BLOD	0.9	0.3	144.1	25.2
UZ-42-32	4.3	9	5.4	0.3	400	210	1.4	0.2	175.9	60.0
UZ-42-33	7.2	15	5.8	0.3	BLOD	BLOD	1.3	0.3	276.7	73.4
UZ-42-34	7.7	9	10.3	0.5	BLOD	BLOD	0.8	0.1	165.4	56.1
UZ-42-35	3.1	5	10.9	0.5	BLOD	BLOD	1.2	0.3	62.3	28.1
UZ-42-36	5.9	7	6.0	0.3	BLOD	BLOD	1.4	0.3	218.2	83.8
UZ-43-1	4.6	21	9.9	0.5	BLOD	BLOD	0.6	0.1	85.9	19.6
UZ-43-2	10.5	35	16.6	0.8	BLOD	BLOD	1.0	0.3	116.2	20.9
UZ-43-3	8.5	24	21.2	1.1	BLOD	BLOD	0.7	0.1	74.2	15.9
UZ-43-4	3.5	17	3.5	0.3	BLOD	BLOD	1.6	0.2	185.7	47.6
UZ-43-5	23.4	45	25.2	1.7	18600	5400	1.3	0.4	171.8	28.9
UZ-43-6	10.2	31	14.5	0.6	BLOD	BLOD	0.7	0.1	130.2	24.6
UZ-43-7	18.9	55	51.6	2.9	BLOD	BLOD	1.1	0.3	67.9	10.2
UZ-43-8	8.5	33	15.1	1.0	970	390	1.1	0.3	104.7	19.9
UZ-43-9	27.1	58	58.6	2.7	BLOD	BLOD	1.2	0.3	85.7	12.4
UZ-43-10	7.5	15	13.8	0.7	BLOD	BLOD	0.8	0.2	100.8	26.8
UZ-43-11	7.4	32	13.0	0.7	BLOD	BLOD	1.1	0.2	104.7	19.7
UZ-43-12	3.1	11	3.3	0.2	BLOD	BLOD	1.0	0.2	172.9	53.6
UZ-43-13	14.6	28	25.0	2.0	720	400	1.1	0.2	107.7	22.5
UZ-43-14	8.9	48	22.1	1.1	BLOD	BLOD	1.0	0.2	74.5	11.7
UZ-43-15	14.6	48	19.6	1.1	BLOD	BLOD	0.8	0.2	137.5	21.9

UZ-43-16	6.8	19	10.8	0.8	34200	6700	1.4	0.3	116.8	28.5
UZ-43-17	3.0	13	7.6	0.5	BLOD	BLOD	0.8	0.2	74.2	21.2
UZ-43-18	9.8	20	14.1	1.6	BLOD	BLOD	1.0	0.3	128.3	32.5
UZ-43-19	3.3	7	9.0	0.5	BLOD	BLOD	1.5	0.9	67.3	25.9
UZ-43-20	8.0	27	14.1	0.7	BLOD	BLOD	1.2	0.2	104.6	21.1
UZ-43-21	5.9	17	8.5	0.5	BLOD	BLOD	1.1	0.1	127.2	32.1
UZ-43-22	5.3	23	13.2	0.7	BLOD	BLOD	1.3	0.2	74.8	16.3
UZ-43-23	7.5	17	10.5	0.7	BLOD	BLOD	0.8	0.2	132.2	33.5
UZ-43-24	13.7	32	21.6	1.0	BLOD	BLOD	1.0	0.2	116.9	21.8
UZ-43-25	3.9	11	8.7	0.5	BLOD	BLOD	1.5	0.2	82.8	25.6
UZ-43-26	6.5	22	10.2	0.5	BLOD	BLOD	1.1	0.1	116.7	25.9
UZ-43-27	8.1	45	12.8	0.7	BLOD	BLOD	1.5	0.4	117.6	19.3
UZ-43-28	7.7	46	14.0	0.7	BLOD	BLOD	1.4	0.2	101.0	16.2
UZ-43-29	6.7	27	14.9	0.8	1090	500	0.9	0.2	82.8	16.8
UZ-43-30	20.0	80	30.1	1.3	BLOD	BLOD	1.3	0.2	122.7	15.4
UZ-43-31	5.6	13	8.2	0.4	6900	1600	1.2	0.2	125.3	35.7
UZ-43-32	4.8	17	14.3	0.9	BLOD	BLOD	1.1	0.2	61.8	15.6
UZ-43-33	3.5	16	4.8	0.5	BLOD	BLOD	1.1	0.2	135.5	36.5
UZ-43-34	6.2	30	10.9	0.6	BLOD	BLOD	1.4	0.3	105.9	20.6
UZ-43-35	7.8	29	10.9	0.8	BLOD	BLOD	1.4	0.1	132.8	27.0
UZ-43-36	30.7	60	47.7	2.5	BLOD	BLOD	1.4	0.2	119.2	17.2
UZ-43-37	14.2	37	15.7	0.8	BLOD	BLOD	1.3	0.2	166.6	29.4
UZ-44-1	14.9	40	24.4	1.1	BLOD	BLOD	0.9	0.2	138.5	23.8
UZ-44-2	25.1	42	50.4	2.0	770	340	1.2	0.2	112.8	18.8
UZ-44-3	1.5	6	1.4	0.2	2900	1200	1.5	0.3	246.8	107.8
UZ-44-4	8.3	18	16.7	0.7	BLOD	BLOD	1.1	0.3	112.4	27.5
UZ-44-5	13.1	33	18.1	0.8	BLOD	BLOD	0.9	0.2	163.1	30.3
UZ-44-6	27.1	34	28.0	1.8	BLOD	BLOD	1.3	0.3	219.5	41.6
UZ-44-7	12.6	31	12.0	0.6	BLOD	BLOD	1.0	0.2	238.9	46.2
UZ-44-8	9.8	40	36.6	1.9	BLOD	BLOD	1.3	0.7	60.5	10.5

UZ-44-9	5.2	21	10.3	0.6	BLOD	BLOD	1.3	0.2	113.1	26.1
UZ-44-10	18.8	65	18.3	1.3	BLOD	BLOD	1.4	0.3	232.6	35.1
UZ-44-11	66.3	113	137.5	6.5	BLOD	BLOD	1.2	0.3	109.3	12.7
UZ-44-12	3.7	10	7.6	0.5	1010	800	1.2	0.1	109.6	35.9
UZ-44-13	17.4	37	46.9	1.9	BLOD	BLOD	1.1	0.2	84.0	14.8
UZ-44-14	14.9	55	10.9	0.8	BLOD	BLOD	1.2	0.2	307.6	49.5
UZ-44-15	9.9	38	12.6	0.6	BLOD	BLOD	1.3	0.2	176.7	30.9
UZ-44-16	9.6	38	15.0	0.7	BLOD	BLOD	1.1	0.1	145.0	25.6
UZ-44-17	12.0	50	17.6	0.9	BLOD	BLOD	1.0	0.3	154.9	24.4
UZ-44-18	37.4	92	74.9	3.0	BLOD	BLOD	1.3	0.3	113.2	13.8
UZ-44-19	15.3	30	21.1	1.3	BLOD	BLOD	1.1	0.5	164.5	32.7
UZ-44-20	18.7	55	23.2	1.1	BLOD	BLOD	1.2	0.2	182.9	27.6
UZ-44-21	12.6	53	11.7	0.6	BLOD	BLOD	1.1	0.2	242.5	37.4
UZ-44-22	14.6	45	26.0	1.1	BLOD	BLOD	1.0	0.3	127.3	20.7
UZ-44-23	63.4	147	122.9	5.1	BLOD	BLOD	1.3	0.3	116.8	12.2
UZ-44-24	10.1	29	14.8	0.8	BLOD	BLOD	1.0	0.2	154.1	30.8
UZ-44-25	15.3	64	23.7	1.6	BLOD	BLOD	1.4	0.4	146.3	22.0
UZ-44-26	18.7	60	45.6	2.0	9000	750	1.1	0.3	93.0	13.5
UZ-44-27	17.9	66	23.6	1.3	BLOD	BLOD	1.2	0.3	172.2	24.7
UZ-44-28	7.4	24	33.0	70.0	2400000	2100000	0.8	0.2	50.7	108.1
UZ-44-29	19.6	40	24.7	1.2	BLOD	BLOD	1.2	0.2	180.2	31.1
UZ-44-30	45.1	73	93.0	3.6	BLOD	BLOD	1.3	0.2	110.0	14.6
UZ-44-31	15.8	43	21.6	1.3	620	340	1.4	0.2	166.0	28.4
UZ-44-32	9.9	32	16.4	1.1	BLOD	BLOD	1.4	0.2	136.8	26.7
UZ-44-33	9.3	35	9.3	0.5	BLOD	BLOD	1.5	0.2	226.4	41.7
UZ-44-34	8.7	25	12.9	0.6	800	270	1.3	0.2	154.0	32.5
UZ-44-35	8.4	23	20.9	0.9	600	290	1.6	0.2	91.3	20.0
UZ-44-36	10.2	55	16.8	0.8	BLOD	BLOD	1.3	0.3	137.4	20.8
UZ-44-37	10.9	35	9.4	0.7	720	320	1.1	0.2	262.7	49.9
UZ-44-38	17.2	42	15.1	0.9	BLOD	BLOD	1.3	0.3	257.7	44.6

UZ-44-39	13.3	58	17.4	0.8	BLOD	BLOD	1.2	0.1	173.5	25.7
UZ-44-40	10.5	30	9.9	0.6	BLOD	BLOD	1.1	0.2	239.2	47.4
UZ-44-41	7.9	25	13.0	0.8	BLOD	BLOD	1.2	0.3	137.5	29.7
UZ-44-42	5.5	22	8.4	0.5	BLOD	BLOD	0.9	0.2	149.5	33.8
UZ-45-1	9.8	28	14.8	0.8	BLOD	BLOD	0.9	0.2	150.1	30.3
UZ-45-2	22.6	29	27.3	1.9	BLOD	BLOD	1.1	0.3	187.3	38.3
UZ-45-3	6.1	11	10.3	0.7	BLOD	BLOD	1.0	0.2	133.5	41.7
UZ-45-4	3.2	12	6.2	0.3	BLOD	BLOD	0.9	0.1	116.4	34.6
UZ-45-5	11.2	22	21.4	0.8	BLOD	BLOD	1.4	0.2	119.2	26.4
UZ-45-6	10.4	35	13.4	0.7	BLOD	BLOD	1.0	0.2	174.8	32.0
UZ-45-7	3.8	9	9.5	0.8	BLOD	BLOD	1.1	0.1	90.2	31.2
UZ-45-8	18.3	64	20.2	1.2	BLOD	BLOD	1.1	0.3	205.2	30.1
UZ-45-9	5.5	16	9.4	0.6	BLOD	BLOD	0.7	0.3	131.7	34.4
UZ-45-10	5.7	14	8.1	0.4	BLOD	BLOD	0.9	0.3	159.9	44.2
UZ-45-11	10.1	40	12.1	0.6	BLOD	BLOD	1.1	0.2	188.3	32.7
UZ-45-12	3.7	11	8.9	0.5	BLOD	BLOD	0.6	0.2	94.3	29.2
UZ-45-13	7.6	28	6.3	0.4	BLOD	BLOD	1.2	0.3	275.5	56.2
UZ-45-14	4.5	11	12.9	0.8	BLOD	BLOD	0.5	0.1	79.4	24.7
UZ-45-15	5.0	22	9.3	0.4	BLOD	BLOD	1.1	0.1	122.0	27.3
UZ-45-16	16.1	44	31.1	1.4	BLOD	BLOD	1.1	0.2	117.0	19.3
UZ-45-17	9.3	46	16.5	0.8	BLOD	BLOD	1.0	0.3	128.1	21.0
UZ-45-18	8.7	34	9.6	0.6	BLOD	BLOD	1.0	0.2	204.7	38.9
UZ-45-19	8.0	29	12.1	0.8	BLOD	BLOD	0.9	0.1	149.8	30.3
UZ-45-20	10.9	24	15.9	0.9	BLOD	BLOD	1.1	0.5	155.5	33.7
UZ-45-21	7.0	29	9.4	0.6	BLOD	BLOD	1.0	0.3	169.1	34.0
UZ-45-22	5.2	22	5.6	0.3	BLOD	BLOD	1.3	0.1	209.1	46.8
UZ-45-23	4.1	14	5.3	0.3	BLOD	BLOD	1.0	0.1	174.8	48.3
UZ-45-24	10.9	33	10.3	0.6	BLOD	BLOD	1.1	0.2	239.8	45.7
UZ-45-25	8.7	28	10.2	0.5	BLOD	BLOD	1.3	0.3	193.7	38.9
UZ-45-26	4.0	16	7.7	0.4	BLOD	BLOD	1.1	0.3	116.5	30.3

UZ-45-27	6.4	22	7.7	0.4	BLOD	BLOD	0.8	0.2	190.1	42.6
UZ-45-28	3.7	21	8.4	0.4	BLOD	BLOD	1.6	0.3	100.0	22.8
UZ-45-29	8.1	31	12.2	0.6	BLOD	BLOD	1.1	0.3	151.7	29.3
UZ-45-30	10.1	35	15.4	0.8	BLOD	BLOD	1.0	0.2	148.1	27.2
UZ-45-31	9.4	20	9.0	0.7	BLOD	BLOD	1.0	0.3	237.6	57.8
UZ-45-32	6.9	29	9.7	0.5	BLOD	BLOD	1.6	0.2	162.1	32.4
UZ-45-33	4.0	18	7.0	0.4	BLOD	BLOD	1.0	0.1	128.1	31.8
UZ-45-34	6.7	22	9.0	0.5	BLOD	BLOD	0.7	0.2	166.9	37.7
UZ-45-35	10.6	34	14.4	0.8	BLOD	BLOD	1.0	0.2	167.7	31.2
UZ-45-36	2.8	13	5.3	0.3	BLOD	BLOD	1.1	0.1	117.1	33.5
UZ-45-37	16.6	70	54.8	2.5	BLOD	BLOD	1.3	0.2	68.4	9.4
UZ-45-38	6.9	17	8.5	0.4	BLOD	BLOD	1.5	0.2	183.9	46.3
UZ-45-39	8.8	36	9.6	0.6	BLOD	BLOD	0.6	0.1	207.5	38.1
UZ-45-40	2.4	8	4.9	0.3	BLOD	BLOD	0.9	0.1	112.2	40.5
UZ-45-41	3.8	15	7.6	0.4	BLOD	BLOD	1.1	0.2	113.2	30.3
UZ-45-42	9.8	28	14.8	0.8	BLOD	BLOD	0.9	0.2	150.1	30.3
UZ-48-1	2.9	5	4.3	0.3	19800	3200	1.8	0.5	113.9	51.8
UZ-48-2	6.4	11	5.6	0.4	20900	5200	1.6	0.5	197.9	61.6
UZ-48-3	5.6	11	4.3	0.3	17400	4600	2.1	0.2	226.8	70.3
UZ-48-4	4.0	7	6.0	0.5	4700	1700	1.1	0.4	115.0	44.6
UZ-48-5	16.3	47	11.6	0.4	BLOD	BLOD	1.7	0.3	241.5	37.5
UZ-48-6	4.2	6	6.2	0.5	38400	8900	3.1	0.6	116.6	48.8
UZ-48-7	0.7	1	4.4	0.4	3700	2200	2.3	0.5	25.6	25.7
UZ-48-8	4.0	7	4.9	0.2	1460	400	3.3	1.1	138.0	52.8
UZ-48-9	3.2	6	7.2	0.4	3410	550	1.4	0.4	76.1	31.5
UZ-48-10	5.3	7	6.9	0.4	1230	220	1.2	0.3	130.6	50.2
UZ-48-11	3.2	4	6.5	0.3	1200	210	1.3	0.3	83.3	41.9
UZ-48-12	26.5	49	36.6	1.5	550	190	2.0	0.5	124.8	19.2
UZ-48-13	7.1	14	7.5	0.4	BLOD	BLOD	1.3	0.8	163.8	45.1
UZ-48-14	6.3	10	6.3	0.3	1000	220	2.7	1.1	172.3	55.5

UZ-48-15	1.0	2	6.0	0.3	2540	400	1.5	0.5	28.9	20.5
UZ-48-16	4.0	18	7.1	0.3	1330	240	1.4	0.1	96.4	23.5
UZ-48-17	2.4	5	6.0	0.3	1010	200	1.3	0.3	69.1	31.2
UZ-48-18	3.0	4	5.9	0.3	1270	230	1.5	0.3	88.0	44.3
UZ-48-19	3.1	6	6.4	0.3	1130	240	1.2	0.1	82.8	34.2
UZ-48-20	2.5	3	5.3	0.3	1190	240	1.3	0.2	80.9	47.0
UZ-48-21	35.4	89	48.8	2.2	BLOD	BLOD	1.5	0.6	124.9	15.3
UZ-48-22	30.1	62	31.7	1.3	3940	390	1.6	0.5	163.5	22.8
UZ-48-23	4.4	9	5.9	0.4	18700	4800	1.4	0.3	127.1	43.5
UZ-48-24	3.7	13	6.7	0.3	1300	260	1.2	0.3	93.8	26.6
UZ-48-25	2.8	7	3.8	0.2	1660	510	1.1	0.1	126.7	48.8
UZ-48-26	7.6	32	5.7	0.2	2110	300	1.5	0.2	229.3	42.6
UZ-48-27	5.8	16	4.6	0.3	1360	310	1.4	0.3	216.5	56.5
UZ-48-28	3.8	10	5.5	0.3	1410	320	1.5	0.1	117.6	38.0
UZ-48-29	1.9	3	5.1	0.3	1570	320	1.5	0.3	63.9	37.2
UZ-48-30	2.9	7	6.3	0.4	1320	360	1.6	0.1	80.0	30.8
UZ-48-31	2.2	4	3.1	0.2	1440	260	1.1	0.1	118.9	60.0
UZ-48-32	1.5	3	3.7	0.3	6100	2300	1.1	0.2	68.5	39.9
UZ-48-33	1.7	5	3.4	0.2	2000	430	1.0	0.1	85.6	38.8
UZ-48-34	5.1	12	3.9	0.2	2060	610	1.4	0.1	220.9	65.4
UZ-49-1	47.0	130	80.3	3.5	BLOD	BLOD	1.4	0.2	128.2	13.9
UZ-49-2	16.7	22	32.1	1.5	BLOD	BLOD	1.2	0.2	113.8	25.4
UZ-49-3	22.4	49	48.7	2.9	BLOD	BLOD	0.9	0.4	100.5	16.3
UZ-49-4	37.5	91	60.3	2.8	BLOD	BLOD	1.4	0.3	136.0	16.8
UZ-49-5	18.6	35	36.6	2.3	1350	460	1.1	0.3	111.3	20.7
UZ-49-6	51.6	125	80.3	4.7	5600	2300	1.5	0.5	140.7	16.4
UZ-49-7	41.9	152	81.4	3.6	BLOD	BLOD	1.4	0.5	112.7	11.7
UZ-49-8	13.0	33	25.4	1.1	BLOD	BLOD	1.1	0.3	111.6	20.7
UZ-49-9	38.8	137	88.8	7.2	BLOD	BLOD	1.6	0.5	95.6	12.1
UZ-49-10	39.3	110	63.1	4.8	BLOD	BLOD	1.5	0.3	136.3	17.8

UZ-49-11	23.6	72	53.2	2.5	BLOD	BLOD	1.2	0.4	97.3	13.1
UZ-49-12	43.8	158	74.5	3.8	700	320	1.5	0.4	128.6	13.6
UZ-49-13	22.8	56	21.0	1.1	BLOD	BLOD	1.4	0.5	237.1	35.8
UZ-49-14	16.6	26	33.2	1.4	1030	440	1.2	0.2	109.7	22.6
UZ-49-15	39.0	118	65.5	3.1	BLOD	BLOD	1.2	0.4	130.2	14.8
UZ-49-16	12.2	35	20.9	1.4	BLOD	BLOD	1.2	0.4	127.5	23.9
UZ-49-17	46.1	114	69.3	7.1	7900	1900	1.2	0.3	145.4	21.3
UZ-49-18	29.7	121	47.8	1.4	BLOD	BLOD	1.3	0.3	136.0	14.5
UZ-49-19	47.9	119	78.7	4.5	710	280	1.3	0.3	133.1	15.7
UZ-49-20	23.2	83	32.5	1.5	BLOD	BLOD	1.3	0.3	156.2	20.0
UZ-49-21	30.0	76	46.8	3.3	BLOD	BLOD	1.3	0.3	140.1	20.0
UZ-49-22	36.3	117	91.1	6.1	BLOD	BLOD	1.3	0.4	87.3	10.8
UZ-49-23	44.6	177	52.8	2.7	BLOD	BLOD	1.4	0.4	184.9	18.9
UZ-49-24	27.8	91	30.5	1.6	BLOD	BLOD	1.2	0.2	199.4	25.1
UZ-49-25	30.4	121	56.6	3.9	BLOD	BLOD	1.4	0.4	117.5	14.5
UZ-49-26	18.0	30	31.0	1.7	BLOD	BLOD	1.3	0.2	127.2	25.0
UZ-49-27	21.4	56	42.2	2.1	BLOD	BLOD	1.3	0.4	110.9	16.6
UZ-49-28	50.5	151	71.5	5.8	700	330	1.3	0.3	154.5	19.2
UZ-49-29	25.1	48	37.7	1.8	BLOD	BLOD	1.3	0.2	145.8	23.2
UZ-49-30	31.9	71	56.3	3.1	BLOD	BLOD	1.6	0.5	124.1	17.2
UZ-49-31	39.6	87	83.5	3.5	BLOD	BLOD	1.5	0.5	103.9	12.9
UZ-49-32	23.6	67	34.4	1.5	1470	510	1.6	0.3	150.0	20.7
UZ-49-33	38.3	97	63.4	2.3	660	320	1.3	0.2	132.1	15.5
UZ-49-34	20.9	69	29.7	1.2	BLOD	BLOD	1.3	0.4	154.0	20.8
UZ-49-35	58.0	112	107.1	5.7	BLOD	BLOD	1.3	0.3	118.5	14.0
UZ-49-36	36.5	70	66.2	4.5	BLOD	BLOD	1.3	0.2	120.8	17.5
UZ-50-1	26.2	125	45.8	2.0	930	290	1.6	0.5	125.1	13.7
UZ-50-2	46.6	145	69.9	3.0	2790	370	1.8	0.5	145.9	15.2
UZ-50-3	40.1	207	62.3	2.5	1010	260	1.5	0.3	140.7	13.1
UZ-50-4	31.8	99	39.2	1.4	1890	350	1.6	0.4	177.4	20.7

UZ-50-5	20.0	69	451.0	26.0	2540	690	1.7	0.3	9.7	1.4
UZ-50-6	12.8	37	12.7	1.1	700	430	1.1	0.3	220.6	42.3
UZ-50-7	26.3	119	32.5	1.5	1290	360	1.6	0.4	177.2	20.0
UZ-50-8	24.8	62	35.3	1.6	2300	360	1.7	0.5	153.9	22.0
UZ-50-9	22.9	90	27.3	1.7	1120	360	1.5	0.3	183.3	24.0
UZ-50-10	33.2	63	56.4	2.3	1040	390	1.6	0.4	128.9	18.1
UZ-50-11	37.2	172	70.8	5.7	1600	400	1.6	0.3	115.0	13.8
UZ-50-12	40.2	109	53.1	3.9	2600	420	1.6	0.4	165.7	21.4
UZ-50-13	34.1	64	76.9	2.9	1620	350	1.9	0.6	97.1	13.5
UZ-50-14	24.1	105	55.8	3.1	1170	420	1.4	0.2	94.5	11.5
UZ-50-15	25.3	124	38.5	1.3	1100	270	1.7	0.3	143.7	15.3
UZ-50-16	66.9	191	136.7	5.5	1030	300	1.7	0.5	107.1	10.2
UZ-50-17	39.1	102	52.2	3.0	2750	460	1.6	0.3	164.1	20.3
UZ-50-18	52.6	141	62.9	3.1	2700	470	1.6	0.4	183.1	19.8
UZ-50-19	35.5	144	75.7	3.1	760	270	1.8	0.5	102.6	10.7
UZ-50-20	29.5	72	37.9	1.6	2230	320	1.4	0.2	170.5	22.8
UZ-50-21	25.5	55	118.0	11.0	2990	580	1.6	0.4	47.3	8.1
UZ-50-22	36.0	73	58.1	3.6	2210	460	1.5	0.2	135.7	19.1
UZ-50-23	35.2	73	73.4	2.9	1260	520	1.8	0.5	104.8	13.8
UZ-50-24	52.8	164	73.6	3.0	2240	400	1.6	0.4	156.9	15.6
UZ-50-25	45.4	108	110.1	4.1	1610	420	1.7	0.4	90.2	10.2
UZ-50-26	45.3	101	88.9	5.1	1060	310	1.5	0.4	111.6	13.8
UZ-50-27	28.1	97	34.0	1.8	670	330	1.6	0.3	181.0	22.4
UZ-50-28	57.7	166	72.2	3.7	720	290	1.6	0.4	174.9	18.2
UZ-50-29	32.7	110	36.0	1.9	2110	420	1.9	0.7	198.8	23.6

Appendix N

Kyzylkum-Nurata AFT Radial Plots

1 Single grain apatite fission track data for samples taken from the Kyzylkum-Nurata segment plotted using Vermeesch (2009). Single grain ages are coloured according to their respective uranium 238 (U) measurements.

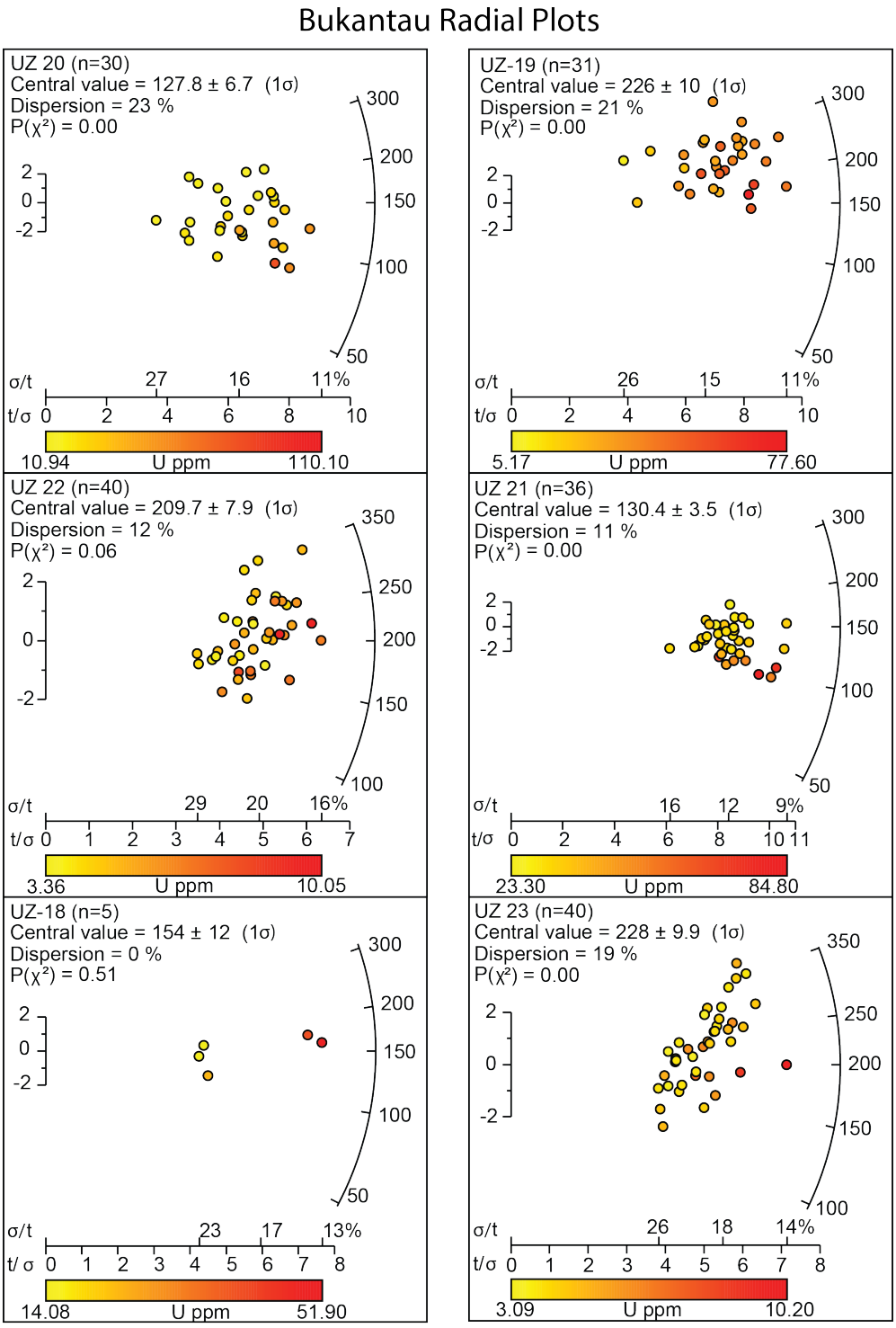

2

Kuldjuktau Radial Plots_1

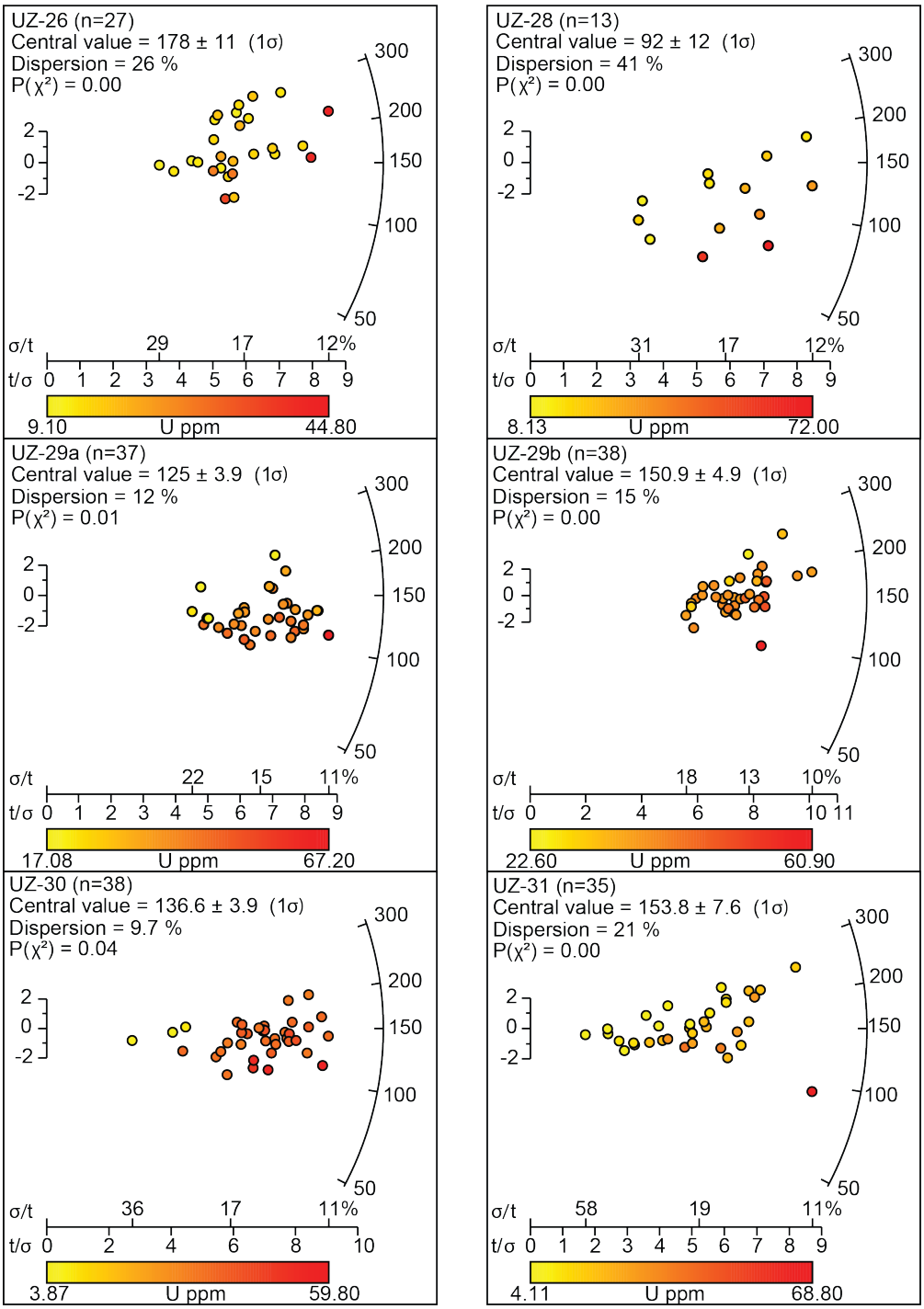

3

Kuldjuktau Radial Plot_2

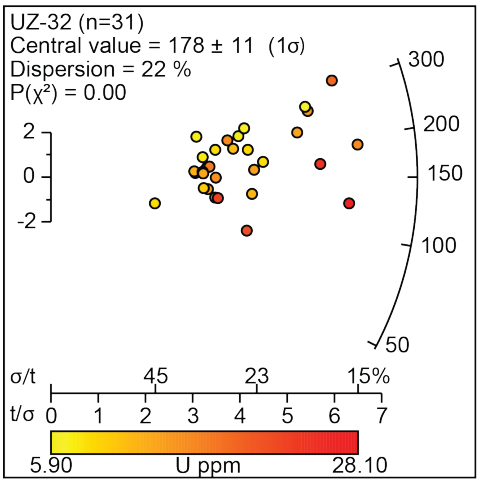

4

Northern Nurata Radial Plots_1

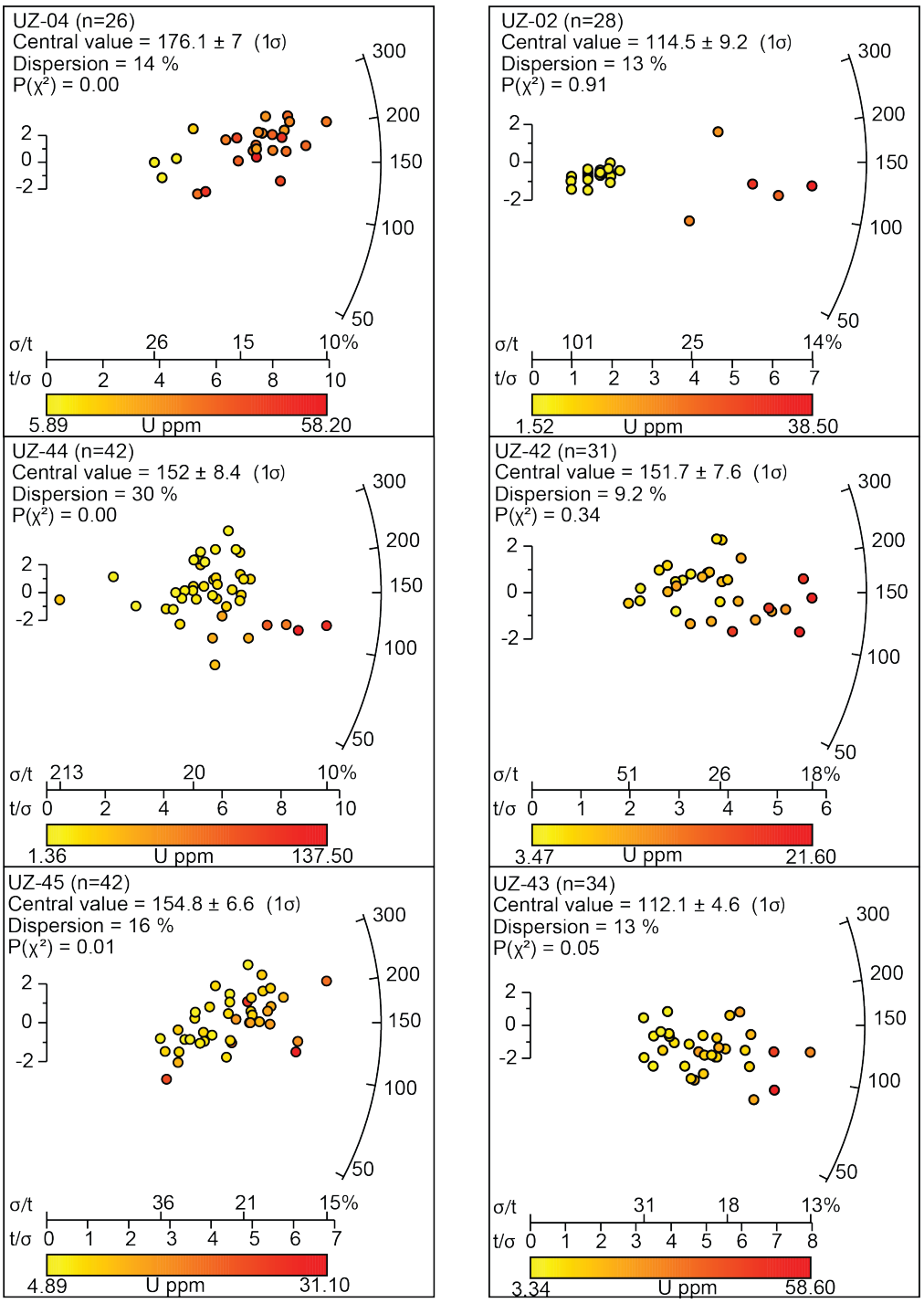

5

South Nurata Range

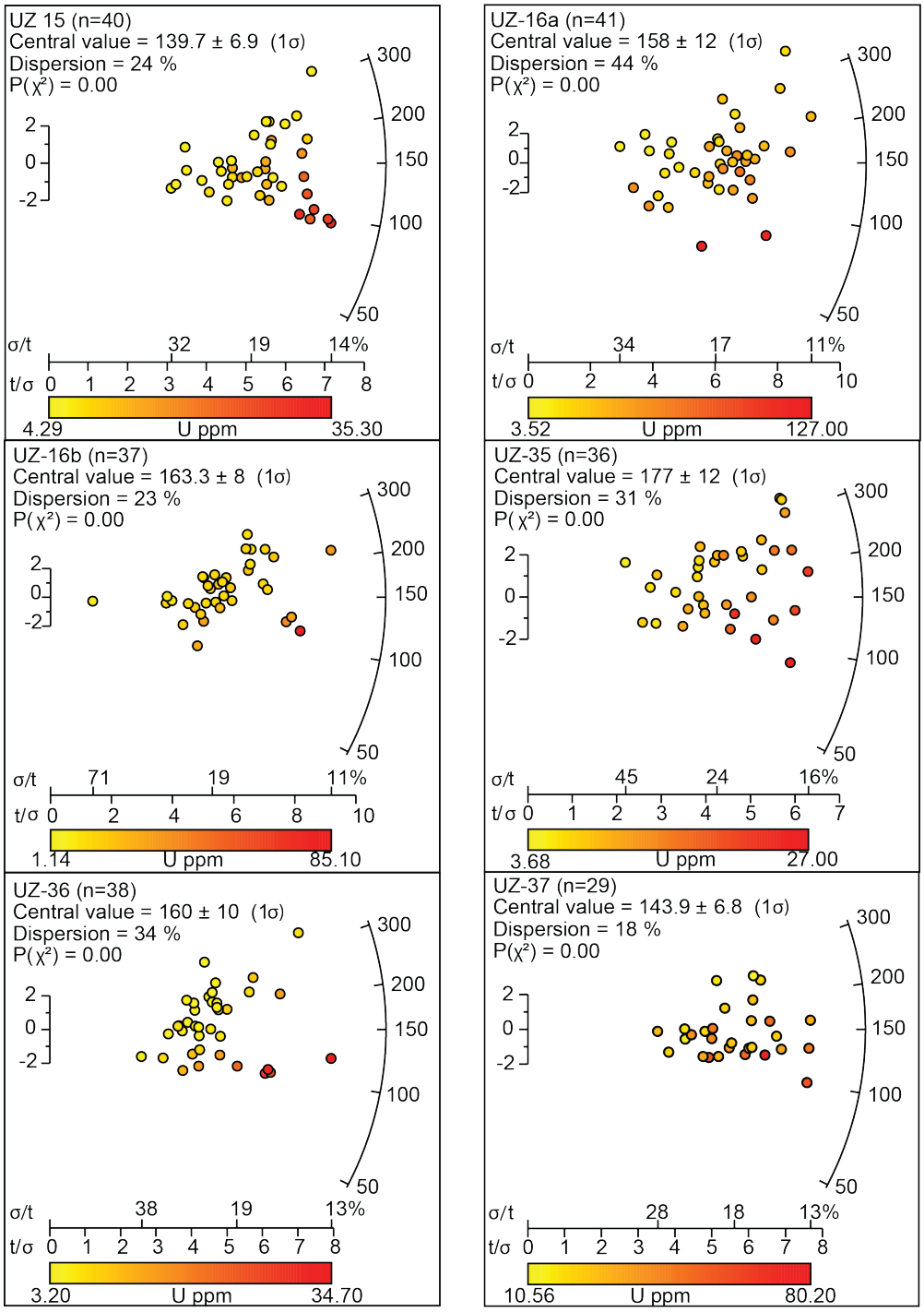

6

South Nurata Range_2

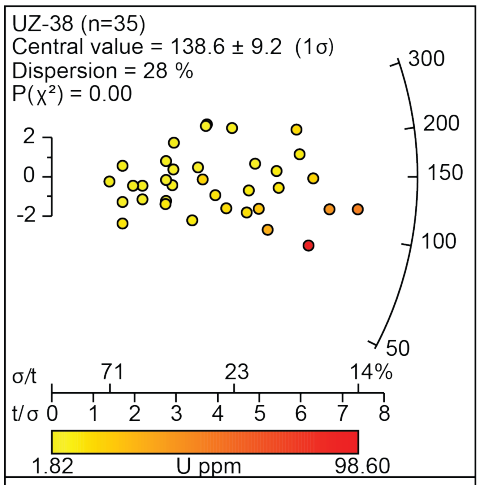

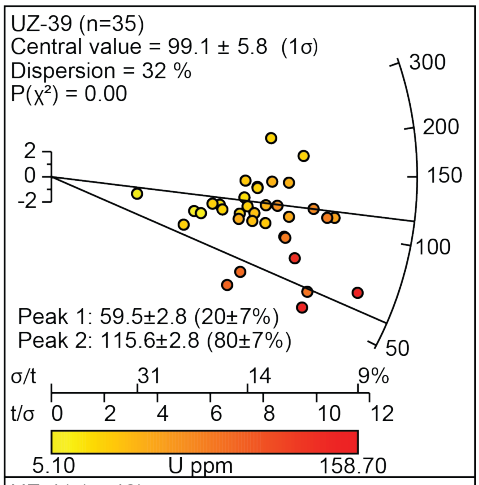

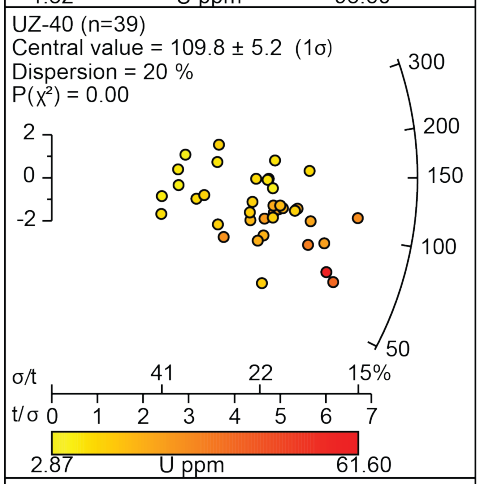

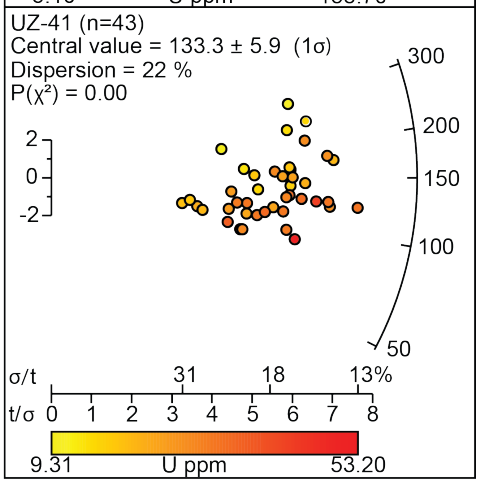

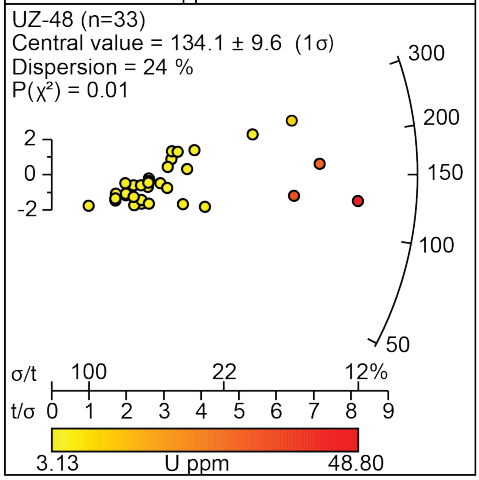

7

Karatyube Massif Radial Plots_1

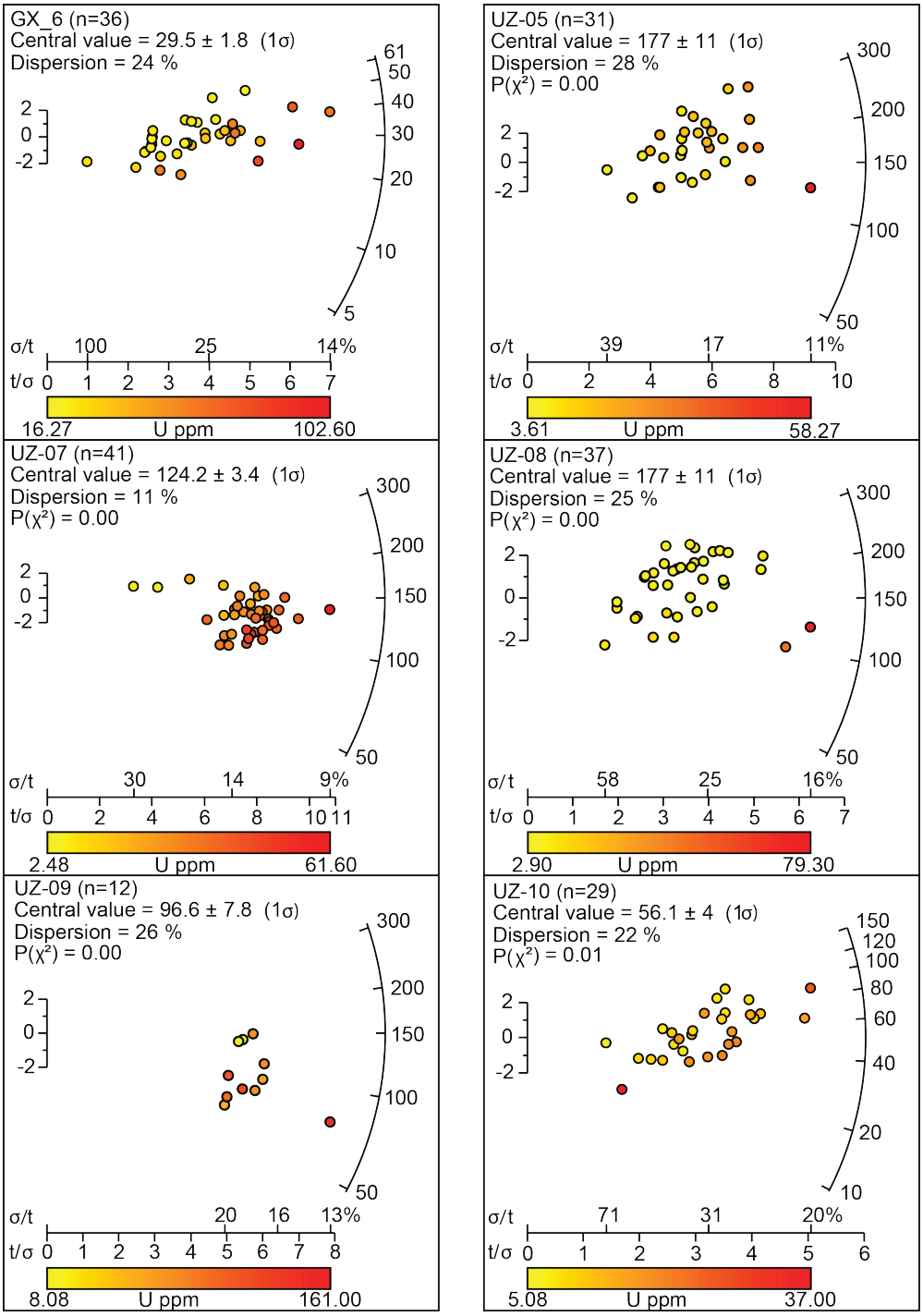

8

Karatyube Massif Radial Plots_2

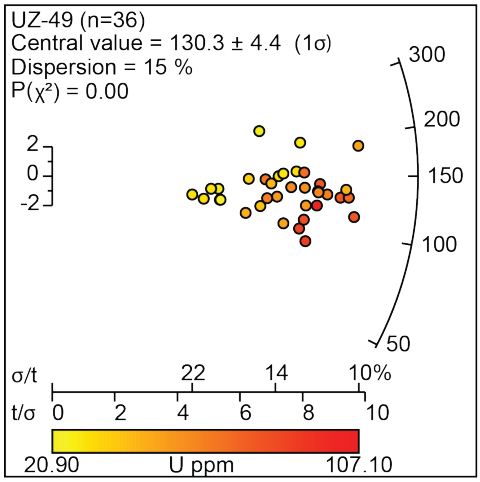

9

Ziadin Mountains Radial Plots

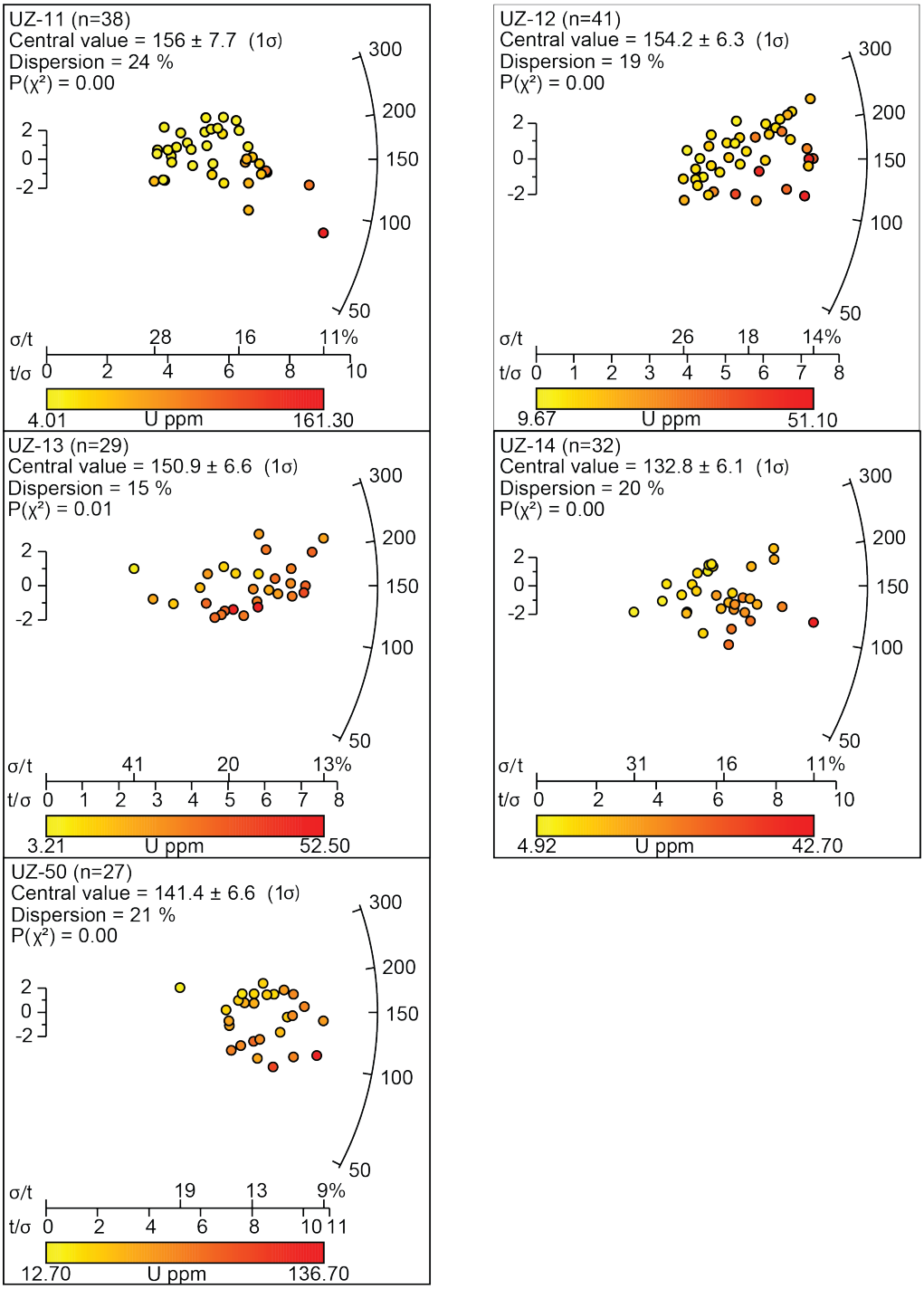

10

Aydar Radial Plots

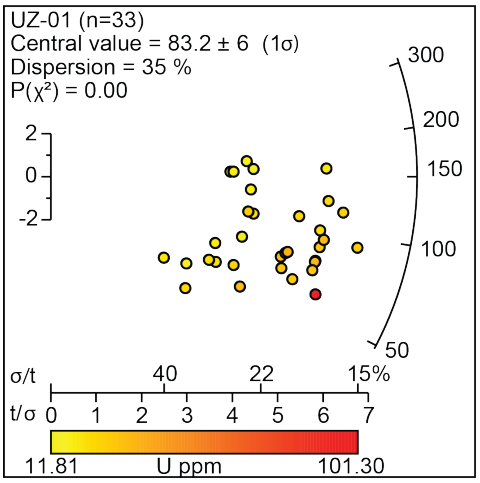

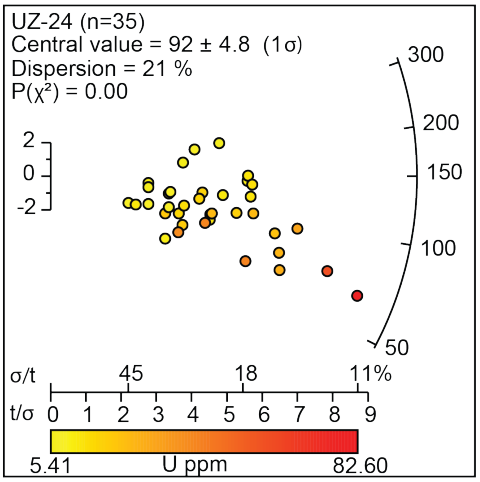

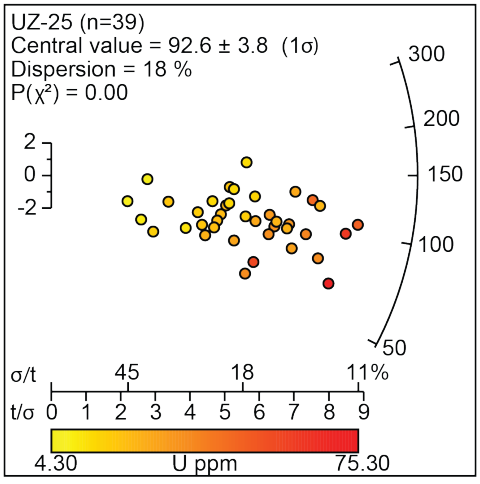

Appendix O

Kyzylkum-Nurata Thermal History Models

1 Individual time-temperature plots for each sample modelled using Gallagher (2012). For modelling parameters see Appendix File 5.

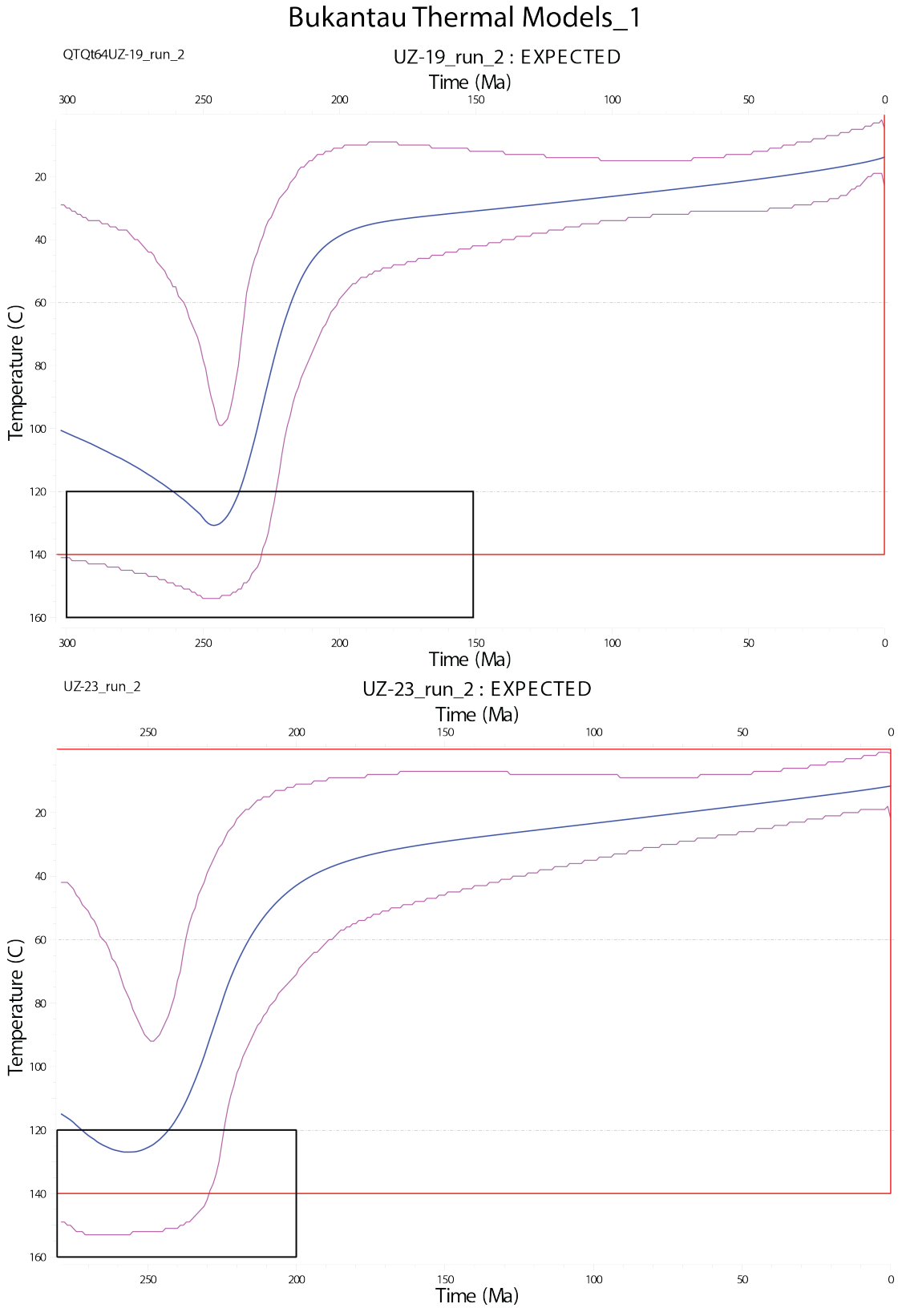

2

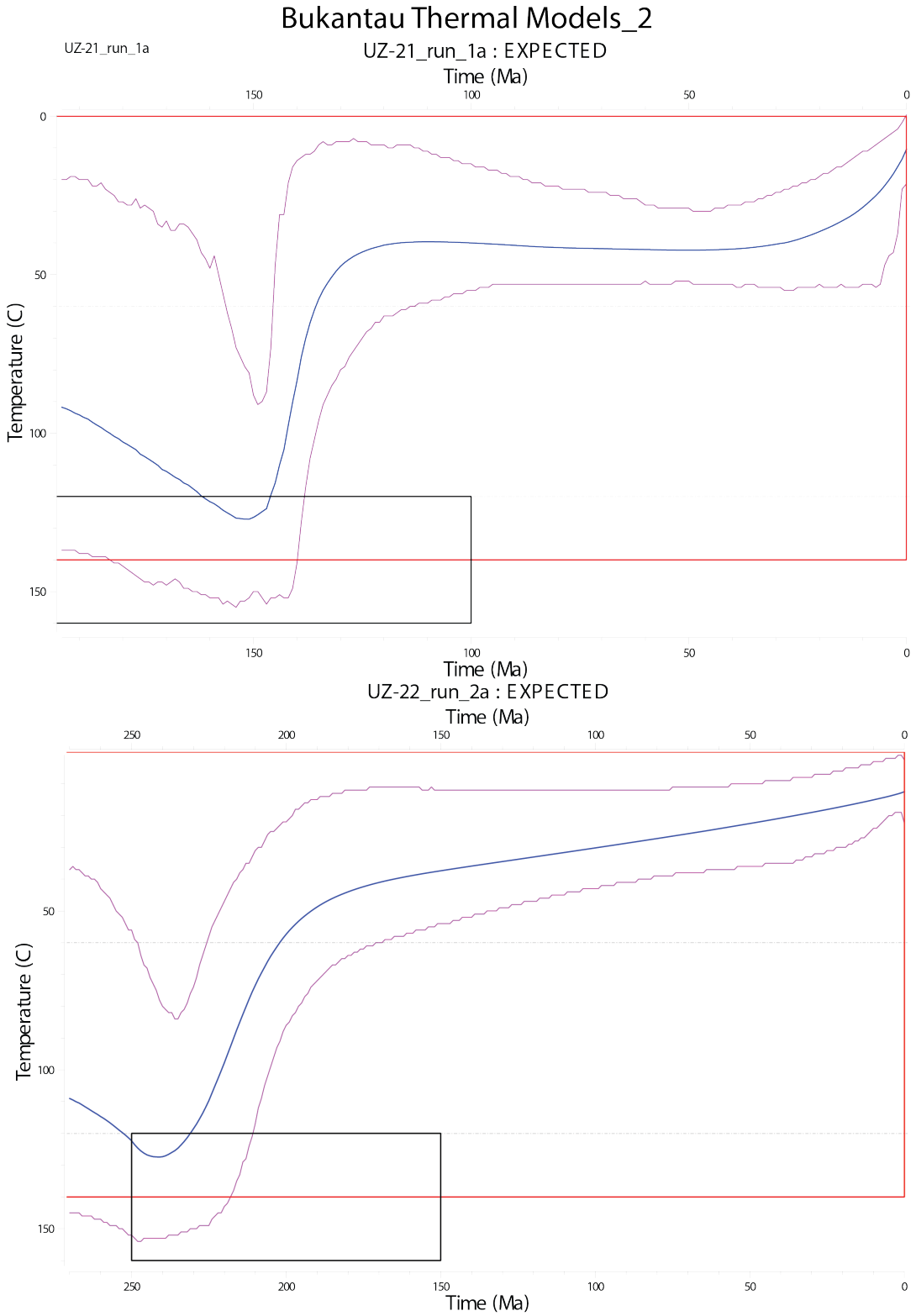
Bukantau Thermal Models_2
UZ-21_run_1a
UZ-21_run_1a : EXPECTED
Time (Ma)
150
100
50
0
Temperature (C)
0
50
100
150
Time (Ma)
UZ-22_run_2a : EXPECTED
Time (Ma)
250
200
150
100
50
0
Temperature (C)
50
100
150
Time (Ma)

3

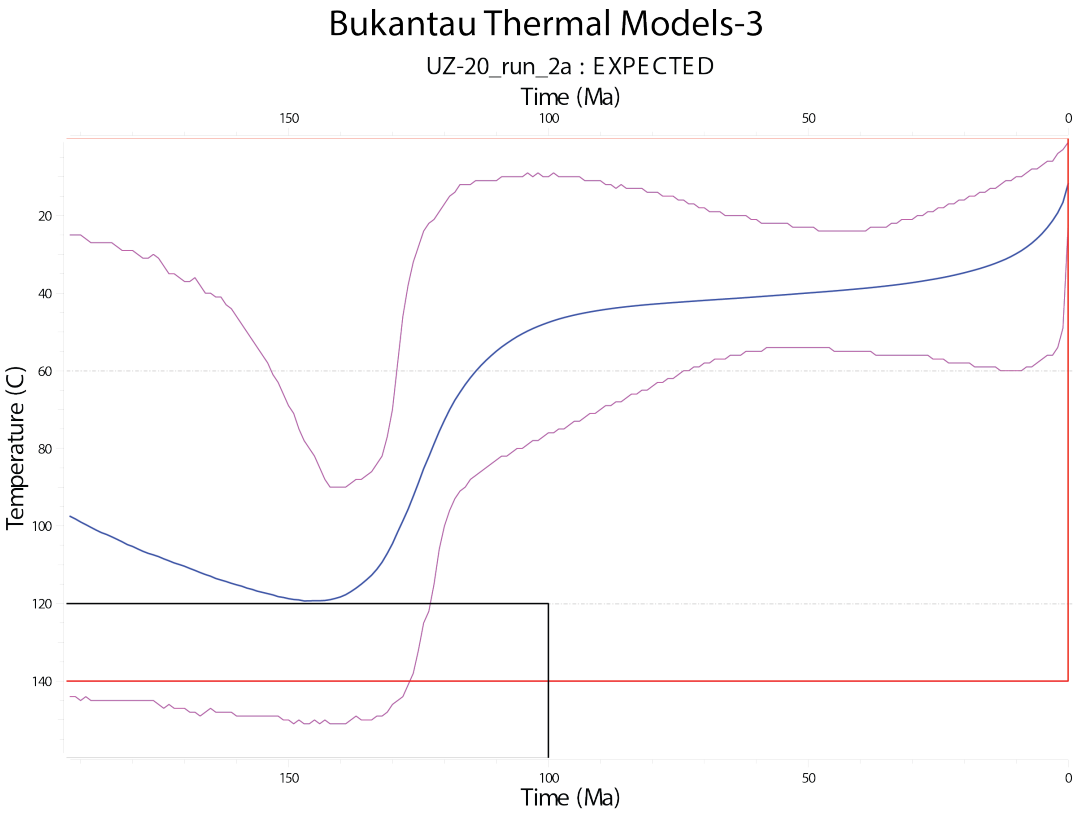
Bukantau Thermal Models-3
UZ-20_run_2a : EXPECTED
Time (Ma)
150
100
50
0
Temperature (C)
20
40
60
80
100
120
140
Time (Ma)

4

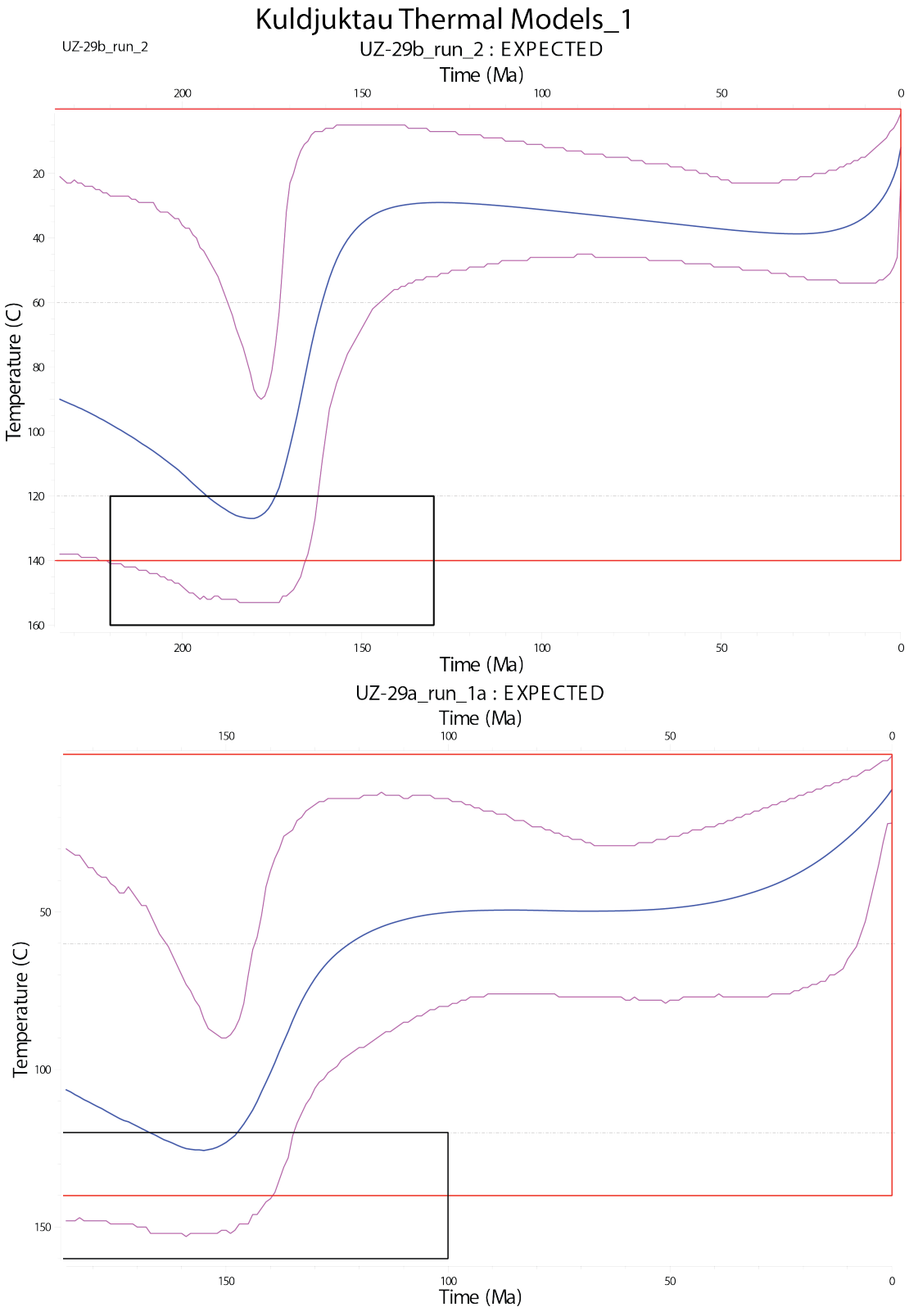
Kuldjuktau Thermal Models_1
UZ-29b_run_2
UZ-29b_run_2 : EXPECTED
Time (Ma)
200
150
100
50
0
Temperature (C)
20
40
60
80
100
120
140
160
Time (Ma)
UZ-29a_run_1a : EXPECTED
Time (Ma)
150
100
50
0
Temperature (C)
50
100
150
Time (Ma)

5

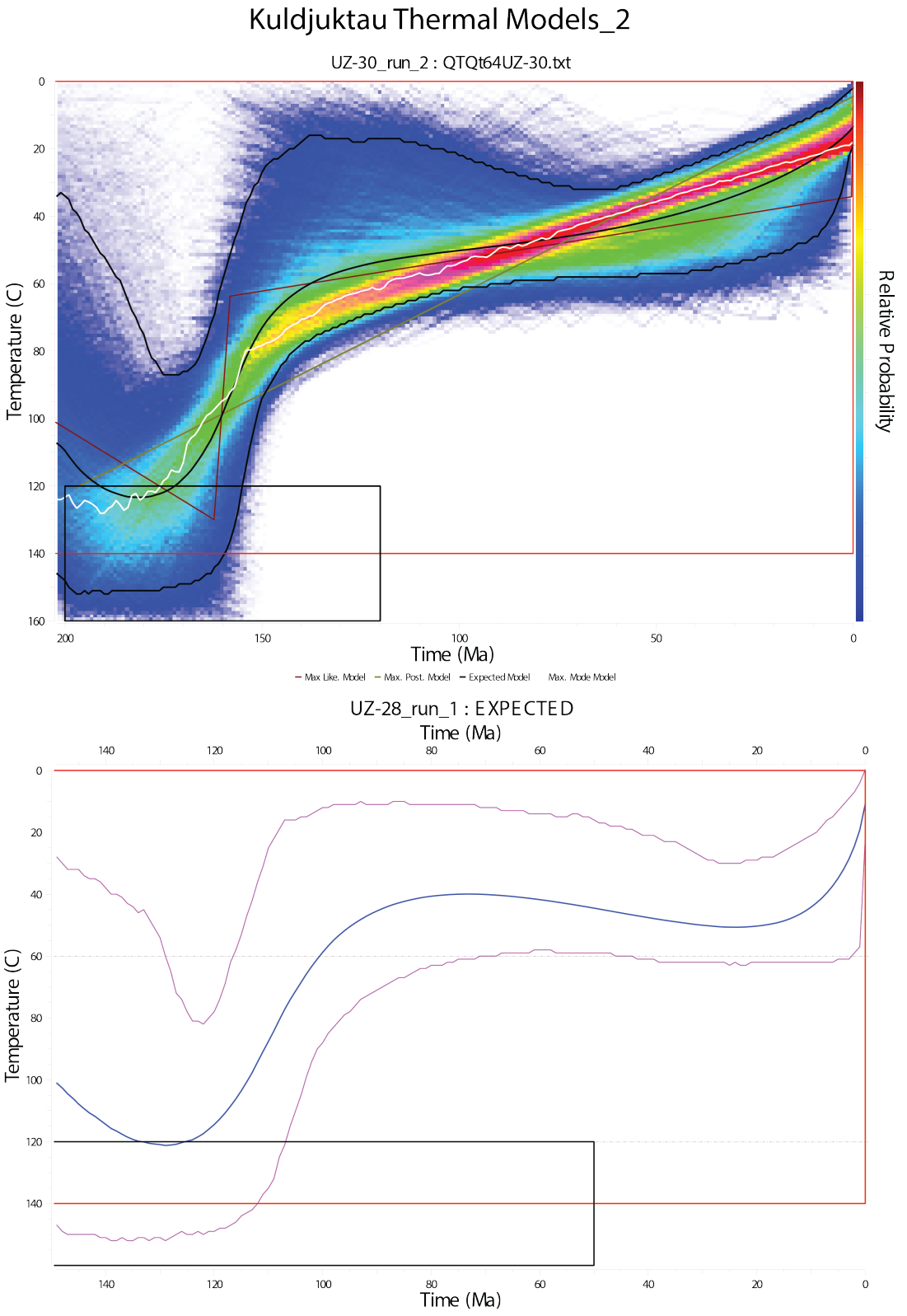
Kuldjuktau Thermal Models_2
UZ-30_run_2 : QTQt64UZ-30.txt
Temperature (C)
Time (Ma)
Relative Probability
Max Like. Model
Max. Post. Model
Expected Model
Max. Mode Model
UZ-28_run_1 : EXPECTED
Time (Ma)
Temperature (C)
Time (Ma)

6

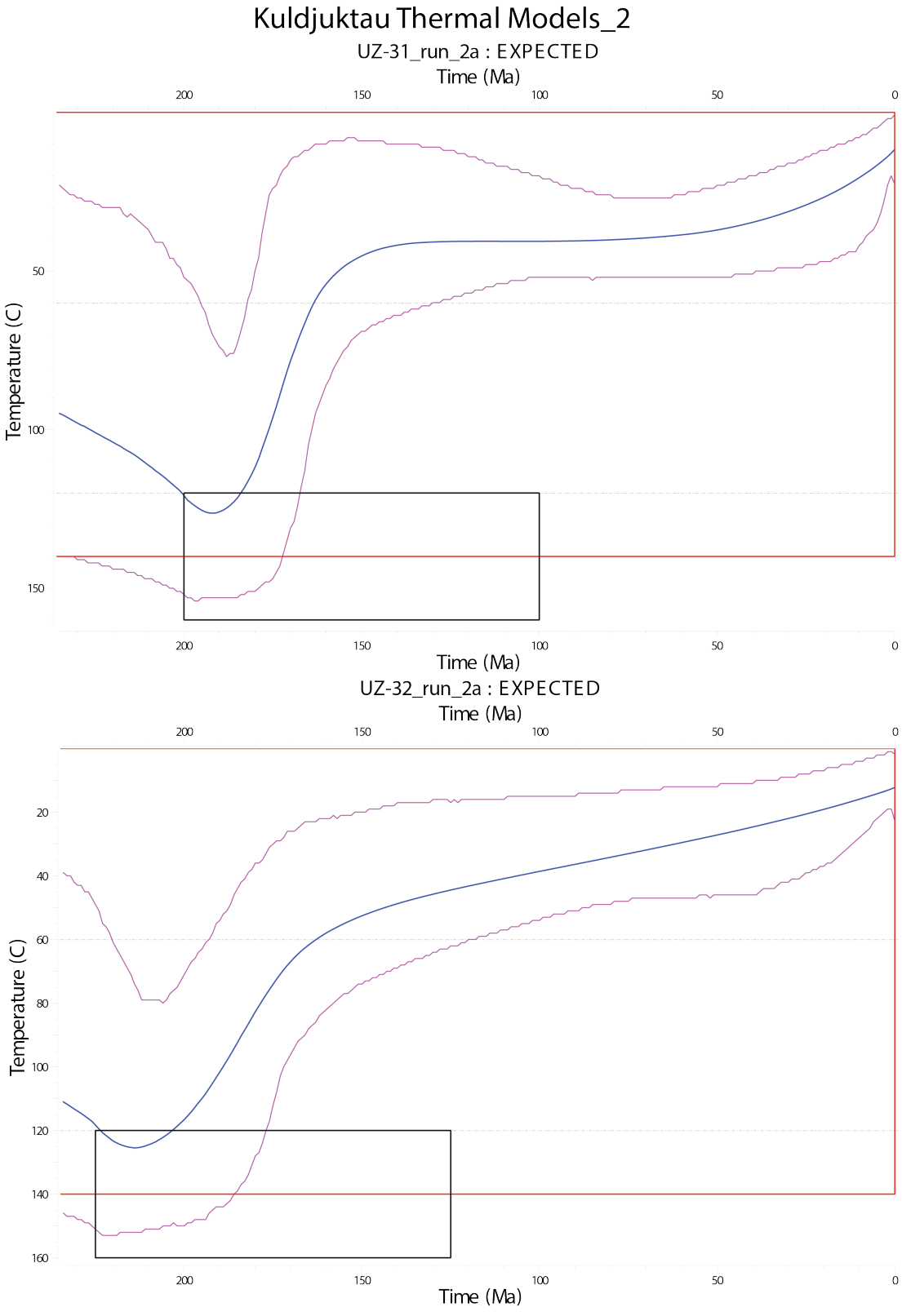
Kuldjuktau Thermal Models_2
UZ-31_run_2a : EXPECTED
Time (Ma)
200
150
100
50
0
Temperature (C)
50
100
150
Time (Ma)
UZ-32_run_2a : EXPECTED
Time (Ma)
200
150
100
50
0
Temperature (C)
20
40
60
80
100
120
140
160
Time (Ma)

7

Nurata Range Thermal Models_1

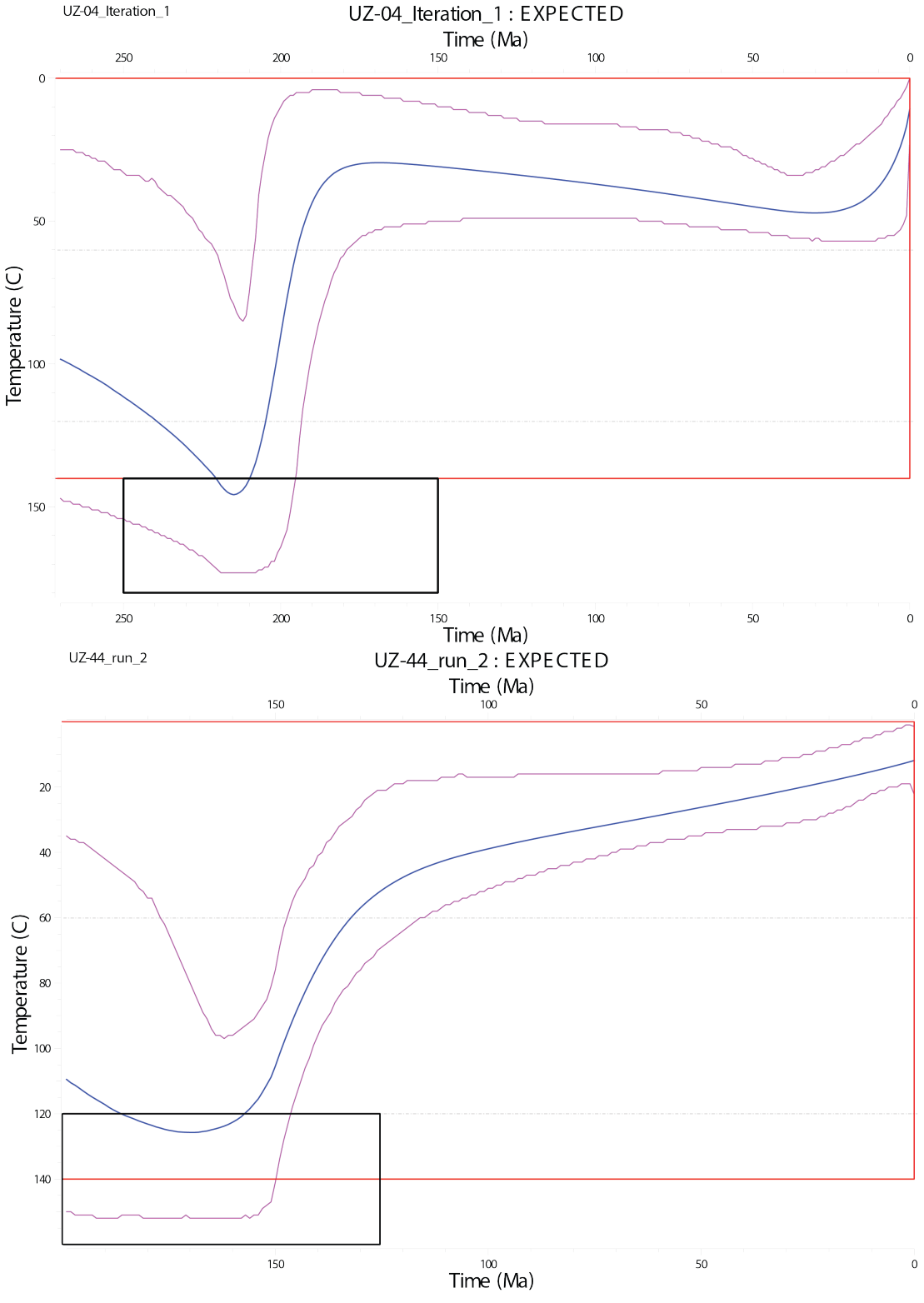

8

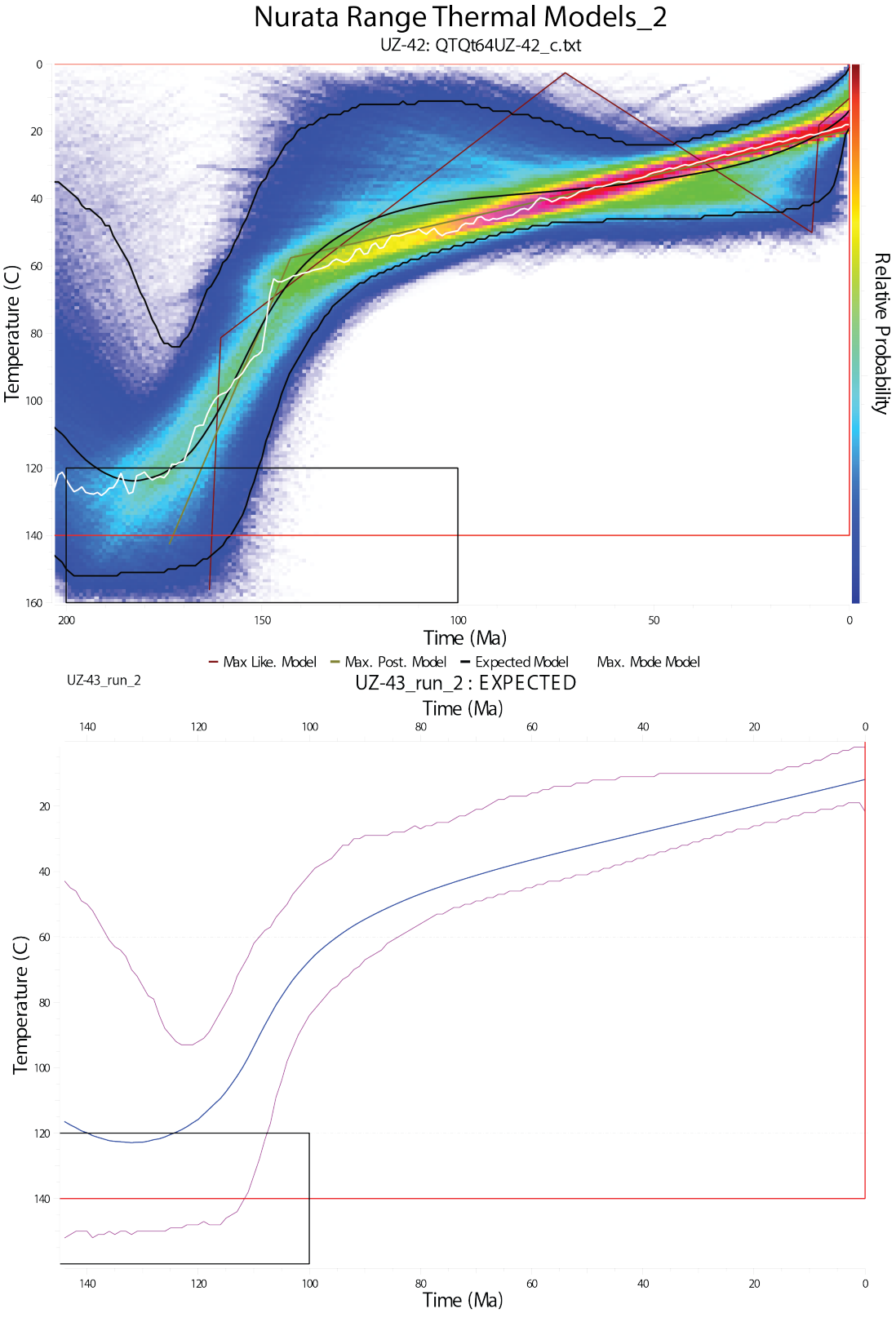
Nurata Range Thermal Models_2
UZ-42: QTQt64UZ-42_c.txt
Temperature (C)
Time (Ma)
Relative Probability
Max Like. Model
Max. Post. Model
Expected Model
Max. Mode Model
UZ-43_run_2
UZ-43_run_2 : EXPECTED
Time (Ma)
Temperature (C)
Time (Ma)

9

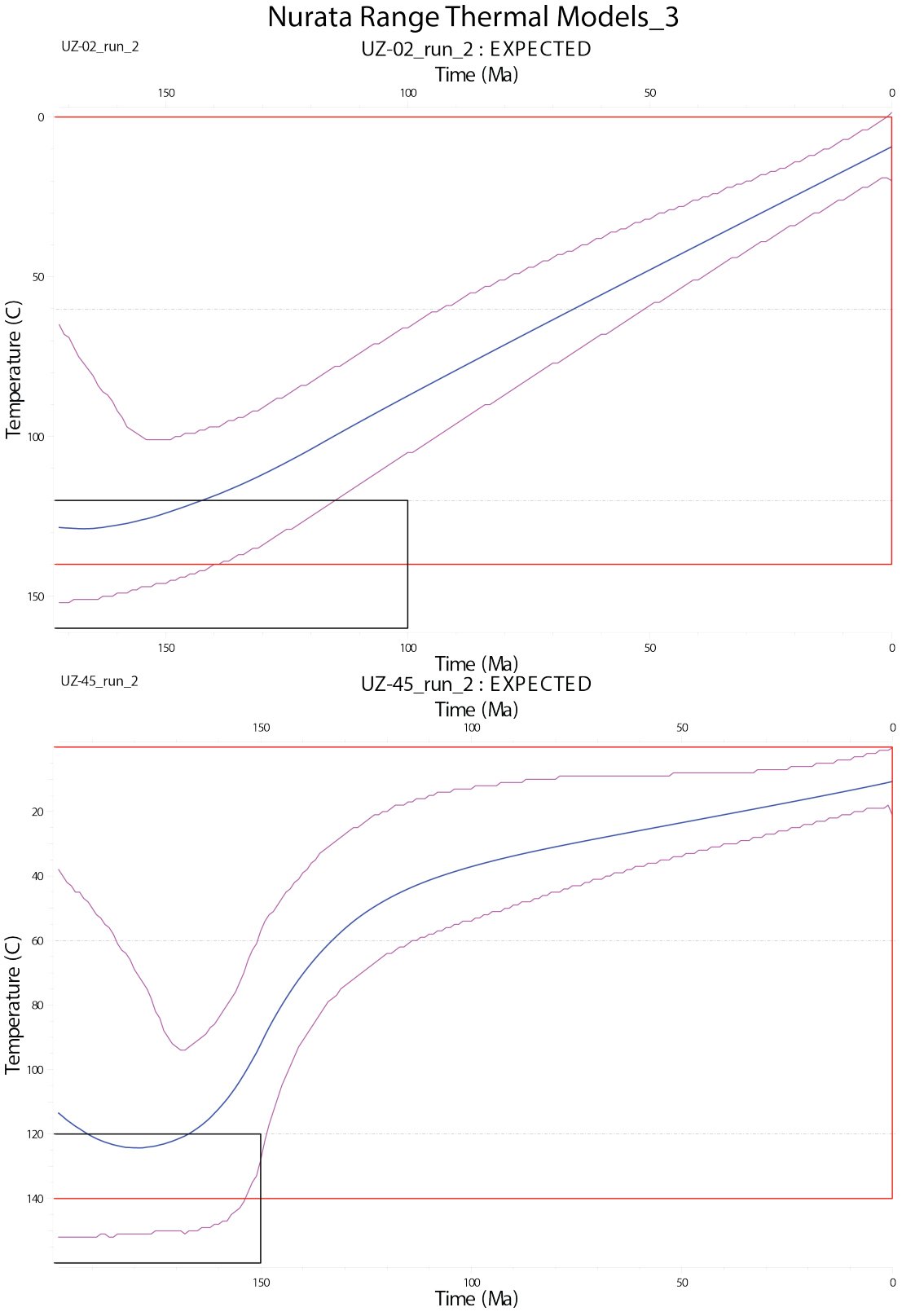
Nurata Range Thermal Models_3
UZ-02_run_2
UZ-02_run_2 : EXPECTED
Time (Ma)
150
100
50
0
Temperature (C)
0
50
100
150
Time (Ma)
UZ-45_run_2
UZ-45_run_2 : EXPECTED
Time (Ma)
150
100
50
0
Temperature (C)
20
40
60
80
100
120
140
Time (Ma)

10

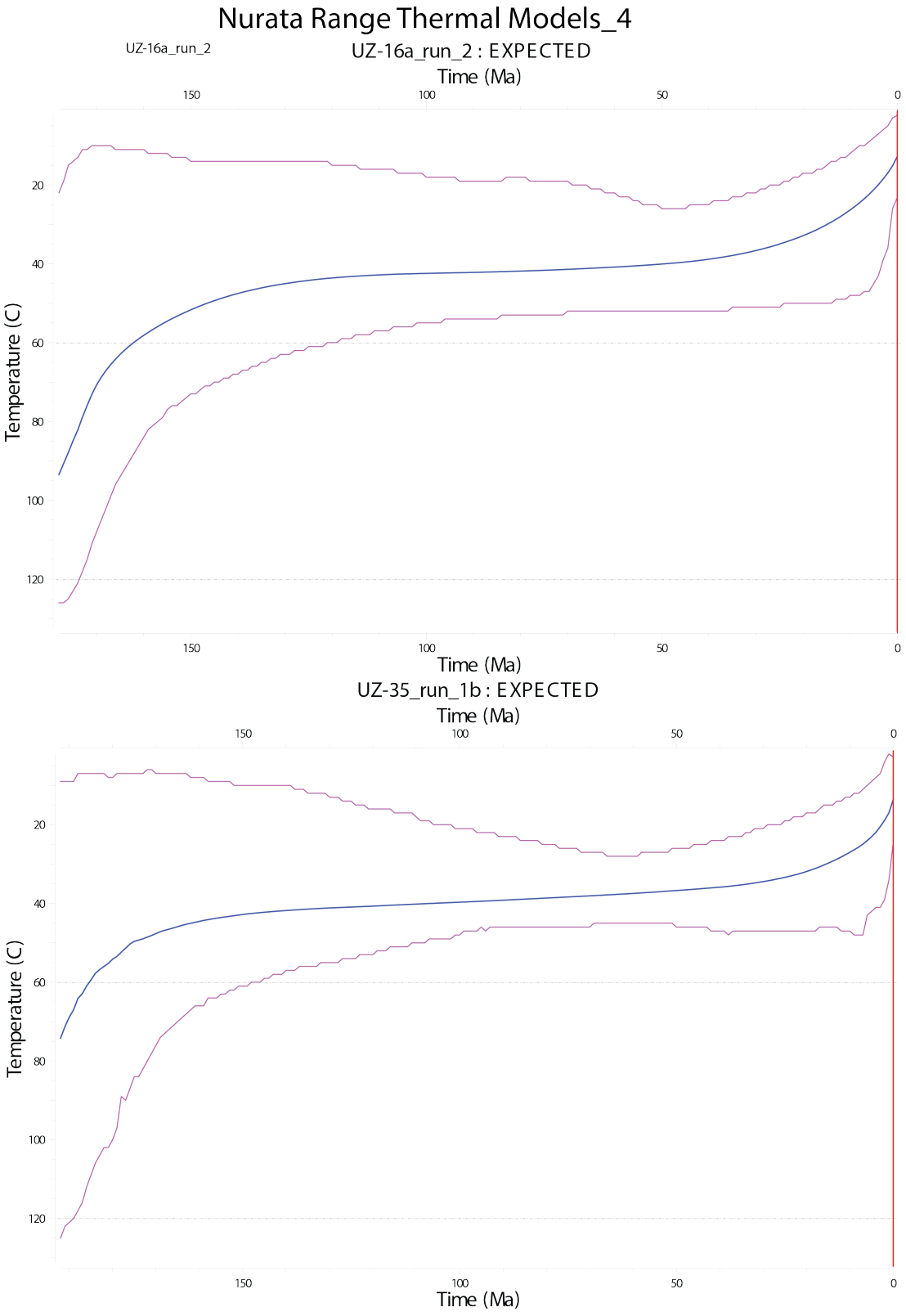
Nurata Range Thermal Models_4
UZ-16a_run_2
UZ-16a_run_2 : EXPECTED
Time (Ma)
150
100
50
0
20
40
60
80
100
120
Temperature (C)
Time (Ma)
UZ-35_run_1b : EXPECTED
Time (Ma)
Temperature (C)
Time (Ma)

11

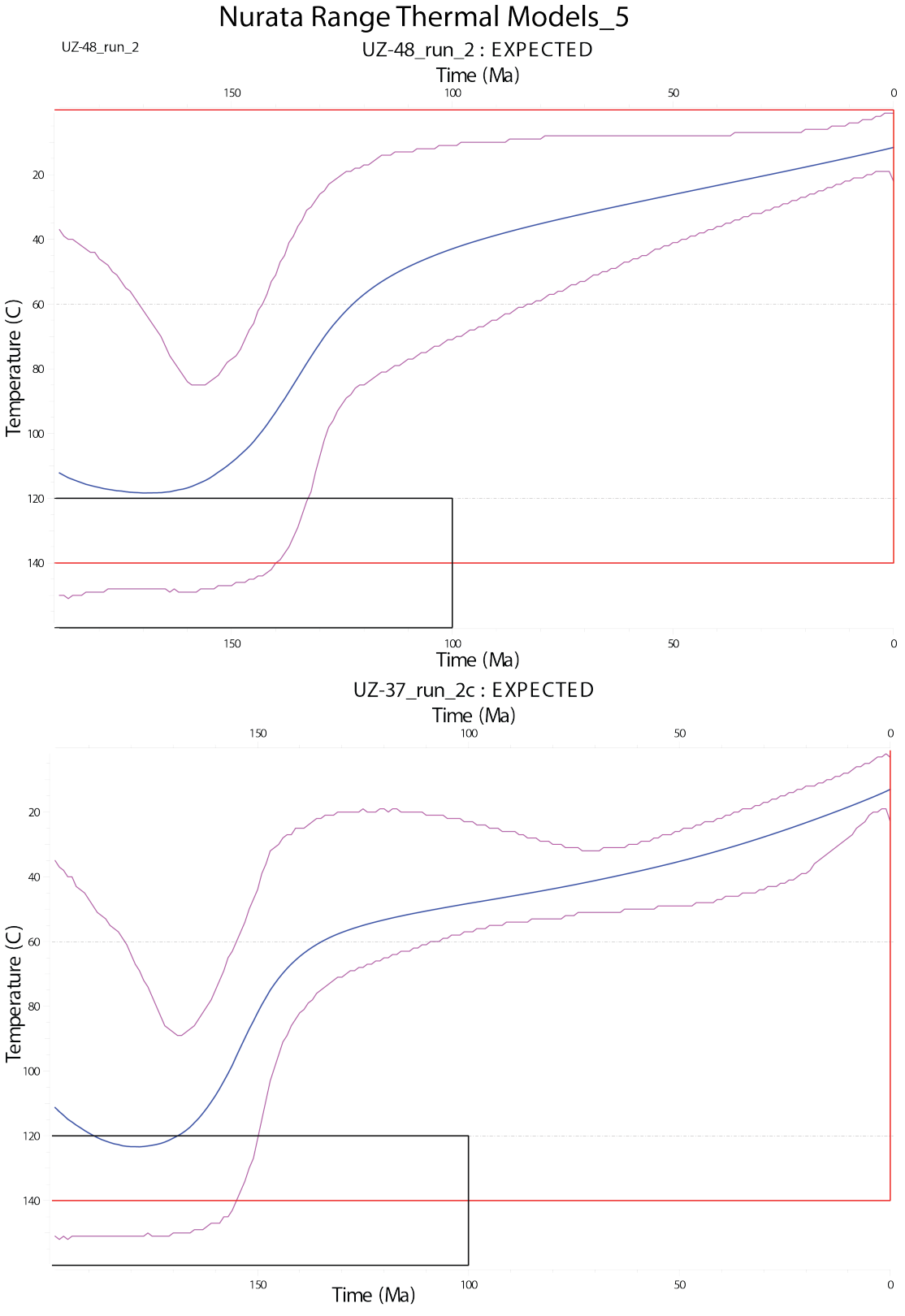
Nurata Range Thermal Models_5
UZ-48_run_2
UZ-48_run_2 : EXPECTED
Time (Ma)
150
100
50
0
20
40
60
80
100
120
140
Temperature (C)
Time (Ma)
UZ-37_run_2c : EXPECTED
Time (Ma)
Temperature (C)
Time (Ma)

12

Nurata Range Thermal Models_6

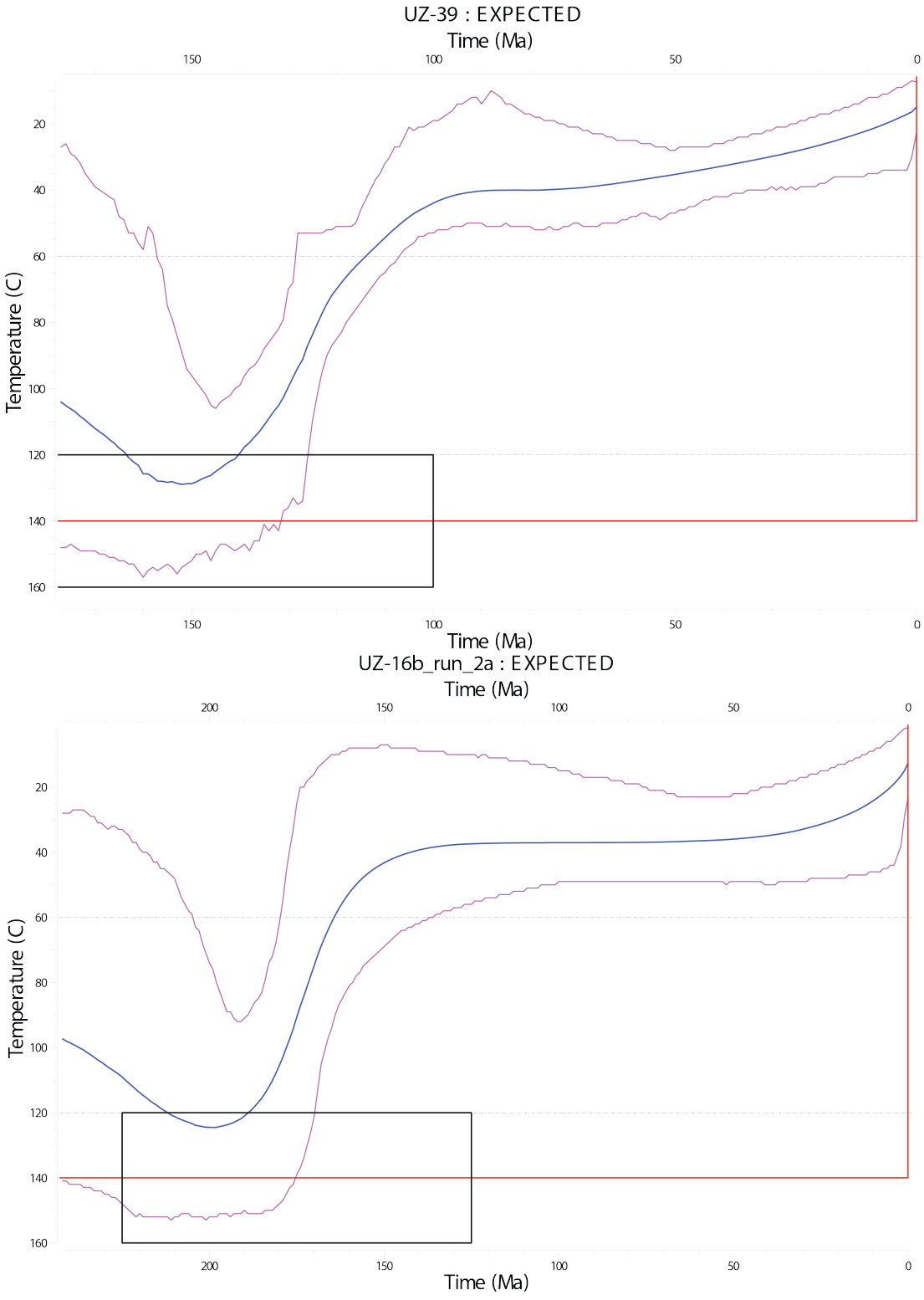

13

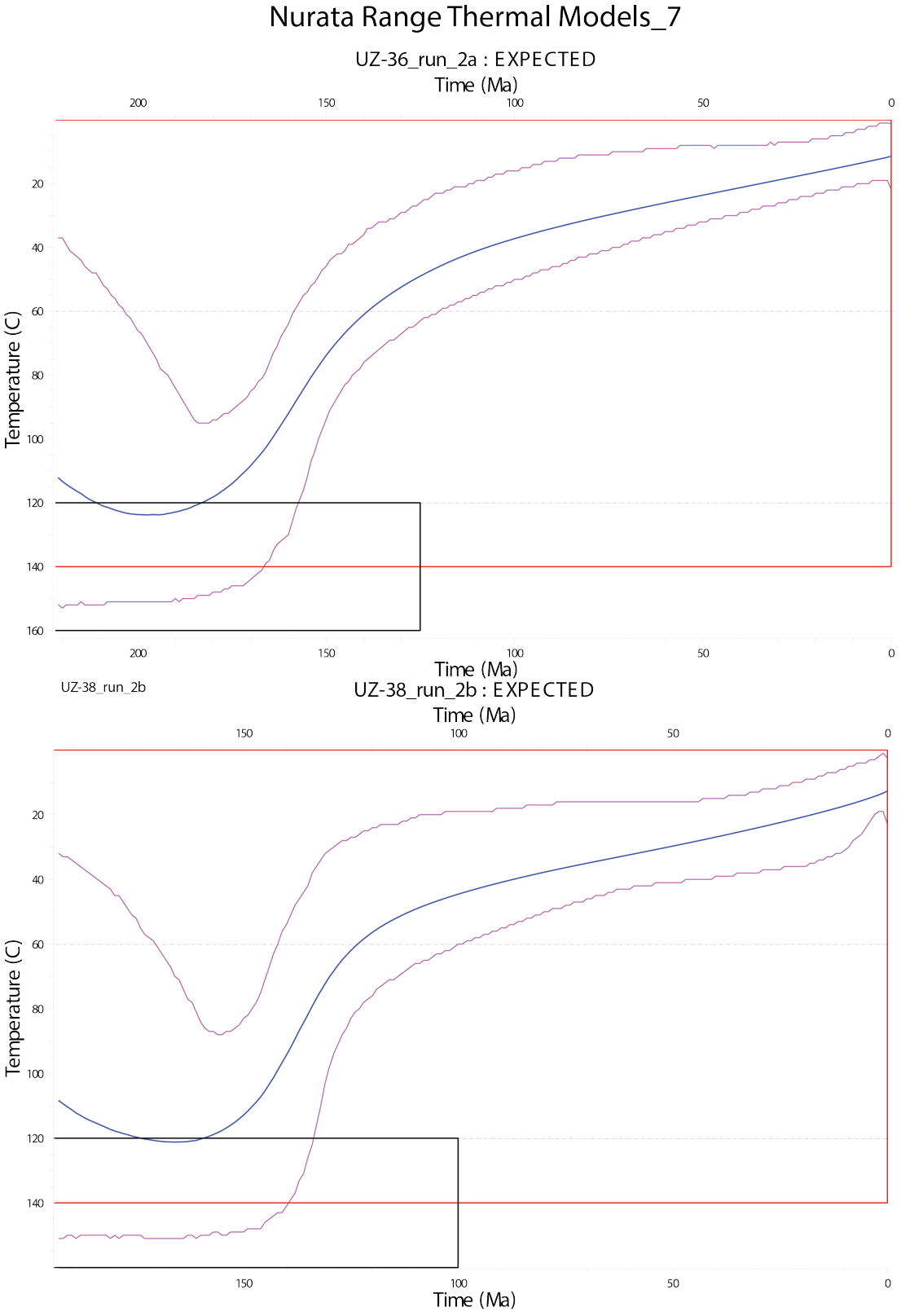
Nurata Range Thermal Models_7
UZ-36_run_2a : EXPECTED
Time (Ma)
200
150
100
50
0
20
40
60
80
100
120
140
160
Temperature (C)
Time (Ma)
UZ-38_run_2b
UZ-38_run_2b : EXPECTED
Time (Ma)
150
100
50
0
20
40
60
80
100
120
140
Temperature (C)
Time (Ma)

14

Nurata Range Thermal Models_8

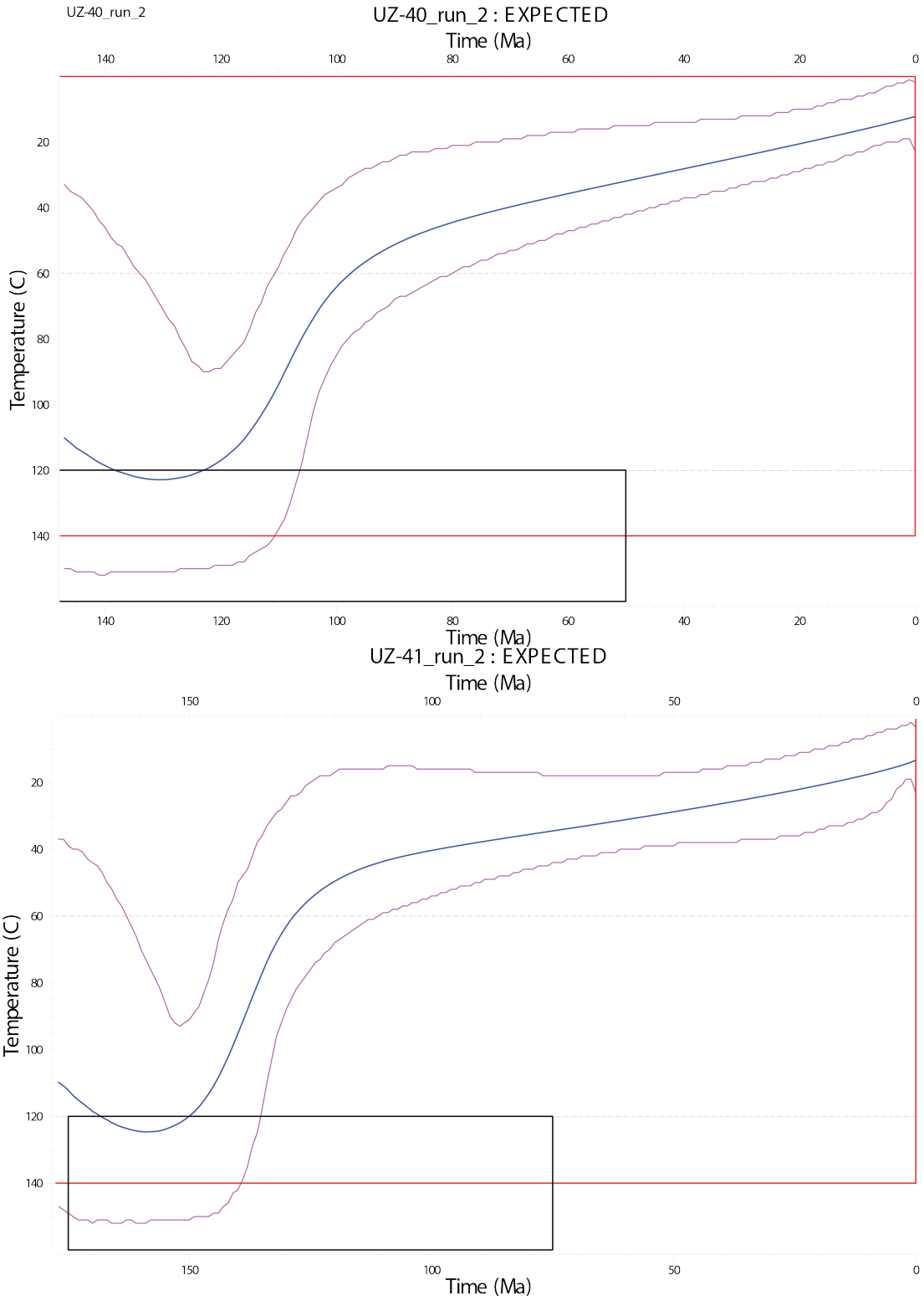

15

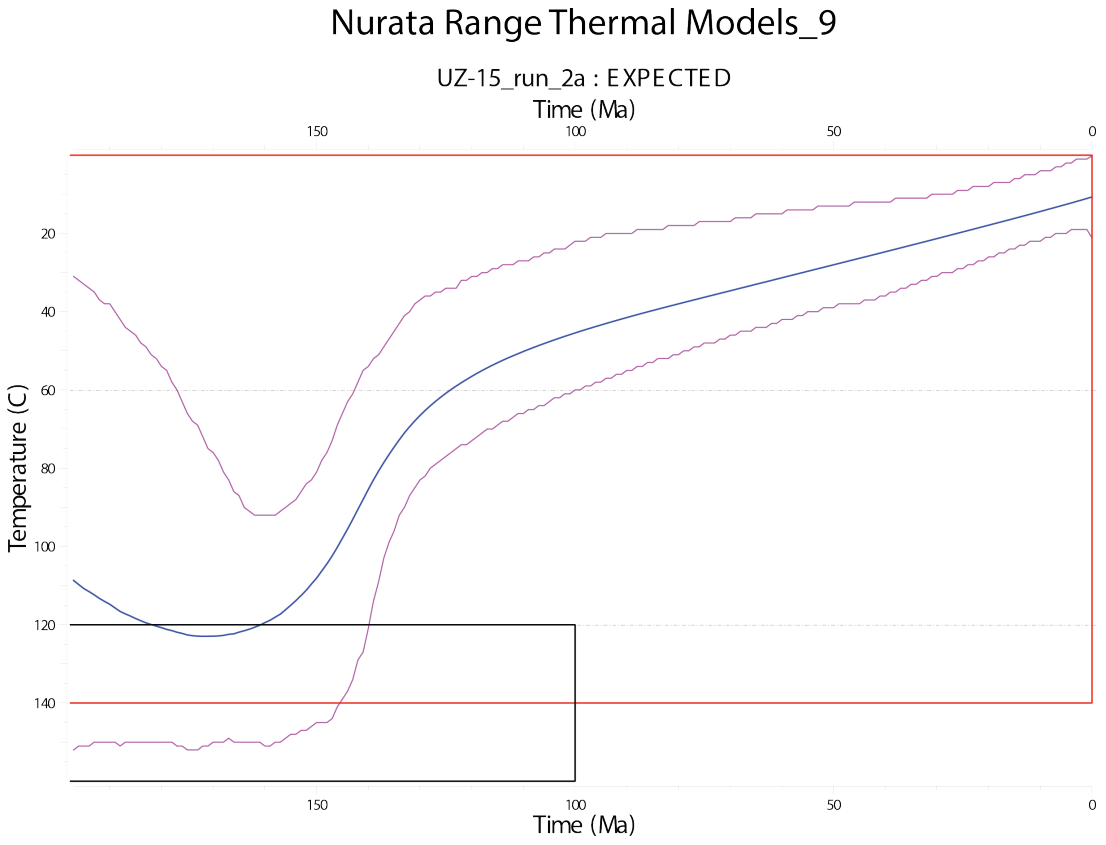
Nurata Range Thermal Models_9
UZ-15_run_2a : EXPECTED
Time (Ma)
150
100
50
0
20
40
60
80
100
120
140
Temperature (C)
150
100
50
0
Time (Ma)

16

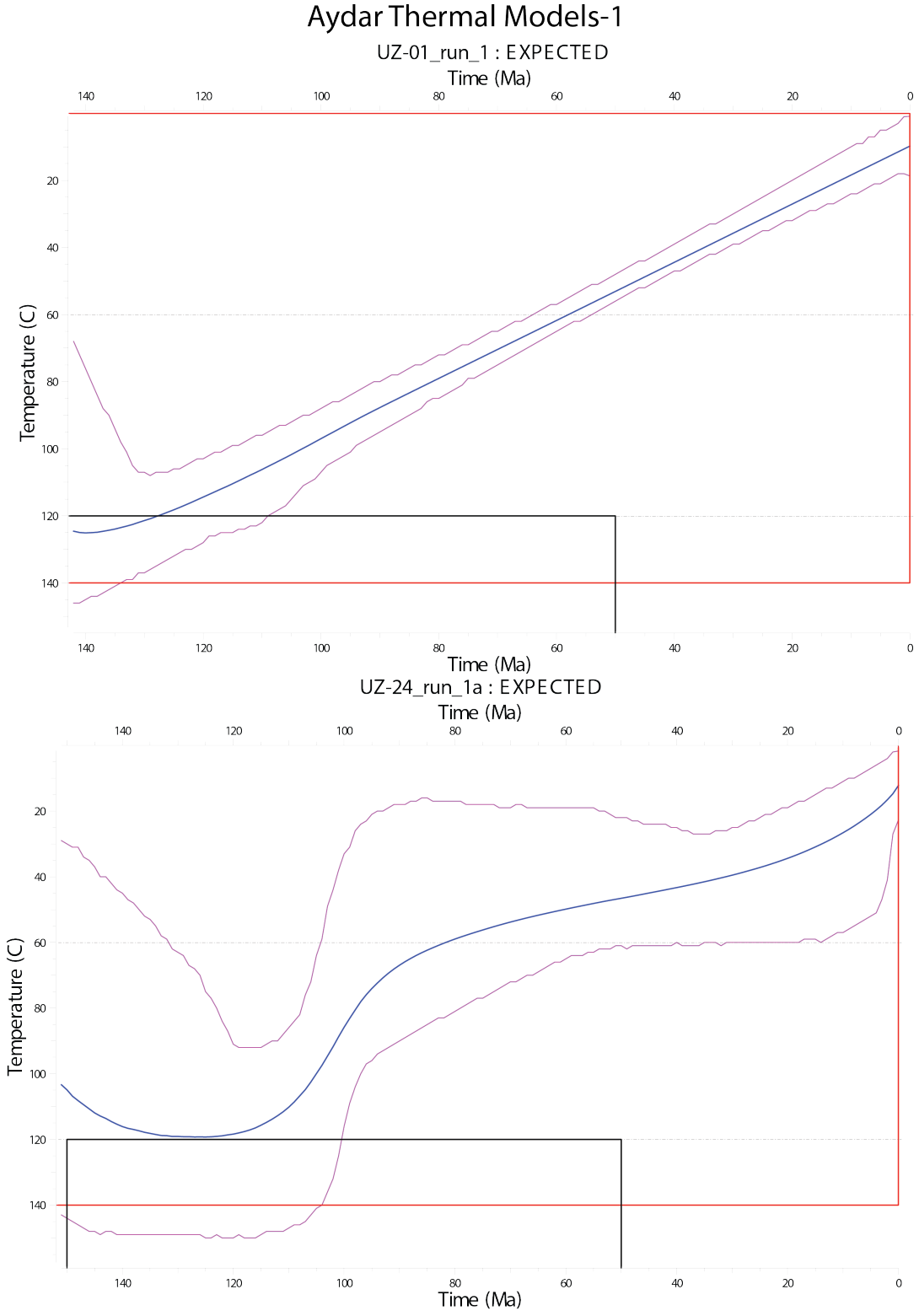
Aydar Thermal Models-1
UZ-01_run_1 : EXPECTED
Time (Ma)
Temperature (C)
UZ-24_run_1a : EXPECTED
Time (Ma)
Temperature (C)

17

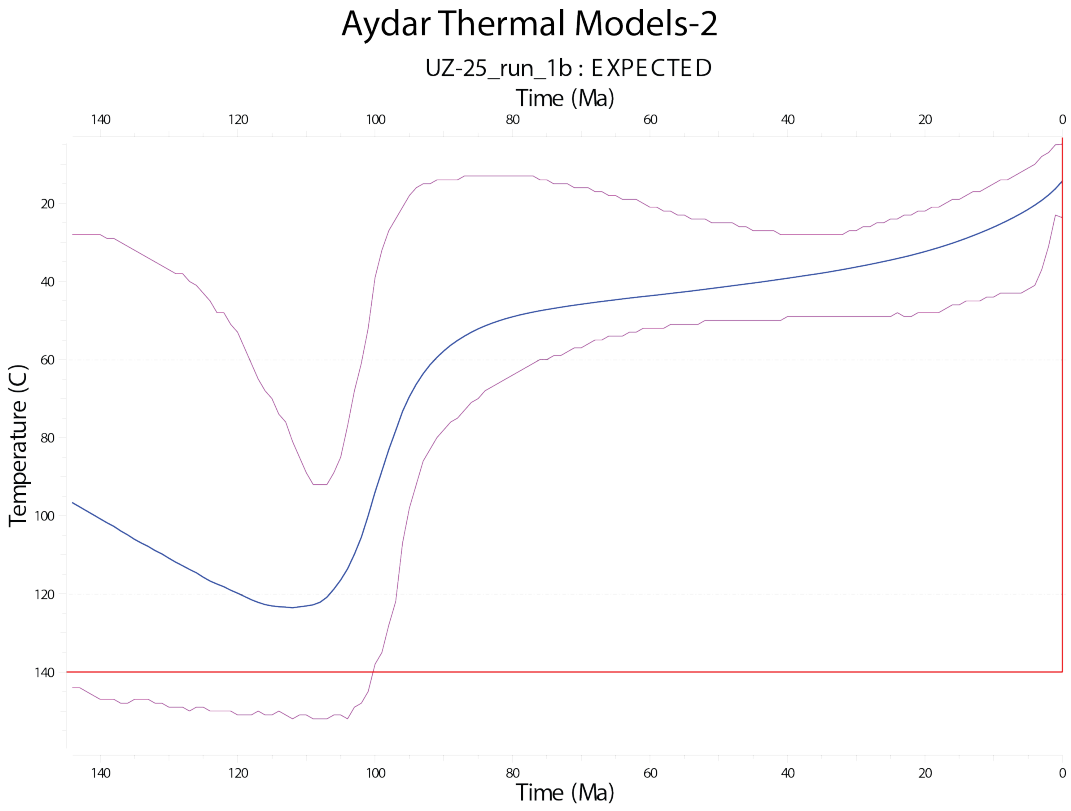
Aydar Thermal Models-2
UZ-25_run_1b : EXPECTED
Time (Ma)
140
120
100
80
60
40
20
0
Temperature (C)
20
40
60
80
100
120
140
Time (Ma)

18

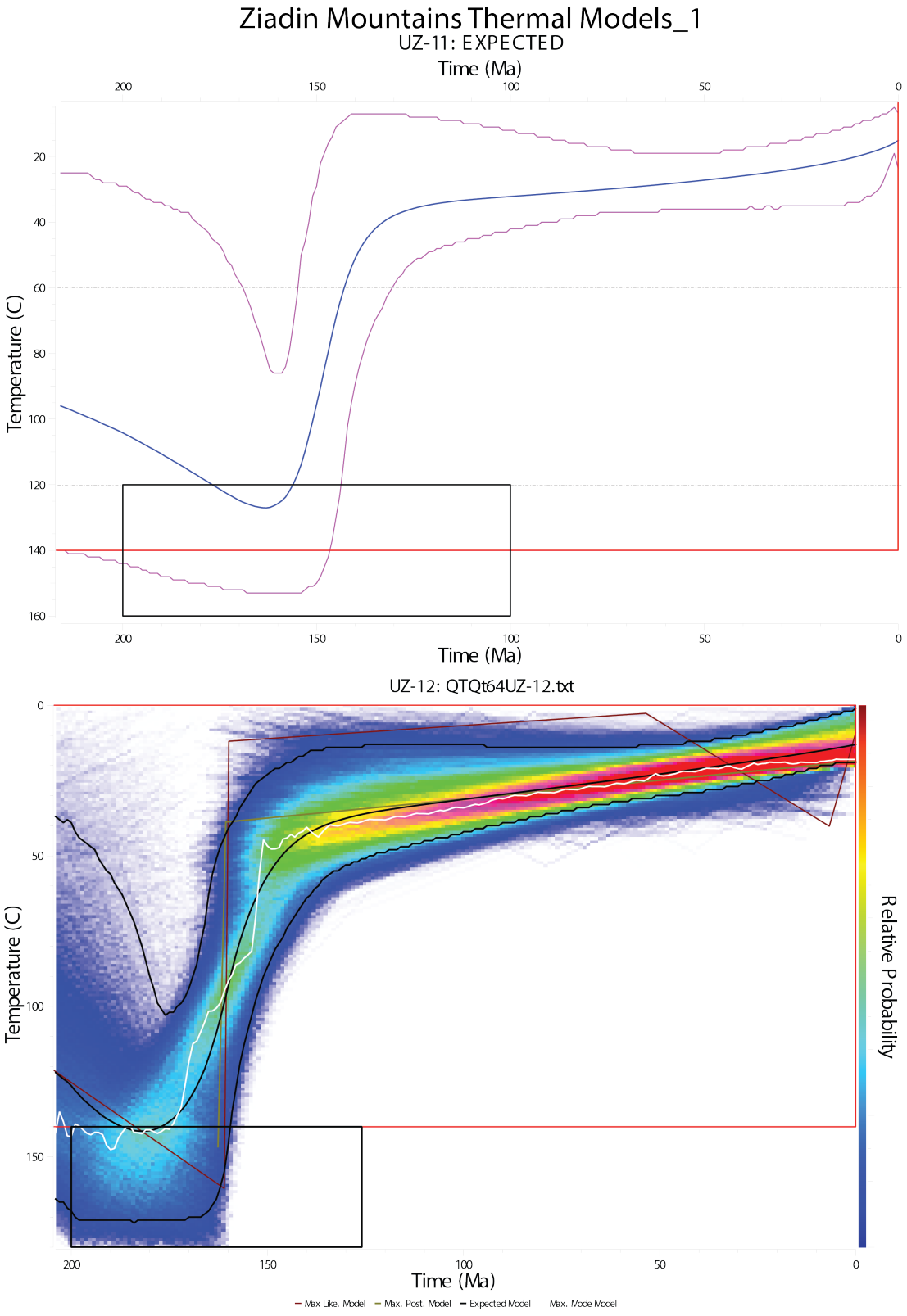
Ziadin Mountains Thermal Models_1
UZ-11: EXPECTED
Time (Ma)
200
150
100
50
0
Temperature (C)
20
40
60
80
100
120
140
160
Time (Ma)
UZ-12: QTQt64UZ-12.txt
Temperature (C)
0
50
100
150
Relative Probability
Time (Ma)
Max Like. Model
Max. Post. Model
Expected Model
Max. Mode Model

19

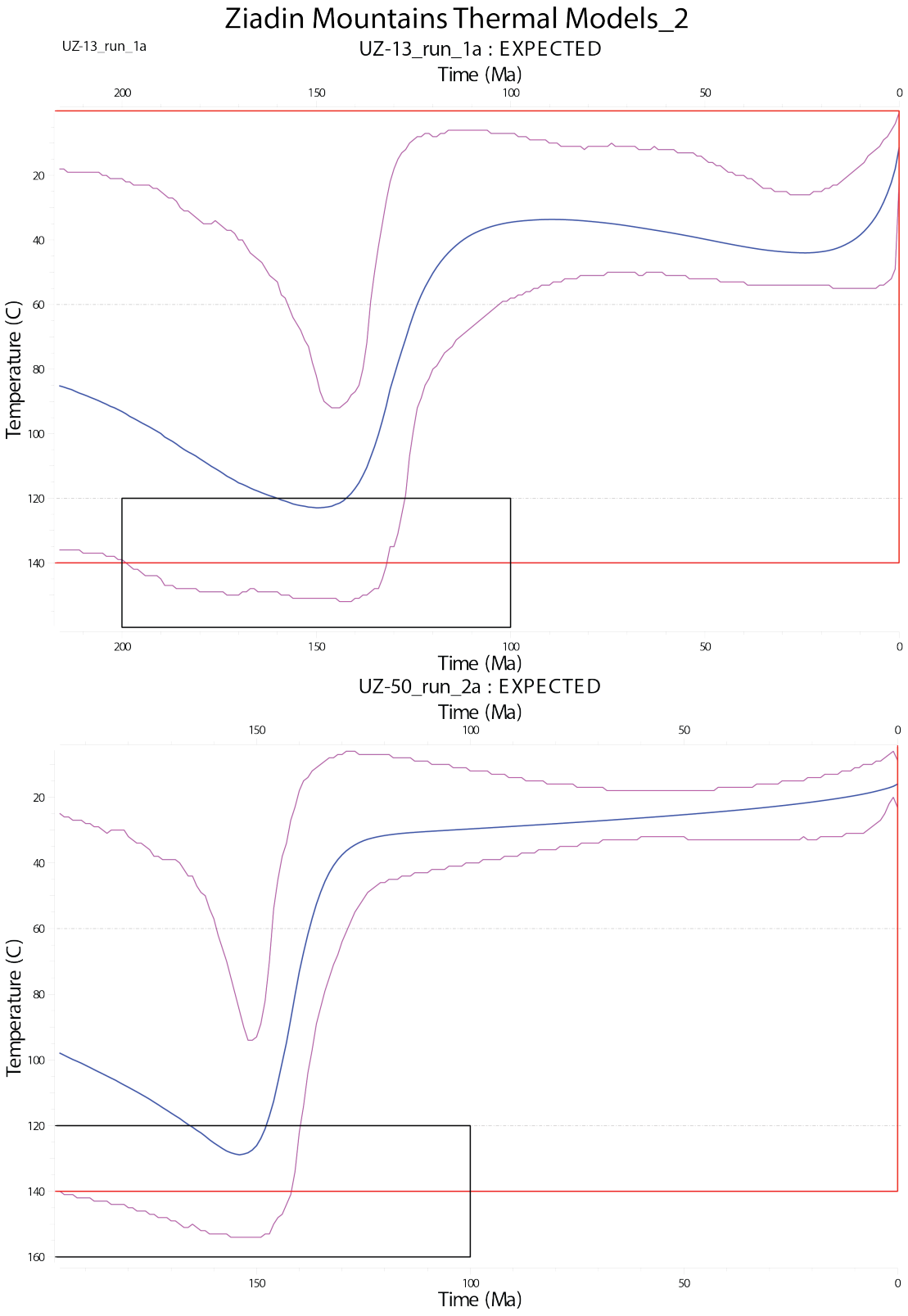
Ziadin Mountains Thermal Models_2
UZ-13_run_1a
UZ-13_run_1a : EXPECTED
Time (Ma)
200
150
100
50
0
20
40
60
80
100
120
140
Temperature (C)
Time (Ma)
UZ-50_run_2a : EXPECTED
Time (Ma)
150
100
50
0
20
40
60
80
100
120
140
160
Temperature (C)
Time (Ma)

20

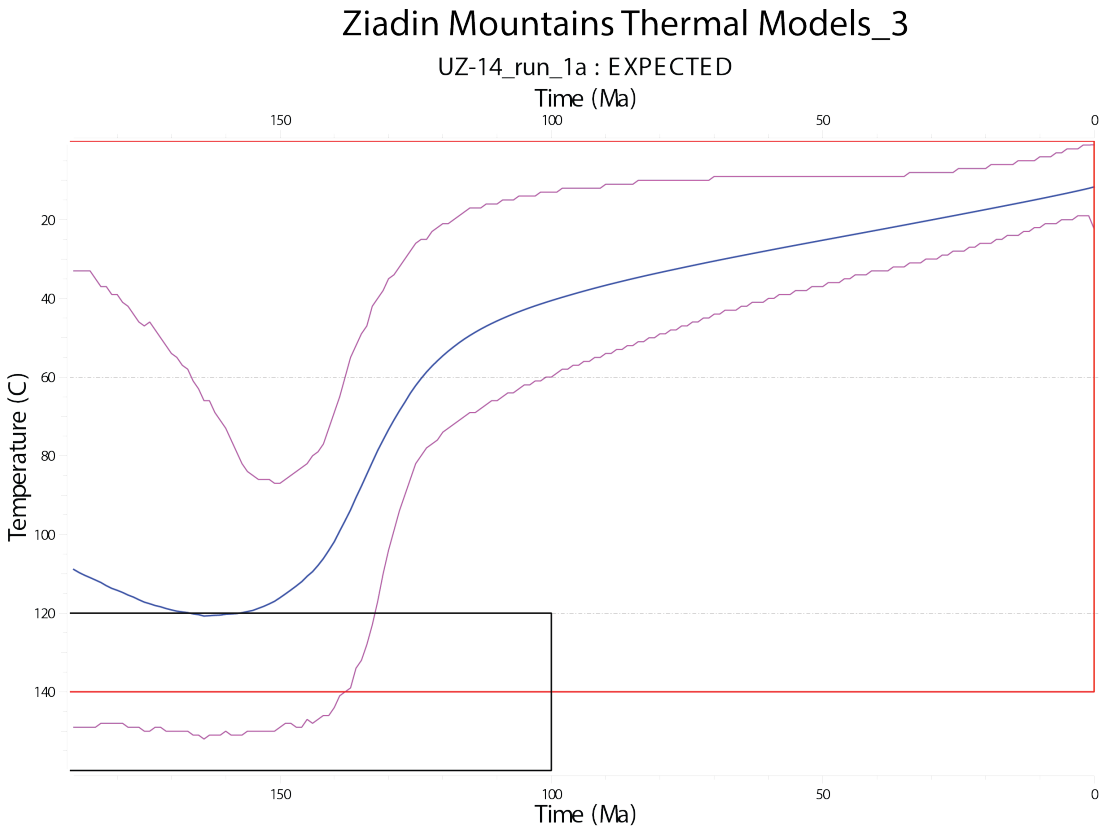
Ziadin Mountains Thermal Models_3
UZ-14_run_1a : EXPECTED
Time (Ma)
150
100
50
0
Temperature (C)
20
40
60
80
100
120
140
Time (Ma)

21

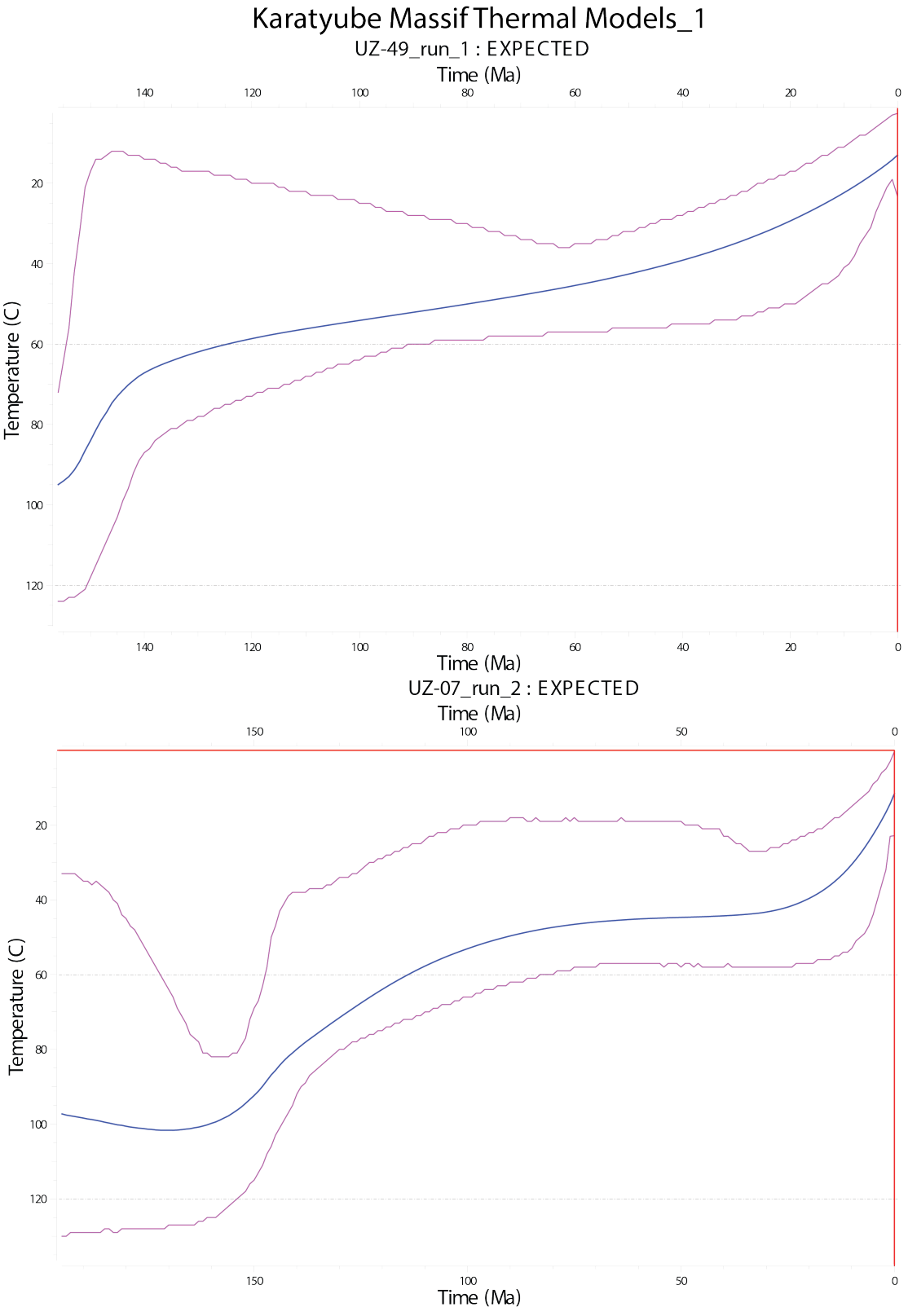
Karatyube Massif Thermal Models_1
UZ-49_run_1 : EXPECTED
Time (Ma)
140
120
100
80
60
40
20
0
Temperature (C)
20
40
60
80
100
120
Time (Ma)
UZ-07_run_2 : EXPECTED
Time (Ma)
150
100
50
0
Temperature (C)
20
40
60
80
100
120
Time (Ma)

22

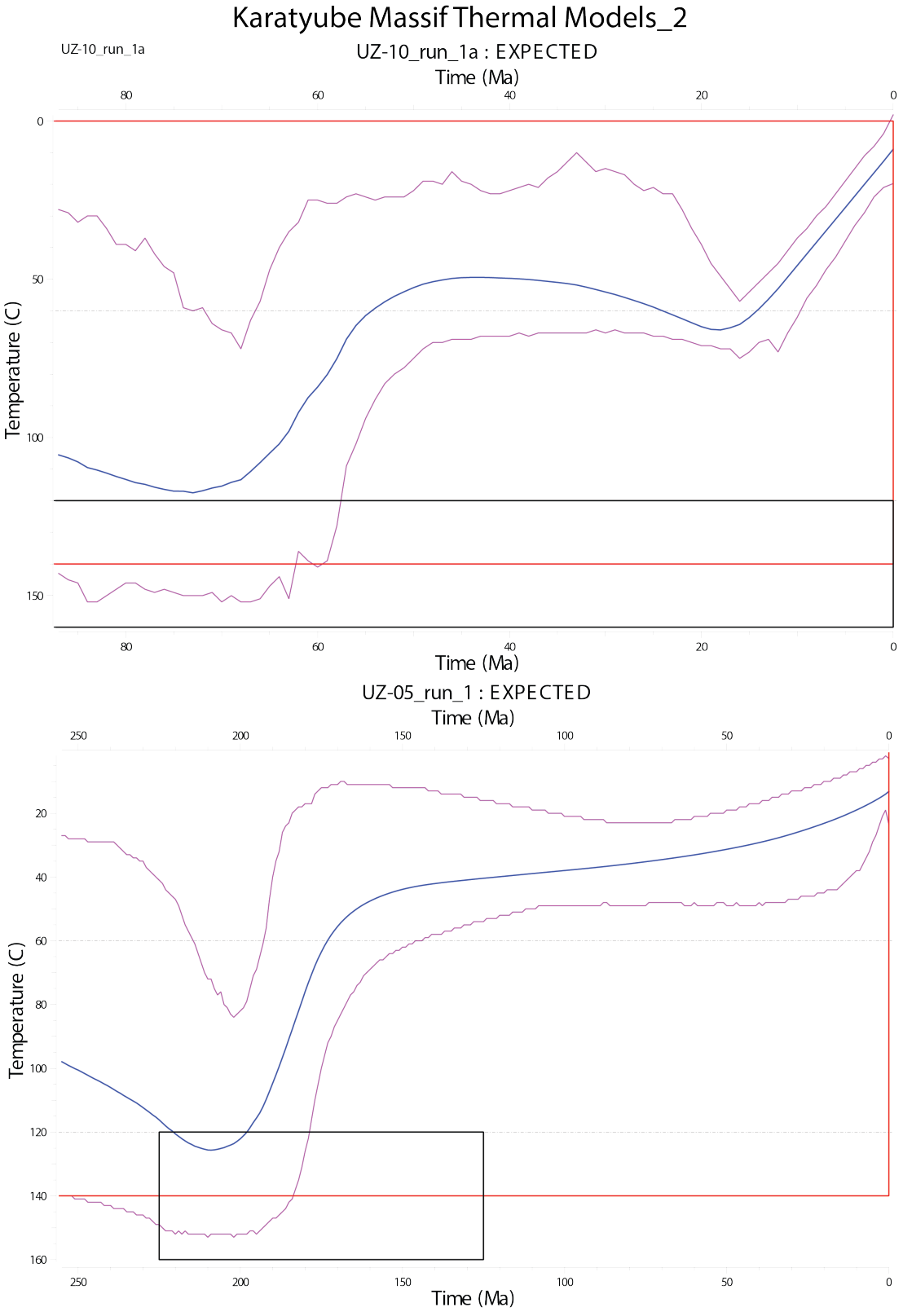
Karatyube Massif Thermal Models_2
UZ-10_run_1a
UZ-10_run_1a : EXPECTED
Time (Ma)
80
60
40
20
0
0
50
100
150
Temperature (C)
Time (Ma)
UZ-05_run_1 : EXPECTED
Time (Ma)
250
200
150
100
50
0
20
40
60
80
100
120
140
160
Temperature (C)
Time (Ma)

23

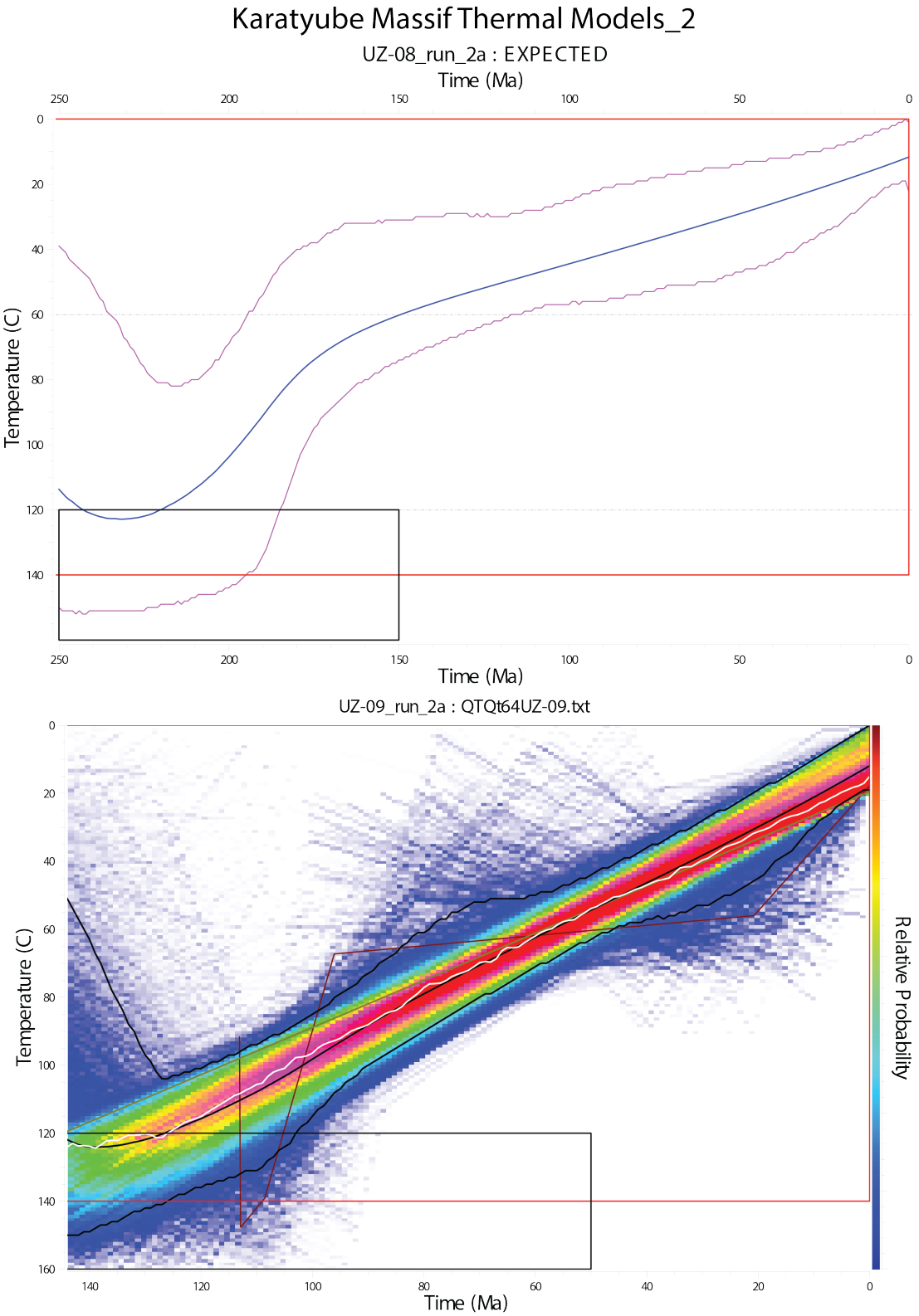
Karatyube Massif Thermal Models_2
UZ-08_run_2a : EXPECTED
Time (Ma)
Temperature (C)
UZ-09_run_2a : QTQt64UZ-09.txt
Relative Probability

Appendix P

Kyzylkum-Nurata Thermal Modelling Constraints

Thermal history modelling parameters following Flowers et al. (2015).

Supplementary File 5: Thermal history model input table for simulations of the Kyzylkum-Nurata Segment, Uzbekistan and Tajikistan, based on framework established by Flowers et al. (2015)

1. Thermochronologic Data

Samples and data used in simulations

Simulation inputs			Data Source	All data
Sample Region	AHe	AFT		
Bukantau				
UZ-19		×	Supplementary File 1 and 4	yes
UZ-20		x	Supplementary File 1 and 4	yes
UZ-21	×	×	Table 2 and Supplementary File 1 and 4	yes
UZ-22		×	Supplementary File 1 and 4	yes
UZ-23		×	Supplementary File 1 and 4	yes
Kuldjuktau				
UZ-28		×	Supplementary File 1 and 4	yes
UZ-29a		×	Supplementary File 1 and 4	yes
UZ-29b		×	Supplementary File 1 and 4	yes
UZ-30		×	Supplementary File 1 and 4	yes
UZ-31		×	Supplementary File 1 and 4	yes
UZ-32		×	Supplementary File 1 and 4	yes
Nurata Range				
UZ-02		×	Supplementary File 1 and 4	yes
UZ-04		×	Supplementary File 1 and 4	yes
UZ-15		×	Supplementary File 1 and 4	yes
UZ-42		×	Supplementary File 1 and 4	yes
UZ-43		×	Supplementary File 1 and 4	yes
UZ-44		×	Supplementary File 1 and 4	yes
UZ-16a		×	Supplementary File 1 and 4	yes
UZ-16b		×	Supplementary File 1 and 4	yes
UZ-35		×	Supplementary File 1 and 4	yes
UZ-36		×	Supplementary File 1 and 4	yes
UZ-37		×	Supplementary File 1 and 4	yes
UZ-38		×	Supplementary File 1 and 4	yes
UZ-39	×	×	Table 2 and Supplementary File 1 and 4	yes
UZ-40		×	Supplementary File 1 and 4	yes
UZ-41		×	Supplementary File 1 and 4	yes
UZ-48		×	Supplementary File 1 and 4	yes
Tymski				
UZ-11		×	Supplementary File 1 and 4	yes
UZ-12		×	Supplementary File 1 and 4	yes
UZ-13		×	Supplementary File 1 and 4	yes
UZ-14		×	Supplementary File 1 and 4	yes
UZ-50		×	Supplementary file 1 and 4	yes
Syr Darya				
UZ-01	×	×	Table 2 and Supplementary File 1 and 4	yes
UZ-24		×	Supplementary File 1 and 4	

UZ-25	×	×	Table 2 and Supplementary File 1 and 4	yes
Gissar				
UZ-05		×	Supplementary File 1 and 4	yes
UZ-07		×	Supplementary File 1 and 4	yes
UZ-08		×	Supplementary File 1 and 4	yes
UZ-10	×	×	Table 2 and Supplementary File 1 and 4	yes
UZ-49		×	Supplementary File 1 and 4	yes

Data treatment, uncertainties, and other relevant constraints

AHe Data

He dates (Ma): Single grain AHe ages were from Supplementary File 2 modelled individually

Error (Ma) applied in modeling: error of 1σ was used from Supplementary file 1

r (μm): Equivalent spherical radius of each grain

AFT data

Cl wt%: From Supplementary file 1

Lengths: Length data for all samples is available in Supplementary File 4

Initial mean track length: 16.3 μm

Track length reduction standard: 0.893

2. Additional geological information

Assumption	Explaination and data source
As all the samples were granitoid and there was no evidence for re-heating. Samples we assumed to have come from >120°C through the APAZ	

3. System- and model-specific parameters

He radiation damage model : Flowers et al. 2009

FT annealing model : Ketcham et al. 2007

FT c-axis projection : Not used

Modeling code : QTQt 5.6.0 PC

Statistical fitting criteria : Default QTQt values

MCMC Parameters : Burn-in = 200,000, Post-burn-in = 200,000

Appendix Q

Garm Methods

Q.1 Apatite U/Pb Dating (AUPb)

Apatite U/Pb dating uses concentrations and the decay rate of $^{238,\ 235}$U into $^{206,\ 207}$Pb to determine the timing of cooling through the 550-450°C temperature window (Chew & Donelick 2012, Thomson et al. 2012, Cochrane et al. 2014). The Apatite U/Pb ages for this study were acquired using a New Wave 213 laser ablation system connected to an Agilent 7500 ICPMS at The University of Adelaide. Spot ablations were performed in constant energy mode using a 32 μm spot and a 5 Hz laser repetition rate. Each analysis comprised a 20s background and 30s ablation. The applied data reduction method followed Chew et al. (2011, 2014), using in-house Excel spread sheets. NIST 610 was used as primary standard and Durango apatite (McDowell et al. 2005) and in-house apatite standard EL-1 (Arkaroola pegmatite; McLaren et al. 2002) were used as secondary standard. Given that NIST 610 is not matrix-matched to the apatite samples, down-hole elemental fractionation was monitored and corrected for using the secondary apatite standards. Fractionation corrections prove to be rather minimal which is likely related with the low energy ablation that was used (typically 2-3 J/cm^2). Common Pb correction was carried out after downhole fractionation correction using Pb evolution models (Stacey & Kramers 1975). More details on this approach can be found in Chew et al. (2014).

Q.2 Apatite fission track analysis(AFT)

The apatite fission track method is based on the temperature dependent annealing of mineral lattice damage features, called 'fission tracks', that are created by the spontaneous decay of ^{238}U (Wagner & Van den haute 1992). Fission tracks record the thermal history of a rock sample through the apatite partial annealing zone of ~120-60°C (APAZ, Green et al. 1986). Apatite grains were picked and mounted in epoxy resin and sample mounts were ground and polished to expose internal sections. They were subsequently chemically etched in a 5 M HNO^3 solution for 20s at 20°C to reveal the natural spontaneous fission tracks. Fission track analysis was performed at The University of Adelaide using an AutoScan system. The concentration of uranium (U) and chlorine (Cl) of each apatite grain was measured using Laser Ablation-Inductively Coupled Plasma Mass Spectrometry using an identical system setup as for the apatite U/Pb analyses (simultaneous analysis). Data reduction and age calculation was carried out following analytical procedures described in Hasebe et al. (2004) and De Grave et al. (2012). Calibrations were carried out using NIST 610, 612, 614 and Durango apatite standards. Ages and errors were obtained and calibrated to Durango using an in-house excel spreadsheet. Given the low track densities in the apatite samples from the Garm block, duplicate samples were sent off for Cf-irradiation at The University of Melbourne in order to increase the likelihood of measuring sufficient amount of confined tracks for thermal history reconstructions (Donelick & Miller 1991).

Given that the Garm samples have very large variations in uranium concentration between grains (4.5 to 333 ppm), the potential dependence of uranium concentrations on the fission track age was tested by plotting individual grain ages in RadialPlotter (Vermeesch 2009) using Uranium concentrations as a colour-coded discriminator. High fluctuations in Uranium may potentially influence annealing kinetics and therefore lead to differential preservation of thermal events within a given sample (Hendriks & Redfield 2005). As well as plotting against U, the more reliable kinetic indicator of Cl concentration was also was plotted against single grain AFT age, in order to determine a relationship between Cl concentration and age (Figure 5). Uranium concentrations can however not be used as a kinetic parameter and therefore Chlorine concentrations were used as a kinetic parameter in the subsequent thermal history modelling.

Q.3 Apatite and zircon (U-Th)/He analysis (AHe and ZHe)

The (U-Th-Sm)/He thermochronometers are based on the diffusivity of ^{4}He. For apatite, the thermochronometer has a thermal sensitivity at 80-40°C, making it valuable for constraining the most recent thermal cooling event (Zeitler et al. 1987, Farley 2002). For zircon, the method records the thermal history at ~190-170°C (Reiners et al. 2002, Guenthner et al. 2013). The (U-Th-Sm)/He analyses for this study were undertaken at the John de Laeter Centre, Curtin University and followed the protocols described in Danišík et al. (2012,a).

Apatite and zircon crystals were hand-picked following the recommendation of (Farley 2002), then photographed, measured for physical dimensions and loaded in Pt (apatite) and Nb (zircon) microtubes. ^{4}He was extracted from apatite and zircon at ~900°C and ~1,250°C, respectively, under ultra-high vacuum using a diode laser and measured by isotope dilution on a Pfeiffer Prisma QMS-200 mass spectrometer. A "re-extract" was run after each sample to verify complete outgassing of the crystals. He gas results were corrected for blank, determined by heating empty microtubes using the same procedure. After the ^{4}He measurements, tubes containing the crystals were retrieved from the laser cell, spiked with ^{235}U and ^{230}Th and dissolved. Sample, blank, and spiked standard solutions were analysed by isotope dilution for ^{238}U and ^{232}Th, and by external calibration for ^{147}Sm on an Agilent 7500 ICP-MS. The total analytical uncertainty (TAU) was calculated as a square root of sum of squares of uncertainty on He and weighted uncertainties on U, Th, Sm and He measurements, and is typically <5% (1σ). The raw (U–Th)/He ages were corrected for alpha ejection (Ft correction) after (Farley et al. 1996), whereby a homogenous distribution of U, Th and Sm was assumed for the crystals. Replicate analyses of internal standard Durango apatite (n = 10) measured over the period of this study, yielded mean (U–Th–Sm)/He ages of 31.3 ± 1.7 Ma (1σ), consistent with the reference Durango (U–Th–Sm)/He age of 31.02 ± 1.01 Ma (McDowell et al. 2005). For Fish Canyon zircon this study obtained 28.6 ± 0.8 Ma (n = 10), which is in excellent agreement with the reference He age of Reiners (2005), which is 28.3 ± 1.3 Ma.

Q.4 Thermal History Modelling

QTQt (Gallagher 2012) was used as modelling software in order to constrain the low-temperature (~120-40°C) thermal history of the samples. Three thermal models were produced for samples which provided fission track length information, one for Gm-21, one for Gm-19, and one for Gm-17, 16, and 15. Samples Gm-17, Gm-16, and Gm-15 were combined as they came from different rock types in the same sample location. Both samples Gm-21, and Gm-17, 16, and 15 were modelled using AFT data alone, while Gm-19 was modelled using AFT data and the measured (U-Th-Sm)/He data. Modelling was carried out using the Ketcham et al. (2007) annealing algorithm with wt% chlorine (Donelick et al. 2005) as kinetic parameter and the Flowers et al. (2009) He diffusion algorithm. The modelling ran completely unconstrained for 200,000 iterations using a prior between surface temperatures and 160°C at 50 Ma (corresponding to the older than the oldest measured track in the distribution). The modelling output shows all possible models in time-temperature space in function of their probability, with warmer colours being most probable. The solid white and black represents the "QTQt expected" model and therefore constrains the most likely time-temperature path for this study. A summary table has been produced based on Flowers et al. (2015) (Supplementary file 5).

Appendix R

Garm AUPb Data

Table R.1: Table of the single grain uranium and lead ratios, and individual apatite uranium lead ages. ^{207}Pb, ^{206}Pb, ^{235}U, and ^{238}U are the different isotopes of lead and uranium measured.

Sample	$^{207}Pb/^{235}U$	1σ	$^{206}Pb/^{238}U$	1σ	$^{207}Pb/^{206}Pb$	1σ	Age$\pm1\sigma$(Ma)
Gm-16-01	1.287	0.044	0.049	0.001	0.168	0.005	261.7±7.6
Gm-16-02	3.308	0.137	0.064	0.001	0.333	0.025	249.4±17.5
Gm-16-03	1.566	0.058	0.052	0.001	0.191	0.004	265.0±9.2
Gm-16-04	1.057	0.04	0.045	0.001	0.157	0.01	244.3±5.8
Gm-16-05	1.364	0.053	0.047	0.001	0.186	0.018	241.0±8.6
Gm-16-06	4.657	0.221	0.072	0.001	0.421	0.006	227.4±16.2
Gm-16-07	6.833	0.584	0.096	0.002	0.507	0.01	231.9±15.9
Gm-16-08	2.273	0.084	0.054	0.001	0.269	0.01	240.1±8.8
Gm-16-09	2.284	0.11	0.054	0.001	0.269	0.005	240.8±8.1
Gm-16-10	5.04	0.246	0.074	0.001	0.404	0.005	242.6±15.7
Gm-16-11	1.646	0.06	0.048	0.001	0.206	0.016	240.4±8.5
Gm-16-12	2.34	0.08	0.059	0.001	0.263	0.007	267.1±8.7
Gm-16-13	1.186	0.046	0.047	0.001	0.17	0.007	251.0±5.5
Gm-16-14	2.858	0.14	0.058	0.001	0.301	0.006	241.4±9.7
Gm-16-15	2.917	0.137	0.062	0.001	0.274	0.004	271.1±9.1
Gm-16-16	2.14	0.091	0.055	0.001	0.24	0.01	257.2±8.3
Gm-16-17	1.452	0.053	0.051	0.001	0.169	0.007	272.9±8.4

Gm-16-18	3.219	0.177	0.065	0.001	0.32	0.006	259.2±11.4
Gm-16-19	1.647	0.073	0.05	0.001	0.203	0.01	252.0±7.2
Gm-16-20	1.57	0.064	0.049	0.001	0.199	0.01	249.7±7.0
Gm-16-21	2.288	0.085	0.057	0.001	0.243	0.006	268.2±7.8
Gm-16-22	2.051	0.076	0.053	0.001	0.25	0.006	244.0±7.3
Gm-16-23	3.033	0.123	0.062	0.001	0.308	0.004	254.8±10.0
Gm-16-24	1.976	0.087	0.053	0.001	0.23	0.016	252.4±9.6
Gm-16-25	9.777	0.781	0.121	0.003	0.563	0.014	233.8±16.3
Gm-17-01	19.526	1.609	0.18	0.003	0.65	0.014	279.0±20.7
Gm-17-02	7.16	0.296	0.095	0.001	0.51	0.01	254.7±8.4
Gm-17-03	8.055	0.44	0.102	0.002	0.50	0.012	279.9±10.2
Gm-17-04	14.242	0.915	0.135	0.002	0.624	0.014	238.7±14.9
Gm-17-05	6.697	0.336	0.087	0.001	0.511	0.012	231.0±9.0
Gm-17-06	15.89	1.326	0.159	0.003	0.656	0.016	240.2±20.9
Gm-17-07	14.732	0.966	0.159	0.003	0.647	0.014	249.9±18.3
Gm-17-08	8.499	2.159	0.10	0.004	0.487	0.033	284.1±28.3
Gm-17-09	4.072	0.373	0.072	0.002	0.368	0.017	274.7±11.7
Gm-17-10	13.458	0.825	0.144	0.002	0.644	0.014	231.3±16.4
Gm-17-11	7.451	0.351	0.094	0.001	0.502	0.011	255.8±8.8
Gm-17-12	4.404	0.194	0.07	0.001	0.419	0.01	237.0±6.7
Gm-17-13	5.743	0.257	0.084	0.001	0.457	0.01	259.1±7.9
Gm-17-14	7.365	0.374	0.091	0.001	0.503	0.012	246.3±9.1
Gm-17-15	6.47	0.291	0.083	0.001	0.467	0.01	248.7±7.5
Gm-17-16	14.826	1.027	0.153	0.003	0.617	0.014	277.8±17.4
Gm-17-17	15.139	1.069	0.156	0.003	0.621	0.014	277.3±17.7
Gm-17-18	19.657	1.719	0.161	0.003	0.663	0.015	232.7±19.5
Gm-17-19	17.422	1.351	0.158	0.003	0.641	0.015	256.9±18.6
Gm-21-01	0.957	0.031	0.046	0.001	0.128	0.003	257.3±4.6
Gm-21-02	0.989	0.031	0.045	0.001	0.134	0.003	245.7±4.5
Gm-21-03	0.937	0.03	0.045	0.001	0.126	0.003	250.9±4.4

Gm-21-04	1.311	0.049	0.049	0.001	0.164	0.004	253.8±6.1
Gm-21-05	1.132	0.038	0.047	0.001	0.151	0.004	247.2±5.2
Gm-21-06	1.151	0.039	0.046	0.001	0.152	0.004	245.2±5.3
Gm-21-07	1.052	0.036	0.046	0.001	0.143	0.004	247.3±5.0
Gm-21-08	1.335	0.05	0.05	0.001	0.162	0.004	258.6±6.1
Gm-21-09	1.063	0.037	0.046	0.001	0.139	0.004	250.2±4.9
Gm-21-10	1.372	0.054	0.048	0.001	0.184	0.005	240.2±6.8
Gm-21-11	0.996	0.035	0.045	0.001	0.137	0.004	246.8±4.8
Gm-21-12	1.912	0.084	0.055	0.001	0.204	0.006	261.3±8.6
Gm-21-13	1.308	0.048	0.05	0.001	0.159	0.004	259.7±5.9
Gm-21-14	1.464	0.059	0.051	0.001	0.183	0.005	251.8±7.0
Gm-21-15	1.392	0.054	0.049	0.001	0.176	0.005	248.9±6.6

Appendix S

Garm Single Grain AFT Data

Table S.1: Apatite fission track data and chemistry: ρ_s is the density of spontaneous tracks within the region of interest and is expressed as 10^5 tracks/cm^2. N_s is the total number of counted spontaneous tracks per sample. ^{238}U is the average concentration in ppm of uranium 238 measured in each grain. ^{35}Cl is the average concentration in ppm of chlorine 35 measured in each grain; concentrations were obtained using laser ablation–inductively coupled plasma–mass spectrometry (LA-ICP-MS). BLOD is below limits of detection, and thus could not provide a concentration value and was not used in calculating sample concentration averages.Dpar is the length of spontaneous track etch pits in μm. t is the AFT single grain age for each sample in Ma.

Sample	ρ_s	N_s	^{238}U	$\pm1\sigma$	^{35}Cl	$\pm1\sigma$	Dpar	$\pm1\sigma$	t	$\pm1\sigma$
Gm-11-1	1.3	3	18.7	2.3	BLOD	BLOD	0.6	0.2	16.7	9.7
Gm-11-2	0.6	2	18.3	1	BLOD	BLOD	1.5	0.5	7.6	5.4
Gm-11-3	1.3	3	11.8	0.9	BLOD	BLOD	1.1	0.3	26.4	15.3
Gm-11-4	0.6	2	19	0.6	BLOD	BLOD	2.1	0.6	7.3	5.2
Gm-11-5	0.4	1	28.2	2.8	BLOD	BLOD	0.7	0.3	3.2	3.2
Gm-11-6	0.2	1	14.8	2.6	BLOD	BLOD	1.3	0.7	3.2	3.2
Gm-11-7	0.6	5	20	0.6	830	460	1.4	0.7	7.8	3.5
Gm-11-8	0.3	3	19.5	1.2	BLOD	BLOD	0.9	0.1	3.9	2.2
Gm-11-9	0.5	4	10.2	2	BLOD	BLOD	1	0.2	12.2	6.1
Gm-11-10	0.2	1	16.5	0.7	BLOD	BLOD	1.1	0.4	3.2	3.2
Gm-11-11	1	4	25.8	3	BLOD	BLOD	1.6	0.5	9.2	7.3
Gm-11-12	0.3	1	17.4	5.9	BLOD	BLOD	0.8	0.4	3.6	3.6
Gm-11-13	0.9	3	22.9	12	BLOD	BLOD	1.7	0.8	10.3	6.5

Gm-15-1	4.2	27	146.2	4.2	290	120	1.9	0.6	7.2	1.4
Gm-15-2	1	4	17	1.3	820	160	1.1	0.3	14	7
Gm-15-3	5.5	27	161.8	7.2	250	120	3.2	0.3	8.5	1.7
Gm-15-4	1.2	12	30.9	2.1	600	170	2.1	1	9.7	2.8
Gm-15-5	3.1	11	27.3	2.4	BLOD	BLOD	1	0.1	28	8.5
Gm-15-6	6.6	21	145.5	24	BLOD	BLOD	1.4	0.2	11.3	2.6
Gm-15-7	2.2	11	67.8	5.5	620	200	1.1	0.1	8.3	2.5
Gm-15-8	2.6	26	57.7	5.6	480	250	1.5	0.5	11.3	2.3
Gm-15-9	5.4	26	99.9	6.3	BLOD	BLOD	1.4	0.3	11.2	2.3
Gm-15-10	4.8	31	64.4	4	1230	550	1.3	0.3	15.6	3
Gm-15-11	0.7	3	32.2	2	BLOD	BLOD	1.2	0.3	4.7	2.7
Gm-15-12	11.6	64	333	23	BLOD	BLOD	1.5	0.5	7.2	1
Gm-15-13	4.1	26	37.3	2.7	1360	460	1.1	0.4	23	4.8
Gm-15-14	1.9	17	39	2.2	1260	540	1.1	0.3	10.2	2.5
Gm-15-15	2.6	8	73.8	4.2	1370	440	1.5	0.2	7.3	2.6
Gm-15-16	0.8	2	4.5	0.27	1060	580	1.4	0.5	37.3	26.5
Gm-15-17	3.6	14	42.9	5.6	BLOD	BLOD	1.6	0.2	17.3	5.1
Gm-15-18	1.5	4	10.55	0.58	1360	630	1.5	0.3	28.7	14.5
Gm-16-1	3.6	13	211.4	13	350	200	1.1	0.3	4.3	1.2
Gm-16-2	3.8	23	106.1	6.4	BLOD	BLOD	0.8	0.4	9.1	1.9
Gm-16-3	4.2	15	153	11	BLOD	BLOD	1.6	0.1	6.8	1.8
Gm-16-4	1.4	5	44.7	5.4	BLOD	BLOD	1.1	0.3	7.8	3.5
Gm-16-5	5	21	155.5	6.3	BLOD	BLOD	1.4	0.1	8.1	1.8
Gm-16-6	4.6	13	149.1	10	340	230	1.5	0.5	7.8	2.2
Gm-16-7	2.3	7	63.8	2.9	BLOD	BLOD	1.9	0.4	9.2	3.5
Gm-16-8	0.8	3	18.6	1.5	510	300	1.2	0.4	11.2	6.5
Gm-16-9	3.6	9	150.2	5.9	BLOD	BLOD	1.4	0.3	6	2
Gm-16-10	1.6	4	70.9	3.3	470	310	1.2	0.2	5.7	2.8
Gm-16-11	1.9	7	64.3	4	BLOD	BLOD	1.4	0.3	7.6	2.9
Gm-16-12	4.5	9	188.3	7.2	BLOD	BLOD	1.5	0.1	6	2

Gm-16-13	3	9	194.5	11	490	200	1.1	0.5	3.9	1.3
Gm-16-14	1.4	5	21.5	1.9	6000	1700	1.2	0.1	16.6	7.5
Gm-16-15	3.7	13	107.4	6.8	780	390	1.7	0.2	8.7	2.4
Gm-16-16	5	21	182.4	8.4	610	330	1.7	0.4	6.9	1.5
Gm-16-17	2.6	11	68.6	3.3	710	320	1.7	0.2	9.6	2.9
Gm-16-18	2.3	8	84.2	7.2	4100	1800	1.7	0.3	6.8	2.4
Gm-16-19	2	7	123.8	4.7	BLOD	BLOD	1.5	0.6	4.1	1.5
Gm-16-20	4.3	18	213.8	14	BLOD	BLOD	1.4	0.3	5	1.2
Gm-16-21	3.9	19	57.6	2.3	900	420	1.2	0.2	16.9	3.9
Gm-16-22	2.5	9	69.8	4.4	910	440	1	0	9	3
Gm-16-23	2.1	9	117.5	6.3	650	310	1.5	0.1	4.6	1.5
Gm-16-24	2.5	12	152.3	9.6	970	480	1.1	0.4	4.1	1.2
Gm-16-25	5.7	20	220.2	14	1110	580	1.2	0.2	6.5	1.5
Gm-16-26	10.3	41	241.2	10	BLOD	BLOD	1.2	0.4	10.7	1.7
Gm-16-27	5.6	14	134.3	7.3	BLOD	BLOD	1.3	0.6	10.5	2.8
Gm-16-28	2.6	9	128	7.5	BLOD	BLOD	1.2	0.4	5	1.7
Gm-16-29	3.6	13	178.2	8.7	BLOD	BLOD	1.4	0.1	5.1	1.4
Gm-16-30	1	5	22.2	1.2	BLOD	BLOD	1.6	0.3	11.5	5.2
Gm-17-1	1	7	28.8	1.1	510	170	1	0.3	8.7	3.3
Gm-17-2	1.5	12	21.5	0.8	1120	180	1	0.3	17.5	5.1
Gm-17-3	0.8	4	12.3	0.4	280	120	1.4	0.1	17	8.5
Gm-17-4	0.8	4	10.5	0.4	BLOD	BLOD	1	0.1	19.9	10
Gm-17-5	2	10	37.7	1.1	540	150	1.4	0.5	13.6	4.3
Gm-17-6	1.8	9	30	1.3	810	410	1.2	0.5	15.3	5.1
Gm-17-7	0.9	6	19.5	0.5	BLOD	BLOD	1	0.4	11	4.5
Gm-17-8	0.6	3	25.4	0.9	1160	170	1.1	0.4	5.9	3.4
Gm-17-9	0.6	3	10.2	0.8	7200	3000	1.6	0.6	13.7	7.9
Gm-17-10	0.7	3	26	1.1	5700	2400	1.3	0.1	6.9	4
Gm-17-11	0.8	4	12.9	0.4	BLOD	BLOD	1.7	0.6	15.9	8
Gm-17-12	0.7	7	16	0.7	0	0	1	0.4	11	4.2

Gm-17-13	1.3	7	11.8	1.2	470	180	1.4	0.5	26.5	10
Gm-17-14	1	5	17.9	1	480	200	1.4	0.1	14	6.3
Gm-17-15	0.7	5	33.8	0.9	1540	250	1.5	0.6	5.2	2.3
Gm-17-16	1.1	5	28.8	1.3	620	160	1.5	0.6	9.7	4.3
Gm-17-17	1	5	38	0.8	430	170	0.7	0.4	6.6	3
Gm-17-18	1.1	8	36.9	0.4	1100	220	1.5	0.5	7.8	2.8
Gm-17-19	0.5	3	12.1	0.9	460	160	1.3	0.3	9.9	5.7
Gm-17-20	1.6	10	29.9	1.1	BLOD	BLOD	1.1	0.6	13.1	4.2
Gm-17-21	1.9	19	40.5	0.4	360	150	0.5	0.1	11.7	2.7
Gm-17-22	0.4	4	16.1	0.7	BLOD	BLOD	1.1	0.5	6.2	3.1
Gm-17-23	0.9	6	15.9	0.3	480	190	1.1	0.8	14.8	6
Gm-17-24	0.8	8	14.2	0.9	BLOD	BLOD	1.4	0.5	14.1	5
Gm-17-25	0.7	4	14.3	0.8	BLOD	BLOD	1.6	0.6	12.5	6.3
Gm-19-1	17.5	18	64.6	6.4	BLOD	BLOD	1.8	0.2	17.5	4.2
Gm-19-2	8.6	4	33.4	1.2	BLOD	BLOD	1.3	0.1	8.6	5.7
Gm-19-3	5.1	14	108.3	3.7	1690	180	1.7	0.2	5.1	1.4
Gm-19-4	8.7	5	24.1	1	1830	260	1.7	0.2	8.7	3.9
Gm-19-5	15.8	6	27.2	1.1	BLOD	BLOD	1.3	0.1	15.8	6.5
Gm-19-6	4.4	13	73.5	2.6	2700	220	1.7	0.2	4.4	1.2
Gm-19-7	8.2	7	26.8	1.1	1710	260	1.6	0.2	8.2	3.1
Gm-19-8	61.1	104	50.9	1.7	BLOD	BLOD	1.9	0.7	13	3.3
Gm-19-9	26.2	30	96.1	5	2280	740	2	0.8	10.4	2.6
Gm-19-10	41.7	60	27.7	1.9	2200	1100	2.3	0.8	5.2	3.7
Gm-19-11	27.6	47	116.2	7.5	2900	1200	1.9	0.7	8.6	2.2
Gm-19-12	26.9	36	30.1	1.8	BLOD	BLOD	2.1	0.7	25.4	7.5
Gm-19-13	14.7	8	86.8	4.5	BLOD	BLOD	1.9	0	7.2	1.8
Gm-19-14	44.4	63	25.3	1.8	BLOD	BLOD	2.2	0.6	5.5	2.5
Gm-19-15	74.3	146	107.6	6.7	BLOD	BLOD	1.8	0.5	6.5	1.9
Gm-19-16	66.4	89	122	11	3760	830	1.9	0	11.7	2.2
Gm-19-17	62.2	165	47	3.1	1920	900	1.8	0.6	19.8	4.5

Gm-19-18	34.1	58	104.8	6.4	3200	1100	2.1	0.5	11.7	2.7
Gm-19-19	65.9	119	101.8	8.5	3500	1300	2.1	0.6	10.8	2.5
Gm-19-20	44.4	154	118.2	6.2	BLOD	BLOD	1.9	0.7	10.1	1.6
Gm-19-21	28.1	48	27.1	1.6	2500	880	1.9	0.8	3.4	3.4
Gm-19-22	29	114	67.1	4.3	3300	1100	2	0.6	15.1	4.5
Gm-19-23	20.7	39	130.6	7.6	4000	1500	2	0.6	7.1	1.7
Gm-19-24	22.1	34	58.6	5.2	2100	1200	1.7	0.7	11.6	2.7
Gm-19-25	36.3	63	29.9	1.6	4000	1100	2.1	0.5	10.6	4
Gm-19-26	21.6	36	33.7	2.3	2300	1000	1.7	0.6	9.6	4
Gm-19-27	43	45	103.4	5.8	3300	1100	1.8	0.7	8	2.3
Gm-19-28	46.1	56	103.5	7.7	BLOD	BLOD	1.9	0.8	11.1	2.8
Gm-19-29	23.3	28	105.7	5.8	BLOD	BLOD	1.4	0.7	8	2.1
Gm-19-30	18.5	38	108	11	BLOD	BLOD	2	0.5	6.9	1.7
Gm-19-31	42.7	78	103.7	9.9	BLOD	BLOD	1.7	0.8	14.8	3.1
Gm-19-32	62.9	57	76.3	6.6	4700	1200	1.5	0.3	36.7	5
Gm-19-33	60.8	70	92	25	BLOD	BLOD	1.8	0.8	4	1.9
Gm-21-1	21.8	61	245.2	9.8	3390	660	1.6	0.5	22.3	2.9
Gm-21-2	20.4	57	279.5	14	3310	750	1.9	0.8	18.2	2.5
Gm-21-3	10.7	32	272.2	14	3790	860	1.6	0.4	9.8	1.8
Gm-21-4	18	63	157.1	7	3860	600	1.7	0.5	28.7	3.7
Gm-21-5	22.8	57	205.6	12	3140	600	1.8	1.2	27.8	3.8
Gm-21-6	15.3	46	228.3	15	2510	640	1.9	0.8	16.8	2.5
Gm-21-7	12.5	45	212.1	13	2680	740	1.7	0.6	14.8	2.3
Gm-21-8	9.2	22	257.8	17	3300	760	1.8	0.6	8.9	1.9
Gm-21-9	30.8	74	229.4	25	3050	840	1.8	0.6	33.6	4.4
Gm-21-10	24	72	163.7	9.3	4180	930	1.8	0.6	36.7	4.4
Gm-21-11	17.1	48	213.7	14	3300	700	1.6	0.7	20.1	3
Gm-21-12	24.2	58	132.4	5	3120	890	1.6	0.7	45.6	6.1
Gm-21-13	15.7	44	221.9	19	2640	540	1.5	0.4	17.7	2.8
Gm-21-14	13.9	25	260	10	3980	680	1.8	0.9	13.4	2.7

Gm-21-15	11.2	28	102.3	4.4	3550	720	2	0.8	27.4	5.3
Gm-21-16	26.3	63	203.8	7.5	3200	840	2	0.7	32.2	4.2
Gm-21-17	13.3	48	206.4	8.9	2350	840	1.7	0.7	16.2	2.4
Gm-21-18	16.7	40	136.9	6.3	2980	670	1.8	0.7	30.5	4.9
Gm-21-19	15.8	38	161.6	4	3300	800	1.4	0.4	24.5	4.1
Gm-21-20	18.8	45	196.8	9	3020	680	1.8	0.6	23.9	3.6

Appendix T

Garm Helium Data

Table T.1: Single grain zircon (U–Th–Sm)/He and apatite (U–Th–Sm)/He age and chemistry data. For single grain analysis, see Table-3. Concentrations of thorium, uranium and samarium in ng. He is the concentration of helium measured in ncc. Th/U is the ratio of thorium to uranium. Raw is the age (Ma) before the F_{T} correction is made. F_{T} is the alpha-ejection correction parameter of Farley et al. (1996). Age is the age (Ma) after applying the F_{T} correction. TAU is the total analytical uncertainty in %, and eU is the effective uranium (Guenthner et al. 2013).

Sample	^{232}Th	±(%)	^{238}U	±(%)	^{147}Sm	±(%)	He±(%)	TAU	eU	Th/U	Raw±1σ	F_{T}	Age±1σ
Zircon (U-Th-Sm)/He data													
Gm-19-1	0.534	1.4	1.57	1.9	0.004	19.0	43.123±0.7	1.9	1.7	0.3	205.2±3.8	0.73	280.6±15.6
Gm-19-2	0.933	1.4	2.003	1.9	0.004	13.4	62.115±0.8	1.9	2.2	0.5	225.2±4.2	0.75	301.3±17.2
Gm-19-3	0.362	1.5	1.465	1.9	0.004	16.0	30.861±1.1	2.1	1.5	0.3	161.3±3.4	0.82	196.8±12.5
Gm-19-4	0.844	2	4.295	2.3	0.003	14.2	129.133±0.7	2.4	4.5	0.2	231.2±5.4	0.77	301.1±18.2
Gm-21-1	0.655	1.4	4.326	1.9	0.001	15.0	75.415±0.7	1.9	4.5	0.2	136.7±2.6	0.76	180.7±10.5
Gm-21-2	0.714	1.4	5.506	1.9	0.003	17.8	93.363±0.7	1.9	5.7	0.1	133.6±2.6	0.69	194.2±10.2
Gm-21-3	0.501	1.5	2.954	1.9	0.003	20.2	48.557±1.8	2.5	3.1	0.2	128.4±3.3	0.67	191.7±10.3
Gm-21-4	0.424	1.5	2.989	1.9	0.002	16.7	59.846±0.7	2	3.1	0.1	157.0±3.1	0.69	227.5±12.0
Apatite (U-Th-Sm)/He data													
Gm-19-1	0.003	4.5	0.516	3.9	0.038	0.3	0.604±1.6	4.2	0.5	0.1	9.6±0.4	0.77	12.4±0.8
Gm-19-4	0.005	5.3	0.029	5.4	0.006	0.4	0.024±5.2	7.3	0.1	0.2	6.7±0.5	0.62	10.8±1.0
Gm-19-6	0.007	5.3	0.069	5.4	0.006	0.5	0.061±2.5	5.9	0.1	0.1	7.1±0.4	0.60	11.9±0.9
Gm-19-8	0.005	5.3	0.149	5.4	0.01	0.4	0.128±1.9	5.7	0.2	0.1	7.0±0.4	0.63	11.1±0.8
Gm-19-3	0.006	3.9	0.088	3.9	0.007	0.4	0.141±1.4	4.1	0.1	0.1	12.9±0.5	0.59	21.8±1.4
Gm-19-5	0.003	4.6	0.036	3.9	0.013	0.3	0.066±2.3	4.5	0.1	0.1	14.5±0.6	0.68	21.3±1.4
Gm-19-7	0.001	19	0.043	3.9	0.013	0.3	0.101±1.4	4.1	0.1	0.1	19.4±0.8	0.69	28.1±1.8

Appendix U

Garm Thermal Modelling Constraints

Table U.1: Thermal history modelling parameters following Flowers et al. (2015).

Simulation inputs

Sample	ZHe	AFT	AHe	Data Source	All Data Published
Gm-21		×		Supp file 3	yes
Gm-19	×	×	×	Supp file 3 and 4	yes
Gm-17		×		Supp file 3	yes
Gm-16		×		Supp file 3	yes
Gm-15		×		Supp file 3	yes

Data treatment, uncertainties, and other relevant constraints

AHe Data

He dates (Ma): Single grain AHe ages from Supp file 3 modelled individually

Error (Ma) applied in modeling: error of 1σ was used from Supp file 3

r (μm): Equivalent spherical radius of each grain

ZHe Data

He dates (Ma): Single grain ZHe ages from Supp file 3 modelled individually

Error (Ma) applied in modeling: error of 1σ was used from Supp file 3

r (μm): Equivalent spherical radius of each grain

AFT Data

Cl wt%: From Supp file 4

Initial mean track length: 16.3 μm

Track length reduction standard: 0.893

Additional geological information

Samples Gm 17, Gm 16, and Gm 15 are all modelled together as samples are all taken from the same geographical location

System- and model-specific parameters

He radiation damage model: Flowers et al. 2009

F_T *annealing model:* Ketcham et al. 2007

F_T *c-axis projection:* Not used

Modeling code: QTQt 5.6.0 PC

Statistical fitting criteria: Default QTQt values

MCMC Parameters: Burn-in = 200,000, Post-burn-in = 200,000

tT path characteristics: Not indicated

Bibliography

Abdrakhmatov, K. Y., Aldazhanov, S., Hager, B., Hamburger, M., Herring, T., Kalabaev, K., Makarov, V., Molnar, P., Panasyuk, S., Prilepin, M. et al. (1996), 'Relatively recent construction of the Tien Shan inferred from GPS measurements of present-day crustal deformation rates', *Nature* **384**(6608), 450.

Ahmedov, N. (2000), 'Stratified and intrusive formations of Uzbekistan', *Uzbekistan Geological Survey* .

Aitchison, J. C., Ali, J. R. & Davis, A. M. (2007), 'When and where did India and Asia collide?', *Journal of Geophysical Research: Solid Earth* **112**(B5).
URL: *https://agupubs.onlinelibrary.wiley.com/doi/abs/10.1029/2006JB004706*

Alexeiev, D., Kröner, A., Hegner, E., Rojas-Agramonte, Y., Biske, Y., Wong, J., Geng, H., Ivleva, E., Mühlberg, M., Mikolaichuk, A. & Liu, D. (2016), 'Middle to Late Ordovician arc system in the Kyrgyz Middle Tianshan: From arc-continent collision to subsequent evolution of a Palaeozoic continental margin', *Gondwana Research* **39**, 261 – 291.
URL: *http://www.sciencedirect.com/science/article/pii/S1342937X16300065*

Alexeiev, D. V., Bykadorov, V. A., Volozh, Y. A. & Sapozhnikov, R. B. (2017), 'Kinematic analysis of Jurassic grabens of southern Turgai and the role of the Mesozoic stage in the evolution of the Karatau–Talas–Ferghana strike-slip fault, Southern Kazakhstan and Tian Shan', *Geotectonics* **51**(2), 105–120.
URL: *https://doi.org/10.1134/S0016852117020029*

Alexeiev, D. V., Cook, H. E., Buvtyshkin, V. M. & Golub, L. Y. (2009), 'Structural evolution of the Ural–Tian Shan junction: A view from Karatau ridge, South Kazakhstan', *Comptes Rendus Geoscience* **341**(2), 287 – 297. Mécanique de l'orogénie varisque : Une vision

moderne de le recherche dans le domaine de l'orogénie.
URL: *http://www.sciencedirect.com/science/article/pii/S163107130800285X*

Allen, M. B., Alsop, G. I. & Zhemchuzhnikov, V. G. (2001), 'Dome and basin refolding and transpressive inversion along the Karatau Fault system, southern Kazakstan', *Journal of the Geological Society* **158**(1), 83–95.
URL: *http://jgs.lyellcollection.org/content/158/1/83*

Allen, M. B., Anderson, L., Searle, R. C. & Buslov, M. (2006), 'Oblique rift geometry of the West Siberian Basin: tectonic setting for the Siberian flood basalts', *Journal of the Geological Society* **163**(6), 901–904.
URL: *http://jgs.lyellcollection.org/content/163/6/901*

Allen, M. B., Windley, B. F., Chi, Z., Zhong-Yan, Z. & Guang-Rei, W. (1991), 'Basin evolution within and adjacent to the Tien Shan Range, NW China', *Journal of the Geological Society* **148**(2), 369–378.
URL: *http://jgs.lyellcollection.org/content/148/2/369*

Allen, M., Windley, B. & Zhang, C. (1993), 'Palaeozoic collisional tectonics and magmatism of the Chinese Tien Shan, central Asia', *Tectonophysics* **220**(1), 89 – 115.
URL: *http://www.sciencedirect.com/science/article/pii/0040195193902259*

Amidon, W. H. & Hynek, S. A. (2010), 'Exhumational history of the north central Pamir', *Tectonics* **29**(5).
URL: *https://agupubs.onlinelibrary.wiley.com/doi/abs/10.1029/2009TC002589*

Angiolini, L., Andrea, Z., Stefano, Z., Alda, N. & Giovanni, V. (2013), 'The Cimmerian geopuzzle: new data from South Pamir', *Terra Nova* **25**(5), 352–360.
URL: *https://onlinelibrary.wiley.com/doi/abs/10.1111/ter.12042*

Bande, A., Radjabov, S., Sobel, E. R. & Sim, T. (2017a), 'Cenozoic palaeoenvironmental and tectonic controls on the evolution of the northern fergana basin', *Geological Society, London, Special Publications* **427**(1), 313–335.
URL: *http://sp.lyellcollection.org/content/427/1/313*

Bande, A., Sobel, E. R., Mikolaichuk, A., Schmidt, A. & Stockli, D. F. (2017c), 'Exhumation history of the western kyrgyz tien shan: Implications for intramontane basin formation', *Tectonics* **36**(1), 163–180.
URL: *https://agupubs.onlinelibrary.wiley.com/doi/abs/10.1002/2016TC004284*

Bande, A., Sobel, E. R., Mikolaichuk, A. & Torres, A. V. (2017b), 'Talas–Fergana Fault Cenozoic timing of deformation and its relation to Pamir indentation', *Geological Society, London, Special Publications* **427**(1), 295–311.
URL: *http://sp.lyellcollection.org/content/427/1/295*

Bazhenov, M. L., Chauvin, A., Audibert, M. & Levashova, N. (1993), 'Permian and Triassic paleomagnetism of the southwestern Tien Shan: timing and mode of tectonic rotations', *Earth and Planetary Science Letters* **118**(1), 195 – 212.
URL: *http://www.sciencedirect.com/science/article/pii/0012821X93901689*

Beck, R. A., Burbank, D. W., Sercombe, W. J., Riley, G. W., Barndt, J. K., Berry, J. R., Afzal, J., Khan, A. M., Jurgen, H., Metje, J., Cheema, A., Shafique, N. A., Lawrence, R. D. & Khan, M. A. (1995), 'Stratigraphic evidence for an early collision between northwest India and Asia', *Nature* **373**(6509), 55.

Bernet, M. & Garver, J. I. (2005), 'Fission-track analysis of detrital zircon', *Reviews in Mineralogy and Geochemistry* **58**(1), 205–237.

Bershaw, J., Garzione, C. N., Schoenbohm, L., Gehrels, G. & Tao, L. (2012), 'Cenozoic evolution of the Pamir plateau based on stratigraphy, zircon provenance, and stable isotopes of foreland basin sediments at Oytag (Wuyitake) in the Tarim Basin (west China)', *Journal of Asian Earth Sciences* **44**, 136 – 148. Asian Climate & Tectonics.
URL: *http://www.sciencedirect.com/science/article/pii/S1367912011001878*

Biske, Y. S., Konopelko, D. & Seltmann, R. (2013), 'Geodynamics of late Paleozoic magmatism in the Tien Shan and its framework', *Geotectonics* **47**(4), 291–309.

Biske, Y. & Seltmann, R. (2010), 'Paleozoic Tian-Shan as a transitional region between the Rheic and Urals-Turkestan oceans', *Gondwana Research* **17**(2), 602 – 613. The Rheic

Ocean: Palaeozoic Evolution from Gondwana and Laurussia to Pangaea.
URL: *http://www.sciencedirect.com/science/article/pii/S1342937X09002160*

Blackburn, T., Bowring, S. A., Schoene, B., Mahan, K. & Dudas, F. (2011), 'U-Pb thermochronology: creating a temporal record of lithosphere thermal evolution', *Contributions to Mineralogy and Petrology* **162**(3), 479–500.
URL: *https://doi.org/10.1007/s00410-011-0607-6*

Bosboom, R., Dupont-Nivet, G., Grothe, A., Brinkhuis, H., Villa, G., Mandic, O., Stoica, M., Kouwenhoven, T., Huang, W., Yang, W. & Guo, Z. (2014), 'Timing, cause and impact of the late eocene stepwise sea retreat from the tarim basin (west china)', *Palaeogeography, Palaeoclimatology, Palaeoecology* **403**, 101 – 118.
URL: *http://www.sciencedirect.com/science/article/pii/S0031018214001709*

Bosboom, R. E., Dupont-Nivet, G., Houben, A., Brinkhuis, H., Villa, G., Mandic, O., Stoica, M., Zachariasse, W. J., Guo, Z., Li, C. & Krijgsman, W. (2011), 'Late eocene sea retreat from the tarim basin (west china) and concomitant asian paleoenvironmental change', *Palaeogeography, Palaeoclimatology, Palaeoecology* **299**(3), 385 – 398.
URL: *http://www.sciencedirect.com/science/article/pii/S0031018210006954*

Bosboom, R., Mandic, O., Dupont-Nivet, G., Proust, J.-N., Ormukov, C. & Aminov, J. (2015), 'Late Eocene palaeogeography of the proto-Paratethys Sea in Central Asia (NW China, southern Kyrgyzstan and SW Tajikistan)', *Geological Society, London, Special Publications* **427**(1).
URL: *http://sp.lyellcollection.org/content/early/2015/10/12/SP427.11*

Bouilhol, P., Jagoutz, O., Hanchar, J. M. & Dudas, F. O. (2013), 'Dating the India–Eurasia collision through arc magmatic records', *Earth and Planetary Science Letters* **366**, 163 – 175.
URL: *http://www.sciencedirect.com/science/article/pii/S0012821X1300040X*

Brookfield, M. (2000), 'Geological development and Phanerozoic crustal accretion in the western segment of the southern Tien Shan (Kyrgyzstan, Uzbekistan and Tajikistan)', *Tectonophysics* **328**(1-2), 1–14.

Bullen, M., Burbank, D., Garver, J. & Abdrakhmatov, K. (2001), 'Late Cenozoic tectonic evolution of the northwestern Tien Shan: New age estimates for the initiation of mountain building', *GSA Bulletin* **113**(12), 1544.
URL: *http://dx.doi.org/10.1130/0016-7606(2001)113<1544:LCTEOT>2.0.CO;2*

Bullen, M. E., Burbank, D. W. & Garver, J. I. (2003), 'Building the Northern Tien Shan: Integrated Thermal, Structural, and Topographic Constraints', *The Journal of Geology* **111**(2), 149–165.
URL: *https://doi.org/10.1086/345840*

Burbank, D., McLean, J., Bullen, M., Abdrakhmatov, K. & Miller, M. (1999), 'Partitioning of intermontane basins by thrust-related folding, Tien Shan, Kyrgyzstan', *Basin Research* **11**(1), 75–92.

Burov, E. B. & Molnar, P. (1998), 'Gravity anomalies over the Ferghana Valley (central Asia) and intracontinental deformation', *Journal of Geophysical Research: Solid Earth* **103**(B8), 18137–18152.
URL: *https://agupubs.onlinelibrary.wiley.com/doi/abs/10.1029/98JB01079*

Burtman, V. (2000), 'Cenozoic crustal shortening between the Pamir and Tien Shan and a reconstruction of the Pamir–Tien Shan transition zone for the Cretaceous and Palaeogene', *Tectonophysics* **319**(2), 69 – 92.
URL: *http://www.sciencedirect.com/science/article/pii/S0040195100000226*

Burtman, V. S. (1975), 'Structural geology of variscan Tien Shan, USSR', *Am. J. Sci* **275**, 157–186.

Burtman, V. S. (1980), 'Faults of middle Asia', *American Journal of Science* **280**(8), 725–744.

Burtman, V. S. (2010), 'Tien Shan, Pamir, and Tibet: History and geodynamics of phanerozoic oceanic basins', *Geotectonics* **44**(5), 388–404.
URL: *https://doi.org/10.1134/S001685211005002X*

Burtman, V. S. (2015), 'Tectonics and geodynamics of the Tian Shan in the Middle and

Late Paleozoic', *Geotectonics* **49**(4), 302–319.
URL: *https://doi.org/10.1134/S0016852115040020*

Burtman, V. S. & Molnar, P. H. (1993), *Geological and geophysical evidence for deep subduction of continental crust beneath the Pamir*, Vol. 281, Geological Society of America.

Burtman, V. S., Skobelev, S. F. & Molnar, P. (1996), 'Late Cenozoic slip on the Talas-Ferghana fault, the Tien Shan, central Asia', *GSA Bulletin* **108**(8), 1004.
URL: *http://dx.doi.org/10.1130/0016-7606(1996)108<1004:LCSOTT>2.3.CO;2*

Buslov, M. M., Watanabe, T., Smirnova, L. V., Fujiwara, I., Iwata, K., De Grave, J., Semakov, N. N., Travin, A. V., Kir'yanova, A. P. & Kokh, D. A. (2003), 'Role of strike-slip faults in Late Paleozoic-Early Mesozoic tectonics and geodynamics of the Altai-Sayan and East Kazakhstan folded zone', *Geologiya i Geofizika* **44**(1-2), 49–75.

Cao, K., Wang, G.-C., van der Beek, P., Bernet, M. & Zhang, K.-X. (2013), 'Cenozoic thermo-tectonic evolution of the northeastern Pamir revealed by zircon and apatite fission-track thermochronology', *Tectonophysics* **589**, 17 – 32.
URL: *http://www.sciencedirect.com/science/article/pii/S0040195113000218*

Carrapa, B., Mustapha, F. S., Cosca, M., Gehrels, G., Schoenbohm, L. M., Sobel, E. R., DeCelles, P. G., Russell, J. & Goodman, P. (2014), 'Multisystem dating of modern river detritus from Tajikistan and China: Implications for crustal evolution and exhumation of the Pamir', *Lithosphere* **6**(6), 443.
URL: *http://dx.doi.org/10.1130/L360.1*

Carroll, A. R., Graham, S. A., Hendrix, M. S., Ying, D. & Zhou, D. (1995), 'Late Paleozoic tectonic amalgamation of northwestern China: Sedimentary record of the northern Tarim, northwestern Turpan, and southern Junggar Basins', *GSA Bulletin* **107**(5), 571.
URL: *http://dx.doi.org/10.1130/0016-7606(1995)107<0571:LPTAON>2.3.CO;2*

Cawood, P. A., Kröner, A., Collins, W. J., Kusky, T. M., Mooney, W. D. & Windley, B. F. (2009), 'Accretionary orogens through earth history', *Geological Society, London, Special Publications* **318**(1), 1–36.
URL: *http://sp.lyellcollection.org/content/318/1/1*

Charvet, J., Shu, L. S. & Laurent-Charvet, S. (2007), 'Paleozoic structural and geodynamic evolution of eastern Tianshan (NW China): welding of the Tarim and Junggar plates', *Episodes Journal of International Geoscience* **30**(3), 162–186.
URL: *https://hal-insu.archives-ouvertes.fr/insu-00179631*

Chen, Z.-l., Wan, J.-l., Liu, J., Li, S.-x. & Zhen, E.-j. (2006), 'Multi-stage uplift and exhumation of the west Tianshan Mountain: Evidence from the apatite fission-track dating', *Acta Geoscientia Sinica* **27**(2), 97.

Cherniak, D., Lanford, W. & Ryerson, F. (1991), 'Lead diffusion in apatite and zircon using ion implantation and Rutherford Backscattering techniques', *Geochimica et Cosmochimica Acta* **55**(6), 1663 – 1673.
URL: *http://www.sciencedirect.com/science/article/pii/001670379190137T*

Chew, D. M. & Donelick, R. A. (2012), 'Combined apatite fission track and U-Pb dating by LA-ICP-MS and its application in apatite provenance analysis', *Quantitative mineralogy and microanalysis of sediments and sedimentary rocks: Mineralogical Association of Canada Short Course* **42**, 219–247.

Chew, D. M., Sylvester, P. J. & Tubrett, M. N. (2011), 'U–Pb and Th–Pb dating of apatite by LA-ICPMS', *Chemical Geology* **280**(1), 200 – 216.
URL: *http://www.sciencedirect.com/science/article/pii/S0009254110004031*

Chew, D., Petrus, J. & Kamber, B. (2014), 'U–Pb LA–ICPMS dating using accessory mineral standards with variable common Pb', *Chemical Geology* **363**, 185 – 199.
URL: *http://www.sciencedirect.com/science/article/pii/S000925411300510X*

Clift, P. D., Carter, A., Krol, M. & Kirby, E. (2002), 'Constraints on India-Eurasia collision in the Arabian Sea region taken from the Indus Group, Ladakh Himalaya, India', *Geological Society, London, Special Publications* **195**(1), 97–116.
URL: *http://sp.lyellcollection.org/content/195/1/97*

Cochrane, R., Spikings, R. A., Chew, D., Wotzlaw, J.-F., Chiaradia, M., Tyrrell, S., Schaltegger, U. & der Lelij, R. V. (2014), 'High temperature (>350°C) thermochronology and

mechanisms of Pb loss in apatite', *Geochimica et Cosmochimica Acta* **127**, 39 – 56.
URL: *http://www.sciencedirect.com/science/article/pii/S0016703713006674*

Cook, H. E., Apollonov, M. K., Taylor, M. E., Zhemchuzhnikov, S. V., Dubinina, S. V. & Mel'nikova, L. (1991), 'Comparison of two early Paleozoic carbonate submarine fans—western United States and southern Kazakhstan, Soviet Union'.

Cook, H. E., Zhemchuzhnikov, V. G., Zempolich, W. G., Zhaimina, V. Y., Buvtyshkin, V. M., Kotova, E. A., Golub, L. Y., Zorin, A. Y., Lehmann, P. J., Alexeiev, D. V. et al. (2002), 'Devonian and Carboniferous carbonate platform facies in the Bolshoi Karatau, Southern Kazakhstan: outcrop analogs for coeval carbonate oil and gas fields in the North Caspian Basin, Western Kazakhstan'.

Danišík, M., Kuhlemann, J., Dunkl, I., Evans, N. J., Székely, B. & Frisch, W. (2012a), 'Survival of Ancient Landforms in a Collisional Setting as Revealed by Combined Fission Track and (U-Th)/He Thermochronometry: A Case Study from Corsica (France)', *The Journal of Geology* **120**(2), 155–173.
URL: *https://doi.org/10.1086/663873*

Danišík, M., Štěpančíková, P. & Evans, N. J. (2012), 'Constraining long-term denudation and faulting history in intraplate regions by multisystem thermochronology: An example of the Sudetic Marginal Fault (Bohemian Massif, central Europe)', *Tectonics* **31**(2).
URL: *https://agupubs.onlinelibrary.wiley.com/doi/abs/10.1029/2011TC003012*

Danišík, M., McInnes, B. I. A., Kirkland, C. L., McDonald, B. J., Evans, N. J. & Becker, T. (2017), 'Seeing is believing: Visualization of he distribution in zircon and implications for thermal history reconstruction on single crystals', *Science Advances* **3**(2).
URL: *http://advances.sciencemag.org/content/3/2/e1601121*

De Grave, J., Buslov, M. M. & Van den haute, P. (2007), 'Distant effects of India–Eurasia convergence and Mesozoic intracontinental deformation in Central Asia: Constraints from apatite fission-track thermochronology', *Journal of Asian Earth Sciences* **29**(2), 188 – 204. The 19th Himalaya-Karakoram-Tibet Workshop (HKT19) held at Niseko, Hokkaido,

Japan, 10–13 July 2004.
URL: *http://www.sciencedirect.com/science/article/pii/S136791200600071X*

De Grave, J., Glorie, S., Buslov, M. M., Izmer, A., Fournier-Carrie, A., Batalev, V. Y., Vanhaecke, F., Elburg, M. & Van den haute, P. (2011), 'The thermo-tectonic history of the Song-Kul plateau, Kyrgyz Tien Shan: Constraints by apatite and titanite thermochronometry and zircon U/Pb dating', *Gondwana Research* **20**(4), 745 – 763.
URL: *http://www.sciencedirect.com/science/article/pii/S1342937X11001201*

De Grave, J., Glorie, S., Buslov, M. M., Stockli, D. F., McWilliams, M. O., Batalev, V. Y. & Van den haute, P. (2013), 'Thermo-tectonic history of the Issyk-Kul basement (Kyrgyz Northern Tien Shan, Central Asia)', *Gondwana Research* **23**(3), 998 – 1020. Ultrahigh-pressure and high-pressure metamorphic terranes in orogenic belts: reactions, fluids and geological processes.
URL: *http://www.sciencedirect.com/science/article/pii/S1342937X12002377*

De Grave, J., Glorie, S., Ryabinin, A., Zhimulev, F., Buslov, M., Izmer, A., Elburg, M., Vanhaecke, F. & Van den haute, P. (2012), 'Late Palaeozoic and Meso-Cenozoic tectonic evolution of the southern Kyrgyz Tien Shan: Constraints from multi-method thermochronology in the Trans-Alai, Turkestan-Alai segment and the southeastern Ferghana Basin', *Journal of Asian Earth Sciences* **44**, 149 – 168. Asian Climate and Tectonics.
URL: *http://www.sciencedirect.com/science/article/pii/S1367912011001866*

de Jong, K., Wang, B., Faure, M., Shu, L., Cluzel, D., Charvet, J., Ruffet, G. & Chen, Y. (2009), 'New 40Ar/39Ar age constraints on the Late Palaeozoic tectonic evolution of the western Tianshan (Xinjiang, northwestern China), with emphasis on Permian fluid ingress', *International Journal of Earth Sciences* **98**(6), 1239–1258.
URL: *https://doi.org/10.1007/s00531-008-0338-8*

De Pelsmaeker, E., Glorie, S., Buslov, M. M., Zhimulev, F. I., Poujol, M., Korobkin, V. V., Vanhaecke, F., Vetrov, E. V. & De Grave, J. (2015), 'Late-Paleozoic emplacement and Meso-Cenozoic reactivation of the southern Kazakhstan granitoid basement', *Tectonophysics* **662**, 416 – 433. Special issue on Comparative tectonic and dynamic analysis of

cratons, orogens, basins, and metallogeny:.
URL: *https://www.sciencedirect.com/science/article/pii/S0040195115003091*

De Pelsmaeker, E., Jolivet, M., Laborde, A., Poujol, M., Robin, C., Zhimulev, F. I., Nachtergaele, S., Glorie, S., Clercq, S. D., Batalev, V. Y. & Grave, J. D. (2018), 'Source-to-sink dynamics in the Kyrgyz Tien Shan from the Jurassic to the Paleogene: Insights from sedimentological and detrital zircon U-Pb analyses', *Gondwana Research* **54**, 180 – 204.
URL: *http://www.sciencedirect.com/science/article/pii/S1342937X17300679*

Dewey, J., Cande, S. & Pitman, W. (1989), 'The tectonic evolution of the India/Eurasia collision zone.', *Ecolgae Geologicae Helvetiae* **82**, 717–734.

Dill, H., Kus, J., Dohrmann, R. & Tsoy, Y. (2008), 'Supergene and hypogene alteration in the dual-use kaolin-bearing coal deposit Angren, SE Uzbekistan', *International Journal of Coal Geology* **75**(4), 225 – 240.
URL: *http://www.sciencedirect.com/science/article/pii/S0166516208001328*

Dolgopolova, A., Seltmann, R., Konopelko, D., Biske, Y. S., Shatov, V., Armstrong, R., Belousova, E., Pankhurst, R., Koneev, R. & Divaev, F. (2017), 'Geodynamic evolution of the western tien shan, uzbekistan: Insights from u-pb shrimp geochronology and sr-nd-pb-hf isotope mapping of granitoids', *Gondwana Research* **47**, 76 – 109. Continental construction in Central Asia and actualistic comparisons with western Pacific.
URL: *http://www.sciencedirect.com/science/article/pii/S1342937X16304324*

Donelick, R. A. & Miller, D. S. (1991), 'Enhanced tint fission track densities in low spontaneous track density apatites using 252Cf-derived fission fragment tracks: A model and experimental observations', *International Journal of Radiation Applications and Instrumentation. Part D. Nuclear Tracks and Radiation Measurements* **18**(3), 301 – 307.
URL: *http://www.sciencedirect.com/science/article/pii/135901899190022A*

Donelick, R. A., O'Sullivan, P. B. & Ketcham, R. A. (2005), 'Apatite Fission-Track Analysis', *Reviews in Mineralogy and Geochemistry* **58**(1), 49.
URL: *http://dx.doi.org/10.2138/rmg.2005.58.3*

Dumitru, T. A., Zhou, D., Chang, E. Z., Graham, S. A., Hendrix, M. S., Sobel, E. R. & Carroll, A. R. (2001), 'Uplift, exhumation, and deformation in the Chinese Tian Shan', *Memoirs-Geological Society of America* pp. 71–100.

Dunkl, I. (2002), 'Trackkey: a Windows program for calculation and graphical presentation of fission track data', *Computers and Geosciences* **28**(1), 3 – 12.
URL: *http://www.sciencedirect.com/science/article/pii/S0098300401000243*

Ehlers, T. A. & Farley, K. A. (2003), 'Apatite (U–Th)/He thermochronometry: methods and applications to problems in tectonic and surface processes', *Earth and Planetary Science Letters* **206**(1), 1 – 14.
URL: *http://www.sciencedirect.com/science/article/pii/S0012821X02010695*

Farley, K. A. (2002), '(U-Th)/He Dating: Techniques, Calibrations, and Applications', *Reviews in Mineralogy and Geochemistry* **47**(1), 819.
URL: *http://dx.doi.org/10.2138/rmg.2002.47.18*

Farley, K., Wolf, R. & Silver, L. (1996), 'The effects of long alpha-stopping distances on (U-Th)/He ages', *Geochimica et Cosmochimica Acta* **60**(21), 4223 – 4229.
URL: *http://www.sciencedirect.com/science/article/pii/S0016703796001937*

Filippova, I., Bush, V. & Didenko, A. (2001), 'Middle Paleozoic subduction belts: the leading factor in the formation of the Central Asian fold-and-thrust belt', *Russian Journal of Earth Sciences* **3**(6), 405–426.

Fleischer, R. L., Price, P. B., Walker, R. M. & W., R. M. (1975), *Nuclear tracks in solids: principles and applications*, Univ of California Press.

Flowers, R. M., Farley, K. A. & Ketcham, R. A. (2015), 'A reporting protocol for thermochronologic modeling illustrated with data from the Grand Canyon', *Earth and Planetary Science Letters* **432**, 425 – 435.
URL: *http://www.sciencedirect.com/science/article/pii/S0012821X15006317*

Flowers, R. M., Ketcham, R. A., Shuster, D. L. & Farley, K. A. (2009), 'Apatite (U–Th)/He thermochronometry using a radiation damage accumulation and annealing model',

Geochimica et Cosmochimica Acta **73**(8), 2347–2365.
URL: *http://www.sciencedirect.com/science/article/pii/S001670370900043X*

Frankopan, P. (2015), *The silk roads: A new history of the world*, Bloomsbury Publishing.

Gallagher, K. (2012), 'Transdimensional inverse thermal history modeling for quantitative thermochronology', *Journal of Geophysical Research: Solid Earth* **117**(B2).
URL: *https://agupubs.onlinelibrary.wiley.com/doi/abs/10.1029/2011JB008825*

Gallagher, K. & Brown, R. (1997), 'The onshore record of passive margin evolution', *Journal of the Geological Society* **154**(3), 451–457.
URL: *http://jgs.lyellcollection.org/content/154/3/451*

Gallagher, K., Brown, R. & Johnson, C. (1998), 'Fission track analysis and its applications to geological problems', *Annual Review of Earth and Planetary Sciences* **26**(1), 519–572.
URL: *https://doi.org/10.1146/annurev.earth.26.1.519*

Garver, J. I. & Kamp, P. J. (2002), 'Integration of zircon color and zircon fission-track zonation patterns in orogenic belts: application to the Southern Alps, New Zealand', *Tectonophysics* **349**(1), 203 – 219. Low Temperature Thermochronology: From Tectonics to Landscape Evolution.
URL: *http://www.sciencedirect.com/science/article/pii/S0040195102000549*

Garzanti, E. (1999), 'Stratigraphy and sedimentary history of the Nepal Tethys Himalaya passive margin', *Journal of Asian Earth Sciences* **17**(5), 805 – 827.
URL: *http://www.sciencedirect.com/science/article/pii/S1367912099000176*

Gautheron, C., Tassan-Got, L., Barbarand, J. & Pagel, M. (2009), 'Effect of alpha-damage annealing on apatite (U–Th)/He thermochronology', *Chemical Geology* **266**(3), 157 – 170.
URL: *http://www.sciencedirect.com/science/article/pii/S0009254109002630*

Gillespie, J., Glorie, S., Jepson, G., Zhang, Z. Y., Xiao, W. J., Danišík, M. & Collins, A. S. (2017), 'Differential Exhumation and Crustal Tilting in the Easternmost Tianshan (Xinjiang, China), Revealed by Low-Temperature Thermochronology', *Tectonics* **36**(10), 2142–2158.
URL: *https://agupubs.onlinelibrary.wiley.com/doi/abs/10.1002/2017TC004574*

Gleadow, A., Harrison, M., Kohn, B., Lugo-Zazueta, R. & Phillips, D. (2015), 'The fish canyon tuff: A new look at an old low-temperature thermochronology standard', *Earth and Planetary Science Letters* **424**, 95 – 108.
URL: *http://www.sciencedirect.com/science/article/pii/S0012821X15002927*

Gleadow, A., Hurford, A. & Quaife, R. (1976), 'Fission track dating of zircon: Improved etching techniques', *Earth and Planetary Science Letters* **33**(2), 273 – 276.
URL: *http://www.sciencedirect.com/science/article/pii/0012821X76902351*

Gleadow, A. J., Belton, D. X., Kohn, B. P. & Brown, R. W. (2002), 'Fission Track Dating of Phosphate Minerals and the Thermochronology of Apatite', *Reviews in Mineralogy and Geochemistry* **48**(1), 579.
URL: *+ http://dx.doi.org/10.2138/rmg.2002.48.16*

Gleadow, A. J. W. (2007), 'Fission track dating methods, 3rd edition', *School of Earth Sciences, The University of Melbourne* .

Gleadow, A. J. W., Duddy, I. R., Green, P. F. & Lovering, J. F. (1986), 'Confined fission track lengths in apatite: a diagnostic tool for thermal history analysis', *Contributions to Mineralogy and Petrology* **94**(4), 405–415.
URL: *https://doi.org/10.1007/BF00376334*

Glorie, S., Alexandrov, I., Nixon, A., Jepson, G., Gillespie, J. & Jahn, B.-M. (2017), 'Thermal and exhumation history of Sakhalin Island (Russia) constrained by apatite U-Pb and fission track thermochronology', *Journal of Asian Earth Sciences* **143**, 326 – 342.
URL: *http://www.sciencedirect.com/science/article/pii/S1367912017302262*

Glorie, S. & De Grave, J. (2016), 'Exhuming the Meso–Cenozoic Kyrgyz Tianshan and Siberian Altai-Sayan: A review based on low-temperature thermochronology', *Geoscience Frontiers* **7**(2), 155 – 170. Special Issue: Exhuming Asia.
URL: *https://www.sciencedirect.com/science/article/pii/S1674987115000468*

Glorie, S., De Grave, J., Buslov, M., Elburg, M., Stockli, D., Gerdes, A. & Van den haute, P. (2010), 'Multi-method chronometric constraints on the evolution of the Northern Kyrgyz Tien Shan granitoids (Central Asian Orogenic Belt): From emplacement to exhumation',

Journal of Asian Earth Sciences **38**(3), 131 – 146.
URL: *http://www.sciencedirect.com/science/article/pii/S1367912009002636*

Glorie, S., De Grave, J., Delvaux, D., Buslov, M., Zhimulev, F., Vanhaecke, F., Elburg, M. & Van den haute, P. (2012), 'Tectonic history of the Irtysh shear zone (NE Kazakhstan): New constraints from zircon U/Pb dating, apatite fission track dating and palaeostress analysis', *Journal of Asian Earth Sciences* **45**, 138 – 149.
URL: *http://www.sciencedirect.com/science/article/pii/S1367912011004160*

Glorie, S., Grave, J. D., Buslov, M. M., Zhimulev, F. I., Stockli, D. F., Batalev, V. Y., Izmer, A., Van den haute, P., Vanhaecke, F. & Elburg, M. A. (2011), 'Tectonic history of the Kyrgyz South Tien Shan (Atbashi-Inylchek) suture zone: The role of inherited structures during deformation-propagation', *Tectonics* **30**(6).
URL: *https://agupubs.onlinelibrary.wiley.com/doi/abs/10.1029/2011TC002949*

Goldfarb, R. J., Taylor, R. D., Collins, G. S., Goryachev, N. A. & Orlandini, O. F. (2014), 'Phanerozoic continental growth and gold metallogeny of Asia', *Gondwana Research* **25**(1), 48 – 102.
URL: *http://www.sciencedirect.com/science/article/pii/S1342937X13000993*

Gordon Gastil, R., DeLisle, M. & Morgan, J. (1967), 'Some Effects of Progressive Metamorphism on Zircons', *GSA Bulletin* **78**(7), 879.
URL: *http://dx.doi.org/10.1130/0016-7606(1967)78[879:SEOPMO]2.0.CO;2*

Green, P., Duddy, I., Gleadow, A., Tingate, P. & Laslett, G. (1986), 'Thermal annealing of fission tracks in apatite: 1. A qualitative description', *Chemical Geology: Isotope Geoscience section* **59**, 237 – 253. Calibration of the Phanerozoic Time Scale.
URL: *http://www.sciencedirect.com/science/article/pii/0168962286900746*

Green, P. F. (1986), 'On the thermo-tectonic evolution of Northern England: evidence from fission track analysis', *Geological Magazine* **123**(5), 493–506.

Guenthner, W. R., Reiners, P. W., Ketcham, R. A., Nasdala, L. & Giester, G. (2013), 'Helium diffusion in natural zircon: Radiation damage, anisotropy, and the interpretation

of zircon (U-Th)/He thermochronology', *American Journal of Science* **313**(3), 145–198.
URL: *http://www.ajsonline.org/content/313/3/145.abstract*

Hall, R. (2012), 'Late Jurassic–Cenozoic reconstructions of the Indonesian region and the Indian Ocean', *Tectonophysics* **570–571**, 1–41.
URL: *http://www.sciencedirect.com/science/article/pii/S0040195112002533*

Hamburger, M. W., Sarewitz, D. R., Pavlis, T. L. & Popandopulo, G. A. (1992), 'Structural and seismic evidence for intracontinental subduction in the Peter the First Range, Central Asia', *GSA Bulletin* **104**(4), 397.
URL: *http://dx.doi.org/10.1130/0016-7606(1992)104<0397:SASEFI>2.3.CO;2*

Haq, B. U., Hardenbol, J. & Vail, P. R. (1987), 'Chronology of Fluctuating Sea Levels Since the Triassic', *Science* **235**(4793), 1156–1167.
URL: *http://science.sciencemag.org/content/235/4793/1156*

Hasebe, N., Barbarand, J., Jarvis, K., Carter, A. & Hurford, A. J. (2004), 'Apatite fission-track chronometry using laser ablation ICP-MS', *Chemical Geology* **207**(3), 135 – 145.
URL: *http://www.sciencedirect.com/science/article/pii/S0009254104000427*

Hasebe, N., Carter, A., Hurford, A. J. & Arai, S. (2009), 'The effect of chemical etching on LA-ICP-MS analysis in determining uranium concentration for fission-track chronometry', *Geological Society, London, Special Publications* **324**(1), 37–46.
URL: *http://sp.lyellcollection.org/content/324/1/37*

Hegner, E., Klemd, R., Kröner, A., Corsini, M., Alexeiev, D. V., Iaccheri, L. M., Zack, T., Dulski, P., Xia, X. & Windley, B. F. (2010), 'Mineral ages and P-T conditions of Late Paleozoic high-pressure eclogite and provenance of mélange sediments from Atbashi in the south Tianshan orogen of Kyrgyzstan', *American Journal of Science* **310**(9), 916–950.
URL: *http://www.ajsonline.org/content/310/9/916.abstract*

Hendriks, B. & Redfield, T. (2005), 'Apatite fission track and (U-Th)/He data from Fennoscandia: An example of underestimation of fission track annealing in apatite', *Earth and Planetary Science Letters* **236**(1), 443 – 458.
URL: *http://www.sciencedirect.com/science/article/pii/S0012821X05003420*

Hendrix, M. S. (2000), 'Evolution of Mesozoic Sandstone Compositions, Southern Junggar, Northern Tarim, and Western Turpan Basins, Northwest China: A Detrital Record of the Ancestral Tian Shan', *Journal of Sedimentary Research* **70**(3), 520.
URL: *http://dx.doi.org/10.1306/2DC40924-0E47-11D7-8643000102C1865D*

Hendrix, M. S., Graham, S. A., Carroll, A. R., Sobel, E. R., McKnight, C. L., Schulein, B. J. & Wang, Z. (1992), 'Sedimentary record and climatic implications of recurrent deformation in the Tian Shan: Evidence from Mesozoic strata of the north Tarim, south Junggar, and Turpan basins, northwest China', *GSA Bulletin* **104**(1), 53.
URL: *http://dx.doi.org/10.1130/0016-7606(1992)104<0053:SRACIO>2.3.CO;2*

Hetzel, R. & Glodny, J. (2002), 'A crustal-scale, orogen-parallel strike-slip fault in the Middle Urals: age, magnitude of displacement, and geodynamic significance', *International Journal of Earth Sciences* **91**(2), 231–245.
URL: *https://doi.org/10.1007/s005310100208*

Huang, B., Piper, J. D., Wang, Y., He, H. & Zhu, R. (2005), 'Paleomagnetic and geochronological constraints on the post-collisional northward convergence of the southwest Tian Shan, NW China', *Tectonophysics* **409**(1), 107 – 124.
URL: *http://www.sciencedirect.com/science/article/pii/S0040195105003951*

Hurford, A. J. & Green, P. F. (1982), 'A users' guide to fission track dating calibration', *Earth and Planetary Science Letters* **59**(2), 343 – 354.
URL: *http://www.sciencedirect.com/science/article/pii/0012821X82901364*

Hurford, A. J. & Green, P. F. (1983), 'The zeta age calibration of fission-track dating', *Chemical Geology* **41**, 285 – 317.
URL: *http://www.sciencedirect.com/science/article/pii/S0009254183800266*

Jepson, G., Glorie, S., Konopelko, D., Gillespie, J., Danišík, M., Evans, N. J., Mamadjanov, Y. & Collins, A. S. (2018a), 'Thermochronological insights into the structural contact between the Tian Shan and Pamirs, Tajikistan', *Terra Nova* **30**(2), 95–104.
URL: *https://onlinelibrary.wiley.com/doi/abs/10.1111/ter.12313*

Jepson, G., Glorie, S., Konopelko, D., Gillespie, J., Danišík, M., Mirkamalov, R., Mamadjanov, Y. & Collins, A. S. (2018c), 'Low-Temperature Thermochronology of the Chatkal-Kurama Terrane (Uzbekistan-Tajikistan): Insights Into the Meso-Cenozoic Thermal History of the Western Tian Shan', *Tectonics* **0**(0).
URL: *https://agupubs.onlinelibrary.wiley.com/doi/abs/10.1029/2017TC004878*

Jepson, G., Glorie, S., Konopelko, D., Mirkamalov, R., Danišík, M. & Collins, A. S. (2018b), 'The low-temperature thermo-tectonic evolution of the western Tian Shan, Uzbekistan', *Gondwana Research* **64**, 122 – 136.
URL: *http://www.sciencedirect.com/science/article/pii/S1342937X18302107*

Jolivet, M. (2017), 'Mesozoic tectonic and topographic evolution of central asia and tibet: a preliminary synthesis', *Geological Society, London, Special Publications* **427**(1), 19–55.
URL: *http://sp.lyellcollection.org/content/427/1/19*

Jolivet, M., Dominguez, S., Charreau, J., Chen, Y., Li, Y. & Wang, Q. (2010), 'Mesozoic and Cenozoic tectonic history of the central Chinese Tian Shan: Reactivated tectonic structures and active deformation', *Tectonics* **29**(6). TC6019.
URL: *http://dx.doi.org/10.1029/2010TC002712*

Jolivet, M., Heilbronn, G., Robin, C., Barrier, L., Bourquin, S., Guo, Z., Jia, Y., Guerit, L., Yang, W. & Fu, B. (2013), 'Reconstructing the Late Palaeozoic - Mesozoic topographic evolution of the Chinese Tian Shan: available data and remaining uncertainties', *Advances in Geosciences* **37**, 7–18.
URL: *https://hal-insu.archives-ouvertes.fr/insu-00920043*

Jolivet, M., Ritz, J.-F., Vassallo, R., Larroque, C., Braucher, R., Todbileg, M., Chauvet, A., Sue, C., Arnaud, N., De Vicente, R., Arzhanikova, A. & Arzhanikov, S. (2007), 'Mongolian summits: An uplifted, flat, old but still preserved erosion surface', *Geology* **35**(10), 871.
URL: *http://dx.doi.org/10.1130/G23758A.1*

Kapp, P., DeCelles, P. G., Gehrels, G. E., Heizler, M. & Ding, L. (2007), 'Geological records of the Lhasa-Qiangtang and Indo-Asian collisions in the Nima area of central Tibet', *GSA*

Bulletin **119**(7-8), 917.
URL: *http://dx.doi.org/10.1130/B26033.1*

Kempe, U., Graupner, T., Seltmann, R., de Boorder, H., Dolgopolova, A. & van Emmichoven, M. Z. (2016), 'The Muruntau gold deposit (Uzbekistan) – A unique ancient hydrothermal system in the southern Tien Shan', *Geoscience Frontiers* **7**(3), 495 – 528. Special Issue: Giant Mineral Deposits.
URL: *http://www.sciencedirect.com/science/article/pii/S1674987115001139*

Ketcham, R. A., Carter, A., Donelick, R. A., Barbarand, J. & Hurford, A. J. (2007), 'Improved modeling of fission-track annealing in apatite', *American Mineralogist* **92**(5-6), 799.
URL: *http://dx.doi.org/10.2138/am.2007.2281*

Khudoley, A. K. (1993), 'Structural and strain analyses of the middle part of the talassian alatau ridge (middle asia, kirgizstan)', *Journal of Structural Geology* **15**(6), 693 – 706.
URL: *http://www.sciencedirect.com/science/article/pii/019181419390056G*

Käßner, A., Ratschbacher, L., Jonckheere, R., Enkelmann, E., Khan, J., Sonntag, B., Gloaguen, R., Gadoev, M. & Oimahmadov, I. (2017b), 'Cenozoic intracontinental deformation and exhumation at the northwestern tip of the India-Asia collision—southwestern Tian Shan, Tajikistan, and Kyrgyzstan', *Tectonics* **35**(9), 2171–2194.
URL: *https://agupubs.onlinelibrary.wiley.com/doi/abs/10.1002/2015TC003897*

Käßner, A., Ratschbacher, L., Pfänder, J. A., Hacker, B. R., Zack, G., Sonntag, B.-L., Khan, J., Stanek, K. P., Gadoev, M. & Oimahmadov, I. (2017a), 'Proterozoic–Mesozoic history of the Central Asian orogenic belt in the Tajik and southwestern Kyrgyz Tian Shan: U-Pb, $^{40}Ar/^{39}Ar$, and fission-track geochronology and geochemistry of granitoids', *GSA Bulletin* **129**(3-4), 281.
URL: *http://dx.doi.org/10.1130/B31466.1*

Konopelko, D., Biske, G., Seltmann, R., Kiseleva, M., Matukov, D. & Sergeev, S. (2008), 'Deciphering Caledonian events: Timing and geochemistry of the Caledonian magmatic arc in the Kyrgyz Tien Shan', *Journal of Asian Earth Sciences* **32**(2), 131 – 141. Geodynamics

and Metallogeny of the Altaid Orogen.

URL: *http://www.sciencedirect.com/science/article/pii/S1367912007001721*

Konopelko, D., Klemd, R., Mamadjanov, Y., Hegner, E., Knorsch, M., Fidaev, D., Kern, M. & Sergeev, S. (2015), 'Permian age of orogenic thickening and crustal melting in the Garm Block, South Tien Shan, Tajikistan', *Journal of Asian Earth Sciences* **113**, 711 – 727. The Making of Asia.

URL: *http://www.sciencedirect.com/science/article/pii/S1367912015300845*

Konopelko, D., Klemd, R., Petrov, S., Apayarov, F., Nazaraliev, B., Vokueva, O., Scherstén, A. & Sergeev, S. (2017b), 'Precambrian gold mineralization at Djamgyr in the Kyrgyz Tien Shan: Tectonic and metallogenic implications', *Ore Geology Reviews* **86**, 537 – 547.

URL: *http://www.sciencedirect.com/science/article/pii/S0169136816306746*

Konopelko, D. L., Biske, Y. S., Kullerud, K., Seltmann, R. & Divaev, F. (2011), 'The Koshrabad granite massif in Uzbekistan: petrogenesis, metallogeny, and geodynamic setting', *Russian Geology and Geophysics* **52**(12), 1563–1573. Geodynamics, Tectonics, and Metallogeny of Orogenic Belts.

URL: *http://www.sciencedirect.com/science/article/pii/S1068797111002549*

Konopelko, D., Seltmann, R., Apayarov, F., Belousova, E., Izokh, A. & Lepekhina, E. (2013), 'U–Pb–Hf zircon study of two mylonitic granite complexes in the Talas-Fergana fault zone, Kyrgyzstan, and Ar–Ar age of deformations along the fault', *Journal of Asian Earth Sciences* **73**, 334 – 346.

URL: *http://www.sciencedirect.com/science/article/pii/S1367912013002733*

Konopelko, D., Seltmann, R., Mamadjanov, Y., Romer, R., Rojas-Agramonte, Y., Jeffries, T., Fidaev, D. & Niyozov, A. (2017a), 'A geotraverse across two paleo-subduction zones in Tien Shan, Tajikistan', *Gondwana Research* **47**, 110 – 130. Continental construction in Central Asia and actualistic comparisons with western Pacific.

URL: *http://www.sciencedirect.com/science/article/pii/S1342937X16302878*

Konopelko, D., Wilde, S., Seltmann, R., Romer, R. & Biske, Y. S. (2018), 'Early Permian intrusions of the Alai range: Understanding tectonic settings of Hercynian post-collisional

magmatism in the South Tien Shan, Kyrgyzstan', *Lithos* **302–303**, 405–420.
URL: *https://doi.org/10.1016/j.lithos.2018.01.024*

Kröner, A., Windley, B., Badarch, G., Tomurtogoo, O., Hegner, E., Jahn, B., Gruschka, S., Khain, E., Demoux, A. & Wingate, M. (2007), 'Accretionary growth and crust formation in the Central Asian Orogenic Belt and comparison with the Arabian-Nubian shield', *Memoirs-Geological Society of America* **200**, 181.

Laurent-Charvet, S., Charvet, J., Monié, P. & Shu, L. (2003), 'Late Paleozoic strike-slip shear zones in eastern central Asia (NW China): New structural and geochronological data', *Tectonics* **22**(2). 1009.
URL: *http://dx.doi.org/10.1029/2001TC901047*

Li, S., Chung, S.-L., Wilde, S. A., Wang, T., Xiao, W.-J. & Guo, Q.-Q. (2016), 'Linking magmatism with collision in an accretionary orogen', *Scientific reports* **6**, 25751.

Li, Z., Song, W., Peng, S., Wang, D. & Zhang, Z. (2004), 'Mesozoic–Cenozoic tectonic relationships between the Kuqa subbasin and Tian Shan, northwest China: constraints from depositional records', *Sedimentary Geology* **172**(3), 223 – 249.
URL: *http://www.sciencedirect.com/science/article/pii/S0037073804003021*

Macaulay, E. A., Sobel, E. R., Mikolaichuk, A., Kohn, B. & Stuart, F. M. (2014), 'Cenozoic deformation and exhumation history of the Central Kyrgyz Tien Shan', *Tectonics* **33**(2), 135–165.
URL: *https://agupubs.onlinelibrary.wiley.com/doi/abs/10.1002/2013TC003376*

Macaulay, E. A., Sobel, E. R., Mikolaichuk, A., Landgraf, A., Kohn, B. & Stuart, F. (2013), 'Thermochronologic insight into late Cenozoic deformation in the basement-cored Terskey Range, Kyrgyz Tien Shan', *Tectonics* **32**(3), 487–500.
URL: *https://agupubs.onlinelibrary.wiley.com/doi/abs/10.1002/tect.20040*

McCann, T. (2016a), 'The Cretaceous of the South Kyzylkum and Nuratau Region, Western Tien Shan, Central Uzbekistan', *Geological Society, London, Special Publications* **427**(1), 439–489.
URL: *http://sp.lyellcollection.org/content/427/1/439*

McCann, T. (2016b), 'The Jurassic of the Western Tien Shan: the Central Kyzylkum Region, Uzbekistan', *Geological Society, London, Special Publications* **427**(1), 411–437.
URL: *http://sp.lyellcollection.org/content/427/1/411*

McDowell, F. W., McIntosh, W. C. & Farley, K. A. (2005), 'A precise 40Ar–39Ar reference age for the Durango apatite (U–Th)/He and fission-track dating standard', *Chemical Geology* **214**(3), 249 – 263.
URL: *http://www.sciencedirect.com/science/article/pii/S0009254104004218*

McLaren, S., James, D. W., Mike, S. & Ian, M. (2002), 'Thermochronology of high heat-producing crust at Mount Painter, South Australia: Implications for tectonic reactivation of continental interiors', *Tectonics* **21**(4), 2–1–2–18.
URL: *https://agupubs.onlinelibrary.wiley.com/doi/abs/10.1029/2000TC001275*

Mohadjer, S., Ehlers, T. A., Bendick, R., Stübner, K. & Strube, T. (2016), 'A Quaternary fault database for central Asia', *Natural Hazards and Earth System Sciences* **16**(2), 529–542.
URL: *https://www.nat-hazards-earth-syst-sci.net/16/529/2016/*

Molnar, P. & England, P. (1990), 'Late Cenozoic uplift of mountain ranges and global climate change: chicken or egg?', *Nature* **346**(6279), 29–34.

Molnar, P. & Stock, J. M. (2009), 'Slowing of india's convergence with eurasia since 20 ma and its implications for tibetan mantle dynamics', *Tectonics* **28**(3).
URL: *https://agupubs.onlinelibrary.wiley.com/doi/abs/10.1029/2008TC002271*

Molnar, P. & Tapponnier, P. (1975), 'Cenozoic tectonics of Asia: effects of a continental collision', *Science* **189**(4201), 419–426.

Molnar, P. & Tapponnier, P. (1977), 'Relation of the tectonics of eastern China to the India-Eurasia collision: Application of slip-line field theory to large-scale continental tectonics', *Geology* **5**(4), 212.
URL: *http://dx.doi.org/10.1130/0091-7613(1977)5<212:ROTTOE>2.0.CO;2*

Nachtergaele, S., De Pelsmaeker, E., Glorie, S., Zhimulev, F., Jolivet, M., Danišík, M., Buslov, M. M. & De Grave, J. (2017), 'Meso-Cenozoic tectonic evolution of the Talas-

Fergana region of the Kyrgyz Tien Shan revealed by low-temperature basement and detrital thermochronology', *Geoscience Frontiers* .
URL: *http://www.sciencedirect.com/science/article/pii/S1674987117302013*

Najman, Y., Appel, E., Boudagher-Fadel, M., Bown, P., Carter, A., Garzanti, E., Godin, L., Han, J., Liebke, U., Oliver, G., Parrish, R. & Vezzoli, G. (2010), 'Timing of India-Asia collision: Geological, biostratigraphic, and palaeomagnetic constraints', *Journal of Geophysical Research: Solid Earth* **115**(B12). B12416.
URL: *http://dx.doi.org/10.1029/2010JB007673*

Nissen, E., Walker, R. T., Bayasgalan, A., Carter, A., Fattahi, M., Molor, E., Schnabel, C., West, A. J. & Xu, S. (2009), 'The late Quaternary slip-rate of the Har-Us-Nuur fault (Mongolian Altai) from cosmogenic 10Be and luminescence dating', *Earth and Planetary Science Letters* **286**(3), 467 – 478.
URL: *http://www.sciencedirect.com/science/article/pii/S0012821X09004154*

Otto, S. C. (1997), 'Mesozoic-Cenozoic history of deformation and petroleum systems in sedimentary basins of Central Asia; implications of collisions on the Eurasian margin', *Petroleum Geoscience* **3**(4), 327–341.
URL: *http://pg.lyellcollection.org/content/3/4/327*

Paton, C., Hellstrom, J., Paul, B., Woodhead, J. & Hergt, J. (2011), 'Iolite: Freeware for the visualisation and processing of mass spectrometric data', *Journal of Analytical Atomic Spectrometry* **26**(12), 2508–2518.

Pearce, N. J., Perkins, W. T., Westgate, J. A., Gorton, M. P., Jackson, S. E., Neal, C. R. & Chenery, S. P. (1997), 'A Compilation of New and Published Major and Trace Element Data for NIST SRM 610 and NIST SRM 612 Glass Reference Materials', *Geostandards Newsletter* **21**(1), 115–144.
URL: *https://onlinelibrary.wiley.com/doi/abs/10.1111/j.1751-908X.1997.tb00538.x*

Peltzer, G. & Tapponnier, P. (1988), 'Formation and evolution of strike-slip faults, rifts, and basins during the India-Asia Collision: An experimental approach', *Journal of Geophysical*

Research: Solid Earth **93**(B12), 15085–15117.

URL: *https://agupubs.onlinelibrary.wiley.com/doi/abs/10.1029/JB093iB12p15085*

Ratschbacher, L., Hacker, B. R., Calvert, A., Webb, L. E., Grimmer, J. C., McWilliams, M. O., Ireland, T., Dong, S. & Hu, J. (2003), 'Tectonics of the Qinling (Central China): tectonostratigraphy, geochronology, and deformation history', *Tectonophysics* **366**(1), 1 – 53.

URL: *http://www.sciencedirect.com/science/article/pii/S0040195103000532*

Reiners, P. W. (2005), 'Zircon (u-th)/he thermochronometry', *Reviews in Mineralogy and Geochemistry* **58**(1), 151.

URL: *http://dx.doi.org/10.2138/rmg.2005.58.6*

Reiners, P. W., Farley, K. A. & Hickes, H. J. (2002), 'He diffusion and (U–Th)/He thermochronometry of zircon: initial results from Fish Canyon Tuff and Gold Butte', *Tectonophysics* **349**(1), 297 – 308. Low Temperature Thermochronology: From Tectonics to Landscape Evolution.

URL: *http://www.sciencedirect.com/science/article/pii/S0040195102000586*

Reinhard, C. T., Planavsky, N. J., Gill, B. C., Ozaki, K., Robbins, L. J., Lyons, T. W., Fischer, W. W., Wang, C., Cole, D. B. & Konhauser, K. O. (2017), 'Evolution of the global phosphorus cycle', *Nature* **541**(7637), 386.

Ren, R., Han, B.-F., Ji, J.-Q., Zhang, L., Xu, Z. & Su, L. (2011), 'U–Pb age of detrital zircons from the Tekes River, Xinjiang, China, and implications for tectonomagmatic evolution of the South Tian Shan Orogen', *Gondwana Research* **19**(2), 460–470.

Robinson, A. C. (2015), 'Mesozoic tectonics of the Gondwanan terranes of the Pamir plateau', *Journal of Asian Earth Sciences* **102**, 170 – 179. Special Issue on CIMMERIAN TERRANES.

URL: *http://www.sciencedirect.com/science/article/pii/S1367912014004258*

Robinson, A. C., Yin, A., Manning, C. E., Harrison, T. M., Zhang, S.-H. & Wang, X.-F. (2004), 'Tectonic evolution of the northeastern Pamir: Constraints from the northern portion of the Cenozoic Kongur Shan extensional system, western China', *GSA Bulletin*

116(7-8), 953.

URL: *http://dx.doi.org/10.1130/B25375.1*

Roger, F., Jolivet, M. & Malavieille, J. (2010), 'The tectonic evolution of the Songpan-Garzê (North Tibet) and adjacent areas from Proterozoic to Present: A synthesis', *Journal of Asian Earth Sciences* **39**(4), 254 – 269.

URL: *http://www.sciencedirect.com/science/article/pii/S1367912010000866*

Rolland, Y., Alexeiev, D. V., Kröner, A., Corsini, M., Loury, C. & Monié, P. (2013), 'Late Palaeozoic to Mesozoic kinematic history of the Talas–Ferghana strike-slip fault (Kyrgyz West Tianshan) as revealed by 40Ar/39Ar dating of syn-kinematic white mica', *Journal of Asian Earth Sciences* **67-68**, 76 – 92.

URL: *http://www.sciencedirect.com/science/article/pii/S1367912013001132*

Rowley, D. B. (1996), 'Age of initiation of collision between India and Asia: A review of stratigraphic data', *Earth and Planetary Science Letters* **145**(1), 1 – 13.

URL: *http://www.sciencedirect.com/science/article/pii/S0012821X96002014*

Rutte, D., Ratschbacher, L., Khan, J., Stübner, K., Hacker, B. R., Stearns, M. A., Enkelmann, E., Jonckheere, R., Pfänder, J. A., Sperner, B. & Tichomirowa, M. (2017), 'Building the Pamir-Tibetan Plateau—Crustal stacking, extensional collapse, and lateral extrusion in the Central Pamir: 2. Timing and rates', *Tectonics* **36**(3), 385–419. 2016TC004294.

URL: *http://dx.doi.org/10.1002/2016TC004294*

Samygin, S. G. & Burtman, V. S. (2009), 'Tectonics of the Ural paleozoides in comparison with the Tien Shan', *Geotectonics* **43**(2), 133–151.

URL: *https://doi.org/10.1134/S0016852109020058*

Sébastien, L.-C., Charvet, J., Shu, L., Ma, R. & Lu, H. (2002), 'Palaeozoic late collisional strike-slip deformations in Tianshan and Altay, Eastern Xinjiang, NW China', *Terra Nova* **14**(4), 249–256.

URL: *https://onlinelibrary.wiley.com/doi/abs/10.1046/j.1365-3121.2002.00417.x*

Schoene, B. & Bowring, S. A. (2007), 'Determining accurate temperature–time paths from U–Pb thermochronology: An example from the Kaapvaal craton, southern Africa', *Geochim-*

ica et Cosmochimica Acta **71**(1), 165 – 185.
URL: *http://www.sciencedirect.com/science/article/pii/S0016703706020187*

Schurr, B., Lothar, R., Christian, S., Richard, G., Xiaohui, Y. & James, M. (2014), 'Seismotectonics of the Pamir', *Tectonics* **33**(8), 1501–1518.
URL: *https://agupubs.onlinelibrary.wiley.com/doi/abs/10.1002/2014TC003576*

Schwab, M., Lothar, R., Wolfgang, S., Michael, M., Vladislav, M., Valery, L., Fokun, C., Klaus, S., Bruce, N., Wolfgang, F. & L., W. J. (2004), 'Assembly of the Pamirs: Age and origin of magmatic belts from the southern Tien Shan to the southern Pamirs and their relation to Tibet', *Tectonics* **23**(4).
URL: *https://agupubs.onlinelibrary.wiley.com/doi/abs/10.1029/2003TC001583*

Searle, M. P. (1991), *Geology and tectonics of the Karakoram Mountains*, John Wiley & Sons Inc.

Seltmann, R., Konopelko, D., Biske, G., Divaev, F. & Sergeev, S. (2011), 'Hercynian post-collisional magmatism in the context of Paleozoic magmatic evolution of the Tien Shan orogenic belt', *Journal of Asian Earth Sciences* **42**(5), 821 – 838. Continental accretion and intra-continental deformation of the Central Asian Orogenic Belt.
URL: *http://www.sciencedirect.com/science/article/pii/S1367912010002646*

Seltmann, R. & Porter, T. M. (2005), 'The porphyry Cu–Au/Mo deposits of Central Eurasia: 1. Tectonic, geologic and metallogenic setting and significant deposits', *Super porphyry copper and gold deposits: a global perspective* **2**, 467–512.

Sengör, A. (1984), *The Cimmeride Orogenic System and the Tectonics of Eurasia*, number no. 195 *in* 'Geological Society of America Special Paper', Geological Society of America.
URL: *https://books.google.com.au/books?id=nOJYrgEACAAJ*

Şengör, A. M. C., Natal'In, B. A. & Burtman, V. S. (1993), 'Evolution of the Altaid tectonic collage and Palaeozoic crustal growth in Eurasia', *Nature* **364**(6435), 299.

Soares, C. J., Guedes, S., Hadler, J. C., Mertz-Kraus, R., Zack, T. & Iunes, P. J. (2014), 'Novel calibration for LA-ICP-MS-based fission-track thermochronology', *Physics and*

Chemistry of Minerals **41**(1), 65–73.
URL: *https://doi.org/10.1007/s00269-013-0624-2*

Sobel, E. R. (1999), 'Basin analysis of the jurassic–lower cretaceous southwest tarim basin, northwest china', *GSA Bulletin* **111**(5), 709.
URL: *http://dx.doi.org/10.1130/0016-7606(1999)111<0709:BAOTJL>2.3.CO;2*

Sobel, E. R. & Arnaud, N. (2000), 'Cretaceous–Paleogene basaltic rocks of the Tuyon basin, NW China and the Kyrgyz Tian Shan: the trace of a small plume', *Lithos* **50**(1), 191 – 215.
URL: *http://www.sciencedirect.com/science/article/pii/S0024493799000468*

Sobel, E. R., Chen, J. & Heermance, R. V. (2006), 'Late Oligocene–Early Miocene initiation of shortening in the Southwestern Chinese Tian Shan: Implications for Neogene shortening rate variations', *Earth and Planetary Science Letters* **247**(1), 70 – 81.
URL: *http://www.sciencedirect.com/science/article/pii/S0012821X06002834*

Sobel, E. R., Chen, J. & Heermance, R. V. (2006a), 'Late Oligocene–Early Miocene initiation of shortening in the Southwestern Chinese Tian Shan: Implications for Neogene shortening rate variations', *Earth and Planetary Science Letters* **247**(1), 70 – 81.
URL: *http://www.sciencedirect.com/science/article/pii/S0012821X06002834*

Sobel, E. R., Chen, J., Schoenbohm, L. M., Thiede, R., Stockli, D. F., Sudo, M. & Strecker, M. R. (2013), 'Oceanic-style subduction controls late Cenozoic deformation of the Northern Pamir orogen', *Earth and Planetary Science Letters* **363**, 204 – 218.
URL: *http://www.sciencedirect.com/science/article/pii/S0012821X12006954*

Sobel, E. R. & Dumitru, T. A. (1997), 'Thrusting and exhumation around the margins of the western Tarim basin during the India-Asia collision', *Journal of Geophysical Research: Solid Earth* **102**(B3), 5043–5063.
URL: *http://dx.doi.org/10.1029/96JB03267*

Sobel, E. R., Oskin, M., Burbank, D. & Mikolaichuk, A. (2006), 'Exhumation of basement-cored uplifts: Example of the Kyrgyz Range quantified with apatite fission track ther-

mochronology', *Tectonics* **25**(2). TC2008.
URL: *http://dx.doi.org/10.1029/2005TC001809*

Sobel, E. R. & Strecker, M. R. (2003), 'Uplift, exhumation and precipitation: tectonic and climatic control of Late Cenozoic landscape evolution in the northern Sierras Pampeanas, Argentina', *Basin Research* **15**(4), 431–451.
URL: *https://onlinelibrary.wiley.com/doi/abs/10.1046/j.1365-2117.2003.00214.x*

Song, D., Xiao, W., Collins, A. S., Glorie, S., Han, C. & Li, Y. (2018), 'Final Subduction Processes of the Paleo-Asian Ocean in the Alxa Tectonic Belt (NW China): Constraints From Field and Chronological Data of Permian Arc-Related Volcano-Sedimentary Rocks', *Tectonics* **0**(0).
URL: *https://agupubs.onlinelibrary.wiley.com/doi/abs/10.1029/2017TC004919*

Stacey, J. & Kramers, J. (1975), 'Approximation of terrestrial lead isotope evolution by a two-stage model', *Earth and Planetary Science Letters* **26**(2), 207 – 221.
URL: *http://www.sciencedirect.com/science/article/pii/0012821X75900886*

Stübner, K., Lothar, R., Daniel, R., Klaus, S., Vladislav, M., Maria, W. & Gloaguen, R. a. (2013), 'The giant Shakhdara migmatitic gneiss dome, Pamir, India-Asia collision zone: 1. Geometry and kinematics', *Tectonics* **32**(4), 948–979.
URL: *https://agupubs.onlinelibrary.wiley.com/doi/abs/10.1002/tect.20057*

Stockli, D. F., Surpless, B. E., Dumitru, T. A. & Farley, K. A. (2002), 'Thermochronological constraints on the timing and magnitude of Miocene and Pliocene extension in the central Wassuk Range, western Nevada', *Tectonics* **21**(4), 10–1–10–19.
URL: *https://agupubs.onlinelibrary.wiley.com/doi/abs/10.1029/2001TC001295*

Survey, U. G. (2012), 'Geological Map of Uzbekistan', *State Geological Information Centre* .

Tagami, T. (2005), 'Zircon Fission-Track Thermochronology and Applications to Fault Studies', *Reviews in Mineralogy and Geochemistry* **58**(1), 95.
URL: *http://dx.doi.org/10.2138/rmg.2005.58.4*

Tapponnier, P. & Molnar, P. (1979), 'Active faulting and cenozoic tectonics of the Tien Shan, Mongolia, and Baykal Regions', *Journal of Geophysical Research: Solid Earth*

84(B7), 3425–3459.
URL: *https://agupubs.onlinelibrary.wiley.com/doi/abs/10.1029/JB084iB07p03425*

Thiede, R. C., R., S. E., Jie, C., M., S. L., F., S. D., Masafumi, S. & R., S. M. (2013), 'Late Cenozoic extension and crustal doming in the India-Eurasia collision zone: New thermochronologic constraints from the NE Chinese Pamir', *Tectonics* **32**(3), 763–779.
URL: *https://agupubs.onlinelibrary.wiley.com/doi/abs/10.1002/tect.20050*

Thomson, S. N., Gehrels, G., Joaquin, R. & Robert, B. (2012), 'Routine low-damage apatite U-Pb dating using laser ablation–multicollector–ICPMS', *Geochemistry, Geophysics, Geosystems* **13**(2).
URL: *https://agupubs.onlinelibrary.wiley.com/doi/abs/10.1029/2011GC003928*

van Hinsbergen, D. J. J., Lippert, P. C., Dupont-Nivet, G., McQuarrie, N., Doubrovine, P. V., Spakman, W. & Torsvik, T. H. (2012), 'Greater india basin hypothesis and a two-stage cenozoic collision between india and asia', *Proceedings of the National Academy of Sciences* **109**(20), 7659–7664.
URL: *http://www.pnas.org/content/109/20/7659*

van Hinsbergen, D. J. J., Steinberger, B., Doubrovine, P. V. & Gassmöller, R. (2011), 'Acceleration and deceleration of India-Asia convergence since the Cretaceous: Roles of mantle plumes and continental collision', *Journal of Geophysical Research: Solid Earth* **116**(B6). B06101.
URL: *http://dx.doi.org/10.1029/2010JB008051*

Vermeesch, P. (2009), 'RadialPlotter: A Java application for fission track, luminescence and other radial plots', *Radiation Measurements* **44**(4), 409–410.

Vermeesch, P. (2017), 'Statistics for LA-ICP-MS based fission track dating', *Chemical Geology* **456**, 19 – 27.
URL: *http://www.sciencedirect.com/science/article/pii/S0009254117301158*

Vlasov, N., Dyakov, Y. A. & Cherev, E. (1991), 'Geological map of the tajik ssr and adjacent territories, 1: 500,000', *Vsesojuznoi Geological Institute Leningrad, Saint Petersburg* .

Voytenko, V. N. & Khudoley, A. K. (2012), 'Structural evolution of metamorphic rocks in the Talas Alatau, Tien Shan, Central Asia: Implication for early stages of the Talas-Ferghana Fault', *Comptes Rendus Geoscience* **344**(3), 138 – 148. Tectonophysics in Russia and France: A project initiated by Jacques Angelier / La tectonophsique en Russie et en France : Un projet initié par Jacques Angelier.
URL: *http://www.sciencedirect.com/science/article/pii/S1631071312000077*

Wagner, G. A. & Van den haute, P. (1992), 'Fission-track dating', *Kluwer Academic Publishers* p. 285.

Wagner, M., Altherr, R. & Haute, P. V. D. (1992), 'Apatite fission-track analysis of Kenyan basement rocks: constraints on the thermotectonic evolution of the Kenya dome. A reconnaissance study', *Tectonophysics* **204**(1), 93 – 110.
URL: *http://www.sciencedirect.com/science/article/pii/0040195192902728*

Wang, B., Cluzel, D., Shu, L., Faure, M., Charvet, J., Chen, Y., Meffre, S. & de Jong, K. (2009), 'Evolution of calc-alkaline to alkaline magmatism through Carboniferous convergence to Permian transcurrent tectonics, western Chinese Tianshan", journal="International Journal of Earth Sciences', **98**(6), 1275.
URL: *https://doi.org/10.1007/s00531-008-0408-y*

Windley, B. F., Alexeiev, D., Xiao, W., Kröner, A. & Badarch, G. (2007), 'Tectonic models for accretion of the Central Asian Orogenic Belt', *Journal of the Geological Society* **164**(1), 31.
URL: *http://dx.doi.org/10.1144/0016-76492006-022*

Windley, B. F., Allen, M. B., Zhang, C., Zhao, Z.-Y. & Wang, G.-R. (1990), 'Paleozoic accretion and Cenozoic redeformation of the Chinese Tien Shan Range, central Asia', *Geology* **18**(2), 128.
URL: *http://dx.doi.org/10.1130/0091-7613(1990)018<0128:PAACRO>2.3.CO;2*

Xiao, W., Han, F., Windley, B. F., Yuan, C., Zhou, H. & Li, J. (2003), 'Multiple Accretionary Orogenesis and Episodic Growth of Continents: Insights from the Western Kunlun Range,

Central Asia', *International Geology Review* **45**(4), 303–328.
URL: *https://doi.org/10.2747/0020-6814.45.4.303*

Xiao, W. J., Windley, B. F., Huang, B. C., Han, C. M., Yuan, C., Chen, H. L., Sun, M., Sun, S. & Li, J. L. (2009), 'End-Permian to mid-Triassic termination of the accretionary processes of the southern Altaids: implications for the geodynamic evolution, Phanerozoic continental growth, and metallogeny of Central Asia', *International Journal of Earth Sciences* **98**(6), 1189–1217.
URL: *https://doi.org/10.1007/s00531-008-0407-z*

Xiao, W., Li, S., Santosh, M. & ming Jahn, B. (2012), 'Orogenic belts in Central Asia: Correlations and connections', *Journal of Asian Earth Sciences* **49**, 1 – 6. Orogenic Belts in Central Asia: Correlations and connections.
URL: *http://www.sciencedirect.com/science/article/pii/S1367912012000752*

Xiao, W., Windley, B. F., Allen, M. B. & Han, C. (2013), 'Paleozoic multiple accretionary and collisional tectonics of the Chinese Tianshan orogenic collage', *Gondwana Research* **23**(4), 1316 – 1341.
URL: *http://www.sciencedirect.com/science/article/pii/S1342937X12000469*

Yang, W., Jolivet, M., Dupont-Nivet, G. & Guo, Z. (2014), 'Mesozoic–Cenozoic tectonic evolution of southwestern Tian Shan: Evidence from detrital zircon U/Pb and apatite fission track ages of the Ulugqat area, Northwest China', *Gondwana Research* **26**(3), 986 – 1008.
URL: *http://www.sciencedirect.com/science/article/pii/S1342937X13002712*

Yang, W., Jolivet, M., Dupont-Nivet, G., Guo, Z., Zhang, Z. & Wu, C. (2013), 'Source to sink relations between the tian shan and junggar basin (northwest china) from late palaeozoic to quaternary: evidence from detrital u-pb zircon geochronology', *Basin Research* **25**(2), 219–240.

Yin, A. & Harrison, T. M. (2000), 'Geologic Evolution of the Himalayan-Tibetan Orogen', *Annual Review of Earth and Planetary Sciences* **28**(1), 211–280.
URL: *https://doi.org/10.1146/annurev.earth.28.1.211*

Yuan, W., Carter, A., Dong, J., Bao, Z., An, Y. & Guo, Z. (2006), 'Mesozoic–Tertiary exhumation history of the Altai Mountains, northern Xinjiang, China: New constraints from apatite fission track data', *Tectonophysics* **412**(3), 183 – 193.
URL: *http://www.sciencedirect.com/science/article/pii/S004019510500449X*

Zahirovic, S., Matthews, K. J., Flament, N., Müller, R. D., Hill, K. C., Seton, M. & Gurnis, M. (2016), 'Tectonic evolution and deep mantle structure of the eastern Tethys since the latest Jurassic', *Earth-Science Reviews* **162**, 293–337.
URL: *http://www.sciencedirect.com/science/article/pii/S0012825216302872*

Zaun, P. & Wagner, G. (1985), 'Fission-track stability in zircons under geological conditions', *Nuclear Tracks and Radiation Measurements (1982)* **10**(3), 303 – 307.
URL: *http://www.sciencedirect.com/science/article/pii/0735245X8590119X*

Zeitler, P., Herczeg, A., McDougall, I. & Honda, M. (1987), 'U-Th-He dating of apatite: A potential thermochronometer', *Geochimica et Cosmochimica Acta* **51**(10), 2865 – 2868.
URL: *http://www.sciencedirect.com/science/article/pii/0016703787901645*

Zhiyong, Z., Wenbin, Z., Liangshu, S., Jinglin, W., Wei, Y., Bihai, Z. & Jinbao, S. (2011), 'Multi-stage exhumation of the NE Tarim Precambrian bedrock, NW China: constraints from apatite fission track thermochronology in the Kuluketage area', *Terra Nova* **23**(5), 324–332.

Zonenshain, L., Kuzmin, M., Natapov, L. & Page, B. (1990), *Central Asian Foldbelt, Western Part: Central Kazakhstan and Tien Shan*, American Geophysical Union (AGU), pp. 55–72.
URL: *https://agupubs.onlinelibrary.wiley.com/doi/abs/10.1029/GD021p0055*